Ecole Centrale de Lille

THÈSE

N° d'ordre : 28

pour obtenir le titre de
Docteur en Sciences de l'Ecole Centrale de Lille
Discipline : Mécanique

par

Jie LIN

Etude détaillée des structures cohérentes de la zone tampon de la turbulence de paroi à l'aide de données de PIV stéréoscopique

Doctorat délivré conjointement par l'Ecole Centrale de Lille
et l'Université de Sciences et Technologies de Lille

Soutenue le 03 Novembre 2006 devant le jury composé de:

Président		M. Gilmar Mompéan, Professeur,	USTL Polytech,	Lille
Rapporteurs	:	M. Jean Paul Bonnet, HDR, Directeur de Recherche,	LEA-CNRS,	Poitiers
		M. Jean Cousteix, HDR, Directeur du DMAE,	ONERA,	Toulouse
Examinateurs	:	M. Marc Michard, Professeur Associé,	INSA,	Lyon
		M. Laurent Jacquin, Professeur, Directeur du DAFE,	ONERA,	Meudon
Directeur de thèse	:	M. Michel Stanislas, Professeur,	Ecole Centrale,	Lille
Invités	:	M. Jean Marc Foucaut, Maître de Conférence,	Ecole Centrale,	Lille
		M. Jean Philippe Laval, Chargé de recherche,	LML-CNRS,	Lille

L'imagination est plus
importante que le savoir.
A. Einstein

Remerciements

Ce travail a été réalisé au sein du Laboratoire Mécanique de Lille et de l'Ecole Centrale de Lille. C'est le moment d'exprimer mes remerciements, simples mais de tout coeur.

Je souhaite tout d'abord remercier mon directeur de thèse Monsieur Michel STANISLAS, pour m'avoir encadré lors de ce travail avec énormément d'enthousiasme et beaucoup de patience. J'ai bénéficié de ses connaissances et sa rigueur scientifique tout au long de mes recherches.

J'aimerais également exprimer toute ma gratitude à Monsieur Jean-Marc FOUCAUT et Monsieur Jean-Philippe LAVAL, qui sont devenu, au cours de ces quatre années, bien plus que de simples co-encadrants. Outre les connaissances qu'il a pu me transmettre, je garderais cette volonté d'une démarche scientifique menée pas à pas.

Messieurs Jean Paul BONNET et Monsieur Jean COUSTEIX ont accepté la tâche ardue d'être rapporteurs de ce travail. Je les en remercie sincèrement. Je remercie également Monsieur Gilmar MOMPEAN de m'avoir fait l'honneur de présider mon jury. Qu'il trouve ici l'expression de toute ma gratitude. Je remercie tout autant Monsieur Marc MICHARD et Monsieur Laurent JACQUIN pour avoir pris part au jury en tant qu'examinateur.

Mes remerciements vont également à Monsieur Johan CARLIER et Madame Patricia CATHALIFAUD pour l'intérêt qu'ils ont porté à ce travail et dont les remarques et les suggestions m'ont permis d'améliorer mes connaissance sur le sujet.

De nombreuses personnes ont participé au bon déroulement de ces travaux. J'exprime toute ma gratitude à mes collègues et amis pour leurs encouragements et leurs attentions lors de la réalisation de ce travail. Les pauses à la cafétéria que nous avons partagées ont ainsi contribuées à compenser le stress qui s'accentuait de jour en jour.

Mes remerciements s'adressent à Monsieur Guy CAIGNAERT et Monsieur Isam SHAHROUR, directeurs du Laboratoire Mécanique de Lille, qui m'ont accueilli au sein du laboratoire.

J'adresse également tous mes remerciements à l'ensemble du personnel de l'Ecole Centrale de Lille et du Laboratoire de Mécanique de Lille pour leur soutien moral et matériel qui m'a permis de mener à bien ce travail.

Mes parents et ma soeur m'ont toujours soutenu dans mes projets. La confiance qu'ils m'ont accordée m'a poussé à faire constamment de mon mieux pour qu'ils puissent en être fiers. Je leur doit beaucoup plus que je ne peux exprimer dans ces quelques lignes.

Enfin, parce que cette période de doute et de stress n'est pas toujours facile au quotidien pour l'entourage, j'aimerais remercier, mon amie Yuan ZHOU, par son soutien constant et ses encouragements, qui m'ont rendue tellement plus facile à vivre.

Résumé détaillé

Une étude à base de PIV Stéréoscopique dans une couche limite turbulente a été réalisée pour caractériser les structures cohérentes et trouver des relations spatiales entre elles. Cette étude est présentée en 8 chapitres.

Chapitre 1 et 2 : Problématique et objectifs

L'étude de la couche limite turbulente est importante pour l'industrie. Par exemple en aéronautique ou dans l'automobile elle intervient lorsque l'on cherche à limiter le coût à dépenser pour vaincre la traînée. D'un point de vue plus général, on s'intéresse à l'étude de la couche limite turbulente de plaque plane et plus particulièrement de la zone proche de la paroi. La zone tampon est une région qui joue un rôle très important dans le processus de génération de la couche limite turbulente. Cette région contient des structures cohérentes. Ceci a déjà été prouvé par de nombreux auteurs. Les structures cohérentes principales sont les tourbillons, les 'streaks', les 'ejections' et les 'sweeps'.

Theodorsen (1952) a montré que la déformation de vorticité transversale peut créer des tourbillons en fer à cheval ou en épingle à cheveux (nommés 'harpins'). Les 'streaks' sont des régions étroites d'écoulement lent ou rapide. Elles sont allongées dans le sens de l'écoulement. Les 'ejections' sont des régions d'écoulement lent qui s'éloigne de la paroi alors que les 'sweeps' sont des régions d'écoulement rapide qui se dirige vers la paroi. Depuis plus de 50 ans, les structures cohérentes et l'organisation de ces différentes structures cohérentes ont été étudiées par de nombreux auteurs. Mais il reste de nombreuses questions en suspens. Par exemple, quel est le mécanisme de formation de chaque structure ? Quelles relations et interactions existent-ils entre les différentes structures cohérentes ? Dans cette étude, nous allons essayer de répondre à ces questions essentielles.

Le premier objectif de cette étude est d'utiliser des données de PIV stéréoscopique pour caractériser les structures cohérentes. Ceci passe par la détection, l'identification et la quantification de ces structures. Cette étude doit mener à la proposition d'un modèle d'organisation général.

Chapitre 3 : Installation expérimentale et traitement de la PIV Stéréoscopique

Installation expérimentale

Le Laboratoire de Mécanique de Lille possède une soufflerie de grande dimension dont la couche limite peut atteindre une épaisseur de 30 cm pour un nombre de Reynolds Re_θ de 7800. Dans cet écoulement, une base de données a été obtenue expérimentalement à l'aide de la PIV Stéréoscopique qui donne accès aux trois composantes de la vitesse dans un plan. La base de données comprend dix plans parallèles à la paroi situés de 14.5 à 48 unités de paroi. La résolution spatiale est de l'ordre de 5 unités de paroi. La vitesse infinie U est de l'ordre de 3 m/s et la vitesse de frottement u_τ est de l'ordre de 0.12 m/s. Ainsi,

une unité de paroi ($\Delta y^+ = 1$) représente 0,125 mm. Chaque plan contient 500 champs de vitesse de manière à pouvoir faire des statistiques sur les grandeurs étudiées. La taille des champs est de 65*40 mm^2 ($\approx 530^+ * 300^+$)

Traitement de la PIV Stéréoscopique

Pour obtenir les champs de vitesse instantanée, on doit choisir une méthode d′analyse des images de SPIV. Dans la littérature, différentes méthodes sont proposées. Parmis ces méthodes, le ′Vector warping′, l′′Image mapping′ et la méthode de Soloff sont les méthodes les plus courantes. Les méthodes de ′Vector warping′ et de Soloff consistent à analyser les images avant de projeter les champs et de reconstruire. La méthode d′′Image mapping′ consiste à analyser entre la projection des images et la reconstruction. La méthode de soloff combine la reconstruction et la projection. De plus, pour chaque méthode, d′autres améliorations (méthode de ′shift′, méthode d′interpolation...) pour estimer. le champ de vitesse 2D3C peuvent être apportées et sont ici explorées afin d′optimiser les critères suivent :

- Précision
- Influence de shift sub-pixel
- densité spectrale de puissance
- Densité de probabilité
- Temps CPU

  ...

La méthode de Soloff à 3 plans de calibration avec ′shift′ entier est finalement choisie. La résolution spatiale est de 12 pixels ce qui fait environ 5 unités de paroi et la fenêtre d′interrogation finale est de 32*32 pixels^2. Ce qui donne un chevauchement de 62.5%.

Chapitre 4 : Analyse statistique des champs de vitesse

Après avoir appliqué la méthode choisie au chapitre précèdent, les champs de vitesse instantanés sont obtenus. A partir de ces champs on a calculé les caractéristiques statistiques suivantes de l′écoulement qui sont :

- Vitesse longitudinale moyenne,
- Contraintes de Reynolds,
- Densité spectrale de puissance,
- Densité de probabilité,
- Dissymétrie et aplatissement,
- Angle de la vitesse

Les résultats sont en bon accord avec la littérature. Il y a cependant des différences avec les résultats obtenus par le fil chaud, probablement à cause du gradient de vitesse qui existe près de la paroi à l′échelle des sondes à fils croisés et de l′obstruction du porte sonde.

Chapitre 5 : Corrélation spatiale double des vitesses

Dans ce chapitre, les corrélations spatiales doubles des vitesses à une dimension et à deux dimensions ont été calculées et analysées en détail. Les corrélations calculées sont :

- Auto corrélation de vitesse longitudinale
- Auto corrélation de vitesse transversale
- Auto corrélation de vitesse normale
- Corrélation croisée de vitesse longitudinale et transversale
- Corrélation croisée de vitesse longitudinale et normale
- Corrélation croisée de vitesse transversale et normale

Cette analyse met en évidence la présence des structures cohérentes, streaks, ejections, sweeps et tourbillons longitudinaux. De plus, elle permet d′obtenir des informations globales sur la structuration moyenne de l′écoulement et de disposer d′ordre de grandeur de leurs échelles.

Chapitre 6 : Détection et caractérisation des structures cohérentes

Afin de quantifier les dimensions des structures cohérentes, celle-ci sont détectées a partir de champs de vitesse instantanées puis une analyse statistique est réalisée. La procédure de détection des structures est réalisée en quatre étapes. Dans la première étape, une fonction de détection est choisie pour chaque type de structure. Cette fonction est définie à l′aide des propriétés des structures cohérentes. Dans cette étude, cette fonction dépend des coordonnées x, y, z. Dans une deuxième étape, on applique un seuillage à cette fonction pour obtenir une image binaire. Puis, dans la troisième étape, un filtrage à base de morphologie mathématique est appliqué pour améliorer les fonctions indicatrices. Dans la dernière étape, un nettoyage est utilisé pour rejeter les objets dégénérés. Dans cette étape, on prend la surface comme critère de validité. Les images finales des structures cohérentes instantanées seront obtenues après nettoyage. La Fig. 1 montre un exemple de détection des ′low speed streaks′. Avec cette méthode de détection, on obtient des images instantanées de structures cohérentes pour les ′streaks′, les ′ejections′ et les ′sweeps′.

Dans cette étude, le plan de mesure comme l′axe des tourbillons longitudinaux sont parallèles à la paroi. Les tourbillons longitudinaux. Ceci exclu toutes les méthodes de détection classique basées sur les gradients comme la vorticité. Ainsi la méthode présentée est une alternative nouvelle de détection de structure dans la cas où l′axe des tournillons se trouve dans le plan de mesure. Celle-ci est développée pour deux types de tourbillons longitudinaux : les tourbillons individuels et les tourbillons contrarotatifs (Fig. 2). On va prendre le tourbillon individuel comme exemple. La Fig. 2 est basée sur le profil de fluctuation de vitesse normale de ce tourbillon dans la direction transversale. Dans le plan de coupe ABCD, on peut trouver des régions avec de grandes fluctuations de vitesse (VF) et des régions avec de grands gradients de vitesse (GO). Ces régions sont dans un ordre bien précis. La détection d′un tourbillon est basé sur la combinaison de ces différentes

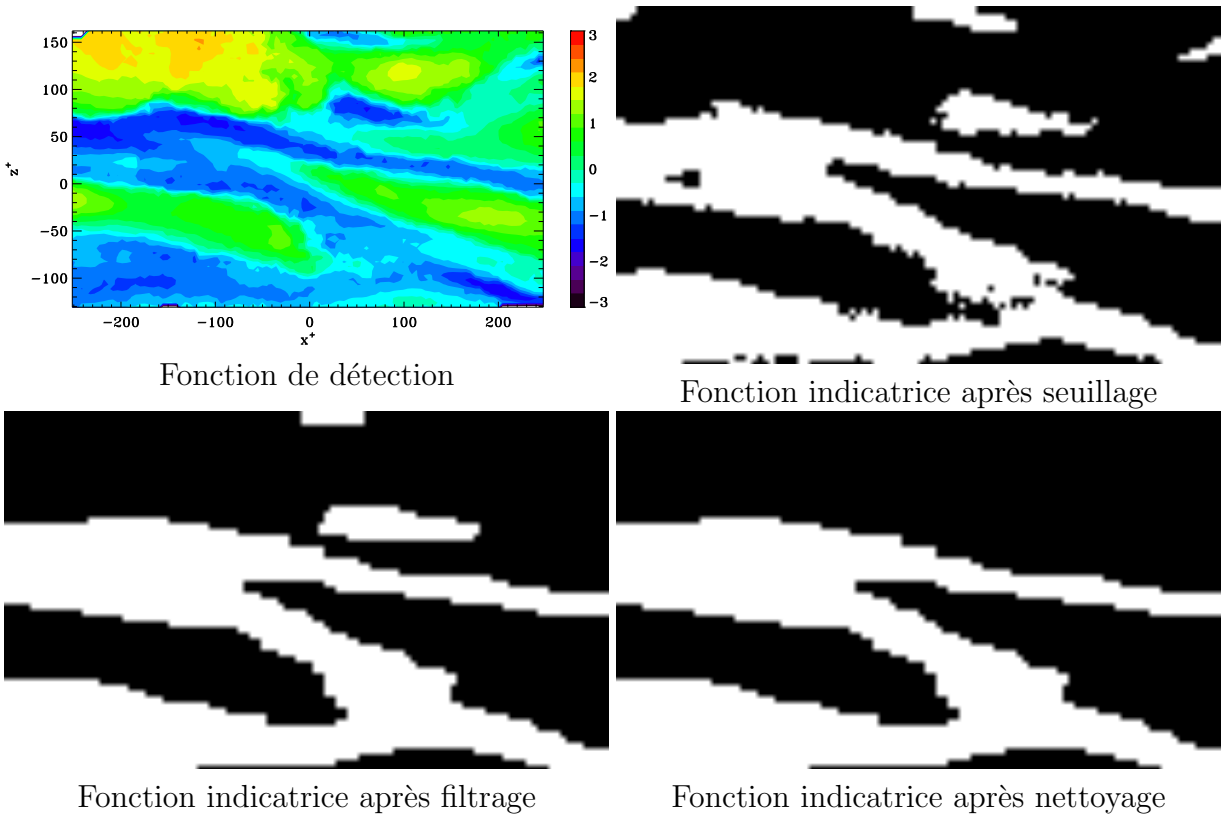

Fonction de détection

Fonction indicatrice après seuillage

Fonction indicatrice après filtrage

Fonction indicatrice après nettoyage

FIG. 1 – Exemple de détection des ′low speed streaks′

régions. D′abord, on détecte les objets ′fluctuation de vitesse′ (VF) et les objets ′gradient′ (GO) comme précédemment. Ensuite on dilate les objets ′gradient′ pour créer des fenêtres de recherche. Ensuite on examine les positions relatives et les tailles de ces objets pour détecter les tourbillons. On obtient alors la fonction indicatrice des tourbillons. Pour les tourbillons contrarotatifs, les principes de détection sont les mêmes que les tourbillons individuels avec une combinaison un peu plus complexe.

Après avoir obtenu toutes les images instantanées de chaque structure cohérente, une analyse statistique permet d'obtenir leurs caractéristiques :

- Fréquence d′apparition
- Angle transversal
- Largeur
- Longueur
- Surface
- Distance transversale

  ...

Ces caractéristiques sont ensuite elles-mêmes analysées à l′aide de statistiques classiques :

- Moyenne

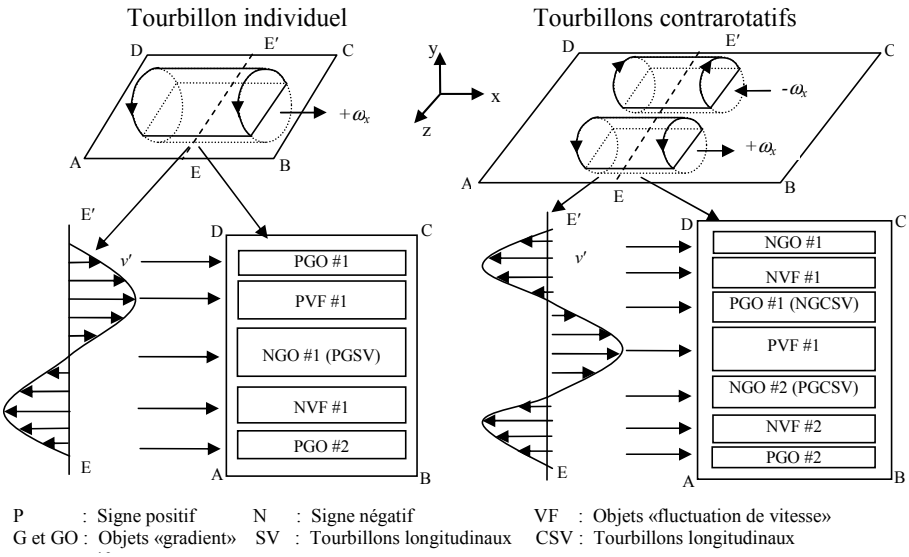

FIG. 2 – Modèle de détection des tourbillons longitudinaux

- RMS
- Histogramme
- Valeur médiane
- Coefficient de variation
- Dissymétrie et Aplatissement

  ...

Cette analyse montre qu'il existe des liens forts entre les différentes structures. Ainsi, de manière remarquable, la distance transversale est comparable quelque soit le type de structure cohérente. De plus, la loi de variation de densité de probabilité est la même pour la même caractéristique des différentes structures. Les longueurs des tourbillons longitudinaux, des 'ejections' et des 'sweeps' sont également comparables.

Chapitre 7 : Organisation des structures cohérentes

Après avoir obtenu les images indicatrices instantanées pour chaque structure cohérente, nous avons calculé les corrélations spatiales entre les différents structures :

- Auto corrélation et corrélation croisée des 'low et high speed streaks'
- Auto corrélation et corrélation croisée des 'ejections' et des 'sweeps'
- Auto corrélation et corrélation croisée des tourbillons négatifs et positifs
- Corrélation croisée des objets de grande vitesse de touillions positifs et négatifs
- Corrélation croisée des 'low et high speed streaks' avec les 'ejections' et les 'sweeps'
- Corrélation croisée des 'low et high speed streaks' avec les tourbillons négatifs et positifs
- Corrélation croisée des 'ejections' et des 'sweeps' avec les tourbillons négatifs et positifs

Les résultats de ces corrélations et les analyses statistiques précédentes fournissent des informations sur l'organisation de ces structures dans l'écoulement.

Chapitre 8 : Conclusions et perspectives

Conclusions

Nous avons montré que la SPIV est une méthode adaptée à l'étude de la turbulence de paroi. L'approche par reconnaissance de forme, quant à elle, lorsqu'elle est utilisée avec précaution, peut être une bonne méthode de détection des structures cohérentes. Dans cette étude, c'est la première fois que les caractéristiques de ces structures ont été déterminées avec autant de détails. Les résultats de notre étude sont en bon accord avec la littérature. Cette étude propose un modèle quantitatif d'organisation spatiale de ces structures dans la région inférieure à 50 unités de la paroi.

Les résultats montrent que la distance transversale moyenne entre les 'low (ou high) speed streaks' voisins est environ de 120 unités de paroi. Cette valeur est presque la même que celle pour les 'ejections' et les 'sweeps' ou les tourbillons longitudinaux. Généralement cette distance augmente avec la distance à la paroi pour toutes les structures cohérentes. La présente étude mesure également la distance entre les 'low (ou high) speed streaks' les plus proches. Elle est d'environ 8-12% plus petite que la distance précédente, ce qui met en évidence la propriété d'alignement de ces types de structures. La distance entre les deux jambes des tourbillons contra-rotatifs est environ 45 unités de paroi, ce qui est comparable à la largeur des 'low speed streaks'. Exceptée pour la fréquence d'apparition, les histogrammes de la même statistique suivent la même loi de distribution pour les structures différentes : Distribution de Laplace pour l'angle transversal, distribution log-normale pour la largeur et la longueur, distribution exponentielle pour la surface et distribution de Rayleigh pour la distance dans le sens de l'envergure. Une population significative de chaque structure possède un angle transversal non nul.

La présente étude montre que les tourbillons longitudinaux sont centrés dans la région $20 < y^+ < 30$. Dans cette région, on a souvent observé un maximum ou un minimum des caractéristiques étudiées, particulièrement pour les éjections et les tourbillons longitudinaux. Le diamètre moyen des tourbillons longitudinaux augmente avec la distance de paroi.

Les 'streaks' sont les structures les plus grandes dans la présente étude. Les 'low speed streaks' ont une largeur d'environ 35 unités de paroi tandis que les 'high speed streaks' ont environ 45 unités de paroi. En raison de la taille limitée du champ de vitesse, la longueur des 'streaks' ne peut pas être mesurée si elle est plus grande que 500 unités de paroi (la dimension longitudinale du champ de vitesse). Les 'ejections' ont une largeur d'environ 20 unités de paroi et une longueur d'environ 110 unités de paroi. Les 'sweeps' sont plus larges et plus courts que les 'ejections'. Leur largeur et longueur moyennes sont d'environ 25 et 90 unités de paroi respectivement. Les tourbillons longitudinaux ont une longueur comparable avec celle des 'ejections' et des 'sweeps'.

Les corrélations entre les structures montrent que les 'ejections' et les 'sweeps' sont

fortement associés aux tourbillons longitudinaux. Les ′ejections′ et les ′sweeps′ sont liés respectivement aux ′low et high speed streaks′. Les corrélations indiquent également que les ′low speed streaks′ et les ′ejections′ sont sur la droite en amont des tourbillons longitudinaux négatifs et sur la gauche en amont des tourbillons positifs tandis que les ′high speed streaks′ et les ′sweeps′ sont respectivement sur la gauche et droite en aval. Les ′ejections′ et les ′sweeps′ sont plus près des tourbillons longitudinaux que des ′streaks′ dans les directions longitudinale et transversale.

Les corrélations des fluctuations de vitesse et des structures cohérentes prouvent que, pour un tourbillon longitudinal, la partie avec des fluctuations négatives de vitesse normales, est en amont de la partie avec des fluctuations positives. De plus, cette étude montre que les ′streaks′ sont associés à un paquet de tourbillons longitudinaux. Ceci mène à la conclusion que des ′low speed streaks′ sont formés à l′intérieur d′un paquet de tourbillons longitudinaux alors que les ′high speed streaks′ sont sur l′extérieur. Comme ′ejections′ et ′sweeps′ sont associés aux ′low et high speed streaks′ respectivement, la conclusion ci-dessus est également vraie pour les ′ejections′ et les ′sweeps′. L′analyse statistique prouve que la différence de l′angle transversal entre les jambes positives et négatives d′un tourbillon longitudinal a une valeur positive au-dessus de $y^+ = 30$. Ceci indique que la plupart de ces tourbillons ont une forme en Ω dans cette région. En plus, l′analyse des corrélations croisées entre les tourbillons longitudinaux négatifs et positifs met en évidence des phénomènes d′appariement décrit par Tomkins et Adrian (2003), et qui sont localisés la plupart du temps dans la région $33 < y^+ < 44$.

Les résultats soutiennent le modèle d′Adrian et collaborateur (2000) exceptée pour la localisation des ′sweeps′. Il ont suggéré que les ′sweeps′ sont crés dans la couche supérieure alors qu′ils sont associés aux tourbillons longitudinaux attaché à la paroi dans la présente étude. Dans cette étude, le modèle d′Adrian et collaborateur (2000) a été amélioré et des dimensions caractéristiques ont été proposées.

Perspectives

Basé sur cette étude, plusieurs perspectives peuvent être proposées. La première est de poursuivre l′étude pour la région supérieure a y^+=50. La deuxième est de faire varier le nombre de Reynolds pour voir son influence sur les caractéristiques des structures et sur leur organisation. Ensuite, on pourrait étudier l′évolution temporelle de ces structures. Enfin, il serait intéressant de comparer les résultats de PIV avec des résultats de DNS qui fournit une vrai information 3D.

Table des matières

Table des figures

Liste des tableaux

Nomenclature

Latin symbols

A_C	Area of complete object
C_C	Clean factor for complete object
C_B	Clean factor for incomplete object
C_T	Threshold for detection function F_d
C_T^{uv}	Threshold for detection function F_d^{uv}
C_T^v	Threshold for detection function F_d^v
C_T^{grad}	Threshold for detection function F_d^{grad}
d	Spanwise distance between two nearby objects
d_n	Spanwise distance between two closest objects
E_1	Error estimation parameter : mean value of modulus
E_{11}	Spectrum of the u velocity component
E_2	Error estimation parameter : standard deviation of the modulus
E_{22}	Spectrum of the v velocity component
E_{33}	Spectrum of the w velocity component
F	Flatness factor
F_d	Detection function
F_i	Indicative function
F_d^{grad}	Detection function based on the velocity gradient in the spanwise direction
$F_{u'}$	Flatness of the fluctuation of the streamwise velocity
F_d^{uv}	Detection function based on the product of the streamwise and wall-normal velocities
F_d^v	Detection function based on the wall-normal velocity
$F_{v'}$	Flatness of the fluctuation of the wall-normal velocity
$F_{w'}$	Flatness of the fluctuation of the spanwise velocity
H	Vertical distance between the lens of camera and the light sheet
L	Streamwise distance between the lens of camera and the light sheet
k	Wave number
k_c	PIV cut-off wave number
L_f	Field size
k_{min}	Minimum wave number accessible with PIV
L_A	Length of complete object
M_0	Median value
M_S	Structuring element
N	Frequency of appearance
p	Pressure
R_{AB}	Correlation tensor of a signal A with a signal B
Re_θ	Reynolds number
R_{mm}	Ratio of the most-probable value to the mean

S	Skewness factor
S_{IW}	Interrogation window size
$S_{u'}$	Skewness of the fluctuation of the streamwise velocity
$S_{v'}$	Skewness of the fluctuation of the wall-normal velocity
$S_{w'}$	Skewness of the fluctuation of the spanwise velocity
U_∞	Free stream velocity
U	Streamwise velocity after reconstruction (in plane velocity)
U_1	Streamwise velocity obtain from camera #1 by a 2D2C analysis before reconstruction
U_2	Streamwise velocity obtain from camera #2 by a 2D2C analysis before reconstruction
u_τ	Skin friction velocity
u	Instantaneous streamwise velocity
u'	Fluctuation of the streamwise velocity
$\overline{U}$	Mean streamwise velocity
v	Instantaneous wall-normal velocity
v'	Fluctuation of the wall-normal velocity
V	Wall-normal velocity after reconstruction (out plane velocity)
$\overline{V}$	Mean wall-normal velocity
w	Instantaneous spanwise velocity
w'	Fluctuation of the spanwise velocity
W	Spanwise velocity after reconstruction (in plane velocity)
W_1	Spanwise velocity obtain from camera #1 by 2D2C analysis before reconstruction
W_2	Spanwise velocity obtain from camera #2 by 2D2C analysis before reconstruction
W_a	Width of object
$\overline{W}$	Mean spanwise velocity
(X_1, Y_1, Z_1)	Position of the lens of camera #1
(X_2, Y_2, Z_2)	Position of the lens of camera #2
x	Streamwise coordinate
(x, y, z)	Position of the measurement point
y	Wall-normal coordinate
z	Spanwise coordinate

Greek symbols

ΔX_i^j	Displacement in the image plane (two dimensions (i)) obtained from two cameras (j), i,j = 1, 2
Δx_i	Displacement in the object plane (three dimensions), i =1, 2 , 3
Δx	Streamwise displacement
Δz	Spanwise displacement
φ	Spanwise angle
φ_c	Difference of the spanwise angle between PGCSV and NGCSV of the same vortex
ν	Kinematic viscosity
ρ	Density of the fluid
α	Velocity angle (tan(α)=v/u or w/u)
σ_u	Standard deviation of the velocity component u
$\sigma_{u'}$	Standard deviation of the fluctuation of the velocity component u
σ_v	Standard deviation of the velocity component v
$\sigma_{v'}$	Standard deviation of the fluctuation of the velocity component v
σ_w	Standard deviation of the velocity component w
$\sigma_{w'}$	Standard deviation of the fluctuation of the velocity component w
ψ	Variation coefficient
ψ_0	Variation coefficient of $ln\psi$

Superscript

$\overline{(\,)}$	Mean
$^+$	Normalized by inner layer scale

Abbreviations

CS	Coherent structure
EJ	Ejection
GCSV	A pair of NGSV and PGSV representing the core of legs of a counter-rotating streamwise vortex
GO	Object with high spanwise gradient of the wall-normal velocity fluctuation v'
GSV	GO representing the core of a streamwise vortex
HSS	High speed streak
LSS	Low speed streak
MSI	Image mapping method with Surfacial interpolation and integer shift
MSW	Image mapping method with Surfacial interpolation and Whittaker shift
MWI	Image mapping method with Whittaker interpolation and integer shift
MWW	Image mapping method with Whittaker interpolation and Whittaker shift
NGCSV	NGSV representing the core of the negative leg of a counter-rotating streamwise vortex
NGSV	GO representing the core of a negative streamwise vortex
NGO	GO with negative gradient
NVF	Object with high negative wall-normal velocity fluctuation v'
PGCSV	PGSV representing the core of the positive leg of a counter-rotating streamwise vortex
PGO	GO with positive gradient
PGSV	GO representing the core of a positive streamwise vortex
PVF	Object with high positive wall-normal velocity fluctuation v'
Q_1	Quadrant one of the plane (u', v')
Q_2	Quadrant two of the plane (u', v')
Q_3	Quadrant three of the plane (u', v')
Q_4	Quadrant four of the plane (u', v')
S3I	Soloff method with 3 calibration planes and integer shift
S3W	Soloff method with 3 calibration planes and Whittaker shift
S5I	Soloff method with 5 calibration planes and integer shift
S5W	Soloff method with 5 calibration planes and Whittaker shift
SW	Sweep
VF	Object with high wall-normal velocity fluctuation v'
WI	Vector Warping method with integer shift
WW	Vector Warping method with Whittaker shift

Chapitre 1

Introduction

1.1 Background

Most flows in daily life are turbulent. For example, the flows in pumps, compressors, pipe lines, and the flows around airplanes, automobiles, ships, and submarines, are generally turbulent. Two properties of turbulent flows are very important. One is that a turbulent flow is unsteady both in time and in space. The other is that a turbulent flow contains eddy structures with characteristic length, velocity and time scales which are spread over a very wide range. The two properties make the mathematical description of turbulence complicated and eliminate the use of an exact mathematical theory in the calculation of practical problems. Although the concept of turbulence is generally accepted and understood, it is difficult to give a precise definition. The first detailed definition was given by Von Karman (1937) : ′Turbulence is an irregular motion which in general makes its appearance in fluids, gaseous or liquid, when they flow past solid surfaces or even when neighbouring streams of the same fluid flow past or over one another′. The word ′irregularity′ in the definition emphasize the chaotic nature of turbulence. However, distinct average values of turbulence, such as velocity, pressure and temperature, can also be obtained by the theory of probability. Hinze (1975) gave a more precisely definition as : ′Turbulent fluid motion is an irregular condition of flow in which the various quantities show a random variation with time and space coordinates, so that statistically distinct average values can be discerned′. Even with this definition, it is sometimes tricky to objectively distinguish turbulence from a complicated laminar flow. Thus far, no fully satisfactory definition has been found.

According to Hinze (1975), turbulence can be divided into two categories. One is called ′wall turbulence′ which presents the turbulence generated and continuously affected by fixed walls ; the other is referred to as ′free turbulence′ which presents the turbulence in the absence of walls. Wall turbulence is very common and known as turbulence which is directly influenced by a solid boundary. Many possibilities of this turbulence exist according to the configuration of the boundary. The rigid wall is one of the most important boundary. Even in this case, two main groups can be identified. One comprises the flows around rigid bodies, while the other consists of the flows within a space bounded by rigid walls. The simplest case of these two groups are respectively the two-dimensional boundary

layer flow along a flat plane with zero pressure gradient in the free stream and the fully developed flow through a round tube with uniform cross-section. Clearly, the substantial difference between the two groups is that the domain of wall turbulence increases along the body in the downstream direction in the first group but remains restricted to the space bounded by the rigid wall in the second group.

The first group of wall turbulence is known as ′boundary layer flows′ as the wall turbulence remains within a relatively thin layer between the surface of the body and the outside undisturbed free stream. This layer usually increases in absolute thickness in the downstream direction. In this layer, the turbulence is directly affected by the wall, at least in a region close to it. This effect occurs respectively through the action of viscous stresses for a smooth wall and through the action of forces resulting from the flow around the roughness elements for a rough wall. In wall turbulence, if the wall is smooth, a region close to the wall, where the behaviour of the flow is determined by the fluid viscosity, exists at any Reynolds number. Moreover, the direct effect of fluid viscosity on the gross structure of the turbulence become smaller and more negligible with the wall distance. Therefore, two regions are distinguished when a turbulent flow develops along a rigid boundary. The first one is the region adjacent to the wall where the flow is directly affected by the condition at the wall. As mentioned above, this condition is represented respectively by the fluid viscosity in case of a smooth wall and by the wall roughness in case of a rough wall. This region is referred to as the ′wall region′ or the ′inner region′. The second region, which is beyond the wall region, is only indirectly affected by the wall through its wall shear stress and usually referred to as the ′outer region′.

In case that the wall is perfectly smooth, there is an extremely thin layer in the wall region where the flow is predominantly viscous. This thin layer is named the ′viscous sublayer′. Beyond this viscous sublayer, there is a region called as ′transition region′ or ′buffer region′ where the inertial effects become more and more important with respect to the viscous effects. Until some distance from the wall, a fully turbulent region, where direct viscous effects are negligible and inertial effects dominate the flow, can be found. It should be noted that the turbulent flow in the wall region is different from that in the outer region. The turbulence is directly influenced by the wall in the former region but not in the latter one, though some interaction may exist between the two regions. The viscous sublayer and the buffer region are both very thin compared with the local thickness of the boundary layer. Additionally, The total ′wall region′ covers roughly 15% of the whole boundary layer (Hinze (1975)).

Turbulent boundary layer near a flat wall is a basic flow phenomenon, which is of importance for the development of aviation, shipbuilding and chemical industry, and for the design of the hydraulic structure, etc. Moreover, investigation of the wall region helps one to understand the process of the turbulent energy generation and transport. The motion in the near wall region of a turbulent boundary layer is not entirely random but formed by organized structures. Many researchers have made great efforts on this subject (e.g. Theodorsen (1952), Kline and Runstadler (1959), Kline *et al.* (1967), Schlichting (1979), Hinze (1975), etc.). In the wall region, three kinds of eddy structures are presently most documented : low and high speed streaks, Ejections and Sweeps, and various vortices (e.g. hairpin vortex, horseshoe vortex, streamwise vortex, etc.). The relations and interactions

between all these coherent structures, which should explain the self-sustaining mechanism of near wall turbulence, have been investigated by many researchers (e.g. Panton (1997)and Adrian *et al.* (2000)). However, the mechanisms responsible for their formation and their contribution to the generation and the preservation of wall turbulence still remain to be solved.

1.2 Objectives

Taking advantage of the Stereoscopic Particle Image Velocimetry (SPIV) method, 2-dimensions and 3-components (2D3C) instantaneous velocity fields were obtained from the datasets recorded by Pérenne *et al.* (2004). Then, the coherent structures were identified from the resulting velocity fields, in order to obtain the mean characteristics, spatial distribution as well as the interactions between these structures. From this analysis, it was expected to obtain more information about the spatial organization of these structures.

1.3 Outline

In Chapter 2, the previous theories and achievements on the coherent structures in a boundary layer flow are reviewed and summarised. Chapter 3 firstly describes the details of the experiment. Then the earlier developments in PIV and SPIV are introduced and summarised. Following that, an optimal algorithm is selected to process the SPIV dataset in order to obtain 2D3C instantaneous velocity fields.In Chapter 4, the basic characteristics of the present turbulent flow (e.g. mean streamwise velocity, velocity fluctuations, Reynolds Shear Stress, spectrum, Probability Density Function (PDF), skewness and flatness) are calculated. In addition, they are compared with those of Hot Wire Anemometry (HWA) and Direct Numerical Simulation (DNS). In Chapter 5, two point spatial auto- and cross-correlations are calculated directly from the instantaneous velocity fields. The results show the existence and spatial distribution of coherent structures (e.g. streaks, ejections and sweeps, vortices). Pattern recognition method is used to identify these coherent structures and to calculate their statistical characteristics in Chapter 6. In Chapter 7, two-point spatial correlations are performed to investigate the detailed spatial distributions between different coherent structures and to explain the organization of them. Chapter 8 concludes the present study and gives the perspectives for future work.

Chapitre 2

Literature Review

As mentioned above, three main coherent structures exist in near wall turbulence : Streaks, Ejections and Sweeps, Vortices.

2.1 Streaks

2.1.1 General introduction

Hama (1954) was the first to evidence the existence of coherent structures near the wall. He observed the streaky structure in his flow visualization experiments. This structure reveals that very near to the wall, the instantaneous spanwise velocity distribution consists of alternating regions of high and low speed fluids. By flushing a turbulent pipe flow of coloured water with clear fluid, Ferrell *et al.* (1955) found the dye was swept from the outer portions of the boundary layer, leaving only streamwise traces of dyed fluid close to the wall with a fairly periodic transverse spacing. Since then, the streaky structure has been identified and examined by a number of authors under different experimental conditions.

Kline *et al.* (1967) investigated boundary layers subject to different pressure gradients by using hydrogen bubble wire visualization technique. They observed that the low speed streaks exist in all cases, including those in which relaminarization can occur (Fig. 2.1). Even being disrupted, the streaks can quickly re-establish themselves. Additionally, streaks show a remarkable degree of persistence and regularity. Hama and J. (1963) studied the transition procedure in the laminar boundary layer and found that the streaky structures can even be found in a transitional boundary. Bippes (1972) investigates a transitional boundary layer on a concave surface and observed these streaky structures by using the same hydrogen bubble wire visualization technique as Kline *et al.* (1967). The visualization picture he obtained is extraordinarily similar to those obtained by Kline *et al.* (1967) in a fully turbulent boundary layer. Therefore, Kline (1978) suggested that streaks constitute a universal feature of bounded shear flows and that the presence of streaks is a sufficient condition for establishing whether a given boundary layer flow is turbulent.

Thereafter, many properties of the streaks have been investigated. The streaky struc-

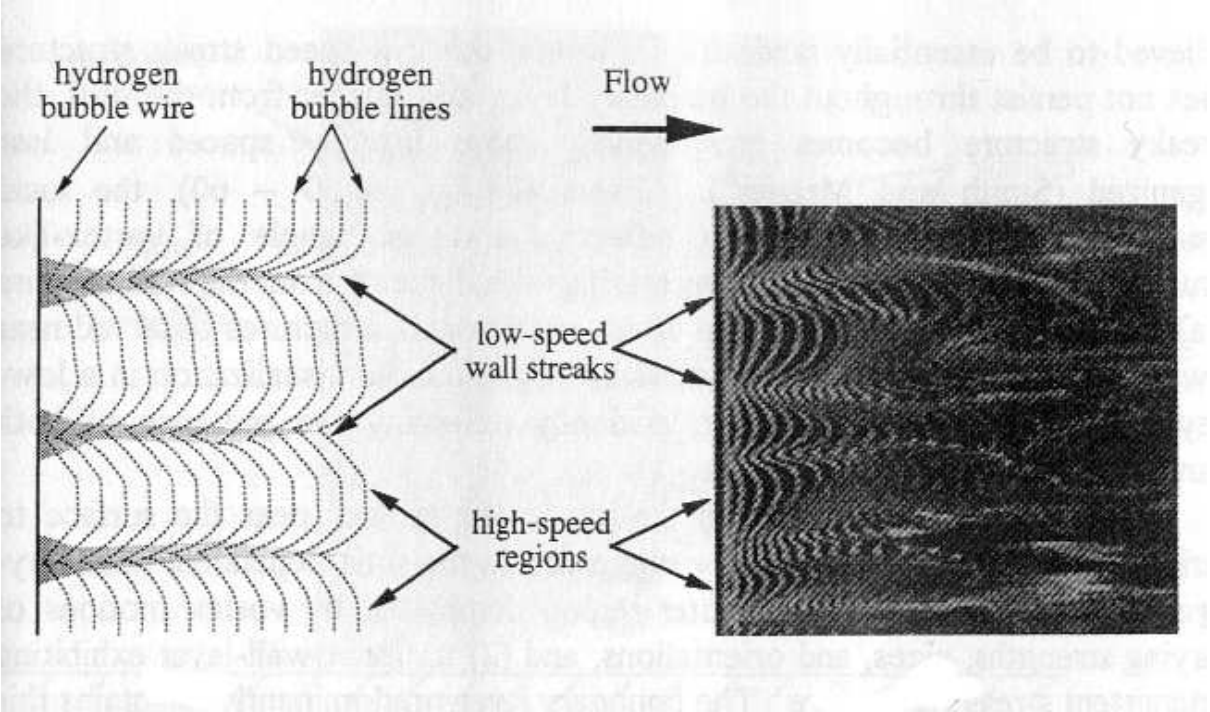

FIG. 2.1 – Structure of a flat plate turbulent boundary-layer visualised with hydrogen bubbles at $y^+ = 9.6$ (Kline *et al.* (1967)). The flow direction is from left to right.

tures are most clearly present close to the wall. Moving away from the wall, fewer and fewer streaks are found. The low-speed streaks observed from flow visualization studies show that they are not rigidly directed along the streamwise direction (Talmon *et al.* (1986)). They show meanders in the spanwise direction where they merge together or separate. Moreover, this meandering is time dependent, as can be seen in Fig. 2.2. Meandering property of low speed streaks in the spanwise direction is also known from results obtained from the numerical simulations and theoretical modelling. The investigation of a database generated with direct numerical simulation by Johansson *et al.* (1991) showed that the development of asymmetry in the spanwise direction is important for the evolution of near-wall structures. Based on that, they assumed that the inhibition of spanwise motion of the near wall streaky pattern might be the primary reason for skin friction reduction. Landahl (1990) has investigated the sublayer streaks by means of a simplified theoretical model. He found that asymmetry structures will grow in the streamwise direction and turn into streaks by the small three-dimensional disturbances initially localized in the spanwise direction while symmetric structures showed little or no such behaviour.

Compared to low speed streaks, high speed streaks were less investigated. Talmon *et al.* (1986) found that high speed streaks are related to regions of high value of Reynolds stress. The studies of Suzuki and Kasagi (1993) and Robinson (1991) associated the high speed streaks with an exchange of wall-normal velocity to streamwise and spanwise velocity. Johansson *et al.* (1991) observed that high speed streaks are surrounded by spanwise

diverging fluid.

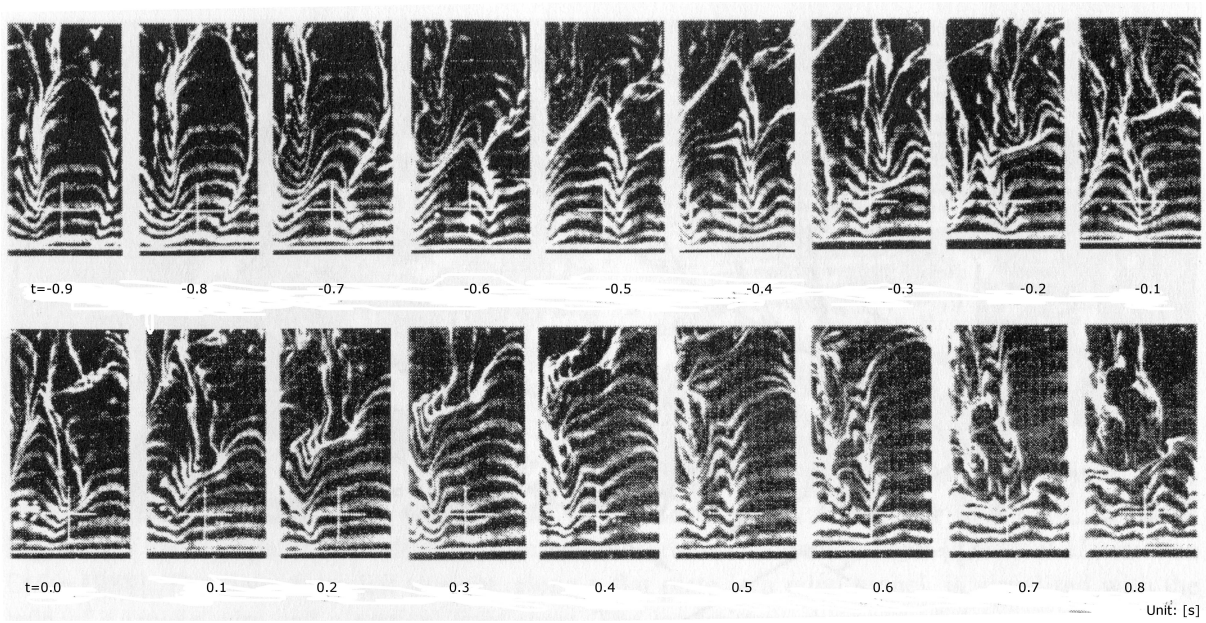

FIG. 2.2 – Time-dependent low speed streaks meanders at $y^+ = 29$ (Talmon *et al.* (1986)). The flow direction is from Bottom to top and LDV measurement location is indicated with a white $'+'$ signal.

2.1.2 Origin of streaks

The origin of streaks has always been an interesting topic for research. Many models have been proposed, among which two are quite popular. One explains the streaks as a consequence of wall normal motion while the other considers the combined action of lift-up, shear and diffusion as the origin of streaks.

For the first explanation, two popular models of wall normal motion are available. Stuart (1965) was the first one to explain the origin of streaks, from streamwise vortices inducing normal motions which cause the streaks. This conclusion was confirmed by some authors (e.g. Blackwelder and Eckelmann (1979) ; Blackwelder (1983) ; Ersoy and A. (1985), Aubry *et al.* (1988), etc.). They suggested that streaks are caused by long counter-rotating streamwise vortex pairs (Fig. 2.3). Rows of vortices elongated and rotated in the direction of the mean flow, which advects the fluid from the wall and to the wall in alternating lines. The fluid advected from the wall is moving slower than average at this distance from the wall, whereas fluid advected to the wall is moving faster. This creates the wavy streamwise velocity profile at a fixed distance from the wall. This is a simple model which requires long streamwise vortex pairs embedded within the wall layer which are not well evidenced in both experiments and numerical simulation studies. The second model suggested that hairpin vortex is responsible for streaks (Fig. 2.4). When the

hairpin vortex moves downstream, a trace is left behind in the form of an elongated streak. Fig. 2.4 shows different possibilities for a symmetric hairpin vortex or for an asymmetric core vortex. This second model was approved by many researchers (e.g. Acarlar and R. (1987) ; Smith *et al.* (1991) ; Haidari and R. (1994) ; Asai *et al.* (1996). etc). Besides these two models, other similar patterns of wall normal motions generating streaks were also proposed by numerous researchers. At present, the idea that the streaks is dictated by wall-normal motions is generally accepted. One can find detailed explanations from the work of Panton (1997), Jang *et al.* (1986), Brooke and Hanratty (1993), Butler and Farrell (1993), Waleffe *et al.* (1993), Hamilton *et al.* (1995), Nikitin and Chernyshenko (1997), Schoppa and Hussain (1998), Waleffe (2003), etc.). Even after several decades of research, no general agreement on which pattern of wall-normal motions is responsible for streaks was made. This can be explained by the fact that streaks are easy to observe in experiments or direct numerical simulations but it is more difficult to find the corresponding pattern of wall-normal motions.

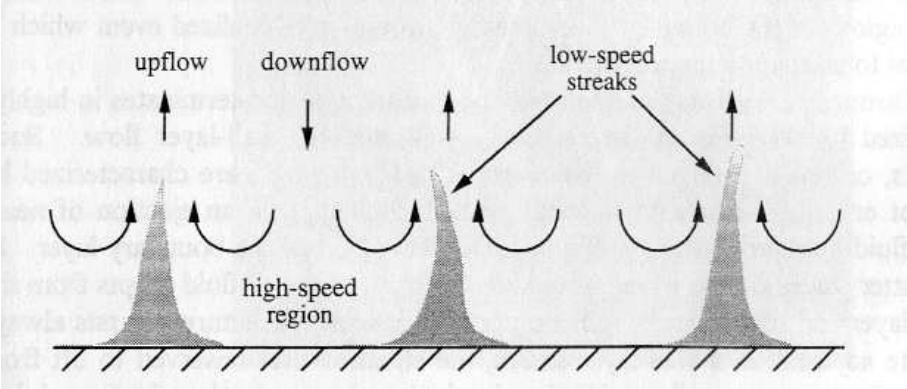

FIG. 2.3 – Schematic illustating how counter-rotating streamwise vortex pairs generate streaks (Blackwelder and Eckelmann (1979))

The second model suggests that the combined action of lift-up, shear and diffusion generates streaks (e.g. Landahl (1990),Butler and Farrell (1993), Chernyshenko and Baig (2005), etc.). In this model, the wall normal velocity definitely has no pattern and the velocity streaks are supposed to be created by the same mechanism as streaks of a passive scalar. Fig. 2.5 shows the process in terms of a passive scalar. In Fig. 2.5, the surface indicates the boundary of the region of high concentration of a passive scalar released from the wall. In Fig. 2.5a, the surface is assumed to be flat, but the lift-up by wall-normal motion will cause some hunches and deform the surface to a shape in Fig. 2.5b. If a visualization plane, parallel to the wall at some distance from the initial position of the boundary, was selected at this moment, it will cut through these hunches shown in Fig. 2.5b. Then this visualization plane only shows several cycle or ellipse shaped contours plotted according to the concentration level of the scalar instead of a streaky pattern as expected, due to the fact that the wall-normal motions are assumed to have no pattern. It reveals that lift-up by isotropic wall normal motions does not create streaks. Now the

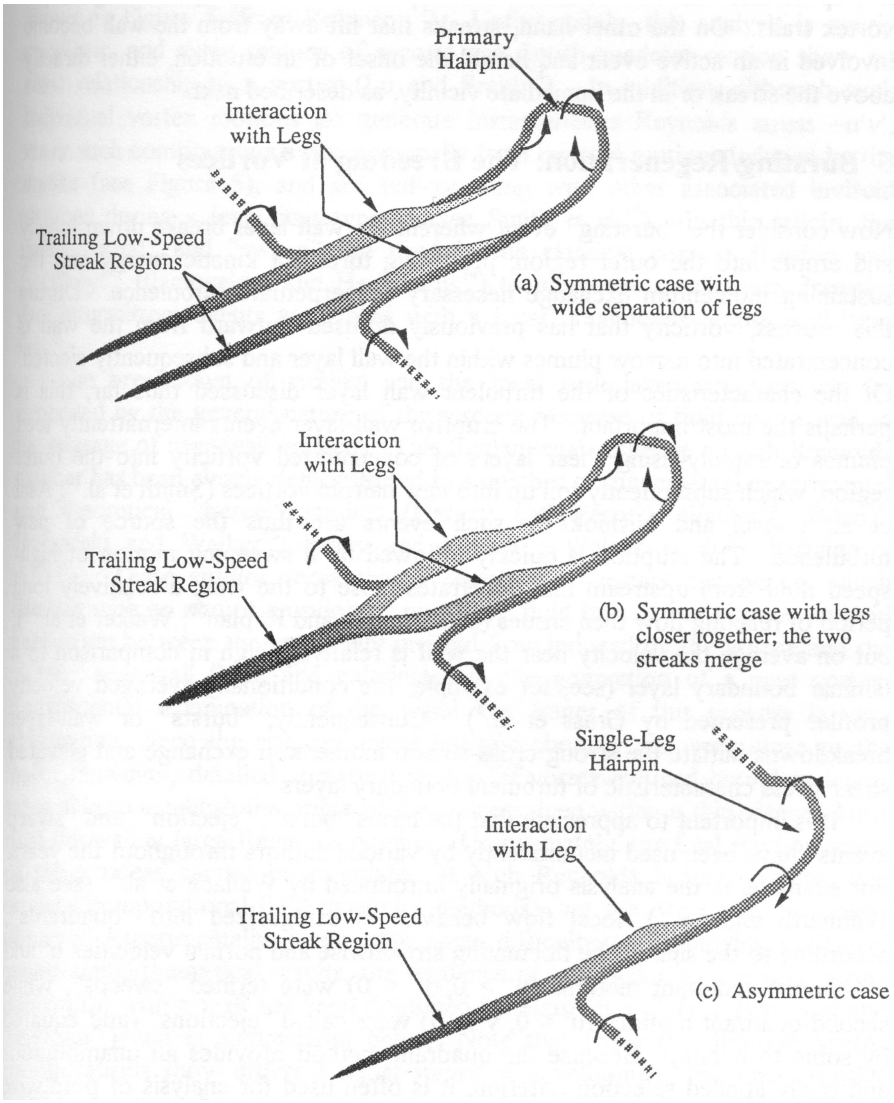

FIG. 2.4 – Schematic illustating how hainpin-liked vortex generates streaks (Smith *et al.* (1991))

mean shear starts to work. It first tilts and stretches the lifted volumes as it is shown in figure Fig. 2.5c, which only causes a downstream shift or a deformation of these contour in the visualization image obtained from Fig. 2.5b. Still, no streaky pattern appears. However, tilting and stretching lead to an increase of the wall normal gradient and then the wall normal diffusion occurs in Fig. 2.5d. Finally, a streaky pattern appears in the visualization plane.

Since the effect of lift-up, shear and diffusion of a flow are governed by the linearised Navier-Stokes equations and these effects are sufficient to explain the origin of streaks in the second theory, the possibility of using the linearised Navier-Stokes equations to investigate streaks is well accepted. Landahl (1990) studied the linear response of the

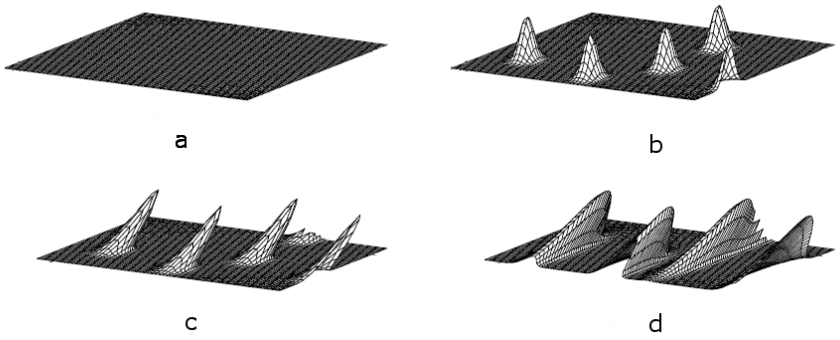

FIG. 2.5 – Combined action of lift-up, shear and diffusion. a :orignal surface ; b : lift-up by isotropic wall-normal motions ; c : effect of mean shear ; d : effect of diffusion (Chernyshenko and Baig (2005)

mean shear flow to random forces in the near wall turbulent flow. His results about the evolution of coherent structures agree well with those obtained by a VITA (Variable Interval Time Averaging) technique (Blackwelder and Kaplan (1976)). Lee *et al.* (1990) compared the predictions of the rapid distortion theory based on linearised equations with the results of direct numerical simulations. They found that the dominant mechanism in the production and maintenance of the preferred structures (for example, streaks) in all turbulent shear flows at high shear rate is a selective amplification of eddies primarily by the linear interaction with mean shear. Butler and Farrell (1993) investigated streaks by calculating the optimal perturbations of a channel flow linearised around the turbulent mean velocity. They found that the optimal perturbations predict streaks, but they had to limit the lifetime of the perturbation by the eddy turnover time in order to obtain streak spacing agreeing with experiment. The second model was used and supported by some researcher, however, it is not as widely accepted as the first one for explaining the origin of streaks. The reason can be insufficient information about how linearised equations can give predictions about the essentially non-linear phenomena of turbulence.

Similar to how various alternatives (e.g. streamwise vortices, hairpins, etc.) exist in the first theory of streak origin, in the second theory, the described mechanism of streak formation by non-structured wall normal motions is not unique. Various mechanisms can also be proposed within the second conceptual framework. Moreover, these two theories are not exclusive. The characteristics of streaks in real turbulent flows are naturally determined by both wall normal motions and the combined action of lift-up, shear and diffusion. However, the question, which is the dominant one, is still under investigation.

2.1.3 Statistical characteristics

2.1.3.1 Investigation methods

The first systematic and quantitative investigation of streaks was carried out by Runstadler *et al.* (1963). Their results showed that the mean spacing between streaks could be quantified and correlated. Thereafter, the physical characteristics of the low speed streaks have been examined by a number of researchers with different measurement techniques. There exist generally two prevailing methods to extract the streak spacing : visual inspection and spectral techniques based on the autocorrelation or its Fourier transform, the spatial spectrum. Visual inspection may be performed directly on the video screen, as in Kaftori *et al.* (1994), or on a sequence of still images, which have been extracted from a high-speed video, as in Smith and Metzler (1983). A set of rules has been developed to guide the examiners in localizing the streaks in pictures taken by the visualization inspection method. An additional threshold may be used to eliminate the weak or underdeveloped streaks.

Spectral method can estimate the characteristic streaks spacing directly from the location of the first peak of the autocorrelation. Alternatively the characteristic spatial frequency can be determined by the peak frequency of the spatial spectrum, which is the Fourier transform of the autocorrelation. There are two drawbacks to the spectral methods. One is that as the amount of data (i.e. the number of data frames) increases, the averaged autocorrelation tends to get flattened and then make the results irresponsible (Gupta *et al.* (1971) and Fortuna and Hanratty (1972)). Therefore, Achia and Thompson (1977) developed a so-called $'$AD-HOC$'$ method which extracts and averages the lag of the first peak in each individual autocorrelation function to overcome this problem. Another drawback is that spectral methods provide only an estimate of the distribution of the mean streak spacing. Thus, it does not provide other characteristics of the streak spacing such as the histogram of the spacing which can be obtained by visual inspection methods. Both methods gained wide use among researchers.

2.1.3.2 Results of statistical characteristics

Schraub and Kline (1965) established the mean spanwise spacing ($\overline{\lambda}$) between low speed streaks by using primarily flow visualization techniques for low Reynolds number flows ($R_e < 1500$). They found the mean spanwise spacing is generally about 100$\pm$20 wall units. Many researchers (e.g. Oldaker and Tiederman (1977), Achia and Thompson (1977), Lee *et al.* (1974), Blackwelder and Eckelmann (1979), Kreplin and Echelmann (1979), etc.) have confirmed this value with different visual and probe experiment techniques. Schraub and Kline (1965) were also the first ones to examine the variation of streak spacing with wall distance by using both visual inspection and spectral methods. They found that streak spacing appears to increase for $y^+ \geq 7$, however, no explanation was provided for this increase. Nakagawa and Nezu (1981), using both visual techniques and hot film probe correlation techniques, showed an apparent increase in streak spacing for $y^+ > 10$ and proposed an estimation of this spacing as $2y^+$ when $y^+ > 100$. They suggested that the increase in scale may be due to a pairing interaction of the low speed streaks as they move outward from the wall, resulting in the increase in scale. An extended

study of the low-speed streaks has been carried out by Smith and Metzler (1983) using flow visualization experiment at $740 < R_e < 5380$. They found that the mean spanwise spacing of low speed streaks is about 100^+ based on a detection threshold. For a higher Reynolds number $4700 < R_e$, Gupta *et al.* (1971) investigated the spatial structure in the viscous sub-layer using an array of hot-wires distributed in the spanwise direction. They used a VITA correlation technique to determine the spanwise separation between streaks in the viscous sublayer. Their results show that the mean spacing increase with Reynolds number (up to 10000), which reveals a dependence of this spacing on Reynolds number. This conclusion is also confirmed by recent research (Kahler (2004), Lagraa *et al.* (2004), Carlier and Stanislas (2005)). In case of low Reynolds numbers, the non-dimensional mean streak spacing was suggested to be invariant (Kline *et al.* (1967), Achia and Thompson (1977), Oldaker and Tiederman (1977), Nakagawa and Nezu (1981), Smith and Metzler (1983), and Hetsroni and Rozenblit (1994)). This value is generally accepted as $\overline{\lambda} = 100 \pm 20$ wall units for $y^+ \leq 10$ and increases for $y^+ > 10$. Recent research shows that streak spacing can provide a new way to investigate turbulence. For instance, Grass and Mansour-Tehrani (1996) used the mean spacing to investigate the effect of surface roughness while Oldaker and Tiederman (1977) and Hetsroni *et al.* (1997) used it to study the effect of drag-reducing solutions on the streaky structure.

Blackwelder and Eckelmann (1979) used a combination of hot film probes and flush mounted surface elements to measure the length of the streak structures in a low Reynolds number oil channel. They found that streamwise length scales can extend beyond $\Delta x^+ > 1000$ according to the connected regions of low axial velocity in the region $5 \leq y^+ \leq 30$. Oldaker and Tiederman (1977) also found that streaks may exceed $\Delta x^+ > 1000$ by their dye visualization experiment. Kreplin and Echelmann (1979), using the same oil-channel facility as Blackwelder and Eckelmann (1979), confirmed these results by their probe correlation studies. By using a SPIV experiment, Carlier and Stanislas (2005) confirmed this result by their own experiments and agreed that the streamwise size of streaks is generally between 500 and 2000 wall units. Moreover, they also found that the size of streak is between 20 and 40 wall units in width.

2.2 Ejections and Sweeps

2.2.1 General introduction

Ejections and sweeps (Fig. 2.6), which are defined as regions of an abrupt outward motion of fluid with low streamwise velocity or inward motion of fluid with high streamwise velocity, play a major role in the process of turbulent generation. Investigation of ejections, sweeps and interactions between them can provide more insight into the process of Reynolds stress production. One of earliest studies on these structures was carried out by Corino and Brodkey (1969). They investigated the wall region of a fully developed turbulent pipe flow by photographing the motions of colloidal-size solid particles suspended in flows with a high-speed-camera moving with the flow. They observed that a distinct pattern existed in the wall region and was characterized by a deterministic sequence of events occurring randomly in space and time. This pattern was a function of the distance from the wall. The area $0 < y^+ < 5$ (sublayer region) was found not to be laminar ; it was characterized by velocity fluctuations of small magnitude and disturbed by fluid coming from the adjacent region. The area $5 < y^+ < 30$ was characterized by ejections of fluid away from the wall. These ejections were found to occur intermittently and randomly in space and time, and were part of a sequence of events. The first event of this sequence was a deceleration, in which the axial velocity was characterized by the essential disappearance of the velocity gradient and by a velocity defect as great as 50% of the local mean velocity. The second event was an acceleration, in which a mass of fluid coming from upstream and entering at about $y^+ = 5$ was directed towards the wall at angles of 0-15° and interacted with the fluid in the decelerated region. The third event was an ejection, in which a mass of fluid coming from the decelerated region moved away from the wall. The fourth event was a sweep, in which a mass of high speed fluid entrying from upstream moved almost parallel to the wall. This latter high speed fluid was often a part of the same mass of fluid which gave rise to the acceleration stage. The above cycle was repeated randomly in space and time.

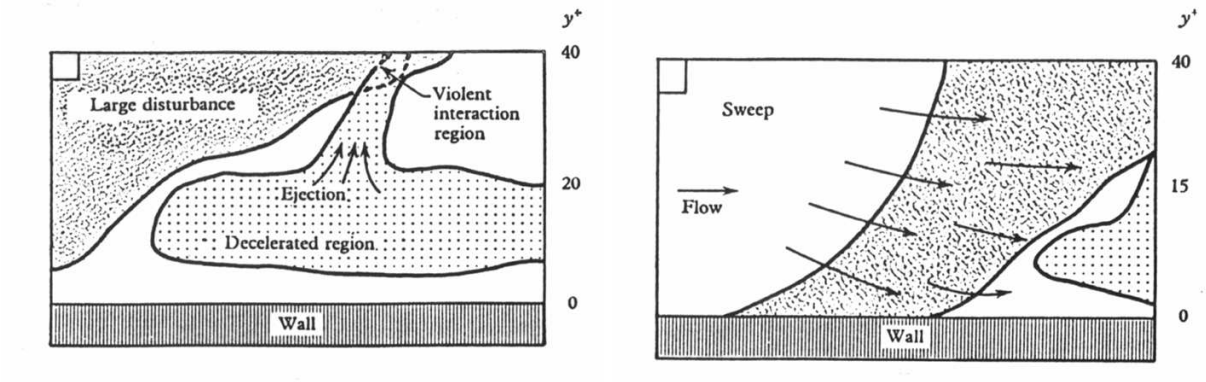

a b

FIG. 2.6 – Illustration of ejection (a) and sweep (b), Corino and Brodkey (1969)

2.2.2 Detection algorithms

Different algorithms were employed to investigate these types of coherent structures. Most of them focused on the burst or ejection events that occur in the near wall region.

Wallace *et al.* (1972) introduced a quadrant algorithm to investigate the production of Reynolds stress by using hot-film anemometry techniques. This quadrant algorithm separates the $u'v'$ signal into four parts (Fig. 2.7). where u' and v' are the time-dependent streamwise and wall normal velocity fluctuations respectively, quadrant two ($u' < 0$, $v' > 0$) and quadrant four ($u' > 0$, $v' < 0$) were associated with the ejection and sweep events respectively (called as Q2 and Q4 events respectively). Quadrant one ($u' < 0$, $v' < 0$) and quadrant three ($u' > 0$, $v' > 0$) were related to the interactions between them (called as Q1 and Q3 events respectively).

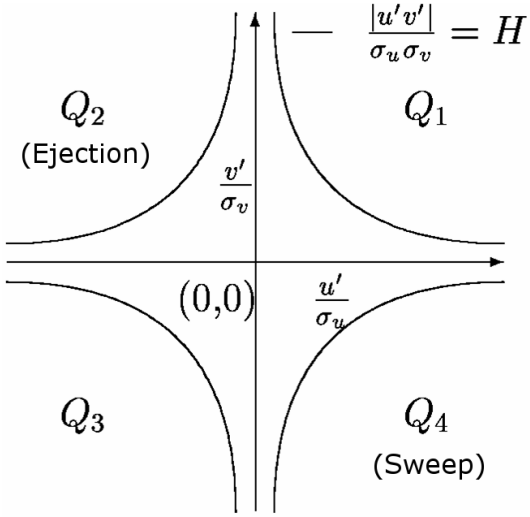

FIG. 2.7 – Illustration of quadrant algorithm (Wallace *et al.* (1972))

Blackwelder and Kaplan (1976) introduced a VITA algorithm (Variable Interval Time Averaging) (Fig. 2.8). The VITA algorithm based on the magnitude of the short-term RMS of a fluctuation signal compared to the long-term RMS value for the same signal. The VITA algorithm computes a short-term RMS value for a fluctuation signal (e.g. velocity, temperature, etc.) within a specified length of time. If the short-term RMS value is above a specified threshold with respect to the RMS value for the entire time series, then an ejection (or a burst) event is counted. The unique aspect of the VITA algorithm is that the characteristic large, positive velocity gradient does not occur when applying the algorithm to a random noise signal. It suggests that the VITA algorithm detects an event which is particular to turbulent wall flows, and this event has been generally assumed to be a burst. With the VITA algorithm, Chen and Blackwelder (1978) and Johansson and Alfredsson (1982) found that the results show two different events. One has a strong negative velocity gradient and the other has a strong positive gradient. Therefore, they added a slope condition to ensure only events with an accelerating streamwise velocity

component were counted. Without the slope condition, the resulting structure detected by the VITA algorithm may mix different types of events.

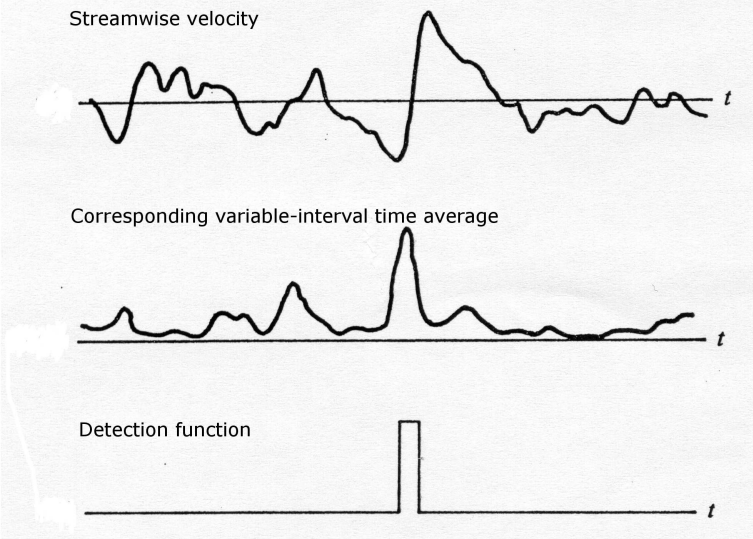

FIG. 2.8 – Illustration of VITA algorithm (Blackwelder and Kaplan (1976))

In addition to the most used algorithms (quadrant and VITA), many other algorithms exist. Rao *et al.* (1971) identified ejections as regions of energetic activity by using a band-pass filter to the streamwise velocity signal. Lu and Willmarth (1973) used a u-level algorithm. The u-level algorithm counts a burst when a fluctuation of streamwise velocity falls below a certain threshold with respect to the long-time RMS value. Rajagopalan and Antonia (1984) used a burst detection algorithm based on strong activity in the high frequency component of velocity. They found that the conditional average of this algorithm differed significantly from that obtained with the VITA algorithm. Zaric (1975) and Zaric (1982) focused on the low streamwise velocity region. They attempted to identify the ejections by searching out in the regions where the streamwise momentum was changing rapidly. Guezennec (1985) used a shear-stress detection method at the wall to identify bursts. When the fluctuation of streamwise shear stress ($\tau_x^{'}$) is greater than a given threshold ($+k_{\mathrm{X}}$) with respect to the long-term RMS ($\tau_{\mathrm{X}}^{'}$) a sweep motion is detected. Likewise when ($\tau_{\mathrm{X}}^{'} < -k_{\mathrm{X}}\ \tau_{x_{ms}}^{'}$) an ejection motion is counted.

Conditional averaging techniques were widely used to process the velocity signal in the studies mentioned above. Most of conditional average velocity signals always carry characteristics that can be directly related to the threshold used in the detection algorithm. For instance, the VITA algorithm is generally triggered by either a large positive or negative velocity gradient while it intends to measure periods of large variance in the velocity ; the quadrant algorithm has a large negative uv spike in its conditional average signals ; the high frequency velocity component detection has a high frequency oscillation in a conditional average signal. Consequently the reliability of these conditional averages is questionable, especially in the sense of being representative of the characteristics of an

ejection (or burst) event.

Different methods were used to solve this problem. Chen and Blackwelder (1978) and Subramanian *et al.* (1982) used temperature contaminated fluid in the wall region to improve the velocity based detection algorithms. They detected the fluid away from the wall by temperature difference as the wall was heated very slightly in their experiments. Conditional averages were calculated by detecting temperature fronts which had a sudden decrease in temperature and extended across the entire boundary layer. The resulting conditional average displayed a strong positive gradient similar to the VITA results. This algorithm has one disadvantage : no distinction can be made between ejections that are actively moving away from the wall and those which occurred further upstream. Bogard and Tiederman (1987b) used another method to overcome the drawback of the original conditional average method. In their study, discrete ejections from a burst event were identified using fluorescent-dye flow visualization. Simultaneous velocity measurements were made with a X-type hot film probe located at $y^+ = 15$. Conditional sampling of the velocity data was based on the flow visualization data series that were recorded when an ejection was in contact with the probe. Furthermore, the stage of growth of the ejection, and its position with respect to the velocity probe, were taken into account when the conditional-sampling analyses were carried out. Recently, PIV (and SPIV) technique was introduced to investigate the near wall turbulence (e.g. Adrian (1991), Carlier and Stanislas (2005), etc.). Similar to the method of Bogard and Tiederman (1987b), one can identify the coherent structures directly from the instantaneous velocity field obtained by PIV (or SPIV) experiments and perform the characteristic analysis on them.

Subramanian *et al.* (1982) have also made a comparison between the VITA and *uv* quadrant algorithms. They applied the VITA algorithm to the temperature signal in a slightly heated boundary layer (as mentioned above). The conditional averages of the *uv*-signal has a relatively small amplitude, which may be partly due to the low threshold used. The conditional averages obtained with the *uv*-quadrant algorithm and the VITA algorithm were found to differ considerably. They also made a study similar to that of Offen and Kline (1974) by using a rake consisting of 10 temperature-sensitive probes as their reference. When a temperature front was identified across the boundary layer an event was considered to occur. A X-type hot-film probe was used for the VITA and *uv*-quadrant detections, with the parameters modified to obtain the same number of events per unit time as with rake. The correspondence was generally found to be rather weak. At $y^+ = 40$, it was 42% for the VITA algorithm and only 15% for the uv-quadreant algorithm. This may be explained by the large spanwise separation between the rake and the X-type hot-film probe used to provide data in the experiment.

Alfredsson and Johansson (1984) compared the VITA and *uv* quadrant algorithms in a fully developed turbulent channel flow. Different from Subramanian *et al.* (1982), a close correspondence was found between VITA events and ejection type of events detected with the *uv*-quadrant algorithms. In contrast to the previous finding of double peak (Blackwelder and Kaplan (1976), Chen and Blackwelder (1978)), they found that the *uv*-pattern obtained with the VITA algorithm has only one peak. In contrast to the VITA results, conditional average obtained by Alfredsson and Johansson (1984) using the quadrant algorithm did not show an acceleration of the streamwise velocity to a value greater than

the mean velocity.

Bogard and Tiederman (1987a) performed a comparison of the effectiveness of the above-mentioned algorithms. They compare the results obtained from different algorithms based on the same data series recorded by a X-type hot-film probe in their flow visualization experiment. They found that the effectiveness of each of the detection algorithms was found to be highly dependent on the operational parameters (e.g. threshold level and averaging or window time, etc.). The results of their study suggested that the quadrant algorithm was the most reliable in the sense that it had a high probability of detecting real ejections and a low probability of detecting false ones.

Tubergen and G. (1993) compared not only all the previous mentioned algorithms but also their combinations. They suggest that the Zaric algorithm demonstrates better ejection detection but does not exhibit a region of threshold independence for ejections grouped into bursts. The best single-component ejection detector with threshold independence for bursts is the u-level algorithm. The two-components system combining of VITA and u-level, is the best overall ejection detector and also has a region of threshold independence for the bursting period.

2.2.3 Property and statistical characteristics

By using the above-mention algorithms, ejections and sweeps were investigated in many studies using different experimental methods or numerical simulations.

Grass (1971) using the hydrogen-bubble technique, studied visually and quantitatively the turbulent boundary layer in a free surface channel flow. His research mainly concentrated on surface roughness effects. Irrespective of wall roughness, he observed two well-defined flow events. These were ejections of low momentum fluid outwards and ′inrushes′ of high momentum fluid toward the wall (sweep). The measurements indicated that the process of turbulent energy production is intermittent and that it occurs through the contributions of both ejections and sweeps. Grass concluded that the contribution of the sweeps to the turbulent energy production was mainly limited to the wall region. The role of the ejections events extended to the outer region where very large positive contributions were measured.

Talmon *et al.* (1986) investigated the simultaneous flow visualization and Reynolds stress ($-\overline{u'v'}$) by a hydrogen bubble visualization experiment. They found ′dark spots′ that appear in the visualization of the low-speed streaks as an area where the hydrogen bubbles have disappeared. These dark spots appear at the centre line of the streak and are immediately pushed away by a high-speed region. This study showed that the contribution of these dark spots to the Reynolds stress is much larger than that of the instantaneous low or high-speed regions. They assumed that these spots, and therefore the streaks, are closely related to ejections. Wark and Nagib (1991) suggested a direct link between the space-time correlations and the quadrant-detected coherent structures. Specifically, the convection velocities inferred from both the long-time correlations and the conditional probability density functions were consistent. Jeong *et al.* (1997) carried out a numerical simulation in a turbulent channel flow. They concluded that a phase difference in space between streamwise and normal velocity fluctuations created by coherent

structure advection caused sweep (Q4) events to dominate ejection (Q2) events and also created counter-gradient Reynolds stresses (such as Q1 and Q3 events) above and below these coherent structures. Delo *et al.* (2004) evidenced that the ejection events are associated with the lift up of low speed streaks by using a volumetric imaging technique. They found that ejections of near-wall fluid appeared to be spatially organized and related to the passage of the large-scale agglomerations. Stoesser *et al.* (2005) carried out a large eddy simulation (LES) in an open channel flow over a layer of spheres. They evidenced not only the existence of ejections and sweeps but also the amalgamation process that leads to ejection of fluid into the outer layer associated with vortex growth.

Not only the existence of the ejection (or sweep) was evidenced, their statistical characteristics were also investigated by many researchers. Raupach (1981) found that sweep motions accounted for most of the Reynolds stress produced in the viscous sublayer, with ejections contributing more outside of the viscous sublayer. His results are consistent with those of Wallace *et al.* (1972) but inconsistent with the results of Lu and Willmarth (1973) for the sublayer region. Lu and Willmarth concluded that ejection motions were dominant for the entire region. As reported by them, 77% of the contribution to Reynolds shear stress $-\overline{u'v'}$ is by ejection motions and 55% from sweep motions. The excess over 100% explained by the negative Reynolds shear stress generated by the interaction between outward high speed flow (Q1 events) ($u'>0$ and $v'>0$) and inward low speed flow (Q3 event) ($u'<0$ and $v'<0$).

Corino and Brodkey (1969) estimated roughly that 70% of the positive Reynolds stress ($-u'v'$) could be attributed to the ejections and 30% by difference to the sweeps. More experimental findings, such as interactions between the events, frequency of occurrence and Reynolds number effects, can be found in Corino and Brodkey (1969). Wallace *et al.* (1972) found that ejections and sweeps generated approximately equal positive contributions to the Reynolds stress (70% from ejections 70% from sweeps), while each of wallward and outward interactions made a negative contribution of about 20% at $y^+ = 15$. Moreover, they suggested the values being a weak function of wall distance. By using hot-wire anemometry and conditional sampling techniques, Willmarth and Lu (1972) studied the structure of the Reynolds stress near the wall. Their results showed that 60% of the positive contribution to the Reynolds stress ($-\overline{u'v'}$) occurred when the sublayer velocity was less than the local mean. Positive contributions to the instantaneous $u'v'$, 62 times higher than the local mean average, were measured. According to them, the process of turbulent energy production in the wall region was intermittent and 99% of the contribution to $-\overline{u'v'}$ occurred during 55% of the total time. Carlier and Stanislas (2005) used a threshold in their quadrant-detection process. They found that ejections and sweeps occupy 25% of the experiment area and generate 85% of Reynolds shear stress $-\overline{u'v'}$.

Praturi and Brodkey (1978) studied a turbulent boundary layer flow by photographing the motions of small tracer particles using a stereoscopic medium speed camera system moving with the flow. He found that the ejections originated in a region $5 < y^+ < 30$ and travelled up to $y^+ = 100$ or more. In some rare cases, they can travel up to $y^+ = 300$. These ejections were small scale straight line motions. They moved at angles of 45°-90° to the wall as observed in the convected frame.

2.3 Vortices

In wall turbulence, vortices participate in the generation and preservation of wall turbulence by interaction with wall or with neighboring coherent structures. Among them, horseshoe and hairpin vortices are mostly discussed and studied. Many researchers have made great efforts on this topic using different experiments and numerical simulations.

2.3.1 Horseshoe and hairpin vortices

2.3.1.1 General introduction

Theodorsen (1952) was the first to suggest the existence of horseshoe vortices (Fig. 2.9) and the model of them in wall turbulence. He found that the perturbations of the spanwise vortex lines of the mean flow can be stretched by the shear into intensed hairpin vortices. His model is probably the simplest structural model but explains most of the features observed in wall turbulence. He proposed that hairpin (or horseshoe) vortices are the major momentum-transporting structures in shear turbulence. Theodorsen also proposed that a hairpin vortex is initiated by the instability of the instantaneous velocity profiles evolving into transverse vortices. These hairpin vortices were supposed to be tilted at about 45° downstream, mainly due to the stretching of the mean velocity gradient and to the mechanism of self-induction which lifts them up.

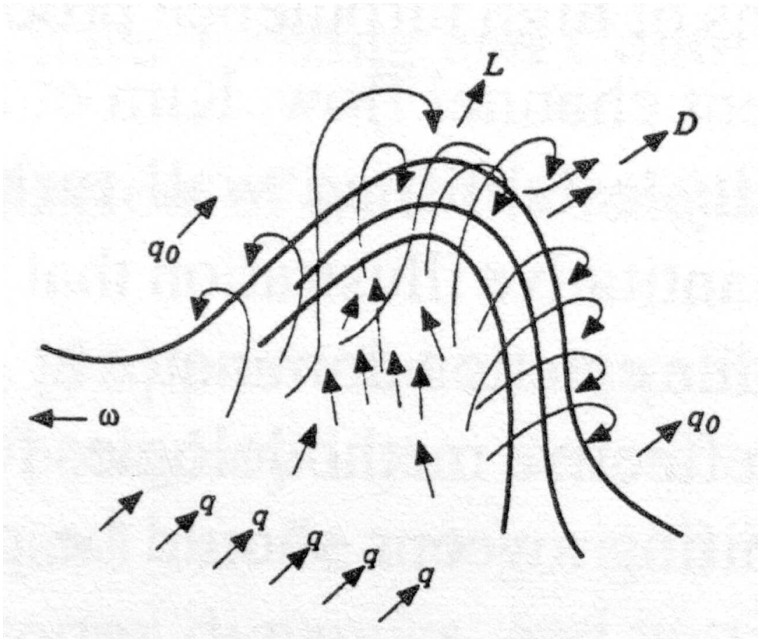

FIG. 2.9 – Illustration of horseshoe vortex (Theodorsen (1952))

Schubauer and Skramstad (1948), and Klebanoff *et al.* (1962), with the ′vibrating ribbon′ technique, introduced a two dimensional disturbance in the form of a spanwise

vortex varying harmonically in intensity with time in a boundary layer. Their results on the process of deformation of this spanwise vortex into so-called U-shape loop, are illustrated in Fig. 2.10. In the first stage, a straight vortex-line is assumed that has just been separated, in stage 2 the slight deformation in the streamwise-spanwise plane of the vortex causes a normal velocity component v as indicated by arrows. The top-part of the vortex is transported into a region of high velocity, the valley-part is transported into a low velocity region. This movement further produces a stretching effect in the streamwise direction of the U-shape loop as shown in stage 3. We thus see that streamwise components of the vortex develop, so that farther downstream eddies with axes inclined in the streamwise direction occur, forming pairs with opposite sign of vorticity. The U-shape loop is drifted away from the wall, with a velocity that is higher for the parts with greater curvature. Consequently the tip of the U-shaped loop has the highest velocity away from the wall (Fig. 2.11a). Arriving in region with increasing streamwise velocity, due to the accompanying stretching of the U-shape loop, the vorticity increases. Due to self-induction effect, the downstream tip of the vortex loop lifts away from the wall. Since it then arrives in a higher mean velocity region, the tip of the loop becomes more peaked due to a stretching effect. At the same time the local intensity of the streamwise and normal velocity components around the tip is strongly increased. This is caused primarily by the spanwise vorticity component of the vortex, which arises when the vortex tip drifts away from the wall. It induces a dent in the U-loop vortex near its tip, and deform the U-shape loop to the Ω shape. In both the plane view and the side view (Fig. 2.11b), the tip of the stretched u-loop takes a typical bottle neck or Ω shape, again due to self induction effects. Hama (1962) found a similar result by injecting dye at the wall in a turbulent shear flow.

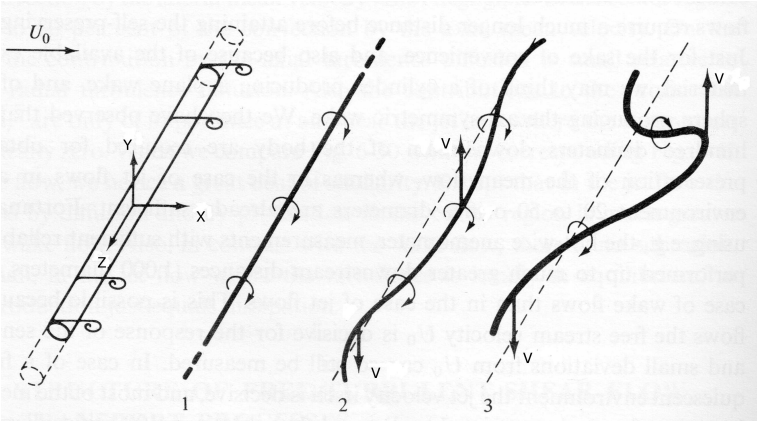

FIG. 2.10 – Illustration of U-loop vortex generation (Hinze (1975))

The flow visualizations of Nychas *et al.* (1973) were generally consistent with a hair-pin vortex picture, although they were interpreted somewhat differently. Nychas *et al.* (1973) recorded the trace of solid particles in a water flow, using a moving camera, and identified transverse vortices in the outer layer which were formed at the top of a shear

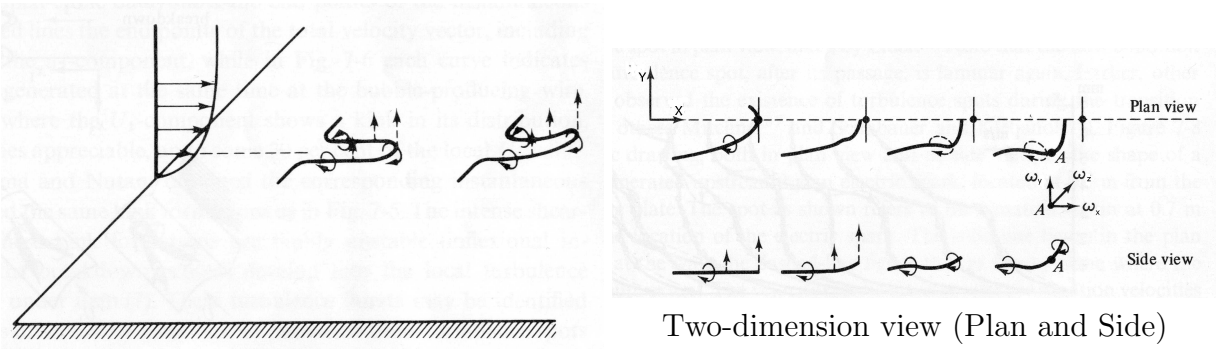

Three-dimension view

Two-dimension view (Plan and Side)

FIG. 2.11 – Illustration of deformation of a U-loop vortex to a Ω-shaped vortex, (Hinze (1975)

layer extending from the near-wall region to the outer region. They attributed the shear layer to low-speed fluid interacting with upstream high-speed fluid. They observed that the transverse vortices were not triggered by low-speed streaks, but as the result of the shear layer rolling up, instead of a pre-existing hairpin. This experiment also provided a connection between the transverse vortices and the unsteady events in the near-wall layer that are associated with the widely recognized bursting process.

Townsend (1976) found that the legs of horseshoe vortices would remain attached to the wall during their development. The mean spacing between these legs is about 100 wall units, but the aspect ratio of the horseshoe vortices is Reynolds number dependent (Head and Bandyopadhyay (1981)). Moreover, these eddy structures appear more elongated at higher Reynolds number and then are called hairpin vortices.

Smith (1984) extended the above mentioned Theodorsen's model and reported hydrogen bubble visualizations of hairpin loops at low Reynolds number, while a formation mechanism like Theodorsen's was evidenced in homogeneous shear flow (Rogers and Moin (1987) ; Adrian and Moin (1988)). However, Theodorsen's model must be modified in the strongly inhomogeneous region near a wall to include long quasi-streamwise vortices which are about 50 wall units apart and connected to the head of the hairpin by vortex necks inclined at roughly 45° to the wall (Robinson (1991),Robinson (1993)). Adrian (1991) performed a PIV experiment to examine the structure of wall turbulence in the streamwise wall-normal plane of a fully developed low-Reynolds-number channel flow. According to their results, shear layers which were inclined at angles of less than 45° from the wall can grow up from the wall. Regions containing high Reynolds stress were associated with the near-wall shear layers. Typically, these shear layers terminated in regions of rolled-up spanwise vorticity, which were explained to be the heads of hairpin vortices.

Robinson (1991) detected hairpin vortices using a pressure criteria in the direct numerical simulation result obtained by Spalart (1988) in a flat plate boundary layer. He noticed that these hairpin vortices generally appear more asymmetric than sketched in the literature, having more a cane shape (with two legs of different length) than the usual symmetric hairpin shape put forward by most previous authors. In recent years, asymmetric hairpins or 'cane′ vortices have been more commonly observed than symme-

tric hairpins (e.g. Guezennec *et al.* (1987), Robinson (1993), Jeong *et al.* (1997), etc). It should be noted that available evidence suggests that these structures (symmetric and asymmetric hairpin and horseshoe vortices) are variations of a common basic structure at different stages of evolution or in different surrounding flow environments.

Hairpin vortex generally travels in a group. This phenomena was first observed by Bandyopadhyay (1980) and Head and Bandyopadhyay (1981), in the flow visualization experiments on a zero-pressure-gradient boundary layer. Recently, more and more studies support this finding. Smith *et al.* (1991) showed that a single vortex of sufficient circulation could induced a trailing group of hairpins that are convected at the same speed as the leading structure. His results are confirmed by Zhou *et al.* (1999) who studied a low Reynolds number DNS datasets ($Re_\theta = 180$). Adrian *et al.* (2000), performed PIV experiments in streanwise-wall-normal plane of a zero-pressure-gradient boundary layer over a Reynolds number range of $930 < Re_\theta < 6845$. They observed that packets of hairpin vortex heads appear regularly in the viscous sublayer and logarithmic layers. Moreover, they found that 5 to 10 hairpins are united as a group moving at a uniform streamwise velocity. The length of the group can extend over 2δ. Christensen and Adrian (2001) performed a series of PIV experiments in streamwise-wall-normal plane of a turbulent channel flow at $Re_\tau = 547$ and 1734. Using linear stochastic estimation for the conditional average of the two-dimensional velocity field associated with swirling motion, they concluded that the mean structure consists of a series of swirling motions located along a line inclined at 12°-13° from the wall, which is consistent with the earlier observations of packets of hairpin vortices. Marusic (2001) investigated this phenomenon using the attached eddy model by calculating structure angles, two-point velocity correlations and autocorrelations and comparing them to experimental measurements across a zero-pressure-gradient turbulent boundary layer. His results showed that packets of eddies were required in order to match measured boundary layer turbulence statistics near the wall. Tomkins and Adrian (2003), using PIV measurements of streamwise-spanwise plane of a turbulent boundary layer in the logarithmic layer and beyond at $Re_\theta = 2500$, showed long low-streamwise-momentum zones enveloped by positive and negative vortex cores representing packets of hairpin structures. Delo *et al.* (2004) investigated zero pressure gradient incompressible turbulent boundary layer using a volumetric imaging technique in a low Reynolds number ($Re_\theta = 700$). They found a large scale behavior that is consistent with the statistical signature of hairpin vortex packets embedded within the flow. They also found multiple swirling motions inclined away from the wall and aligned in the streamwise direction.

2.3.1.2 Origin of hairpin vortices

Smith and Walker (1997) proposed a regeneration scenario in which parent hairpin vortices spawn offspring hairpins, both behind the head (or 'arch') (spanwise) and beside each of the legs (streamwise). In this scenario, vortex formation is driven by unsteady separation near the wall (Doligalski and Walker (1984)), in which the parent hairpin produces localized ejections near its head and legs. Then the resulting inflectional shear flow is rolled up by Kelvin-Helmholtz instability (Helmholtz (1868)) and gives birth to new hairpins. In contrast, Zhou *et al.* (1999) revealed that a sufficiently strong single hairpin can generate a packet of hairpin vortices in both upstream and downstream direction of

the parent hairpin. In this mechanism, first, the induction of the parent vortex generates intense local shear layers, composed predominantly of spanwise vorticity. Then, these shear layers roll up into arch vortices related with the existing streamwise-oriented legs. Finally, they are stretched by the mean shear into offspring hairpin vortices which is separated from the parent hairpin vortex. These observations are also consistent with the conditional-average initial condition studied by Kim *et al.* (1987), who emphasized the role of localized vorticity stretching above the parent legs in generating the offspring arch vortex.

2.3.2 Streamwise vortices

2.3.2.1 General introduction

Besides horseshoe and hairpin vortices, the streamwise vortices (Fig. 2.12) is also one of the principal elements of the turbulent sequence. The streamwise vortices has been observed and studied in the near-wall region by numerous researchers with different experiment and numerical methods.

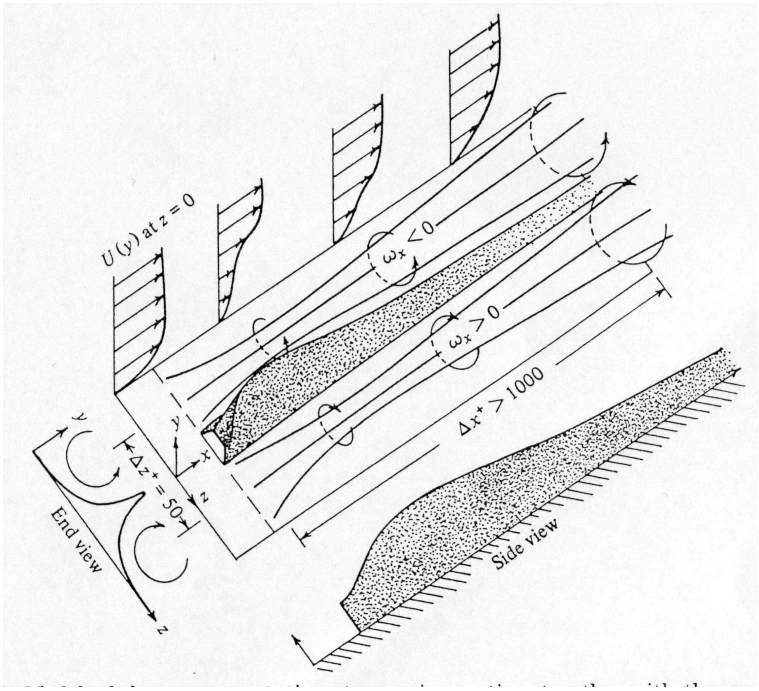

FIG. 2.12 – Illustation of streamwise vortex (Blackwelder and Kaplan (1976))

Bakewell and Lumley (1967) found pairs of counter rotation vortices which are considered as the eddy structures. These vortices consist of the largest amount of energy as observed by their proper orthogonal decomposition technique. Using hydrogen bubbles, Kim *et al.* (1971) observed a rotational motion near the wall which they interpreted as streamwise vortices. Blackwelder and Eckelmann (1979) found that the most probable

stress pattern on the wall was consistent with counter rotating streamwise vortices. Smith and Metzler (1983) filmed hydrogen bubbles in the cross plane near the wall and observed frequent counter rotating motions in the near wall region. Aubry *et al.* (1988) used a dynamical systems approach to study the behavior of streamwise vortices in the near-wall region of turbulent boundary layers. They were able to achieve a great reduction in the complexity of the observed flow by using a severely truncated modal decomposition and by considering only the region very near the wall. Most of the earlier results were obtained by assuming some symmetrical aspects of the flow or detection method, and consequently observed symmetrical vortices in the resulting average structures. More recently it has been pointed out that the symmetry was imposed by the observation method. Guezennec and Choi (1989) found that the streamwise vortices do not necessarily appear in pairs and rarely have the same amplitude.

2.3.2.2 Origin of streamwise vortices

Numerous theories (e.g. Bernard *et al.* (1993), Waleffe *et al.* (1993), Schoppa and Hussain (2002), etc.) concerning the generation of the streamwise vortices exist. Most of them can be classified into 5 groups : hairpin vortex related mechanism, streamwise vorticity (ω_{X}) sheet roll up, instability of curvature and shear stress near the wall, oblique mode theory and streak instability.

Hairpin vortex related mechanism

Many researchers related the streamwise vortices to the hairpin vortices. They suggest that streamwise vortices are the legs near the wall of the hairpin vortices or are secondary vortices in the trailing legs near the wall of these hairpin vortices. Therefore, the origin of streamwise vortices is the same as that for hairpin vortex which is already discussed above.

Streamwise vorticity (ω_{X}) sheet roll up

Brooke and Hanratty (1993) studied the spatio temporal velocity field from DNS data. They found that an opposite-signed offspring vortex forms immediately underneath a parent streamwise vortex due to the fact that no hairpin type vortices were found in the studied field. Brooke and Hanratty demonstrated that the production of offspring ω_{X} is dominated by the vorticity generation term -$(\partial w/\partial \mathrm{x})(\partial u/\partial \mathrm{y})$, where $\partial w/\partial \mathrm{x}$ (wall-normal vorticity ω_{Y}) is generated by the parent vortex inclination to the wall. Bernard *et al.* (1993) found similar results by identifying streamwise vortices in instantaneous velocity vector patterns (v, w) in successive spanwise-wall-normal planes. Moreover they suggest that new vortices tend to form from strong wall-normal vorticity ω_{Y}, typically on the sweep side of the parent vortex. Both of them proposed a scenario that streamwise vortices are generated by the roll-up of streamwise vorticity ω_{X} sheet by two-dimensional self-advection. Two distinct mechanisms of this roll up motion were proposed : dipole-like head-tail formation due to the wall image vorticity (Jimenez and Orlandi (1993) and lifting of the wall-generated streamwise vorticity ω_{X} (due to the no-slip condition) by a parent vortex, as in vortex wall-rebound (Orlandi (1990)). In all studies cited here a parent vortex is required. Schoppa and Hussain (1997) and Schoppa and Hussain (2002), however, showed that vortex can occur in the absence of a parent vortex. Unlike other researchers, they suggest that vortex generation does not involve streamwise vorticity generation at

the wall (by the no-slip condition) or vorticity layer roll up. Instead, the vortex generation is inherently three-dimensional, with direct stretching of near-wall streamwise vorticity ω_X sheets leading to streamwise vortex collapse.

Instability of curvature and shear stress near the wall

Streamwise vortices are also considered as a consequence of centrifugal and wave-shear instabilities near the wall. Brown and Thomas (2002) showed that the condition for Taylor-Gortler instability (sufficient concave curvature of near-wall streamlines) is locally satisfied above $y^+ \approx 50$. Phillips *et al.* (1996) studied a Craik-Leibovich instability mechanism with streamwise-dependent perturbation growth on shear flows with small-amplitude streamwise undulation. They obtained evidence of Craik-Leibovich-based streamwise vortex formation near a (rigid) wavy wall. They suggested that the vortex is locally representative of the fluctuating streamwise velocity field in near-wall turbulence. Even the induction by spanwise vortices can induce streamline curvature or streamwise waviness in flow field. It is not clear how the instability-generated streamwise vortices make their contribution to this process. Hence, the necessary feedback mechanism for successive episodes of instability and vortex generation is not apparent.

Oblique mode theory

Benney (1961) addressed the generation of streamwise-elongated regions of longitudinal vorticity as a mechanism of transition to small-scale turbulence. He increased the second-order perturbations by the nonlinear interaction of (initially unstable) primary oblique modes in his theoretical studies in the case of a mixing layer. Benney found that the generation of a streamwise-mean secondary flow is inherent to the nonlinear interaction of three-dimensional oblique modes. The secondary motion consists of four counter-rotating cells of longitudinal vorticity per spanwise-wavelength, which implies the generation of spanwise-alternating streamwise vortices. Different from Benney (1961), Schoppa and Hussain (2002) found that the linear growth can also produce nonlinear interactions. Jang *et al.* (1986) applied the ′Direct resonance′ approach of Benney and Gustavsson (1981) to the growth of coherent (wave) motion in triple flow decomposition into mean, coherent, and incoherent parts (Reynolds and Hussain (1981)). The direct resonance mechanism produced rapid growth of oblique wall-normal vorticity modes, but applied only to modes which satisfy a resonance condition, and thus provided a scale selectivity. These wall-normal vorticity modes can then interact non-linearly to form streamwise vortices and streaks of the correct spacing. Subsequently, however, Waleffe *et al.* (1993) examined direct resonance and noted that some non-resonant modes were amplified more than the resonant modes, eliminating any scale selection due to the resonance mechanism. Furthermore, they found that the creation of streamwise vortices by the interactions of oblique modes was dominated by the interactions of the wall-normal velocity modes, rather than the wall-normal vorticity modes as required for scale selection in the direct resonance theory.

Streak instability

Kline *et al.* (1967) studied low-speed fluids using flow visualization method. He observed spatial oscillations of local U(y) shear layers of the Kelvin-Helmholtz type, prior to a ′breakdown′ into smaller scales. Robinson (1991) investigated the evolution of instantaneous structures visualized via DNS. He proposed that lifted low-speed streaks, left

behind by (faster advecting) streamwise vortices, contain a locally unstable U(y) shear on the streak crest which then gives rise to new spanwise 'arch′ vortices. One 'leg′ of the arch is said to be stretched into a streamwise vortex, which in turn generates a new unstable streak in its wake to close the cycle. Accounting for the entire streak U(y, z) distribution instead of U(y), such a streak-crest U(y) instability mechanism conceptually corresponds to varicose modes, which exhibit a hairpin-type perturbation symmetry. As an alternative explanation of Robinson's observations, new spanwise 'arch′ vortices can form due to growth of sinuous disturbances, accompanied by generation of new streamwise vortices. In this scenario, an arch vortex is generated by rollup of an internal shear layer on the top of a streak, which links up with the downstream end of a nearby streamwise vortex due to the shear-induced collapse of the connecting vortex lines. Due to circulation pile-up inherent to vorticity layers of finite extent, vortex rollup commences at the tip of the internal shear layer, much like a wing-tip vortex. In this scenario, no perturbations are required for internal shear layer rollup, and hence the arch formation is not actually an instability process, although vorticity concentration by two-dimensional self-advection is similar to Kelvin-Helmholtz instability.

Swearingen and Blackwelder (1987) proposed an alternative streak instability mechanism. They analysed the streak ′breakdown′ induced by Gortler vortices and found a dominant sinuous mode of transition. From flow visualization and measurements revealing correlation of large fluctuation amplitudes with z inflections of U, they also inferred that turbulence production is caused by local, ′wake-like′ instability of the U(z) shear layers flanking low-speed streaks. Hall and Horseman (1991) and Yu and Liu (1991), also investigated streak U(y, z) distributions generated by Gortler vortices (nonlinear). They found that the growth rates of varicose modes are relatively small compared to the dominant sinuous modes even with exceedingly strong streak-crest U(y) shear. Furthermore, for streak U(y, z) distributions more representative of near-wall turbulence, varicose modes are found to be stable. Finally, the dominant varicose instability requires a formation of two-legged hairpin vortices which are indeed rarely found near the wall. Yu and Liu (1991) also revealed that Gortler U(y, z) streak distributions, representative of the Swearingen and Blackwelder experiments, are in fact unstable to (predominant) sinuous modes. Applying the 'minimal flow unit′ concept of Jimenez and Moin (1991) to plane Couette flow, Hamilton *et al.* (1995) studied vortex regeneration. They observed an interesting cyclic flow evolution and identified a three-step closed cycle : (i) streak formation by streamwise vortices, (ii) streak 'breakdown′ via (normal-mode) sinuous instability, and (iii) 'regeneration′ of streamwise vortices due to nonlinear interactions in the post-breakdown flow.

Even with these theory, the origin of the streamwise vortices is still not clear and is one of the remaining mysteries of near wall flows, and many other questions still remain (e.g. the evolution of them in different directions, interaction with other structures...).

2.3.3 Statistical characteristics

These streamwise vortices inhabit the near wall region and appear randomly in space and time. They have diameters ranging from 10 to 40 wall units and are centred at 10 to

50 wall units from the wall. There has been considerable speculation that they may be associated with other vortex layer. Based on the conditional analysis of hot-film signals, Blackwelder and Eckelmann (1979) inferred that streamwise vortices evolve by counter-rotating pairs near the wall. As shown in Fig. 2.12, their centres are located at about 25 wall units from the wall which agrees well with the result of early researchers (Gupta *et al.* (1971), Lee *et al.* (1974) and Kreplin (1976)). Blackwelder and Eckelmann also found that these vortices are separated by 50 to 100 wall units in the transverse direction, and that their radius is about 15 wall units and their length of the order of 200 wall units. Kim *et al.* (1987) found nearly the same sizes by the analysis of the vorticity fluctuation profiles in a DNS of a turbulent channel flow.

2.4 Organization of coherent structures

The first detailed description of organization and self-sustaining mechanism of coherent structures was proposed by Theodorsen (1952) (Fig. 2.9). According to his theory, the instability of the streamwise instantaneous velocity profiles is supposed to be the source of creation of transverse vortices. Under the action of the mean velocity gradient and 3D character of the flow, these transverse vortices evolve rapidly into deformed vortex tubes, looking like streamwise or hairpin vortices. Both vortical structures explain the formation of the low speed streaks close to the wall. These low speed streaks seem to be at the origin of the above-mentioned instability, through the ejection (or burst) process which generally consists of several ejections (and vortices) and is responsible for the mass transfer away from the wall. This outward mass transfer is necessarily compensated by sweep motions toward the wall. The result of these two events occurring close to the wall is a strong production of turbulence in this region. This wall generated turbulence is then diffused away and dissipated slowly in the turbulent bulges. In the concept of a regeneration cycle of turbulence, the production of new vortical structures is presently attributed either to the instability of the instantaneous velocity profile due to the streaks or to an induction mechanism by the already existing vortices. Some authors invoke both mechanisms. At low Reynolds number, Jimenez and Pinelli (1999) have shown by DNS that the self-sustaining of wall turbulence appears to be local to the near-wall region and does not depend strongly on the outer part. Essentially, it involves vortical structures (which play a central role), low speed streaks and ejections. It is still unclear whether this is also true with a high Reynolds number.

Hinze (1975) suggested that a $'$cyclic$'$ process with a distinct and recognizable average spacing in both spanwise and streamwise direction is repeated randomly in turbulent boundary layer (Fig. 2.13). He found that many features of this process are similar to the laminar-turbulent transition process. Therefore he suggested that the $'$cyclic$'$ process starts with a horseshoe-shaped vortex which is beginning to be formed locally at the wall due to a large-scale disturbance present in the outer region and outer part of the wall region. This vortex is firstly deformed by the flow into a more and more elongated U-shaped loop in the streamwise direction. Afterward, due to the self-induction process, the tip of the loop moves away from the wall and then enters into regions with high streamwise velocity. Consequently the vorticity increases due to stretching processes. At the same time, an outward flow which has a strong normal velocity near the tip, appears between the legs of the U-loop. Between the vortex and the wall, a local deceleration of the fluid is effected. This outflow transports low-momentum fluid away from the wall, thus producing a positive and considerable contribution to the shear stress. Moreover, at distances $x^+ = 5$ to 30, an intense horizontal shear-layer is formed, showing up in the instantaneous velocity profile of the u component as a dent with inflection points. The resulting local inflectional instability and breakdown of the flow surrounding the original tip of the vortex produces a turbulence burst. The pressure waves associated with the turbulence burst are propagated through the whole boundary layer. The fluid with high turbulence intensity produced during the burst is convected downstream and moves farther away from the wall. Since at the same time high-momentum fluid is entering from upstream, the above fluid

is convected in an accelerated flow or swept in downstream direction. The above pressure waves may add themselves to the movement of fluid toward the wall, resulting in a sweep-inrush flow. The inrush process has already been proceeded and initiated by a negative normal velocity downstream of the tip of the U-shaped loop before its breakdown. The sweep inrush flow makes a very small angle (5°-10°) with the wall, which is also observed as the entry of higher momentum fluid in almost horizontal direction at the wall. Both the ejection burst process and the sweep inrush flow contribute to the generation of shear stress, and then are responsible for the turbulence production, mainly in the region y^+ = 10 to 15 from the wall. The horizontal movement during the sweep inrush period will be strongly retarded near the wall. It may eventually, in conjunction with the action of overtaking faster moving fluid at the greater distance from the wall, develop into another horseshoe-type vortex.

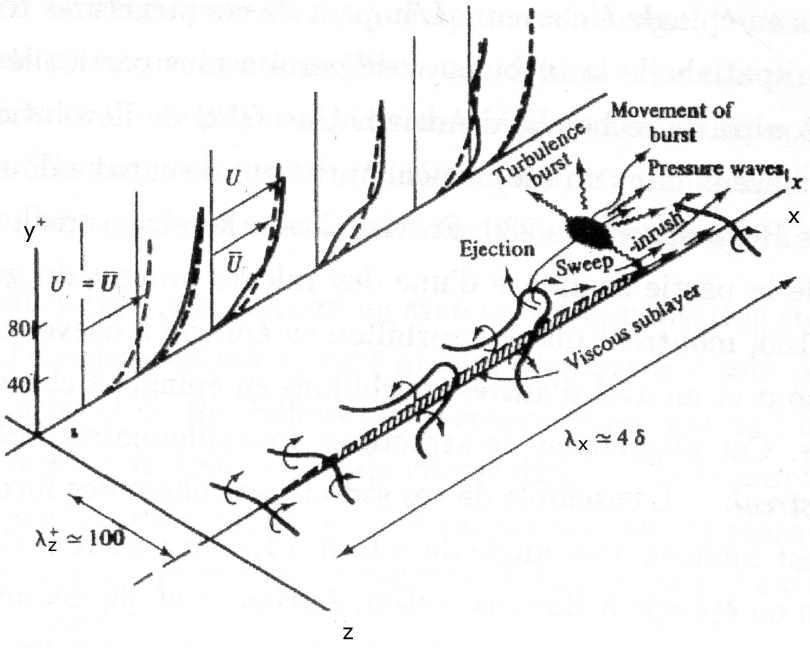

FIG. 2.13 – Organization model of Hinze (1975) in near wall turbulence

Smith and Walker (1997) (see Panton (1997)), based on the results of the early studies from their group, found that hairpin vortices in a shear flow are able to interact with other three-dimensional vortices to yield larger-scale flow structures, and regenerate new vortices through an interaction with the viscous wall layer. Smith and Walker suggested that hairpin vortex deformation is the key element and plays a central role. Based on the summary of their study and also early studies of other researchers, Smith and Walker summarized the key aspects of coherent structures in the near wall region and proposed a model of organization and self-sustain of coherent structures. This model show how vortex interactions sustain the development, evolution, and maintenance of a turbulent boundary layer (Fig. 2.14)

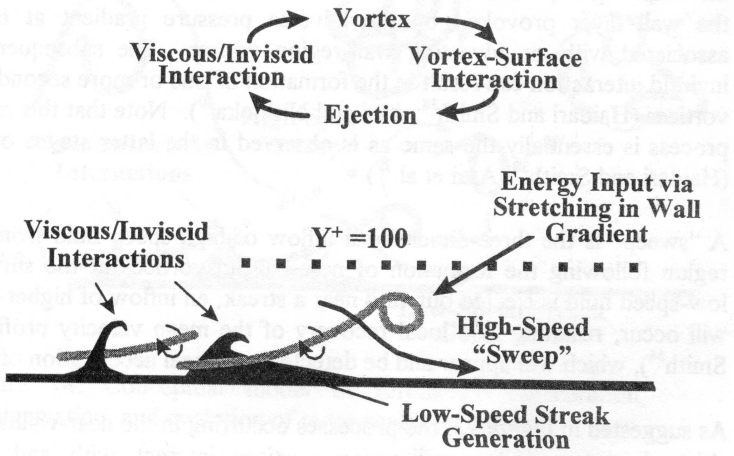

FIG. 2.14 – Organization model of Smith and Walker (1997) in near wall turbulence

The model starts from a hairpin vortex in the wall region. The evolution of the hairpin vortex near the wall can induce low speed streaks. Depending on the strength of the original vortex, an alternative process occurs. If the original vortex is sufficiently strong or close enough to the wall, a burst may occur as a result of the sustained action of the hairpin vortex in the wall layer. The process is reflected as a local viscous-inviscid interaction that initiates close to the streak, appears to destabilize it, and culminates in the ejection of a portion of the streak and secondary vorticity into the out region. If original vortex is relatively weak and close enough to the wall, it can cause a streak to form. In this case, the vortex action may be insufficient to precipitate a local wall-layer breakdown. Then, a streak will either diffuse or be overrun by so-called ′subsequent impinging′ hairpin vortices (generated independently upstream). The ′subsequent impinging′ vortices will create the appearance of waviness and swaying which is a commonly observed behaviour for visualized low-speed streaks. Action by subsequent hairpin vortices can either refocus or buffet the original streak. A refocusing can cause the original streak to grow further (possibly combination or amalgamation with other adjacent streaks), and then a subsequent breakdown is possible. Therefore, no matter the strength of the original vortex, a breakdown process will occur. This breakdown can lead to a so-called ′burst′ phenomena with ejection of wall-layer fluid in proximity to a low-speed streak into the outer region. Moreover, this breakdown constitutes a localized unsteady separation of the wall layer provoked by the adverse pressure gradient at the surface associated with an advection wall-region vortex. The subsequent viscous inviscid interaction can result in the formation of one or more secondary hairpin vortices (Haidari and R. (1994), Asai *et al.* (1996)). This regenerative process is essentially the same as is observed in the latter stages of transition (Haidari and R. (1994)). When low speed fluid is ejected outward near a streak, an inflow of high speed fluid (sweep) will occur to recover the mean velocity profile (Lu and Smith (1991)) which will appear and be detected as a local acceleration of the flow. As shown in Fig. 2.14 , the processes occurring in the near-wall are cyclical, although not periodic, wall-region vor-

tices interact with and cause ejections of wall-region fluid, which subsequently roll up to form new vortices by a viscous-inviscid interaction with the high speed, outer-region fluid. This process defines a continuing cycle which contains both the elements which sustain turbulence (three dimensional vortices) and the process for regeneration (viscous-inviscid interactions).

Adrian *et al.* (2000) combined their own results and that from Zhou *et al.* (1999) and proposed an idealized model of the organization and mechanism of wall turbulence based on the hairpin packet theory (Fig. 2.15). In this model, hairpin packets originate at the wall from a disturbance whose character is not specified except that it creates a pool of low momentum at the wall (e.g. ejection) from another hairpin, a random pressure fluctuation, or a culmination of flow induced by surrounding events such as wall tangent flows that converge to a stagnation point and then erupt upwards. First, the primary hairpin is formed. Then, it is stretched and intensified by the difference between the streamwise velocity at its legs and its head, and grows continuously in time, changing from a hairpin-shape to an omega-shape. If its strength is sufficient, it generates a new upstream hairpin by inducing a strong, three-dimensional ejection event that interacts with high-speed fluid behind the primary hairpin. The secondary hairpin increases in size with time. After a certain time, the secondary hairpin begins to create a tertiary hairpin. Besides the secondary upstream hairpin, the primary hairpin is also capable to generate a new hairpin downstream, and even this hairpin may generate others (Zhou *et al.* (1999)). The model implies that turbulence structures arise at the wall, and grow by continuous straining of the hairpins, coupled with induction interactions within the hairpin vortex packet. However, lack of information about interactions of these packet is a weakness of this model.

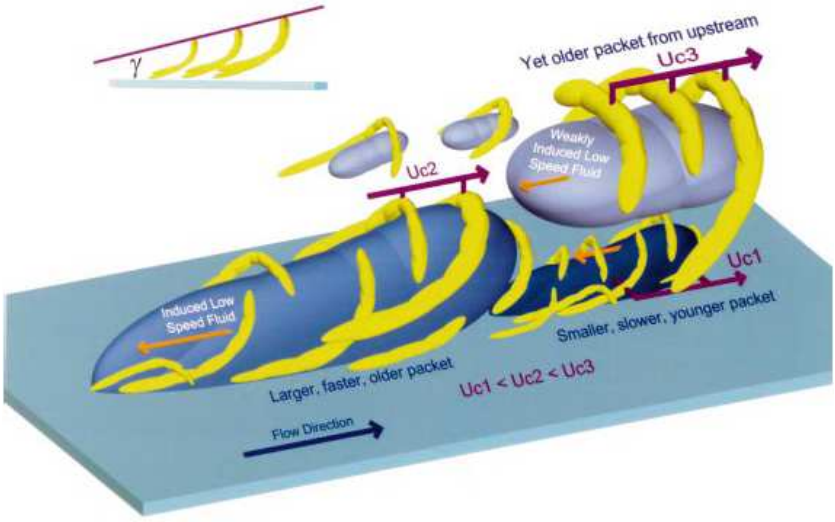

FIG. 2.15 – Organization model of Adrian *et al.* (2000) in near wall turbulence, U_{c1}, U_{c2} and U_{c3} are the convection velocities of each hairpin packet respectively

Chapitre 3

PIV Processing

3.1 PIV and SPIV

3.1.1 Introduction

PIV is a quantitative, non-intrusive method for the measurement of fluid velocity in large areas. For the last 15 years, due to the strong improvement of laser, video camera and computer, PIV has undergone major developments and has become a powerful technique to investigate fluid mechanics (e.g. Adrian (1991), Westerweel (1997), Raffel *et al.* (1995), Foucaut *et al.* (2004a), etc.). The conventional implementation of PIV uses only one camera to record the motion of small tracer particles in a thin light sheet. By using such a configuration, only two in-plane components of the fluid velocity can be obtained in the plane of observation. The two components provide a wealth of information for many flows, however it is sometimes rather difficult to understand the true physical significance of the observed flow phenomena without the third component. This is particularly true in turbulence. Therefore, it is necessary to measure all three components of the velocity in order to understand the organization of flow. Moreover, the out of plane component can introduce errors due to the optical projection (Lourenco (1986)). Stereoscopic PIV have been developed to resolve these problems (Prasad and Adrian (1993)). In SPIV, a stereoscopic camera system is used, in which the motion of the tracer particles is viewed from two different directions. Due to the out of plane motion, the two cameras see the tracer particles travel over slightly different distances. From the differences in the apparent in-plane motion it is possible to reconstruct all three components of the displacement. In the past decade, this method has been well developed and applied by a number of researchers (e.g. Prasad and Adrian (1993), Soloff *et al.* (1997), Willert (1997), Westerweel and van Oord (1999), Coudert and Schon (2001), etc.). It has been shown that the SPIV method can reach as good an accuracy as standard PIV (Pérenne *et al.* (2004)). However, the assessment of turbulence statistics with this technique has not been characterized in detail. In this chapter, the details of different methods for processing SPIV images are discussed and applied to near wall turbulence.

3.1.2 Stereoscopic PIV algorithms

Besides the pinhole model (Wieneke (2005)) that was not tested in the present study, three main algorithms are presently available to process SPIV images : Vector Warping (Coudert and Schon (2001)), Image Mapping (Coudert and Schon (2001)) and the Soloff technique (Soloff *et al.* (1997)). These three methods are detailed in Pérenne *et al.* (2004) and are summarized in the flowchart in Fig. 3.1.

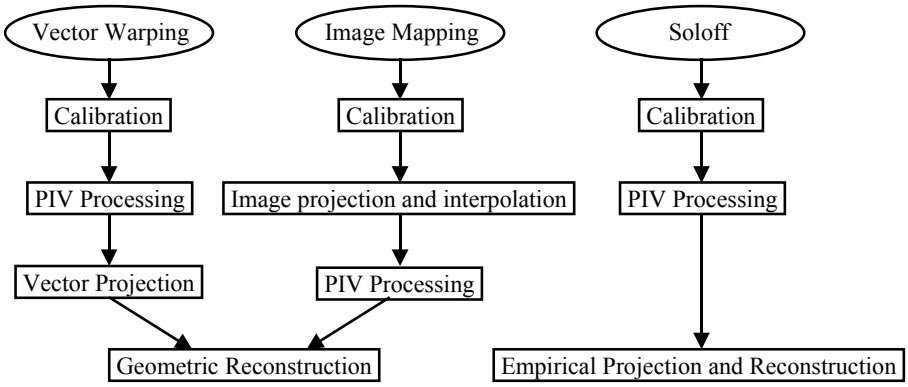

FIG. 3.1 – Flowchart of Vector Warping, Image Mapping and Soloff method

3.1.2.1 Vector Warping and Image Mapping methods

Empirical back projection

To process SPIV measurements, one needs to build an accurate relationship between the image plane of each camera and the object space. This is referred to as back-projection. The function for this relationship is usually generated empirically by using a calibration grid. It allows to map each point of the image plane onto the corresponding point in the object space, which corresponds to the measurement point. The perspective back-projection function was proposed by Raffel *et al.* (1995) as a ratio of second order polynomial. In general, a least square fit between a large number of couples (object-image points) is used to determine the coefficients of this function. Except for the variations in the analytical form, this procedure is considered as standard. Recently, Fei and Merzkirch (2004) proposed a third order polynomial function in order to increase the accuracy of this projection. In the present study, a ratio of second order polynomial was chosen (Raffel *et al.* (1995)). This polynomial method allows to take into account some optical distortion. In addition to its higher order (at least equivalent to fourth order), the ratio of polynomial function is based on an analytical projection function that takes into account the perspective effect of the Scheimpflug deformations. Both Vector Warping and Image Mapping use the empirical back projection to project the vectors and images respectively into the object space. Both methods use the geometric reconstruction to obtain the 2D3C velocity fields (Willert (1997)). However, the procedures of the two methods are different and described in detail below.

Vector Warping

A uniform mesh is firstly generated in the object plane and projected to obtain a deformed mesh in each camera image plane. This eliminates the need for any vector interpolation processing during the reconstruction process. On each point of the deformed mesh, the 2D2C-vector field is then calculated by using a standard PIV processing for each camera. After this processing the two vector fields are back projected into the object space. The velocity vectors of each camera are referenced at the same point of the initial uniform mesh. Finally, a geometrical reconstruction method is applied to obtain a 2D3C-vector field from the 2D2C-vector fields from each camera (Eq. 3.1-3.2) :

$$\begin{aligned} U &= \frac{U_1 tan\alpha_2 - U_2 tan\alpha_1}{tan\alpha_2 - tan\alpha_1} \\ V &= \frac{U_2 - U_1}{tan\alpha_2 - tan\alpha_1} \\ W &= \frac{1}{2}(W1 + W2 + (U_2 - U_1)\frac{tan\beta_1 - tan\beta_2}{tan\alpha_1 - tan\alpha_2}) \\ &\text{with} \end{aligned} \tag{3.1}$$

$$tan\alpha_1 = \frac{X_1 - \mathrm{x}}{\mathrm{y} - Y_1} \quad tan\alpha_1 = \frac{X_2 - \mathrm{x}}{\mathrm{y} - Y_2}$$

$$tan\beta_1 = \frac{Z_1 - \mathrm{x}}{\mathrm{y} - Y_1} \quad tan\beta_1 = \frac{Z_2 - \mathrm{x}}{\mathrm{y} - Y_2} \tag{3.2}$$

The coordinate system for reconstruction is presented in Fig. 3.2. U, V and W are the resulting three velocity components after reconstruction along the X, Y and Z coordinates axis respectively. *U1* and *W1* refer to the two in-plane components obtained by 2D2C analysis from camera #1 while *U2* and *W2* are obtained from camera #2. (X_1, Y_1, Z_1) and (X_2, Y_2, Z_2) are the positions of the lenses of camera #0 and camera #1 respectively in the object space while (x, y, z) is the position of the measurement point.

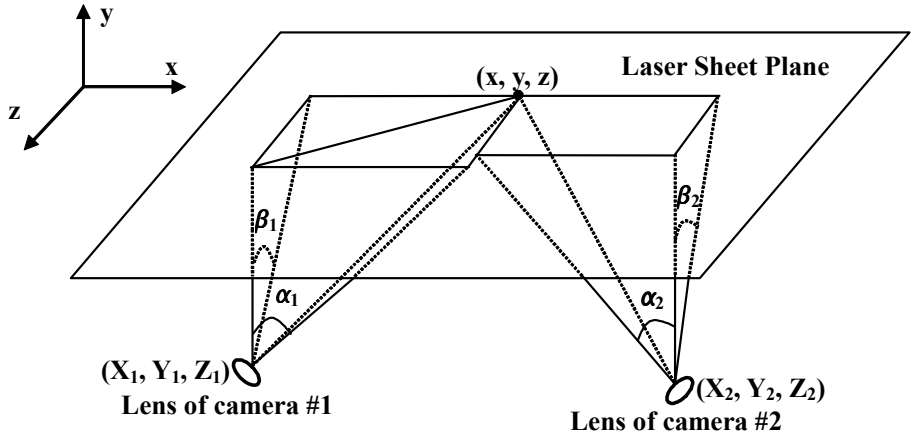

FIG. 3.2 – Reconstruction in a stereoscopic PIV configuration

Image Mapping

The recorded PIV images are firstly back-projected, or 'mapped', to the object space pixel by pixel and interpolated on a new regular grid. The fields of 2D2C vectors are then calculated directly from these images by using standard PIV processing on a common regular grid. Subsequently, the geometric reconstruction method is used to obtain a 2D3C-vector field from two 2D2C-vector fields as with the vector warping method. The same reconstruction process is used for both methods. It should be mentioned that for both image mapping and vector warping, the geometrical reconstruction needs the value of some geometrical parameters (such as the position of the lens, see Eq. 3.2), which are difficult to measure accurately on the experimental setup.

3.1.2.2 Soloff method

Optical distortion due to inaccurate optical alignment, lens non-linearity, refraction by optical windows, fluid interfaces and other optical elements of an experiment can generate inaccuracy by introducing spatial variations of magnification. It is important to compensate for these distortions because fractional changes in the magnification have a one-to-one effect on the accuracy of the measured velocity. Soloff *et al.* (1997) introduced a general empirical calibration procedure, which allows to obtain a specific matrix of the distorted imaging system, and an algorithm to accurately compute the velocity fields from measurements of distorted PIV images. From the calibration that is made by recording several images of a target, Soloff *et al.* (1997) proposed to optimize a mathematical formalism that combines the projection and the reconstruction (Eq. 3.3).

$$\begin{Bmatrix} \overline{\Delta X_1^1} \\ \overline{\Delta X_2^1} \\ \overline{\Delta X_1^2} \\ \overline{\Delta X_2^2} \end{Bmatrix} = \begin{Bmatrix} F_{1,1}^1 & F_{1,2}^1 & F_{1,3}^1 \\ F_{2,1}^1 & F_{2,2}^1 & F_{2,3}^1 \\ F_{1,1}^2 & F_{1,2}^2 & F_{1,3}^2 \\ F_{2,1}^2 & F_{2,2}^2 & F_{2,3}^2 \end{Bmatrix} \begin{Bmatrix} \overline{\Delta \mathrm{x}_1} \\ \overline{\Delta \mathrm{x}_2} \\ \overline{\Delta \mathrm{x}_3} \end{Bmatrix} \tag{3.3}$$

Here, the superscripts 1 and 2 indicate the left and right camera respectively. $\overline{\Delta X}$ is the displacement in the image plane (two-dimensions) and $\overline{\Delta \mathrm{x}}$ is the displacement in the object plane (three-dimension). F refers to the corresponding mapping function. The subscripts 1 and 2 represent the two in-plane displacements while the subscripts 3 stands for the out-of-plane displacement. The Soloff method is based on a third order polynomial function for the in-plane components and a second order one for the out-of-plane component. At least two target images (with an accurately known spacing) are necessary to calibrate the Soloff method. In this study, three or five target images were used.

3.1.2.3 Comparison of the three methods

The main difference among the three methods is that the Soloff technique uses empirical optical projection and reconstruction while Vector Warping and Image Mapping use empirical optical projection but geometrical reconstruction. Considering Vector Warping and Image Mapping only, Vector Warping projects the vectors and Image Mapping

interpolates images. Fig. 3.2 shows the flowchart of the three methods. The drawback of the Warping or Soloff methods is that the PIV analysis is conducted in the image plane, which leads to a local magnification that is not the same along the field. The interrogation window, which has a constant size in pixel in the image plane, then varies in size in the object space. On the contrary, the mapping method projects the images in the object space, making the magnification constant, but it distorts the particle images and introduces interpolation errors.

3.1.2.4 Calibration and correction of positions of the image planes

Calibration is a way to determine the relationship between the position in the object space and that in the image plane. For this purpose, it is necessary to acquire images of a calibration target whose location in the object space is known. By using these calibration targets, a generalized function to project the data from the image plane onto the object space can be found. According to the literature, a second-order polynomial (Westerweel and van Oord (1999)) and a second-order ration of polynomial (Willert (1997)) were used for a 2D calibration while a cubic and a quadratic polynomial (Soloff *et al.* (1997)) and bicubic splines (Lawson and Wu (1997)) were developed for a 3D calibration. In an experiment, however, it is difficult to make the position of the light sheet and the calibration plane exactly the same. There are always small offsets and tilts between calibration and measurement planes. Coudert and Schon (2001) proposed a method to correct the offset and tilt between them. The method works as follows. A set of single exposure PIV images from each camera recorded at the same time is firstly back projected as in the mapping method. A standard PIV processing is then used to calculate the displacement fields of the particle images illuminated at the same time by the same laser pulse. If the measurement and the calibration planes are perfectly superimposed, the mean displacement is zero (computed from about 50 vector fields). Normally one can observe a small displacement from which an offset and tilt between the calibration and measurement planes can be deduced. Following that, a correction procedure is carried out to improve the projection function.

3.2 Experiment description

3.2.1 Wind tunnel

The experiment was carried out in a boundary layer wind tunnel (Carlier (2001)) (Fig 3.3). This wind tunnel is 1x2 m^2 in cross section and 21.6 m in length. In order to use optical methods, the last 5 m of the working section are transparent on all sides. An air-water heat exchanger is located in the plenum chamber to keep the temperature within ± 0.2 °C. The turbulent boundary layer is studied on the bottom wall of the wind tunnel test section. This flow presents a tiny longitudinal pressure gradient which is negligible and has no effect on the near wall turbulence. The Reynolds number based on the momentum thickness Re_θ can reach 20600 with a boundary layer thickness δ of about 0.3 m. The external velocity in the testing zone of the wind tunnel can vary from 0 to 10 m/s with a

stability better than 0.5%.

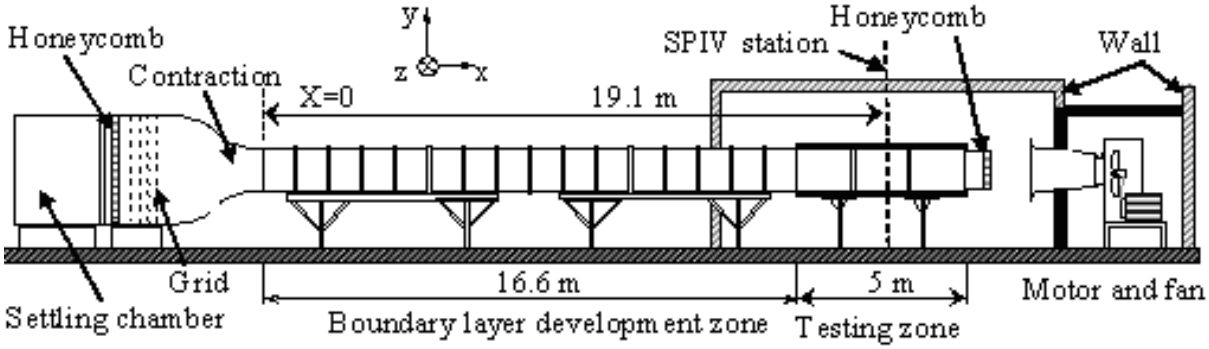

FIG. 3.3 – Front view of the turbulent boundary layer wind tunnel

3.2.2 SPIV setup

The purpose of the experiment was to obtain 3C velocity fields in planes parallel to the wall of a boundary layer, as close as possible to the wall. A Nd-YAG pulsed laser, with 2x250 mJ of energy at 15 Hz, was used to generate the light sheet. This light sheet was shaped using a conventional optical set-up (one sperical and one cylindrical lens) with a thickness of about 0.75 mm. The light sheet passed through a lateral window located 1 m away from the measurement area. Two PCO SENSICAM cameras (1280*1024 Pixel^2) were positioned under the wind tunnel as shown in Fig. 3.3. The cameras were set with the Scheimpflug conditions (Willert (1997)). The H and L parameters defined in Fig. 3.4 are : H $\cong$ 52 cm and L $\cong$ 50 cm. These distances, which are necessary for the geometrical reconstruction, are measured with respect to the centre of the field of view. The line joining the two cameras is parallel to the main flow (camera #1 being upstream). The flow is from left to right in the images delivered by both cameras. The light sheet propagates in the test section along z. Both cameras stand on the same ground under the wind tunnel upstream and downstream of the light sheet in order to obtain symmetric light scattering conditions. The focal length of the camera lenses was 105 mm. The field of view extends over 6.5x4.0 cm^2 and $f_{\#}$ = 5.6 is used for both cameras during the experiments. The average magnification is approximately 50 μm/pixel in the object space. The depth of field is 3.5 mm. The focus was set at the middle value of the explored y domain and kept there for the remainder of the experiment (including the acquisition of calibration images). The experiments were performed at U = 3 m/s (free stream velocity). With this velocity, the Reynolds number Re_θ , based on the momentum thickness, is 7800. The friction velocity u_τ is of the order of 0.12 m/s. A wall unit ($\Delta y^+ = 1$) is 0.125 mm. Ten planes parallel to the wall were characterized. A total of 500 image pairs in each plane were recorded for each camera. The first plane was placed as near as possible to the wall while avoiding too much reflections. The spacing between two neighbouring planes was about 4 wall units.

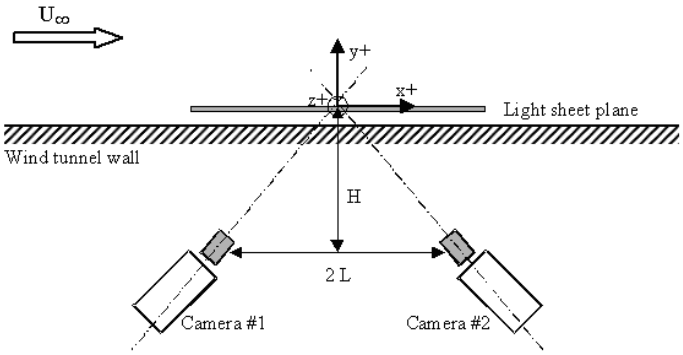

FIG. 3.4 – Setup of the experiment and frame of reference for data analysis

In this experiment, the airy disk diameter is about 8.2 μm, which gives a size of the order of 1.6 pixel according to the theory of Adrian (Adrian (1991)). In order to measure this size more precisely, the auto-correlation of the particle image was calculated. Fig. 3.5 shows the PDF of the particle image size. In this figure, σ_{sp} and σ_{st} are the standard deviations of the particle image size in the streamwise and spanwise direction respectively. The curves follow nearly a Gaussian distribution. In the present study, two times standard deviation is used as the particle image size. Therefore, the particle image size is about 1.5 pixels and 1.3 pixels in the streamwise and spanwise direction respectively. This slight anisotropy is attributed to the stereoscopic distortion. As the particle is considered as a sphere, the average diameter is about 1.4 pixels.

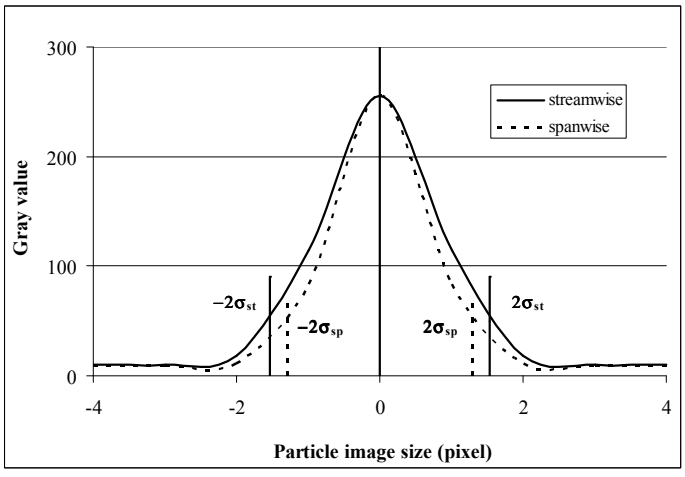

FIG. 3.5 – PDF of the particle image size

3.3 SPIV processing

3.3.1 Method definition

As mentioned above, various methods including Image Mapping, Vector Warping and Soloff are available to obtain 2D3C results from SPIV. For each method, there are also several different choices of tools or parameters. Therefore, it is necessary to select one method with the best set of parameters for computation. In this section, the image number 10 of plane 5 was used in the first step to make a comparison of the instantaneous velocity fields provided by the different processing choices. Then, a statistical comparison was conducted using PDFs and spectra computed on the first 100 images of the plane 5.

The following methods were compared : Image Mapping with Surfacial (Ursenbacher (2000)) or Whittaker (Scarano and Riethmuller (2000)) method to interpolate the image, Vector Warping and Soloff. For each method, the PIV analysis was performed with Integer and sub-pixel Whittaker shift. In the case of Soloff, 3 and 5 calibration planes were taken. Table 3.1 lists the details of the methods and their abbreviations used in this paper. For all the methods, a three-step multi-grid approach was employed (window sizes : 64*64, 32*32 and 32*32 pixel^2).

Short name	Method	Specialty	Shift method
MSI	Image Mapping	Surfacial interpolation	Integer shift
MSW	Image Mapping	Surfacial interpolation	Whittaker shift
MWI	Image Mapping	Whittaker interpolation	Integer shift
MWW	Image mapping	Whittaker interpolation	Whittaker shift
S3I	Soloff	3 calibration planes	Integer shift
S3W	Soloff	3 calibration planes	Whittaker shift
S5I	Soloff	5 calibration planes	Integer shift
S5W	Soloff	5 calibration planes	Whittaker shift
WI	Vector Warping		Integer shift
WW	Vector Warping		Whittaker shift

Tab. 3.1 – Methods description

As described earlier, calibration and its correction should be carried out before PIV processing. In the present study, 60 pairs of the first images of camera #1 and camera #2 are sufficient to calculate the average offset and tilt between calibration and measurement planes with a good convergence. By taking this value into account, the projection functions were corrected and the real position of the light sheet was determined (see Table 3.2). Fig. 3.6 shows the misalignment error between calibration plane 7 and laser plane 5 as an example. The vectors in Fig. 3.6 are quite constant, which means that the calibration and measurement planes are nearly parallel. The mean displacement in Fig. 3.6 is 0.58 mm, which implies a separation between calibration plane 7 and laser plane 5 of about 0.29 mm in depth (as the Scheimpflug conditions was used). This distance is taken into account in the correction process (Coudert and Schon (2001)). The gain in accuracy provided by the correction will be discussed further downstream.

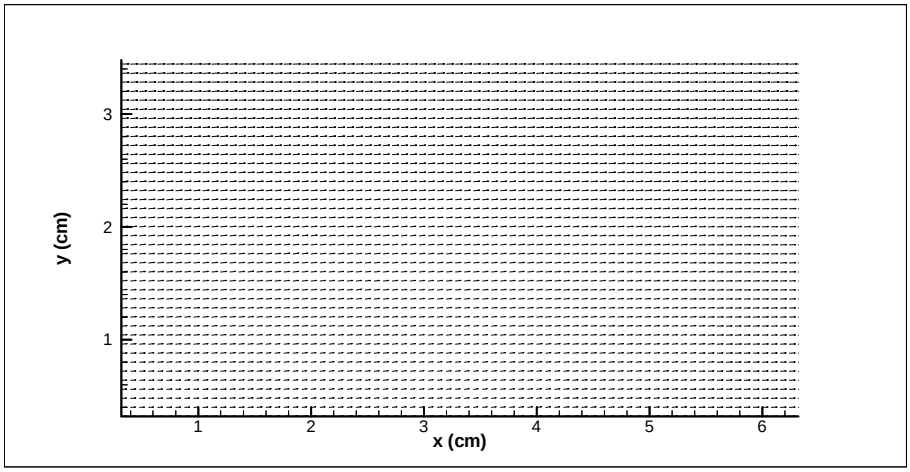

FIG. 3.6 – Offset and tilt between calibration (No.7) and measurement planes (plane 5)

#	Calibration position [mm]	Laser position [mm]	Laser position [Wall units]	Dt [μs]
1	0.68	1.81	14.5	600
2	1.15	2.32	18.5	600
3	1.61	2.78	22.2	400
4	2.07	3.29	26.3	400
5	**2.53**	**3.71**	29.7	350
6	**2.99**	4.16	33.3	350
7	**3.42**	4.63	37	350
8	**3.91**	5.07	40.6	350
9	**4.37**	5.5	44	300
10	4.83	5.99	48	300
11	5.29			

TAB. 3.2 – Absolute positions of the calibration and measurement levels

In order to select suitable calibration plane(s) for each method, the location of each calibration and laser plane are listed in Table 3.2. Laser plane 5 is considered as an example. Based on Table 3.2, calibration plane 7 was used for Image Mapping and Vector Warping, calibration plane 6, 7, 8 were used for the Soloff method with 3 calibration planes and calibration plane 5, 6, 7, 8, 9 were used for the Soloff method with 5 calibration planes. Table 3.2 gives also the PIV time delay for each plane, which was optimized to give a mean displacement of the order of 10 pixels in each field.

3.3.2 Comparison between various methods

3.3.2.1 Accuracy

The comparison starts by comparing the accuracy of computation of the different methods. As the exact result is unknown, only relative comparisons between the different methods are possible. For this purpose, the two following error estimations were computed :

- Mean value of the modulus :

$$E_1 = \frac{\sum_{i=1}^{N} \sqrt{(u_1^i - u_2^i)^2 + (v_1^i - v_2^i)^2 + (w_1^i - w_2^i)^2}}{N} \tag{3.4}$$

- Standard deviation of the modulus :

$$E_2 = \sqrt{\frac{\sum_{i=1}^{N} (\sqrt{(u_1^i - u_2^i)^2 + (v_1^i - v_2^i)^2 + (w_1^i - w_2^i)^2} - E_1)^2}{N-1}} \tag{3.5}$$

Here, (u_1, v_1, w_1) and (u_2, v_2, w_2) are the three instantaneous velocity components for respectively the reference and compared method. N is the total number of velocity vectors in the field. The values of E_1 and E_2 for the different methods are presented in Table 3.3.

# line	Reference	Comparing with	E_1 (pixel)	E_2 (pixel)
1	WI	WW	0.12	0.35
2	S3I	S3W	0.11	0.22
3	MSI	MSW	0.09	0.58
4	MWI	MWW	0.11	0.59
5	MSI	MWI	0.15	0.61
6	MSW	MWW	0.18	0.6
7	MWI	MSW	0.17	0.59
8	S3I	S5I	0.04	0.26
9	MSI	WI	0.59	0.7
10	WI	S3I	0.13	0.63
11	MSI	S3I	0.75	0.67

TAB. 3.3 – Accuracy of the different methods

Table 3.3 shows that the differences of the two parameters E_1 and E_2 between Integer shift and Whittaker (sub-pixel shift) are quite small for both Vector Warping (line 1) and Soloff methods (line 2). This can be explained by the fact that the Whittaker shift, which is expected to reduce the peak locking, does not show any strong improvement from a statistical point of view (Foucaut *et al.* (2004b)). The peak-locking effect appears mainly on the PDF of the velocity. This will be discussed in the next paragraph. As far as the Image Mapping method is concerned, the comparison between two different shifts (line 3 and 4) gives a smaller value of E_1 than the comparison of two different interpolation methods (line 5 and 6). The values of E_2 of lines 3 and 4 keep the same

order of magnitude but are generally two times higher than those with Vector Warping or Soloff methods (line 1 or 2). This suggests that both interpolation and shift methods have strong influence on Image Mapping. Clearly, several successive interpolations (i.e. MWW or MSW) can damage the shape of the particle images and thus the correlation peak. However, it would be possible to couple both interpolations necessary for the projection and the sub-pixel shifting at the same step. The fact of using only one interpolation for both operations should improve the accuracy but increase the computational time (interpolation is necessary at each pass of computation). As shown in line 8 of Table 3.3, the results of the Soloff method with 3 calibration planes and 5 calibration planes are similar to each other. This implies that, in the present configuration (light sheet thickness, low distortion), it is not necessary to use 5 planes to calibrate the Soloff method. The comparison between MSI and WI in line 9 shows high values of both E_1 and E_2. These are introduced by the projection of images and strong differences are evident in the results. The comparison between Vector Warping and the Soloff methods (line 10) shows a small value of E_1 and a large value of E_2. The difference between Soloff and Vector Warping can only be attributed to the reconstruction that decreases the noise effect in the case of Soloff. This is confirmed by the comparison between MSI and S3I (line 11), which shows high values of E_2 but also of E_1. Besides the influence of the projection of images already evidenced in line 9, the reconstruction is the other source of this difference.

3.3.2.2 Effect of sub-pixel shift

As shown in Table 3.3, the effect of sub-pixel shift is not evidenced by the comparison of lines 1 to 4. The reconstruction probably has a filtering effect, which decreases the peak locking. Therefore, the histogram of the decimal part of the velocity, in pixels, is calculated to analyse the effect of this peak locking. Fig. 3.7 compares the histogram of the 2D2C PIV analysis (before reconstruction) for cameras #1 and #2 (C1 and C2) in the case of Soloff methods : S3I and S3W. Foucaut *et al.* (2004b) show a strong improvement when Whittaker interpolation is used for sub-pixel shifting. In the present case, this improvement is less visible probably due to a particle image diameter smaller than two pixels (Foucaut *et al.* (2004b)). Even if the Whittaker interpolation is used, a small peak locking effect can still be shown for the u component (u_{2C}). This effect is still larger for the w component (w_{2C}). Fig. 3.8 shows the histogram of the decimal part of the velocity after reconstruction by the Soloff method for the streamwise component u, the out-of-plane component v and for the spanwise component w (less affected by the stretching of the SPIV). Due to the perspective effect of SPIV, a mean magnification was used to convert physical units to pixels. It is clear that the peak locking is filtered and that S3I and S3W give essentially the same histogram for both components presented in Fig. 3.8. Only some small oscillations remain due to a combination of peak locking, projection (variation of magnification along x) and reconstruction (between both 2D2C fields). To analyse the effect of these oscillations, the PDF of the velocity fluctuations can be studied. Furthermore, to characterize the measurement noise level, it is also interesting to look at the influence of the processing algorithm on the spectrum (Foucaut *et al.* (2004a)) of the velocity fluctuations. For this purpose, the S3I, S3W, MWI and WI methods were selected from the previous analysis to process 100 images pairs, which were used to obtain

the spectrum and PDF of the three velocity components.

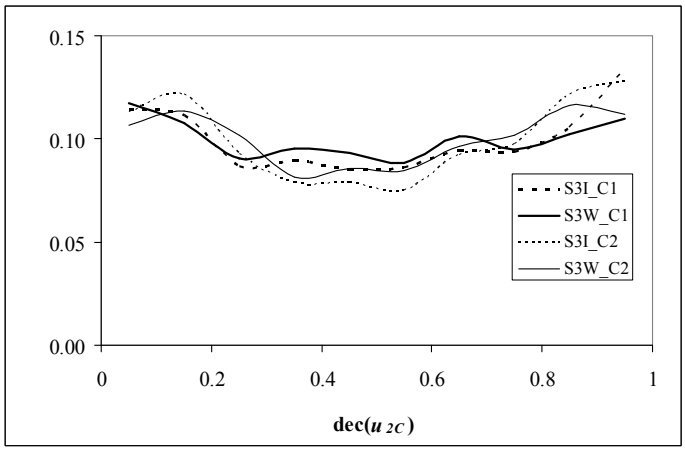

a

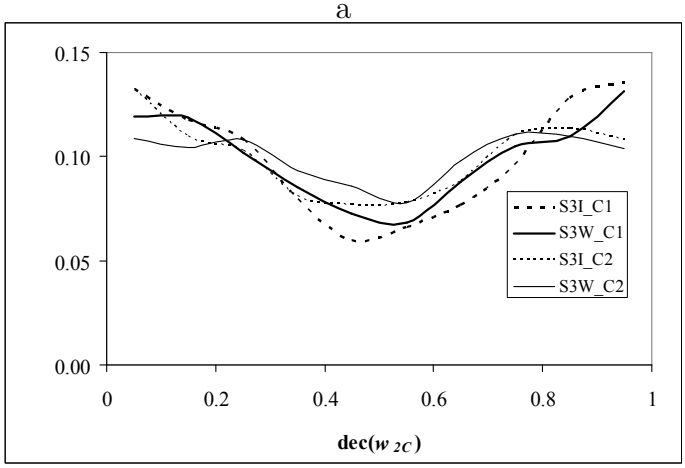

b

FIG. 3.7 – Decimal part histogram of the component u (a) and v (b) of each camera before projection and reconstruction

3.3.2.3 Spectra

The component u and v are computed from U_1 and U_2 (Eq. 3.1). As the angle of view is close to 45° in the present experiment, the behaviour of these two components is similar. The w component is perpendicular to the plane of the cameras and it is thus less affected by the stereoscopic reconstruction. In Fig. 3.9, E_{11}, E_{22} and E_{33} are spectra of the u, v and w components respectively and k is the wave number. According to the theory of Foucaut *et al.* (2004a), k_c is the PIV cut-off wave number ($k_c = 2.8/\mathrm{S}_{IW}$, where S_{IW} is the interrogation window size). The PIV results are qualified only in the region $k \leq k_c$. Fig. 3.9 shows that the results of the four selected methods are almost the same in the valid region of PIV. The noise level, that is attained by the spectrum in the high frequency part, is very close for each method. As in 2D2C PIV (Foucaut *et al.* (2004b)), a

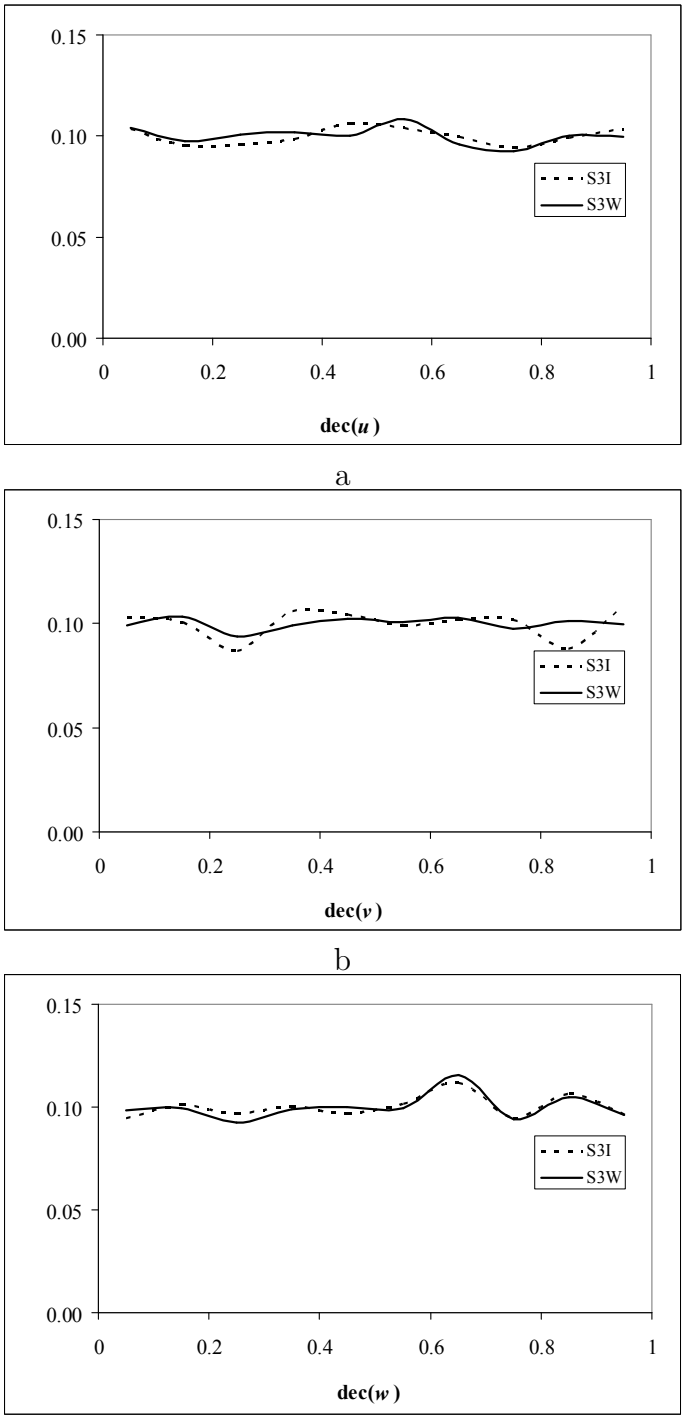

FIG. 3.8 – Decimal part histogram of the component u (a), v (b) and w (c) after projection and reconstruction

sub-pixel shift does not improve the spectrum as compared to the integer shift. It means that from the spectral point of view, all these methods can be used.

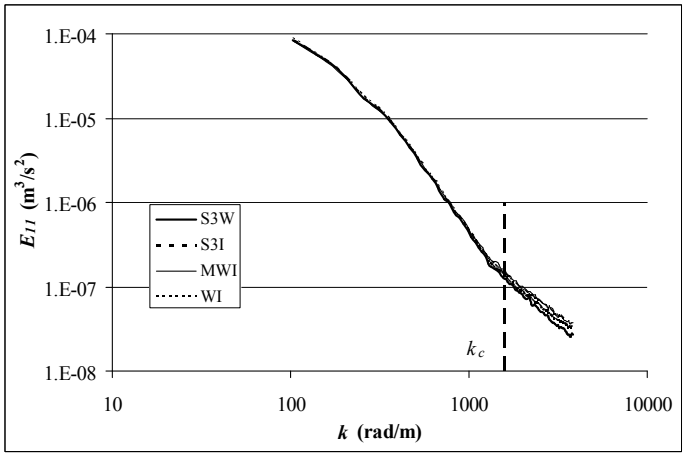

a

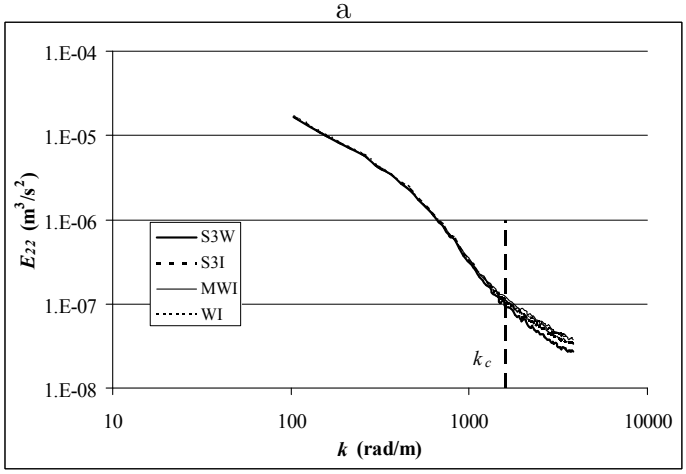

b

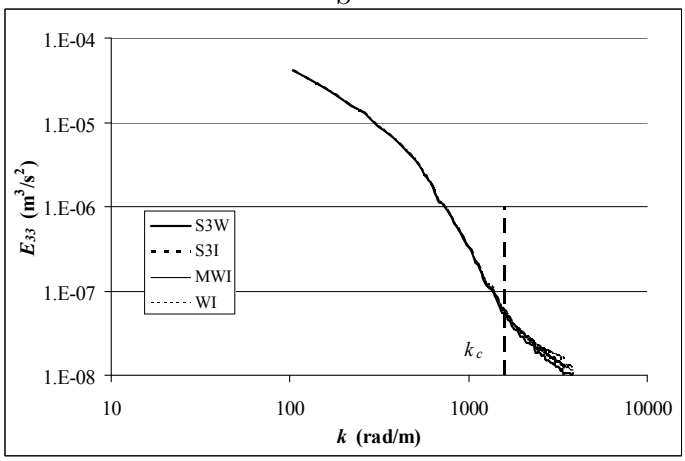

c

FIG. 3.9 – Comparison of the velocity spectra of the component u (a), v (b) and w (c) for different methods

3.3.2.4 PDF

In Fig. 3.10, the PDFs of WI, S3I and S3W are very similar but MWI seems rather different from the others. The differences cannot be attributed to the reconstruction because

Image Mapping and Vector Warping use the same reconstruction process. They may arise from the fact that the Image Mapping method interpolates the deformed images before PIV processing whereas the Vector Warping and Soloff methods are performed directly on the CCD images. As explained before, the perspective effect generates a difference in physical window size along the field and thus introduces a kind of smoothing in the statistics. This effect is clearly visible in Fig. 3.10a and 3.10b as in Fig. 3.7. Moreover, the image Mapping method makes the magnification constant. As a consequence, particle images that are slightly affected by the interpolation are now deformed. This probably induces the modification of the peak locking that appears in Fig. 3.10c. The method S3W using the Whittaker sub-pixel shift does not efficiently remove the peak locking. Fig. 3.11a-3.11c show the PDF in pixel of the 3 components at three typical wall distances. $y^+ = 14.5$ (plane 1) and $y^+ = 48.0$ (plane 10) are the closest and furthest to the wall in the range of wall distances studied, while $y^+ = 29.7$ is in the middle. Some fluctuations similar to peak-locking are clearly visible in Fig. 3.11a and 3.11c. However, the fluctuations do not appear in Fig. 3.11b because the out-of-plane component presents a smaller dynamic range. They are probably smoothed out in this case. In Fig. 3.11a, the result at y^+=14.5 shows different behaviour from those at $y^+ = 29.7$ and 48.0. This difference mainly arises from the fact that the dynamic range and the ratio of this range to the mean velocity of the u component, is very large in this position, which causes the large range of the oscillations. Besides, the large velocity gradient at this position also has some influence. In Fig. 3.11c, small peaks can be found in the PDF at $y^+ = 14.5$, which results mainly from the large velocity gradient at this position. The reduced amplitude of the peak locking benefits from the decrease of the velocity gradient away for the wall. Furthermore, the periodic distance of the main peaks is equal for all three planes, which implies a nearly constant dynamic range of the velocity fluctuation w'.

To study the magnitude of the velocity gradient and its variation with the wall distance, Fig. 3.12 shows the difference of particle displacement normalized by the particle image size between the top and the bottom of the light sheet which has a thickness of about 0.75 mm (e.g. Keane and Adrian (1990), Foucaut *et al.* (2004b)). In 2D2C PIV, the criterion proposed by these authors to minimize the effect of gradient is $Du/di < 0.5$. In the present experiment, this parameter, computed from the mean gradient using the Van-Driest model (Van Driest (1978)), decreases as the distance to the wall increases and it seems acceptable when reaching $y^+ = 26.3$ (plane 4). But there are still oscillations of the PDF in this plane. This is probably due to the fluctuation of the instantaneous velocity gradient around this mean value and to a residual peak locking due to the particle image size (about 1.4 pixels).

3.3.2.5 Time consumption

The time needed by the different methods was computed and is listed in Table 3.4. It is estimated from a computation on a small sample of images (based on a computer with a PIII 800 processor and 256M RAM). The methods with Whittaker shift take the longest time for computation, about 4 times longer than the rest. For the Image Mapping method, Whittaker interpolation needs much more time than Surfacial interpolation when the computation is carried out with the same shift method.

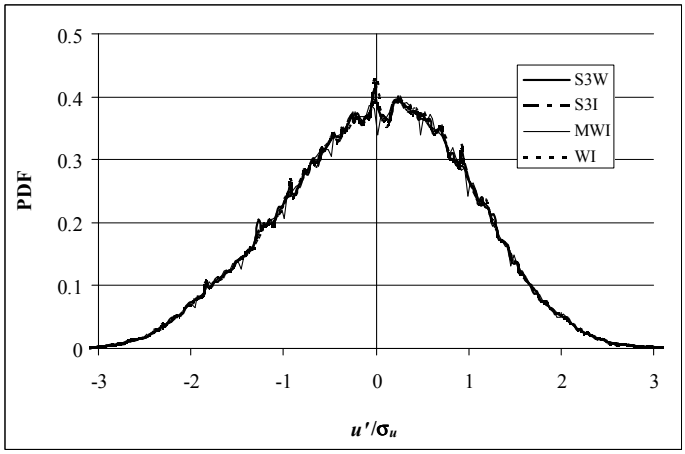

a

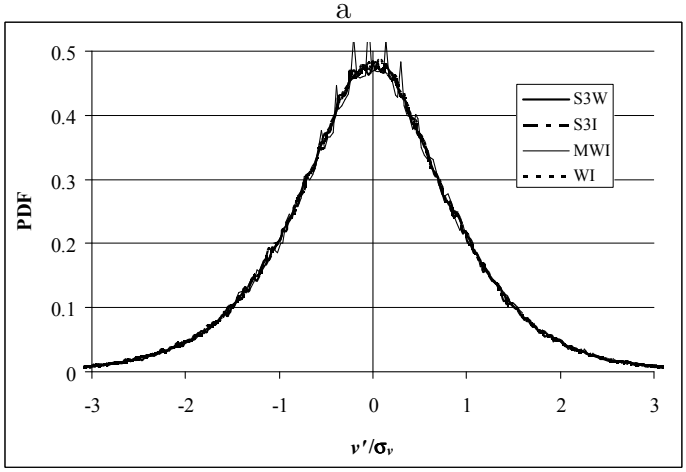

b

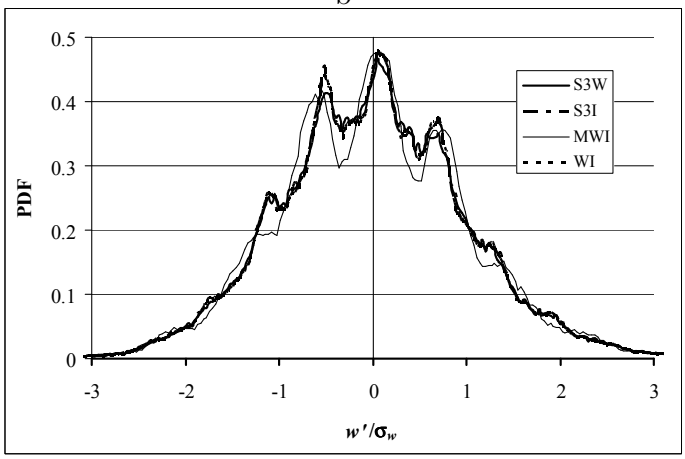

c

FIG. 3.10 – Comparison of the PDF of the normalized fluctuations of the three component u (a), v (b) and w (c) for different methods

3.3.3 Method selection

Based on the above results, the following arguments can be put forward : Regarding the Image Mapping method, the procedure of image interpolation can introduce errors that

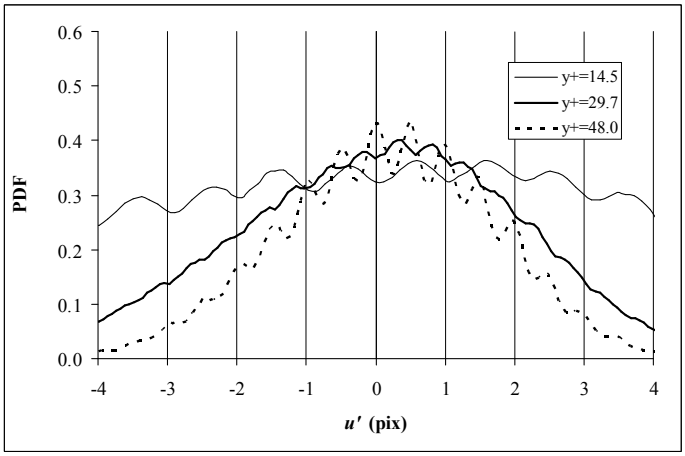

a

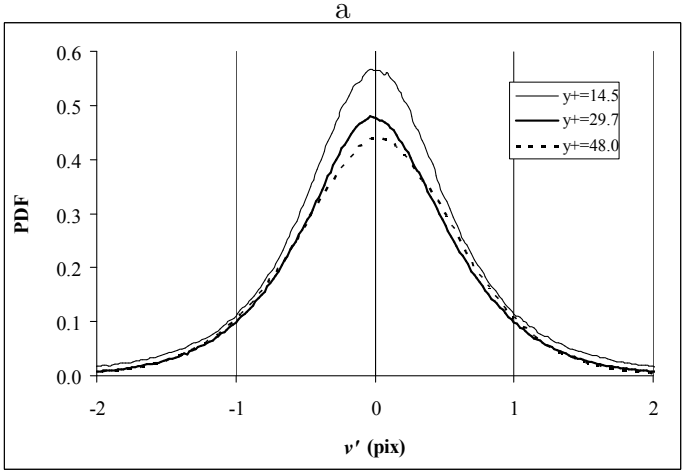

b

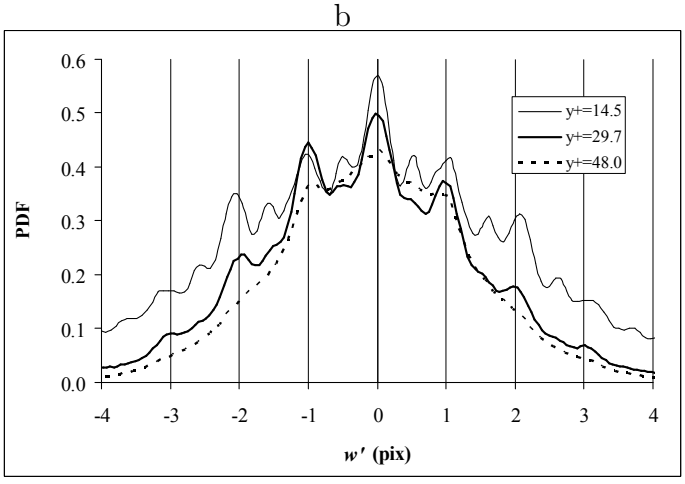

c

FIG. 3.11 – PDF of the fluctuations of the three component u (a), v (b) and w (c) in pixel at three typical wall distances : $y^+ = 14.5$ (plane1), $y^+ = 29.7$ (plane5) and $y^+ = 48.0$ (plane10)

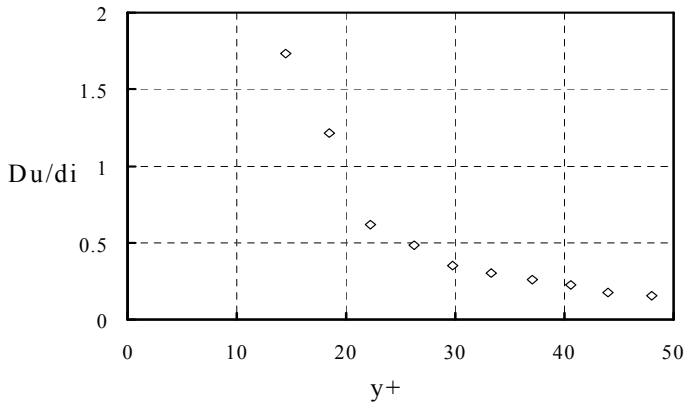

FIG. 3.12 – Difference of velocity between the top and the bottom of the light sheet versus y^+

Method	MSI	MSW	MWI	MWW	S3I	S3W	S5I	S5W	WI	WW
Time estimated for 500 image pairs (hours)	20	100	50	130	20	110	20	110	25	110

TAB. 3.4 – Time consumption of the different methods

are impossible to avoid. Proper interpolation method such as Whittaker reduces the errors and thus improves the accuracy of the results. In addition, for window shifting, Whittaker is a sub-pixel shift that in principle is more accurate than the Integer shift. As discussed before, the Image Mapping method using Whittaker interpolation and Whittaker shift cannot be used together because two successive interpolations affect the correlation peak shape. Therefore, the most accurate method should retain Whittaker interpolation only once : for the image mapping or for the window shifting. However, it needs much more computational time in both cases compared to other interpolation techniques. Focusing on the PDFs in Fig. 3.10, it is clear that the mapping method causes more peak locking than the methods based on vector projection.

With respect to the Vector Warping method, when Whittaker shift is used, the computation is heavier and the accuracy of the results does not improve much. Therefore, to save computer time it is recommended to use Integer shift when the Vector Warping method is selected.

As for the Soloff method, Table 3 shows that the Soloff with 5 calibration planes and with 3 calibration planes give pretty similar results. Therefore, it is not necessary to use 5 calibration planes. Additionally, the difference between the Whittaker and Integer shifts is so small that the Whittaker shift is useless in view of the extra computation effort. Consequently, the Soloff method with 3 calibration planes and Integer shift appears as the best compromise when the Soloff method is considered.

When using Image Mapping and Vector Warping methods, it is required to measure

geometric parameters such as the angle of the camera and the distances between the optical centres of camera lenses and calibration planes. The errors on the measurement of these parameters will affect the result of both methods. For the Soloff method, these parameters are not required. In this regard, the Soloff technique avoids these measurement errors and thus possibly provides more accurate results. Fei and Merzkirch (2004)) found a method for determining the viewing direction in the 'angular displacement' stereoscopic system by means of a digital imaging procedure. The method appears to improve the accuracy of results by avoiding the direct measurement of geometrical parameters of the set-up. They found that their results are quite similar to that of the Soloff method, which supports the reliability of the Soloff approach.

As a conclusion of this synthesis, it appears that the Soloff method with 3 calibration planes and an Integer shift (S3I) is the best choice in the present state of the art. It was thus used for the present analysis of all 10 planes. Using this method, the correction technique proposed by Coudert and Schon (2001) could be studied. Fig. 3.13 and 3.14 show the efficiency of this correction. The SPIV algorithm was applied to plane 5 ($y^+ = 29.7$) using two different sets of calibration planes : (4 to 6) called N° 5 expected when the experiment was done and (6 to 8) called N° 7 which was selected according the result of correction (Table 3.2). As shown in Table 3.2, the calibration plane N° 5 is shifted by about 1.2 mm from the light sheet location N° 5 while the calibration plane N° 7 is much closer. The results are computed with correction (noted C) or without correction (noted NC). Fig. 3.13 illustrates the PDF of the u, v and w components in each case. When the correction is applied, the PDF is comparable whatever the calibration plane is. Fig. 3.14 leads to the same conclusion from the spectrum. Table 3.5 presents the comparison of the parameter E_1 and E_2 (see Eq. 3.2) for the correction. Line 1 shows a small difference between the results obtained with correction from the two calibration planes N° 5 and N° 7. If calibration plane N° 7 is used without correction, the differences with the corrected results increase a little but stay acceptable (line 2). The small increases of E_1 and E_2 come from the distance of 0.3 mm (about 6 pixels) between the calibration plane N° 7 and the measurement plane N° 5. In line 3 and 4, when the calibration plane N° 5 is used without correction the results are remarkably different from other combinations. Considering the fact that the correction of calibration only takes little time but can improve the accuracy of the results, correction is strongly recommended.

# line	Reference	Comparing with	E_1 (pixel)	E_2 (pixel)
1	CP7_C	CP5_C	0.11	0.4
2	CP7_NC	CP7_C	0.24	0.5
3	CP5_NC	CP5_C	0.66	0.63
4	CP5_NC	CP7_C	0.67	0.66

TAB. 3.5 – Accuracy of the correction process

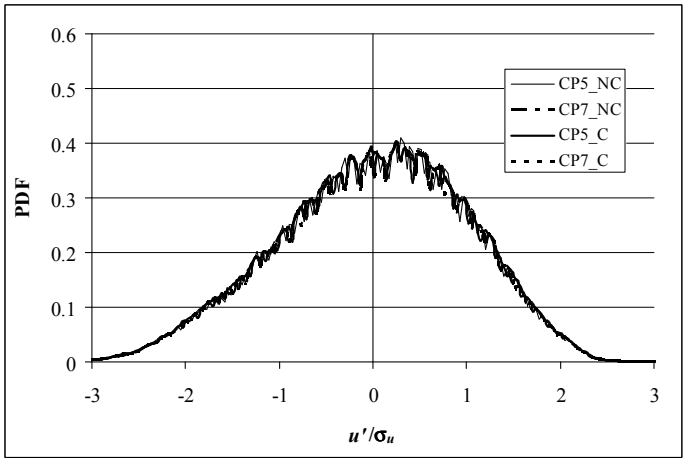

a

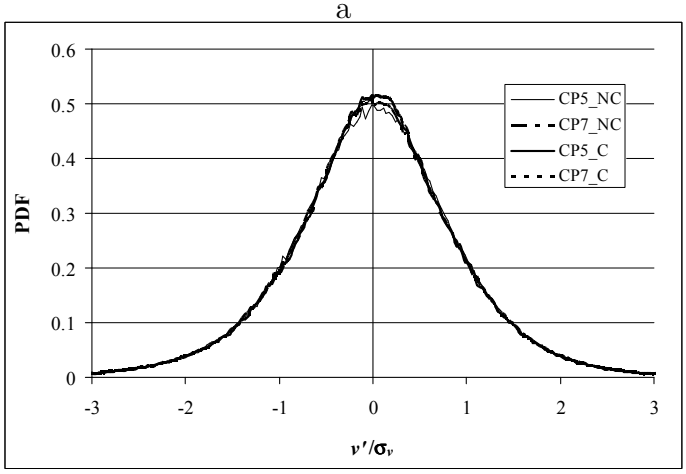

b

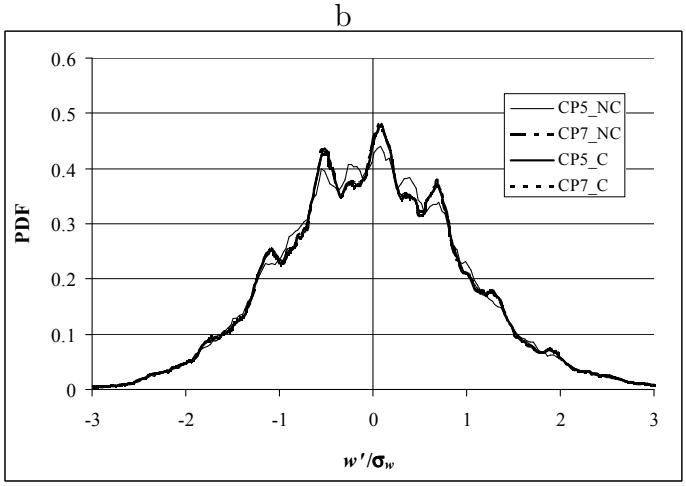

c

FIG. 3.13 – Comparison of the PDF of the normalized fluctuations of the component u (a), v (b) and w (c) effect of correction

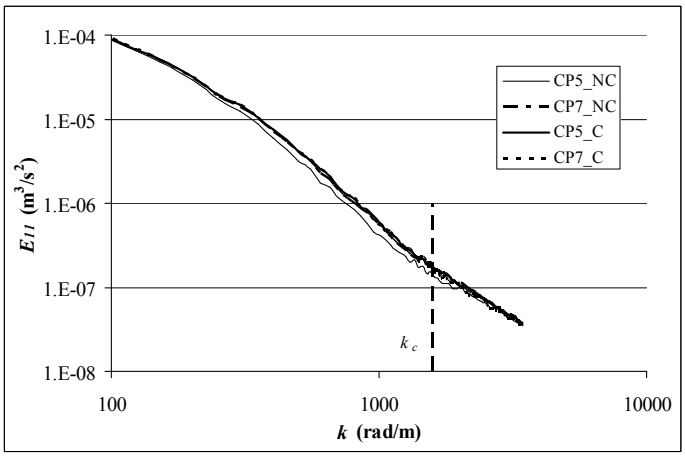

a

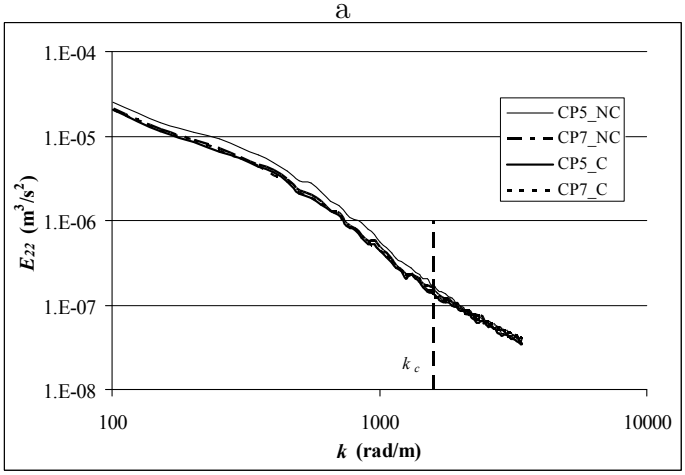

b

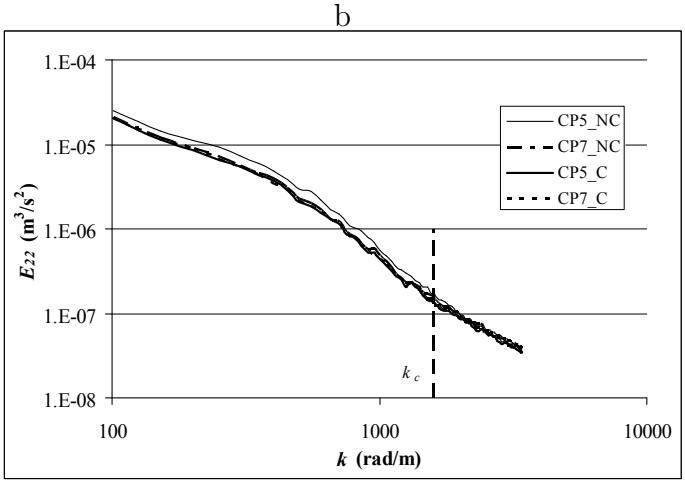

c

FIG. 3.14 – Comparison of the spectra of the component u (a), v (b) and w (c) effect of correction

3.4 Summary

The present experiment of Stereo PIV was carried out to investigate a fully developed turbulent boundary layer along a flat plate. This experiment recorded 500 image pairs for each of 10 planes parallel to the wall. The studied wall distance is in the range from y^+ = 14.5 to 48 with a spacing about 4^+. The Reynolds number based on the momentum thickness Re_θ was 7800. Three methods are available to analyse the database, namely Image Mapping, Vector Warping and the Soloff technique. They were compared in order to select the most suitable method of analysis for our database. The comparison took into consideration different interpolation and shift methods. The whole comparison was based on the estimation of computation time, the estimation of accuracy, the spatial spectra and velocity PDFs. The results favoured the Soloff method over all the others. For the Soloff method, the difference between Whittaker and Integer shift PIV processing and the difference between using 3 and 5 calibration planes was negligible. As a result, the Soloff method with 3 calibration planes for projection and reconstruction, using integer shift for PIV analysis was chosen as the most suitable method for the database. The improvement provided by the correction process (Coudert and Schon (2001)) was presented. Recently, Calluaud and David (2004) and Wieneke (2005) proposed a method based on the pinhole model. This model is based on previous work in the field of computer vision. It can incorporate some limited optical distortion and has the advantage of using less parameters in the least square fit than the Soloff method (24 instead of about 80). Scarano *et al.* (2005) compared this method with the image warping method with misalignment correction. They found that the two methods are practically equivalent for a correctly aligned system. In the present study, the Soloff method was found to be the best compromise to analyse turbulent PIV data, but the differences with the other two methods (mapping and warping) were fairly limited. The main advantage for the moment of the Soloff method is its generality and overall accuracy and it seems that any reconstruction method, properly applied leads to errors smaller than the PIV processing errors. In the present study, when processing the database of SPIV, three passes are used to calculate standard 2D2C vector field. The window sizes are respectively 64*64, 32*32, and 32*32 (pixel^2) with a final spacing of 12 pixel (0.6 mm) corresponding to a mean overlapping of 67.5%. Here, the 67.5% overlapping is used to obtain better spatial resolution for detection of coherent structures in future work. The results were saved in a database built using the Pivnet 2 Netcdf format (Willert (2004)).

Chapitre 4

Statistical Analysis of the Velocity Field

Using the selected S3I method with correction, a statistical analysis was performed to obtain the mean streamwise velocity, the Reynolds stresses, the velocity spectrum and PDF as well as skewness and flatness in the 10 planes. These statistical results were then compared with those of Hot Wire Anemometry (Carlier (2001)), numerical models (Van Driest (1978)) and DNS (Spalart (1988)). Plane 4 ($y^+ = 26.3$) was chosen to look at the spectra and PDF because it is in the middle of the range of wall distances studied and it corresponds to the limit of validity for the velocity gradient inside the light sheet (Fig. 3.12). In addition, the joint PDFs and velocity angles were computed and compared with the results of Kahler (2004).

In the rest of the thesis, the result which is normalized using the skin friction velocity u_τ ($= \sqrt{\tau_w/\rho}$, where ρ is the density of the fluid) and ν, is donoted with a superscript $+$.

4.1 Mean streamwise velocity

Fig. 4.1 shows the mean streamwise velocity profile in the near wall region ($y^+ < 50$). In this figure the solid symbols correspond to Hot Wire measurement (Carlier and Stanislas (2005)) for different Reynolds numbers ($Re_\theta = 11400$ (▲), 14800 (■) and 20600 (●)). The hollow symbols correspond to the 10 planes measured with PIV. The straight line represents the viscous sub-layer equation $u^+ = y^+$. The dot line represents the Van Driest model (Van Driest (1978)). This figure shows that the mean velocity obtained by SPIV is in perfect agreement with that of Hot Wire Anemometry and Van Driest model.

4.2 Velocity fluctuations

Besides the mean streamwise velocity, the fluctuations of all three components are also basic characteristics of the turbulent boundary layer and thus need to be analysed. Fig. 4.2 shows a comparison of the profiles of the fluctuations obtained by the two methods (SPIV and HWA). These results are also compared with the results of the DNS by Spalart

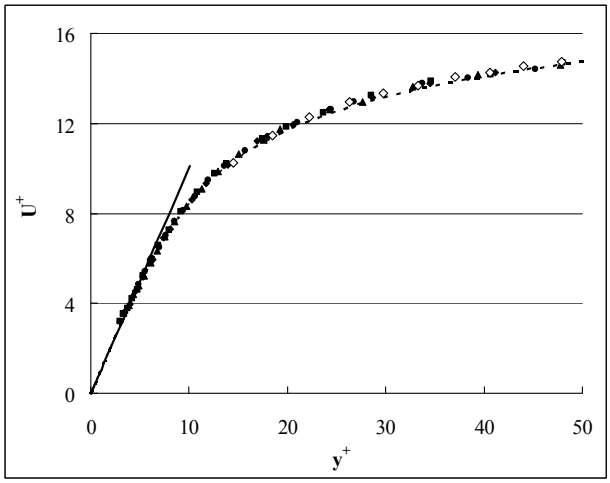

FIG. 4.1 – Comparison of mean streamwise velocity distributions of SPIV (♢) and Hot Wire Anemometry $11400 < Re_\theta < 21000$ (▲ ■ ●) [Carlier (2001)] ; Viscous sub layer (-) ; Van Driest model(...)

(1988). The Reynolds number of this simulation is $Re_\theta = 1410$. The $\sqrt{\overline{v'^2}}$ profile is very similar for all the methods down to $y^+ = 15$. Under this value, no PIV measurements is available and the hot wire starts to show a wall interference due to the probe size. For $\sqrt{\overline{u'^2}}$ and $\sqrt{\overline{w'^2}}$, the results of the hot wire measurement are slightly higher than those of the DNS. The result obtained with SPIV ($Re_\theta = 7800$) is between both, but closer to the HWA. The differences with DNS are attributed to the low Reynolds number influence. However, when it is very close to the wall, the difference of $\sqrt{\overline{v'^2}}$ or $\sqrt{\overline{w'^2}}$ between the results of SPIV and HWA increases. The main reason is that X-wire probes show an increasing bias when approaching the wall. This is due to wall interference and velocity gradients at the scale of the probe (0.5 mm). Considering this effect, the results reveal an excellent behaviour of the SPIV measurement.

4.3 Reynolds shear stress

As is well known, Reynolds shear stress is a critical parameter of the turbulence. Fig. 4.3 shows the data obtained by the two experimental methods (HWA and SPIV) compared with the results of DNS (Spalart (1988)) and with the Van Driest model (Van Driest (1978)). This model has been improved taking into account the weak pressure gradient of the test section $\partial p/\partial x = 0.057$ pa/m ($\partial p^+/\partial x^+ = 3.65\times10^{-4}$). The results of SPIV are similar to those of the Van Driest model and of the DNS. However, the results of HWA deviate considerably from the others, which once again shows the influences of the near wall interference and gradients at the scale of the probe. This explains the low values of the turbulent shear stress of HWA. Small oscillations are visible in the PIV results due to the lack of convergence on this small term.

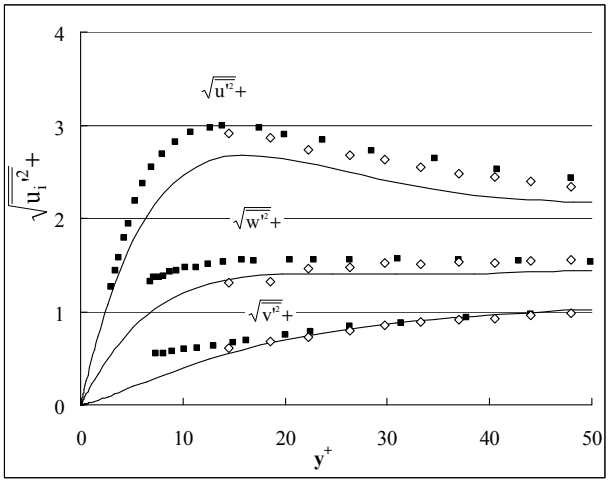

FIG. 4.2 – Comparison of the profiles of fluctuations of SPIV Re_θ (◊),Hot Wire Anemometry (■) [Carlier (2001)] and DNS (-) [Spalart (1988)]

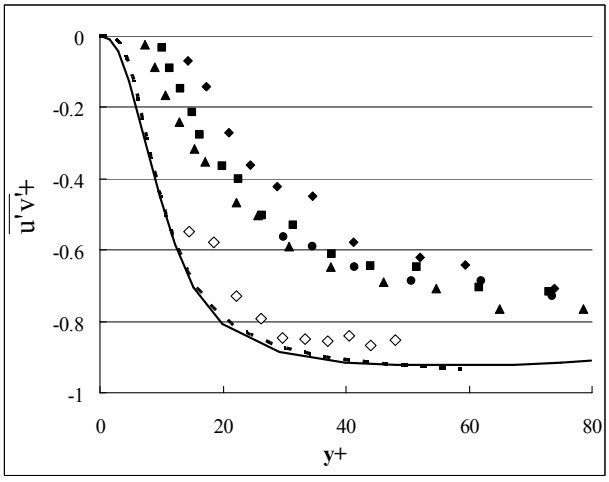

FIG. 4.3 – Comparison of mean Reynolds shear stress of SPIV (◊), Hot Wire Anemometry $11400 < Re_\theta < 21000$ (▲■●) [Carlier (2001)], Van Driest model (...) [Van Driest (1978)] and DNS (-) [Spalart (1988)]

4.4 Spectra

For the comparison of the spectra, the results at $y^+ = 14.5$ and 26.3 (plane 1 and 4 respectively) were used. The wall distance $y^+ = 14.5$ was selected because it is the closest to the wall. The wall distance $y^+ = 26.3$ was chosen because it is in the middle of the field investigated and it corresponds to the limit of validity for the velocity gradient inside the light sheet (Fig. 3.12).

Fig. 4.4 and 4.5 present the comparison of spectra obtained from SPIV and from HWA using a local Taylor hypothesis (Hinze (1975)). In Fig. 4.4 and 4.5, k_{min} is the minimum wave number accessible with PIV ($k_{min} = 2\pi/L_f$, L_f being the field size) and k_c is the cut-off wave number of PIV due to the windowing effect (Foucaut *et al.* (2004a)). The PIV results are qualified to compare with the results of HWA only in the region between k_{min} and k_c.

Fig. 4.4 and 4.5, E_{11} and E_{22}, the spectra of the u and v velocity component respectively, are consistent in most parts. The deviation occurs mainly in the high-frequency regions and it decreases considerably from $y^+ = 14.5$ to $y^+ = 26.3$. The large deviation at $y^+ = 14.5$ is caused by the strong velocity gradient. In the present study, the laser sheet has a thickness of the order of 0.3 mm. As explained in Chapter 3, the closer to the wall, the greater the velocity gradient is. Therefore, the effect of gradient in the laser sheet is likely to be strong close to the wall thus increases the noise of the SPIV results. Above $y^+ = 26.3$ (plane 4), the difference between SPIV and HWA in E_{11} and E_{22} reaches a relatively stable stage as the velocity gradient decreases to a neglected level.

Fig. 4.4 and 4.5, E_{33}, the spectra of the w velocity component, shows a great deviation between the results of SPIV and HWA at $y^+ = 14.5$. This deviation reduces gradually until $y^+ = 26.3$ where E_{33} shows a perfect fit with the result of the Hot Wire Anemometry. This is not only due to the wall interference and strong velocity gradients near the wall at the scale of the HWA probe (0.5 mm) but also owing to the velocity gradient in the laser sheet of SPIV. E_{33} shows that the results of SPIV can reach the same noise level as HWA. However, for E_{11} and E_{22}, the results of HWA always show a lower noise level than SPIV. Besides the effect of the velocity gradient in the laser plane, this is probably due to the variation in magnification across the field and to the stretching effect in the x direction linked to the stereoscopic set-up. According to the experimental set-up used, the w component is always perpendicular to the axis of the lenses and is less affected than the u component by the reconstruction process. The v component is built from the same elements as u hence shows a similar behavior.

4.5 PDF

Fig. 4.6 shows the PDF of the u', v' and w' component respectively. The PDF of w' shows much higher oscillation than that of u' and v'. As explained before, this is due to a peak locking effect amplified by the gradient through the light sheet. For v' (or u'), these oscillations are smoothed out by the stretching in the reconstruction procedure. Only a small difference in the height of the peak of v' is observable due to the noise caused by the strong velocity gradient near the wall. This difference disappears above $y^+ = 26.3$ (above

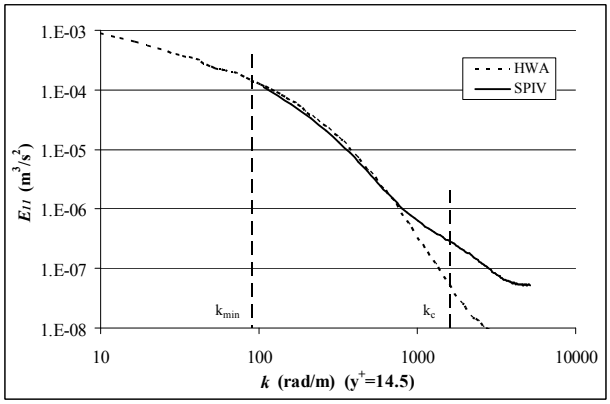

a

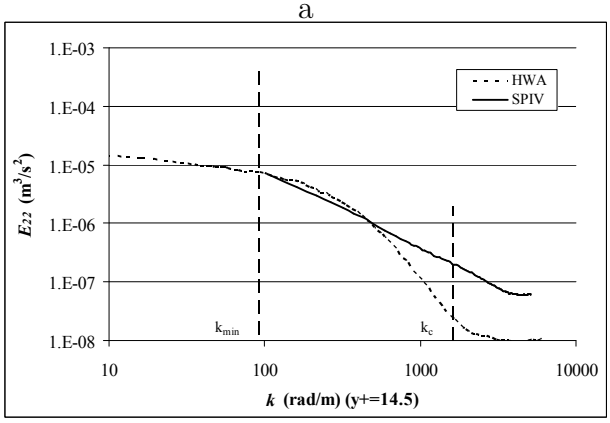

b

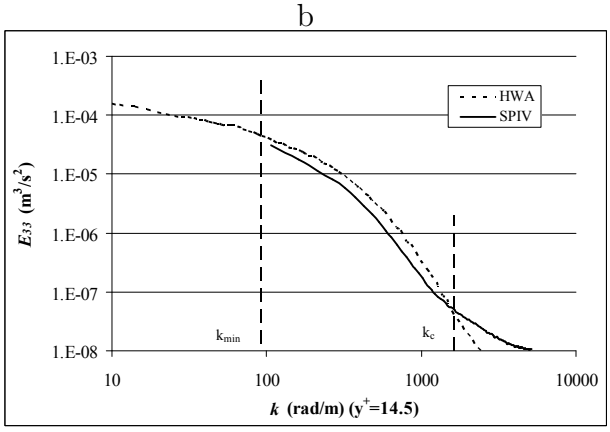

c

FIG. 4.4 – Velocity spectrum of the u, v and w component at $y^+ = 14.5$ comparison with HWA.

this wall distance Fig. 3.12 shows that the gradient effect is negligible).

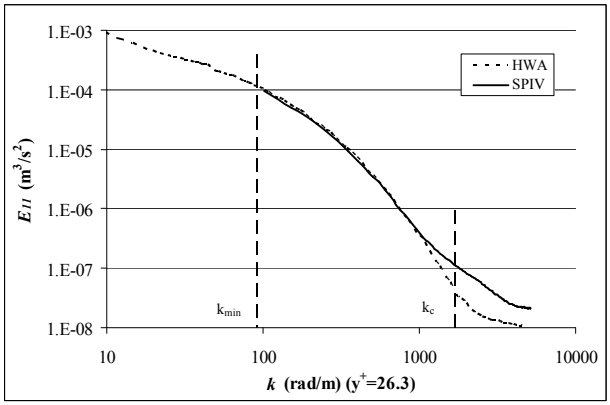

a

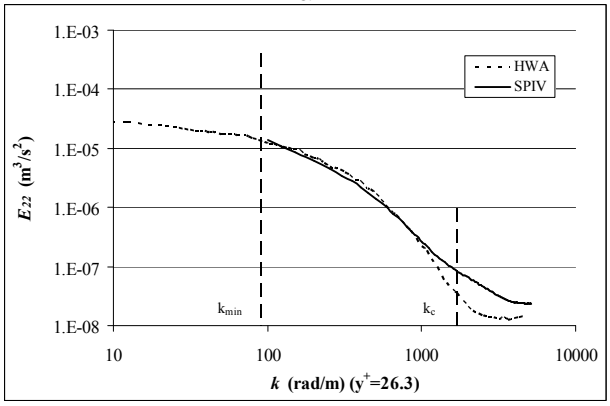

b

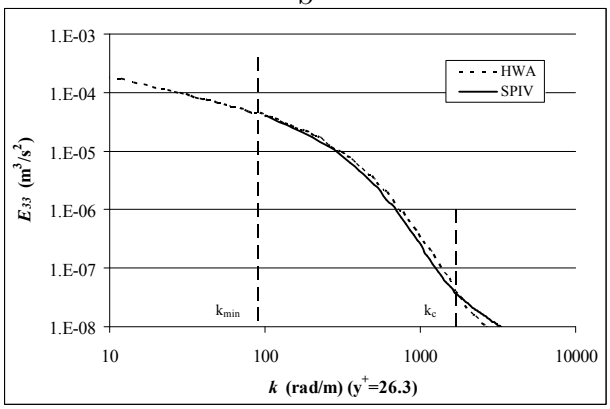

c

FIG. 4.5 – Velocity spectrum of the u, v and w component at $y^+ = 26.3$, comparison with HWA.

4.6 Skewness and Flatness

As is well known, the third order moment of a random signal (e.g. signal A) S_A describes the asymmetry or skewness of the corresponding probability density function while the fourth order moment F_A (also referred to as flatness) reveals the frequency of

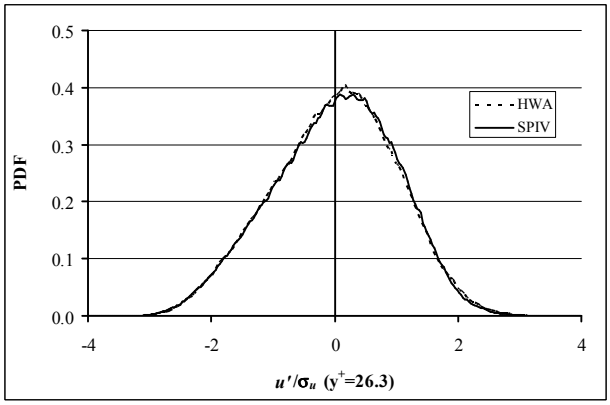

a

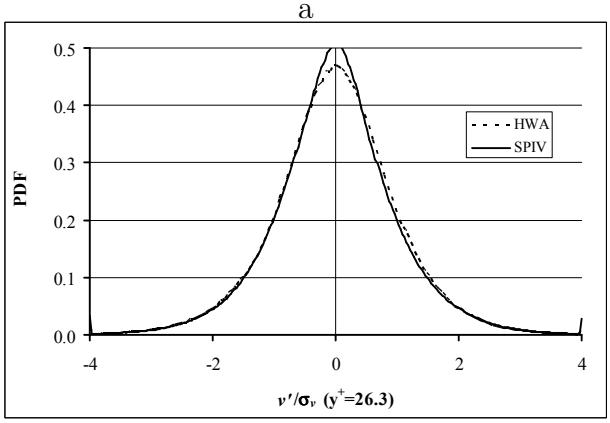

b

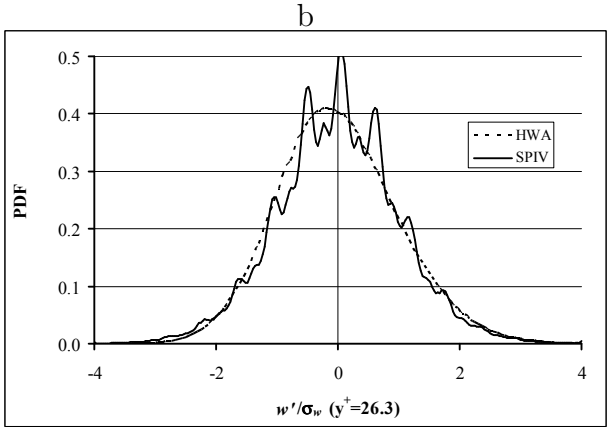

c

FIG. 4.6 – PDF of the normalized fluctuations of the u, v and w component at $y^+ = 26.3$, comparison with HWA.

occurrence of events far from the axis. These parameters are defined as :

$$S_A = \frac{\overline{A^3}}{\overline{A^2}^{3/2}} \tag{4.1}$$

$$F_A = \frac{\overline{A^4}}{\overline{A^2}^2} \tag{4.2}$$

For the skewness factor, $S_A = 0$ is expected if the probability density function of A is symmetric. In turbulence, the three velocity fluctuations ($u\acute{}$, $v\acute{}$ and $w\acute{}$) often have a nearly Gaussian distribution. For such a distribution, $S_A = 0$ and $F_A = 3$ are obtained.

Fig. 4.7 to 4.9 show respectively the profiles of skewness factors $S_{u'}$, $S_{v'}$ and $S_{w'}$ for the three velocity fluctuations. In Fig. 4.7, the skewness factor for the streamwise fluctuations $S_{u'}$ is in very good agreement with the results of HWA (Carlier and Stanislas (2005)). For $S_{u'}$, both results indicate an increase toward the wall known to be due to the strong intermittency in the viscous sub-layer. Above $y^+ = 15$, $S_{u'}$ is more or less constant and nearly zero, indicating a Gaussian behavior which is confirmed by the shape of the PDF. These results are in agreement with those of Fernholz and Finley (1996), who found that this location varies between $y^+ = 15$ and 20 for various Reynolds numbers. The positive value near the wall indicates that the frequency of occurrence of high positive streamwise fluctuations (high speed streaks and sweeps) is higher than that of high negative fluctuations in this region.

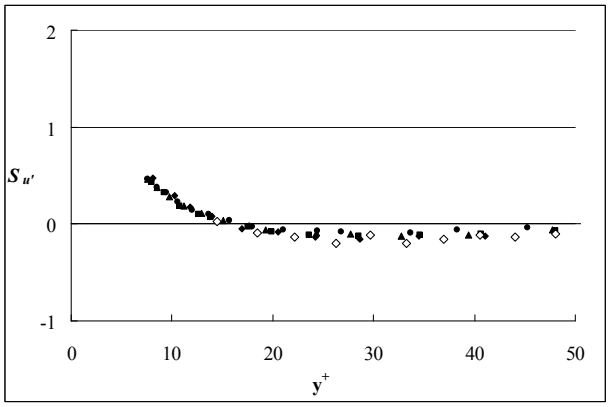

FIG. 4.7 – Skewness factor $S_{u'}$

In Fig. 4.8, $S_{v'}$ agrees also very well with HWA. Again it is nearly zero above $y^+ = 20$. The larger scatter compared to $S_{u'}$ is attributed to the small value of this component compared to $u\acute{}$ (Fig. 4.2). The positive value of $S_{v'}$ evidences the asymmetry of the PDF close to the wall, indicating the predominance of ejections on the statistical behaviour of this component.

The skewness factor $S_{w'}$ should be zero in a truly two-dimensional boundary layer due to the symmetry of the mean flow in the spanwise direction. This is confirmed by the

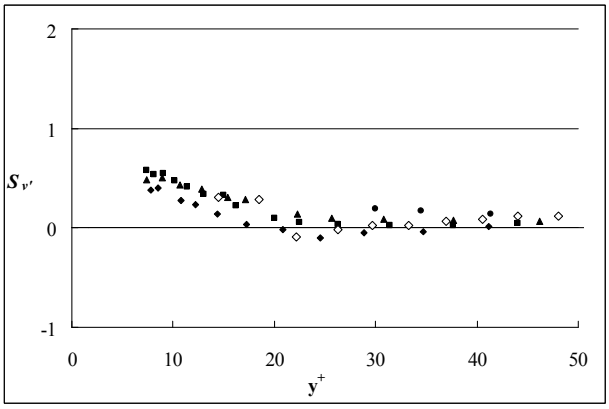

FIG. 4.8 – Skewness factor $S_{v'}$

present SPIV results in Fig. 4.9, where the factor $S_{w'}$ is nearly zero. The HWA results have a slightly positive value of about 0.25 which is comparable to that found by Fernholz and Finley (1996). It is attributed to a bias in the HWA measurements due either to a slight rotation of the probe around its axis or to the local velocity gradient at the scale of the probe.

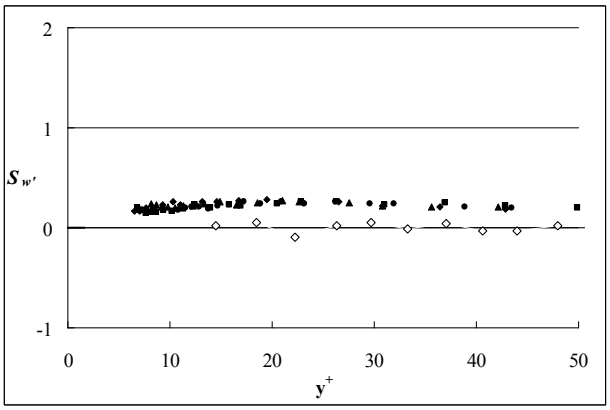

FIG. 4.9 – Skewness factor $S_{w'}$

Fig. 4.10 to 4.12 show respectively the profiles of skewness factors $F_{u'}$, $F_{v'}$ and $F_{w'}$. Fig. 4.10 compares the flatness factor $F_{u'}$ obtained in the present study with that obtained by HWA (Carlier and Stanislas (2005)). Again the SPIV results are in very good agreement with HWA. For $y^+ \geq 15$, the present SPIV results show that $F_{u'}$ increases slightly from 2.4 at $y^+ = 15$ to 2.8 at $y^+ = 39.7$ and then levels off afterwards. Ueda and Hinze (1975) found a relationship between the position of the maximum of the streamwise normal Reynolds stress ($\overline{u'^2}$), the zero value of $S_{u'}$, and the minimum of $F_{u'}$. These characteristic points are at the same distance from the wall. In the present case, the maximum of ($\overline{u'^2}$) is at

about $y^+ = 14$ (Fig. 4.2), the zero crossing of $S_{u'}$ is at around $y^+ = 16$ in Fig. 4.7, and the minimum value of $F_{u'}$ is near to y^+ =12. Considering the experimental errors involved, the results confirm the relationship obtained by Ueda and Hinze (1975). Similar to $S_{u'}$, $F_{u'}$ is known to increase toward large positive values in the viscous sub-layer ($y^+ \leq 5$) due to intermittency.

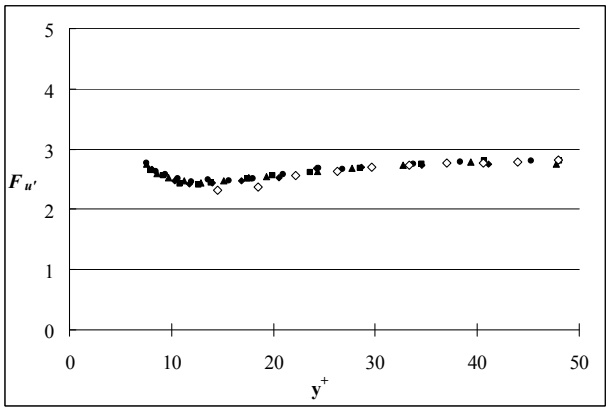

FIG. 4.10 – Flatness factor $F_{u'}$

Fig. 4.11 presents the flatness factor $F_{v'}$ compared with HWA. In SPIV, this parameter decreases sharply between $y^+ = 14.5$ and 22.2. When $y^+ > 22.2$, $F_{v'}$ decreases slowly with increasing wall distance and is in good agreement with the results of HWA for various Reynolds numbers. This result was also obtained by other researchers (e.g. Balint *et al.* (1991), Spalart (1988)and Fernholz and Finley (1996)). The large values at $y^+ = 14.5$ and 18.5 can be associated with the intermittent character of near wall flow in the buffer layer. The differences with the results of HWA at $y^+ = 14.5$ and 18.5 are attributed to the velocity gradient at the size of the X-wire probe close to the wall.

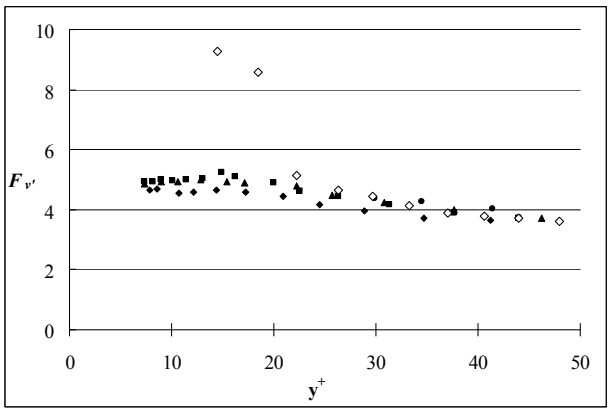

FIG. 4.11 – Flatness factor $F_{v'}$

Fig. 4.12 compares $F_{w'}$ obtained by SPIV and HWA. There is a very good agreement. $F_{w'}$ is nearly constant. The value of 3.4 is the same as Fernholz and Finley (1996).

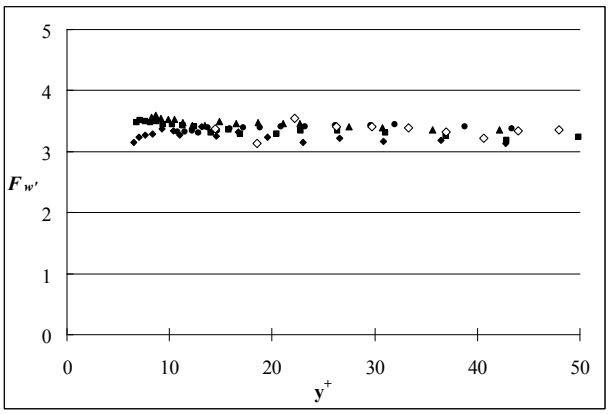

FIG. 4.12 – Flatness factor $F_{w'}$

4.7 Joint PDF

To study the spatial distribution of the velocity, the joint PDFs were calculated for the velocity fluctuation (u', v') and (u', w') respectively (Fig. 4.13 and 4.14). Three typical wall distances were selected : $y^+ = 14.5$, 29.3 and 48.0 (plane 1, 5, 10 respectively). As mentioned above, $y^+ = 14.5$ and 48.0 are the closest and furthest position from the wall in the range of wall distance studied while $y^+ = 29.3$ is in the middle.

For each plane, the two joint PDFs ((u', v') and (u', w')) show strong differences in both size and shape. The PDF (u', v') shows a strong asymmetrical behaviour. It indicates the existence of coherent structures such as 'ejections' ($u' < 0$, $v' > 0$) and 'sweeps' ($u' > 0$, $v' < 0$). Clearly, from the shape of the PDF(u', v'), the counter-sign regions (ejections and sweeps) dominate over the other two with same signs. The PDF (u', w') is symmetrical : PDF(u, w) = PDF(u, $-w$). It results from the homogeneity of the flow in the spanwsie direction. The PDF (u', w') also shows an interesting behaviour, that is, large negative streamwise fluctuations u' are frequently associated with small spanwise fluctuations w' and large spanwise fluctuations with positive streamwise fluctuations. In Fig. 4.13 and 4.14, the difference in the range of velocity fluctuations confirms the relation of standard deviation of the three velocity components $u_{rms} > w_{rms} > v_{rms}$ (see Fig. 4.2). Moreover, these figures show that the amplitude of velocity fluctuations decreases in the streamwise direction but increases in spanwise and wall-normal direction with wall distance.

4.8 Velocity angle

Fig. 4.15 shows the PDFs of the flow angle α between the instantaneous velocity component u and v, which allows to study the direction of the transport of the low and

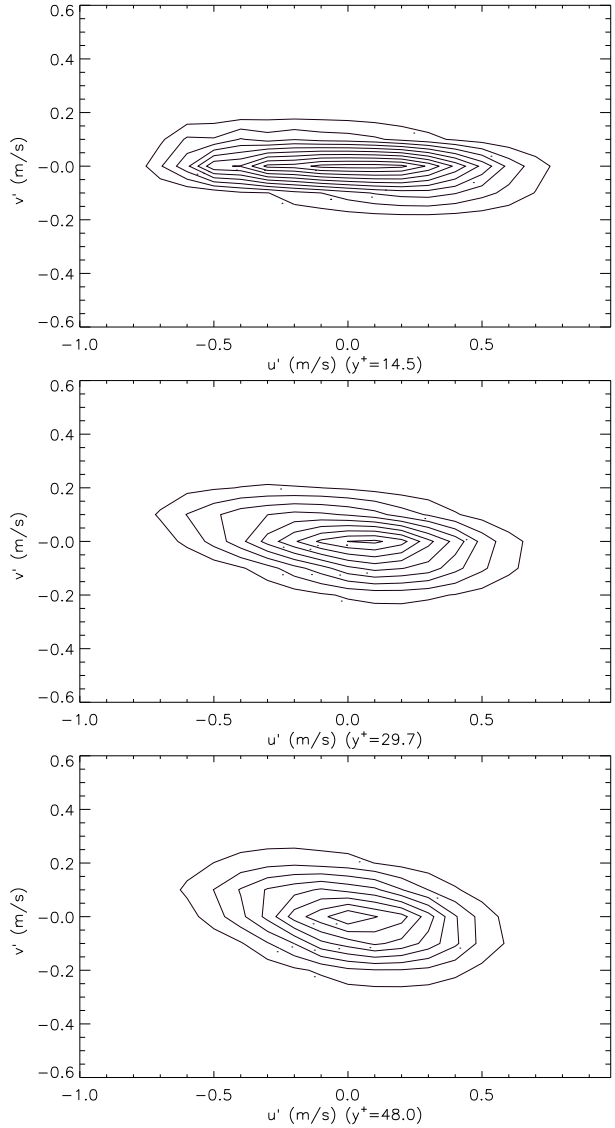

FIG. 4.13 – Joint PDF of the velocity fluctuations (u', v')

high momentum fluids towards and away from the wall. This distribution is asymmetric with a large range of scales for positive angles but a peak located on the negative side. The negative part, where the sign of the two velocity components is opposite, has a larger surface area than the positive part and seems more important to the characteristics of the flow.

To study this angle in more detail, the distribution of the flow angles for an instantaneous streamwise velocity u smaller and larger than the mean U ($\alpha|u < U$ and $\alpha|u > U$ respectively) were calculated separately. Both results are asymmetric in terms of the scale range, the location of the peak and the proportion. When u is smaller than U, the result shows both a peak and a large range (especially for the plane far from the wall) in the positive domain. The positive part has about two times the surface of the negative one.

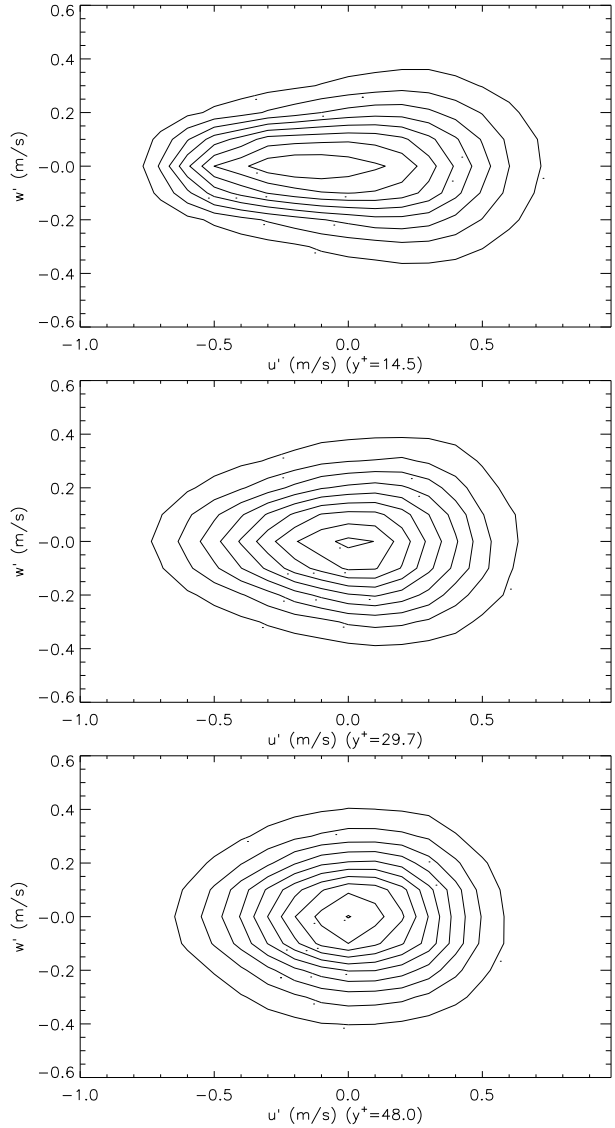

FIG. 4.14 – Joint PDF of the velocity fluctuations (u', w')

The asymmetry indicates that the probability of finding a low speed fluid moving away from the wall is much higher than towards the wall. The former is called a Q2 event or ′ejection′ (Wallace *et al.* (1972)) and the latter is referred to as a Q3 event. In contrast, when u is larger than U, the result shows a peak and a large range in the negative domain. The negative part is about two times of the positive one. It reveals that the chances of finding high speed fluid moving towards the wall are much higher than moving away from the wall. The former is called a Q4 event or ′sweep′ and the latter is referred to as a Q1 event. The comparison of the proportion yields that P(Q2) > P(Q4) >> P(Q3) > P(Q1). This result shows that Q2 and Q4 events (Ejections and Sweeps) dominate over Q1 and Q3 events. Moreover, the largest angles are always associated with Q2 and Q4 events. In Fig. 4.15, the distributions have a similar pattern above $y^+ = 2.2$.

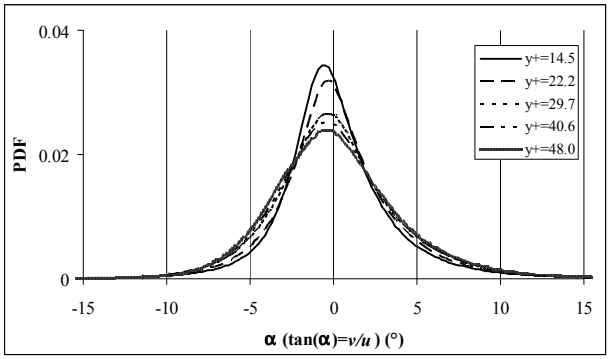

a

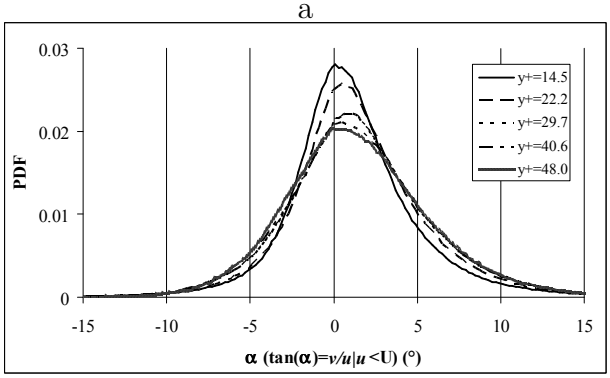

b

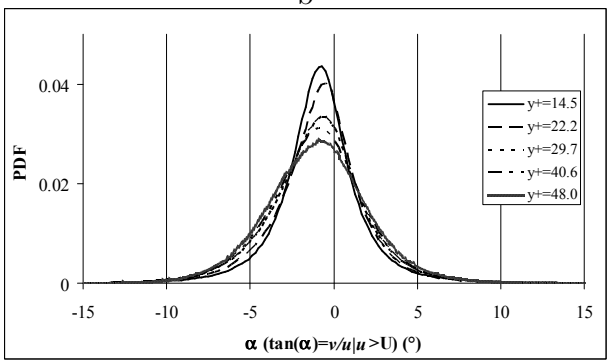

c

FIG. 4.15 – Flow angle between the u and v component

Fig. 4.16 shows the mean flow angle $\overline{\alpha}$ between the u and v component. An interesting feature is that the behaviors at $y^+ = 14.5$ and 18.5 are different from other wall distances where all the results are similar. This difference can result from the influence of the wall. The absolute value of $\overline{\alpha}|u < U$ is larger than that of $\overline{\alpha}|u > U$. Moreover, $\overline{\alpha}$ has always a positive value. These results can be explained by the fact that instantaneous velocities were used to calculate the flow angle. The present results were also compared with those of Kahler (2004). Both results are in good accordance. Fig. 4.17 shows the RMS of flow angles between the u and v component. Evidently, it is comparable with the results of Kahler (2004).

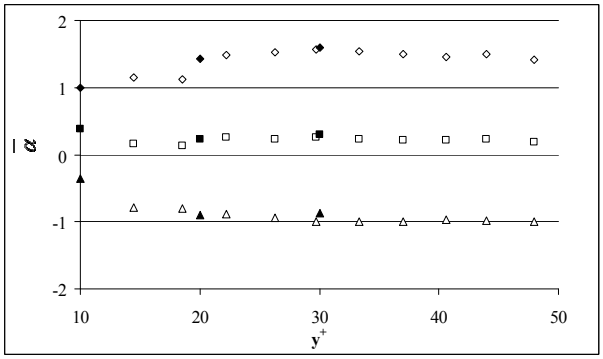

FIG. 4.16 – Mean flow angle between the u and v component, comparison with Kahler (2004). Present study : $\overline{\alpha}$ (□), $\overline{\alpha}|u < U$ (◊), $\overline{\alpha}|u > U$ (△) ; Kahler (2004) : $\overline{\alpha}$ (■), $\overline{\alpha}|u < U$ (♦), $\overline{\alpha}|u > U$ (▲)

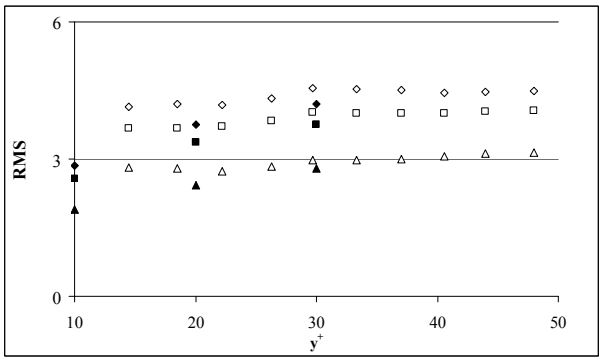

FIG. 4.17 – RMS of flow angles between the u and v component, comparison with Kahler (2004). Present study : $\overline{\alpha}$ (□), $\overline{\alpha}|u < U$ (◊), $\overline{\alpha}|u > U$ (△) ; Kahler (2004) : $\overline{\alpha}$ (■), $\overline{\alpha}|u < U$ (♦), $\overline{\alpha}|u > U$ (▲)

4.9 Summary

Using this processing method, the whole database was analysed. The results were presented in terms of the mean streamwise velocity, velocity fluctuations, Reynolds shear stresses, the spectra and PDFs, skewness and flatness. They were compared with those of Hot Wire Anemometry, DNS and the Van Driest model. The comparisons show that the results of SPIV are in good accordance with those of other methods. In general, the results of SPIV are closer to those of the Van Driest model and DNS than to HWA in the very near wall region. This study concludes that SPIV is a suitable method to study near wall turbulence. In addition to the above-mentioned characteristics, joint PDFs and velocity angles are also computed and compared with the results of SPIV of Kahler (2004). The comparison shows that two studies are in very good agreement, validating the quality of the present measurement.

Chapitre 5

Velocity correlations

5.1 Introduction

A first step toward the study of coherent structures is done by computing the two-point spatial correlation tensor. The interest of this tensor for the study of near wall turbulence with PIV has been shown by Stanislas *et al.* (1999), from 2D2C PIV fields in planes normal to the wall and parallel to the flow. The advantage of SPIV results is to provide the out-of-plane component. Kahler (2004) did the same analysis and gave some results concerning coherent structures. The spatial auto-correlations and spatial cross-correlations are discussed in this section. These correlation tensors were computed based on the velocity fluctuations (u', v' and w'). The mean of u' as well as v' and w', is equal to zero, which leads to $\sigma_{u'} = \sigma_u$, $\sigma_{v'} = \sigma_v$ and $\sigma_{w'} = \sigma_w$. As the database has only two dimensions (streamwise and spanwise) in the present study, the two-dimensional two-point correlation function and the one-dimensional two-point correlation function are defined as follows :

Two-dimensional two-point correlation function :

$$R_{u_i'u_j'}(\Delta x^+, \Delta z^+) = \frac{\overline{u_i'(x^+, z^+)u_j'(x^+ + \Delta x^+, z^+ + \Delta z^+)}}{\sigma_{u_i'}\sigma_{u_j'}} \tag{5.1}$$

Streamwise one-dimensional two-point correlation function :

$$R_{u_i'u_j'}(\Delta x^+, \Delta z^+ = 0) = \frac{\overline{u_i'(x^+, z^+)u_j'(x^+ + \Delta x^+, z^+)}}{\sigma_{u_i'}\sigma_{u_j'}} \tag{5.2}$$

Spanwise one-dimensional two-point correlation function :

$$R_{u_i'u_j'}(\Delta x^+ = 0, \Delta z^+) = \frac{\overline{u_i'(x^+, z^+)u_j'(x^+, z^+ + \Delta z^+)}}{\sigma_{u_i'}\sigma_{u_j'}} \tag{5.3}$$

Where $u_i^{'}$, and $u_j^{'}$ are the two selected velocity fluctuations (they are the velocities $u^{'}$, $v^{'}$ or $w^{'}$ in the present study). The number of PIV samples is 500 for each plane. Δx^+

and Δz^+ are respectively the displacements in the streamwise and spanwise directions respectively.

For all the following two-dimensional correlation figures, if no special statement is made, the contours are plotted in intervals of 0.05 and the zero contours are illustrated by a dash-dotted line. The solid lines show the positive correlation regions while the dotted lines represent the negative ones. For the one-dimensional correlation figures, the results for 6 selected wall distance are plotted in order to show the variation of the correlations with wall distance.

It should be noted that for the two-dimensional correlation, for example Fig.5.1, the plane view is from below to above. The positive and negative Δz^+ are on the top and bottom half of the correlation image respectively, corresponding the right and left side of the flow with respect to the streamwise direction.

5.2 Spatial auto-correlations

5.2.1 Streamwise velocity fluctuations

Fig. 5.1 shows an example of two-point spatial auto-correlations of the streamwise velocity fluctuations $R_{u'u'}$ at $y^+ = 14.5$. The correlation contours have a strong elliptical shape, with the principal axis in the streamwise direction, and the minor axis in the spanwise direction. It indicates the existence of an organization that has a significant spatial coherence in both streamwise and spanwise directions. These structures have a long extension in the streamwise direction and a short one in the spanwise direction. According to the definition of two-point spatial auto-correlations (Eq. 5.1), these structures are regions with high velocity fluctuations and are named low or high-speed streaks (Smith and Metzler (1983)).

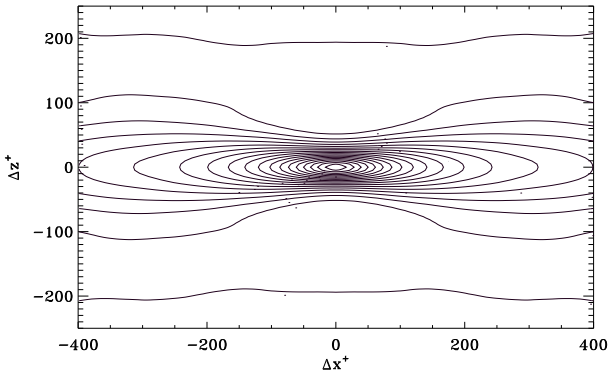

FIG. 5.1 – Two-dimensional spatial auto-correlations of the streamwise velocity fluctuations $R_{u'u'}$ at $y^+ = 14.5$

To obtain more information on the variation of the streamwise and spanwise dimensions of these structures with wall distance, one-dimensional spatial auto-correlations are computed at $\Delta x^+ = 0$ and $\Delta z^+ = 0$ respectively and plotted in Fig. 5.2. In Fig. 5.2a, the correlation function decreases monotonously with increasing streamwise displacement

Δx^+, but increases with wall distance. At $y^+ = 14.5$, the streamwise extend of the correlation can be estimated of the order of 500^+. At $y^+ = 48$, due to the limited field of view, it is difficult to estimate where the correlation goes down to zero, but probably beyond 1000^+. This is a very large change on a very small range. In Fig. 5.2b, the spanwise correlations computed at $y^+ = 14.5$ and 18.5 show a distinct minimum, while all the others decrease monotonously with increasing Δz^+. This can be explained twofold. Firstly, the same as given by Kahler (2004), there is a decreasing dynamic velocity range with increasing wall distance, which implies that the coherent regions rapidly lose their identities. The second reason is that other coherent structures may occur and develop as wall distance increases, which can hide the signature of streaks.

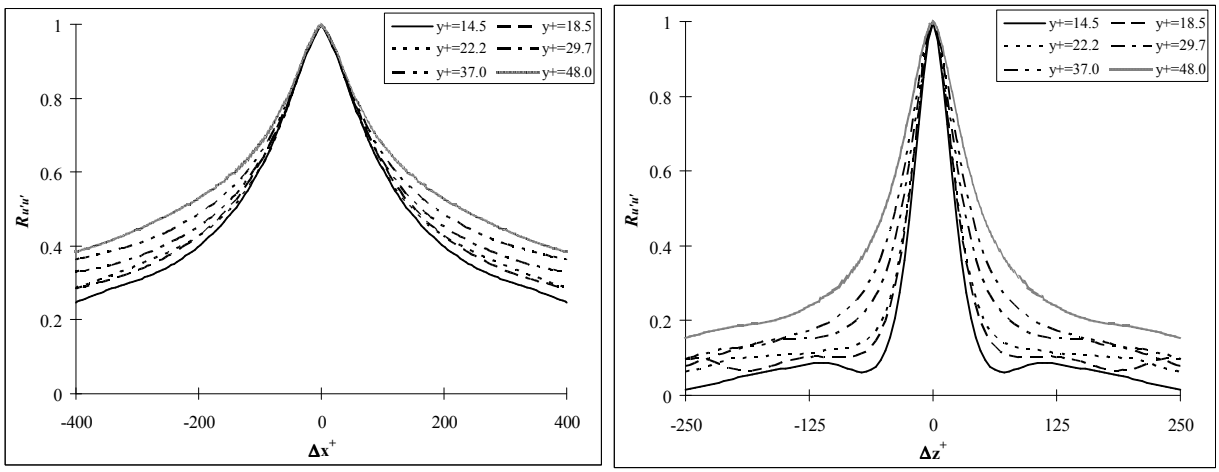

a : $R_{u'u'}$, with $\Delta z^+ = 0$ b : $R_{u'u'}$, with $\Delta x^+ = 0$

FIG. 5.2 – One-dimensional spatial auto-correlation of the streamwise velocity fluctuations $R_{u'u'}$ at selected wall distances

Clearly, the correlations in Fig. 5.2 include the contributions of both low and high speed regions. It is interesting to subdivide them according to the sign of the streamwise velocity fluctuation before computing the correlations. This conditional-correlation approach allows the identification of low and high speed regions and the study of the statistical properties of them separately. The results are shown in Fig. 5.3.

In Fig. 5.3, $R_{(u'<0)(u'<0)}$ denotes the correlation in the low speed regions while $R_{(u'>0)(u'>0)}$ is for the high speed ones. Fig. 5.3 shows that for both low and high speed regions, an increase of size with wall distance is visible in both streamwise and spanwise directions. At the same wall distance, low speed regions are narrower than high speed ones in the spanwise.

Both Fig. 5.3a and 5.3c show a continuous decrease in the correlations, implying that the size of both kinds of regions may extend more than 400 wall units in the streamwise direction. Due to the limited size of the velocity field in the present study, it is not possible to measure the maximum streamwise extend of the correlation. In Fig. 5.3a, except for the relatively smaller value of the peak at $y^+ = 14.5$, all curves are nearly the same when $|\Delta x^+| < 100$. When $|\Delta x^+| > 100$, the curves for $y^+ \leq 30$ are also nearly the same. Only above $y^+ = 30$ and $|\Delta x^+| > 100$, an increase of the size is observed. This result indicates

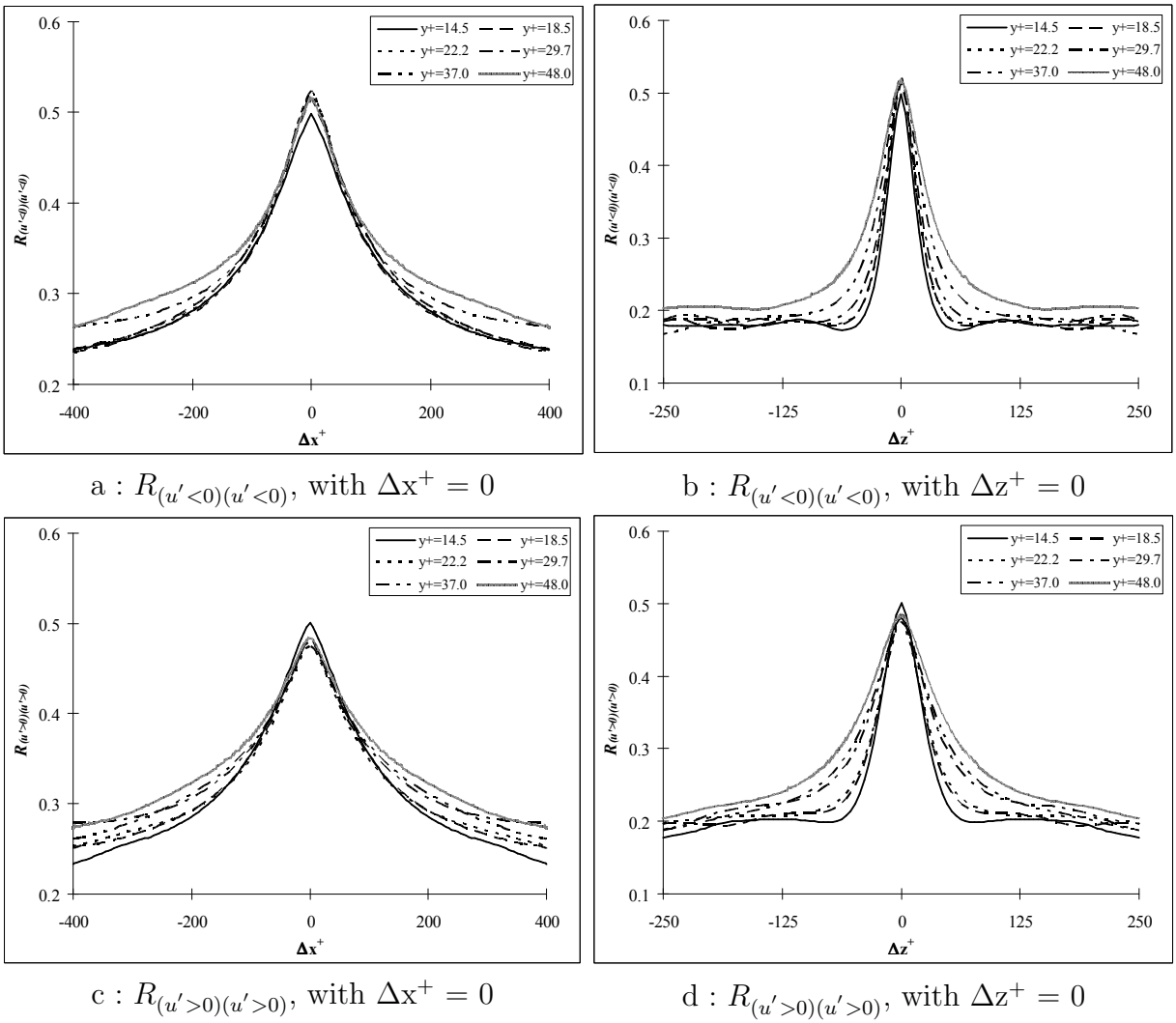

a : $R_{(u'<0)(u'<0)}$, with $\Delta x^+ = 0$

b : $R_{(u'<0)(u'<0)}$, with $\Delta z^+ = 0$

c : $R_{(u'>0)(u'>0)}$, with $\Delta x^+ = 0$

d : $R_{(u'>0)(u'>0)}$, with $\Delta z^+ = 0$

FIG. 5.3 – Conditional one-dimensional spatial auto-correlation of the streamwise velocity fluctuations $R_{u'u'}$ at selected wall distances

that the streamwise extend of low speed region is nearly the same in the buffer layer ($y^+ < 30$) and it increases with wall distance afterward. In Fig. 5.3c, globally, the streamwise extend of high speed regions increases with wall distance.

In Fig. 5.3b and 5.3d, the spanwise distance between the first off-centre maximum and the centre in the spanwise auto-correlation is used to estimate for the mean periodic spanwise spacing between low or high speed regions. However, the maximum is less clear than the minimum due to the fact that the correlation function is computed based on a decreasing number of samples with increasing displacements (Δx^+ and Δz^+, in the present study). Therefore, the distance between the first off-centre minimum and the centre in this spanwise auto-correlation function is considered as half of the mean spanwise periodic spacing. When $y^+ = 14.5$, this distance is about 60 wall units for low speed regions and 70 wall units for high speed regions. For high-speed regions, the distance can not be measured above $y^+ = 14.5$ because the distinct minimum disappears. For low speed regions, this

distance increases with wall distance up to 90 wall units at $y^+ = 33.3$ (which is not shown in Fig. 5.3b) and thereafter the distinct minimum disappears. Comparing Fig. 5.3b and 5.3d, low speed regions are more localized than high speed ones.

In Fig. 5.3, at $y^+ = 14.5$ the main positive peak of the correlation has a smaller value for $R_{(u'<0)(u'<0)}$ (0.495)than for $R_{(u'>0)(u'>0)}$ (0.505). When $y^+ \geq 18.5$, this value increases to a nearly constant (0.525) for low speed regions while it decreases to a nearly constant (0.475) for high speed ones to hold the positive peak with a value of 1 for each wall distance in Fig. 5.2. This reveals that low speed regions are more significant than high speed ones when $y^+ \geq 18.5$ and the opposite holds true for $y^+ \leq 18.5$.

5.2.2 Wall-normal velocity fluctuations

Fig. 5.4 shows an example of two-point spatial auto-correlations of the wall-normal velocity fluctuations $R_{v'v'}$ at $y^+ = 14.5$. The correlation shows also elliptical shaped contours with positive values at the centre. Besides these positive contours, two negative elliptical-shaped peaks are located symmetrically in the spanwise direction. The principal axis of these ellipses is in the streamwise direction and the minor axis in the spanwise direction. The negative contours evidence the existence of coherent structures which are in fact streamwise vortices. In Fig. 5.4, similar to $R_{u'u'}$, the principal axis is longer than the minor one, implying that these vortices have a longer extension in the streamwise direction than in the spanwise, but this extension is obviously much shorter than that for $R_{u'u'}$

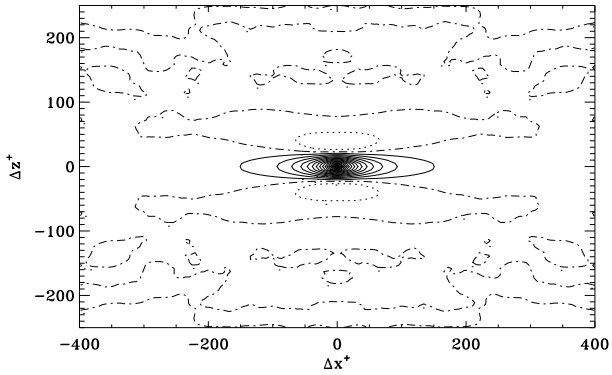

FIG. 5.4 – Two-dimensional spatial auto-correlations of the wall-normal velocity fluctuations $R_{v'v'}$ at $y^+ = 14.5$

Fig 5.5 shows two one-dimensional spatial auto-correlations : at $\Delta z^+ = 0$ and at $\Delta x^+ = 0$ respectively. These correlations show the variation of streamwise and spanwise dimensions of the structures with wall distance. In the streamwise direction, the correlations decrease sharply from the peak at the centre asymptotically to zero with increasing Δx^+. This implies that the streamwise extension of these structures is less than about 200 wall units. In the spanwise direction, the positive correlations decrease sharply from the peak at the centre to the negative minimum then increase slowly to zero. The minimum is located between 35-60 wall units, depending on wall distance.

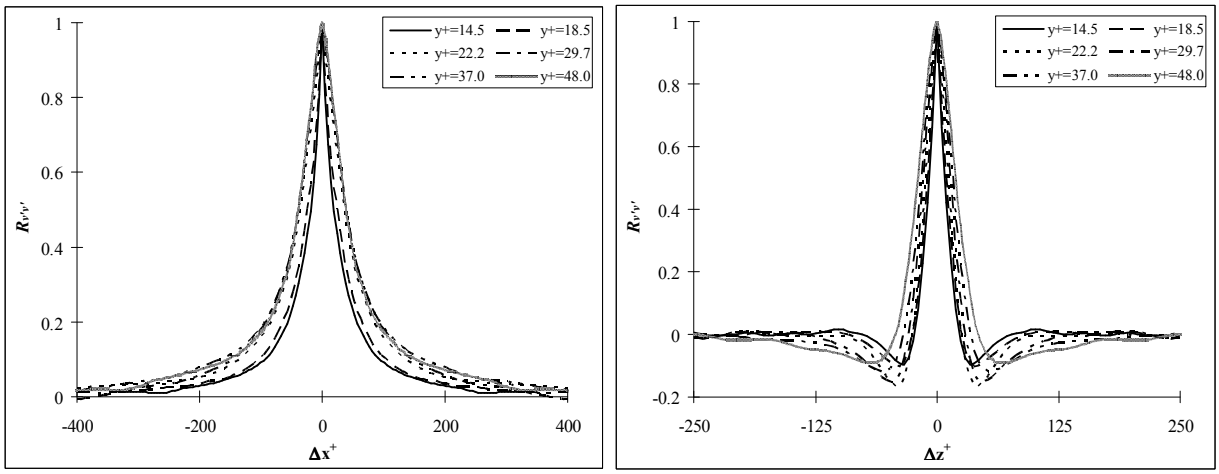

a : $R_{v'v'}$, with $\Delta x^+ = 0$ a : $R_{v'v'}$, with $\Delta z^+ = 0$

FIG. 5.5 – One-dimensional spatial auto-correlation of the wall normal velocity fluctuations $R_{v'v'}$ at selected wall distances

Similar to the streamwise velocity fluctuation, positive and negative fluctuations of the wall-normal velocity component can be separated before computing the correlations. The conditional-correlation $R_{(v'>0)(v'<0)}$ denotes the correlation of positive fluctuations at the fixed point with negative ones at the moving point, allowing to analyse the statistical properties of streamwise vortices. The two-dimensional correlation results are shown in Fig. 5.6 for various wall distances. To show the correlation clearly, colour levels are plotted instead of line contours. In Fig. 5.6, an angle between the principle axis of low correlation contours at centre and the principle axis of the high correlation contours is clearly visible and more pronounced above $y^+ = 22$. This figure also shows that the negative peaks are located in the negative region of the streamwise displacement Δx^+. It suggests that for a streamwise vortex, in case of plane top view, the part with positive wall-normal velocity fluctuations is slightly downstream of the part with negative ones.

In Fig. 5.6, the correlations are computed by correlating regions with negative wall-normal fluctuations to those with positive ones. To explain how the angle appears in Fig. 5.6, Fig. 5.7 gives a scheme of the above-mentioned two regions with different relative positions and the corresponding correlation results. As explained above, the two regions are related to streamwise vortices. In Fig. 5.7, it is assumed that only ideal streamwise vortices exist in the flow, in other words, the regions with negative and positive wall-normal velocity fluctuations related to a streamwise vortex are parallel. Let the variable in Fig. 5.7 be the wall-normal velocity fluctuation v', in the column of 'Data field', the positive wall-normal velocity fluctuations are located in the elliptical region defined by solid lines while the negative ones are in the regions with dashed lines. For the rest of the domain, the fluctuations are assumed to be zero. Fourteen particular contrapositions of negative and positive fluctuation regions are presented. In each case, the column 'Auto-correlation' shows the results of $R_{v'v'}$ while the column 'Conditional correlation' shows the results of $R_{(v'>0)(v'<0)}$. For $R_{v'v'}$, only negative correlation regions are plotted. The dotted lines show the zero-contours, and the dash-dotted lines represent the non-zero contours

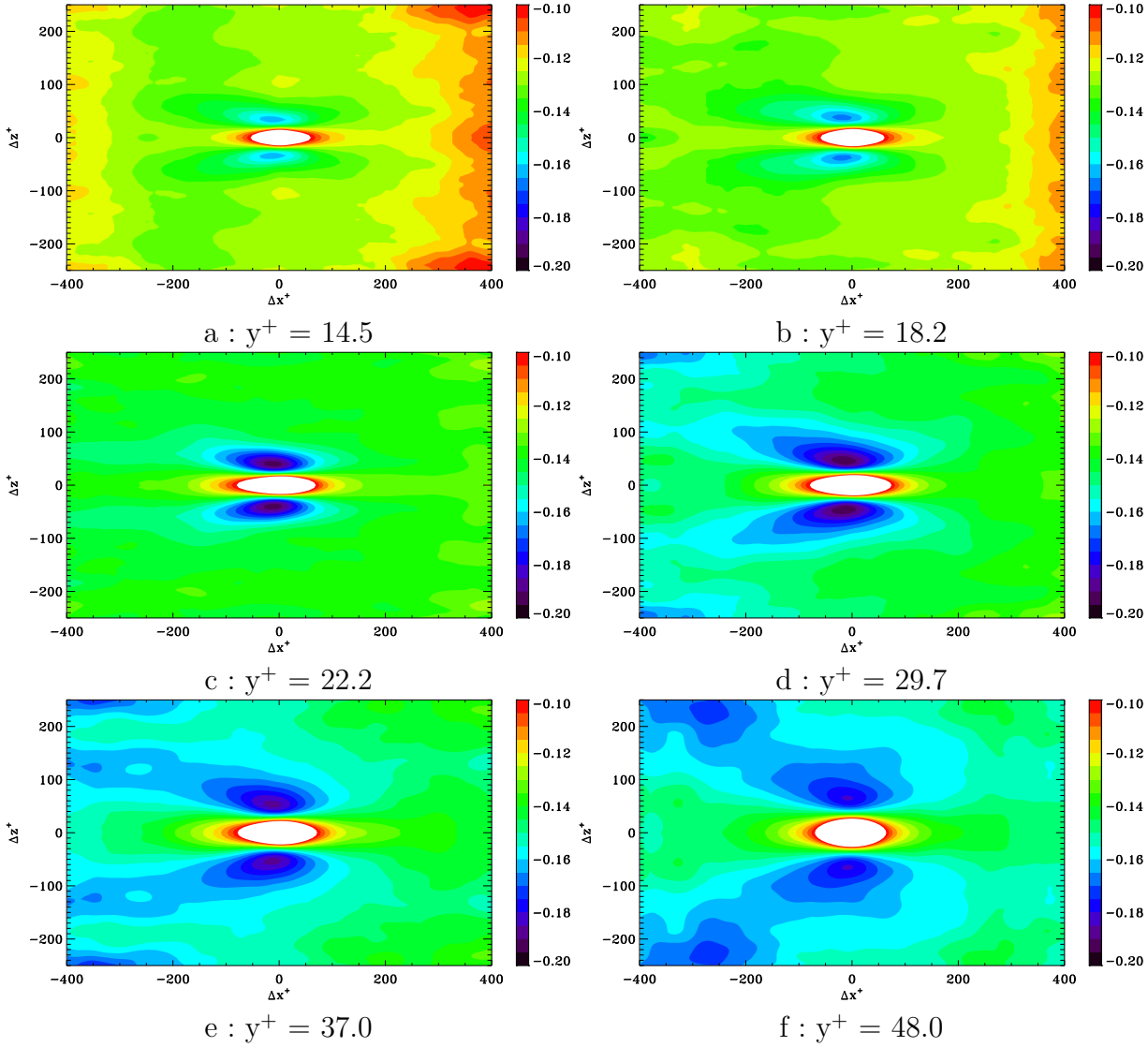

FIG. 5.6 – Conditional two-dimensional spatial auto-correlation of the wall-normal velocity fluctuations $R_{(v'>0)(v'<0)}$ at selected wall distances

(with negative values). The peak of correlation is expected to be in the centre of the ellipse.

As mentioned above, two findings are important in Fig. 5.6. One is the angle between the region with the high coherence and the streamwise coordinate, and the other is the streamwise shift of the negative peaks with respect to the centre ($\Delta x^+ = 0$, $\Delta z^+ = 0$). In the following discussion, the two findings are referred to as Rule #1 and Rule #2 respectively. Comparing the column 'Conditional correlation' with Fig. 5.6, Case 1, 2, 5, 6, 9, 10, 12 and 13 satisfy neither Rule #1 nor Rule #2. Case 3 and 4 satisfy the Rule #2 but not Rule #1, while Case 7 and 8 satisfy Rule #1 but not Rule #2. Only case 11 and 14 satisfy both of Rule #1 and Rule #2. It indicates that the streamwise vortices have a spanwise angle as well when they travel downstream. Moreover, the combined action of

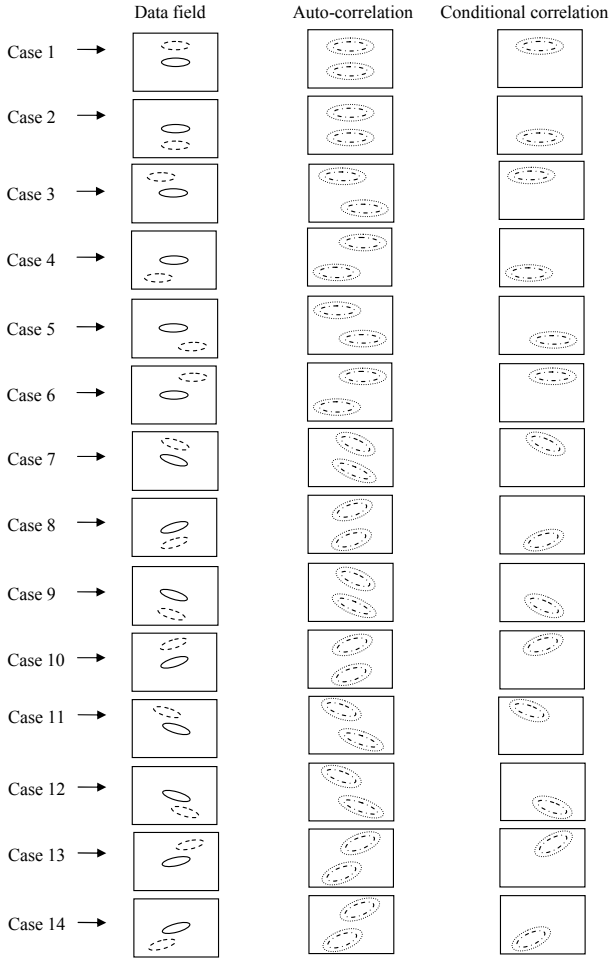

FIG. 5.7 – Illustration of data field and the corresponding correlation result

the auto-correlation of case 11 and 14 in Fig. 5.7, leads to the correlation field similar to that shown in Fig. 5.4. The combination of case 11 and 14 is known as Ω- or Λ-shaped vortices. Fig. 5.7 is based on the ideal streamwise vortex. In a real flow, these vortices may be deformed and the situation is likely to be more complicated. However, the basic principles remain the same.

Fig. 5.8 shows the one-dimensional spanwise spatial correlations $R_{(v'>0)(v'<0)}$ at $\Delta x^+ = 0$ at various wall distances. The distinct minimum in this figure shows again the high degree of coherence in the spanwise direction. The distance between the first off-centre minimum and the centre ($\Delta z^+ = 0$), is widely used to predict the mean diameter of the streamwise vortices. In the region $14.5 < y^+ < 30$, this distance increases from 30 to 40 wall units with wall distance. At the same time, the absolute value of negative peaks increases rapidly in the same region (especially from $y^+ = 18.5$ to $y^+ = 22$). In the region $y^+ > 30$, this distance increases from 40 to 60 wall units with wall distance but the absolute value of negative peaks decreases. In addition, Fig. 5.6 shows that the size of the region with high coherence at $y^+ = 30$ is larger than at other wall distances studied. It suggests that the centre of the wall-attached streamwise vortices locate around

this wall distance. This result agrees well with the results of earlier studies (e.g. Gupta *et al.* (1971), Blackwelder and Eckelmann (1979) and Carlier and Stanislas (2005)). In the region of $y^+ > 30$, the decrease of the absolute value of the negative peak, as well as the size of the region with high coherence (Fig. 5.6), can be explained twofold : one is the occurrence of other coherent structures with increasing wall distance, and the other is the decrease of the intensity of the streamwise vortices due to the interaction with other coherent structures and the lift-up when they travel downstream.

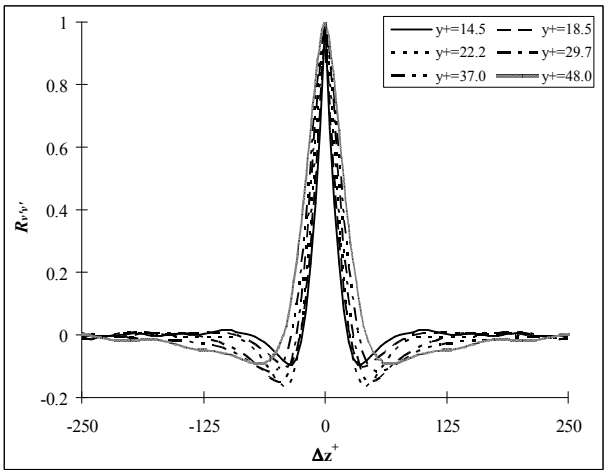

FIG. 5.8 – Conditional one-dimensional spatial auto-correlation of the wall-normal velocity fluctuations $R_{(v'>0)(v'<0)}$ at $\Delta x^+ = 0$ at selected wall distances

It should be noted that in the present study the experiment was performed in the streamwise-spanwise plane. As these vortices always move downstream with a certain angle to the wall, only parts of the cross-section of streamwise vortices can be recorded. This implies that the real streamwise extend of streamwise vortices can be larger than found here.

5.2.3 Spanwise velocity fluctuations

Fig. 5.9 shows examples of the spatial auto-correlation of spanwise velocity fluctuations $R_{w'w'}$ at $y^+ = 14.5$ and at $y^+ = 48$ respectively. These correlation contours have a more circular shape than the previous ones, which indicates that less streamwise or spanwise coherence can be found. As shown inthis figure, the shape becomes more elliptical approaching the wall.

5.3 Spatial cross-correlations

5.3.1 Streamwise and wall-normal velocity fluctuations

To investigate how turbulence is produced and transported, the cross-correlation $R_{u'v'}$ of streamwise velocity fluctuations with wall-normal ones can be computed. In this corre-

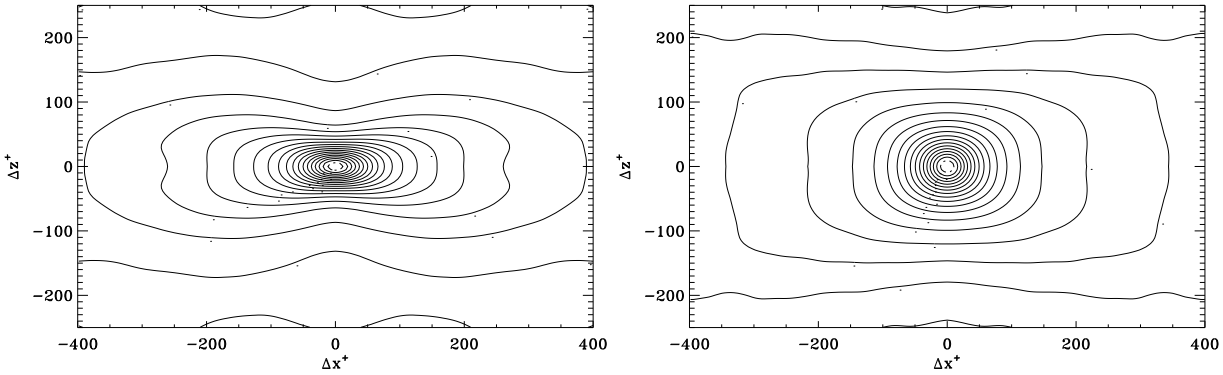

d : $y^+ = 14.5$ d : $y^+ = 48.0$

FIG. 5.9 – Two-dimensional spatial auto-correlation of the spanwise velocity fluctuations $R_{w'w'}$

lation, the streamwise fluctuation $u^{'}$ is fixed while the wall-normal fluctuation $v^{'}$ is shifted in both streamwise and spanwise directions. This correlation was first studied by Tritton (1967) and then used widely by other researchers (e.g. Kahler (2004), Carlier and Stanislas (2005)). It is used to predict the size and shape of the coherent structures which are responsible for producing and transporting turbulence.

Fig. 5.10 shows an example of the two-dimensional cross-correlation $R_{u'v'}$ at $y^+ = 14.5$. Similar to the auto-correlation $R_{v'v'}$, the cross-correlation $R_{u'v'}$ shows elliptical-shape contours with the principal axis of these ellipses in the streamwise direction and the minor axis in the spanwise direction. In contrast to $R_{v'v'}$, $R_{u'v'}$ shows the region of negative contours in the centre of the field while two regions of positive contours located nearly symmetrically in the spanwise direction besides it. The negative contours at the centre imply the existence of coherent structures that are responsible for most of the production of turbulence. The negative sign indicates that the movement of low speed fluid away from the wall ($u^{'} < 0$, $v^{'} > 0$) and the movement of high-speed fluid towards the wall ($u^{'} > 0$, $v^{'} < 0$) are the predominant processes of turbulence generation and transportation in the near wall region. These results are in good agreement with the conclusions of other studies (e.g. Wallace *et al.* (1972), Carlier and Stanislas (2005)). According to the quadrant analysis proposed by Wallace *et al.* (1972), events in quadrant two ($u^{'} < 0$, $v^{'} > 0$) are called Q2 events and events in quadrant four ($u^{'} > 0$, $v^{'} < 0$) Q4 events. Q2 and Q4 events are also referred to as ejections and sweeps respectively. Events in the other two quadrants, namely Q1 events ($u^{'} > 0$, $v^{'} > 0$) and Q3 events ($u^{'} < 0$, $v^{'} < 0$), are usually considered to be related to the interactions between Q2 and Q4 events.

Streamwise and spanwise one-dimensional cross-correlations are plotted in Fig. 5.11 to show the variation of streamwise and spanwise dimensions of these structures with wall distance. In Fig. 5.11, the absolute value of the negative peak is the smallest in the region $y^+ \leq 18.5$ and is nearly the same above $y^+ = 22$. This indicates that the normalized Reynolds shear stress $\overline{u'v'}/\sigma_u\sigma_v$ is relatively smaller in the region very near to the wall ($y^+ = 14.5$ to 18.5) than in the region away from the wall ($22<y^+<48$). It should be noted that $R_{u'v'}$ jumps from -0.3 at $y^+ = 18.5$ to 0.395 at $y^+ = 22.2$, indicating a strong production of Reynolds shear stress in this region.

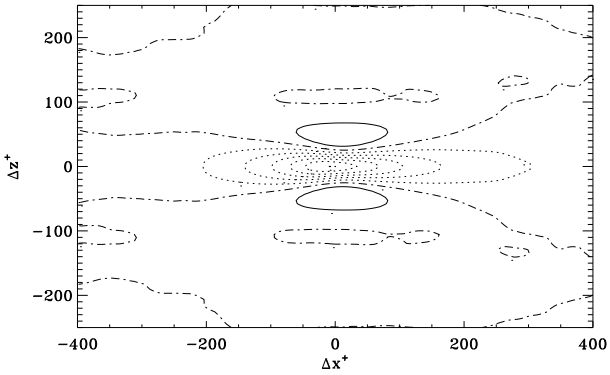

FIG. 5.10 – Two-dimensional spatial cross-correlations of streamwise velocity fluctuations with wall-normal ones $R_{u'v'}$ at $y^+ = 14.5$

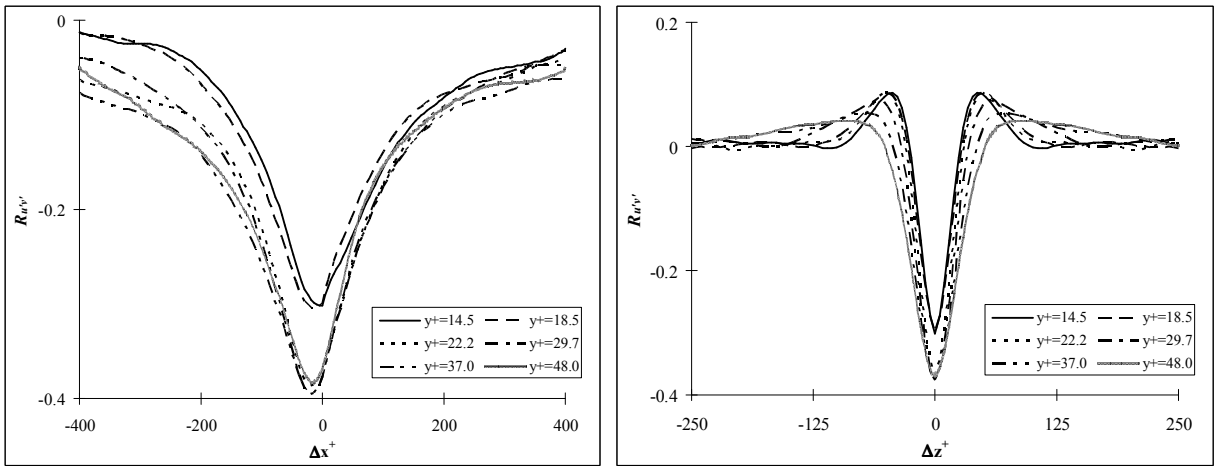

a : $R_{u'v'}$, with $\Delta x^+ = 0$ a : $R_{u'v'}$, with $\Delta z^+ = 0$

FIG. 5.11 – One-dimensional spatial cross-correlation of streamwise velocity fluctuations with wall-normal ones $R_{u'v'}$ at selected wall distances

As indicated above, the u' and v' signals can be separated into four quadrants according to their signs. It is interesting to compute the conditional cross-correlation to investigate the property of possible coherent structures in each quadrant. Fig. 5.12 shows the conditional one-dimensional cross-correlations for each quadrant.

Fig. 5.12a and 5.12b show the results of the correlation $R_{u'v'(u'>0 \text{and} v'>0)}$. In Fig. 5.12a, when $|\Delta x^+| < 60$, all the correlations are nearly the same. However, when $|\Delta x^+| > 60$, a clear asymmetry of the correlation appears. The range of the correlations with negative streamwise displacement is larger than that with positive ones. In this region, the coherence is still comparable at various wall distances. In Fig. 5.12b, all the correlations are similar, except for $y^+ = 48$ where the size of the region with high coherence is slightly larger than that at other wall distances.

Fig. 5.12c and 5.12d show the results of the correlation $R_{u'v'(u'<0 \text{and} v'>0)}$. Fig. 5.12c shows that wall distance can be separated into two groups according to the correlations.

One is in the region $y^+ \leq 18.5$ and the other is in the region $y^+ \geq 18.5$. The asymmetry between upstream and downstream is visible, but fairly low. Q2 events extend more

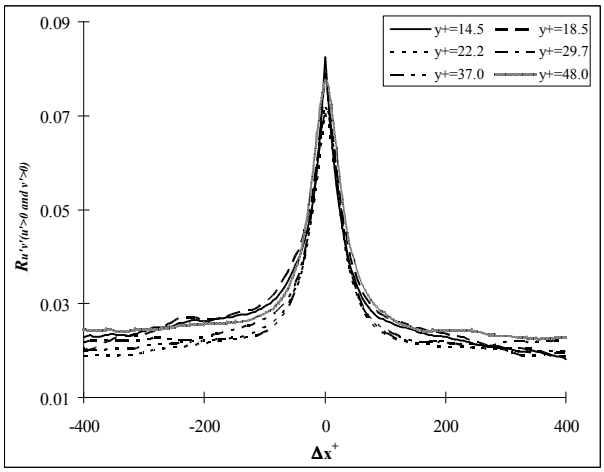

a : $R_{u'v'}(u > 0 \; and \; v > 0)$, with $\Delta x^+ = 0$

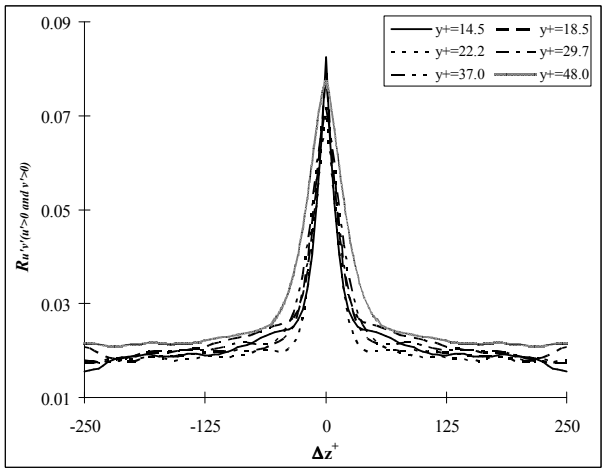

b : $R_{u'v'}(u > 0 \; and \; v > 0)$, with $\Delta z^+ = 0$

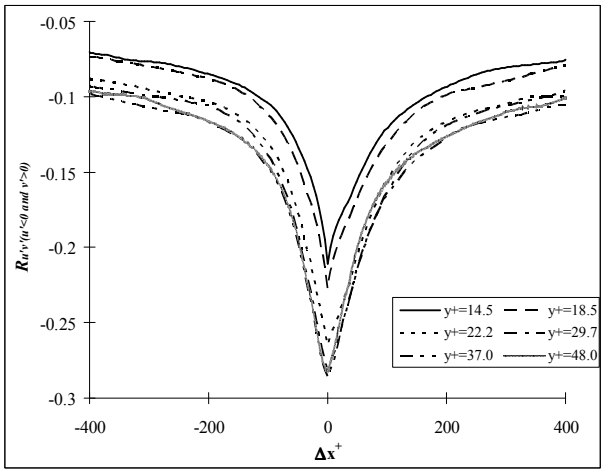

c : $R_{u'v'}(u < 0 \; and \; v > 0)$, with $\Delta x^+ = 0$

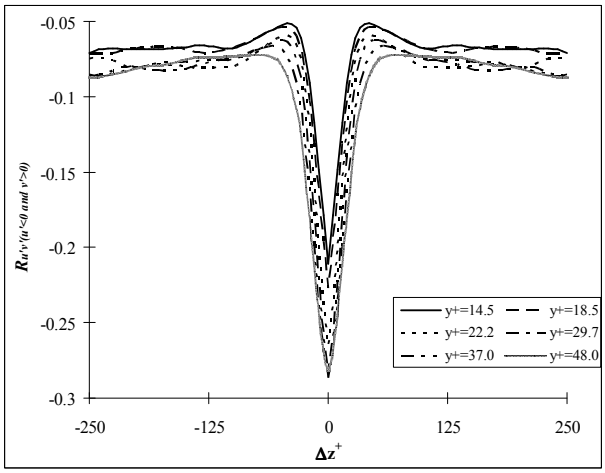

d : $R_{u'v'}(u < 0 \; and \; v > 0)$, with $\Delta z^+ = 0$

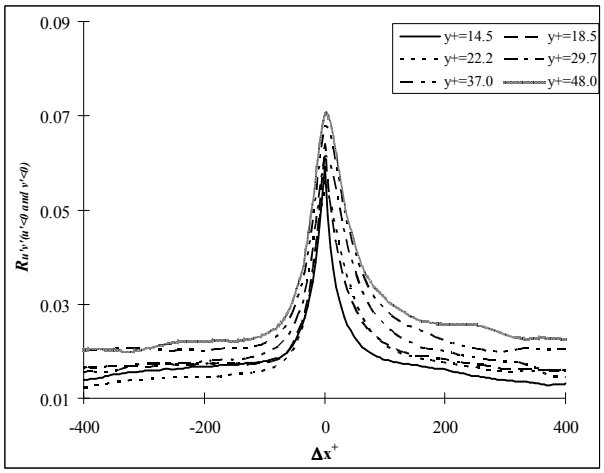

e : $R_{u'v'}(u < 0 \; and \; v < 0)$, with $\Delta x^+ = 0$

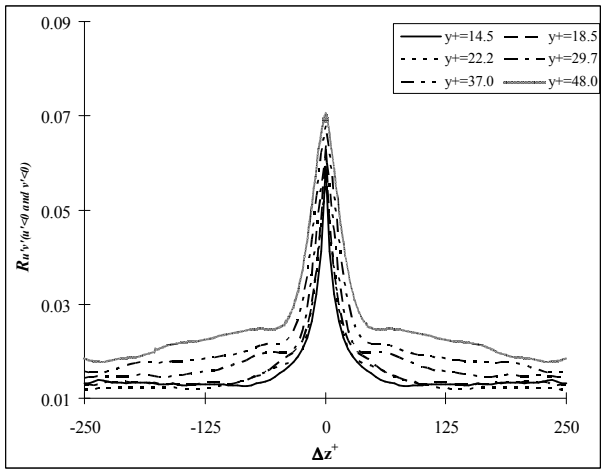

f : $R_{u'v'}(u < 0 \; and \; v < 0)$, with $\Delta z^+ = 0$

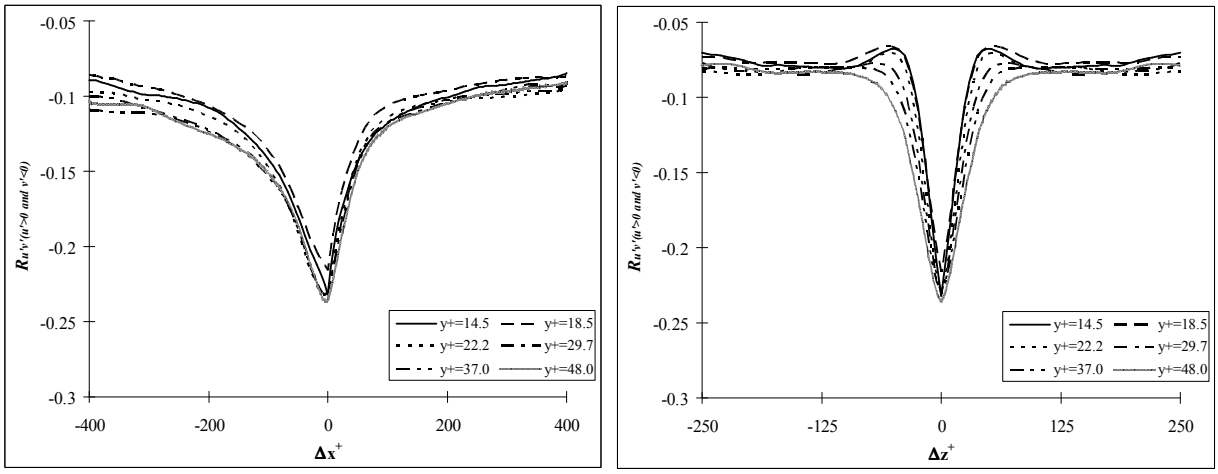

g : $R_{u'v'}(u > 0\ and\ v < 0)$, with $\Delta x^+ = 0$ h : $R_{u'v'}(u > 0\ and\ v < 0)$, with $\Delta z^+ = 0$

FIG. 5.12 – Conditional one-dimensional spatial cross-correlation of streamwise velocity fluctuations with wall-normal ones $R_{u'v'}$ in each quadrant at selected wall distances

downstream than upstream. The relatively large difference between the correlation at y^+ = 18.5 and 22.2 indicates that the streamwise extend of Q2 events in the region very close to the wall are much smaller than further away from the wall. Fig. 5.12d shows the same trend as in Fig. 5.12c, which is observable but not so clearly marked. The off-center spanwise distance of the distinct maximum is about 40 wall units at $y^+ = 14.5$ and it increases with wall distance up to about 60 wall units at $y^+ = 48$. This indicates that the spanwise dimension of the Q2 events increases with wall distance.

Fig. 5.12e and 5.12f show the results of the correlation $R_{u'v'(u'<0 \text{and} v'<0)}$. In Fig. 5.12e, in the region $y^+ > 22$, the size of correlated region and the level of coherence increase with wall distance. A clear asymmetry of the correlation appears. On the contrary to the Fig. 5.12a, the range of the correlations with negative streamwise displacement is smaller than that with positive ones. In Fig. 5.12f, an increase in size and level of coherence with wall distance is evidenced.

Fig. 5.12g and 5.12h show the results for $R_{u'v'(u'>0 \text{and} v'<0)}$. Opposite to Fig. 5.12c, the correlations are very similar at all wall distances. This indicates that the Q4 events have a size at least of the order of 50 wall units in the spanwise direction and are fairly long in the streamwise direction. Moreover, a strong asymmetry is visible with a longer extend in upstream. Fig. 5.12h shows that, on the contrary, the spanwise extend of the Q4 events increases with wall distance from 50 wall units at $y^+ = 14.5$ to 70 wall units at $y^+ = 48$ with a clear marked extrema from $y^+ = 14.5$ to 22.

As shown in Fig. 5.12a, when $\Delta x^+ < 0$, the wall distance studied can be separated into two groups according to the coherence : $y^+ < 18.5$ and $y^+ > 22$. Examining Fig. 5.12a, 5.12c, 5.12e and 5.12g, it can be concluded that this phenomenon mainly results from the Q2 events. Additionally, the correlations in Fig. 5.12a, 5.12c, 5.12e and 5.12g show an asymmetry with respect to $\Delta x^+ = 0$, especially for Q3 and Q4 events. With the same displacement and wall distance, the correlation in the negative part ($\Delta x^+ < 0$) is higher than in the positive part ($\Delta x^+ > 0$) for Fig. 5.12a and 5.12g, while the opposite is true

for Fig. 5.12c and 5.12e. This indicates that in each quadrant, the high wall-normal and streamwise velocity fluctuations normally do not appear at the same place. The high wall-normal velocity fluctuations are located upstream of the streamwise ones in Q1 and Q4 events but downstream in Q2 and Q3 events.

The absolute values of the main peaks $R_{u'v',max}$ of the conditional cross-correlations, are plotted in Fig. 5.13. Several conclusions can be drawn based on these values. First, the intensity in Q1 and Q3 events is very similar. Second, the contribution of Q2 and Q4 events to the generation of Reynold shear stress is respectively about 3.5 times higher in modules than that of Q1 and Q3 events. This manifests that the former two events dominate the turbulence generation and transportation. Third, Q4 events are more responsible for the generation of turbulence than Q2 events when very close to the wall (y^+ <18.5), while the opposite is true for $y^+ > 18.5$. Finally, the distribution of the contribution to the turbulence production with wall distance is different for Q2 and Q4 events. For Q2 events, it increases with wall distance in the region $y^+ < 30$ and is nearly constant afterwards. For Q4 events, it keeps nearly constant in the whole range studied. In the region $y^+ > 30$, the contribution of Q2 events to the generation of turbulence is about 20% higher than that of Q4 events. These results roughly agree with previous results (e.g. Corino and Brodkey (1969) and Wallace *et al.* (1972)).

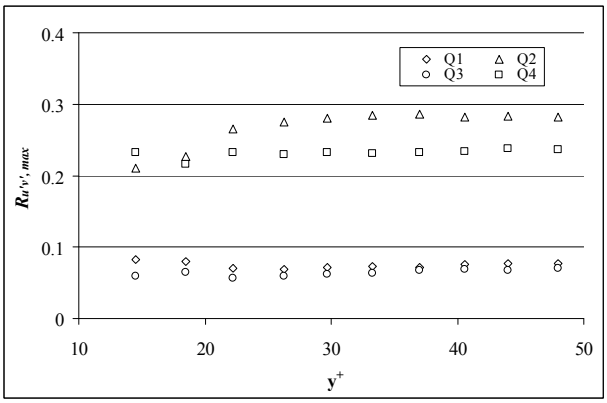

FIG. 5.13 – Absolute value of the main peak of $R_{u'v',max}$ in each quadrant at various wall distances

5.3.2 Streamwise and spanwise velocity fluctuations

In addition to the turbulence generation and its transportation in the streamwise and wall-normal directions, the flow motions in the streamwise and spanwise directions are also important to be investigated. Fig. 5.14 shows the two-dimensional cross-correlation of streamwise velocity fluctuations with spanwise ones $R_{u'w'}$ at various wall distances. In this figure, two nearly elliptic regions with high correlation values, locate almost symmetrically with respect to $\Delta z^+ = 0$ in the spanwise direction. Both regions are with opposite signs (the positive is above $\Delta z^+ = 0$ while the negative is below it) and are shifted with respect to the center ($\Delta x^+ = 0$, $\Delta z^+ = 0$) in both streamwise and spanwise directions. The elliptic regions show the existence of a well-organized spanwise motion, especially close to

the wall. It should be noted that two small regions with relatively high coherence appear clearly on the left side of Fig. 5.14d.

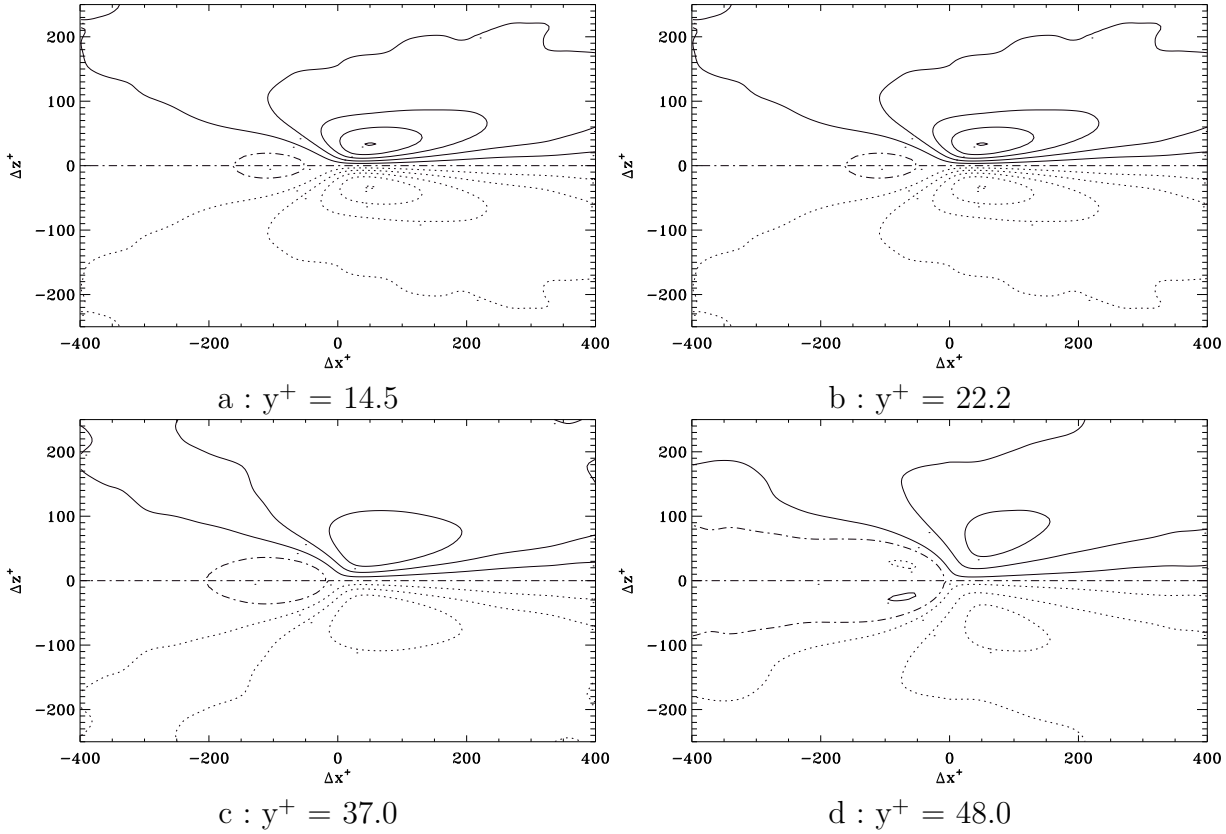

FIG. 5.14 – Two-dimensional spatial cross-correlations of streamwise with wall-normal velocity fluctuations $R_{u'w'}$

To investigate separately the contribution of low and high speed regions to this correlation, the $u^{'}$ signal is divided into two groups according to its signs and then the conditional cross-correlations $R_{(u'<0)w'}$ and $R_{(u'>0)w'}$ are computed. Fig. 5.15 shows an example of these correlations at $y^+ = 22.2$. Clearly at the same wall distance, the peaks are not located at the same position for both correlations and their values are different.

To investigate the above conditional correlations, Fig. 5.16 shows the absolute value of the peak of the cross-correlations of $R_{(u'<0)w'}$ and $R_{(u'>0)w'}$ at various wall distances. The error bars represent an error of 5% of the absolute value. These values show a tendency of decrease with wall distance, which implies that the further away from the wall, the weaker the coherent structures are. As shown in profiles of the RMS of velocity (Chapter 4), spanwise fluctuations are small near the wall but they increase sharply with increasing wall distance. On the contrary, the streamwise fluctuations are high near the wall but decrease sharply with increasing wall distance. In addition, the rate of decrease in streamwise velocity fluctuations is much higher than the rate of increase in the spanwise velocity fluctuations (especially very close to the wall : $y^+ < 22$). This explains in part the decrease of $R_{u'w',max}$ as shown in Fig. 5.16. The figure also shows that the peak value of $R_{(u'<0)w'}$ is slightly smaller than that of $R_{(u'>0)w'}$.

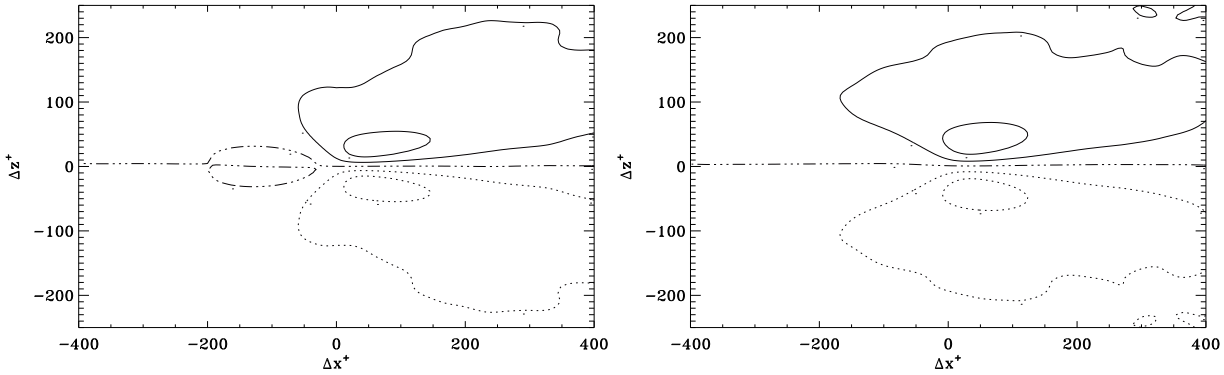

a : $R_{(u'<0)w'}$ b : $R_{(u'>0)w'}$

FIG. 5.15 – Conditional two-point spatial cross-correlations of streamwise velocity fluctuations with wall-normal ones $R_{(u'<0)w'}$ and $R_{(u'>0)w'}$ at $y^+ = 22.2$

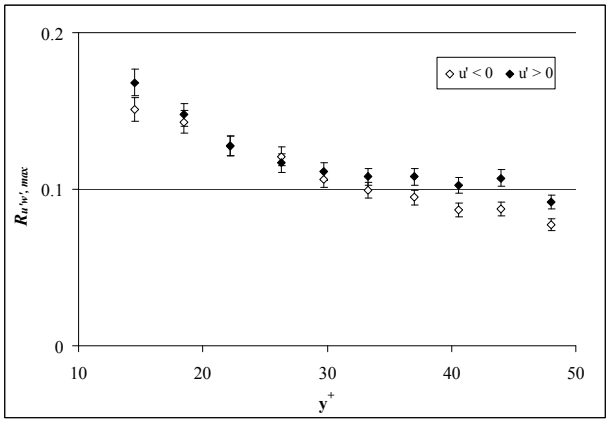

FIG. 5.16 – Absolute value of the peak of $R_{(u'<0)w'}$ and $R_{(u'>0)w'}$ at selected wall distances

Fig. 5.17 shows the streamwise and spanwise off-centre distances of the peak of the cross-correlations of $R_{(u'<0)w'}$ and $R_{(u'>0)w'}$ at various wall distances. The error bars represent an error of 5 wall units which is the grid size of the correlation field. In the region $y^+ < 27$, the streamwise distance appears more or less constant around 60 and 43 wall units for $R_{(u'<0)w'}$ and $R_{(u'>0)w'}$ respectively. Then, it grows to about 72 and 67 wall units at $y^+ = 48.0$ and stays constant afterwards. Fig. 5.17 shows that the spanwise off-centre distance of $R_{(u'<0)w'}$ increases from about 24 wall units at $y^+ = 14.5$ to about 60 wall units at $y^+ = 48$. The rate of the increase in the buffer layer $y^+ \leq 30$ is much lower than that in the region $y^+ > 30$. For $R_{(u'>0)w'}$, this spanwise off-centre distance increases linearly from 29 wall units at $y^+ = 14.5$ to 77 wall units at $y^+ = 48$.

As $R_{u'w'}$ is a correlation of u' with w' and u' is also an indicative parameter of streaks, there should be a relation between the correlations $R_{u'w'}$ and $R_{u'u'}$. Fig. 5.18 shows the spanwise distance between positive and negative peaks of $R_{(u'<0)w'}$ (Fig. 5.14a) together with the half of mean spanwise distance between low speed regions obtained with the help of auto-correlation results in Fig. 5.3b. The error bars represent an error of 5 wall units. As shown in Fig. 5.3b, the coherence intensity decreases with wall distance. Therefore,

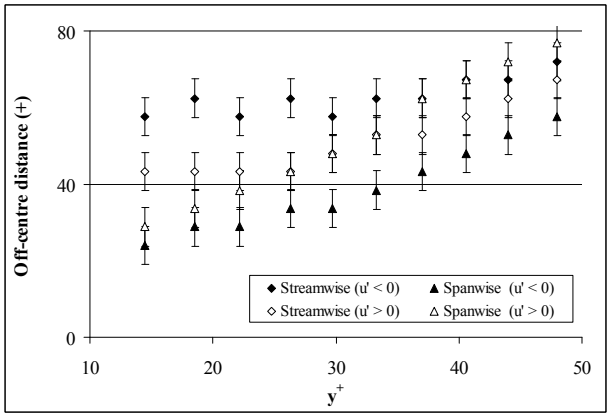

FIG. 5.17 – Mean streamwise and spanwise off-centre distance of both positive and negative peaks of $R_{u'w'}$ at selected wall distances

in Fig. 5.18, the half of mean spanwise distances is obtained only for six positions near the wall where the distinct minimum is visible (some of the results are not shown in Fig. 5.3b). Fig. 5.18 shows that half of the mean spanwise distance between the low speed regions is very similar to the spanwise distance between the negative and positive peaks of correlation, indicating that the spanwise distance between the peaks of correlation is supposed to be equal to half the mean spanwise distance between the low speed regions. As shown in Fig. 5.3d, for $R_{(u'>0)(u'>0)}$, the distinct minimum only appears at $y^+ = 14.5$ and it is located at 70 wall units. This value is comparable to the spanwise distance between the negative and positive peaks of $R_{(u'>0)w'}$ (58 wall units).

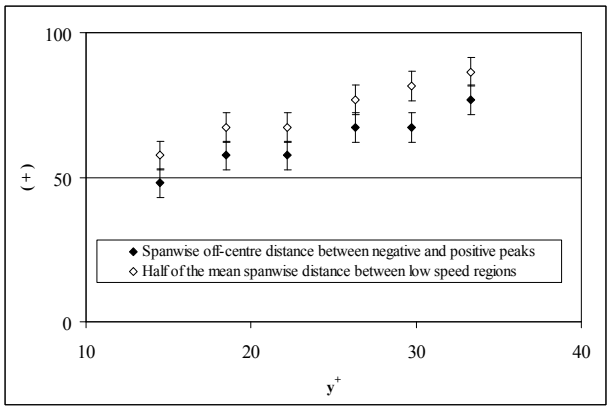

FIG. 5.18 – Comparison of the spanwise off-centre distance between negative and positive peaks with half of the mean spanwise distances between low speed regions

5.3.3 Wall-normal and spanwise velocity fluctuations

The last interesting cross-correlation is between the wall-normal and spanwise velocity fluctuations $R_{v'w'}$. Fig. 5.19 shows the two-dimensional $R_{v'w'}$ at various wall distances.

Similar to $R_{u'w'}$, two elliptic regions with high correlation are located symmetrically with respect to the axis $\Delta z^+ = 0$. These two regions are of opposite signs and shifted with respect to the centre ($\Delta x^+ = 0$, $\Delta z^+ = 0$) in both streamwise and spanwise directions. Different from the correlation $R_{u'w'}$, the positive region is below while the negative one is above the axis. The elliptic regions show the existence of a well-organized spanwise motion, in particular close to the wall. Secondary peaks appear on the left side of Fig. 5.19c at $y^+ > 37$. The further away from the wall, the clearer these peaks are. This phenomenon will be interpreted in detail in Chapter 7.

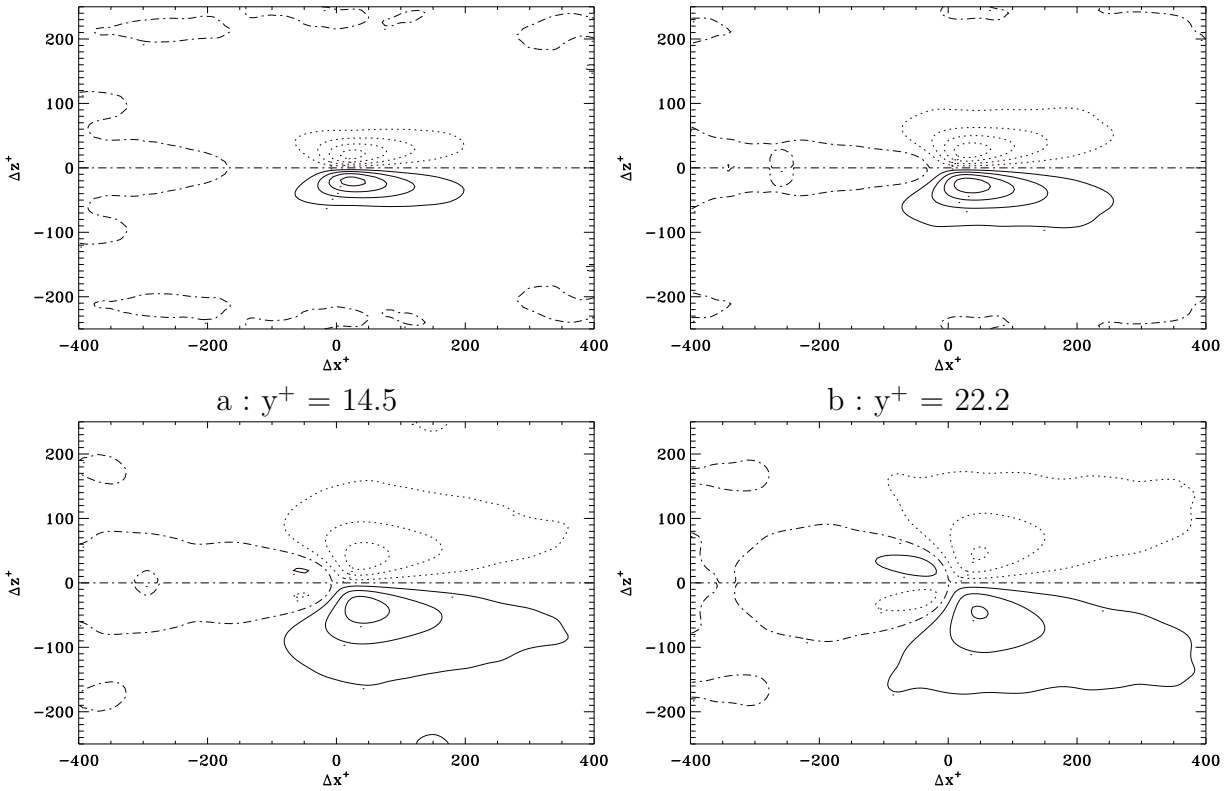

a : $y^+ = 14.5$ b : $y^+ = 22.2$

c : $y^+ = 37.0$ d : $y^+ = 48.0$

FIG. 5.19 – Two-dimensional spatial cross-correlations of streamwise with wall-normal velocity fluctuations $R_{v'w'}$

As for $R_{u'w'}$, the v' signal is divided into two groups according to its signs in order to perform the conditional cross-correlations $R_{(v'<0)w'}$ and $R_{(v'>0)w'}$. Fig. 5.20 shows an example of these correlations at $y^+ = 22.2$. At the same wall distance, the location as well as the value of the peak is different for both correlations.

Fig. 5.21 shows the absolute value of the peaks of $R_{(v'<0)w'}$ and $R_{(v'>0)w'}$ at various wall distances. The error bars represent an error of 5% of the absolute value. In the region $y^+ \leq 22.2$, , this value is nearly the same when $y^+ \leq 18.5$ and then it jumps to a maximum at $y^+ = 22.2$ for $R_{(v'<0)w'}$ while it is nearly a constant for $R_{(v'>0)w'}$. In the region $y^+ > 22$, this value is comparable for both $R_{(v'<0)w'}$ and $R_{(v'>0)w'}$ and it decreases with wall distance.

Fig. 5.22 shows the streamwise and spanwise off-centre distances of the peaks of

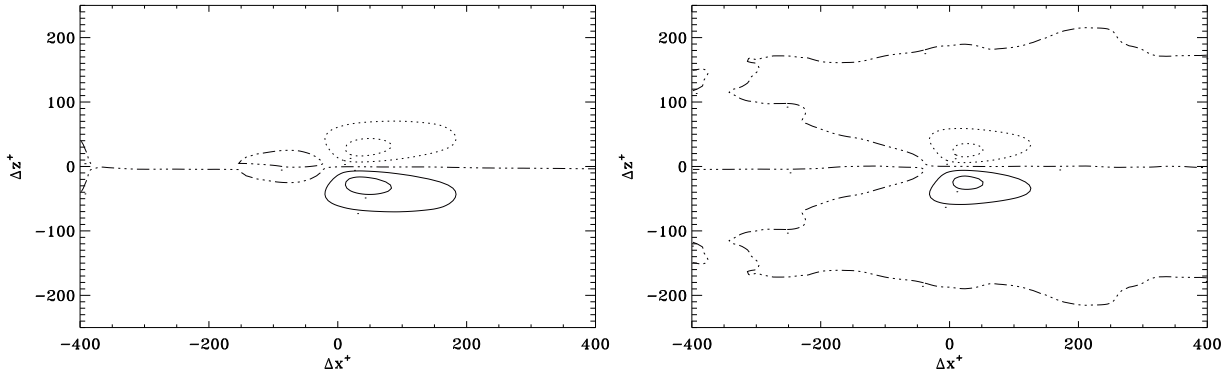

a : $R_{(v'<0)w'}$ b : $R_{(v'>0)w'}$

FIG. 5.20 – Conditional two-point spatial cross-correlations of streamwise with wall-normal velocity fluctuations $R_{(v'<0)w'}$ and $R_{(v'>0)w'}$ at $y^+ = 22.2$

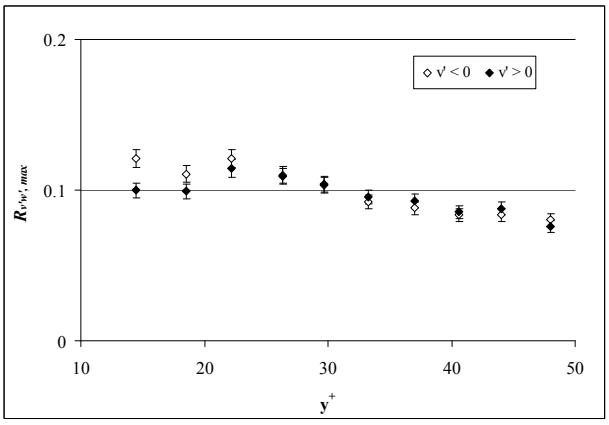

FIG. 5.21 – Absolute value of the peak of $R_{(v'<0)w'}$ and $R_{(v'>0)w'}$ at selected wall distances

$R_{(v'<0)w'}$ and $R_{(v'>0)w'}$ at various wall distances. The error bars represent an error of 5 wall units. Globally, both distances increase with wall distance. The streamwise distance for $R_{(v'<0)w'}$ is much larger than that of $R_{(v'<0)w'}$ while the spanwise distance is comparable between them. For $R_{(v'<0)w'}$, the streamwise distance is nearly the same as the spanwise one. Moreover, off-centre distances (in both streamwise and spanwise directions) in Fig. 5.22 are smaller than those in Fig. 5.17 at the same wall distance. These phenomena will be interpreted in detail in Chapter 7.

As v' is one of the indicative parameter for streamwise vortices, it is interesting to compare the spanwise off-centre distance from $R_{(v'<0)w'}$ and $R_{(v'>0)w'}$ to those from $R_{(v'>0)(v'<0)}$. Fig. 5.23 shows this comparison of the spanwise off-centre distance of the peaks of $R_{(v'<0)w'}$ and $R_{(v'>0)w'}$ with those of $R_{(v'>0)(v'<0)}$. The latter is usually applied to estimate the radius of the streamwise vortices. Fig. 5.18 shows that the the distances of $R_{(v'>0)(v'<0)}$ are small but comparable to those of $R_{(v'<0)w'}$ and $R_{(v'>0)w'}$. Detailed explanation of this can be found in Chapter 7.

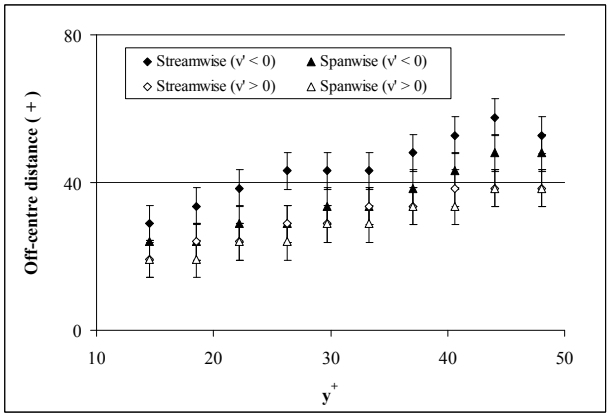

FIG. 5.22 – Mean streamwise and spanwise off-centre distance of both positive and negative peaks of $R_{v'w'}$ at selected wall distances

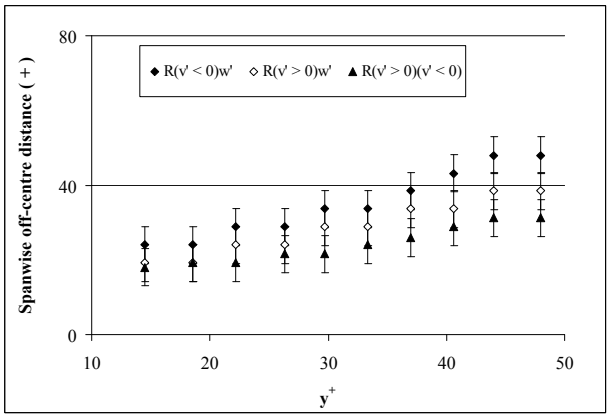

FIG. 5.23 – Comparison of the spanwise off-centre distance of the peaks of $R_{(v'<0)w'}$ and $R_{(v'>0)w'}$ with those of $R_{(v'>0)(v'<0)}$

5.4 Comparison

As shown in Fig. 5.17, the peaks (both negative and positive) are shifted in the streamwise and spanwise directions with respect to the centre ($\Delta x^+ = 0$, $\Delta z^+ = 0$). This result agrees well with that of Lee *et al.* (1974). They measured the streamwise and spanwise velocities of a pipe flow ($y^+ < 5$) at various spanwise locations close to the wall as a function of time. Besides a maximum and a minimum in the correlation between streamwise and spanwise velocity components, they found a time delay between these velocities as well. This time delay can be transformed into the spatial shift shown in Fig. 5.14 using a local Taylor hypothesis. In other words, regions with high positive and negative spanwise velocities are found both downstream and shifted in the spanwise direction with respect to a region with high streamwise velocity. Lee et al. also proposed that the spanwise distance between positive and negative peaks of $R_{u'w'}$ should be equal to the half of mean spanwise distance between low speed regions, which is proved by the present study.

Kahler (2004) found that the spanwise off-centre distance of the minimum of correlation $R_{v'v'}$ is about 44 and 53 wall units at $y^+ = 20$ and 30 respectively. These values are comparable to the present results. Kahler (2004) suggested that in the region $20 \leq y^+ \leq 30$ the streamwise off-centre distance of the extrema of correlation $R_{u'w'}$ is about 57 wall units, which is also in good agreement with the present results. However, Kahler found that the spanwise off-centre distance of these extrema is about 38 and 50 wall units at $y^+ = 20$ and 30 respectively. These values are much larger than the present results shown in Fig. 5.17. However, in Kahler (2004), the cross-correlation $R_{u'w'}$ is slightly asymmetric with respect to $\Delta z^+ = 0$ due to the lack of convergence and this distance was measured only in the region $\Delta z^+ > 0$. If the measurement were taken in the region $\Delta z^+ < 0$, the distance would be about 33 and 40 wall units respectively in the above-mentioned two wall locations. These distances are nearly the same as the present results.

5.5 Summary

In order to obtain information about the global characteristics of coherent structures, the size, shape, and intensity of various two points correlations were examined in detail. The results show that the characteristics of coherent structures depend strongly on wall distance, especially for the intensity of the correlation and spanwise spacing.

The auto-correlation $R_{u'u'}$ evidences the existence of streaks in the near wall turbulent flow. Conditional correlations $R_{(u'<0)(u'<0)}$ and $R_{(u'>0)(u'>0)}$ shows that both low and high streaks are elongated in the streamwise direction. These correlations shows that the streamwise extend is around 1000 and 800 wall units for low and high speed streaks respectively. The size of these structures increases with wall distance in both streamwise and spanwise directions. At the same wall location, low speed streaks are longer but narrower than high speed ones. At $y^+ = 14.5$, the spanwise distance is about 120 wall units for low speed streaks and about 140 wall units for high speed ones. It increases with wall distance for both types of structures. The above results are in good agreement with those obtained by other researchers.

The auto-correlation $R_{v'v'}$ and conditional correlation $R_{(v'>0)(v'<0)}$ show that the streamwise dimension of streamwise vortices is less than about 200 wall units, and that the diameter of these vortices increases with wall distance from about 40 wall units at $y^+ = 22.2$ to about 60 wall units at $y^+ = 48$. $R_{v'v'}$ and $R_{(v'>0)(v'<0)}$ suggests that the wall-attached streamwise vortices are centred between $y^+ = 20$ and 30. In addition, the conditional correlation $R_{(v'>0)(v'<0)}$ implies the existence of the Λ- and Ω-shape vortices.

The cross-correlation $R_{u'v'}$ in the whole field and the conditional correlations $R_{u'v'}$ in each quadrant show that the contribution of Q2 (ejections) and Q4 (sweeps) to the production of the turbulence is about 3.5 times higher than that of Q1 and Q3, indicating the former two events dominate this process. Moreover, conditional correlations $R_{u'v'}$ of Q2 and Q4 suggests that very close to the wall ($y^+ < 18.5$), Q4 events have a more important contribution to the production of turbulence than Q2 events. The opposite holds true in the region $y^+ > 18.5$.

The cross-correlations $R_{u'w'}$ and $R_{v'w'}$ indicate that regions with high spanwise velocity fluctuations can be found both downstream and shifted in the spanwise direction

with respect to regions with high streamwise or wall-normal velocity fluctuations. The correlation degree of $R_{u'w'}$ and $R_{v'w'}$ decreases with wall distance. The off-centre distance of the extrema increases with wall distance in both streamwise and spanwise directions. Moreover, for $R_{u'w'}$, the off-centre spanwise distance of the extrema is found to be close to the half of the spanwise spacing of low speed streaks.

Chapitre 6

Detection and Statistics on Coherent Structures

6.1 Pattern recognition

The aim of pattern recognition is to classify data (patterns) based on either a priori knowledge or on statistical information extracted from the patterns. The patterns to be classified are usually groups of measurements or observations, defining points in an appropriate multidimensional space. A complete pattern recognition system consists of an experiment capturing device (e.g. sensor, camera, etc.) that gathers the observations to be classified or described ; a feature extraction mechanism that computes numeric or symbolic information from the observations ; and a classification or description scheme that does the actual job of classifying or describing observations, relying on the extracted features.

The classification or description scheme is usually based on the availability of a set of patterns that have already been classified or described. This set of patterns is termed the training set and the resulting learning strategy is characterised as supervised. Learning can also be unsupervised, in the sense that the system is not given a priori labelling of patterns, instead it establishes the classes itself based on the statistical regularities of the patterns.

The classification or description scheme usually uses one of the following approaches : statistical, syntactic (or structural), or neural. Statistical pattern recognition is based on statistical characterisations of patterns, assuming that the patterns are generated by a probabilistic system. Structural pattern recognition is based on the structural relationships of features. Neural pattern recognition employs the neural computing paradigm that has emerged with neural networks. The detail theory and main application of pattern recognition can be found in the books of Paulus and Hornegge (1998) and Gonzalez and Woods (2001).

In the present study, pattern recognition was used to identify and investigate coherent structures specific of near wall turbulence : streaks, ejections, sweeps and streamwise vortices.

It is performed in four steps :

1. Detection function definition : to define the detection function according to the property of structures.
2. Thresholding : to generate binary indicative images.
3. Mathematical morphology : to remove noise and improve the quality of each binary image.
4. Cleaning : to remove the mis-detected objects.

Details of these procedures are explained in the following sections.

6.1.1 Detection function definition

To identify the structure objects, a detection function F_d or a group of detection functions F_d^i which describe(s) their basic characteristic(s), has to be defined. The function is generated according to the property of the structures which are inferred from the observations in the experiments or numerical simulations. In general, a detection function can be defined as :

$$F_d = f(var_1, var_2, ...var_n) \tag{6.1}$$

Where, $var_1, var_2, ...var_n$ are parameters characterising the structures to be detected.

6.1.2 Thresholding

The thresholding is a standard procedure in the digital image processing. A gray level digital image a[m,n] defined in a 2D discrete space is derived from an analog image a(x,y) in a 2D continuous space through a sampling process that is referred to as digitization (Gonzalez and Woods (2001)). In this process, the 2D continuous image a(x,y) is divided into N rows and M columns. The intersection of a row and a column is termed a picture element, an image element, a pel or a pixel. Pixel is the most widely used term.

Using the method of binary segmentation (Gonzalez and Woods (2001)), the digital image can be transformed to a binary image which has only two possible values : 1 or 0. Based on a threshold level, the value of a pixel in the digital image is defined as 1 if its gray-level intensity is larger than the threshold level, and 0 if it is less than or equal to the threshold. Fig. 6.1 shows an example of a digital binary image.

In the present study, the detection function F_d obtained from SPIV data is a real scalar field defined on a discrete (M, N) grid in R^2, which can easily be thresholded directly, leading to a binary discrete function analog to a binary image. This binary image is called here an indicative function F_i, which is defined as :

$$F_i = \begin{cases} 1 \text{ when } F_d \geq C_T \\ 0 \text{ otherwise} \end{cases} \tag{6.2}$$

$$\tag{6.3}$$

or

$$F_i = \begin{cases} 1 \text{ when } F_d \leq C_T \\ 0 \text{ otherwise} \end{cases} \tag{6.4}$$

Here, C_T refers to the threshold.

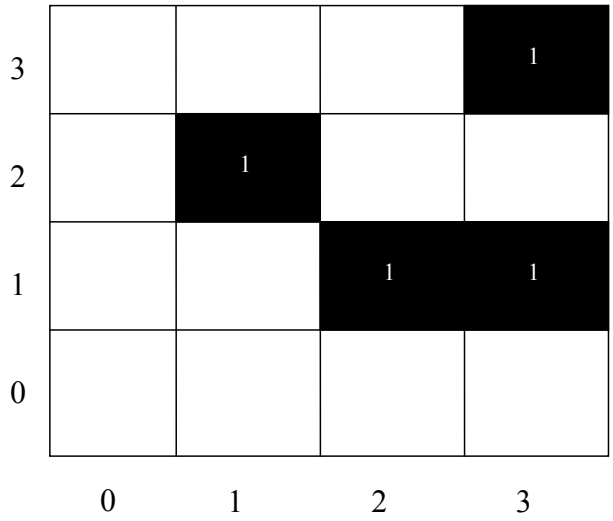

FIG. 6.1 – Example of a digital binary image

6.1.3 Mathematical morphology

The indicative function F_i, is a binary image obtained directly from the thresholding procedure. To remove the noise and to improve the quality of the image, a mathematical morphology procedure is employed.

6.1.3.1 Introduction

Mathematical morphology is a methodology for image analysis, which aims at quantitatively describing the geometrical structure of image objects. It was initiated in the late 1970's to analyse binary images from geological and biomedical data (Matheron (1975), Meyer (1977)) as well as to formalize and extend earlier or parallel work (Preston and Duff (1984)) on binary pattern recognition based on cellular automata and Boolean/threshold logic. In the mean time, it was extended to gray-level images (Serra (1982). In 1990, it was brought to the mainstream of image/signal processing and related to other nonlinear filtering approaches (Maragos and Schafer (1990)). Finally, it was generalized to arbitrary lattices (Serra (1988), Heijmans (1994)). The above evolution of ideas has formed what is called nowadays the field of morphological image processing, which is a broad and coherent collection of theoretical concepts, nonlinear filters, design methodologies, and applications systems. Its rich theoretical framework, algorithmic efficiency, easy implementability on special hardware, and suitability for many shape-oriented problems have propelled its widespread usage and further advancement by many academic and industry groups working on various problems in image processing, computer vision, and pattern recognition.

6.1.3.2 Morphology operators for a binary set

Let us consider a set of elements, A $= [a_1, a_2, ...a_m]$, of a commutative group in a n-dimensional (nD) integer space Z^n, each $a_{i=1,2,...m}$ is thus an nD integer vector in Z^n. Any digital binary image can be represented as such a set. For example, the digital binary

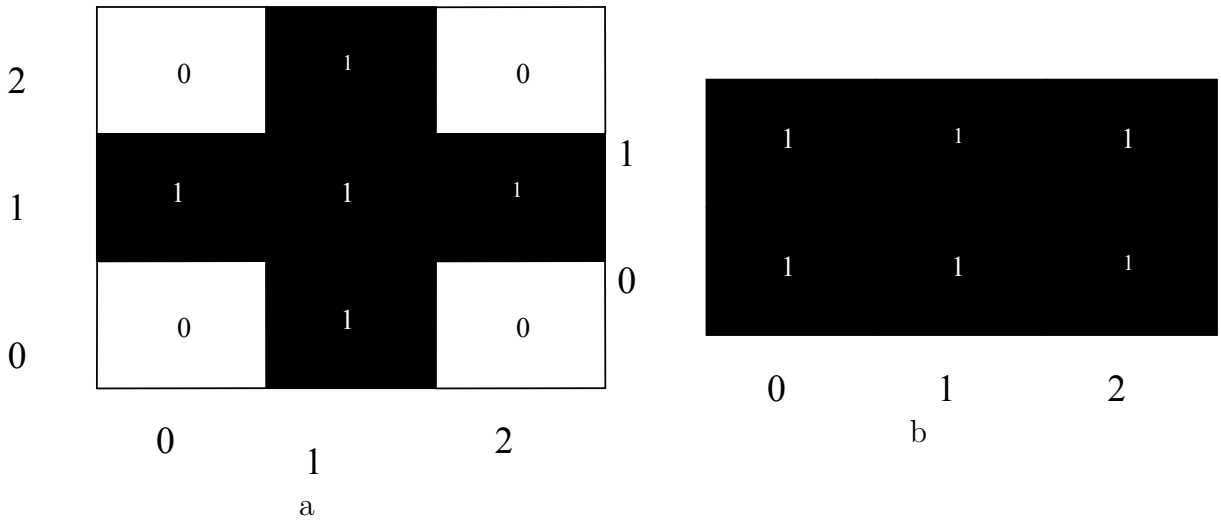

FIG. 6.2 – Examples of structuring element for a binary set, a : circular structuring element with a radius of 1 ; b : rectangular structuring element with 3 in length and 2 in width

image in Fig. 6.1 can be presented by A = [(2,1), (2,3), (1,2), (3,3) in Z^2. Following Matheron (1975), the basic morphological transformations that can be applied to such a discrete binary set are dilation and erosion, which are based on Minkowski algebra.

Dilation and erosion

Let B be also a set of the same commutative group as, B = $[b_1, b_2, ...b_l]$. The dilation of A by B, noted $\delta_B(A)$, is the Minkowski addition ($\oplus$) of A and B while the erosion, noted $\epsilon_B(A)$, is the Minkowski subtraction ($\ominus$) of B from A. They are defined by :

$$\begin{aligned} \delta_B(A) &= A \oplus B = \bigcup(\{x\} + B; \{x\} \in A) \\ \epsilon_B(A) &= A \ominus B = \bigcup(\{x\}\,; \{x + B\} \in A) \end{aligned} \tag{6.5}$$

In practice, the set A will be the input binary data set created by the filtering or thresholding procedure, which has values 1 for the image objects and 0 for the background. The set B will be referred to as a structuring element. For a binary set, the structuring element contains two values : 1 and 0. It can be defined as any shape according to the application. Fig. 6.2 shows examples of a circular structuring element with a radius of 1 and a rectangular structuring element of 2*3.

Erosion generally decreases the sizes of objects and removes small anomalies by eliminating objects with a size smaller than the structuring element. With binary images, erosion completely removes objects smaller than the structuring element and removes perimeter pixels from larger image objects. Dilation generally increases the sizes of objects, filling in holes and broken areas, and connecting areas that are separated by spaces smaller than the size of the structuring element. With binary images, dilation connects areas that are separated by spaces smaller than the structuring element and adds pixels to the perimeter of each image object. Fig. 6.3 shows an example of dilation and erosion on a binary image.

Opening and Closing

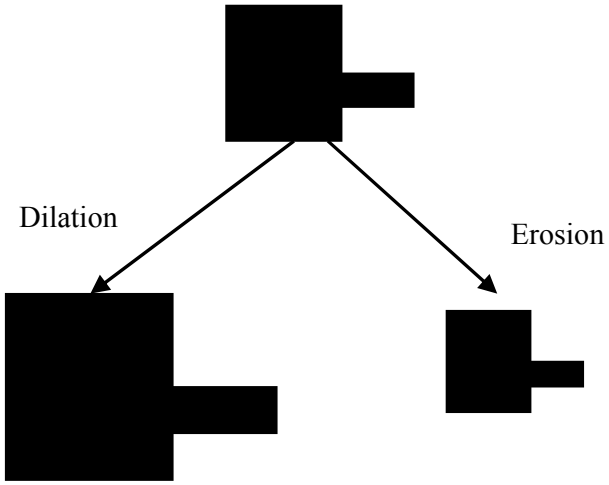

FIG. 6.3 – Example of dilation and erosion

According to the definition, single dilation or erosion expands or reduces the image objects and thus results in the global geometric distortion of unsuppressed features. To avoid this effect, dilation and erosion are often combined in pairs to be used, in either of two ways, to produce other fundamental morphological operations called closing and opening. Opening breaks narrow isthmuses, eliminate small islands and sharp peaks or capes. Closing fuses narrow breaks and long thin gulfs, and fills in the thin gulfs and small holes.

The opening of A by B is simply the erosion of A by B followed by dilation by B and is defined as :

$$A_B^{\vee} = (A \ominus B) \oplus B \tag{6.6}$$

The closing of A by B is simply the dilation of A by B followed by erosion by B and is defined as :

$$A_B^{\wedge} = (A \oplus B) \ominus B \tag{6.7}$$

An example of opening and closing on a binary image is shown in Fig. 6.4.

6.1.3.3 Application to the present study

To improve the present binary image (indicative function F_i), a closing operation is used firstly to connect separated objects and to fill in holes by changing the value of F_i from 0 to 1 in the corresponding position. Then an opening operation is employed to remove isolated small objects, sharp peaks or capes by changing the value of F_i from 1 to 0 in the corresponding position. As mentioned above, a structuring element needs to be defined before processing those operations. In the present study, the structuring element is referred to as parameter M_s and is chosen according to the shape of objects expected.

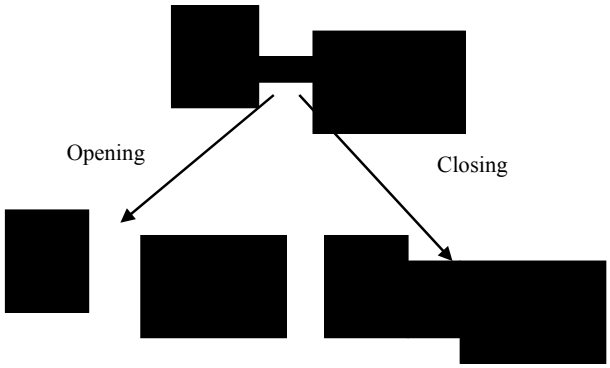

FIG. 6.4 – Example of opening and closing

For example, a rectangular (or square) structuring element is suitable for the elongated objects. Large structuring elements are not recommended in the present mathematical morphological procedure due to the following reasons : First, they can connect several separate coherent structures together. Second, they can cut those structures that have a large angle with respect to the axis of coordinates into several small pieces. Third, they can eliminate small and incomplete objects cut by the border of the image during the erosion operation.

6.1.4 Cleaning procedure

After the mathematical morphology procedure, many small objects, whose surfaces are larger than that of the structuring element but not enough to be considered as coherent structures, remain in the images. They should be removed before statistical analysis. Therefore, a cleaning procedure with two parameters is introduced to remove these objects by considering their areas. One is for the objects that are cut by borders and the other is for the small objects totally embedded in the images. They are named $'$clean factor for incomplete objects cut by borders$'$ (referred to as C_B) and $'$clean factor for complete objects$'$ (referred to as C_C) respectively. Let us take A_s as the object area. The cleaning procedure is defined as :

$$\text{For a complete object } F_i = \begin{cases} 0 \text{ when } A_s \leq C_C \\ 1 \text{ otherwise} \end{cases} \tag{6.8}$$

$$\text{For an incomplete object } F_i = \begin{cases} 0 \text{ when } A_s \leq C_B \\ 1 \text{ otherwise} \end{cases} \tag{6.9}$$

6.1.5 Various conditions and interesting characteristics

As the pattern recognition method is used in a limited area, the coherent structure objects may have various locations. Taking this into account, four circumstances are considered when statistical results are computed. This is illustrated in Fig. 6.5 where 0 and 1

indicate background (white) and objects (grey) respectively. In the first case (Fig. 6.5a), objects are embedded totally in the image area without holes inside or branches. The principal statistical characteristics that can be computed are frequency of appearance (N) (number of objects per image), spanwise angle (φ), width (W), length (L), spanwise distance (d) between two nearby objects, streamwise distance (d_s) and area (A_c). In the present study, spanwise distance between two clostest objects can be also obtained and it is named (d_n). For example, in Fig. 6.5a, there are three objects. Take the object at the bottom as a reference, the middle object can be referred to as a closest object while the upper one as a nearby object. The spanwise distance between the bottom object and its closest neighbour is named not only d but also d_n. Clearly, d includes all d_n.

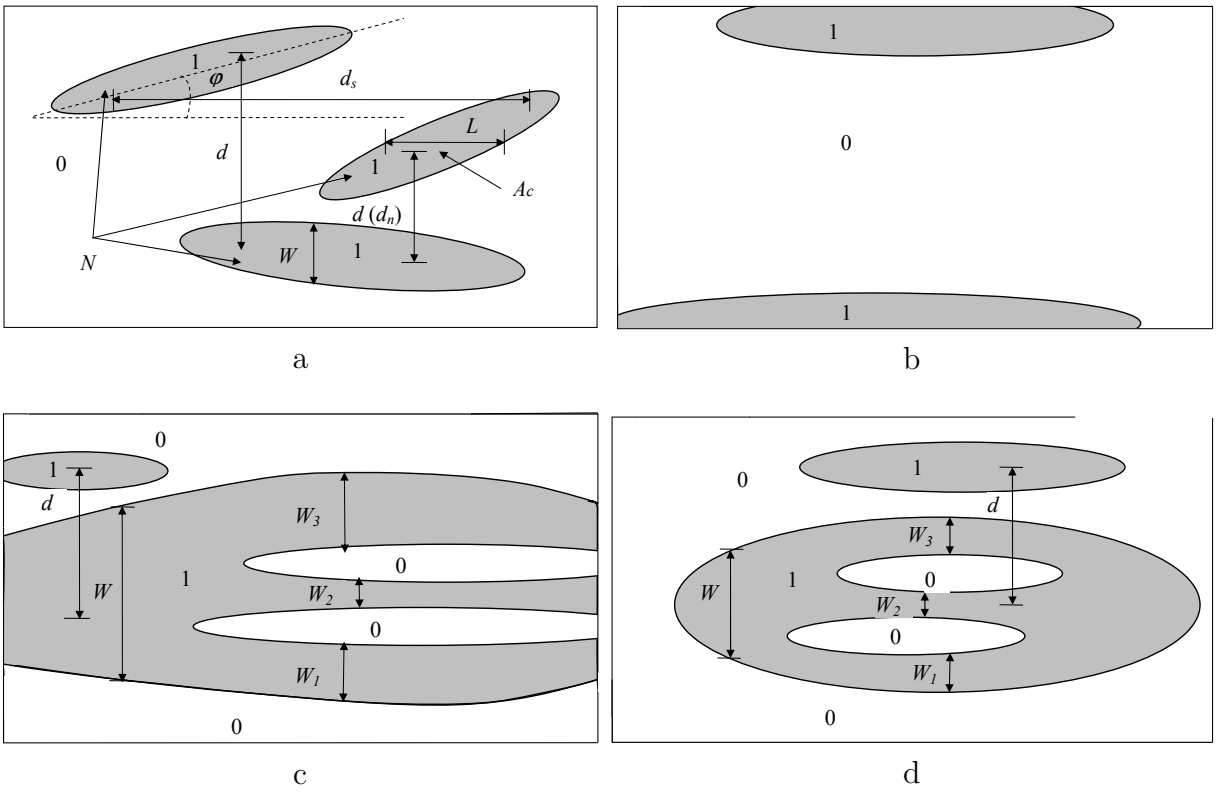

FIG. 6.5 – Various conditions for statistical analysis

In the second case (Fig. 6.5b), objects are cut by the spanwise borders. Only the number of object (N) can be obtained. The other parameters cannot be calculated since there is no information on the portion of objects beyond the image.

In the third and fourth cases (Fig. 6.5c-d), objects have more than one branch or have large holes inside them. The distance between objects can be determined similarly as in case one. Given that the images are M lines in the streamwise direction x and N columns in the spanwise direction z, the width can, however, be calculated by two methods. The first method (referred to as 'total') : $W_t^j = \sum_{i=1}^{b} W_i$; the second method (referred to as 'average') : $W_a^j = (\sum_{i=1}^{b} W_i)/b$. Here, j is the index of the column, b is the number of branches and W_i is the width of each branch. The distance and the width are measured in the spanwise direction z for each column. The mean distance $\overline{d}$ is taken as the average of

all measurements. The width of each object is calculated by averaging the corresponding samples W_t^j or W_a^j, giving W_t or W_a respectively. These, of course, can be averaged again over all the objects, yielding mean width $\overline{W_t}$ or $\overline{W_a}$. In Fig. 6.5a, the length L can not represent correctly the streamwise extend of the object when it has an angle with respect to the streamwise direction. Therefore, in the case that the object has a rectangular or elliptical shape, its mean length is computed based on its mean width and area. This length is referred to as L_A and is defined as $L_A = A_c/W_t$ or $L_A = A_c/W_a$.

6.2 Streaks

6.2.1 Detection functions and parameters

6.2.1.1 Detection function definition

It is well known that low and high speed streaks (LSS and HSS respectively) correspond to low and high streamwise velocity (u component) distribution relative to the mean $\overline{u}$, in other words, high velocity fluctuations of the streamwise component. According to this definition, different methods have been proposed to identify low speed streaks. Gupta *et al.* (1971) have used a VITA method to detect streaks in their experiment investigation using hot wires. Smith and Metzler (1983) have performed an experiment with a high-speed video system and hydrogen bubble-wire flow visualization. They identified low speed streaks by considering the differential in momentum flux between the adjacent high and low-speed regions. By applying the auto-correlation method to the streamwise velocity fluctuation u', Kahler (2004) has evidenced the existence of streaks. However, most of these detections were specified to calculate one or several spatial characteristics (mainly frequency of appearance and spanwise spacing). Benefiting from instantaneous velocity fields obtained from PIV experiments, Carlier and Stanislas (2005) are one of the early researchers who have made efforts to obtain the instantaneous streak images. They applied a threshold directly to the normalized streamwise velocity fluctuation field to generate the instantaneous binary image of streaks. All above mentioned methods are based on the streamwise velocity or its fluctuations. As both of them are widely agreed to be the characteristic variables of streaks, it is reasonable to choose one or the other as the detection variable. In the present study, the velocity fluctuations are normalized with the standard deviation. The detection function (F_d) of streaks is defined as :

$$F_d = f(u'(m,n,\mathrm{y}^+), \sigma_u(\mathrm{y}^+)) = \frac{u'(m,n,\mathrm{y}^+)}{\sigma_u(\mathrm{y}^+)} \tag{6.10}$$

Where u' is the instantaneous velocity fluctuation of the streamwise component u, σ_u is the standard deviation, (m, n) is the position in the (M, N) grid, and y^+ is the wall distance at which the SPIV measurement is performed.

6.2.1.2 Thresholding

The above detection function F_d (Eq. 6.10), obtained from SPIV data, is a real scalar field defined on a discrete (M,N) grid. Streaks are detected by applying a threshold C_T directly to F_d. The value of C_T is taken positive. The corresponding indicative function F_i of streaks are defined as :

$$\text{Low speed streaks } F_i = \begin{cases} 1 \text{ when } F_d < -C_T \\ 0 \text{ otherwise} \end{cases} \tag{6.11}$$

$$\text{High speed streaks } F_i = \begin{cases} 1 \text{ when } F_d > C_T \\ 0 \text{ otherwise} \end{cases} \tag{6.12}$$

It should be noted that the structures and the background are represented respectively by white and black in all binary indicative images.

In the present study (see Appendix B.1), C_T was selected as 0.6 at $y^+ = 14.5$. As is well known, σ_u^n decreases with wall distance when $y^+ >$ 10-15. Also, beyond a certain distance from the wall streaks are known to disappear. Considering these facts, the threshold C_T for the other wall distances was chosen as $0.6 * \sigma_u^{max}/\sigma_u^n$. Here, σ_u^n is the standard deviation of the streamwise velocity component u at position n, and σ_u^{max} is the maximum standard deviation of the present flow and is equal to 0.35 according to our previous study (Lin *et al.* (2004)). According to this method, there is a streak only when u' (fluctuation of the streamwise velocity) is larger than a constant value whatever the wall distance is. Table 6.1 gives the resulting values of C_T at each wall distance.

Plane #	1	2	3	4	5	6	7	8	9	10
y^+	14.5	18.5	22.2	26.3	29.7	33.3	37.0	40.6	44.0	48.0
σ_u^n	0.348	0.344	0.329	0.322	0.316	0.307	0.298	0.293	0.288	0.281
$C_T = 0.6 * \sigma_u^{max}/\sigma_u^n$	0.60	0.61	0.63	0.65	0.66	0.68	0.70	0.72	0.72	0.74

TAB. 6.1 – Threshold C_T in ten planes of measurement (σ_u^{max}= 0.35)

6.2.1.3 Mathematical morphology

Since streaks are elongated in the streamwise direction, a rectanglar structuring element was chosen : $M_S(W, L)$, in which W is the width in the spanwise direction and L is the length in the streamwise direction. The values of W and L are given in wall units. The structuring element was selected as $M_S = (10^+, 50^+)$ for both low and high speed streaks (see Appendix B.1).

6.2.1.4 Cleaning

The two clean factors C_B and C_C are given in square wall units. The values $C_B = 1750^{+2}$ and $C_C = 2500^{+2}$ were chosen for both low and high speed streaks. It should be noted that the value of C_B is larger than half of the value of C_C due to the fact that streaks are much larger than the average size of complete objects obtained in the present study. Details about the selection of these parameters are described in Appendix B.1.

Fig. 6.6 shows an example of detection function and the corresponding indicative image of streaks at the different steps of the detection procedure.

6.2.2 Statistics on streaks

6.2.2.1 Frequency of appearance of streaks

One interesting characteristic of streaks is the frequency of appearance, in other words, the number of streaks in a certain area. In the present study, the area (field of view) is

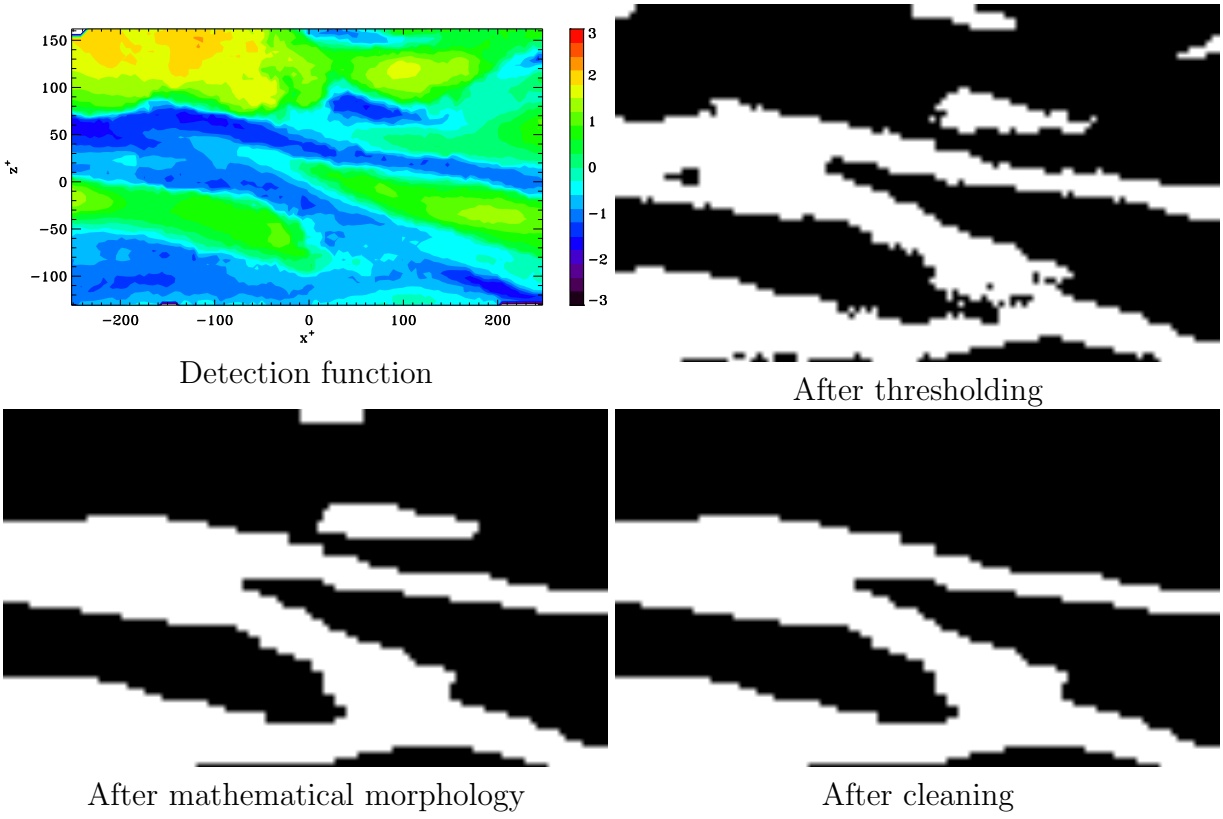

FIG. 6.6 – Detection image and indicative images

$530^{+}*300^{+}$ in a streamwise-spanwise plane. Fig. 6.7a shows frequency of appearance (N) of detected streaks based on this area at various wall distances. In the present study, Low and High Speed Streaks are represented by LSS and HSS respectively in all the figures if no other specification is made. In Fig. 6.7a, the error bars represent an error of 5% of the mean. In the buffer layer ($y^{+} \leq 30$), low and high speed streaks show a different behavior. As wall distance increases, the frequency N decreases rapidly for high speed streaks but is nearly the same or decreases very slowly for low speed ones. In the bottom region of the logarithm layer ($y^{+} > 30$), the frequency of both types of streaks show the same decreasing rate with wall distance. On average, about 2.9 low speed streaks and 2.8 high speed ones are expected per area of $530^{+}*300^{+}$ at $y^{+} = 14.5$ while about 2.1 low speed and 1.6 high speed streaks at $y^{+} = 48$.

Many streaks show a bifurcating behaviour. Fig. 6.7b shows the frequency of appearance of bifurcate streaks at various wall distances. This frequency is about 0.6 for both of low and high speed streaks. For low speed streaks, it shows an increasing trend approaching the wall. Comparing with Fig. 6.7a, it suggests that about 22-26% of low speed streaks and about 23-35% of high speed streaks have branches. As explained in Appendix B.1, the dimension of the parts with branches are comparable with the whole size of streaks.

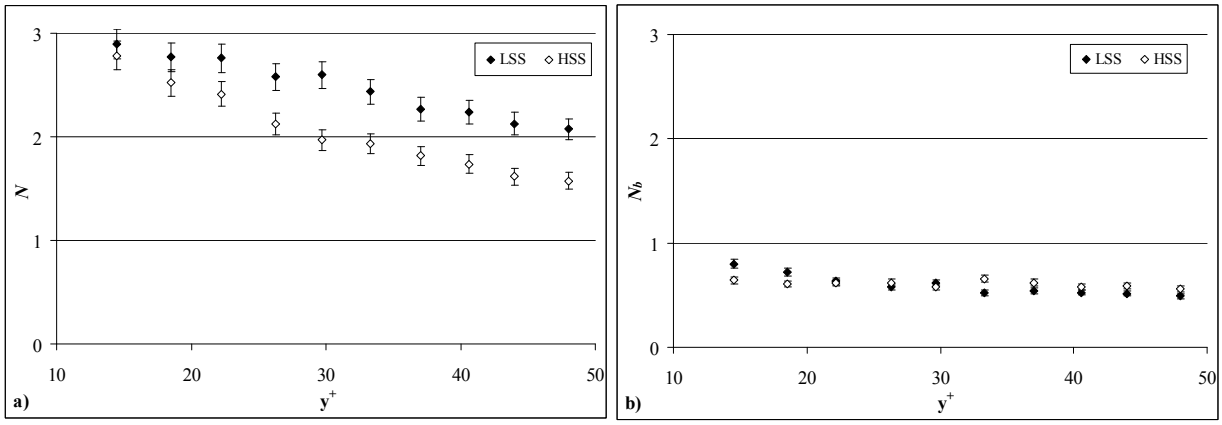

FIG. 6.7 – Frequency of appearance of streaks, a : Frequency of appearance of detected streaky objects N ; b : Frequency of appearance of bifurcate streaks N_b

6.2.2.2 Spanwise angle

The streaks are generally expected to be parallel to the streamwise direction. Benefiting from the instantaneous indicative images of streaks obtained in the streamwise-spanwise plane, the angle of streaks with respect to the streamwise direction can be calculated. Due to the limitation in the size of SPIV images, streaks, which are cut by the spanwise border of the image, were excluded from calculation of the angle. Fig. 6.8 shows the variation of the mean spanwise angle $\overline{\varphi}$ with wall distances. The values of $\overline{\varphi}$ are nearly zero for both low and high speed streaks, which suggests that on average streaks move parallel to the streamwise direction as expected. The near-zero value also confirms the homogeneous property of the flow in the spanwise direction. The small fluctuations in Fig. 6.8 result from the lack of convergence. Fig. 6.8 also shows the mean absolute spanwise angle $|\varphi|$. For low speed streaks, $|\varphi|$ increases slightly with wall distance from 5.9° at $y^+ = 14.8$ to 8.3° at $y^+ = 48.0$. Comparing to low speed streaks, $|\varphi|$ of high speed ones shows a more random distribution. It has an average value about 7.5°.

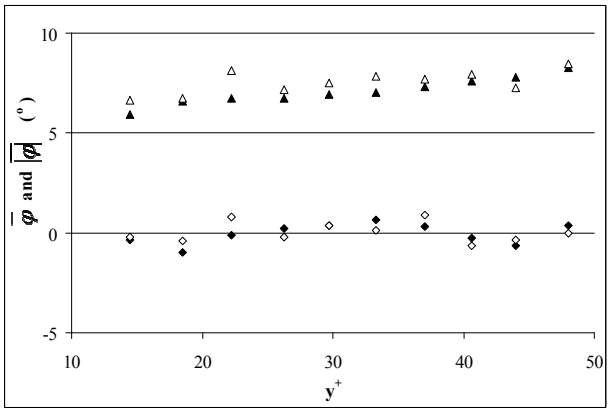

FIG. 6.8 – Mean spanwise angle $\overline{\varphi}$ and mean absolute spanwise angle $\overline{|\varphi|}$. $\overline{\varphi}$ (LSS) : ♦ ; $\overline{\varphi}$ (HSS) : ◊ ; $\overline{|\varphi|}$ (LSS) : ▲ ; $\overline{|\varphi|}$ (HSS) : △.

Fig. 6.9 shows the RMS of φ, which is around 10° for both low and high speed streaks. Both types of streaks have a similar behavior : a slight increase with wall distance. Fig. 6.9 also shows the RMS of $|\varphi|$. Low and high speed streaks have nearly the same mean value of the RMS : about 7.2°. Besides this mean value, the distribution of the RMS of $|\varphi|$ is also similar. Except for the values, the distribution of $|\varphi|$ is nearly the same as that of φ.

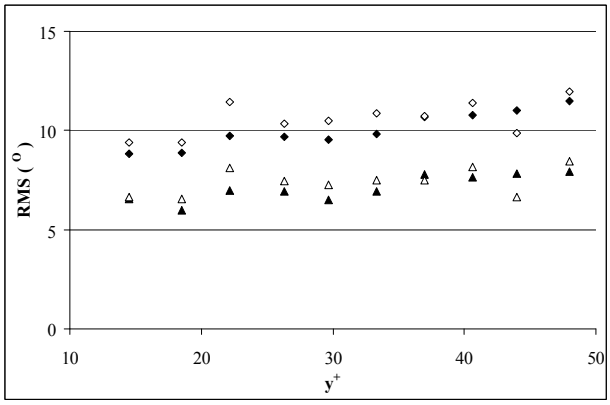

FIG. 6.9 – RMS of spanwise angle φ and absolute spanwise angle $|\varphi|$. φ (LSS) : ♦; φ (HSS) : ◊; $|\varphi|$ (LSS) : ▲; $|\varphi|$ (HSS) : △.

To investigate the spanwise angle in more detail, the histograms of φ for low and high speed streaks are shown respectively in Fig. 6.10 at selected wall distances. The histograms are closer to a Laplace distribution than to a Gaussian one. Different from the average behaviour, many streaks move with a spanwise angle up to about 15°. Some of them even travel downstream with an angle of more than 25°. The high values of spanwise angle indicate the meandering property of streaks. In Fig. 6.10, with the increase in wall distance, a plateau begins to appear around 10-12°. This plateau is more visible in the histogram of high speed streaks than low speed ones.

The histograms are closer to a Laplace distribution than to a Gaussian one. The probability density function of a Laplace distribution is defined as :

$$P(x) = \frac{1}{2b} e^{-|x-\mu|/b} \tag{6.13}$$

Where, μ is the mean and b is the parameter of rate of change.

In order to characterize the distribution of φ statistically, skewness (S) and flatness (F) are calculated and shown in Fig. 6.11. Skewness (S) is nearly zero for all wall distances, revealing the symmetry property of the distribution and confirming again the spanwise homogeneity. The value of flatness (F) is in the range of 5 to 8, which is comparable to 6, the standard value for a Laplace distribution. The variation of F near the wall should be attributed to the convergence.

6.2.2.3 Width

In Fig. 6.12, the mean width $\overline{W_a^+}$ of streaks is shown at various wall distances. The error bars represent an error of 5% of the mean. For low speed streaks, the mean width

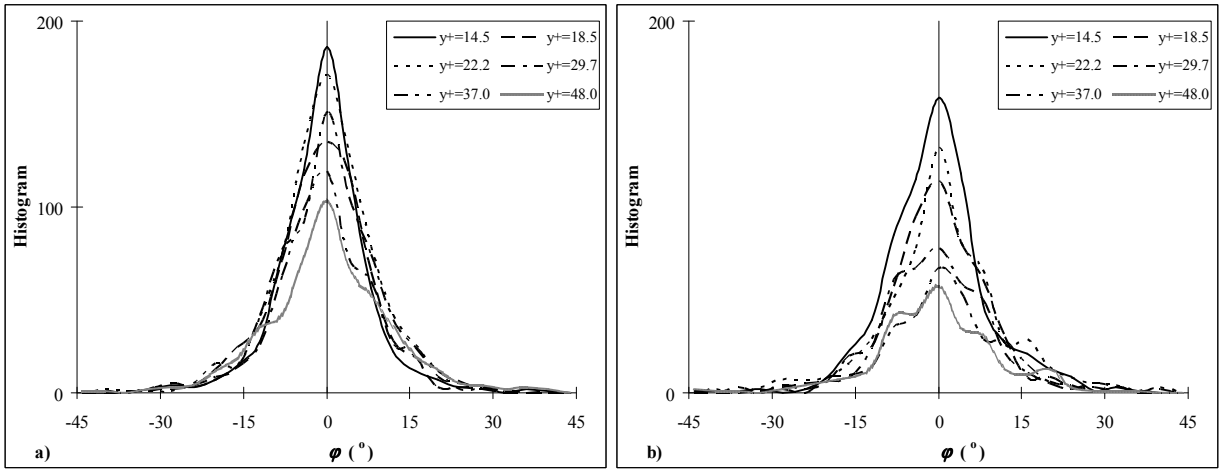

FIG. 6.10 – Histogram of the spanwise angle φ of streaks at selected wall distance, a : LSS ; b : HSS.

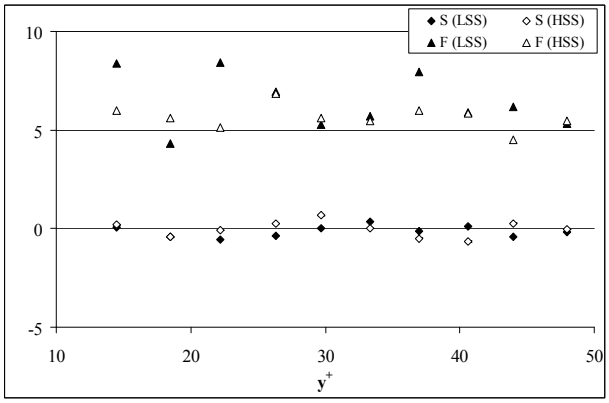

FIG. 6.11 – Skewness (S) and flatness (F) of the spanwise angle φ of streaks

$\overline{W_a^+}$ is nearly a constant at about 31 wall units in the region $14.5 < y^+ < 33$. After that, it increases slowly with the wall distance up to 39 wall units at $y^+ = 48$. For high speed streaks, the mean width $\overline{W_a^+}$ is fluctuating between 42 and 47 wall units. Fig. 6.12 also gives the RMS of the width W_a^+ of streaks. It shows that the RMS is about 16 wall units for low speed streaks and 23 wall units for the high speed ones in the whole y^+ range.

Histograms of the width of streaks are given in Fig. 6.13. These distributions are far from Gaussian, looking more like a lognormal distribution. Consequently, the most probable value is rather different from the mean value. For example, they are 20 and 30 wall units respectively for low speed streaks at $y^+ = 14.5$. As shown in Fig. 6.13, the distribution of high speed streaks is significantly wider than the low speed ones. The most probable value is between 20 and 30 wall units for low speed streaks and between 25 and 35 wall units for high speed ones. It is interesting to compare the characteristics of the present distribution to a true lognormal one.

According to Hastings and Peacock (1975), let us consider that the variable A has a lognormal distribution, and $\overline{A}$ and σ_A are the corresponding mean value and standard

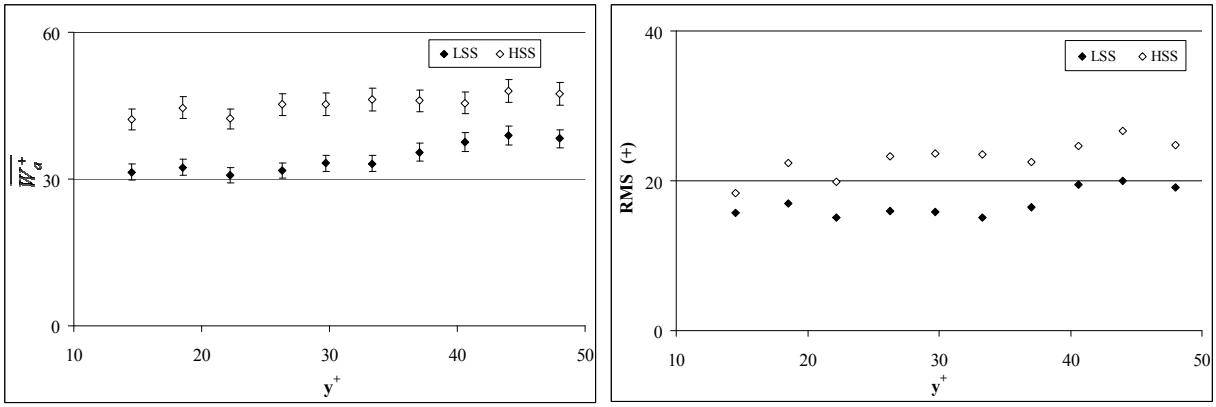

FIG. 6.12 – Mean and RMS of the width W_a^+ of streaks

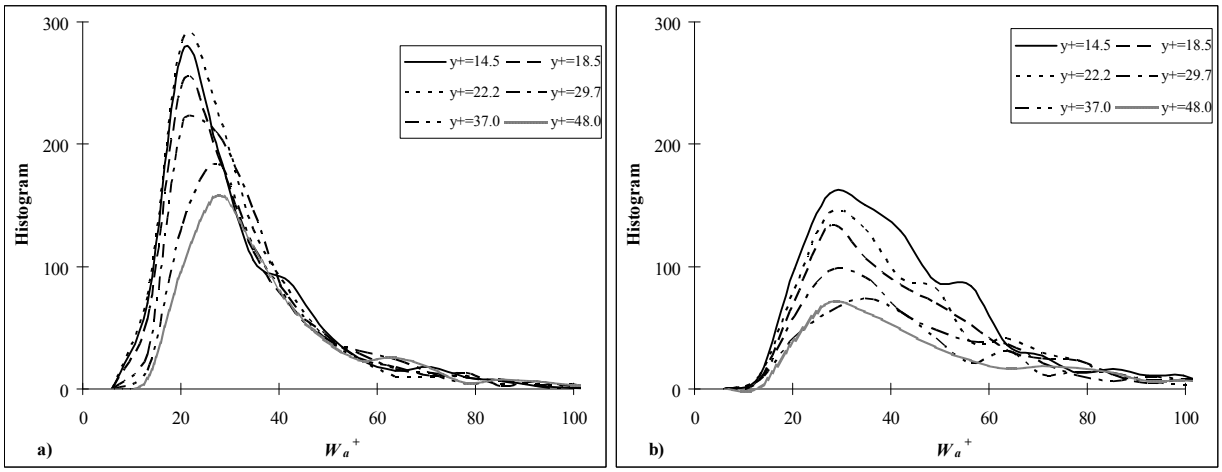

FIG. 6.13 – Histogram of the width W_a^+ of streaks at selected wall distances, a : LSS ; b : HSS

deviation respectively. The variation coefficient ψ is defined by :

$$\psi = \frac{\overline{A}}{\sigma_A} \tag{6.14}$$

The form of the probability density function is given by :

$$P(A) = \frac{e^{-\frac{1}{2}(\frac{1}{\psi_0} ln \frac{A}{M_0})^2}}{A\psi_0\sqrt{2\pi}} \tag{6.15}$$

where

$$M_0 = \overline{A}(1+\psi^2)^{-\frac{1}{2}} \tag{6.16}$$

$$\psi_0 = (ln(1+\psi^2))^{\frac{1}{2}} \tag{6.17}$$

$$\tag{6.18}$$

Here, M_0^+ is the median value of A and ψ_0 the variation coefficient of $ln\psi$. Employing Eq. 6.14, Eq. 6.16 and Eq. 6.17, the coefficient ψ and the median value M_0^+ of the width W_a^+ of streaks are calculated and shown in Fig. 6.14. The range of ψ of all 10 distribution is $0.45 < \psi < 0.52$ and $0.43 < \psi < 0.56$ for low and high speed streaks respectively. The difference in the range of ψ can be explained by the fact that the distribution of W_a^+ for high speed streaks is wider than for low speed ones as shown clearly by Fig. 6.13. ψ_0 is about 4-6% smaller than ψ for both types of streaks at all wall distance studied. Compared with Fig. 6.12, the value of M_0^+ in Fig. 6.14 has nearly the same distribution as $\overline{W_a^+}$, except that it is about 9-12% smaller.

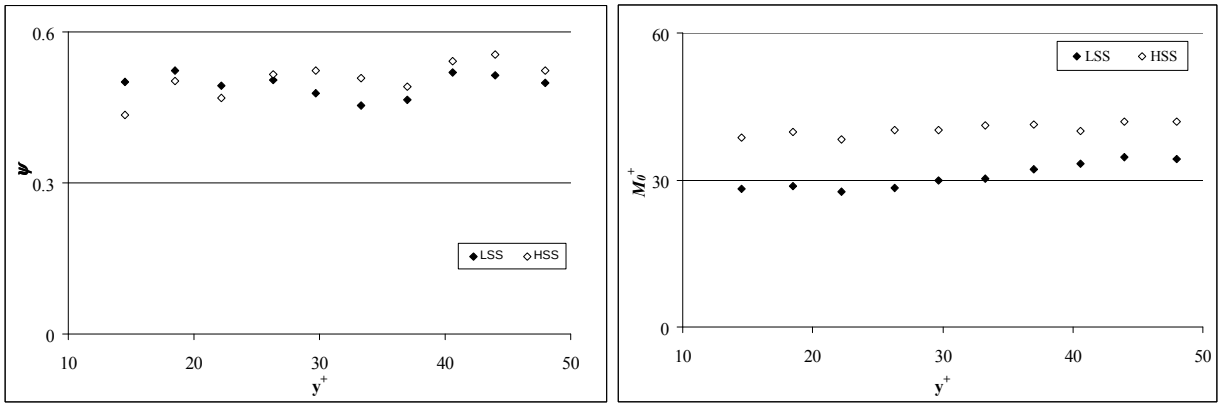

FIG. 6.14 – Coefficient variation ψ and median value M_0^+ of the width W_a^+ of streaks

According to Eq. 6.15, the theoretical skewness and flatness of the lognormal distribution are defined by :

$$S = \sqrt{e^{\psi_0^2}(2 + e^{\psi_0^2})} \tag{6.19}$$

$$F = e^{4\psi_0^2} + 2e^{3\psi_0^2} + 3e^{2\psi_0^2} - 3 \tag{6.20}$$

Using Eq. 6.19-6.20, the theoretical skewness (S) and flatness (F) of lognormal distributions corresponding to ψ_0 and M_0^+ in Fig. 6.14, are obtained and compared with the present results in Fig. 6.15. For both S and F, the present results are comparable with theoretical ones. In general, for S, the agreement is better for high speed streaks than for low speed ones. However, for F, the opposite is true. This result indicates that the distribution of W_a^+ is more symmetric for high speed streaks than for low speed ones as shown in Fig. 6.13. According to Hastings and Peacock (1975), for a true lognormal distribution, the ratio of the most-probable value to the mean value R_{mm}, can be calculated by Eq .6.21. Fig. 6.16 shows that the present results are consistent with the theoretical values. It reveals again that the width of streaks follows nearly a lognormal distribution.

$$R_{mm} = (1 + \psi^2)^{-\frac{3}{2}} \tag{6.21}$$

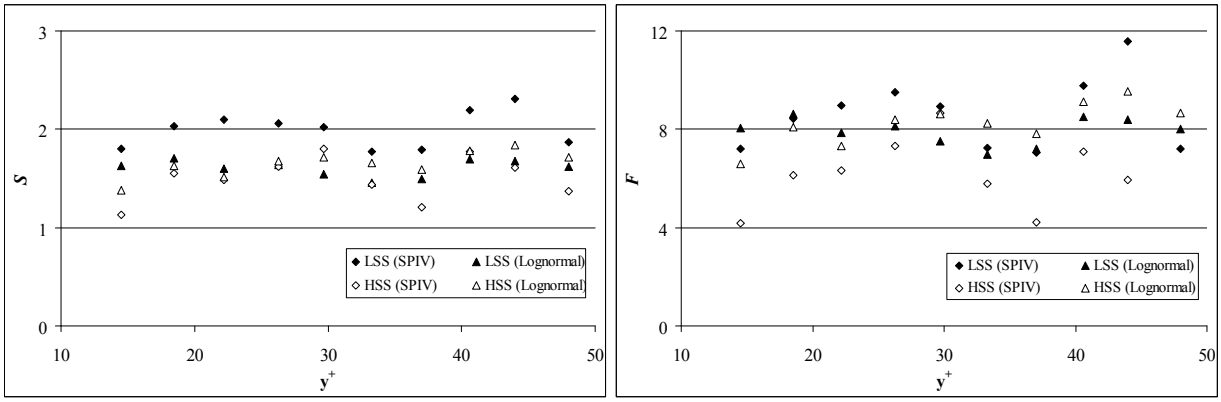

FIG. 6.15 – Comparison of skewness (S) and flatness (F) of the width W_a^+ of streaks of the present study with the theoretical values obtained according to lognormal distributions

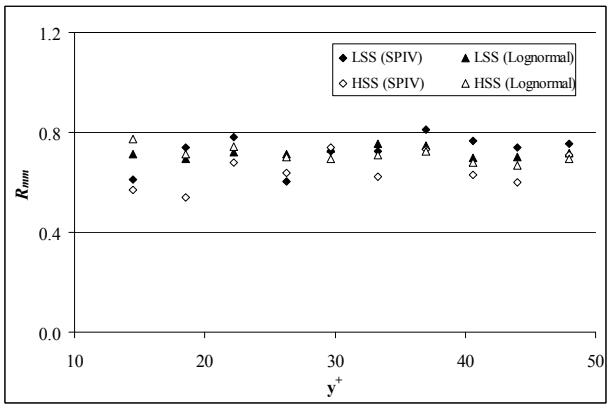

FIG. 6.16 – Ratio of the most probable value to the mean value R_{mm} of the width W_a^+ of streaks

6.2.2.4 Spanwise distance

The mean spanwise distance $\overline{d^+}$ between the center of two nearby streaks is widely referred to as the spanwise periodic spacing $\overline{\lambda}$ in literature. Fig. 6.17 shows $\overline{d^+}$ for low and high speed streaks at various wall distances. The error bars represent an error of 5% of the mean. The mean distance $\overline{d^+}$ is nearly the same for both types of streaks at the same wall distance. It varies between 114 and 135 wall units. Fig. 6.17 also suggests that the mean distance $\overline{d^+}$ is slightly smaller in the buffer layer than in the log layer. Fig. 6.17 also gives the RMS of d^+. The value of this RMS is about 42 wall units for low speed streaks and 39 wall units for high speed streaks.

The instantaneous indicative images of streaks allow to obtain the histogram of the distance d^+. In Fig. 6.18, the number of samples decrease sharply with wall distance in the logarithm layer. This can be explained by the following two reasons. One is that the number of streaks decreases with the wall distance as shown in Fig. 6.7. The other is that streaks become wider with the wall distance (see Fig. 6.12). The wider streaks are, the more likely they will be cut by the spanwise border of the field and thus the number of samples will decrease. Moreover, the streamwise extension of streaks may decrease with

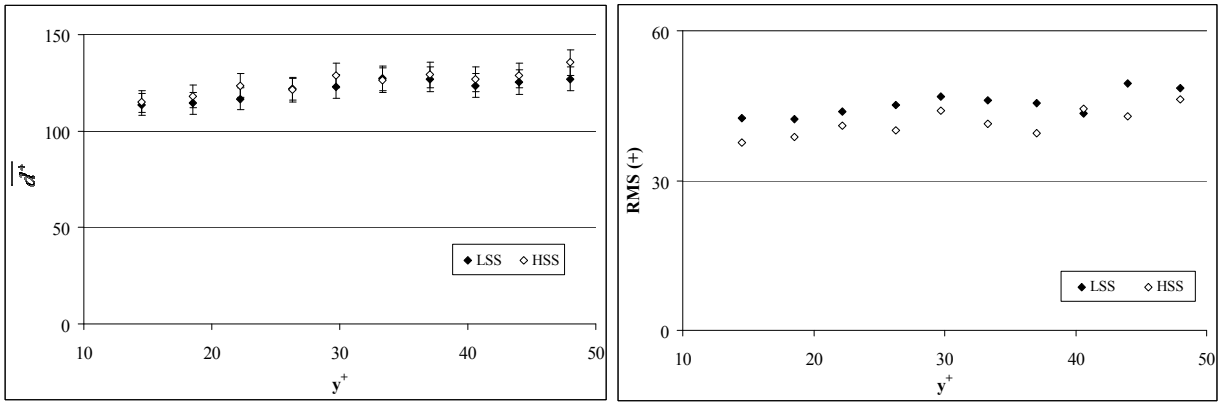

FIG. 6.17 – Mean and RMS of the spanwise distance between the nearby streaks d^+

wall distance as velocity fluctuations decrease. The shorter streaks are, the fewer samples there are. Unfortunately, due to the relatively small size of the SPIV field used, it is not possible to measure the length of streaks.

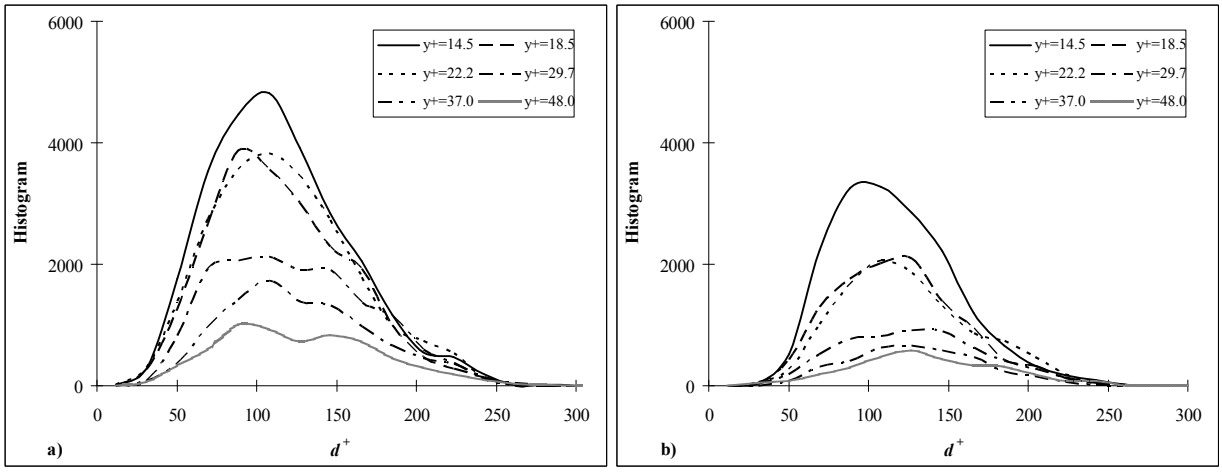

FIG. 6.18 – Histogram of the spanwise distance between the nearby streaks d^+ at selected wall distance , a : LSS ; b : HSS

Except for oscillations that may arise from the lack of convergence, both histograms of low and high speed streaks are close to a Rayleigh distribution (Weisstein (1999)). The probability distribution function of this distribution is defined as :

$$P(x) = \frac{(\mathrm{x} - a)e^{-(\mathrm{x}-a)^2}/2s^2}{s^2} \tag{6.22}$$

Where, a is the shift to the origin, s is the parameter of rate of change, and $\mathrm{x} \in [a, \infty]$.

To characterise the histogram from the statistical point of view, skewness (S) and flatness (F) are calculated and are given in Fig. 6.19. These parameters are compared with those obtained from a Rayleigh distribution. For such a distribution, skewness (S) and flatness (F) are defined by Eq. 6.23-6.24. For both low and high speed streaks, the values of the two parameters are nearly the same. Skewness (S) has a value about 0.4

and flatness (F) has a value of about 2.8. These values are comparable respectively to S = 0.63 and F = 3, the standard values for a Rayleigh distribution.

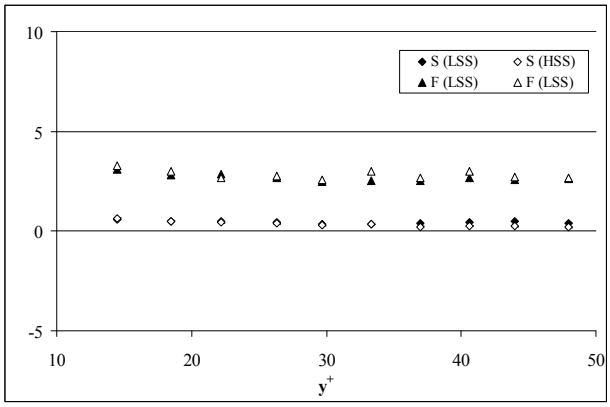

FIG. 6.19 – Skewness (S) and flatness (F) of the spanwise distance d^+ between the nearby streaks

$$S = \frac{2(\pi - 3)\sqrt{\pi}}{(4 - \pi)^{3/2}} \tag{6.23}$$

$$F = \frac{6\pi^2 - 24\pi + 16}{(4 - \pi)^2} + 3 \tag{6.24}$$

Most of the former studies were conducted to measure only the spanwise distance between two nearby streaks d^+. In the present study, however, instantaneous streak indicative images provide the possibility to measure the spanwise distance between the centre of two closest streaks and its mean value (referred to as d_n^+ and $\overline{d_n^+}$ respectively) (Fig. 6.5a). Fig. 6.20 shows the mean distance $\overline{d_n^+}$ at various wall distances. Comparing with Fig. 6.17, the distance $\overline{d_n^+}$ is about 13 wall units smaller than $\overline{d^+}$ for low speed streaks and about 9 wall units for high speed streaks. This difference indicates a staggering of the two closest streaks in the streamwise direction (Fig. 6.5a). Except for the difference in value, $\overline{d^+}$ and $\overline{d_n^+}$ have a similar distribution with wall distance, which manifests the reliability of the measurement. Fig. 6.20 also shows that the RMS is around 39 wall units for both low and high speed streaks on average.

Fig. 6.21 shows the histograms of the spanwise distance d_n^+ at selected wall distances for low and high speed streaks respectively. Similar to d^+, d_n^+ has a nearly Rayleigh distribution. Comparing with Fig. 6.18, it appears that about 60-70% of d^+ are d_n^+ (Fig. 6.5a). As for d^+, skewness (S) and flatness (F) are given in Fig. 6.22. The values of S and F are nearly the same as those of d^+.

6.2.2.5 Percentage of area

Table 6.2 shows the percentage of the total area of low and high speed streaks in the whole field with various wall distance. With the selected detection parameters, low and high speed streaks cover about 59% of the area of the whole field at $y^+ = 14.5$. This

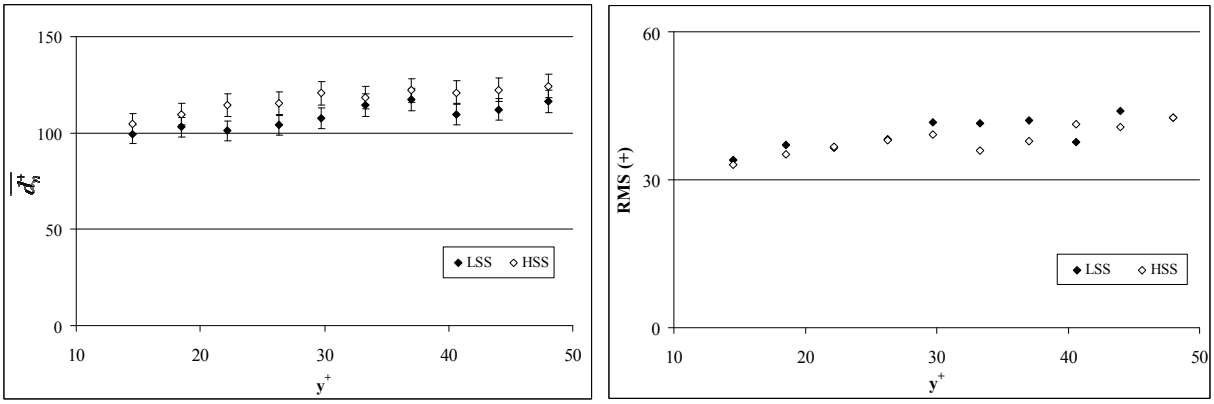

FIG. 6.20 – Mean and RMS of the spanwise distance between the closest streaks d_n^+

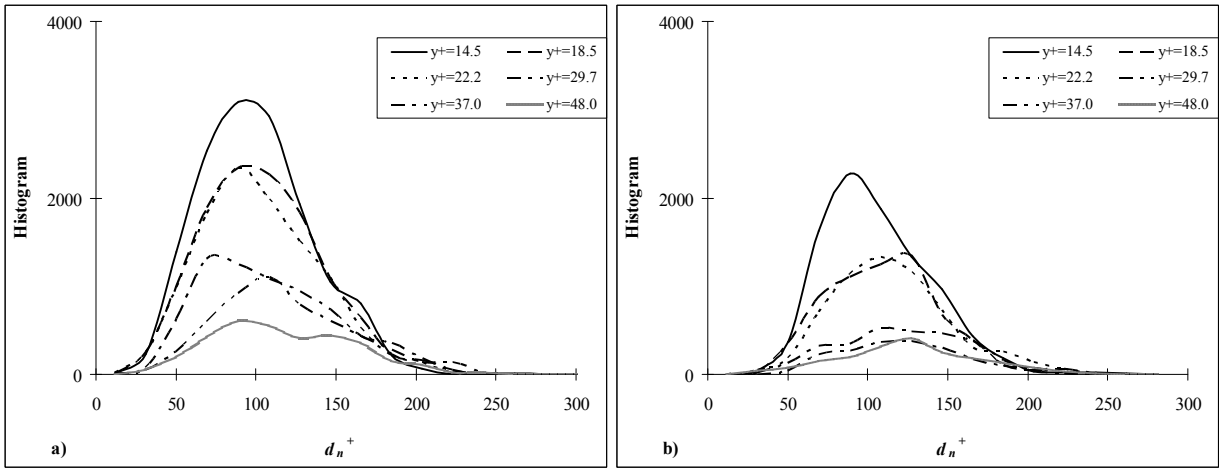

FIG. 6.21 – Histogram of the spanwise distance between the closest streaks d_n^+ at selected wall distance, a : LSS ; b : HSS

percentage decreases nearly linearly to about 45% at $y^+ = 48$ with wall distance. Table 6.2 shows that the percentage of total area of high speed streaks is almost equal to that of the low speed ones.

6.2.2.6 Mean normalized velocity fluctuations

Fig. 6.23 gives mean normalized velocity fluctuations in streaks at various wall distances. The mean streamwise normalized fluctuations in low speed streaks are comparable to those in high speed ones. In low speed streaks, remarkably, high positive mean wall-normal fluctuations are observed. Similarly, high negative mean wall-normal fluctuations are found in high speed streaks. These findings confirm that ejections are associated with low speed streaks while sweeps are linked to high speed ones. The absolute value of the mean wall-normal fluctuation is comparable in both low and high speed streaks very close to the wall ($y^+ < 18.5$). In the region $y^+ > 18.5$, it is slightly larger in low speed streaks that high speed ones. The nearly zero value of the mean spanwise fluctuation in both low and high speed streaks results from the spanwise homogeneity.

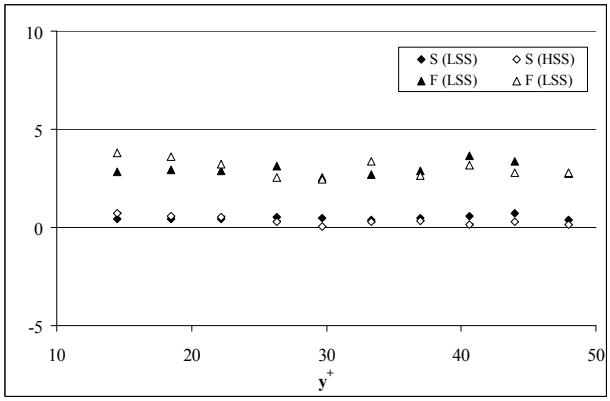

FIG. 6.22 – Skewness (S) and flatness (F) of the spanwise distance between the closest streaks d_n^+

y^+	14.5	18.5	22.2	26.3	29.7	33.3	37.0	40.6	44.0	48.0
Total area of LSS/ Area of whole field	0.29	0.28	0.26	0.25	0.25	0.23	0.23	0.23	0.22	0.22
Total area of HSS/ Area of whole field	0.30	0.29	0.27	0.27	0.26	0.26	0.24	0.24	0.23	0.23

TAB. 6.2 – Percentage of the total area of low and high speed streaks with various wall distance

6.2.3 Comparison

The mean distance $\overline{d^+}$ between low speed streaks are compared with earlier studies in Fig. 6.24. Smith and Metzler (1983) obtained their results at $Re_\theta = 2030$, using a high speed video camera and a hydrogen bubble-wire in water. In spite of the differences in the experimental methods and conditions, the present results are comparable with their results, except at $y^+ = 30$ where Smith and Metzler (1983) observed a much larger value (see Fig. 6.24). Both the present study and Smith and Metzler's show an increase of $\overline{d^+}$ with wall distance. It should be noted that the increase of $\overline{d^+}$ is much stronger according to their study than in the present study. Moreover, Kahler (2004) conducted an analysis using the spatial correlation method. Fig. 6.24 shows that the result of Kahler's study is smaller than the other results. The difference can be explained by the fact that it is obtained directly from the spatial correlation of negative streamwise velocities fluctuations, while the present results are obtained from the binary indicative images of streaks. Carlier and Stanislas (2005) used standard 2D2C PIV on a larger field of view ($1250^+ * 800^+$), at the same Reynolds number as here, to investigate streaks at $y^+ = 15$. Their results are in good agreement with the present study.

Table 6.3 shows a comparison of the percentages in our study with those of Carlier (2001). It shows that our percentage is greater. The reason can be that we used a threshold of 0.6-0.75 (from wall distance $y^+ = 14.5$ to $y^+ = 48$) while Carlier (2001) used a constant value of 1.0. With the same threshold, the results become more similar, which indicates

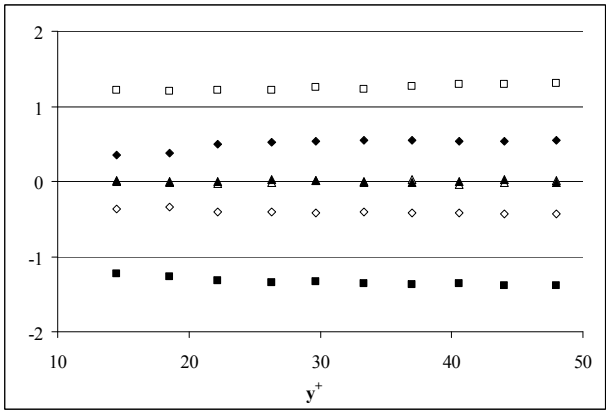

FIG. 6.23 – Mean normalized velocity fluctuations in streaks. $\frac{u'}{\sigma_u}$ (LSS) : ■; $\frac{v'}{\sigma_v}$ (LSS) : ♦; $\frac{w'}{\sigma_w}$ (LSS) : ▲; $\frac{u'}{\sigma_u}$ (HSS) : □; $\frac{v'}{\sigma_v}$ (HSS) : ◊; $\frac{w'}{\sigma_w}$ (HSS) : △

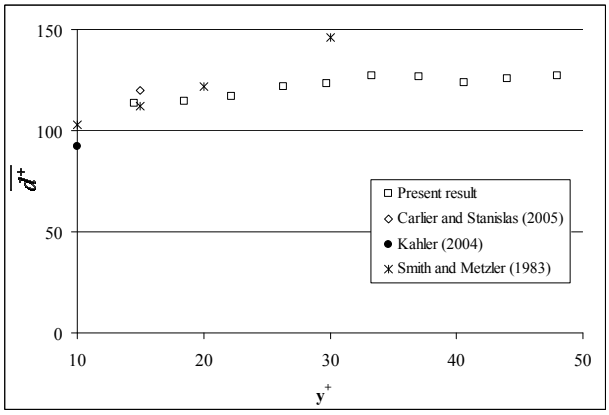

FIG. 6.24 – Comparison of the mean spanwise distance $\overline{d^+}$ of low speed streaks

that the choice of the threshold is important for the study.

Carlier (2001), with a threshold C_T equal to a value of 1, found that the width $\overline{W_a^+}$ is about 30 wall units for low speed streaks and 50 wall units for high speed streaks at $y^+ = 15$. These values are similar to the present results.

According to Nakagawa and Nezu (1981) and Smith and Metzler (1983), the distance between nearby low speed streaks d^+ follows a lognormal distribution. To compare with their results, the variation coefficient ψ, skewness (S) and flatness (F) are presented. Fig. 6.25 compares ψ obtained from the present results with those found by Smith and Metzler (1983). It shows that the present results are smaller than those of Smith and Metzler (1983) but still comparable. Fig. 6.26 gives skewness (S) and flatness (F) of d^+ obtained from the experiments compared with the theoretical values computed from ψ_0 (Eq.6.17, 6.19 and 6.20). The experimental results turn out to be very similar. For both skewness (S) and flatness (F), the theoretical values are about two times higher than those obtained by experiments. This suggest the distribution of d^+ does not have a lognormal distribution. As proposed above, d^+ is near to a Rayleigh distribution (see Fig. 6.18). This proposition can be validated by the values of skewness and flatness in Fig. 6.26.

	Present results						Carlier's results		
y^+	14.5	18.5	26.3	26.3	48.0	48.0	15.0	25.0	50.0
Threshold C_T	0.60	1.00	0.65	1.00	0.75	1.00	1.00	1.00	1.00
Total area of LSS/Total area of LSS and HSS	0.50	0.51	0.48	0.50	0.49	0.50	0.48	0.52	0.52
Total area of LSS and HSS/Area of whole field	0.59	0.34	0.52	0.31	0.45	0.31	0.31	0.29	0.31

TAB. 6.3 – Percentage of the total area of low and high speed streaks, comparison with the results of Carlier (2001)

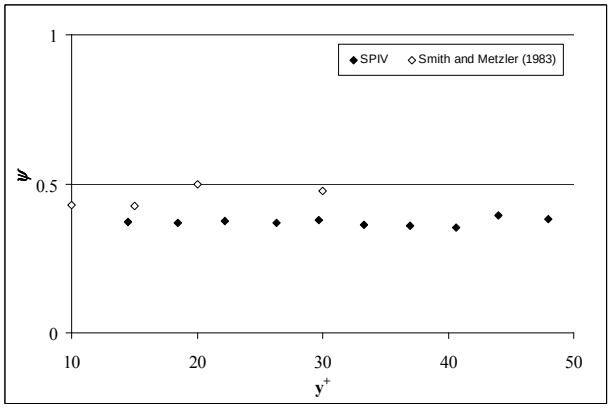

FIG. 6.25 – Comparison of variation coefficient ψ of the spanwise distance d^+ of low speed streaks obtained in the present study with the results of Smith and Metzler (1983)

6.2.4 Summary

Using a pattern recognition method, both low and high speed streaks were identified and the corresponding binary streak images were created. From these data, the characteristics of streaks were investigated in detail in the region $14.5 < y^+ < 48$.

Globally, the frequency of appearance of both low and high speed streaks decreases with wall distance in the whole range studied. However, both the value and the variation of this frequency show different behavior for both types of streaks. In the buffer layer ($y^+ \leq 30$), with an increasing wall distance, the frequency decreases rapidly for high speed streaks but is nearly the same or decreases very slowly for low speed ones. In the bottom region of the logarithm layer ($y^+ > 30$), the frequency of low and high speed streaks decreases nearly linearly with the same decreasing rate with wall distance. On average, about 2.9 low speed streaks and 2.8 high speed ones are expected per area of $530^+ * 300^+$ at $y^+ = 14.5$ while about 2.1 low speed streaks and 1.6 high speed ones at $y^+ = 48$. In general, about 22-26% of low speed streaks and about 23-35% of high speed

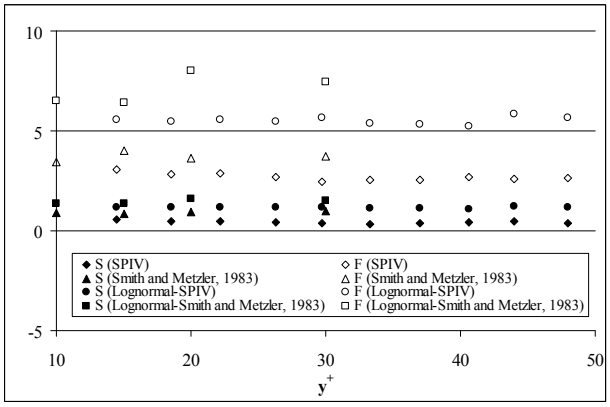

FIG. 6.26 – Comparison of skewness *(S)* and flatness *(F)* of the spanwise distance d^+ of low speed streaks obtained in the present study with the results of Smith and Metzler (1983), and theoretical values from lognormal distribution

streaks show a bifurcating behavior.

The mean spanwise angle of both low and high speed streaks is nearly zero, indicating the homogeneous property in the spanwise direction. For the mean absolute spanwise angle, the variation with wall distance is different between low and high speed streaks. It increases slightly with wall distance from 5.9° at $y^+ = 14.5$ to 8.3° at $y^+ = 48$ for low speed streaks while it varies around 7.5° for high speed streaks. The histogram of the spanwise angle follows nearly a Laplace distribution. It shows that many streaks have a spanwise angle larger than 15°, evidencing the meandering behaviour of these structures.

The mean width of low speed streaks is nearly constant at about 31 wall units in the region $14.5 < y^+ < 33$. Above that region, it increases slowly with the wall distance up to 39 wall units. For high speed streaks, the mean width varies between 42 and 47 wall units in the whole range studied. Clearly, high speed streaks are wider than low speed ones. For both types of structures, the histogram of the width is close to a lognormal distribution.

The mean spanwise distance between the centre of two nearby low speed streaks is nearly the same as that of high speed ones at the same wall distance. It varies between 114 and 135 wall units. The present results suggest that this distance is slightly smaller in the buffer layer than in the bottom of the log layer. Its histogram follows nearly a Rayleigh distribution. In the present study, it is the first time that the spanwise distance between the centre of two closest low (or high) streaks and its mean value were investigated. In comparison with the mean spanwise distance between the centre of two nearby streaks, this mean distance is about 13 wall units smaller for low speed streaks and about 9 wall units smaller for high speed streaks. This difference indicates a staggering of two closest streaks in the streamwise direction. Except for the difference in value, the two distances (between two nearby streaks and between two closest streaks) have a similar distribution with wall distance.

Low and high speed streaks cover about 59% of the area of the whole field at $y^+ = 14.5$. This percentage decreases nearly linearly to about 45% at $y^+ = 48$ with wall distance. The total area of high speed streaks is almost equal to that of the low speed ones. The present study shows that the magnitude of the RMS of three velocity components are

comparable in low and high speed streaks. In low speed streaks, high positive wall-normal fluctuations are observed together with high negative streamwise ones. The contrary is true in high speed streaks. Remarkably, the magnitude of these fluctuations is nearly the same in both type of the structures.

6.3 Ejections and sweeps

6.3.1 Functions and parameters of detection

6.3.1.1 Detection functions and parameters

Ejections and sweeps, which are important coherent structures related to the turbulence generation process, are defined as regions of an abrupt outward motion with low streamwise velocity or inward motion with high streamwise velocity respectively. Corino and Brodkey (1969) are one of the earliest who have observed these structures. Thereafter, different techniques were employed to detect those structures. Most of them focused only on the burst or ejections that occur in the near wall region. Among them, the four most widely used techniques are : Variable -Interval Time-Averaging (VITA), Zaric technique, quadrant analysis (also called uv-level) and u-level. The VITA technique, firstly used by Blackwelder and Kaplan (1976), is based on the intermittent character of the short-time variance of a turbulent signal. The detection criterion is completed by using a threshold level on the VITA variance signal. Chen and Blackwelder (1978) and Bogard and Tiederman (1987a) had modified this technique to detect ejections by adding an additional criterion on the velocity gradient, du/dt. Only when the gradient is negative, ejections can be recorded. The Zaric technique (Zaric (1975)) was used to detect ejections by searching the regions in the flow where the streamwise momentum is changing rapidly. The quadrant technique was introduced by Wallace *et al.* (1972) and is based on the detection of the second-quadrant uv signal above a specified magnitude. The u-level technique used by Lu and Willmarth (1973), identifies ejections by detecting the region with high negative streamwise velocity fluctuations. All the four techniques are listed in Table. 6.4 and details can be found in the corresponding articles. In this table, u and v are the instantaneous streamwise and spanwise velocity components respectively. u' and v' are the corresponding fluctuations while u_{rms} and v_{rms} are the standard deviations. H is the threshold level and takes a positive value.

Many efforts were made to evaluate the above methods. For example, Alfredsson and Johansson (1984) compared the VITA, the quadrant and the u-level techniques. They found that the results obtained by the VITA and the quadrant techniques are similar. They have also observed that some events with large uv-peaks detected by this two techniques do not correspond to any strong activity in the u-component. Bogard and Tiederman (1987a) made an evaluation of the effectiveness of the VITA, the quadrant, the u-level techniques and their combinations with flow visualization. They suggest that the quadrant technique has the greatest reliability with a high probability of detecting ejections and a low probability of false detections. Following this, in the present study the quadrant technique is used to detect ejections and sweeps. As explained in Chapter 6.2.1, the velocity fluctuations were normalized by the standard deviations. Then the normalized velocity fluctuations were used to define the detection functions. According to the quadrant technique, three detection functions, F_d^{uv}, F_d^u and F_d^v are defined as :

Technique	Detection function	Detection criteria	references
VITA	$F_d^1 = \frac{1}{T}\int_{t-\frac{1}{2}T}^{t+\frac{1}{2}T} u^2(x_i,t)dt - (\frac{1}{T}\int_{t-\frac{1}{2}T}^{t+\frac{1}{2}T} u(x_i,t)dt)^2$	$F_d^1 > H{u_{rms}}^2$	Blackwelder and Kaplan (1976)
	$F_d^2 = \frac{du}{dt}\|begin$	$F_d^1 > H{u_{rms}}^2$ and $F_d^2 < 0$	Chen and Blackwelder (1978)
	$F_d^3 = \frac{du}{dt}\|center$	$F_d^1 > H{u_{rms}}^2$ and $F_d^3 < 0$	Bogard and Tiederman (1987a)
Zaric	$F_d^1 = u'(\frac{du'}{dt})$	$F_d^1 > Hu_{rms}(\frac{du}{dt})_{rms}$ and $F_d^2 < 0$	Zaric (1975)
	$F_d^2 = \frac{du}{dt}$ $F_d^3 = u'$	$F_d^1 > Hu_{rms}(\frac{du}{dt})_{rms}$ and $F_d^3 < 0$	Zaric (1975) Tubergen and G. (1993)
Quadrant	$F_d^1 = u'v'$ $F_d^2 = u'$ $F_d^3 = v'$	$F_d^1 < -Hu_{rms}v_{rms}$ $F_d^2 < 0$ $F_d^3 > 0$	Wallace *et al.* (1972) Lu and Willmarth (1973) Carlier and Stanislas (2005)
u-Level	$F_d = u'(t)$	$F_d < -Hu_{rms}$	Lu and Willmarth (1973)

TAB. 6.4 – Review of previous methods to detect ejections

$$F_d^{uv} = \frac{u'(m,n,\mathrm{y}^+)v'(m,n,\mathrm{y}^+)}{\sigma_u(\mathrm{y}^+)\sigma_v(\mathrm{y}^+)} \tag{6.25}$$

$$F_d^{u} = \frac{u'(m,n,\mathrm{y}^+)}{\sigma_u(\mathrm{y}^+)} \tag{6.26}$$

$$F_d^{v} = \frac{v'(m,n,\mathrm{y}^+)}{\sigma_v(\mathrm{y}^+)} \tag{6.27}$$

Where u' and v' are the instantaneous velocity fluctuations of the streamwise and spanwise component u and v respectively, σ_u and σ_v are the corresponding standard deviations, (m, n) is the position in the (M, N) grid, and y^+ is the wall distance at which the SPIV measurement is performed.

6.3.1.2 Thresholding

As for streaks, the detection functions, F_d^{uv}, F_d^u and F_d^v (Eq. 6.27), are real scalar fields defined on a discrete (M, N) grid. To obtain the indicative functions F_i of ejections and sweeps, three thresholds, C_T^{uv}, C_T^u and C_T^v, are applied to F_d^{uv}, F_d^u and F_d^v respectively. The values of thresholds are taken as positive. The indicative function F_i is then defined as :

$$\text{Ejection}: \quad F_i = \begin{cases} 1 \text{ when } F_d^{uv} < -C_T^{uv},\ F_d^u < 0 \text{ and } F_d^v > C_T^v \\ 0 \text{ otherwise} \end{cases} \tag{6.28}$$

$$\text{Sweep}: \quad F_i = \begin{cases} 1 \text{ when } F_d^{uv} < -C_T^{uv},\ F_d^u > 0 \text{ and } F_d^v < -C_T^v \\ 0 \text{ otherwise} \end{cases} \tag{6.29}$$

In the present study (see Appendix B.2), C_T^u was selected as zero as used by other studies (e.g. Wallace *et al.* (1972), Carlier and Stanislas (2005)). However, different from previous studies, C_T^v was taken as 0.6 instead of zero. This non-zero value of C_T^v reduces the erroneous detection of strong streaks as ejections or sweeps. The suitable value of C_T^{uv} was chosen as 1.0. However, to compare with early studies, other values will also be used when the statistical characteristics are computed.

6.3.1.3 Mathematical morphology

Similar to streaks, ejections and sweeps are also elongated in the streamwise direction and thus a rectangular (or square) structuring element was chosen : $M_S(W, L)$, in which W is the width in the spanwise direction and L is the length in the streamwise direction. The values of W and L are given in wall units. The structuring element was selected as $M_S = (10^+, 10^+)$ for both ejections and sweeps (see Appendix B.2). Since the selected structuring element is small, it can also be employed in the case that a higher C_T^{uv} is used.

6.3.1.4 Cleaning

As explained in Appendix B.2, two clean factors C_B and C_C, which are given in square wall units, were used to improve the indicative images of ejections and sweeps. The values $C_B = 375^{+^2}$ and $C_C = 750^{+^2}$ were chosen for both types of coherent structures. These two values are based on a threshold $C_T^{uv} = 1.0$. Since they are relatively small, they can be used also for a higher threshold.

Fig. 6.27 shows an example of the detection function and the corresponding indicative images of ejections at the different steps of the detection procedure.

6.3.2 Statistics on ejections and sweeps

6.3.2.1 Frequency of appearance

As for streaks, the frequency of appearance (N) in the area of $530^+ * 300^+$ was computed. Fig. 6.28 shows the profile of (N) as a function of the wall distance. The error bars represent an error of 5% of the mean. In the present study, ejections and sweeps are abbreviated EJ and SW respectively in all the figures if no other specification is made. For ejections, the maximum ($N = 5.2$) is located around $y^+ = 22$. In the region $y^+ < 22$, the frequency of appearance decreases rapidly approaching the wall. In the region $y^+ > 22$, it decreases less rapidly with wall distance. For sweeps, it decreases linearly with wall distance in the whole range. The maximum is expected to locate very close to the wall. In the region $y^+ > 22$, the rate of decrease is almost the same for ejections and sweeps.

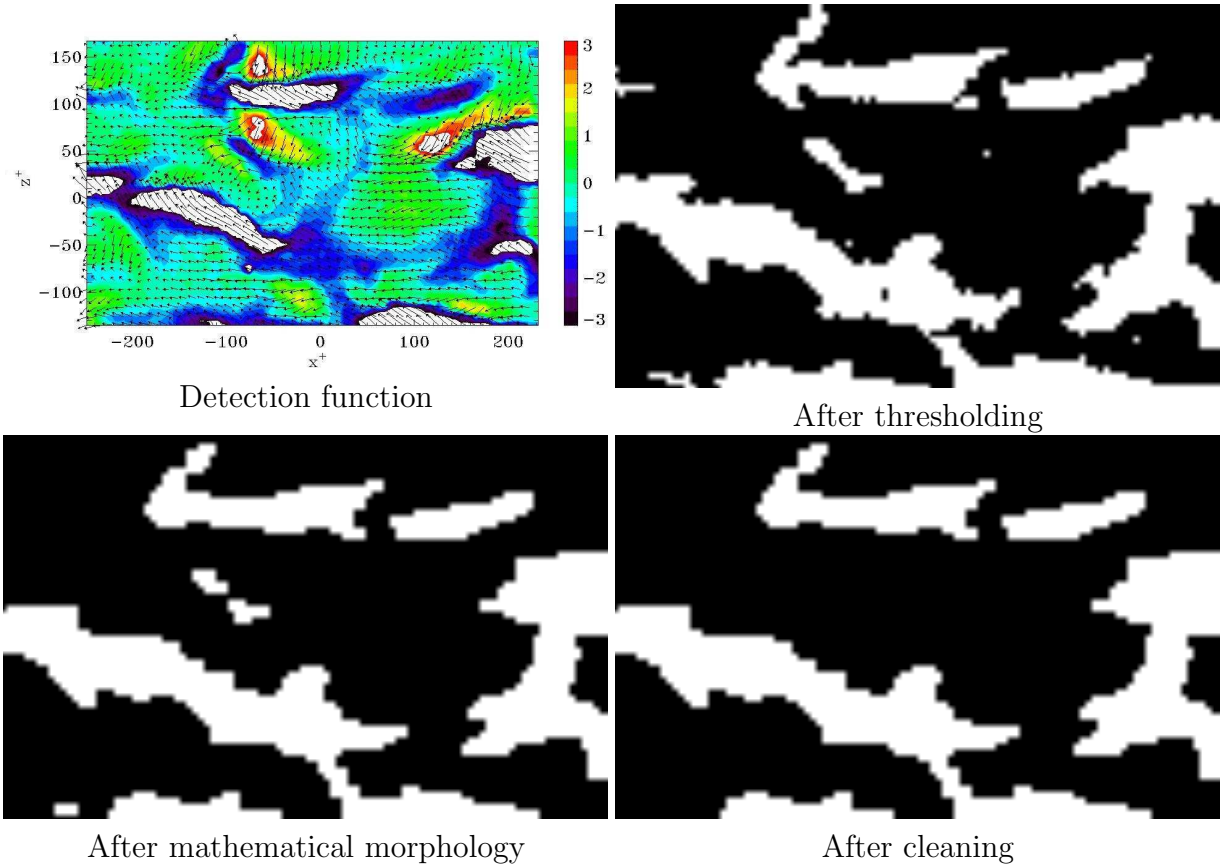

FIG. 6.27 – Detection image and indicative images of ejections

Moreover, in this region, the frequency of appearance of ejections is nearly 50% larger than that of sweeps.

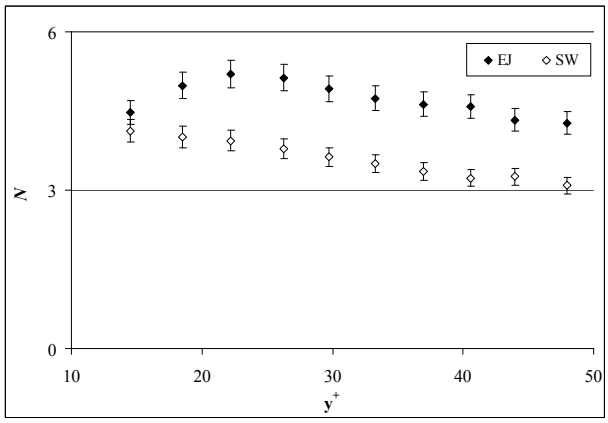

FIG. 6.28 – Frequency of appearance (N) of ejections and sweeps

6.3.2.2 Spanwise angle

To study the direction of motions of ejections and sweeps in the streamwise-spanwise plane, the spanwise angle (φ) is investigated. Fig. 6.29 shows the distribution of its mean value $\overline{\varphi}$ as a function of the wall distance for both ejections and sweeps. As expected from the homogenous property in the spanwise direction, a near-zero value is obtained. The small variations can be attributed to the lack of convergence. Fig. 6.29 also shows the mean of the absolute spanwise angle $\overline{|\varphi|}$. At $y^+ = 14.5$, $\overline{|\varphi|}$ is about 10 degrees for both ejections and sweeps. In the region $y^+ < 22$, it decreases slightly from 10 to 8 degrees with wall distance for ejections while it has nearly a constant value (about 10 degrees) for sweeps. Afterward, in the region $y^+ > 22$, it increases nearly linearly with wall distance to about 11.5 and 14.5 degrees for ejections and sweeps respectively. The value of $\overline{|\varphi|}$ of ejections is about 3 degrees larger than that of sweeps in this region. The large value of $\overline{|\varphi|}$ (> 8 degrees) indicates that many ejections and sweeps move also in the spanwise direction when they travel downstream, especially when far away from the wall.

Fig. 6.30 gives the RMS of φ and $|\varphi|$ respectively. At $y^+ = 14.5$, for both ejections and sweeps, the RMS of φ has nearly the same value (about 14 degrees) while the RMS of $|\varphi|$ has also nearly the same value (about 10 degrees). Except for the difference in values, the distributions of the RMS of φ and $|\varphi|$ are similar to those of $\overline{|\varphi|}$ (Fig. 6.29) for ejections and sweeps respectively : a) decreasing with wall distance for ejections and being constant for sweeps in the region $y^+ < 22$; b) increasing for both ejections and sweeps afterwards (in the region $y^+ > 22$). In the latter region, for ejections or sweeps, the RMS of φ is about 5 degrees larger than that of $|\varphi|$. In the same region, the RMS of ejections is about 3 degrees larger than that of sweeps for both φ and $|\varphi|$. In Fig. 6.29, all the RMS are fairly large (> 8 degrees).

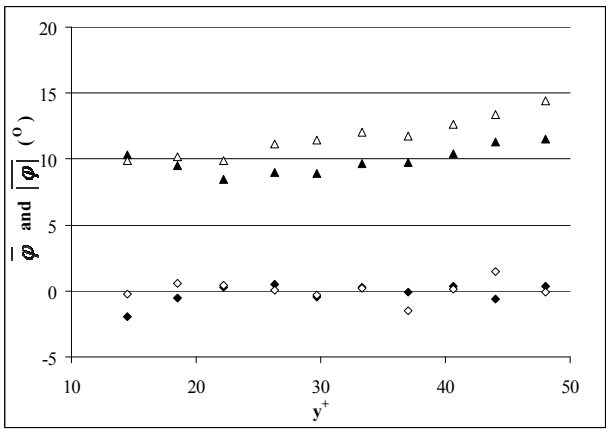

FIG. 6.29 – Mean spanwise angle $\overline{\varphi}$ and mean absolute spanwise angle $\overline{|\varphi|}$. $\overline{\varphi}$ (EJ) : ♦ ; $\overline{\varphi}$ (SW) : ◊ ; $\overline{|\varphi|}$ (EJ) : ▲ ; $\overline{|\varphi|}$ (SW) : △.

The above discussion is only based on the average behaviour. To investigate the spanwise angle φ in more detail, Fig. 6.31 shows its histograms for both ejections and sweeps. It shows clearly that many ejections and sweeps travel downstream with large spanwise angle (up to 30 degrees). When $|\varphi| < 15$, the histogram is changing with wall distance.

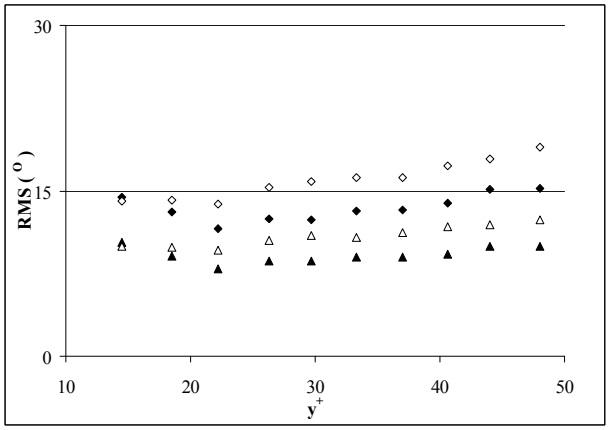

FIG. 6.30 – RMS of the spanwise angle φ and the absolute spanwise angle $|\varphi|$. φ (EJ) : ♦ ; φ (SW) : ◊ ; $|\varphi|$ (EJ) : ▲ ; $|\varphi|$ (SW) : △.

However, when $|\varphi| > 15$, the histograms are nearly the same in whole range of wall distance studied. The variation in the value of the central peak partly results from different frequency of appearance at each wall distance studied (Fig. 6.28).

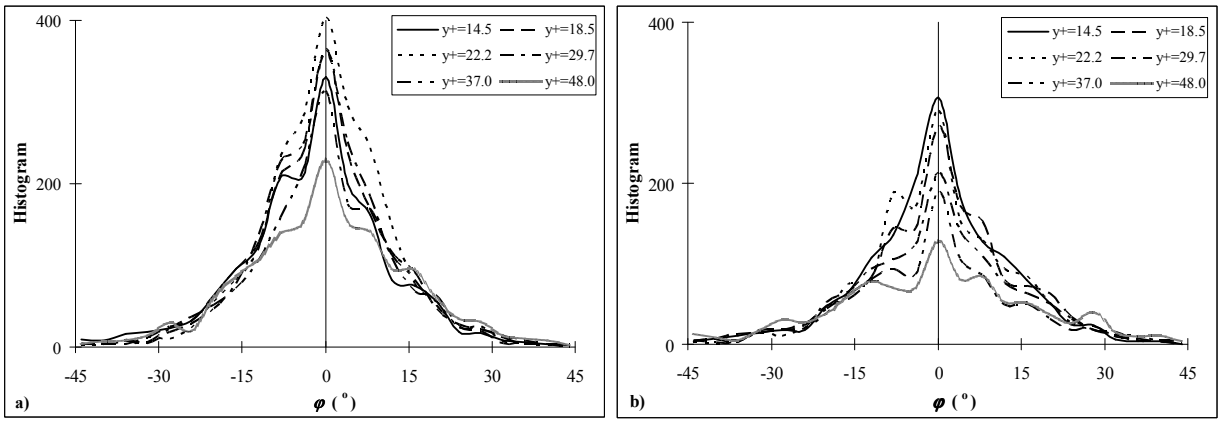

FIG. 6.31 – Histogram of the spanwise angle φ at selected wall distances. a : ejections ; b : sweeps.

From these histograms, the spanwise angle of ejections and sweeps was divided into three groups based on the absolute value : $|\varphi| < 6$, $6 < |\varphi| < 15$ and $|\varphi| > 15$. Fig. 6.32 gives the percentage of each group as a function of wall distance. In the first group, for ejections, the percentage increases in the range $y^+ < 22$ and then decreases linearly afterwards. For sweeps it decreases slowly in the whole range. The second group shows a nearly constant percentage (34%) for both ejections and sweeps in the whole range of wall distance under study. In the last group, the behaviour is just opposite to that in the first group. Fig. 6.32 also shows that ejections are relatively more parallel to the streamwise direction around $y^+ = 25$ while for sweeps, closer to the wall, more parallel to the streamwise direction. Considering the tendency about $y^+ = 48$, the probability of small angles should be overwhelmed by that of large ones for both ejections and sweeps.

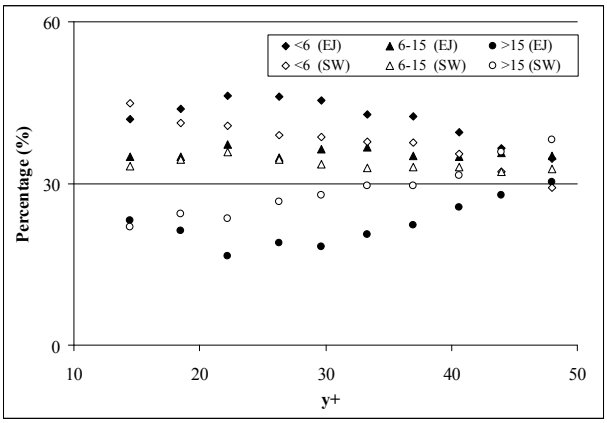

FIG. 6.32 – Percentage of the spanwise angle ($|\varphi|$) in three different ranges

The histograms in Fig. 6.31 are close to a Laplace distribution (Eq. 6.13) except for small oscillations due to the lack of convergence. To characterize them globally, skewness (S) and flatness (F) are given in Fig. 6.33. For both ejections and sweeps, the near-zero value of skewness indicates the good symmetry property of the histogram. It also suggests the homogeneity in the spanwise direction. The flatness has a value about 5, which is smaller than the standard value of a Laplace distribution, which is 6.

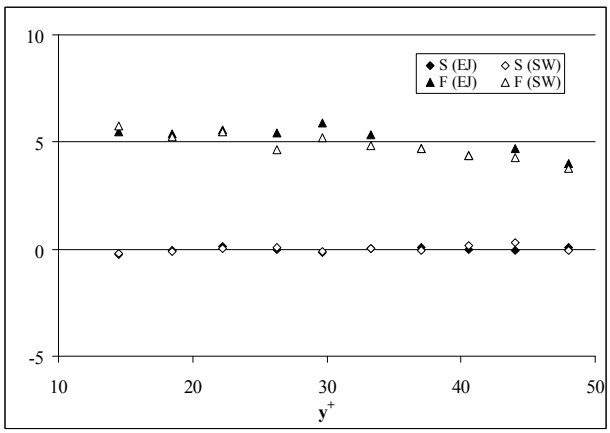

FIG. 6.33 – Skewness (S) and flatness (F) of the spanwise angle φ

6.3.2.3 Width

Except for the frequency of appearance and the spanwise angle, another interesting characteristic of ejections and sweeps is the size, including width W_a^+, length $L_A^+$and area A_c^+. Fig. 6.34 shows the mean width $\overline{W_a^+}$ of ejections and sweeps respectively at various wall distances. The error bars represent an error of 5% of the mean. For ejections, the mean width keeps nearly a constant value (18 wall units) in the region $y^+ < 22$ and increases linearly to about 24 wall units at $y^+ = 48$. For sweeps, a nearly linear increase with wall distance is evidenced in the whole range. It starts from about 22 wall units at

$y^+ = 14.5$ to about 30 wall units at $y^+ = 48$. Sweeps are about 25% wider than ejections on average. Fig. 6.34 also shows the RMS of the width W_a^+ at various wall distances. Both RMS of ejections and sweeps increase linearly with wall distance. The RMS of the width of sweeps is about 40% larger than that of ejections. It is about 1/5 of the corresponding $\overline{W_a^+}$, showing that this parameter is fairly constant in the region near the wall.

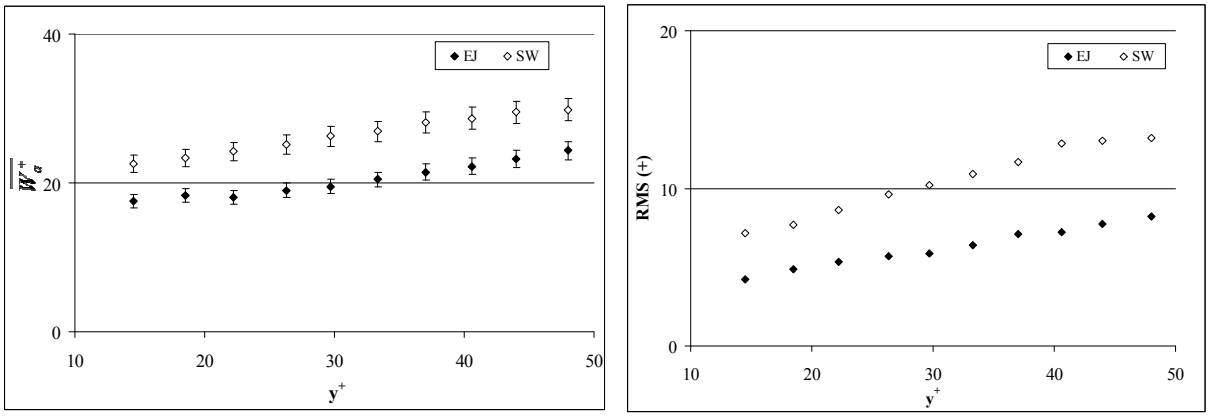

FIG. 6.34 – Mean and RMS of the width W_a^+ of ejections and sweeps

To study the distribution of W_a^+ in more detail, Fig. 6.35 shows some histograms at selected wall distances. As indicated by the RMS in Fig. 6.34, the histograms of ejections have a much smaller range compared to those of sweeps. For ejections, the maximum of the histogram locates at about $W_a^+ = 15$ up to $y^+ = 30$ and shifts progressively to $W_a^+ = 20$ at $y^+ = 48$. For sweeps, the location of this maximum is always at about $W_a^+ = 20$. In the range $W_a^+ > 25$ for ejections and $W_a^+ > 32$ for sweeps, the larger the wall distance, the higher the histogram. In other words, the population of structures with large width increases with wall distance. This indicates that both ejections and sweeps become larger with increasing wall distance as shown in Fig. 6.34, but the peak of this histogram which hardly moves with wall distance is indicative of a strong coherent motion. Similar to streaks, the histograms of the width of ejections and sweeps follow nearly a lognormal distribution.

Fig. 6.36 show respectively the variation coefficient ψ and the median value M_0^+ (See Eq. 6.16). For ejections, ψ increases with wall distance in the region $y^+ < 22$, stays nearly constant in the region $22 < y^+ < 30$, and then increases again but less rapidly in the region $22 < y^+ < 48$. For sweeps, this coefficient increases continuously with wall distance in the whole range. The distributions of the median value M_0^+ are the same as those of the mean width $\overline{W_a^+}$ in Fig. 6.34 for ejections and sweeps, the median value being about 5% smaller than the corresponding mean value.

Since the histograms are expected to follow a lognormal distribution. The skewness (S) and flatness (F) obtained in the present study are compared to those computed from the true lognormal distribution in Fig. 6.37. For both ejections and sweeps, the agreement is good in both parameters. The results confirm that the histograms of the width W_a^+ of ejections and sweeps do follow a lognormal distribution.

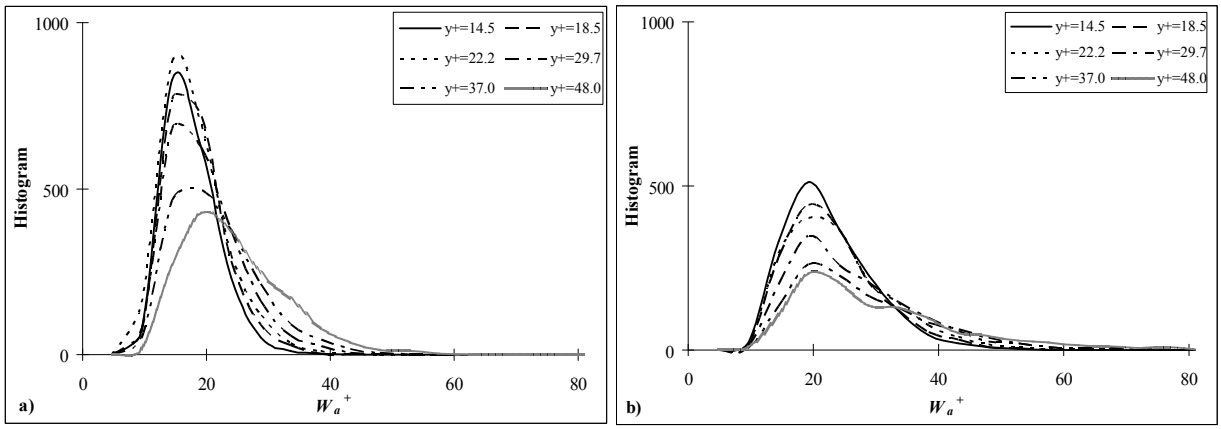

FIG. 6.35 – Histogram of the width W_a^+ of ejections and sweeps at selected wall distances. a : ejections ; b : sweeps.

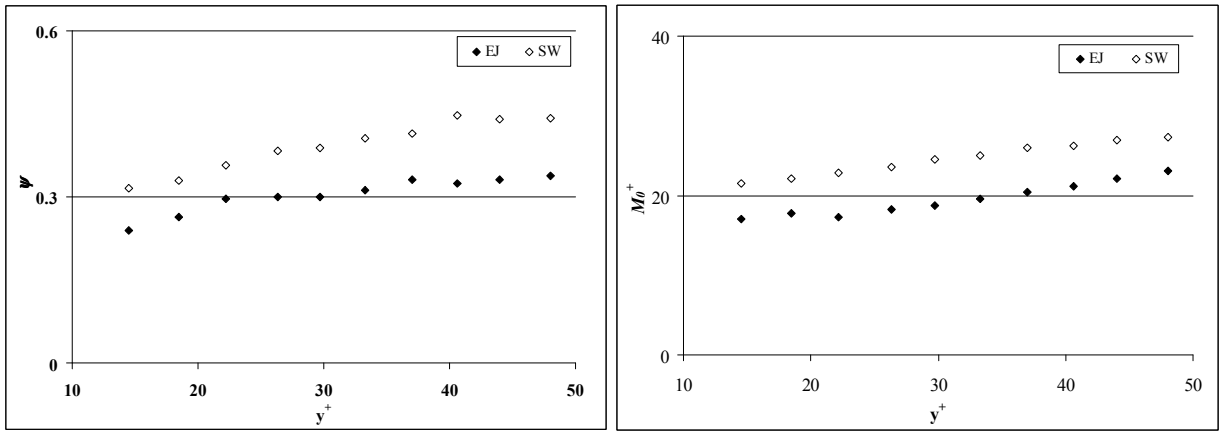

FIG. 6.36 – Variation Coefficient ψ and median value M_0^+ of the width W_a^+ of ejections and sweeps

6.3.2.4 Length

Fig. 6.38 shows the profiles of the mean length $\overline{L_A^+}$ as a function of wall distance. The error bars represent an error of 5% of the mean. For ejections, the studied wall distance range can be split into three regions. In the first region, $y^+ < 22$, the mean length increases rapidly from 92 wall units at $y^+ = 14.5$ to 117 wall units at $y^+ = 22.2$. Then, for $22 < y^+ < 33$, it keeps a nearly constant value of 117 wall units. In the third region, $y^+ > 33$, it decreases slightly to 107 wall units at $y^+ = 48$. Different from ejections, sweeps have a nearly constant mean length $\overline{L_A^+}$ of 90 wall units in the whole range. Different from the width, the length of ejections is generally larger than that of sweeps especially when $y^+ > 22$ (the difference is about 10 wall units). Fig. 6.38 also gives the RMS of the length L_A^+ of ejections and sweeps. The RMS of ejections increases rapidly from 49 to 67 wall units with wall distance up to $y^+ = 22$ and thereafter stays nearly constant around 70 wall units. For sweeps, the RMS has a slight linear increase, from 52 to 59 wall units in the whole range.

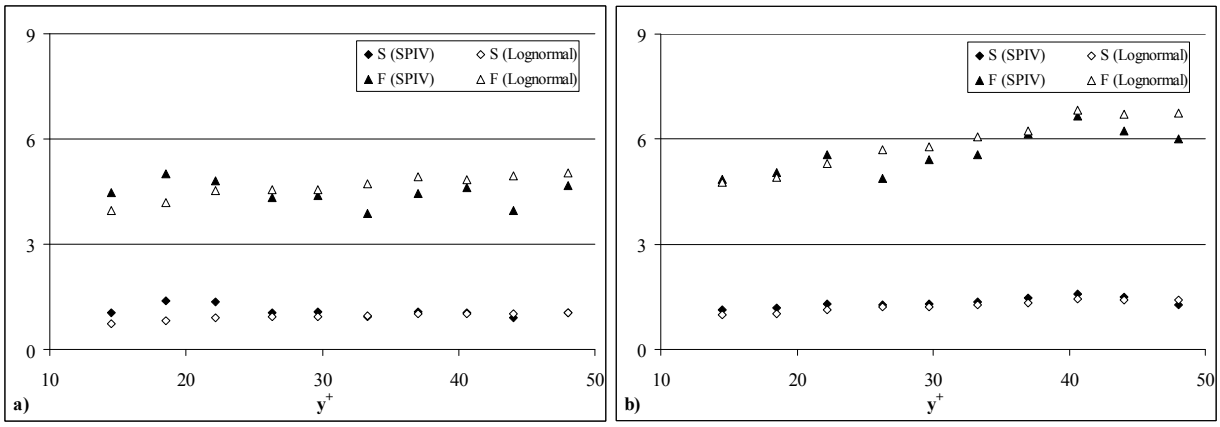

FIG. 6.37 – Comparison of skewness (S) and flatness (F) of the width W_a^+ of ejections and sweeps of the present study with the theoretical values obtained according to lognormal distributions. a : ejections ; b : sweeps

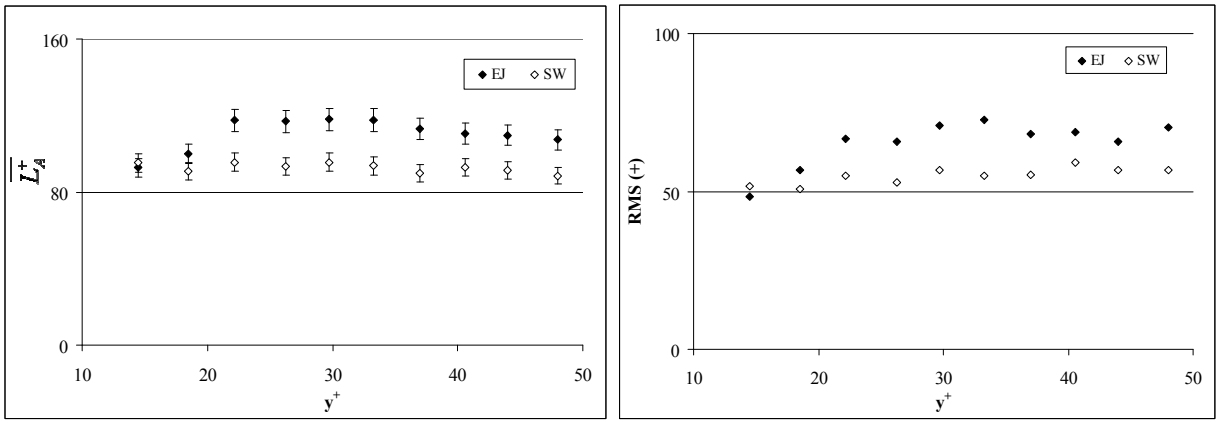

FIG. 6.38 – Mean and RMS of the length L_A^+ of ejections and sweeps

Fig. 6.39 shows the histograms of L_A^+ for ejections and sweeps at selected wall distances. Similar to the width W_a^+, the histograms of the length follow nearly a lognormal distribution. Contrary to the result of the width, the histograms of the length have nearly the same range for ejections and sweeps. For ejections, the location of the peak is 60 at $y^+ = 14.5$ to 18.5 and 73 at $y^+ = 22$ to 37. Afterward, it goes down to 52 at $y^+ = 48$. This is more or less in agreement with tendencies observed in Fig. 6.38. It is difficult to interpret in itself and should be looked at in relation with other coherent structures (e.g. streaks, vortices). For sweeps, there seems to be a convergence problem near the wall ($y^+ = 14.5$ and 22.2). The logic would call for a constant peak at $L_A^+ = 50$.

To study the histograms statistically, Fig. 6.40 shows the profiles of the coefficient ψ of the length of ejections and sweeps as a function of wall distance. The profiles are nearly the same for both types of coherent structures. This coefficient increases slightly with wall distance. The average value is about 0.59. Fig. 6.40 also shows the median value M_0^+ of the lengths of ejections and sweeps. The distributions of the median value are similar to those of the mean length $\overline{L_A^+}$ for ejections and sweeps respectively. In general, the median

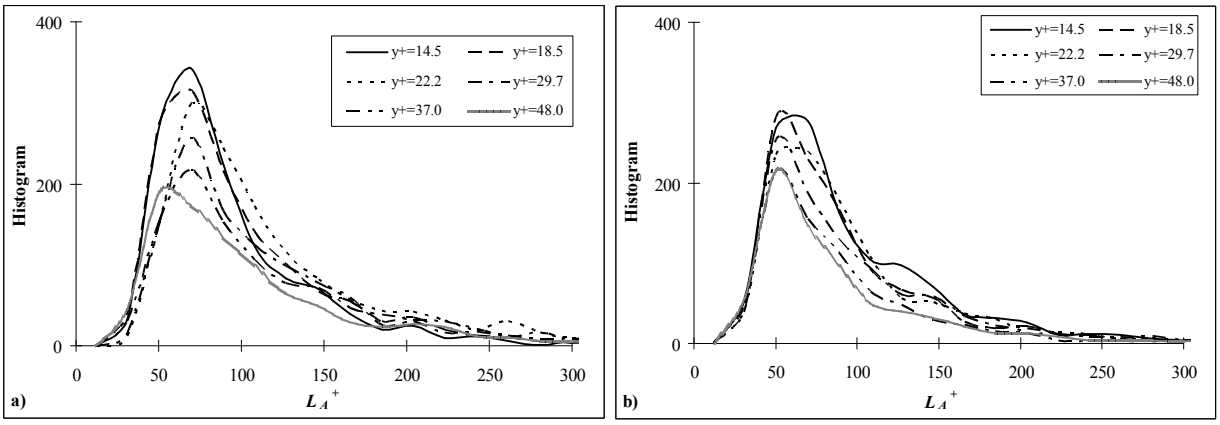

FIG. 6.39 – Histogram of the length L_A^+ of ejections and sweeps at selected wall distances. a : ejections ; b : sweeps

value is about 14% smaller than the mean.

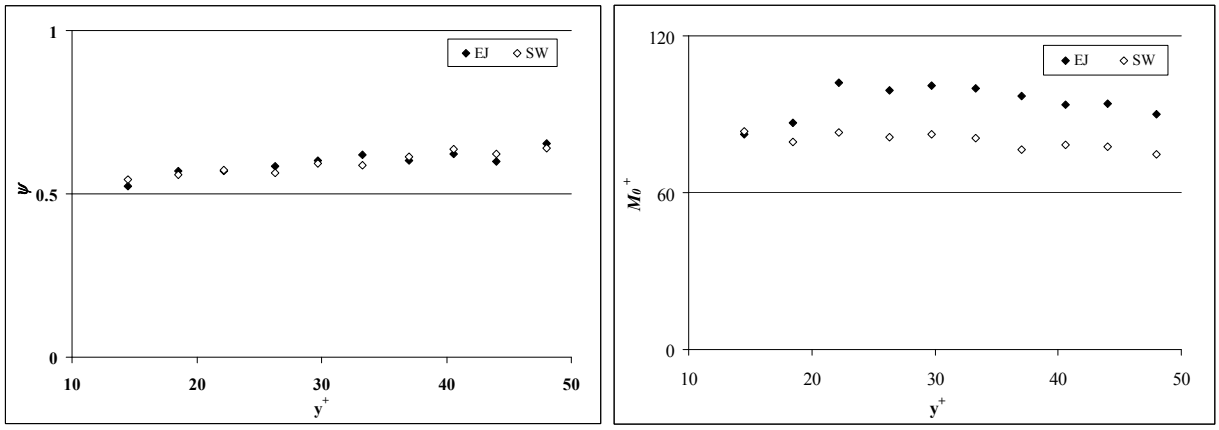

FIG. 6.40 – Variation Coefficient ψ and median value M_0^+ of the length L_A^+ of ejections and sweeps

Fig. 6.41 shows skewness (S) and flatness (F) obtained in the present study. The results are compared to those computed from a true lognormal distribution. For both ejections and sweeps, skewness of the present study is in remarkably good agreement with that from lognormal distributions. However, for flatness, some difference appears due to the lack of convergence. In the present study, the length and the width have nearly the same number of samples. However, the range of the length is about 5 times larger than that of the width. Consequently, the convergence of length is not as good as that of width.

6.3.2.5 Area

Fig. 6.42 shows the profile of the mean area $\overline{A_c^+}$ of ejections and sweeps as a function of wall distance. The error bars represent an error of 5% of the mean. For sweeps, the mean area increases nearly linearly from 2240 square wall units at $y^+ = 14.5$ to 2800 square wall units at $y^+ = 48$. For ejections, the growth is faster in the region $y^+ < 22$ and is

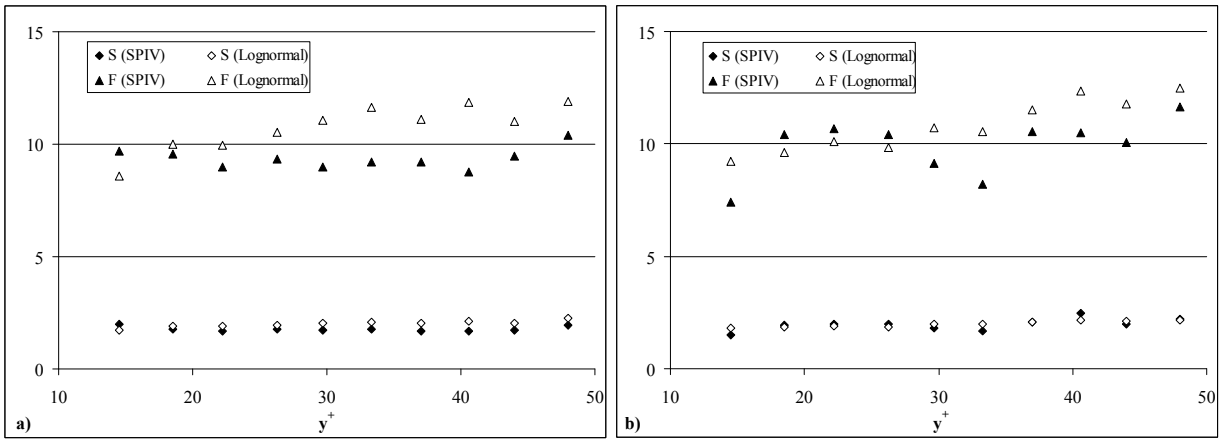

FIG. 6.41 – Comparison of skewness (S) and flatness (F) of the length L_A^+ of ejections and sweeps of the present study with the theoretical values obtained according to lognormal distributions. a : ejections ; b : sweeps

comparable to that of sweeps afterward. Fig. 6.42 indicates that ejections are smaller than sweeps. Examining Fig. 6.34 and 6.38, for sweeps, the growth in area is mainly due to the variation of the mean width $\overline{W_a^+}$. However, for ejections this growth mainly results from the variation of $\overline{W_a^+}$ in the region $22 < y^+ < 33$ and from the combination of variations of $\overline{W_a^+}$ and $\overline{L_A^+}$ for the rest of wall distances studied. Fig. 6.42 also shows the RMS of $\overline{A_c^+}$ for ejections and sweeps. The distribution of the RMS is similar to that of $\overline{A_c^+}$ for both ejections and sweeps : an increase with wall distance in general. The increase starts from 1100 and 1750 square wall units at $y^+ = 14.5$ and ends at 2450 and 3000 square wall units at $y^+ = 48.0$ for ejections and sweeps respectively. It should be noted that here, the RMS is comparable to the mean.

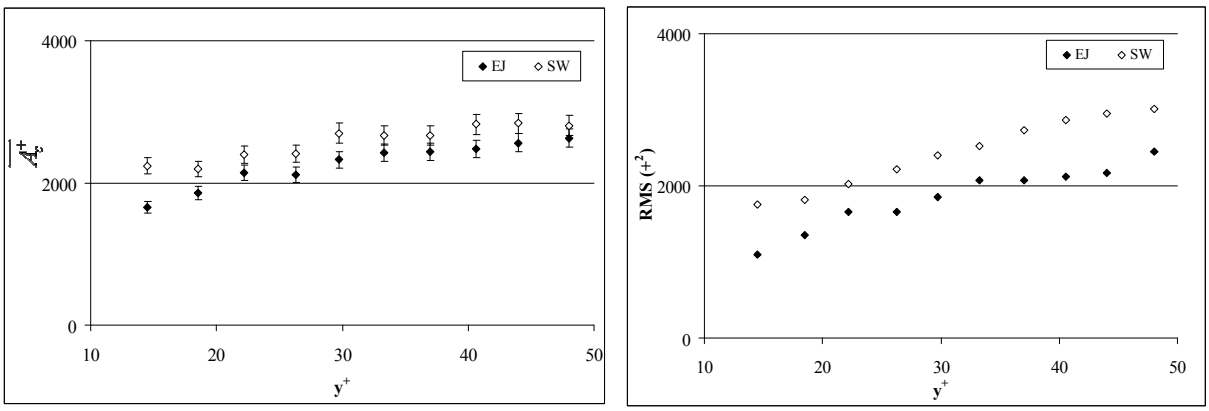

FIG. 6.42 – Mean and RMS of the area A_c^+ of ejections and sweeps

As for other statistics, the histogram of the area A_c^+ of ejections and sweeps are plotted in Fig. 6.43 at selected wall distances. The dash line at $A_c^+ = 820$ square wall units is related to the cleaning factor C_C (see chapter 6.3.1). Different from distributions of the width and the length, the histogram of the area follows nearly an exponential distribution

with a shift about 820 wall units. The probability distribution function of this distribution is given in Eq. 6.30. The fluctuations can be attributed to the lack of convergence. The difference for the two types of coherent structures can be in part explained twofold : firstly ejections are smaller than sweeps ; secondly the frequency of appearance of ejections is higher than that of sweeps.

$$P(x) = \lambda e^{-\lambda(x-a)} \tag{6.30}$$

Where λ is the rate of change, a is the shift to the origin and $x \in [a, \infty]$.

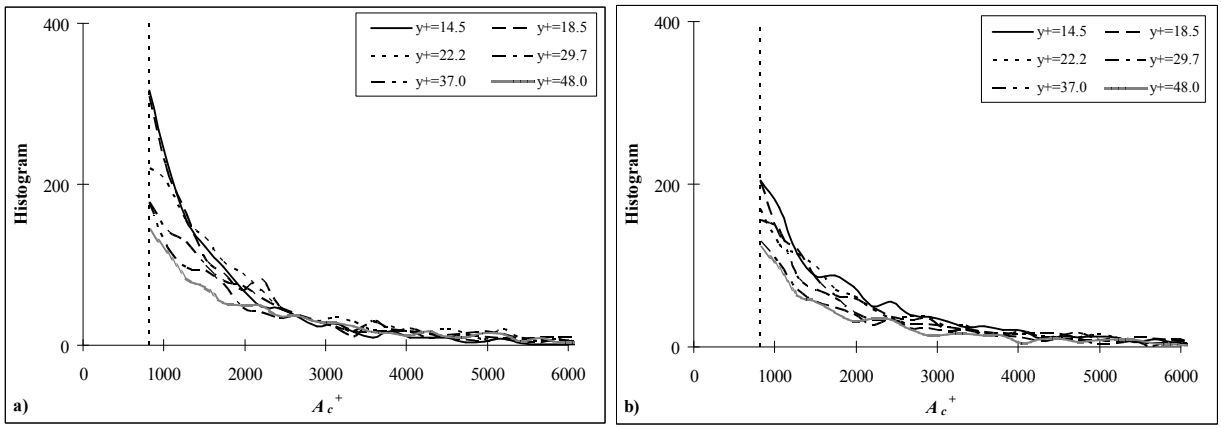

FIG. 6.43 – Histogram of the area A_c^+ of ejections and sweeps at selected wall distances. a : ejections ; b : sweeps.

Fig. 6.44 shows skewness (S) and flatness (F) of the area A_c^+ of ejections and sweeps. For skewness, both coherent structures have a similar value of about 2.5, which is close to the standard value of an exponential distribution that is 2. However, flatness varies between 8.5 and 16. The standard value of flatness for an exponential distribution is 9. Comparing Fig. 6.43 with Fig. 6.35 and Fig. 6.39, the range of the distribution of the area is much larger than those of the width and the length of ejections and sweeps. However the number of samples used to calculate the area is nearly the same as those for the width and the length. Consequently, the convergence of the area is much less than those of the width and length. This explains in part the relatively large difference in flatness between the present results and the exponential distribution.

6.3.2.6 Spanwise distance

Fig. 6.45 gives the profiles of the mean spanwise distance $\overline{d^+}$ of ejections and sweeps as a function of wall distance. The distribution is nearly the same for both coherent structures. The mean spanwise distance varies between 118 and 128 wall units in the whole range of wall distance studied. Fig. 6.45 also shows the RMS of the spanwise distance d^+ of ejections and sweeps. Both of them are nearly constant around 50 wall units.

Fig. 6.46 shows the histograms of the spanwise distance d^+ of ejections and sweeps at selected wall distances. The histograms in Fig. 6.46 are close to a Rayleigh distribution Weisstein (1999), Eq. 6.22). The small oscillations may arise from the lack of convergence.

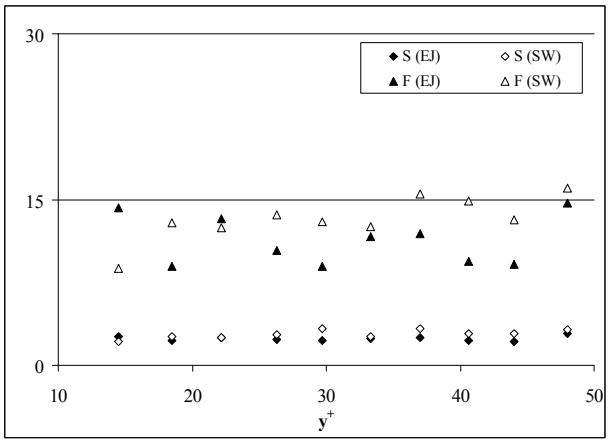

FIG. 6.44 – Skewness (S) and flatness (F) of the area A_c^+ of ejections and sweeps. a : ejections ; b : sweeps

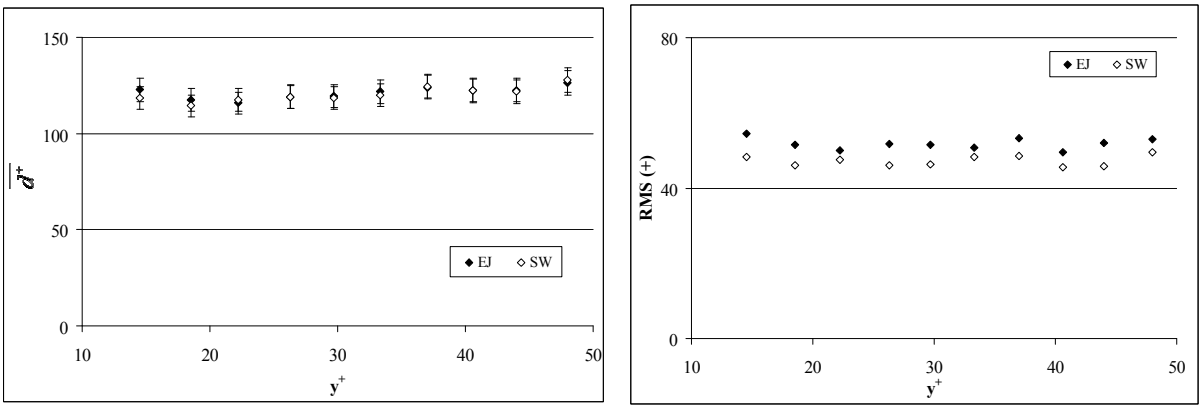

FIG. 6.45 – Mean and RMS of the spanwise distance d^+ of ejections and sweeps

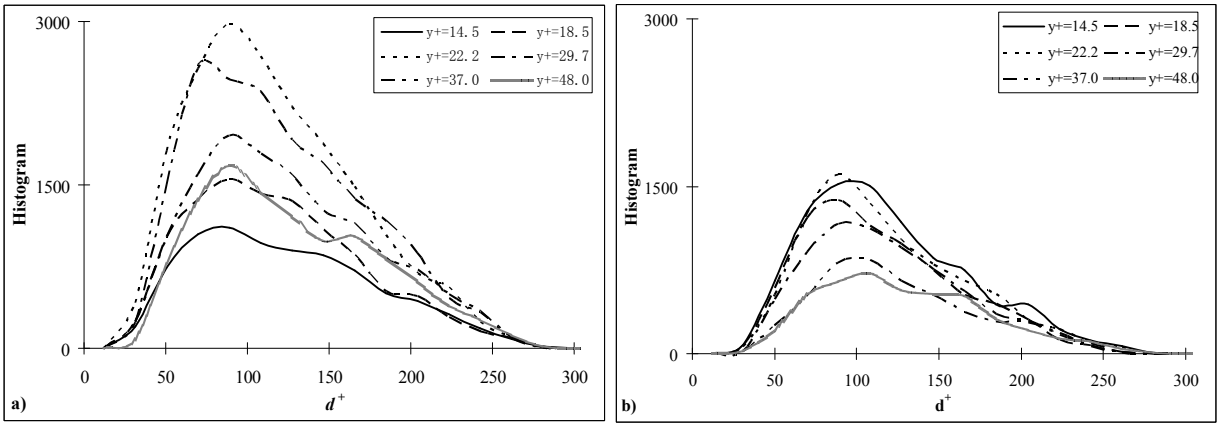

FIG. 6.46 – Histogram of the spanwise distance d^+ of ejections and sweeps at selected wall distances. a : ejections ; b : sweeps

To characterise the histograms statistically, skewness (S) and flatness (F) are compu-

ted and presented in Fig. 6.47. Skewness has a constant value of about 0.52 for ejections and of about 0.60 for sweeps, which indicates the relatively symmetric property of the histograms (Fig. 6.46). These values are comparable to 0.63 which is the standard value for a Rayleigh distribution (Eq. 6.23). Likewise, the present results of flatness are nearly a constant of about 2.6 for ejections and of about 2.8 for sweeps. These values are close to 3.24, the standard value for a Rayleigh distribution (Eq. 6.24). A comparison with a lognormal distribution shows that d^+ is much further from this type of law than from a Rayleigh one.

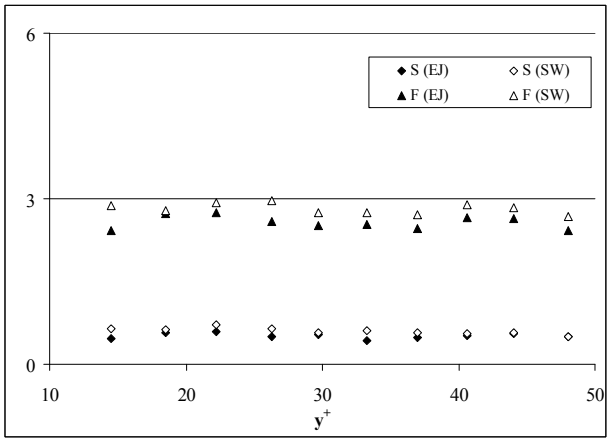

FIG. 6.47 – Skewness (S) and flatness (F) of the spanwise distance d^+ of ejections and sweeps

6.3.3 Conditional statistical analysis

When ejections and sweeps are detected, it is possible to perform various statistical analysis within those structures, for example, the mean velocities in ejections and sweeps. As shown in Chapter 6.3.1, the threshold $C_T^{uv} = 1.0$ were selected. In the following discussion, for each analysis, the results obtained using $C_T^{uv} = 2.0$, 3.0 and 4.0 are also presented to study the influence of this threshold on the statistics investigated. Moreover, as the quadrant method is used to distinguish ejections from sweeps, the statistical analysis are also carried out in each quadrant. In the present study, the four quadrants are named Q1, Q2, Q3 and Q4 respectively. In all the following figures, in EJ-n and SW-n, n is the value of the threshold C_T^{uv} (n=1, 2, 3, 4).

6.3.3.1 Percentage of area

The first interesting conditional characteristic is the proportion of area. Fig. 6.48 shows the percentages of the area of each quadrant. The percentage of Q1 and Q3 is of the order of 18% and independent of wall distance. The percentage of Q2 and Q4 is also similar but of the order of 32%. The percentage of Q2 is slightly smaller than that of Q4.

Fig. 6.49a and 6.49b give profiles of the percentages of area of ejections and sweeps in Q2 and Q4 respectively obtained with various C_T^{uv} as a function of wall distance. For

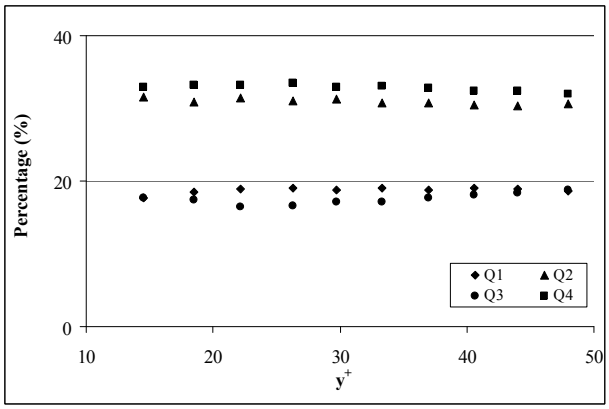

FIG. 6.48 – Percentage of area in each quadrant

ejections, Fig. 6.49a shows that the profiles have a similar pattern for all the thresholds studied. It first increases rapidly in the region $14.5 < y^+ < 26$. Then it remains nearly constant above that region. For sweeps, in Fig. 6.49b the percentage is nearly constant for each threshold. Fig. 6.49 indicates that the threshold has a significant influence on the percentage, indicating that high intensity ejections and sweeps are very localized.

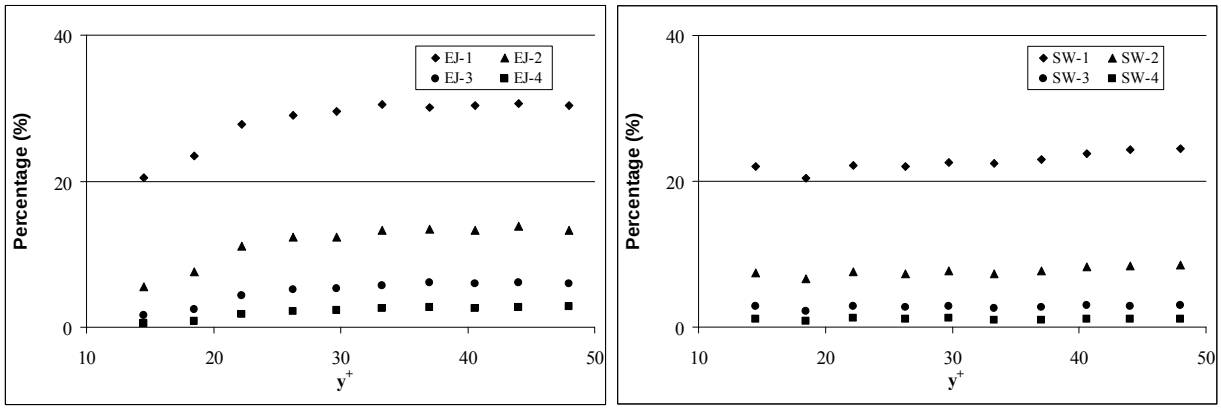

FIG. 6.49 – Percentage of area of ejections and sweeps with various C_T^{uv}. a) Percentage of area of ejections in Q2 ; b) Percentage of area of sweeps in Q4

6.3.3.2 Velocity angle

Fig. 6.50 shows the profile of the mean streamwise velocity angle $\overline{\alpha}$ ($\tan(\alpha)=v/u$) as a function of wall distance in each quadrant as well as in the whole field (all 4 quadrants). The mean angle of the whole field has a very small positive value (about 0.15 degree). The absolute value of the mean angle increases slightly with wall distance for all quadrants. Fig. 6.50 also shows that the mean angle of Q2 is about 2 times that of Q1 and 1.5 times that of Q3 and Q4. This results probably from the fact that the streamwise velocity (u) in Q2 is much smaller than in Q1. It also explains the small positive value of the mean angle of the whole field. Moreover, for low speed regions (Q2 and Q3), Fig. 6.50 shows

that the motions away from the wall are more intense than those moving towards the wall. The opposite is true for high speed regions (Q1 and Q4).

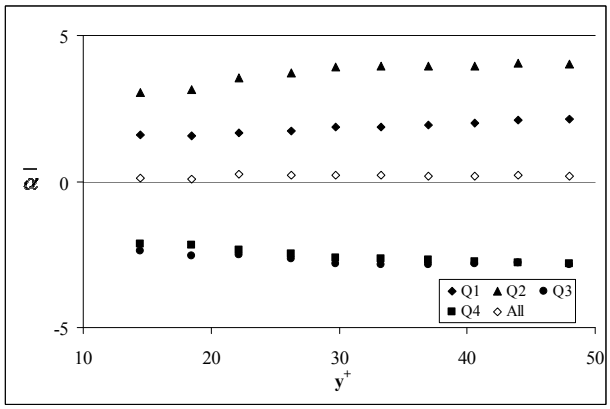

FIG. 6.50 – Mean streamwise velocity angle $\overline{\alpha}$ in each quadrant and in the whole field

Fig. 6.51 gives the mean streamwise velocity angle $\overline{\alpha}$ in ejections and sweeps with various threshold C_T^{uv} as a function of wall distance. Compared to Fig. 6.50, the mean velocity angles in ejections and sweeps are much larger than those in Q2 and Q4 respectively. In Fig. 6.51, the angle increases significantly with C_T^{uv} for ejections but less so for sweeps. Moreover, Fig. 6.51 shows that the angle in ejections is much larger than that in sweeps, especially for strong ones. These findings can be attributed to the difference in streamwise velocity as explained earlier.

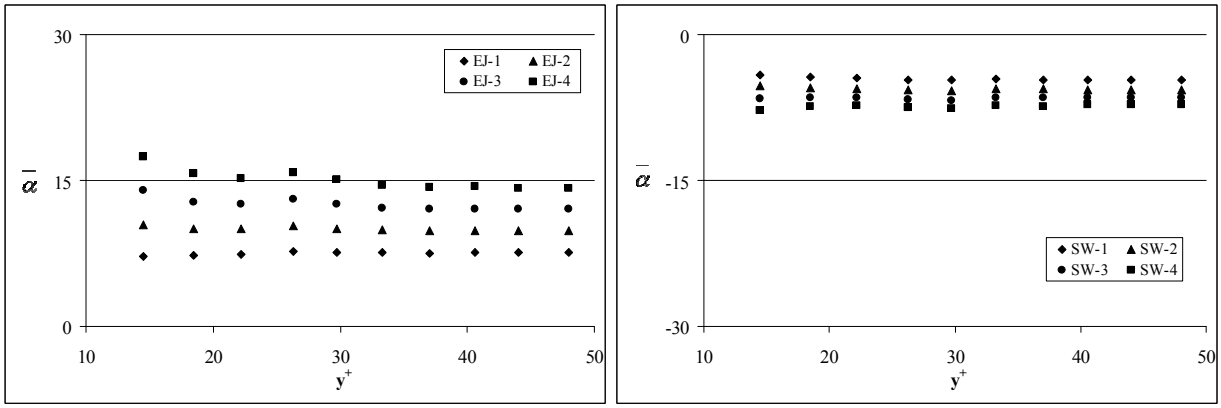

FIG. 6.51 – Mean streamwise velocity angle $\overline{\alpha}$ in ejections and sweeps

6.3.3.3 Reynolds shear stress

The most interesting feature of ejections and sweeps is the contribution to the generation of Reynolds shear stress $-(u'v')^+$. Since ejections and sweeps are involved in Q2 and Q4 respectively, it is also important to study this contribution in each quadrant. Fig. 6.52 shows profiles of the mean Reynolds shear stress $-\overline{u'v'}^+$ in each quadrant as well as in the whole field. The modulus of $-\overline{u'v'}^+$ increases in the region $y^+ < 30$ for Q2, Q4 and

the whole field. It stays almost constant in the region $y^+ > 30$. For Q1 and Q3, a slow linear increase is observed in the whole range. Fig. 6.53 shows the ratio of the modulus of $-\overline{u'v'}^+$ in Q2 and Q4 to that in Q1 and Q3. This ratio is about 2 all over the field.

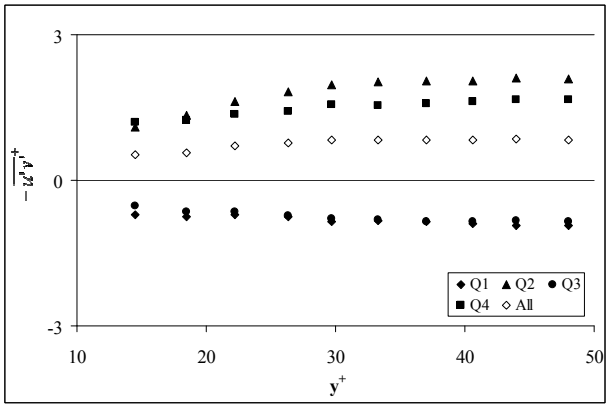

FIG. 6.52 – Mean Reynolds shear stress $-\overline{u'v'}^+$ in each quadrant and in the whole field

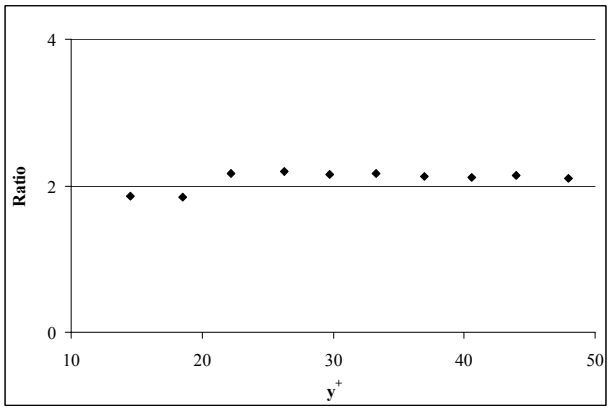

FIG. 6.53 – Ratio of the modulus of the mean Reynolds shear stress $-\overline{u'v'}^+$ in Q2 and Q4 to that in Q1 and Q3

Fig. 6.54 shows the ratios of the mean Reynolds shear stress $-\overline{u'v'}^+$ in ejections and sweeps to those in Q2 and Q4 respectively. For ejections, in the region $y^+ < 22$, the ratio decreases linearly with wall distance. In the region $y^+ > 22$, it is nearly constant. For sweeps, the ratio is constant or decreases slightly with wall distance. Fig. 6.54 shows that the mean value in ejections and sweeps is much larger than those in Q2 and Q4 respectively. For example, even with the small threshold $C_T^{uv} = 1.0$, the ratio is larger than 2.4 for ejections and 2.8 for sweeps. It indicates that ejections and sweeps are remarkably strong structures in Q2 and Q4.

After studying the mean value of $-(u'v')^+$, a forward step is conducted to investigate the distribution of the total Reynolds shear stress $\sum_1^M \sum_1^N \sum_1^{N_f} (-u'v')^+$ in each quadrant. Here, M and N are the number of column and line of the grid (M, N), and N_f is the number of fields recorded by SPIV. Fig. 6.55 shows the ratios of the total Reynolds shear stress

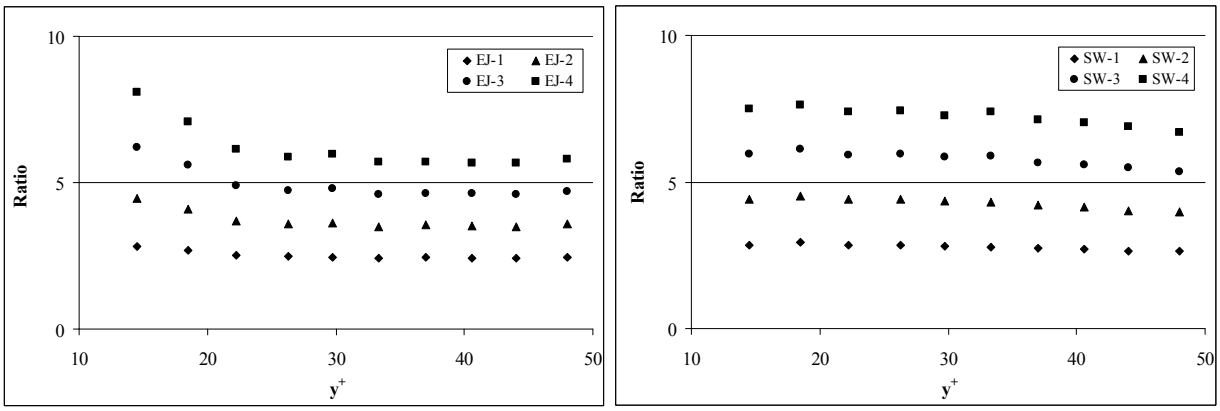

FIG. 6.54 – Ratios of the mean Reynolds shear stress $-\overline{u'v'}^{+}$ in ejections and sweeps to those in Q2 and Q4 respectively. a) Ratios of $-\overline{u'v'}^{+}$ in ejections to that in Q2 ; b) Ratios of $-\overline{u'v'}^{+}$ in sweeps to that in Q4

in each quadrant to that in the whole field. For Q2, the ratio is about 0.72 and hardly varies with wall distance. For Q4, in the region $y^+ < 14.5$, it decreases with wall distance from 0.75 at $y^+ = 14.5$ to 0.62 at $y^+ = 22.2$. At $y^+ = 18.5$ the ratios of Q2 and Q4 are equal (about 0.72). Apart from this point, the ratio of Q4 is larger than that of Q2 in the region $y^+ < 18.5$ while the opposite is true in the region $y^+ > 18.5$. In the region $18.5 < y^+ < 22$, the ratio of Q1 and Q3 decreases from 0.22 to 0.17. In the region $y^+ \leq 18.5$, it is nearly a constant value of 0.22 while in the region $y^+ \geq 22$ it is about 0.17. Fig. 6.55 shows that the ratios of Q2 and Q4 are about 3.5 times those of Q1 and Q3, which indicates that Q2 and Q4 dominate the generation of Reynolds shear stress. In the present study, the ratio of $\sum_1^M \sum_1^N \sum_1^{N_f} (-u'v')^+$ in Q2 to that in Q4 increases from 0.9 at $y^+ = 14.5$ to 1.2 at $y^+ = 48$.

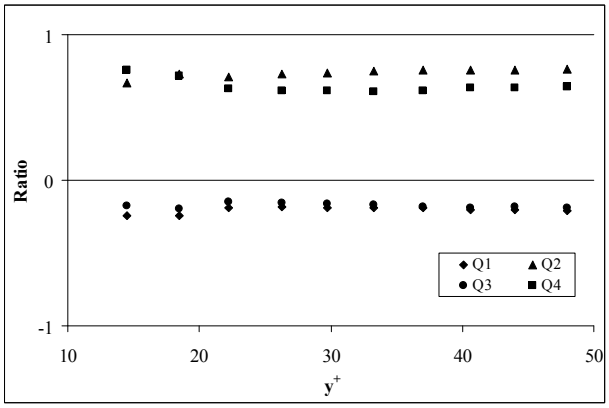

FIG. 6.55 – Ratios of the total Reynolds shear stress $\sum_1^M \sum_1^N \sum_1^{N_f} (-u'v')^+$ in each quadrant to that in the whole field

To study the contribution of ejections and sweeps to the production of the total Reynolds shear stress, Fig. 6.56 shows ratios of the turbulence production in ejections and sweeps to that in the whole field. For ejections, the studied wall distance can be divided

into two regions. For $y^+ < 26$, the ratio increases relatively rapidly from 0.38 at $y^+ = 14.5$ to 0.52 at $y^+ = 26.3$ with wall distance. In the region $y^+ > 26$, it is nearly a constant of about 0.55. For sweeps, on the contrary, the ratio decreases at the region of $y^+ < 26$: from 0.47 at $y^+ = 14.5$ to 0.38 at $y^+ = 26.3$. It is nearly a constant of about 0.38 in the region $y^+ > 26$. With the same threshold, the ratio of ejections is smaller than that of sweeps in the region $y^+ < 18.5$, while it is the opposite in the region $y^+ > 18.5$. This result implies that sweeps are more productive than ejections in the region very near to the wall ($y^+ < 18.5$), and it is the opposite case in the region $y^+ > 18.5$.

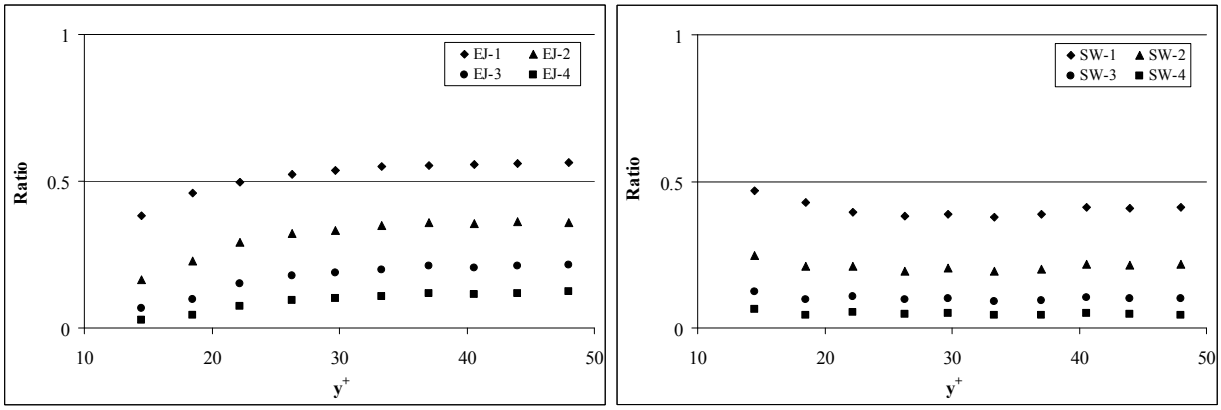

FIG. 6.56 – Ratios of the total Reynolds shear stress $\sum_1^M \sum_1^N \sum_1^{N_f} (-u'v')^+$ in ejections and sweeps to that in the whole field. a) Ratios of $\sum_1^M \sum_1^N \sum_1^{N_f} (-u'v')^+$ in ejections to that in the whole field ; b) Ratios of $\sum_1^M \sum_1^N \sum_1^{N_f} (-u'v')^+$ in sweeps to that in the whole field.

Fig. 6.57 gives ratios of the total Reynolds shear stress in ejections and sweeps to those in Q2 and Q4 respectively. For ejections, in the region $y^+ < 30$, the ratio increases relatively rapidly with wall distance. In the region $y^+ > 30$, however, it is nearly constant. For sweeps, the ratio is nearly a constant in the whole wall distance studied, except for $y^+ = 18.5$ where the ratio is considerably smaller than those of other wall distances. Similar to Fig. 6.56, this result indicates that sweeps dominate the generation of Reynolds shear stress in the region very near to the wall ($y^+ < 18.5$). Beyond this region, ejections are more important than sweeps to the generation of Reynolds shear stress.

In turbulence, the term $-\overline{u'v'}^+ \frac{DU^+}{Dy^+}$ represents the production of turbulent energy. As shown in Fig. 4.1, the Van Driest model (Van Driest (1978)) is in good agreement with the result obtained by SPIV as well as by HWA. Therefore, this model is used to compute the velocity gradient $\frac{DU^+}{Dy^+}$ in the present study. This gradient is defined as :

$$\frac{DU^+}{Dy^+} = \frac{2}{1 + \sqrt{1 + 4(\kappa y^+ (1 - e^{-y^+/A}))^2}} \tag{6.31}$$

Where, κ is the Van Karman constant, and A is the Van Driest parameter. In the present study, $\kappa = 0.39$ and A=26 were used.

Employing Eq. 6.31, $-\overline{u'v'}^+ \frac{DU^+}{Dy^+}$ is computed in each quadrant as well as in the whole field and the results are shown in Fig. 6.58. Globally, the modulus $\left| -\overline{u'v'}^+ \frac{DU^+}{Dy^+} \right|$ decreases

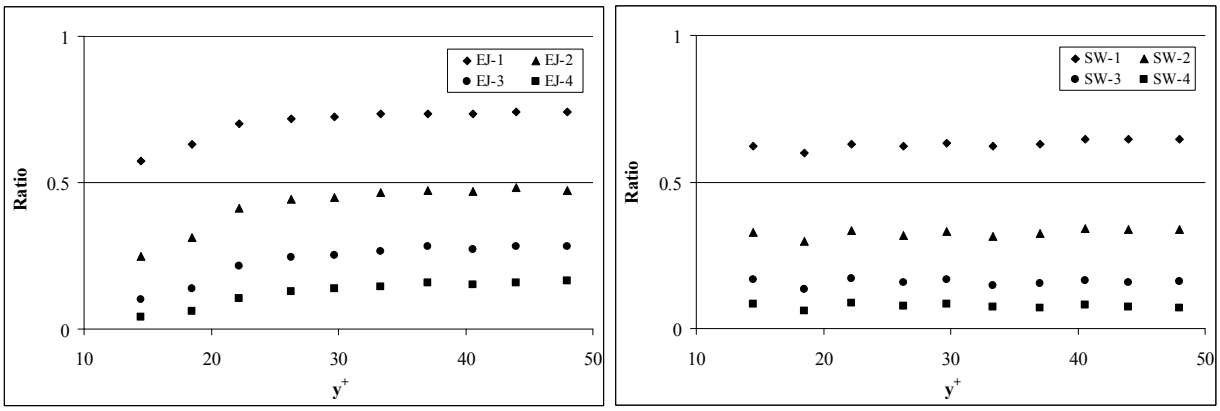

FIG. 6.57 – Ratios of the total Reynolds shear stress $\sum_1^M \sum_1^N \sum_1^{N_f} (-u'v')^+$ in ejections and sweeps to these in Q2 and Q4 respectively. a) Ratio of $\sum_1^M \sum_1^N \sum_1^{N_f} (-u'v')^+$ in ejections to that in Q2 ; b) Ratio of $\sum_1^M \sum_1^N \sum_1^{N_f} (-u'v')^+$ in sweeps to that in Q4.

with wall distance. The further away from the wall, the slower the decrease or the increase is. Remarkably, the production is very similar in Q2 and Q4 on one side and Q1 and Q3 on the other side.

The same as in Fig. 6.55, at $y^+ = 18.5$, the value of Q2 is equal to that of Q4. When $y^+ < 18.5$, the production of Q2 is slightly smaller than that of Q4. The opposite is true in the region $y^+ > 18.5$. These results are in good agreement with those in the literatures (e.g. Hinze (1975)). Fig. 6.58 shows that $\left|-\overline{u'v'}^+ \frac{DU^+}{Dy^+}\right|$ of Q2 and Q4 is about 3.5 times higher than in Q1 and Q3, indicating again that most of turbulent energy is generated in Q2 and Q4.

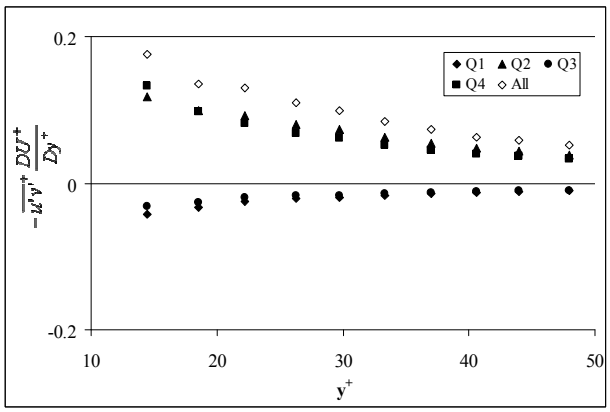

FIG. 6.58 – Turbulent energy $-\overline{u'v'}^+ \frac{DU^+}{Dy^+}$

6.3.4 Comparison

Lu and Willmarth (1973) have computed the contributions of Q2 and Q4 to the total Reynolds shear stress. They found that the contributions are about 77% and 55% for

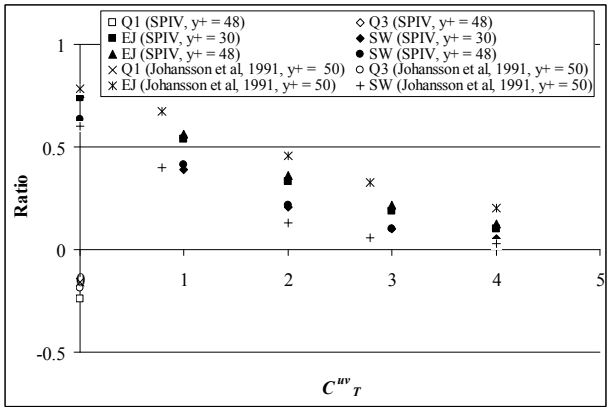

FIG. 6.59 – Comparison of ratios of the total Reynolds shear stress $\sum_1^M \sum_1^N \sum_1^{N_f} (-u'v')^+$ in ejections and sweeps to that in the whole field with various threshold C_T^{uv} of SPIV with those of Johansson *et al.* (1991)

Q2 and Q4 respectively in the region $y^+ > 14$. For Q2, this value is comparable to the present result which is in the range 72% - 76%. However, for Q4, it is much smaller than the present result (62% - 78%). Wallace *et al.* (1972) found that at $y^+ = 15$ this ratio is about 70% for both Q2 and Q4. This is in good agreement with the present results. The discrepancy between the present result and that in Lu and Willmarth (1973) may be caused by the flow geometry and the different techniques used to detect Q2 and Q4 events. Lu and Willmarth (1973) also computed the ratio of $-\overline{u'v'}^+$ in Q2 to that in Q4. According to their result, this ratio increases from about 1.0 at $y^+ = 15$ to 1.15 at $y^+ = 50$. This is similar to the present result.

Johansson *et al.* (1991) used the Variable-Interval Time-Averaging (VITA) technique in a water channel to investigate the Reynolds shear stress distribution. In Fig. 6.59, the results of Johansson *et al.* (1991) show a greater contribution to the Reynolds shear stress of Q2 (as ejections) than the present results. The opposite is true for Q4 (as sweeps). Nevertheless, the agreement between both results is fairly good and indicates a strong influence of the threshold.

In Fig. 6.60, the balance point of Reynolds shear stress generated by ejections and sweeps, usually associated with the maximum production of turbulent energy, was located around y^+ =18 in the present study while it was about y^+ =15 according to Wallace *et al.* (1972). At y^+ =14.5, present results show about 78% and 70% of total Reynolds shear stress generated in Q2 and Q4 respectively. In addition to this, at the balance point (y^+ =18), these values are about 75% for both events while Wallace *et al.* (1972) found a value of 70% at their balance point ($y^+ = 15$). The differences between the present results and those of Wallace *et al.* (1972) are mainly due to characteristics of experiments (such as experiment set-up and technique). In agreement with the results of Wallace *et al.* (1972), away from the balance point, ejections appear to be more important further away from the wall while sweeps show opposite behaviours.

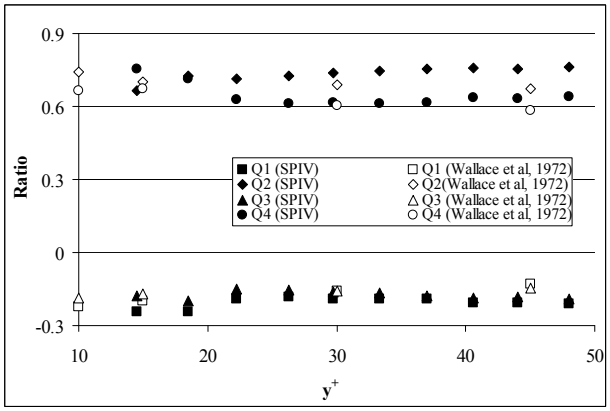

FIG. 6.60 – Comparison of ratios of the total Reynolds shear stress $\sum_1^M \sum_1^N \sum_1^{N_f} (-u'v')^+$ in each quadrant to that in the whole field of SPIV with those of Wallace *et al.* (1972) at various wall distance

6.3.5 Summary

In the present study, the characteristics of ejections and sweeps were investigated in detail for the first time in the region $14.5 < y^+ < 48$. The main conclusions are as follows :

The frequency of appearance of ejections reaches its maximum around $y^+ = 22$. For sweeps, it decreases with wall distance in the whole range. When $y^+ > 22$, the rate of decrease is almost the same for both ejections and sweeps. In a streamwise-spanwise plane, the spanwise angle of ejections and sweeps is close to a Laplace distribution. In the region $y^+ < 22$, the mean of the modulus of the spanwise angle decreases slightly from 10 to 8 degrees with wall distance for ejections while it has a nearly constant value (about 10 degrees) for sweeps. In the region $y^+ > 22$, it increases nearly linearly with wall distance to about 11.5 and 14.5 degrees for ejections and sweeps respectively. These relative larger values (> 8 degrees), indicates that ejections and sweeps have a spanwise angle when traveling downstream, especially far away from the wall. For both ejections and sweeps, the mean spanwise distance varies between 118 and 128 wall units in the whole range. The histogram of the spanwise distance is close to a Rayleigh distribution.

For ejections, the mean width is a constant (18 wall units) when $y^+ < 22$. In the region $y^+ > 22$, it increases slightly with wall distance to about 24 wall units at $y^+ =48$. For sweeps, the mean width increases continuously from about 22 wall units at $y^+ = 14.5$ to about 30 wall units at $y^+ = 48$. The mean length of ejections increases rapidly from 92 wall units at $y^+ = 14.5$ to 117 wall units at $y^+ = 22.2$. In the region $22 < y^+ < 33$, it keeps a nearly constant value of 117 wall units. In the region $y^+ > 33$, it decreases slightly to 107 wall units at $y^+ = 48$. The mean length of sweeps is nearly constant at 90 wall units in the whole range. Both histograms of the width and the length are close to a lognormal distribution. For both ejections and sweeps, the mean area increases almost linearly with wall distance. It increases from 1700 and 2240 square wall units at $y^+ = 14.5$ to 2700 and 2800 square wall units at $y^+ = 48$ for ejections and sweeps respectively. For ejections, the growth is faster in the region $y^+ < 22$ but is similar to that of sweeps afterwards. Globally, ejections are smaller than sweeps in the whole range. The histogram

of the area is close to an exponential distribution.

Q2 and Q4 take respectively about 31% and 33% of the area of the field but produce about 72% and 62% of the total Reynolds shear stress while Q1 and Q3 take about 18% of the area and produce only 17% of the total Reynolds shear stress. With $C_T^{uv} = 1.0$, in the region $14.5 < y^+ < 26$, the percentage of the area of ejections in Q2 increases rapidly from 20% to 30% while its contribution to the production of total Reynolds shear stress in this quadrant increases from 56% to 75%. Afterwards, in the region $y^+ > 26$, these values are nearly constant. Sweeps take only 23% of the area in Q4 but contribute to 62% of the production of total Reynolds shear stress in this quadrant. Very close to the wall ($y^+ < 18.5$), sweeps are dominating the turbulence production compared to ejections. The opposite is true when $y^+ > 18.5$, these values decrease with increasing C_T^{uv}, but their variations with wall distance are nearly the same.

6.4 Streamwise vortices

6.4.1 Functions and parameters of detection

6.4.1.1 Detection function definition

The streamwise vortices have been observed and studied in the near-wall region by numerous researchers with different experimental or numerical methods. The subject, how to find a reliable mathematical criterion to define such vortices, has been discussed by many authors (e.g. Jeong and Hussain (1995)). Different detection criteria (e.g. Q, λ) have been proposed. Among them, most of the methods are used to detect the streamwise vortices from the three dimensional flow obtained by numerical simulations or in cross-section at 45°, 90° or 135° to the streamwise direction. In the present study, experiments were conducted in a streamwise-spanwise plane. This excludes the possible use of the above detection methods.

Fig. 6.61 shows an ideal positive streamwise vortex. In this figure, ABCD is a streamwise-spanwise cross section and EE′ is a cross line. In the bottom left part of Fig. 6.61, the profile of the v' fluctuation along EE′ is plotted according to the property of streamwise vortices. Based on this profile, the cross-section ABCD of the streamwise vortex is shown in the right bottom in Fig. 6.61. It can be decomposed into five regions, according to the strength of wall-normal velocity fluctuation and of its spanwise gradient. In the present study, the following abbreviations have been used to simplify the discussion. High spanwise velocity Gradient Objects of the wall-normal component v' are referred to as GO. The GO are divided into negative (NGO) and positive (PGO) according to the sign of the gradient. High Velocity Fluctuation object of the wall-normal component v is referred to as VF, which can also be classified into NVF and PVF according to the sign of the fluctuation. For the example of the streamwise vortex in Fig. 6.61, the five regions are NGO, PVF, PGO, NVF and NGO from top to bottom. Similarly, for an ideal counter-rotating streamwise vortex as shown in Fig. 6.62, seven regions can be identified according to the profile of fluctuation v' along EE′. They are PGO, NVF, NGO, PVF, PGO, NVF, NGO from top to bottom. Fig. 6.61 and 6.62 indicate that the basic elements involved in a streamwise vortex or one leg of a counter-rotating streamwise vortex are a GO, a PVF and a NVF. Furthermore, the PVF and NVF need to be located on different sides of the GO to ensure they belong to the streamwise vortices (eg. PVF #1, NGO #1, NVF #1 in Fig. 6.61 ; NVF #1, PGO #1, PVF #1, and PVF#1, NGO #2, NVF #2 in Fig. 6.62). This criterion excludes the GO that result from the gradient inside the VF but do not represent streamwise vortices (e.g. PGO #1 and PGO #2 in Fig 6.61 ; NGO #1 and PGO #2 in Fig. 6.62). The GO which are related to Streamwise Vortices, are referred to as GSV. GSV can be separated into negative (NGSV) and positive (PGSV) according to the sign of the streamwise vorticity. For example, the NGO #1 in Fig 6.61 is a PGSV. Among GSV, those related to Counter-rotating Streamwise Vortices (also called streamwise vortex pairs) are referred to as GCSV. NGSCV and PGSCV are used for Negative and Positive legs of a GCSV. For example, PGO #1 and NGO #2 in Fig. 6.62 are respectively NGCSV and PGCSV of one GCSV. It should be noted that **the sign of GO is opposite to that of GSV**.

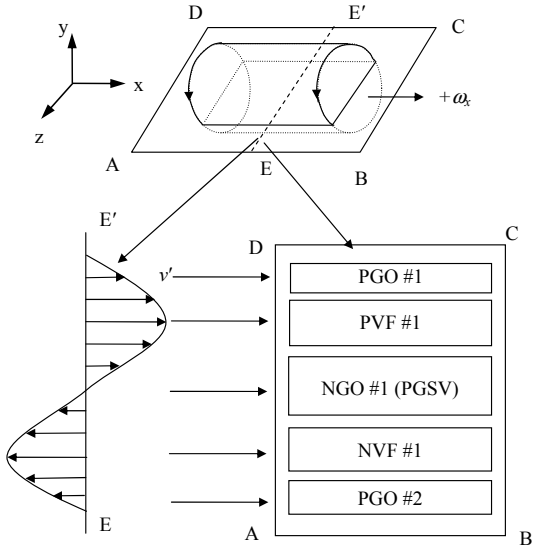

FIG. 6.61 – Illustration of a positive streamwise vortex and its cross-section in streamwise-spanwise plane

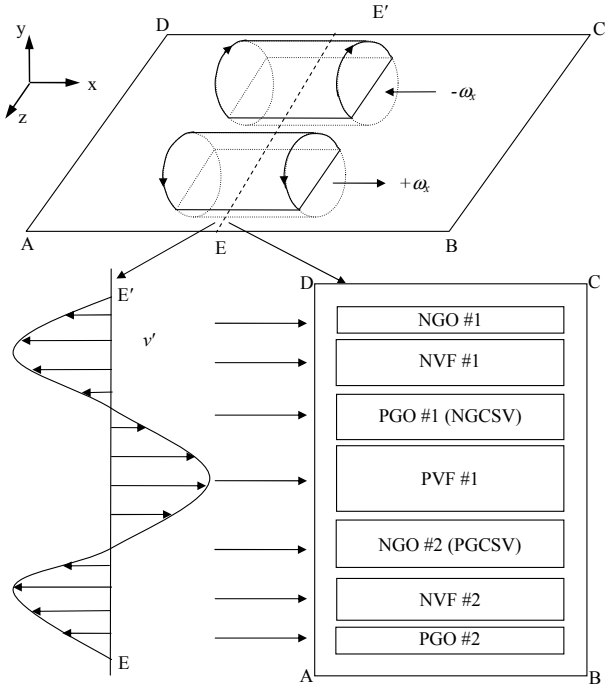

FIG. 6.62 – Illustration of a counter-rotating streamwise vortex and its cross-section in streamwise-spanwise plane

Based on the above discussion, VF and GO need to be identified to detect streamwise vortices. Two detection criteria are selected. One is the velocity fluctuation used to identify VF, and the other is the spanwise gradient of this fluctuation used to identify GO. The corresponding detection functions are referred to as F_d^v and F_d^{grad} respectively. As the velocity fluctuation is normalized by its standard deviation in the present study, this

normalized velocity fluctuation will be used to define F_d^v and F_d^{grad}. As explained before, the streamwise-spanwise 2D3C velocity fields obtained by SPIV are available on a discrete (M, N) grid at 10 different wall distances. Therefore, F_d^v and F_d^{grad} are defined as :

$$F_d^v = f_1(v', \sigma_v) = \frac{v'(m, n, \mathrm{y}^+)}{\sigma_v(\mathrm{y}^+)} \tag{6.32}$$

$$F_d^{grad} = f_2(v', \sigma_v) = \frac{1}{\sigma_v(\mathrm{y}^+)} \frac{\partial(v'(m, n, \mathrm{y}^+))}{\partial \mathrm{z}} \tag{6.33}$$

Where v' is the instantaneous fluctuation of the spanwise velocity component, σ_v re the standard deviations. (m, n) is the position in the (M, N) grid and y^+ is the wall distance at which the SPIV measurement is performed.

F_d^v can be obtained directly from the 2D3C velocity fields. However, a suitable derivation filter needs to be selected to calculate F_d^{grad}. In the literature, many derivation filters exist to compute the velocity gradient in a discrete domain. Among them, five filters have been compared in the present study. To compute the derivatives, a compromise has to be made among various parameters such as the order of the filter, the number of points used for the derivative calculation, the frequency response and the noise amplification. In general, for classical finite difference schemes, the order increases with the number of points used for the computation. The frequency response increases when the truncation error decreases, which is directly linked to the order of the filter. Two standard filters based on centered difference schemes (Eq. 6.34 and 6.35) are proposed with 2nd and 4th order accuracy. A compact difference scheme is proposed as well. The last scheme detailed by Lele (1992) is implicit and requires a matrix inversion. It is given by Eq. 6.38. The bandwidth increases with the order of the filter. In PIV it is not necessary to use large bandwidth filters because the highest frequency resolved is limited. An approach which consists of limiting the order and optimising the noise amplification has been developed by Foucaut and Stanislas (2002) for the PIV results, which leads to the least square difference scheme (Eq. 6.36) and the Richardson extrapolation (Eq. 6.37). These two filters present a limited bandwidth.

1) 2nd order centered difference

$$\left.\frac{\partial A}{\partial \mathrm{x}}\right|_i = \frac{(A_{i+1} - A_{i-1})}{2\delta_{\mathrm{X}}} \tag{6.34}$$

2) 4th order centered difference

$$\left.\frac{\partial A}{\partial \mathrm{x}}\right|_i = \frac{(-A_{i+2} + 8A_{i+1} - 8A_{i-1} + A_{i-2})}{12\delta_{\mathrm{X}}} \tag{6.35}$$

3) 2nd order least square difference

$$\left.\frac{\partial A}{\partial \mathrm{x}}\right|_i = \frac{(2A_{i+2} + A_{i+1} - A_{i-1} - 2A_{i-2})}{10\delta_{\mathrm{X}}} \tag{6.36}$$

4) 2nd order Richardson extrapolation

$$\left.\frac{\partial A}{\partial \mathrm{x}}\right|_i = \frac{(-8A_{i+8} + A_{i+1} - A_{i-1} + 8A_{i-8})}{130\delta_\mathrm{X}} \tag{6.37}$$

5) 6th order compact difference. (This filter uses a tridiagonal matrix resolution.)

$$\frac{1}{3}\left.\frac{\partial A}{\partial \mathrm{x}}\right|_{i-1} + \left.\frac{\partial A}{\partial \mathrm{x}}\right|_i + \frac{1}{3}\left.\frac{\partial A}{\partial \mathrm{x}}\right|_{i+1} = \frac{14}{9}\frac{(A_{i+1} - A_{i-1})}{2\delta_\mathrm{X}} + \frac{1}{9}\frac{(A_{i+2} - A_{i-2})}{4\delta_\mathrm{X}} \tag{6.38}$$

In Eq. 6.34-6.38, A is the signal sample, x is the deviation direction, i is the index of the signal and δ_X is the grid size. To find a suitable deviation filter for the present study, all five filters have been tested on field #3 of plane 5 ($\mathrm{y}^+ = 29.7$). This position is selected due to the fact that the centre of wall-attached streamwise vortices are expected to locate around this position. Field #3 was used because several typical streamwise vortices exist in this image. Fig. 6.63 shows the original wall-normal velocity fluctuation contour of the selected field. Fig. 6.64 shows the corresponding spanwise gradient contour images computed with various derivation filters. Comparing the gradient image with the original velocity fluctuation image, the second order Richardson extrapolation scheme has a strong smoothing effect and thus can not be used. The 2nd and 4th order centered difference schemes as well as 6th order compact difference scheme have a very similar pattern, which shows fairly noisy data. Only the second order least square scheme obtains the gradient image (Fig. 6.64) that is in good agreement with the velocity fluctuation image (Fig. 6.63).Thus this scheme was used in the present study.

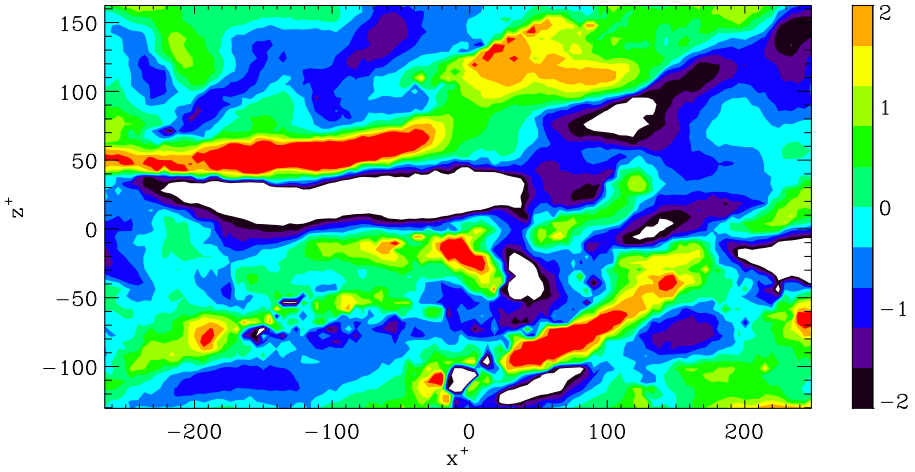

FIG. 6.63 – Normalized wall-normal velocity contour image (Image #3 at $\mathrm{y}^+ = 29.7$)

After the detection functions have been defined for both VF and GO, the next step is to identify these objects from the instantaneous velocity fields. Similar to the detection of streaks, ejections and sweeps, three procedures including thresholding, mathematical morphology and cleaning were employed.

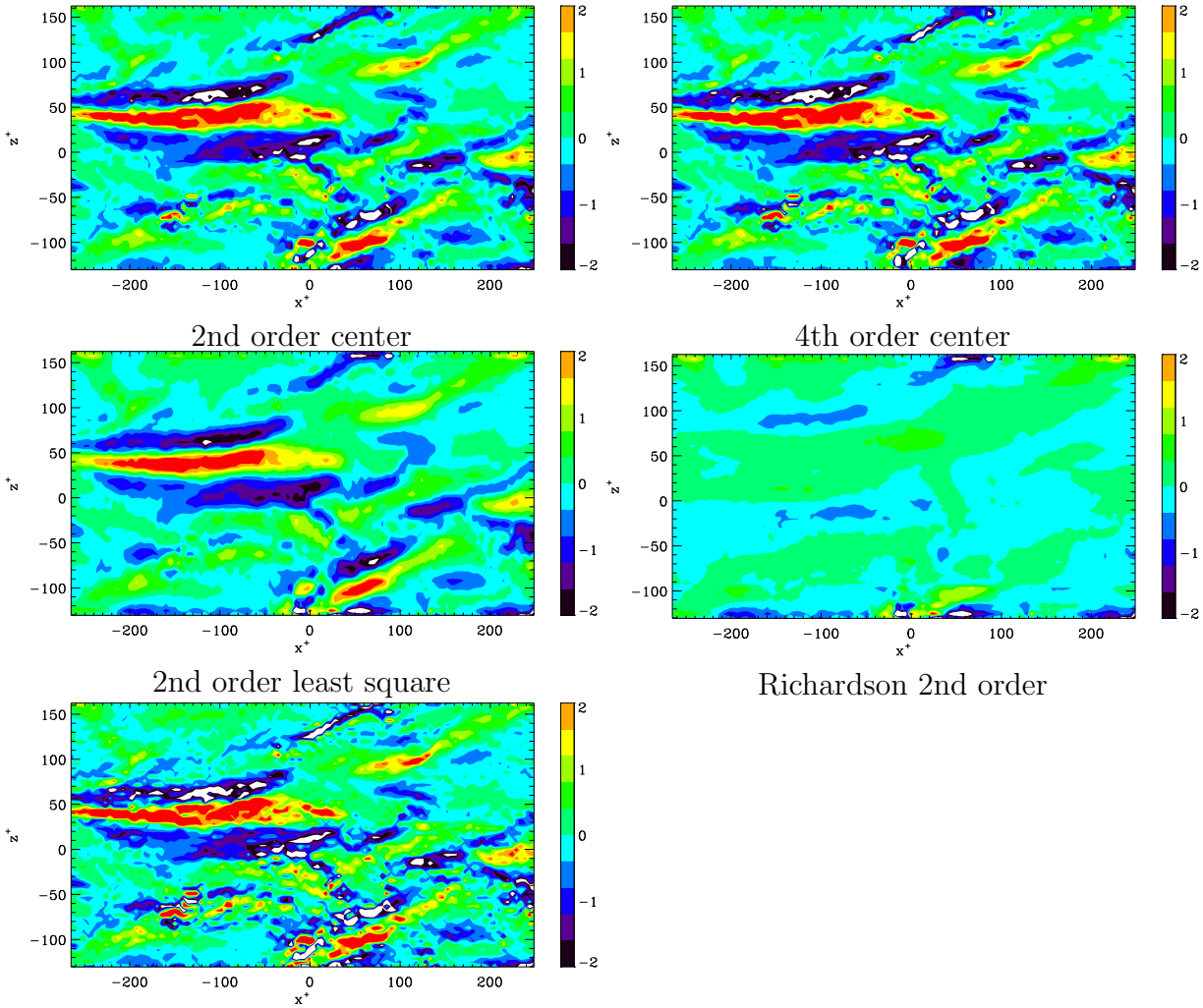

FIG. 6.64 – Normalized wall-normal velocity gradient contour images with various deviation filters (Image #3 at $y^+ = 29.7$)

6.4.1.2 Thresholding

VF can be recognized from the background by thresholding the detection function F_d^v (Eq. 6.33). The corresponding threshold is referred to as C_T^v. To simply the detection procedure, PVF and NVF are identified separately. The corresponding indicative functions of PVF and NVF, F_i^v, are defined as :

$$\text{PVF}: \quad F_i^v = \begin{cases} 1 & \text{when } F_d^v > C_T^v \\ 0 & \text{otherwise} \end{cases} \tag{6.39}$$

$$\text{NVF}: \quad F_i^v = \begin{cases} 1 & \text{when } F_d^v < -C_T^v \\ 0 & \text{otherwise} \end{cases} \tag{6.40}$$

GO are recognized from the background by thresholding the detection function F_d^{grad}

(Eq. 6.33). The corresponding threshold is referred to as C_T^{grad}. To simply the detection procedure, PGO and NGO are identified separately. The corresponding indicative functions of PGO and NGO, F_i^{grad}, are defined as :

$$\text{PGO}: \quad F_i^{grad} = \begin{cases} 1 & \text{when } F_d^{grad} > C_T^{grad} \\ 0 & \text{otherwise} \end{cases} \tag{6.41}$$

$$\text{NGO}: \quad F_i^{grad} = \begin{cases} 1 & \text{when } F_d^{grad} < -C_T^{grad} \\ 0 & \text{otherwise} \end{cases} \tag{6.42}$$

The threshold C_T^v was selected as 1.2 while C_T^{grad} as 1.0 in the present study. Details about the selection of these parameters have been included in Appendix B.3.

6.4.1.3 Mathematical morphology

The examination of the shapes of VF and GO from the indicative images reveals that both of them are elongated in the streamwise direction. Therefore, the structure element is chosen as rectangle (or square) with two parameters : $M_S(W, L)$, in which W is the width in the spanwise direction and L is the length in the streamwise direction. The values of W and L are given in wall units. The structure element was selected as $M_S = (10^+, 10^+)$ for both VF and GO. Details about the selection of these parameters can be found in Appendix B.3.

6.4.1.4 Cleaning

The clean factors $C_B = 500^{+^2}$ and $C_C = 1000^{+^2}$ were chosen in the present study to detect VF. To detect GO, the clean factors $C_B = 375^{+^2}$ and $C_C = 750^{+^2}$ were chosen. Details about the selection of these parameters can be found in Appendix B.3.

Fig. 6.65 shows an example of a detection function and the corresponding indicative images of PVF.

Fig. 6.66 shows an example of a detection function and the corresponding indicative images of PGO.

6.4.2 Detection of streamwise vortices

After VF and GO are detected, a forward step is to investigate the relations between them to identify streamwise vortices. This is done by examining GO one by one. Four steps are employed to achieve this purpose.

In the first step, i.e. examining the indicative images of GO, we found that most of GO that are located in the core area of streamwise vortices are relatively thin. To guarantee that the GO can be connected with VF related to the same streamwise vortex, the investigation began with increasing the size of each GO in the spanwise direction (Fig. 6.69) to create a so-called ′searching window′. A dilation procedure is used to perform this enlargement of GO. As it is well known, the streamwise vortices have a radius of about 20-40 wall units. Therefore, the increase of 10 wall units is chosen on each side of GO in

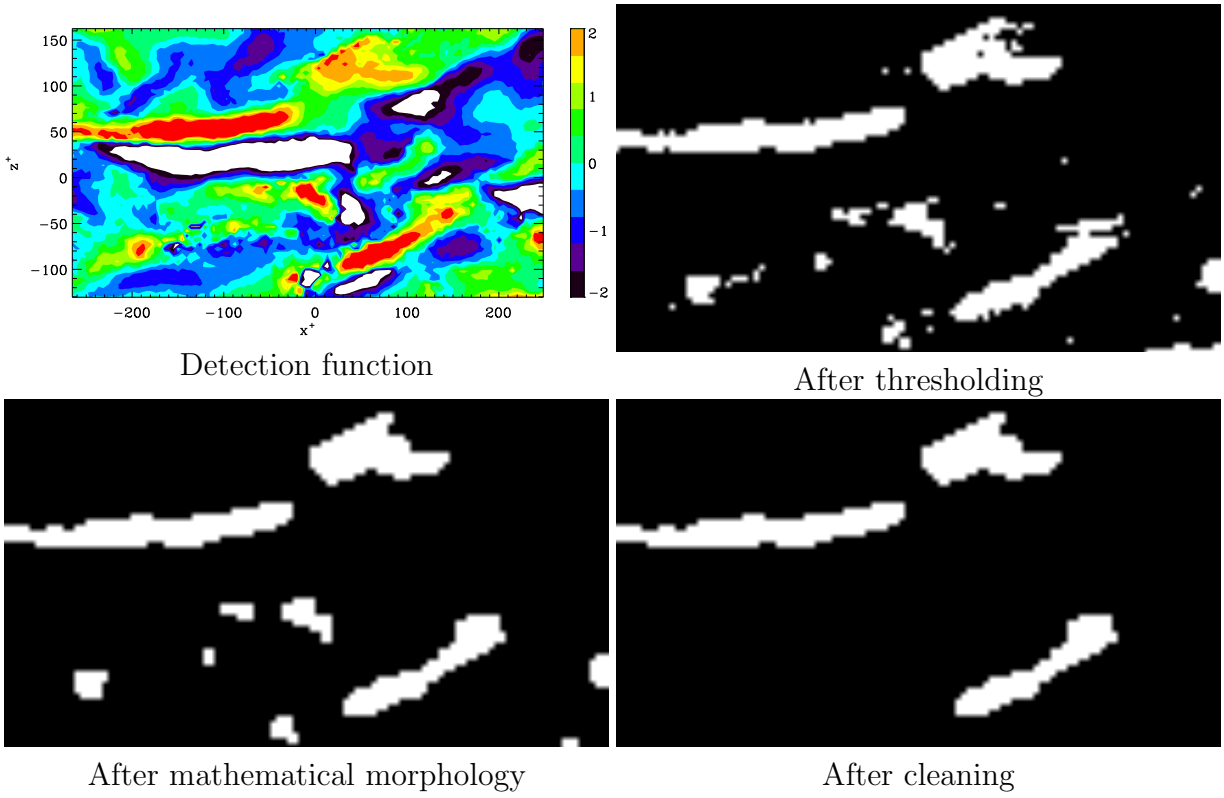

Detection function

After thresholding

After mathematical morphology

After cleaning

FIG. 6.65 – Detection image and indicative images of PVF

the spanwise direction. This value can not be larger due to the fact that it may connect two nearby GO together.

In the second step, the number of points that belong to NVF and PVF in the searching window are counted respectively. A threshold is applied to the number of points in order to exclude the VF that are not related to streamwise vortices. If only NVF or only PVF result from this procedure, we consider that the GO is not related to a streamwise vortex (see Fig. 6.61 and 6.62). Cases where neither NVF nor PVF is obtained are rare. Only when both of the number of points belonging to NVF and PVF are larger than the threshold (10 is used in the present study), they are considered as potential VF related to a streamwise vortex presented by the GO.

The next step is to examine whether the NVF and PVF involved are on each side of the GO. NVF and PVF come not only from streamwise vortices but also from other coherent structures (e.g. ejections and sweeps). Therefore, it is possible that the NVF and PVF exist on the same side of a GO. Obviously, this GO can not represent a streamwise vortex. As shown in Fig. 6.61 and 6.62, the streamwise vortex requires that the NVF and PVF are located on different side of the GO, which represents the core of the vortex.

The last step is to compute the ratio of the area of NVF to PVF involved ($R_{N/P}$). This step ensures that NVF and PVF belonging to the same vortex are comparable in size. As explained before, VF can come from both streamwise vortices and other coherent structures. Therefore, VF that come from other coherent structures, can be mis-detected as those related to the streamwise vortex. To minimize this error, $R_{N/P}$ is required to be

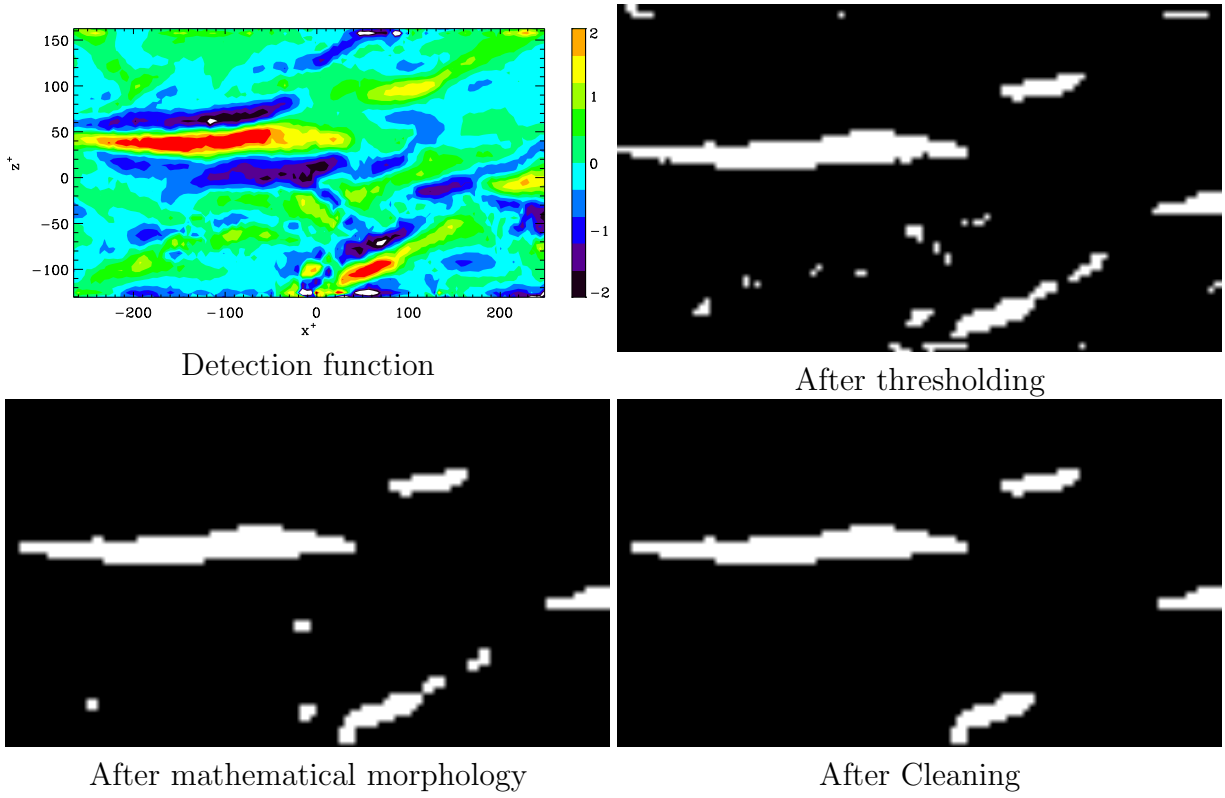

Detection function

After thresholding

After mathematical morphology

After Cleaning

FIG. 6.66 – Detection image and indicative images of GO

in the range $0.2 < R_{N/P} < 5$ in the present study.

When all the above criteria are satisfied, a streamwise vortex is recorded. The GO is consequently marked as a GSV. If the GO is a NGO, the GSV is then correspondingly a PGSV. The opposite is true for PGO. Fig. 6.67 shows the detailed flow chart of the detection procedure of GSV. Whether NGSV and PGSV have a common VF is the criterion to examine whether NGSV and PGSV belong to a GCSV (counter-rotating streamwise vortex or streamwise vortex pair). If the GSV is also a GCSV, the NGSV and PGSV involved are called NGCSV and PGCSV respectively. Fig. 6.68 shows the detection procedure of GCSV. Fig. 6.69 gives an example of the detection of GSV (NGSV).

6.4.3 Statistics on the streamwise vortices

6.4.3.1 Frequency of appearance

Fig. 6.70 shows the frequency of the appearance of NGO and PGO as a function of wall distance in the area of $530^+ * 300^+$. The error bars represent an error of 5% of the mean. The frequency of appearance of both NGO and PGO are very similar, showing again the spanwise homogenous property of the flow. A clear maximum appears at $y^+ = 23$. Fig. 6.70 also shows the frequency of appearance of NGSV and PGSV as a function of wall distance in the same area. It should be noted that NGSV or PGSV include those from individual streamwise vortices, as well as from streamwise vortex pairs. The distributions of NGSV and PGSV are very similar to those of NGO and PGO except for the difference

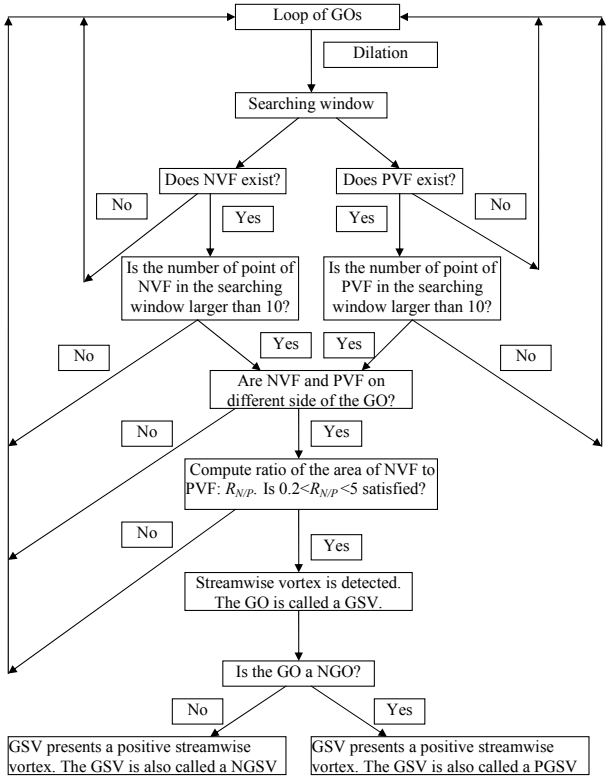

FIG. 6.67 – Flow chart of detection of streamwise vortices or legs of counter-rotating streamwise vortices

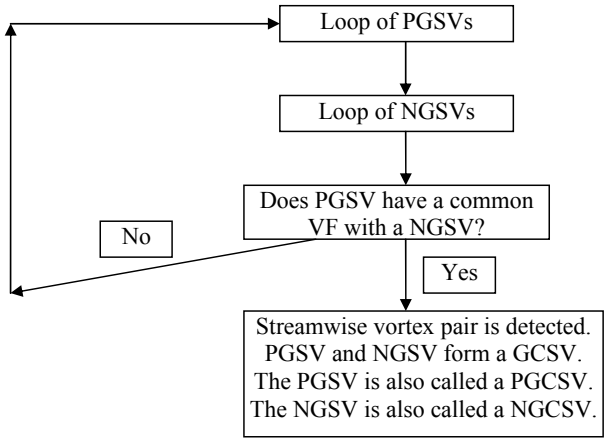

FIG. 6.68 – Flow chart of detection of counter-rotating streamwise vortices

in their values. The frequency of appearance of GCSV is also shown in Fig. 6.70. This figure indicates that the counter-rotating streamwise vortices account for 20% of the total vortices including both individual and counter-rotating ones. The GCSV have similar distribution as GSV. The maximum appears also around $y^+ = 23$.

In Fig. 6.70 the ratio of the frequency of appearance of NGO to NGSV and PGO to PGSV are nearly the same and both are in the range of 2.1 to 2.6. In near wall turbulence,

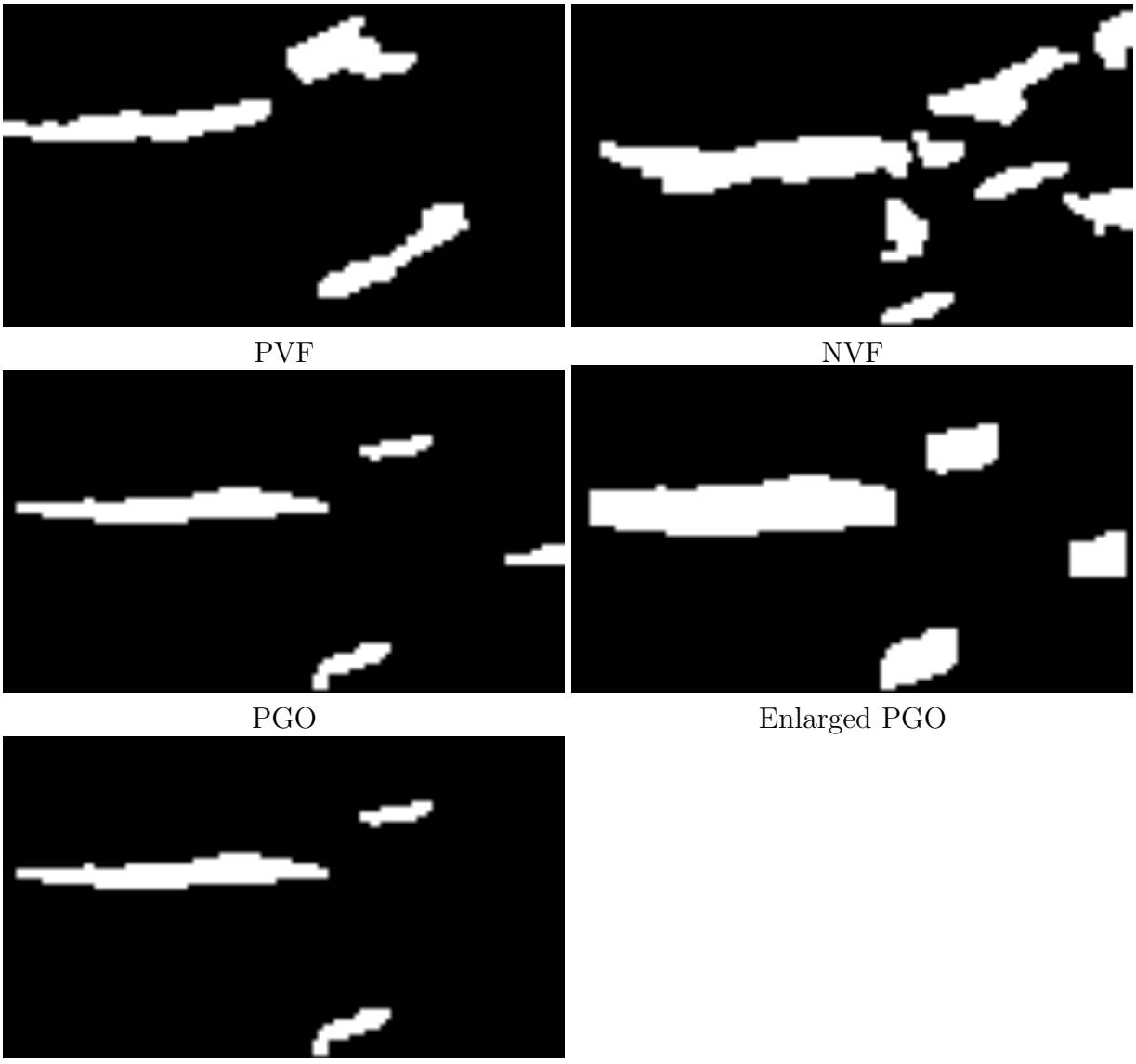

FIG. 6.69 – Illustration of detection of streamwise vortices

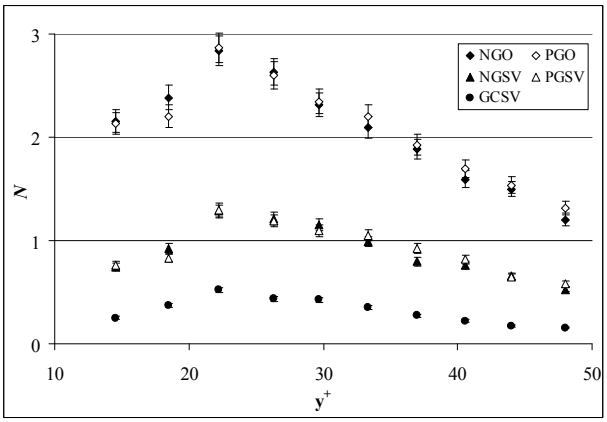

FIG. 6.70 – Frequency of appearance (N) of NGO, PGO, NGSV, PGSV and GCSV

most of the streamwise vortices are either individual or counter-rotating streamwise vortex. As explained in the Chapter 6.4.1, it is observed that an ideal individual streamwise vortex is associated with a series of GO (NGO, PGO, NGO or reverse). Among them, only the middle one locates the vortex core and is called a NGSV or PGSV according to the sign of the gradient. Similarly, an ideal counter-rotating streamwise vortex pair is associated with a series of GO (NGO, PGO, NGO, PGO or reverse). Among them, only the middle two locate the cores of the counter-rotating streamwise vortices and are marked respectively as NGSV and PGSV (also NGCSV and PGCSV). Consequently, the ratio of the frequency of appearance of GO to GSV is 3 in the case of ideal individual streamwise vortices, and 2 in the case of ideal counter-rotating streamwise vortex pairs. However, weak vortices generally create only one or two GO. Additionally, other coherent structures, for example ejections and sweeps, may also generate GO. Moreover, the present experiment has been carried out only in the x-z plane and thus cannot pass through the cores of all vortices. In this case, the GO related to a streamwise vortex (pair) may be relatively weak and thus cannot be detected, which results in a decrease in the frequency of appearance of GO. As a result, the ratio of the frequency of appearance of GO to GSV should be around 2 or 3 but closer to 2, which is in good agreement with what was found in the present study. The results also indicate that the detection procedure has removed efficiently most of GO that do not represent streamwise vortices. This proves the reliability of the detection.

The following sections analyze firstly the statistical characteristics of NGSV and PGSV, followed by the statistical characteristics of NGCSV and PGCSV that were studied. The statistical characteristics investigated were spanwise angle, φ; width, W_a^+; length, L_A^+; area, A_c^+, and spanwise distance, d^+.

According to the homogeneity in the spanwise direction, except for the spanwise angle (which should be opposite), the other statistical characteristics of NGSV and PGSV, and of NGCSV and PGCSV, are the same. Based on this fact, to increase the convergence, the statistical characteristics of GSV are computed from both results of NGSV and PGSV. Similarly, the results of GCSV are obtained from those of NGCSV and PGCSV.

6.4.3.2 Spanwise angle of PGSV

Fig. 6.71 shows the distributions of the mean spanwise angle $\overline{\varphi}$ of PGSV at various wall distances, while Fig. 6.72 shows the RMS (standard deviation) of φ. Fig. 6.71 shows that $\overline{\varphi}$ is near zero. It varies between -1.3 and 1.3 degrees, which is relatively small compared to the RMS (about 17 degrees) given in Fig. 6.72. Considering the spanwise homogenous property of the flow, the small value can be attributed to the lack of convergence. This is also manifested by the random distribution with wall distances in Fig. 6.71. The mean absolute spanwise angle $|\overline{\varphi}|$ is shown in Fig. 6.71. It is nearly a constant in the whole range of wall distance studied. It varies slightly between 11.5 and 14 degrees. Fig. 6.71 shows that the RMS is nearly a constant for both φ and $|\varphi|$ in the whole range of wall distance studied. This constant is about 17 degrees for φ and 11 degrees for $|\varphi|$.

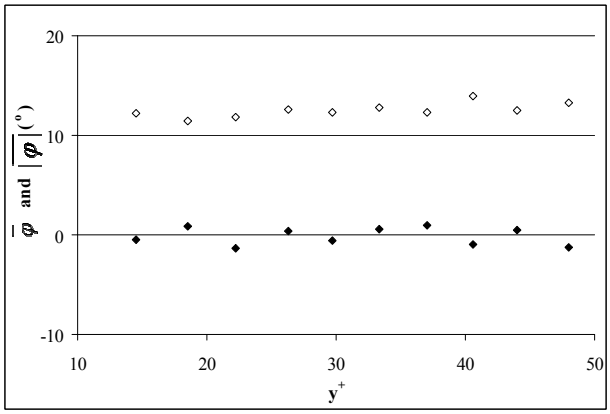

FIG. 6.71 – Mean spanwise angle $\overline{\varphi}$ and mean absolute spanwise angle $\overline{|\varphi|}$ of PGSV. $\overline{\varphi}$: ♦ ; $\overline{|\varphi|}$: ◊.

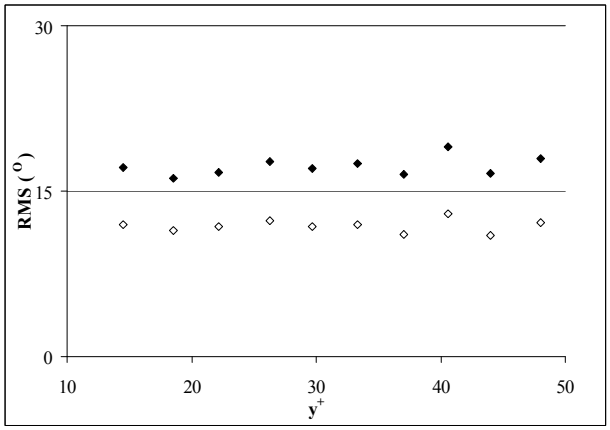

FIG. 6.72 – RMS of the spanwise angle φ and the absolute spanwise angle $|\varphi|$ of PGSV. φ : ♦ ; $|\varphi|$: ◊.

Fig. 6.73 shows the histograms of the spanwise angle φ of PGSV at selected wall distances. According to this figure about 50% of the streamwise vortices have an absolute

spanwise angle between 4 and 16 degrees (corresponding to a threshold of about 30 in the histogram), while about 14% of vortices have an angle larger than 16 degrees. It suggests that most of the streamwise vortices do not move straight downstream, which may explain the meandering property of streaks. In addition to errors from the detection procedure, above $y^+ = 30$ the distribution of φ is slightly asymmetrical with respect to zero. PGSV have more positive angles than negative ones.

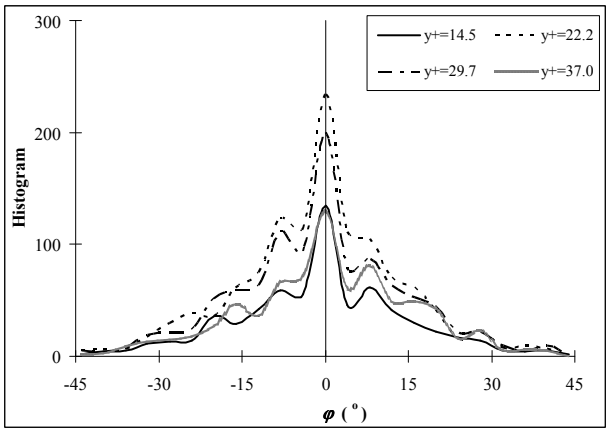

FIG. 6.73 – Histograms of the spanwise angle φ of PGSV at selected wall distances

Fig. 6.74 gives skewness (S) and flatness (F) to characterize the distribution statistically at all 10 wall distances studied. Skewness is nearly zero for all wall distances, revealing the symmetrical property of the distribution. The value of flatness is in the range of 4.5 to 5. This value shows that the distribution is clearly not a Gaussian one. Similar to streaks, ejections and sweeps, the histograms are close to a Laplace distribution (Eq. 6.13) rather than a Gaussian one. The standard value of S and F for the Laplace distribution is 0 and 6 respectively which are comparable to the present results. The differences may be attributed to small oscillations due to the lack of convergence, as shown in Fig. 6.73.

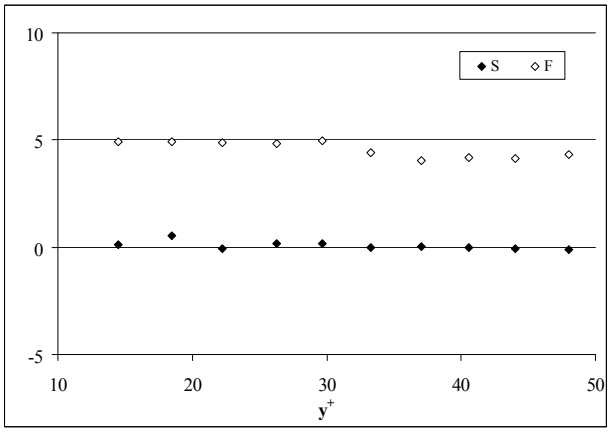

FIG. 6.74 – Skewness (S) and flatness (F) of spanwise angle φ

6.4.3.3 Width of GSV

Fig. 6.75 shows the profile of the mean width $\overline{W_a^+}$ of GSV at various wall distances. The error bars represent an error of 5% of the mean. $\overline{W_a^+}$ has a remarkably constant value of about 16 wall units at all wall distances. The fluctuation is about 0.5 wall units in Fig. 6.75. Fig. 6.75 also presents the RMS of the width W_a^+ of GSV at various wall distances. It shows that the RMS is about 2.8 wall units with a variation of 0.2 wall units at all 10 wall distances studied.

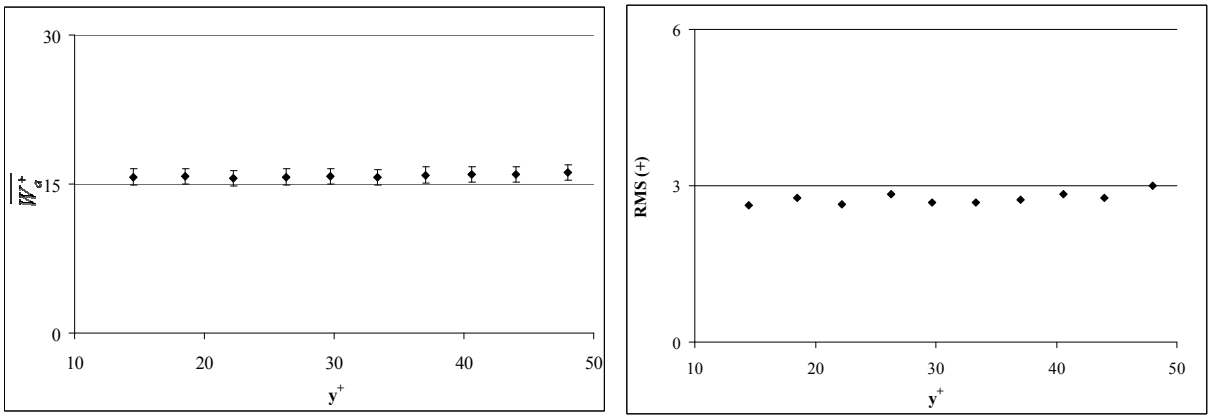

FIG. 6.75 – Mean and RMS of the width W_a^+ of GSV

Fig. 6.76 shows the histograms of the width W_a^+ of GSV. The histograms are close to a lognormal distribution. To characterize the histograms, their characteristics are computed and compared to true lognormal distributions. Fig. 6.77 shows the variation coefficient ψ. This coefficient is nearly a constant (about 0.17) in the whole range of wall distance studied. Fig. 6.77 also gives the median value M_0^+. Comparing with Fig. 6.75, M_0^+ is almost the same as $\overline{W_a^+}$. Fig. 6.78 gives skewness (S) and flatness (F) of the histograms at various wall distances. It shows that skewness obtained from both the present study and lognormal distributions are nearly the same, which is a constant of about 0.9. However, for flatness, there are some differences between the present results and the lognormal distribution. It may result from the lack of convergence. Fig. 6.79 shows the ratio of the most probable value to the mean value, R_{mm}. The results from true lognormal distributions are about 5% higher than the present study. Both results are nearly indenpendent of wall distance.

6.4.3.4 Length of GSV

Fig. 6.80 presents the profiles of the mean length $\overline{L_A^+}$ of GSV at various wall distances. The error bars represent an error of 5% of the mean. The figure shows three interesting regions : (1) When $y^+ < 22$, $\overline{L_A^+}$ decreases slowly towards the wall. As well known (e.g. Kreplin (1976), Kim *et al.* (1987)), the radius of streamwise vortices is normally about 20-40 wall units. Therefore, in this region, most of GSV detected are not from the core area of streamwise vortices and thus are relatively weaker and shorter. (2) When $22 < y^+ < 33$, a plateau appears with a value of about 96 wall units. This plateau indicates that the well-developed wall-attached streamwise vortices are located in this region. (3) When

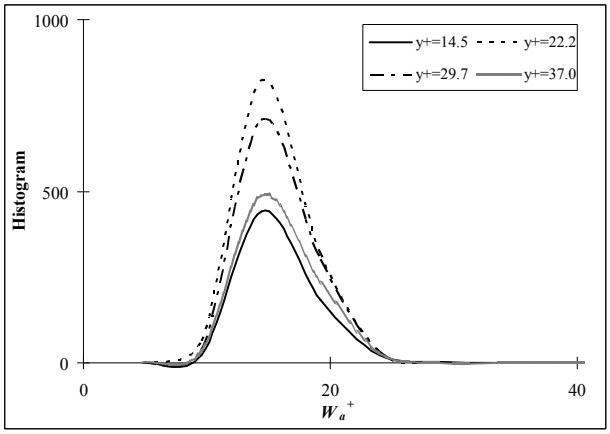

FIG. 6.76 – Histograms of the width W_a^+ of GSV at selected wall distances

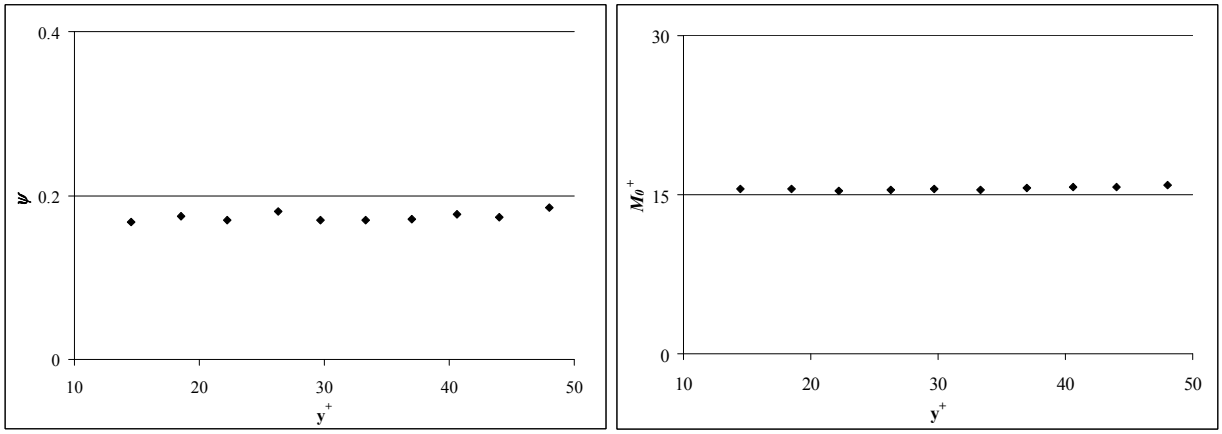

FIG. 6.77 – Variation Coefficient ψ and median value M_0^+ of the width W_a^+ of GSV

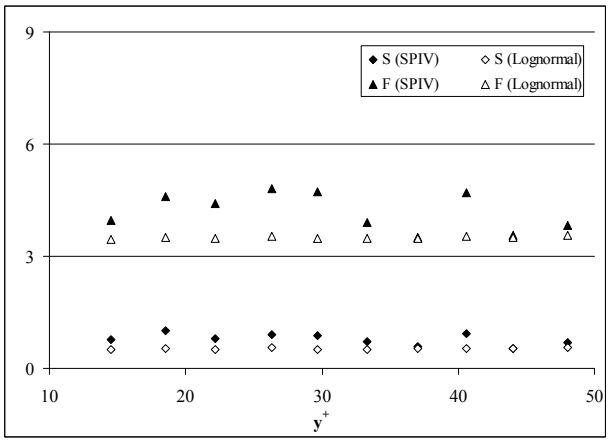

FIG. 6.78 – Comparison of skewness (S) and flatness (F) of the width W_a^+ of GSV of the present study with the theoretical values obtained according to lognormal distributions

$y^+ > 33$, $\overline{L_A^+}$ again decreases slowly but away from the wall. This decrease can be partly

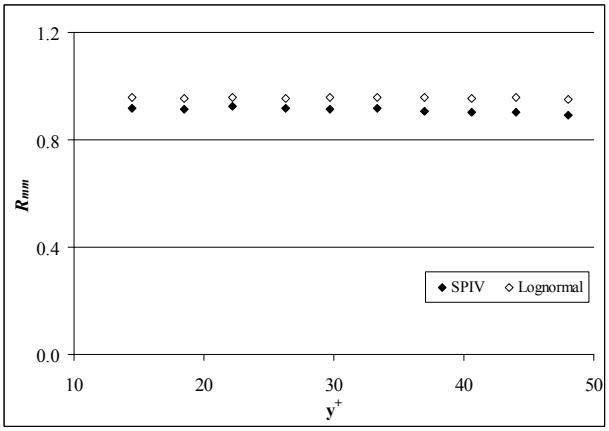

FIG. 6.79 – Ratio of the most probable value to the mean value R_{mm} of the width W_a^+ of GSV

explained by the lift-up of streamwise vortices when they travel downstream and by the fact that the streamwise vortices travel downstream with nearly a constant angle of about 45 degrees with respect to the streamwise-spanwise plan after the lift-up. The RMS of the length L_A^+ of GSV is also given in Fig. 6.80. The distribution of the RMS is similar to that of $\overline{L_A^+}$. The RMS is in the range of 31 to 40 wall units.

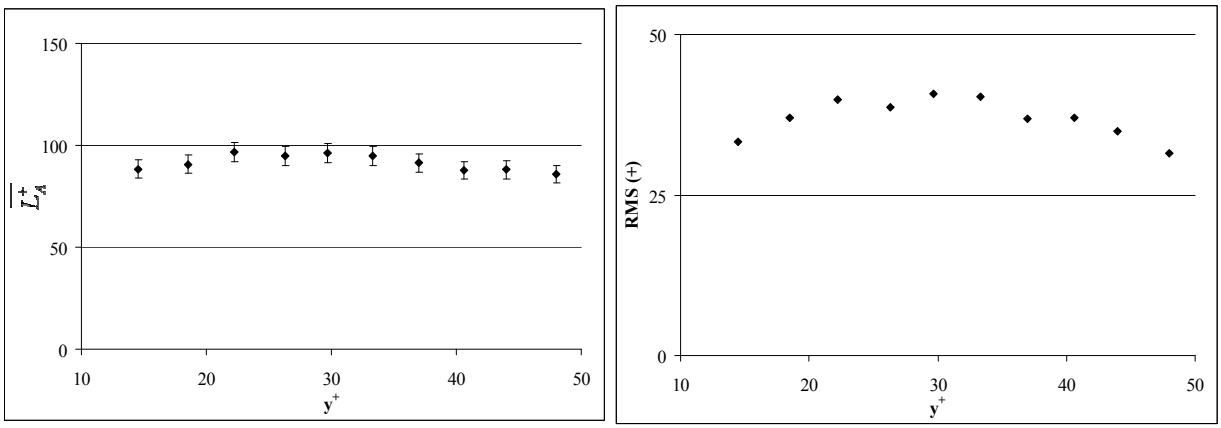

FIG. 6.80 – Mean and RMS of the length L_A^+ of GSV

Fig. 6.81 shows the histograms of the length L_A^+ of GSV at selected wall distances. The peaks are located at nearly the same position (about 75 wall units). Most of GSV have a length in the range of about 50 to 150 wall units. The same as for the width W_a^+, the histograms of L_A^+ in Fig. 6.81 follow nearly a lognormal distribution. Consequently, the most probable value (75 wall units) is rather different from the mean value (about 90-95 wall units).

To study the histograms statistically, the characteristics of the present distributions are compared to a true lognormal one. Fig. 6.82 shows the variation coefficient ψ and the median value M_0^+. Using these values, the ratio R_{mm} (the most probable value to the mean value) is compared to the true lognormal distribution in Fig. 6.83. The results

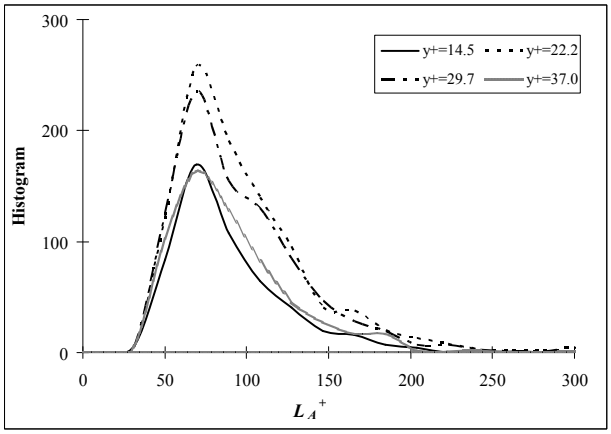

FIG. 6.81 – Histograms of the length L_A^+ of GSV at selected wall distances

from true lognormal distributions have a constant value of about 0.8, while those from the present study vary between 0.68 and 0.81.

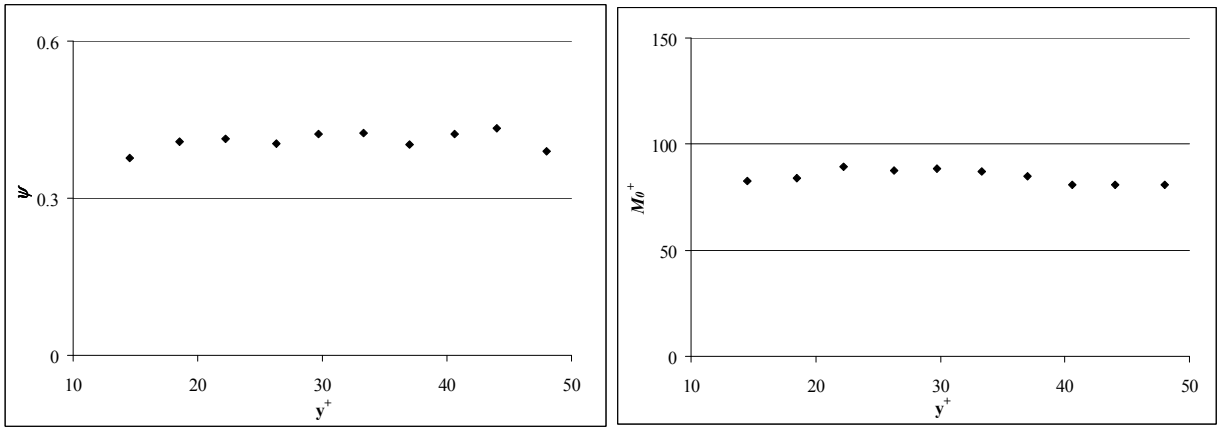

FIG. 6.82 – Variation Coefficient ψ and median value M_0^+ of the length L_A^+ of GSV

Fig. 6.84 gives skewness (S) and flatness (F). The same as for W_a^+, these parameters are compared to those of true lognormal distributions. For skewness, both results are in good agreement, while for flatness they agree well only in the region $y^+ < 40$. As shown in Fig. 6.70, the frequency of appearance is very low when $y^+ > 40$, which leads to a decrease of convergence. This can explain the differences observed in Fig. 6.84.

6.4.3.5 Area of GSV

Fig. 6.85 shows the profiles of the mean area $\overline{A_c^+}$ of GSV at various wall distances. The error bars represent an error of 5% of the mean. The figure shows that the distributions of $\overline{A_c^+}$ of GSV have the same pattern as those of $\overline{L_A^+}$. In general, $\overline{A_c^+}$ is about 1400 square wall units. Fig. 6.85 also shows the RMS of A_c^+, which is about 650 square wall units with a variation of 100 wall units in the whole range of wall distance studied.

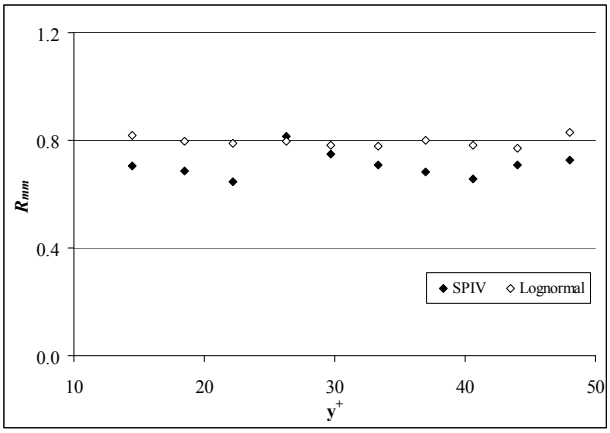

FIG. 6.83 – Ratio of the most probable value to the mean valueR_{mm} of the length L_A^+ of GSV at various wall distances

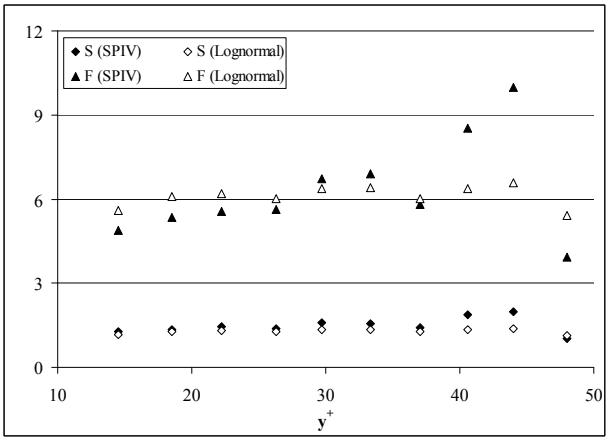

FIG. 6.84 – Comparison of skewness (S) and flatness (F) of the length L_A^+ of GSV of the present study with the theoretical values obtained according to lognormal distributions

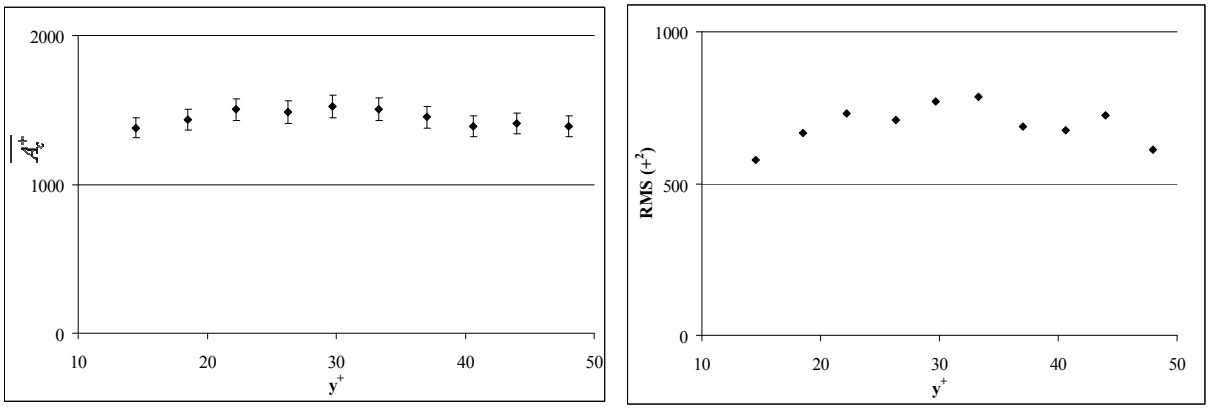

FIG. 6.85 – Mean and RMS of the area A_c^+ of GSV

Fig. 6.86 shows the histograms of the area A_c^+ of GSV. Similar to ejections and sweeps,

the histograms of the area follow nearly an exponential distribution with a shift of about 820 wall units which depends on the cleaning factor C_C. Figures. 6.87 gives skewness (S) and flatness (F) obtained in the present study. Skewness has nearly a constant value of about 1.8, which is close to 2, the standard value of an exponential distribution. Flatness varies between 5.5 and 10.5, which is also close to the standard value of flatness for an exponential distribution, 9. The oscillations of skewness and flatness can be attributed to the lack of convergence as well.

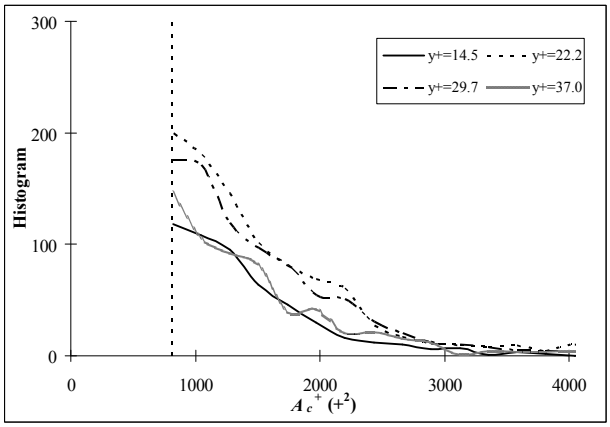

FIG. 6.86 – Histograms of the area A_c^+ of GSV

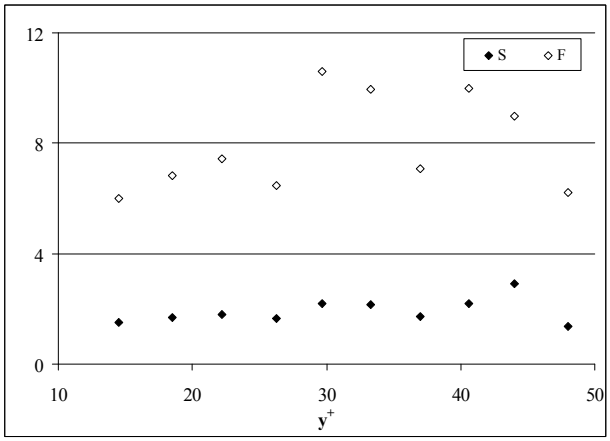

FIG. 6.87 – Skewness (S) and flatness (F) of the area A_c^+ of GSV

6.4.3.6 Spanwise distance of GSV

The profile of the mean spanwise distance $\overline{d^+}$ between GSV is shown in Fig. 6.88. It should be noted that the spanwise distance is measured only between the GSV with the same sign (e.g. between NGSV and between PGSV). The error bars represent an error of 5% of the mean. As shown in Fig. 6.88, the value of $\overline{d^+}$ varies between 107 and 147 wall units. Three interesting regions can be found from this profile. In the first two

regions where y^+ is between 14.5 and 18.5, and between 22 and 40, repectively, $\overline{d^+}$ is nearly constant. The difference between the two regions is that the value of the constant is about 107 wall units in the first region and about 127 in the second. In the third region where $y^+ > 40$, the spanwise distance inceases from about 127 wall units at $y^+ = 40$ to about 147 wall units at $y^+ = 48$. Fig. 6.88 also gives the RMS of the spanwise distance of GSV. It shows that the RMS increases linearly with the wall distance. The RMS is about 50 wall units at $y^+ = 14.5$ and increases up to 64 wall units at $y^+ = 48$.

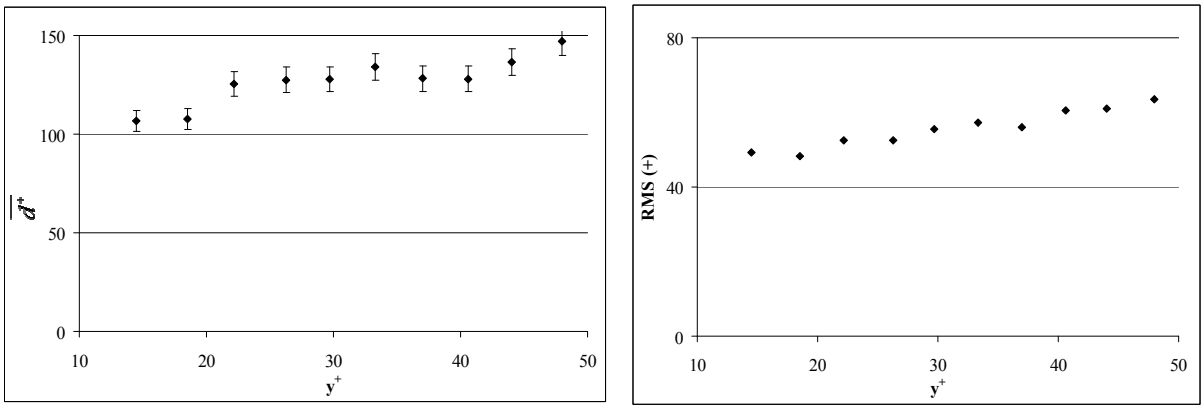

FIG. 6.88 – Mean and RMS of the spanwise distance d^+ between GSV (with the same sign)

Fig. 6.89 shows the histograms of the distance d^+ of GSV at selected wall distances. It indicates that most d^+ are in the range of about 50 to 200 wall units. The fluctuations in this figure result partly from the lack of convergence. To study the histogram statistically, skewness (S) and flatness (F) are given in Fig. 6.90, in which skewness is close to zero and flatness is about 2.5.

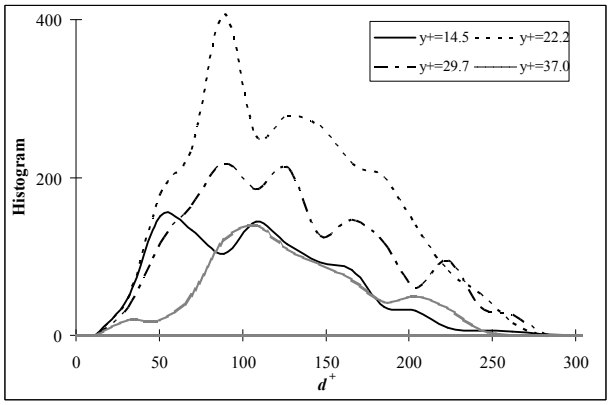

FIG. 6.89 – Histograms of the spanwise distance d^+ between GSV (with the same sign)

6.4.3.7 Spanwise angle of GCSV

Fig. 6.91 shows the distributions of the mean spanwise angle $\overline{\varphi}$ of NGCSV and of the mean of the difference of the spanwise angle $\overline{\varphi_c}$ between the NGCSV and PGCSV that

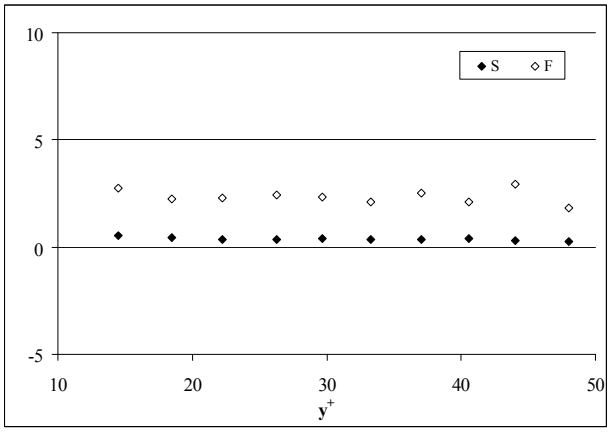

FIG. 6.90 – Skewness (S) and flatness (F) of the spanwise distance d^+ of GSV (with the same sign)

belong to the same counter-rotating streamwise vortex at various wall distances. In the region of $y^+ < 30$, the value of both $\overline{\varphi}$ and $\overline{\varphi_c}$ is nearly zero. However, when $y^+ > 30$, both $\overline{\varphi}$ and $\overline{\varphi_c}$ become non-zero, with $\overline{\varphi_c}$ larger than $\overline{\varphi}$. For $y^+ > 40$, the interpretation is difficult due to the lack of convergence.

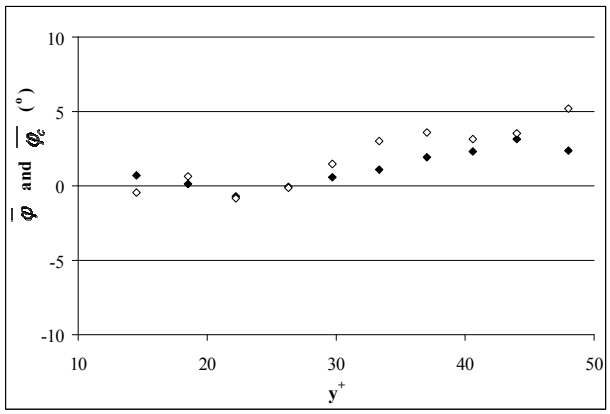

FIG. 6.91 – Mean spanwise spanwise angle $\overline{\varphi}$ of PGCSV, and mean of the difference of the spanwise angle $\overline{\varphi_c}$ between the PGCSV and NGCSV that belong to the same counter-rotating streamwise vortex. $\overline{\varphi}$: ♦ ; $\overline{\varphi_c}$: ◊.

To study these angles in more detail, Fig. 6.92 gives the histograms of the spanwise angle φ of PGCSV and the difference of spanwise angle φ_c between the PGCSV and NGCSV which belong to the same counter-rotating streamwise vortex at selected wall distances. The negative values in the histogram suggest the existence of Λ-shaped vortices (or at least the existence of two close streamwise vortices, this will be explained in the next chapter) while the positive ones evidence the Ω-shaped vortices. Except for small oscillations due to the lack of convergence, the distribution of φ and φ_c is more symmetrical in the region of $y^+ < 30$ than $y^+ > 30$. This suggests that both Λ- or Ω-shaped vortices are comparable in population in the region $y^+ < 30$. It explains zero value of $\overline{\varphi}$ and $\overline{\varphi_c}$

in this region. The asymmetry of the histograms above $y^+ = 30$ shows that Ω-shaped vortices are dominant. This is also evidenced by the positive $\overline{\varphi_c}$ in Fig. 6.91.

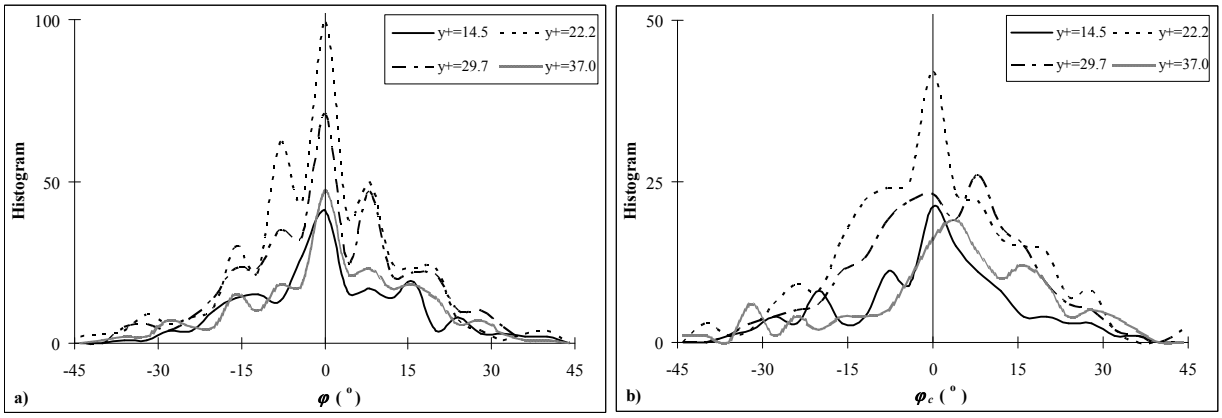

FIG. 6.92 – Histogram of the spanwise angle φ of PGCSV and the difference of spanwise angle φ_c between PGCSV and NGCSV that belong to the same counter-rotating streamwise vortex at selected wall distances. a : φ ; b : φ_c

6.4.3.8 Spanwise distance of GCSV

Fig. 6.93 presents the profile of the mean spanwise distance $\overline{d^+}$ between NGCSV and PGCSV related to the same counter-rotating streamwise vortex at various wall distances. The error bars represent an error of 5% of the mean. In general, $\overline{d^+}$ tends to increase with wall distance. It starts with a value of about 39 wall units at $y^+ = 14.5$ and ends with a value of 53 wall units at $y^+ = 48$. These values are comparable to the width of low speed streaks (31-39 wall units, see Fig. 6.12).

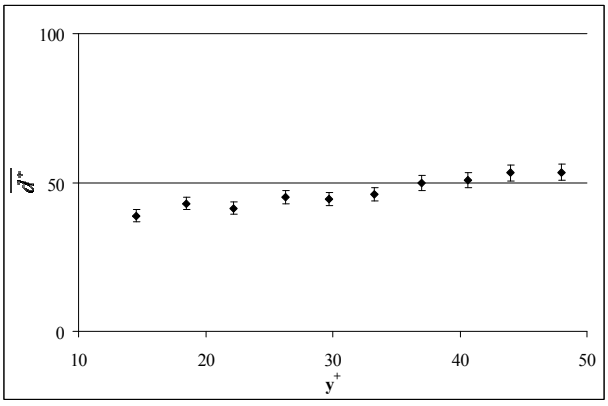

FIG. 6.93 – Mean spanwise distance $\overline{d^+}$ between NGCSV and PGCSV that belong to the same counter-rotating streamwise vortex

Fig. 6.94 shows the histogram of the spanwise distance d^+ between NGCSV and PGCSV that belong to the same counter-rotating streamwise vortex at selected wall distances. It shows that most of d^+ are in the range of 30 - 60 wall units. All the peaks

are located at the same position (about 40 wall units), which is comparable to the mean width of streaks.

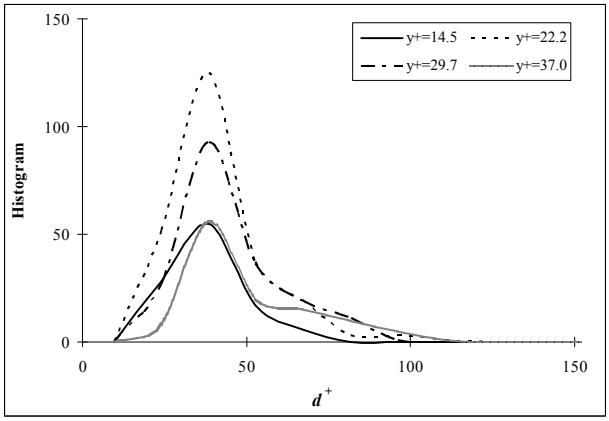

FIG. 6.94 – Histogram of the spanwise distance d^+ between NGCSV and PGCSV related to the same counter-rotating streamwise vortex at selected wall distances

6.4.3.9 Area of GCSV

Fig. 6.95 shows the profile of the mean area $\overline{A_c^+}$ of NGCSV at various wall distances. At the same wall distance, the value of $\overline{A_c^+}$ is only slightly larger than that in Fig. 6.85. It implies that individual streamwise vortices are comparable to counter-rotating ones.

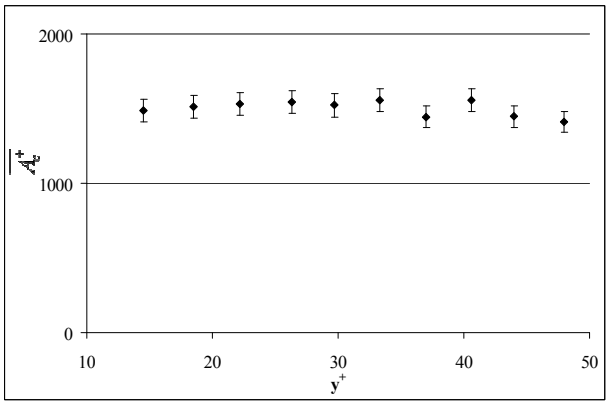

FIG. 6.95 – The mean area $\overline{A_c^+}$ of GCSV

6.4.4 Comparison

Fig. 6.70 shows that the maximum values of the frequency of appearance of NGSV, PGSV as well as of GCSV are located around $y^+ = 25$. According to the present detection method, the frequency of appearance of NGSV and PGSV can represent that of negative and positive streamwise vortices respectively, while GCSV represent counter-rotating

streamwise vortices. The streamwise vortices might be the legs of hairpins. Therefore, the maximum may result from the contribution of streamwise legs of the secondary and tertiary hairpin vortices according to Zhou *et al.* (1999). In their theory of hairpin packet, the core of streamwise legs is located between $y^+ = 12$ and 30 for the primary hairpin vortice in most of their life time, while it is between $y^+ = 30$ and 45 for the secondary and tertiary hairpins. Hence, the decrease of the frequency of appearance of NGSV and PGSV towards the wall can be partly attributed to the decease in the numbers of secondary and tertiary hairpins. Above $y^+ = 25$, the further away from the wall, the more likely the head segment of hairpin vortex can be found instead of leg segments. In other words, the streamwise vortices may lose some of their identification. This explains the decrease of the frequency of appearance away from the wall above $y^+ = 25$.

According to Zhou *et al.* (1999), the streamwise vortices that are related to hairpins, are in the range of 140 to 250 wall units long. However the length $\overline{L_A^+}$ is less than 100 wall units in the present study (Fig. 6.80). The disagreement can be explained by the following reasons. Firstly the value of $\overline{L_A^+}$ is obtained from the well-developed hairpins in the simulation of channel flow at a low Reynolds number in Zhou *et al.* (1999). However, the value obtained in the present study is an average of all kinds of streamwise vortices, including all individual and counter-rotating ones at various lifetimes. Moreover, as explained above, the measurement planes cannot cut through all cores of streamwise vortices, which causes that the lengths of GSV are shorter than the real vortices. Furthermore, the streamwise vortices may travel downstream with an angle inclined to the wall.

In Fig. 6.93, the present results are different from those of Zhou *et al.* (1999). Zhou *et al.* (1999) concluded that the spanwise separation between two legs of a hairpin decreases from about 100 wall units at $y^+ = 12$ to about 30 - 40 wall units at $y^+ = 45$. The present results show a slight increase from 39 wall units at $y^+ = 14.5$ to 53 at $y^+ = 48.0$ Zhou et al.'s results were obtained from the relatively strong and well-developed hairpins or hairpin packets. In contrast, the present results are calculated from all possible counter-rotating streamwise vortices detected from the experiment dataset. Some of them may not be able to evolve yet into well-developed hairpins.

6.4.5 Summary

Due to the orientation of the PIV planes used, a specific detection method was developed to evidence the streamwise vortices. Thanks to this method, the characteristics of these vortices could be extracted.

The frequencies of appearance of positive and negative streamwise vortices are nearly the same in terms of both the value and the distribution with wall distance, indicating the good spanwise homogeneity of the flow. The population of the counter-rotating streamwise vortices is about 20% of the total, including both individual and counter-rotating vortices. The frequency distribution with wall distance is the same for both populations. The present results show that the maximum frequency is located around $y^+ = 23$ for both types of streamwise vortices.

The mean value of the spanwise angle of negative streamwise vortices is close to zero. The mean of the modulus varies between 11.5 and 14 degrees. The histogram of this angle

shows that about 50% of the streamwise vortices have an absolute spanwise angle between 4 and 16 degrees and about 14% of vortices have an angle larger than 16 degrees. This implies that only about 36% of the streamwise vortices move almost parallel to the mean flow. The histogram is close to a Laplace distribution. According to the homegeneous property of the flow, the spanwise angle of positive streamwise vortices is the same as that of the negative ones except for the sign.

The mean width of the gradient objects which represent the core of the streamwise vortices has a remarkably constant value of about 16 wall units with a very small fluctuation of about 0.5 wall units in the whole range studied. Different from the mean width, in the present study, the distribution of the mean length of those objects can be divided into three regions. In the region $y^+ < 22$, it decreases slowly toward the wall. In the region $22 < y^+ < 33$, it is nearly constant about 96 wall units. When $y^+ > 30$, it again decreases slowly but away from the wall. This distribution suggests that the well-developed wall-attached streamwise vortices are located around 25 wall units. Both histograms of the width and the length follow nearly a lognormal distribution. The distribution of the mean area of these objects is similar to that of the length. However, different from the width and the length, the histogram of the area is close to an exponential distribution.

The mean spanwise distance between the positive or negative streamwise vortices is nearly a constant of about 107 wall units in the region $14.5 < y^+ < 18.5$ and about 127 wall units in the region $22 < y^+ < 40$. When $y^+ > 40$, the spanwise distance increases from about 127 wall units at $y^+ = 40$ to 147 wall units at $y^+ = 48$. The histogram of this spanwise distance suggests that most of the samples are in the range of about 50 - 200 wall units.

In the region $y^+ < 30$, the mean spanwise angle of the positive legs of the counter-rotating streamwise vortices, as well as the mean of the difference of the spanwise angle between positive and negative legs of the same counter-rotating streamwise vortex is nearly zero. This results from the comparable population of Λ- and Ω- shaped streamwise vortex in this region. For $y^+ > 30$, both of these angles increase with wall distance. The mean of the difference is larger than the angle of negative legs. Moreover, the histograms of both angles are asymmetric with more positive values. These results evidence the dominance of Ω-shaped counter-rotating streamwise vortices (hairpins) in this region.

The mean spanwise distance between negative and positive legs of the same counter-rotating streamwise vortex, increases from about 39 wall units at $y^+ = 14.5$ to about 53 wall units at $y^+ = 48$. The histogram of this distance shows that most of the samples are in the range of 30 - 60 wall units.

Chapitre 7

Discussion

7.1 Introduction

The results obtained in Chapters 5 and 6 show that some of the characteristics of different coherent structures are very similar. For example, the closer to the wall, the more streaks (both low and high speed streaks) and sweeps can be found. However, for the other coherent structures (e.g. ejections and streamwise vortices), a maximum is located around $y^+ = 22$. A significant population of each structure show a spanwise angle when they travel downstream. These results suggest that all coherent structures may evolve into a regular organization, which is repeating in the flow. Therefore, to investigate the relative position of one structure with respect to another, two-point correlation analysis is conducted on the indicative functions. As the indicative functions have only two values : 1 and 0, the standard deviation is taken as 1 and the mean as 0 to simplify the calculation. Hence, Eq. 5.1-5.3 are rewritten as :

Two-dimensional two-point correlation function :

$$R_{CS_i-CS_j}(\Delta x^+, \Delta z^+) = \overline{F_i^{CS_i}(x^+, z^+) F_i^{CS_j}(x^+ + \Delta x^+, z^+ + \Delta z^+)} \tag{7.1}$$

Streamwise one-dimensional two-point correlation function :

$$R_{CS_i-CS_j}(\Delta x^+, \Delta z^+ = 0) = \overline{F_i^{CS_i}(x^+, z^+) F_l^{CS_j}(x^+ + \Delta x^+, z^+)} \tag{7.2}$$

Spanwise one-dimensional two-point correlation function :

$$R_{CS_i-CS_j}(\Delta x^+ = 0, \Delta z^+) = \overline{F_i^{CS_i}(x^+, z^+) F_i^{CS_j}(x^+, z^+ + \Delta z^+)} \tag{7.3}$$

Where, CS_i and CS_j are Coherent Structures (CS) which can be low or high speed streaks, ejections, sweeps and streamwise vortices related objects (NGSV, PGSV, NVF and PVF) in the present study. $F_i^{CS_i}$ and $F_i^{CS_j}$ are the indicative functions.

As explained in Chapter 4, for the two-dimensional correlations (e.g Fig.7.1), the positive and negative Δz^+ are located respectively on the right and left sides of the flow with respect to the streamwise direction (view from below).

7.2 Two-point correlation analysis of coherent structures

7.2.1 Streaks

Fig. 7.1 shows examples of two-dimensional auto-correlation of low speed streaks $R_{LSS-LSS}$ and high speed streaks $R_{HSS-HSS}$ at $y^+ = 14.5$. The elliptical regions with high correlation located at the centre ($\Delta x^+ = 0$, $\Delta z^+ = 0$) reveal that streaks are elongated in the streamwise direction. To obtain more information on the variation of the correlation in the streamwise and spanwise directions, two one-dimensional auto-correlations : at $\Delta x^+ = 0$ and at $\Delta z^+ = 0$ are calculated and shown in Fig. 7.2. The value of the peak at the center decreases with wall distance, indicating that the area occupied by both low and high speed streaks decreases when moving away from the wall. As in Fig. 5.3b, for the one-dimensional correlation at $\Delta z^+ = 0$, a continuous decrease is observed, implying that both low and high speed streaks are longer than 400 wall units. Due to the limited size of the velocity field, it is not possible to measure the length of streaks. However, according to the shape and the tendency of the curves in Fig. 7.2a and 7.2c, several conclusions can be drawn. First, with the same streamwise displacement Δx^+, the coherence decreases with wall distance, which indicates a decrease in the length of streaks. Second, according to the coherence, the wall distance under study can be categorised into two groups : $y^+ \leq 18.5$ and $y^+ > 18.5$. In each group, the curves are comparable. The coherence in the first group is much higher than that in the second one, revealing that the length of streaks is larger in the region very near the wall than far from the wall. It should be noted that there is a large difference in coherence between the correlation at $y^+ = 18.5$ and at $y^+ = 22.2$.

In Fig. 7.2b and 7.2d ($\Delta x^+ = 0$), all the curves have a transition position where a minimum or a plateau is visible. Generally, the off-centre distance of this position increases from about 55 wall units at $y^+ = 14.5$ to 65 wall units at $y^+ = 48$. As explained in Chapter 5, this off-centre distance is equal to half the spanwise distance between low or high streaks, in agreement with the results in Fig. 6.17. According to these results, the secondary peak should be found around $\Delta z^+ = 165$ and 195 for both low and high speed streaks. However, as shown in Fig. 7.1 and Fig. 7.2 (for other wall distances, two-dimensional auto-correlations of $R_{LSS-LSS}$ and $R_{HSS-HSS}$ can be found in Appendix C.1 - C.2), no clear secondary peak appears. This may result from the strong variability in size and position of the two types of structures as shown by the large range of the histograms in Fig. 6.13 and 6.18.

Fig. 7.3 shows an example of two-dimensional spatial cross-correlation of low speed streaks with high speed ones $R_{LSS-HSS}$ at $y^+ = 14.5$. Two regions with high correlation are located symmetrically with respect to $\Delta z^+ = 0$, indicating the existence of high speed streaks. Fig. 7.4 shows the one-dimensional correlation at $\Delta x^+ = 0$. At $y^+ = 14.5$, the first off-centre maximum indicates the location of the nearby high speed streak. This distance is about 75 wall units. At other wall distances, a plateau is observed which is again indicative of a strong variability in size and position of the two types of structures. The figures of $R_{LSS-HSS}$ at other wall distances (Appendix C.1) clearly shows that in

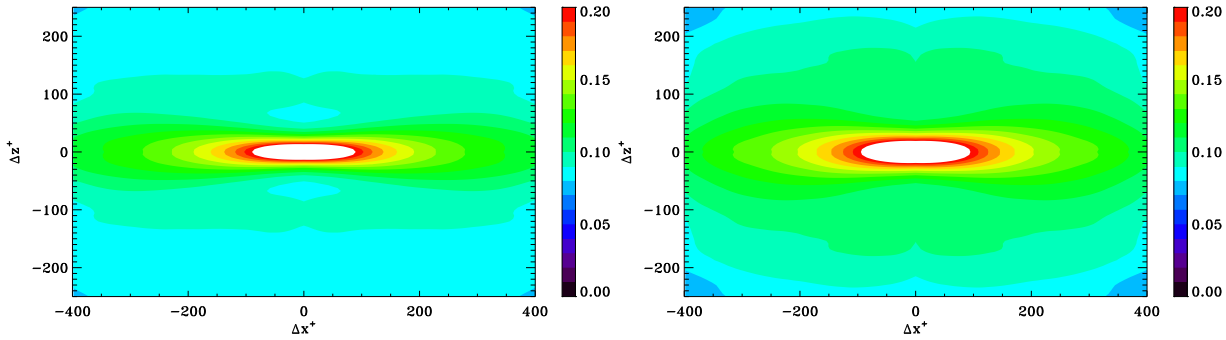

a : $R_{LSS-LSS}$ b : $R_{HSS-HSS}$

FIG. 7.1 – Two-point spatial auto-correlations of streaks at $y^+ = 14.5$

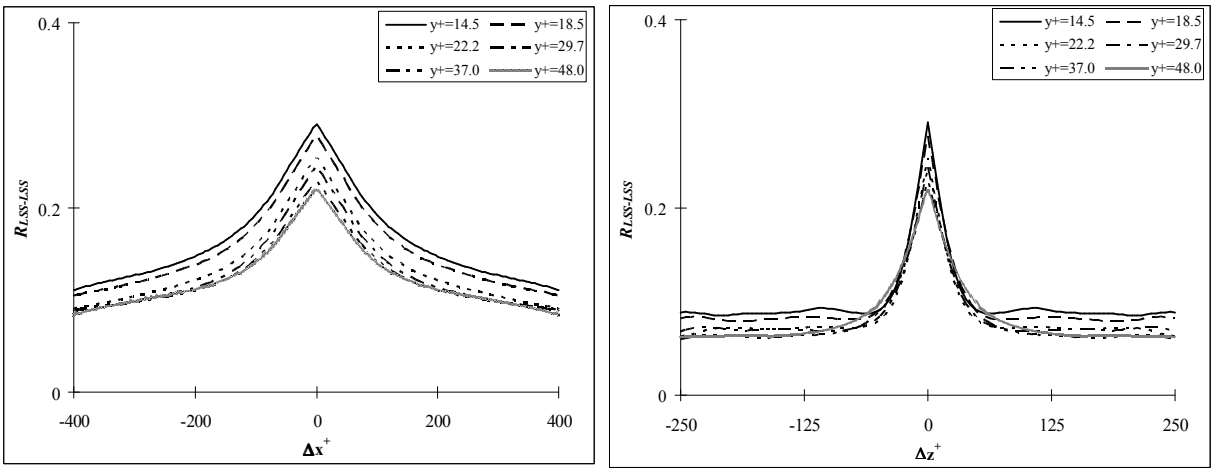

a : $R_{LSS-LSS}$, with $\Delta z^+ = 0$ b : $R_{LSS-LSS}$, with $\Delta x^+ = 0$

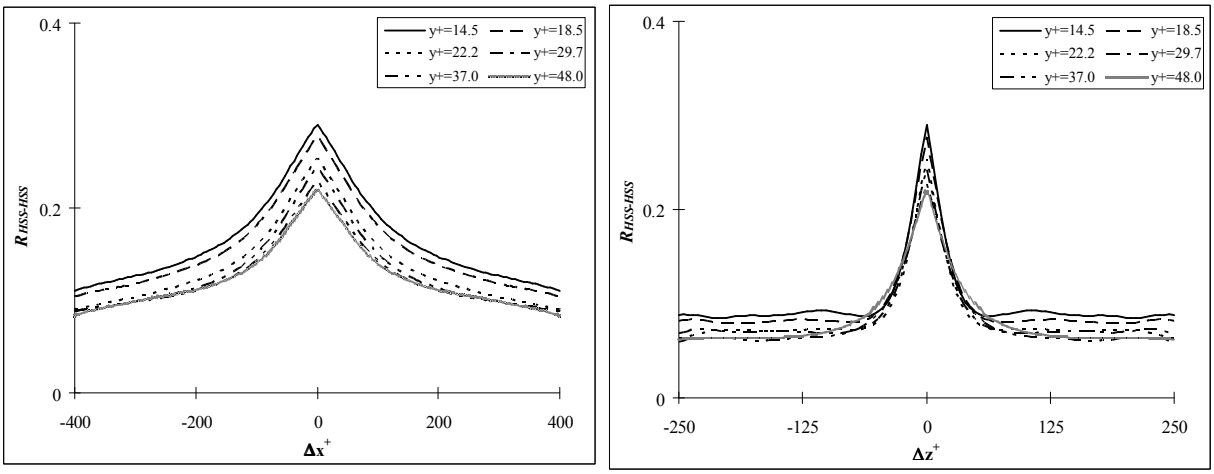

c : $R_{HSS-HSS}$, with $\Delta z^+ = 0$ d : $R_{HSS-HSS}$, with $\Delta x^+ = 0$

FIG. 7.2 – One-dimensional spatial auto-correlation of streaks at selected wall distances

the streamwise-spanwise planes the link between LSS and HSS is much stronger near the wall.

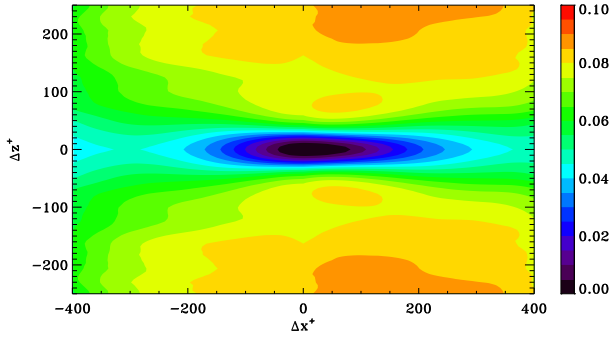

FIG. 7.3 – Two-point spatial cross-correlation of low speed streaks with high speed ones $R_{LSS-HSS}$ at $y^+ = 14.5$

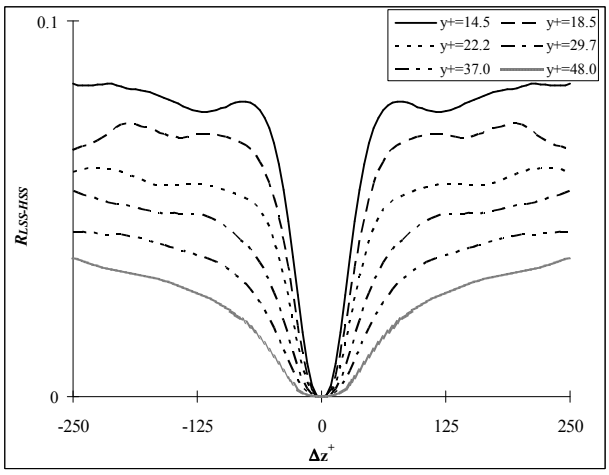

FIG. 7.4 – One-dimensional spatial cross-correlations of low speed streaks with high speed ones at selected wall distances with $\Delta x^+ = 0$

7.2.2 Ejections and sweeps

Fig. 7.5 shows examples of two-dimensional spatial auto-correlation of ejections R_{EJ-EJ} and sweeps R_{SW-SW} at $y^+ = 14.5$. To analyse those correlations in detail, Fig. 7.6 gives two one-dimensional auto-correlations : at $\Delta x^+ = 0$ and $\Delta z^+ = 0$ respectively. Opposite to Fig. 7.2a and 7.2c, Fig. 7.6a and 7.6c shows that the value of the central peak increases with wall distance, indicating an increase in the size of both ejections and sweeps. This is in good agreement with Fig. 6.42. No distinct minimum appears in both Fig. 7.6a and 7.6c. However, a rapid transition is visible around 120 wall units for ejections and 100 wall units for sweeps, giving an estimate of the length of ejections and sweeps, which is in good agreement with Fig. 6.38. For ejections, similar to streaks (Fig. 7.2a and 7.2c), the wall distance can be separated into two groups : $y^+ \leq 18.5$ and $y^+ > 18.5$. In each group, the curves are comparable. However, contrary to streaks, the length of ejections is smaller very near the wall than far from it. A large difference is evidenced between the correlations at $y^+ = 18.5$ and $y^+ = 22.2$. It is also revealed by the rapid increase of the mean length in this region shown in Fig. 6.38.

In Fig. 7.6b and 7.6d, a minimum is evidenced only at $y^+ = 14.5$. The off-centre distance of this minimum is equal to about 45 wall units for ejections and 50 wall units for sweeps. These values are somewhat smaller than half of those in Fig. 6.45.

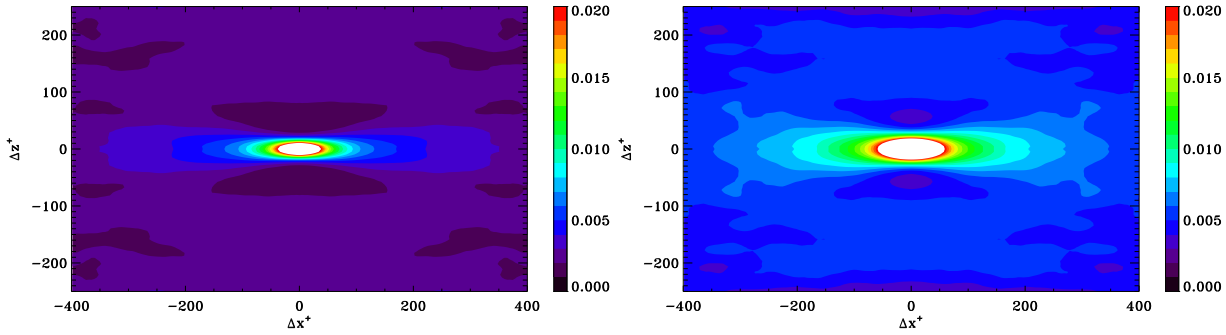

a : R_{EJ-EJ} b : R_{SW-SW}

FIG. 7.5 – Two-dimensional spatial auto-correlations of ejections and sweeps at $y^+ = 14.5$

Fig. 7.7 shows an example of two-dimensional spatial cross-correlation of ejections with sweeps R_{EJ-SW} at $y^+ = 14.5$. Two regions with high correlation are located symmetrically with respect to $\Delta z^+ = 0$ in the spanwise direction. These regions have a small angle (about 5 degrees) with the streamwise direction. Fig. 7.8 shows the one-dimensional correlation at $\Delta x^+ = 0$. As for $R_{LSS-HSS}$, the off-centre distance of this maximum can be used to measure the spanwise distance between neighbouring ejections and sweeps. In Fig. 7.8, it increases from about 50 wall units at $y^+ = 14.5$ to 90 at $y^+ = 48$.

7.2.3 NGSV and PGSV

Fig. 7.9 shows an example of two-dimensional spatial auto-correlation of PGSV $R_{PGSV-PGSV}$ at $y^+ = 22.2$ where the frequency of appearance of those structures is the highest. The secondary peak is not evidenced, revealing a strong variability in size and position of these structures. Additionally, the peaks at the center are clearer at $y^+ = 22.2$ and 26 than at other wall distances, indicating that the cores of wall-attached streamwise vortices are located around $y^+ = 25$.

Fig. 7.10 shows an example of two-dimensional spatial cross-correlation of NGSV with PGSV $R_{NGSV-PGSV}$ at $y^+ = 22.2$. Two regions with high correlation are located symmetrically in the spanwise direction with respect to $\Delta z^+ = 0$, indicating the existence of PGSV beside NGSV. To study the variation of correlation in the spanwise direction in detail, the one-dimensional correlation $\Delta x^+ = 0$ is calculated and shown in Fig. 7.11. The off-centre distance of the peak can be used to measure the spanwise distance between neighbouring PGSV and NGSV. It increases slightly with wall distance from 30 wall units at $y^+ = 14.5$ to 35 wall units at $y^+ = 48$. These small values indicate that the peaks of $R_{NGSV-PGSV}$ are mainly resulting from counter-rotating streamwise vortices. Moreover, the values of these peaks are much smaller than those corresponding to $R_{PGSV-PGSV}$, indicating that the phenomenon of counter-rotating streamwise vortices is much less frequent than individual ones.

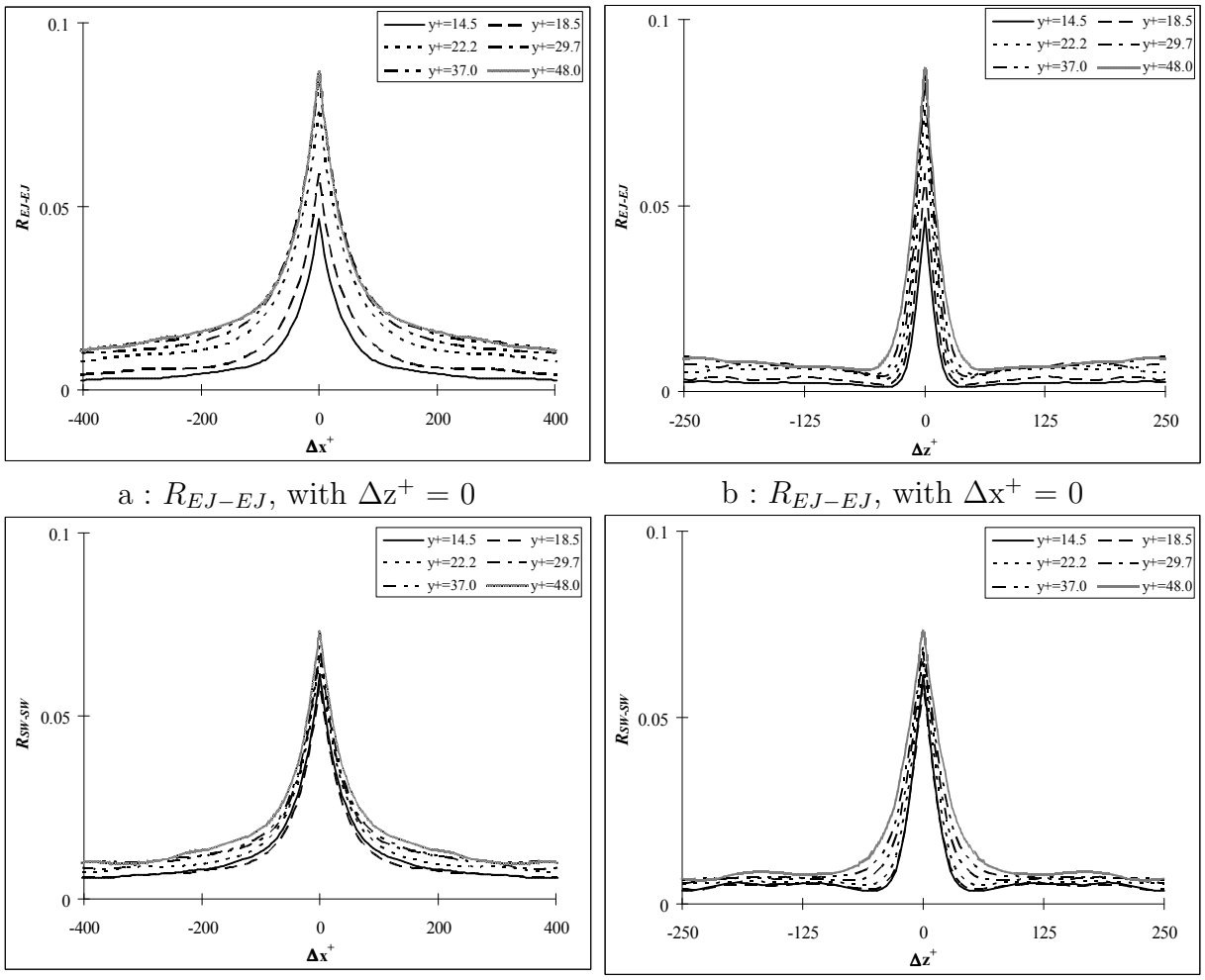

a : R_{EJ-EJ}, with $\Delta z^+ = 0$ b : R_{EJ-EJ}, with $\Delta x^+ = 0$

c : R_{SW-SW}, with $\Delta z^+ = 0$ d : R_{SW-SW}, with $\Delta x^+ = 0$

FIG. 7.6 – One-dimensional spatial auto-correlation of ejections and sweeps at selected wall distances

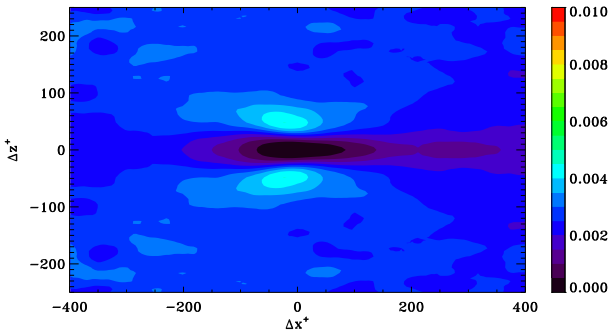

FIG. 7.7 – Two-dimensional spatial cross-correlation of ejections with sweeps R_{EJ-SW} at $y^+ = 14.5$

7.2.4 Streaks with ejections and sweeps

Fig. 7.12a shows an example of two-dimensional spatial cross-correlation of low speed streaks with ejections R_{LSS-EJ} at $y^+ = 14.5$. The region with high correlation at the centre

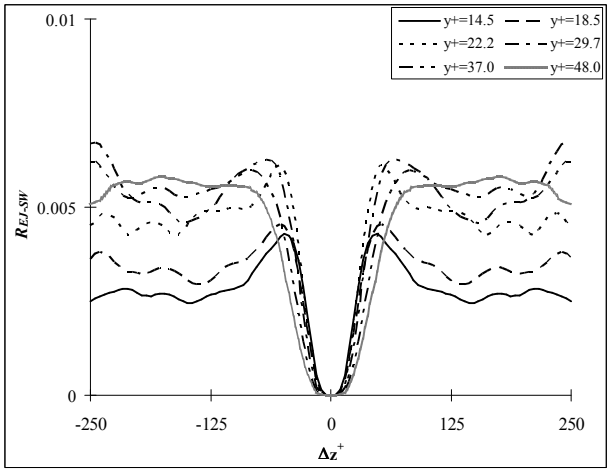

FIG. 7.8 – One-dimensional spatial cross-correlations of ejections with sweeps R_{EJ-SW} at selected wall distances with $\Delta x^+ = 0$

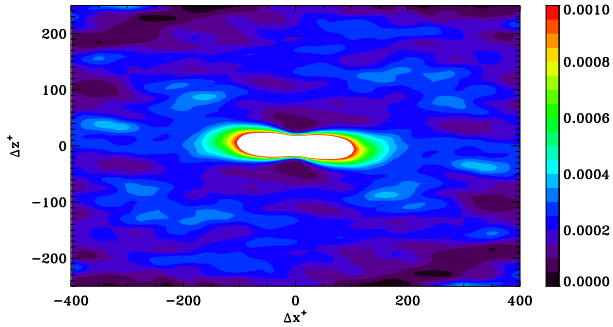

FIG. 7.9 – Two-dimensional spatial auto-correlation of NGSV $R_{PGSV-PGSV}$ at $y^+ = 22.2$

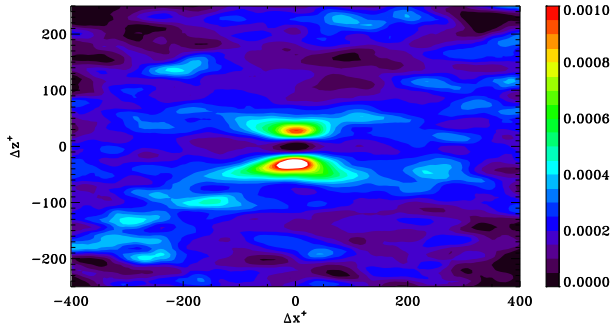

FIG. 7.10 – Two-dimensional spatial cross-correlation of NGSV with PGSV $R_{NGSV-PGSV}$ at $y^+ = 22.2$

($\Delta x^+ = 0$, $\Delta z^+ = 0$) and the minimum on both sides along Δz^+, indicates that ejections are strongly linked to low speed streaks ; in other words, they are part of streaks. Fig. 7.12b shows an example of two-dimensional spatial cross-correlation of low speed streaks with sweeps R_{LSS-SW} at $y^+ = 14.5$. Two peaks are located symmetrically with respect to $\Delta z^+ = 0$. This indicates that sweeps can be found on both sides of low speed streaks in the

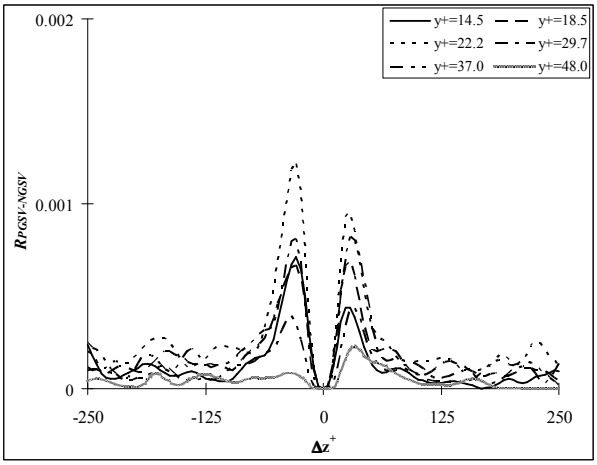

FIG. 7.11 – One-dimensional spatial cross-correlations of PGSV with NGSV $R_{NGSV-PGSV}$ at selected wall distances with $\Delta x^+ = 0$

spanwise direction.

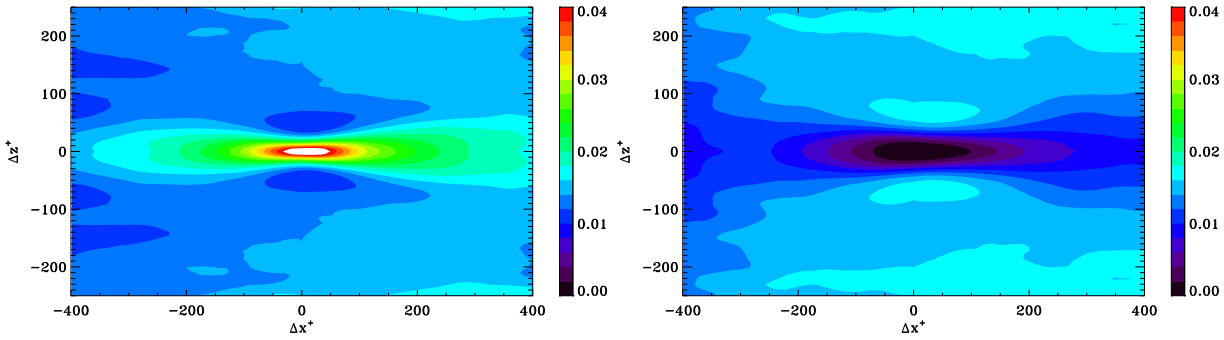

a : R_{LSS-EJ} b : R_{LSS-SW}

FIG. 7.12 – Two-dimensional spatial cross-correlations of low speed streaks with ejections and sweeps at $y^+ = 14.5$

Fig. 7.13b shows the spanwise one-dimensional correlation R_{LSS-SW} at $\Delta x^+ = 0$. For each correlation, a transition position, where a maximum or plateau appears, is visible. The off-centre distance of this position increases from 65 wall units at $y^+ = 14.5$ to about 95 at $y^+ = 48$. As shown in Fig. 7.13, the intensity of the peaks decreases rapidly with wall distance in the region $y^+ > 22$, which results mainly from the fact that the frequency of appearance of both low speed streaks and sweeps decrease with wall distance in this region (see Fig. 6.7a and 6.28).

Fig. 7.14a shows an example of two-dimensional spatial cross-correlation of high speed streaks with ejections R_{HSS-EJ} at $y^+ = 14.5$. Similar to Fig. 7.12b, two peaks located symmetrically with respect to $\Delta z^+ = 0$ are visible. This indicates that ejections can be found on both sides of high speed streaks. Fig. 7.14b shows an example of the cross-correlation of high speed streaks with sweeps R_{HSS-SW} at $y^+ = 14.5$. Similar to R_{LSS-EJ} (Fig. 7.12a), a region with high correlation is located around the centre ($\Delta x^+ = 0$, $\Delta z^+ = 0$), indicating that sweeps are strongly linked to high speed streaks.

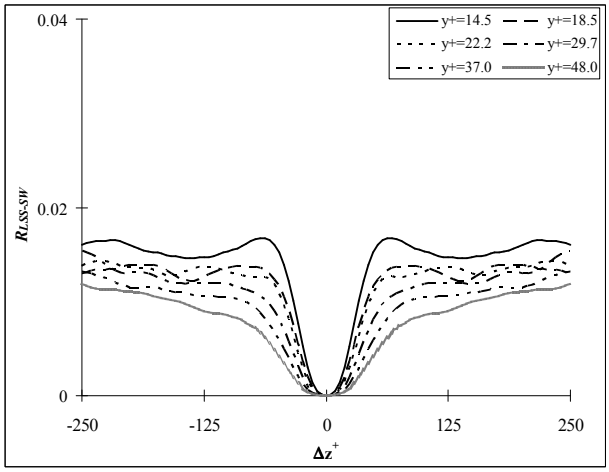

FIG. 7.13 – One-dimensional spatial cross-correlation of low speed streaks with sweeps R_{LSS-SW} at selected wall distances with $\Delta x^+ = 0$

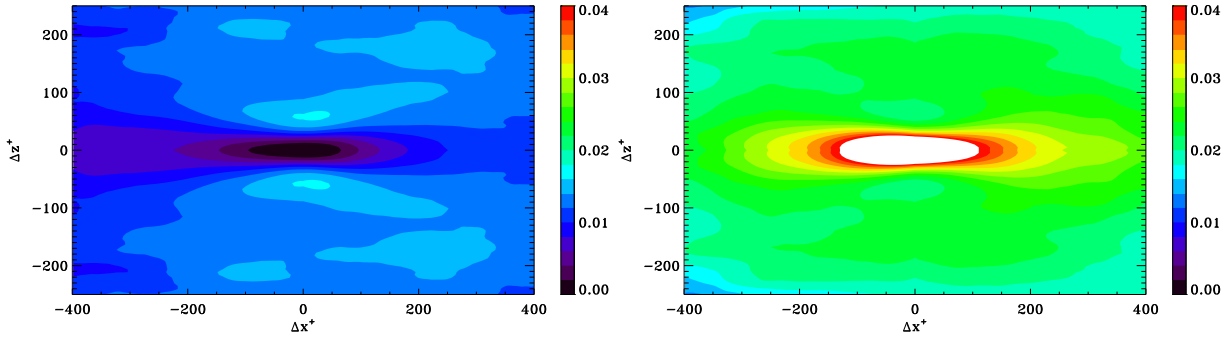

a : R_{HSS-EJ} b : R_{HSS-SW}

FIG. 7.14 – Two-dimensional spatial cross-correlations of high speed streaks with ejections and sweeps at $y^+ = 14.5$

Fig. 7.15 shows the one-dimensional correlation R_{HSS-EJ} at $\Delta x^+ = 0$. For each correlation, a transition position, where a maximum or plateau appears, is visible. The off-centre distance of this transition increases from 65 at $y^+ = 14.5$ to about 95 wall unit at $y^+ = 48$. The maximum disappears in the region $y^+ > 37$, which results mainly from the fact that the frequency of appearance of both high speed streaks and ejections decrease with wall distance (see Fig. 6.7a and 6.28)

7.2.5 Streaks with NGSV and PGSV

Fig. 7.16 shows examples of cross-correlation of low speed streaks with NGSV ($R_{LSS-NGSV}$) and low speed streaks with PGSV ($R_{LSS-PGSV}$) at $y^+ = 14.5$. For $R_{LSS-NGSV}$ (Fig. 7.16a), an elongated region with high correlation appears with a spanwise angle of about 7 degrees. A maximum is evidenced in this region with a negative streamwise Δx^+ and a positive spanwise displacements Δz^+. For $R_{LSS-PGSV}$ (Fig. 7.16b), the angle is also about -7 degrees and both Δx^+ and Δz^+ are positive. This shows that negative streamwise vortices

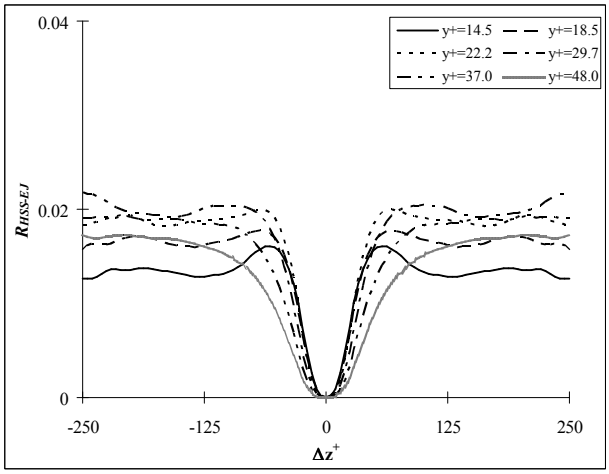

FIG. 7.15 – One-dimensional spatial cross-correlation of high speed streaks with ejections R_{HSS-EJ} at selected wall distances with $\Delta x^+ = 0$

are located on the downstream left of low speed steaks while the positive ones are on the downstream right. For each correlation, the off-centre distance of the maximum is about 24 wall units in the spanwise direction. The same value is observed in the streamwise direction.

Fig. 7.17 gives the spanwise one-dimensional correlation $R_{LSS-NGSV}$ and $R_{LSS-PGSV}$ at $\Delta x^+ = 0$. In coherence with the results on vortices in Chapter 6.4, the maximum of correlation is obtained for y^+ at the range between 20 and 30.

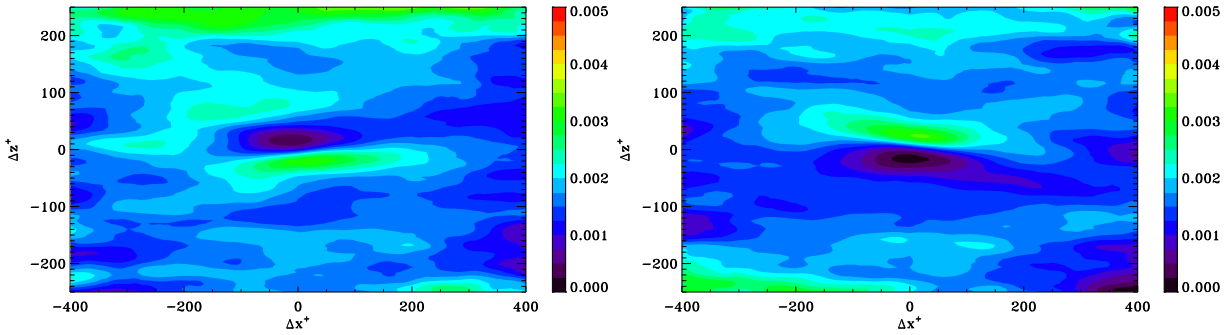

a : $R_{LSS-NGSV}$ b : $R_{LSS-PGSV}$

FIG. 7.16 – Two-dimensional spatial cross-correlations of low speed streaks with NGSV and PGSV at $y^+ = 14.5$

Fig. 7.18 shows examples of cross-correlation of high speed streaks with NGSV ($R_{HSS-NGSV}$) and high speed streaks with PGSV ($R_{HSS-PGSV}$) at $y^+ = 14.5$. For $R_{HSS-NGSV}$, like in Fig. 7.16a, a region of high correlation appears with a spanwise angle of about 7 degrees. Opposite to Fig. 7.16a, the maximum is at the upstream right. For $R_{HSS-PGSV}$, it is at the upstream left with a spanwise angle of about -7 degrees. For both correlations, the off-centre streamwise distance of the maximum increases from 20 at $y^+ = 14.5$ to about 50 at $y^+ = 48$, while the off-centre spanwise distance is from 24 to 60 wall units. Fig. 7.19

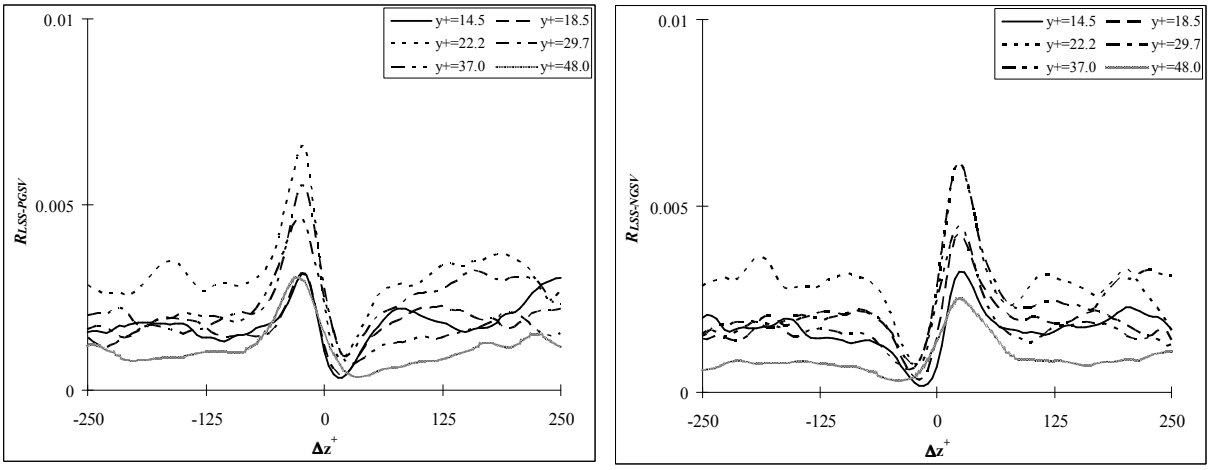

a : $R_{LSS-NGSV}$ b : $R_{LSS-PGSV}$

FIG. 7.17 – One-dimensional spatial cross-correlations of low speed streaks with NGSV and PGSV at selected wall distances with $\Delta x^+ = 0$

shows the spanwise one-dimensional correlation $R_{HSS-NGSV}$ and $R_{HSS-PGSV}$ at $\Delta x^+ = 0$.

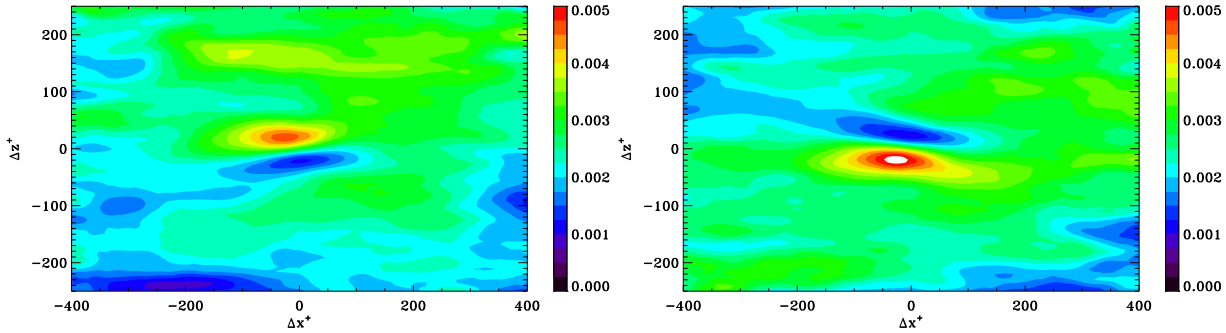

a : $R_{HSS-NGSV}$ b : $R_{HSS-PGSV}$

FIG. 7.18 – Two-dimensional spatial cross-correlations of high speed streaks with NGSV and PGSV at $y^+ = 14.5$

7.2.6 Ejections and sweeps with NGSV and PGSV

Two-dimensional spatial cross-correlation of ejections with NGSV ($R_{EJ-NGSV}$) and of ejections with PGSV ($R_{EJ-PGSV}$) at $y^+ = 14.5$ are shown in Fig. 7.20. Similar to $R_{LSS-NGSV}$ and $R_{LSS-NGSV}$, an elongated region with high correlation appears with a spanwise angle of about 4 and -4 degrees for $R_{EJ-NGSV}$ and $R_{EJ-PGSV}$ respectively. However, these regions are much smaller than those for $R_{LSS-NGSV}$ and $R_{LSS-NGSV}$. The location of the maximum of $R_{EJ-NGSV}$ is evidenced at the downstream left as for $R_{LSS-NGSV}$ but the distance to the centre ($\Delta x^+ = 0$, $\Delta z^+ = 0$) is much smaller. The same kind of relation can be found for $R_{EJ-PGSV}$ and $R_{LSS-NGSV}$. The off-centre distance of the maximum is about 5 wall units in the streamwise direction and 19 wall units in

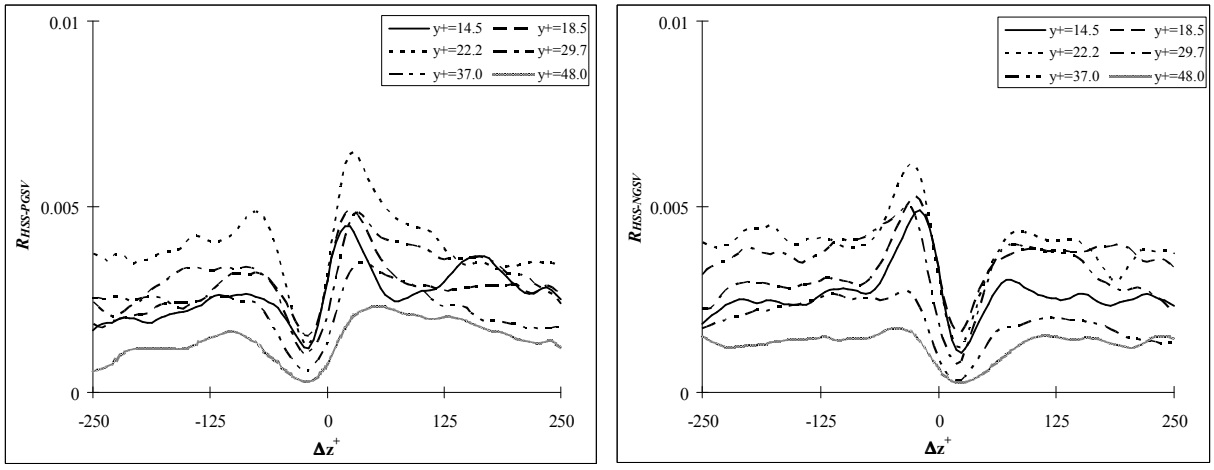

a : $R_{HSS-NGSV}$ b : $R_{HSS-PGSV}$

FIG. 7.19 – One-dimensional spatial cross-correlations of high speed streaks with NGSV and PGSV at selected wall distances with $\Delta x^+ = 0$

the spanwise direction. Fig. 7.21 shows the one-dimensional correlation $R_{EJ-NGSV}$ and $R_{EJ-PGSV}$ at $\Delta x^+ = 0$.

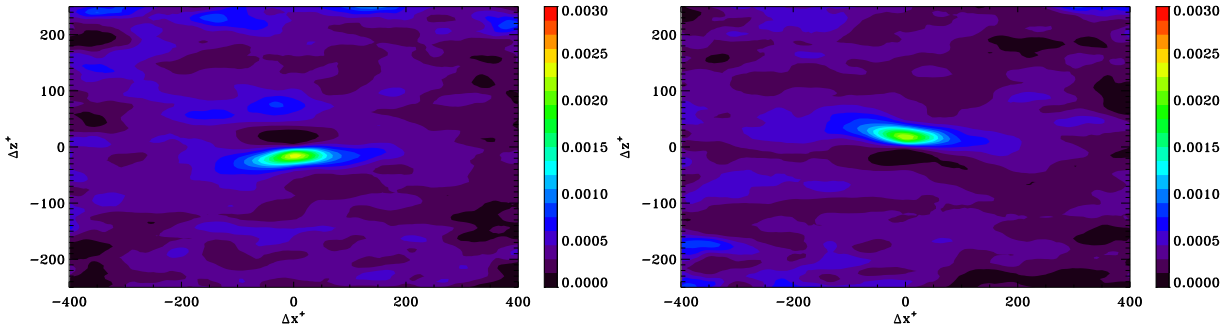

a : $R_{EJ-NGSV}$ b : $R_{EJ-PGSV}$

FIG. 7.20 – Two-dimensional spatial cross-correlations of ejections with NGSV and PGSV at $y^+ = 14.5$

Fig. 7.22 shows the respective examples of two-dimensional spatial cross-correlation of sweeps with NGSV ($R_{SW-NGSV}$) and of sweeps with PGSV ($R_{SW-PGSV}$) at $y^+ = 14.5$. An elongated region with high correlation appears with a spanwise angle of about 4 and -4 degrees for $R_{SW-NGSV}$ and $R_{SW-PGSV}$ respectively. The same as for $R_{HSS-PGSV}$ and $R_{HSS-PGSV}$, the maximum is located upstream right for $R_{SW-NGSV}$ and upstream left for $R_{SW-PGSV}$. In the streamwise direction, the off-centre distance is about 10 wall units. In the spanwise direction, it is about 19 wall units in the region $y^+ < 33$ and about 24 in the region $y^+ > 33$. These values are much smaller than those of $R_{HSS-PGSV}$ and $R_{HSS-PGSV}$. Fig. 7.23 shows the spanwise one-dimensional correlation $R_{SW-NGSV}$ and $R_{SW-PGSV}$ at $\Delta x^+ = 0$.

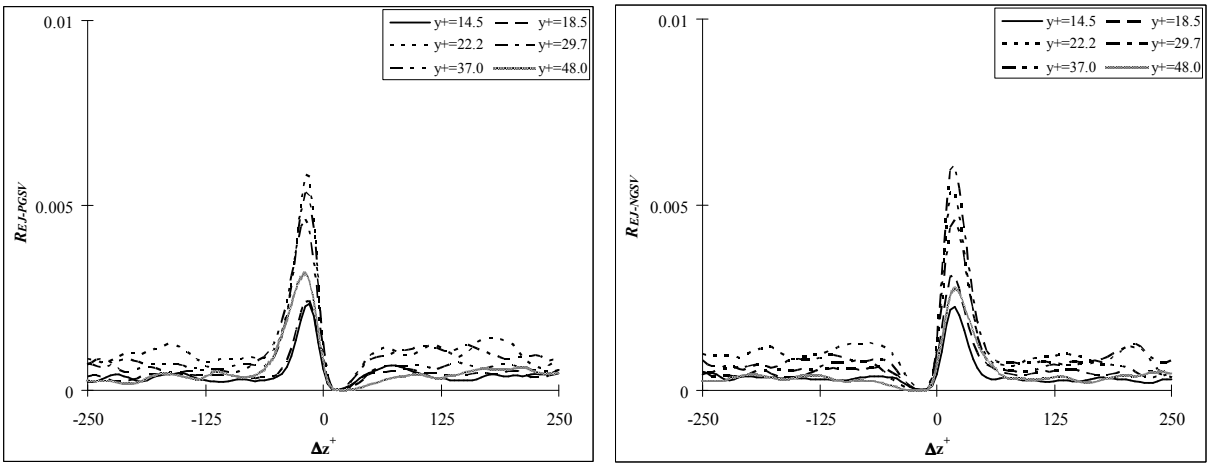

a : $R_{EJ-NGSV}$ b : $R_{EJ-PGSV}$

FIG. 7.21 – One-dimensional spatial cross-correlations of ejections with NGSV and PGSV at selected wall distances with $\Delta x^+ = 0$

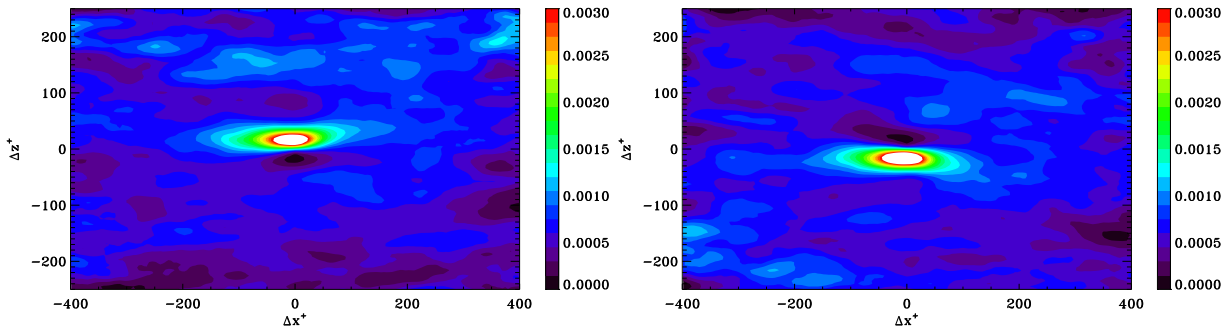

a : $R_{SW-NGSV}$ b : $R_{SW-PGSV}$

FIG. 7.22 – Two-dimensional spatial cross-correlations of ejections with NGSV and PGSV at $y^+ = 14.5$

7.2.7 PVF and NVF

Fig. 7.24 shows an example of two-dimensional spatial cross-correlation of PVF with NVF ($R_{PVF-NVF}$) at $y^+ = 22.2$. Similar to Fig. 5.6, two regions with high correlation appear symmetrically with respect to $\Delta z^+ = 0$. They also show a small angle with the streamwise direction. The maximum is located slightly upstream. The spanwise off-centre distance is a constant (about 34 wall units) in the region $y^+ \leq 22$. Above $y^+ = 22$, it increases up to about 50 wall units at $y^+ = 48$, indicating an increase in diameters of the streamwise vortices. Fig. 7.25 shows the spanwise one-dimensional correlation $R_{PVF-NVF}$ at $\Delta x^+ = 0$.

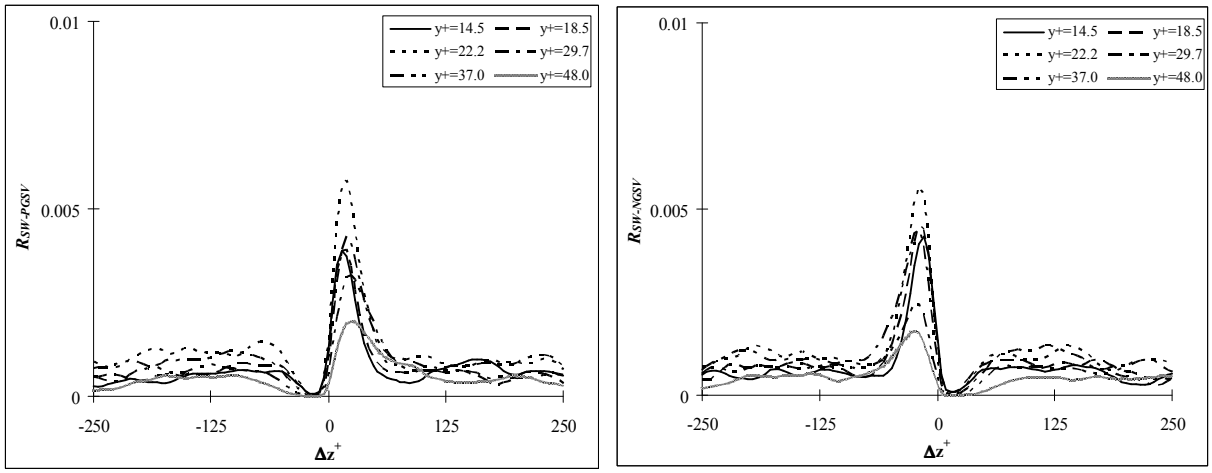

a : $R_{SW-NGSV}$ b : $R_{SW-PGSV}$

FIG. 7.23 – One-dimensional spatial cross-correlations of sweeps with NGSV and PGSV at selected wall distances with $\Delta x^+ = 0$

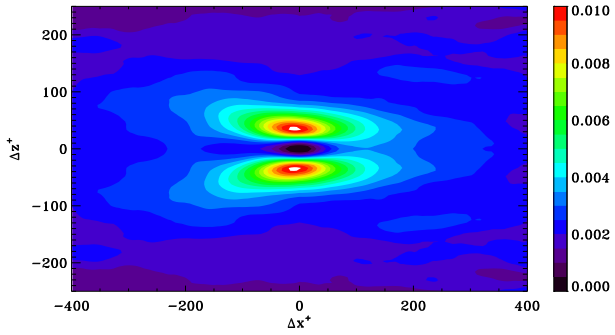

FIG. 7.24 – Two-dimensional spatial cross-correlation of PVF with NVF $R_{PVF-NVF}$ at $y^+ = 22.2$

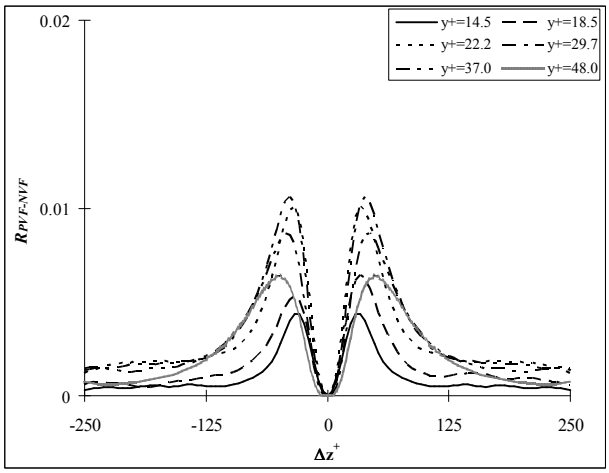

FIG. 7.25 – One-dimensional spatial cross-correlations of PVF with NVF $R_{PVF-NVF}$ at selected wall distances with $\Delta x^+ = 0$

7.3 Conceptual model

As can be seen from the above paragraph, evident links appear between the different coherent structures involved in the near-wall turbulence process. Among those structures, the streamwise vortices appear to play a significant role and are known to be a link with the log layer (Carlier and Stanislas (2005)). It is thus proposed to first insist on the evidence and the characteristics of these structures, as inferred from the present data and then to investigate the links of the other coherent objects (streaks, ejections and sweeps) with these vortices. Finally, the consequences of these results in terms of a structural model of the turbulence near the wall will be investigated. To facilitate the comparison, the principal results are summarized and listed in Table. 7.1. The symbols are defined in Chapter 6. As concluded above, the core of the wall-attached streamwise vortex is located between 20-30 wall units. Moreover, many results show a transition point around $y^+ = 22.2$. Following that, in Table. 7.1, the studied wall region is divided into two parts to simplify the discussion : $14.5 < y^+ < 22$ and $22 < y^+ < 48$.

7.3.1 Evidence and characteristics of streamwise vortices

In the present study, the existence of streamwise vortices was firstly evidenced from the auto-correlation of wall-normal velocity fluctuations $R_{v'v'}$ (Fig. 5.4), which shows a clear elongated correlation zone between fluctuations of opposite signs. In Chapter 6.4, these vortices were put in evidence and characterized by a specific pattern recognition method. Finally, in the earlier section, the $R_{NVF-PVF}$ correlations also clearly evidence these vortices and can even be used to estimate their diameters.

From the above different tools, which allow to detect the streamwise vortices, a certain number of characteristics of these structures were put in evidence :

- In the field of investigation, the streamwise vortices are, on average, centred around $y^+ = 20$ to 30. This is shown by critical points in most of the results and particularly by the maximum frequency of appearance.
- The diameter of the vortices is about 40 wall units at $y^+ = 22.2$, which means that these vortices are wall-attached. It increases with wall distance up to 60 wall units at $y^+ = 48$, which suggests a lift up. The streamwise vortices do not originate at the wall but in the buffer layer, above the peak of turbulent kinetic energy (around $y^+ = 15$).
- The population of counter-rotating streamwise vortices is about 20% of the total (including both individual and counter-rotating vortices). Above $y^+ > 30$, most of them have a Ω-shaped.
- The mean spanwise distance between the same sign streamwise vortices is nearly a constant of about 107 wall units in the region $14.5 < y^+ < 18.5$ and about 127 wall units in the region $22 < y^+ < 40$. When $y^+ > 40$, the spanwise distance increases from about 127 wall units at $y^+ = 40$ to about 147 wall units at $y^+ = 48$. The mean spanwise distance between negative and positive legs of the same counter-rotating streamwise vortex, increases from about 39 wall units at $y^+ = 14.5$ to about 53 wall units at $y^+ = 48$. These spacings will be further interpreted in the following discussion.

		Streamwise vortices (GSV)		Ejections		Sweeps		Low speed streaks		High speed streaks	
y^+		< 22	> 22	< 22	> 22	< 22	> 22	< 22	> 22	< 22	> 22
N		1.5-2.7	2.7-1.1	4.5-5.2	5.2-4.5	4.2-4.0	4.0-3.1	2.9-2.75	2.75-2.1	2.8-2.4	2.4-1.6
φ	Mean	0	0	0	0	0	0	0	0	0	0
	PDF	Laplace		Laplace		Laplace		Laplace		Laplace	
$\lvert\varphi\rvert$	Mean	13±1.5	13±1.5	10-8	8-11.5	10	10-14.5	5.9-6.5	6.5-8.3	7.5±1	7.5±1
W_a^+	Mean	16±1	16±1	18	18-24	22-24	24-30	31	31-39	45±2	45±2
	PDF	Lognormal		Lognormal		Lognormal		Lognormal		Lognormal	
L_A^+	Mean	89-99	99-85	92-117	117-107	90	90	≈1000-1200	≈1000-1200	≈900-1100	≈900-1100
	PDF	Lognormal		Lognormal		Lognormal		/		/	
A_c^+	Mean	1400-1500	1500-1400	1600-2100	2100-2640	2240-2400	2400-2800	/	/	/	/
	PDF	Exponential		Exponential		Exponential		/		/	
d^+	Mean	107-127	127-147	123±5	123±5	123±5	123±5	125±10	125±10	125±10	125±10
	PDF	Rayleigh		Rayleigh		Rayleigh		Rayleigh		Rayleigh	
Other		GCSV									
y^+		< 22	> 22								
N		0.3-0.5	0.5-0.2								
φ	Mean	0	0-4								
φ_c	Mean	0	0-5								
d_c^+	Mean	39-43	43-53								

TAB. 7.1 – Summary of the principal results on coherent structures

- Apparently these ′streamwise′ vortices are not really streamwise. Their mean spanwise angle is zero due to the homogeneous property of the flow, but the histograms show that many streamwise vortices have a relatively large spanwise angle. The mean of the absolute value is nearly a constant of about 13 degrees with a fluctuation of about 1.5 degrees.
- The histogram of the spanwise angle is close to a Laplace distribution. The histogram of the spanwise distance between two nearby streamwise vortices with the same sign, follows nearly a Rayleigh distribution. This distribution also applies to the spanwise distance between negative and positive legs of the same counter-rotating streamwise vortex.

7.3.2 Strong link between ejections and streamwise vortices

Fig. 7.20 shows that there is a strong link between ejections and streamwise vortices. It is of interest to compare their characteristics in order to support this statement. The following characteristics of these structures are put into evidence from the present results :

- As for streamwise vortices, the results show that the wall distance y^+ =22.2 is a critical position for ejections. Their characteristics and their variation with wall distance are different below and above this point.
- The distribution of the frequency of appearance of ejections with wall distance is nearly the same as that of streamwise vortices. The maximum of both structures are located around $y^+ = 22$. The frequency of appearance of ejections is larger than two times that for streamwise vortices. This can be interpreted by the fact that ejections are outward motions and have a wider wall-normal development than the corresponding streamwise vortices.
- The mean width of ejections increases with wall distance. This results partly from the above-mentioned increasing diameter of streamwise vortices in this region. In addition, the width of ejections is slightly smaller than half the diameter of the vortices at the same wall distance.
- The mean spanwise distance between ejections is in the range of 118-128 wall units, which is comparable to that of streamwise vortices.
- The mean of the absolute spanwise angle decreases from 10 degrees at $y^+ = 14.5$ to 8 degrees at y^+ =22.2 and then increases up to 11.5 degrees at y^+ =48. It is slightly smaller than that of streamwise vortices which has a constant value of about 13 degrees.
- The histograms of the spanwise angle and the spanwise distance of ejections follow the same distribution pattern as those of streamwise vortices.
- The mean length of ejections is comparable to that of streamwise vortices. For both structures, the variation with wall distance is the same.

7.3.3 Strong link between sweeps and streamwise vortices

Fig. 7.22 shows that there is a strong link between sweeps and streamwise vortices as well. The following observations are made :

- Above y^+ =22.2, the frequencies of appearance of both sweeps and streamwise vortices decrease with wall distance. However, for sweeps, the maximum of this frequency is not located around y^+ =22.2 as that for the vortices but in fact below y^+ =15. This may be attributed to the fact that sweeps are inward motions in the flow and thus can develop themselves until very near the wall. This interprets also the fact that the frequencies of appearance of sweeps are higher than that of streamwise vortices.
- Similar to the diameter of streamwise vortices, the mean width of sweeps increases with wall distance. However, different from ejections, it is somewhat larger than half of the diameter at the same wall distance.
- The same as ejections, the mean spanwise distance is in the range of 118-128 wall units and is comparable to those of streamwise vortices.

- The mean of the absolute spanwise angle is a constant of about 10 degrees until y^+ =22.2 and then increases up to 14.5 degrees at y^+ =48. These values are comparable to those of streamwise vortices.
- The histograms of the spanwise angle and the spanwise distance of sweeps, follow a Laplace distribution and a Rayleigh distribution respectively, which is the same as for streamwise vortices.
- The mean length of sweeps is nearly the same as that of streamwise vortices in both the value and the variation with wall distance.

The above discussion confirms that ejections and sweeps are both strongly linked to streamwise vortices. However, there exist some differences between the results of ejections and sweeps. This will be discussed in detail later on.

7.3.4 Links between low speed streaks and streamwise vortices and between low speed streaks and ejections

Fig. 7.16 suggests that low speed streaks and streamwise vortices are related. Fig. 7.12 shows that most of ejections are associated with a low speed streak. It is thus of our interest to compare the characteristics of low speed streaks with those of streamwise vortices as well as of ejections. The following observations are made :

- The frequency of appearance of low speed streaks decreases with wall distance as that of streamwise vortices. At the same wall distance, the frequency of low speed streaks is comparable or even larger than that of streamwise vortices. For example, about 2.8 low speed streaks are detected per area of 530^+*300^+ at $y^+ = 22.2$ while only 2.7 are found for streamwise vortices. This seems to be conflicting to the general agreement that a low speed streak should be related to a packet of streamwise vortices (or hairpins) (Adrian *et al.* (2000)). As mentioned in Chapter 6.2, low speed streaks are much longer than the field of the investigation and thus many of them are incomplete (cut by borders of the field). According to the literature, the mean length of streaks is between 1000 - 2000 wall units, which is about 2 - 5 times the size of the present field. This may explain the above result.
- The mean width of low speed streaks is nearly a constant of about 31 wall units in the region $y^+ < 33$. Above that, it increases slowly with the wall distance up to 39 wall units. The value is somewhat smaller than the mean spanwise distance between negative and positive legs of the same counter-rotating streamwise vortex but still comparable. It is about two times that of ejections. The increase in the region $y^+ > 33$ is due probably to the merging of hairpins and the development of the Ω-shaped vortices.
- The mean spanwise distance varies between 115 and 125 wall units. This is comparable to streamwise vortices as well as ejections.
- The mean of the absolute spanwise angle increases from 5.9 degrees at $y^+ = 14.5$ to 8.3 degrees at $y^+ = 48.0$. It is smaller than that of streamwise vortices as well as of ejections. This may be attributed to the above-mentioned vortex packet theory that low speed streaks are induced by several streamwise vortices (or hairpin) (Adrian *et al.* (2000)).

- Compared to streamwise vortices and ejections, the histograms of the spanwise angle and the spanwise distance of low speed streaks have the same distribution pattern. This is also true for the spanwise distance of these structures.

7.3.5 Links between high speed streaks and streamwise vortices and between high speed streaks and sweeps

Fig. 7.18 and Fig. 7.14 show the links between high speed streaks and streamwise vortices as well as between high speed streaks and sweeps. The following observations can be drawn :

- Similar to streamwise vortices, the frequency of appearance of high speed streaks decreases with wall distance. The same argument used for low speed streaks justifies the fact that the frequency of high speed streaks is slightly larger than that of streamwise vortices at the same wall distance.
- The mean width of high speed streaks is nearly a constant of about 45 wall units with a fluctuation of 2 wall units. It is comparable to the mean spanwise distance between negative and positive legs of the same counter-rotating streamwise vortex. This value is about two times that of sweeps.
- The same as low speed streaks, the mean spanwise distance of high speed ones is between 115 and 125 wall units. It is comparable to those of other structures.
- The mean of the absolute spanwise angle is nearly a constant of 7.5. It is comparable to that of low speed streaks but smaller than those of streamwise vortices and sweeps.
- The histograms of the spanwise angle and the spanwise distance of high speed streaks follow the same distribution pattern as those of streamwise vortices and sweeps.

Globally, the characteristics of low and high speed streaks are comparable to those of streamwise vortices, ejections and sweeps, especially in terms of the variation with wall distance and the distribution pattern of histograms. It should be noted that there are also some differences in those characteristics. This will be explained in detail later.

7.3.6 Organization

Thus far, the most popular organization model of near wall turbulence is the one proposed by Adrian *et al.* (2000) (Fig. 7.26), which was presented in Chapter 2. According to this model, four main characteristics can be inferred :

1) Low speed streaks are surrounded by not only symmetrical hairpins but also asymmetrical ones. The legs of hairpins or Ω-shaped vortices are considered as streamwise vortices in the region close to the wall (e.g. $y^+ < 48$ in the present study).
2) The width of low speed streaks is comparable to the distance between the two legs of a hairpin.
3) The hairpins are lifted up except for the region very near to the wall.
4) The spanwise distance between low speed streaks is nearly equal to that of the streamwise vortices (or legs of hairpins) of the same sign.

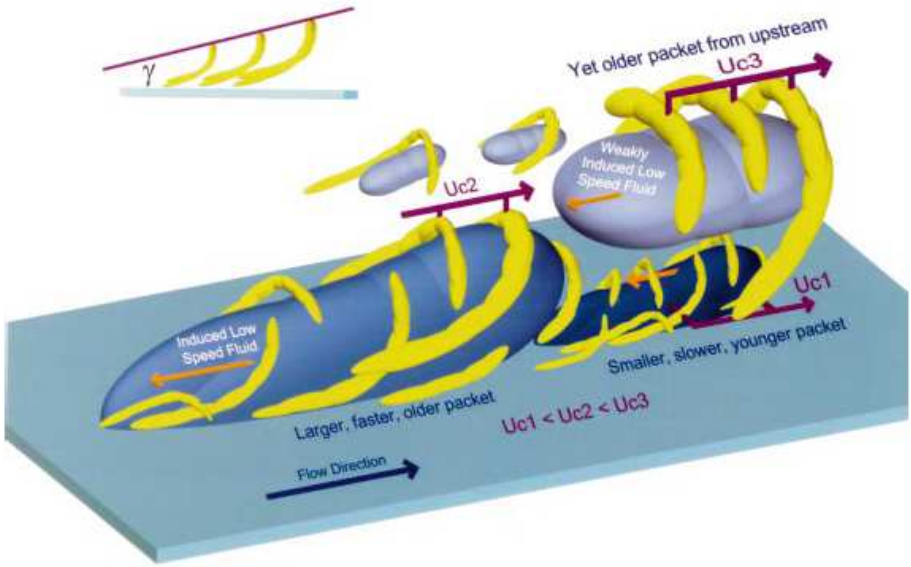

FIG. 7.26 – Organization model of Adrian *et al.* (2000) in near wall turbulence, U_{c1}, U_{c2} and U_{c3} are the convection velocities of each hairpin packet respectively

These characteristics are in complete agreement with the present results as shown above. Besides, Adrian *et al.* (2000) have also given a model concerning ejections and sweeps (Fig .7.27), which suggests that sweeps exist upstream and above the hairpin. In the present study sweeps are found to be associated with mainly streamwise vortices (legs of hairpin). Reconsideration of Fig. 7.26 indicates that the sweeps mentioned in Adrian *et al.* (2000) could be those created by the upstream vortices in the same packet or even those from an upstream upper packet.

In Adrian's model, very few quantitative characteristic parameters are given. In the present study, it is possible to assess some of them, such as size, intensity, direction of the vorticity of the hairpins and relative positions of low speed streaks and hairpins.

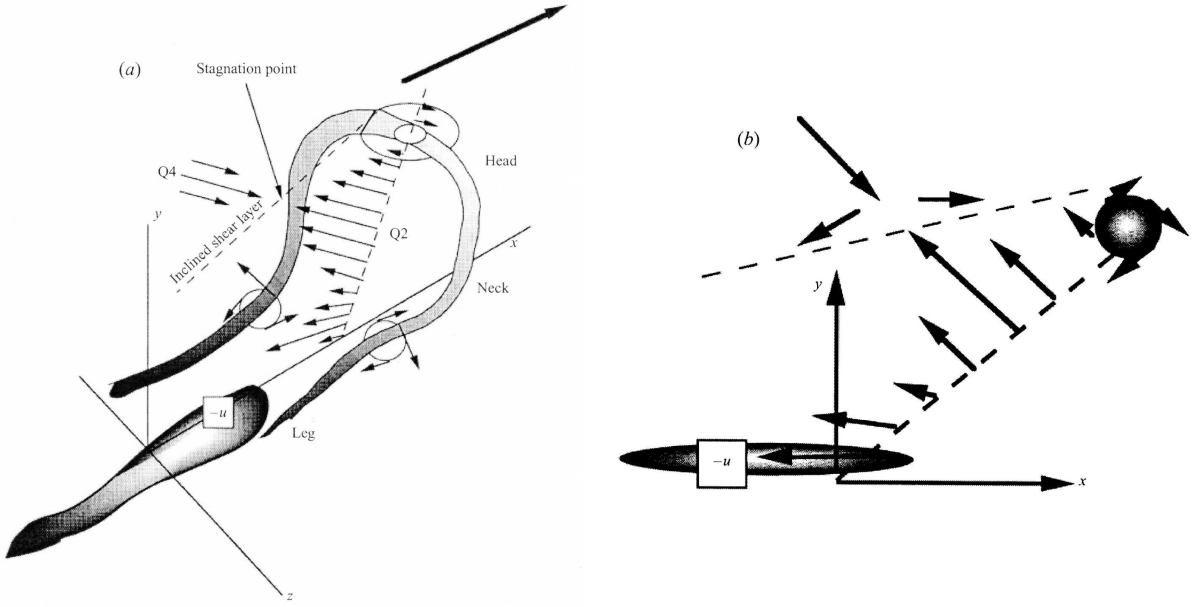

FIG. 7.27 – Organization model of Adrian *et al.* (2000) in near wall turbulence

As shown in Fig. 5.6 and 7.24, regions with positive wall-normal velocity fluctuations are slightly downstream of those with negative ones. This phenomenon can be explained based on the theory proposed by Hinze (1975), which is called ′U-loop deformation of a vortex line′. Fig. 7.28 illustrates the formation of a hairpin or an Ω-shaped vortex. A local disturbance of the spanwise vorticity component ω_Z can result in a symmetric or an asymmetric hairpin which can take a Ω- (case #1) or demi-Ω-shape (case #2 and #3) (to simplify the discussion, both of them are called ′Ω-shaped vortex′ in the following sections). As shown in the third stage in Fig. 7.28, in the region from A to B, the vortex line is supposed to remain nearly unchanged. From B to C a transition region exists, where the spanwise vorticity component ω_Z goes near to zero. The region from C to D is where the streamwise vortex (i.e. the legs of hairpin or cone vortex) can be found. This part should be nearly parallel to the streamwise-spanwise plane where ω_X is dominating. From D to E, another transition region where ω_Y grows, appears due to self-induction and lift-up of vortices. In the region around the head of the hairpin (or Ω-shaped) vortex (from E to F), the spanwise vorticity component ω_Z grows while the two other go back to zero. When the vortices are lifted up, the region from C to D can extend to point A and the vortices will have the shape shown in the fourth stage of Fig. 7.28, which is similar to the hairpins in Fig. 7.26.

In this development model, in the region from C to D, the vortex-induced streamwise velocity above the axis of the vortex is negative. This and the lift up of the low speed fluid reduce the local streamwise velocity of the main flow and thus generate a low speed region indicated in Fig. 7.29. This can cause a flow in rush to the wall on the downstream external side of the vortex, resulting in a lift-up of the vortex and of the related low speed regions (low speed streaks). In the region from E to F, the phenomenon is different. As shown in the Fig. 7.29, the low speed regions are generated below the head of the vortex. This

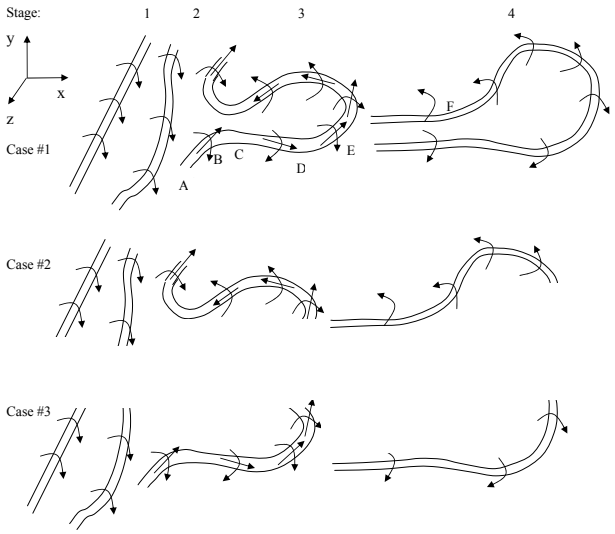

FIG. 7.28 – Conceptual model of the formation of a hairpin or Ω-shaped vortex

result suggests that the low speed regions are within the legs of hairpin vortex (streamwise vortices) but below the head of the hairpin.

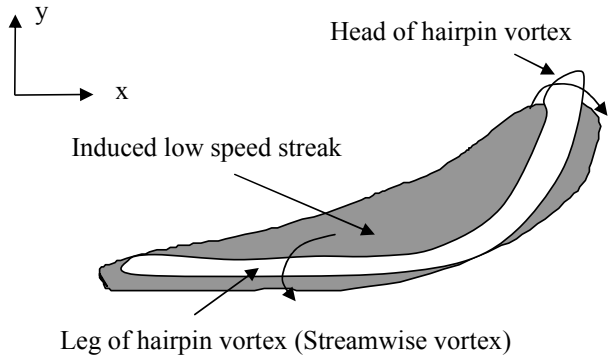

FIG. 7.29 – Organization model of a hairpin vortex and the induced low speed streak

Furthermore, in the region from C to D in Fig. 7.28, the vortex-induced streamwise velocity below the vortex axis and outside the hairpin is positive. This and the above-mentioned rush in of the flow to the wall increase the local streamwise velocity and thus induce high speed streaks. In the region from E to F, high speed regions are generated above the hairpin. These regions are usually much shorter than those in the region CD and not considered as high speed streaks. Fig. 7.30 shows the relative position of the hairpin and its induced high speed streak.

Similar to the generation of low and high speed streaks, ejections and sweeps can also be induced by a hairpin. Fig. 7.31 and 7.32 show respectively the relative position of the hairpin and the induced ejections and sweeps. In the region DE, the sizes of ejections and sweeps are smaller. As shown in Fig. 7.28, in this region, the wall-normal vorticity component ω_Y is much stronger than the other two components ω_X and ω_Z. Therefore, the vortex induced wall normal velocity is rather small. This leads to a smaller size of

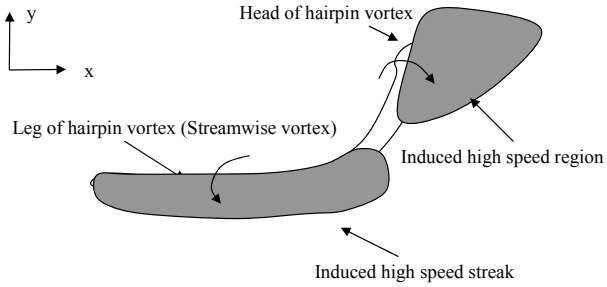

FIG. 7.30 – Organization model of a hairpin vortex and the induced high speed streak

ejections and sweeps.

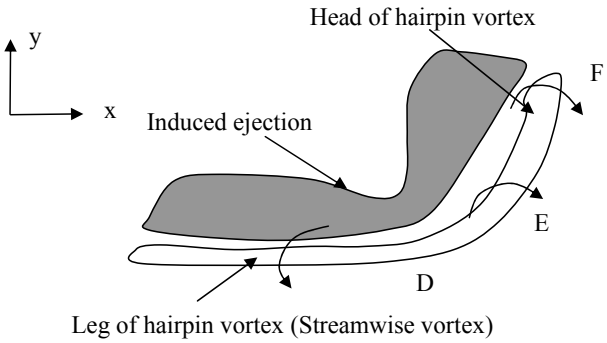

FIG. 7.31 – Organization model of a hairpin vortex and the induced ejection

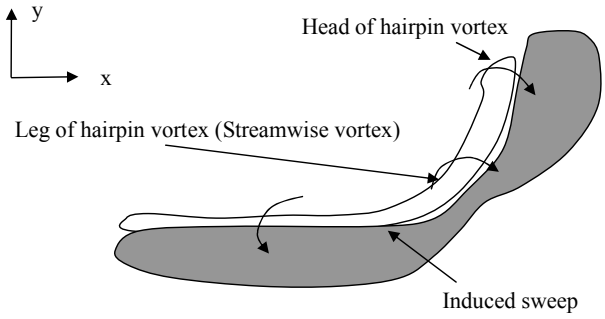

FIG. 7.32 – Organization model of a hairpin vortex and the induced sweep

Fig. 7.33 shows a combination of the above proposed models including the hairpins, low and high speed streaks and the corresponding ejections and sweeps. Fig. 7.33 also shows the projection of the above mentioned model on the streamwise-spanwise and wall-normal-spanwise planes. This model is plotted based on a nearly symmetric hairpin (Ω-shape). It is also valid for asymmetric hairpins. The above discussed model is an ideal average model. In a real flow, due to the effect of interaction and combination, symmetric or asymmetric hairpins and the coherent structures associated with them can form a more complicated structure organization (e.g. Fig. 7.26).

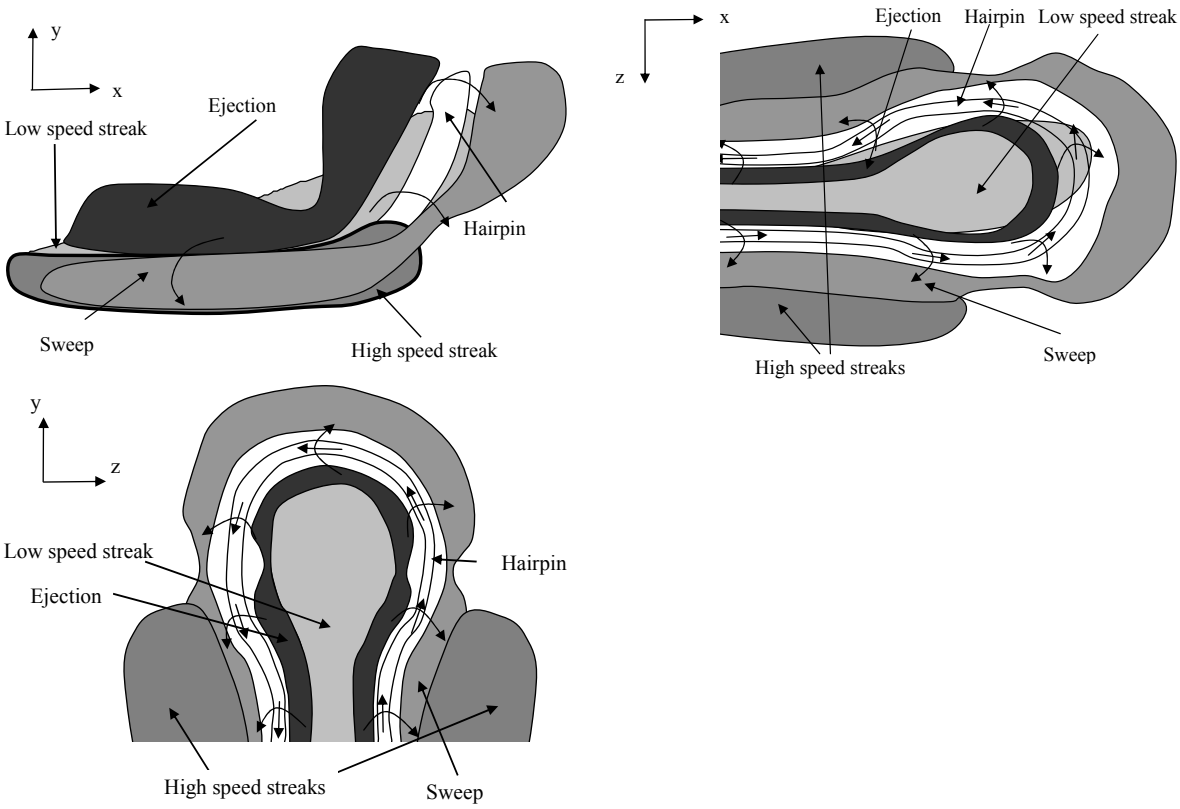

FIG. 7.33 – Organization model in near wall turbulence

In the present study, according to Fig. 7.12, Fig. 7.14, 7.16, 7.18, 7.20 and 7.22 in the streamwise-spanwise plane, three main conclusions are made :

- Ejections and sweeps are associated with low and high speed streaks respectively.
- Low speed steaks and ejections are located on the upstream right of negative streamwise vortices and upstream left of positive ones. Ejections are closer to streamwise vortices than low speed streaks.
- High speed steaks and sweeps are located on the downstream left of negative streamwise vortices and downstream right of positive ones. Sweeps are closer to streamwise vortices than high speed streaks.
- Low and high speed steaks are much larger than ejections, sweeps and streamwise vortices.

Based on these conclusions, in the streamwise-spanwise plane, two basic conceptual models of the organization of streaks, ejections, sweeps and streamwise vortices are proposed in Fig. 7.34. The reference structures are low and high speed streaks respectively. The streaks in Fig. 7.34 are much larger than ejections, sweeps and streamwise vortices. However in Fig. 7.33, these structures have comparable dimensions. The difference can be interpreted by the hairpin packet theory (Adrian *et al.* (2000)). As shown in Fig. 7.26, the large low speed streak is surrounded by several hairpins (symmetric or asymmetric) thus can be considered as a result of a combination of several small streaks induced by each hairpin in the packet. For ejections and sweeps, this combination does not exist.

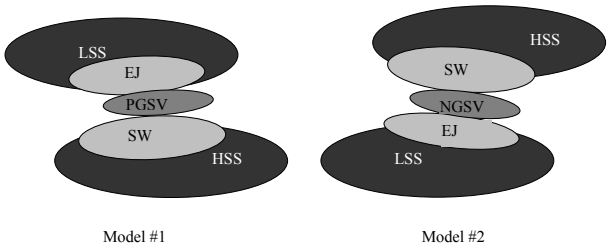

FIG. 7.34 – Basic conceptual models of organization

7.3.7 Interpretation of $R_{v'w'}$ correlations based on the modified model

Based on the models in Fig. 7.33 and 7.34, Fig. 7.35 to 7.37 show an explanation of some specific results of the correlation $R_{v'w'}$ (Fig. 5.19). To simplify this explanation, the vortex is assumed to be formed by a set of individual rings which are named by the location of the center (O_1 - O_5) and have the same diameter. The dash line which is the core of the vortex passes through the centers of all the rings. The rectangle CDEF is a streamwise-spanwise cross section. A_1 and A_2 are the most right and most left intersect positions of the vortex in cross-section CDEF. B_1 and B_2 are the intersect points of ring O_1 with cross-section CDEF. B_O is the center point of line B_1B_2. v'_{max} and w'_{max} are the maximum wall-normal and spanwise velocity fluctuations of the vortex. v'_1 and v'_2 are the wall-normal fluctuation at B_1 and B_2 respectively while w'_1 and w'_2 are the spanwise fluctuations at A_1 and A_2. D_{sv} is the diameter of the vortices. OC represents the distance to the wall. According to this distance, three particular regions are defined : OC $< 0.5D_{sv}$ (case #1), $0.5D_{sv} <$ OC$< D_{sv}$ (case #2) and OC $> D_{sv}$ (case #3).

In Case #1 (Fig. 7.35), the streamwise-spanwise cross-section can cut only the bottom half of a vortex. The correlation $R_{v'w'}$ is mainly from correlating the high spanwise velocity fluctuation w'_1 at A_1 and w'_2 at A_2 with high wall-normal fluctuation v'_1 at B_1 and v'_2 at B_2. As B_1 and B_2 are lower than the center of the vortex (line O_1O_2), three conclusions can be drawn : 1) v'_1 and v'_2 are smaller than v'_{max} ; 2) w'_1 is smaller than w'_{max} and w'_2 is equal to *it* ; 3) B_1B_2 is smaller than the diameter. When OC increases, v'_1, v'_2 and B_1B_2 increase but w'_1 decreases. In Case #2 (Fig. 7.36), the streamwise-spanwise cross-section cut through the core of the vortex. Different from case #1, v'_1 and v'_2 are equal to v'_{max} and B_1B_2 is equal to the diameter D_{sv}. When OC increases, v'_1, v'_2, w'_2 and B_1B_2 keep constant but w'_1 increases. In Case #3 (Fig. 7.37), the streamwise-spanwise cross-section cuts the rising vortex. Unlike Case #2, w'_1 is now equal to w'_{max}. And v'_1, v'_2, w'_1 , w'_2 and B_1B_2 are independent from OC .

As mentioned above, when OC $> D_{sv}$, w'_1 increases with wall distance and levels off at w'_{max}. This offers an explanation to the fact that the weak peaks appear and become more and more intense in the left of Fig. 5.19 when the wall distance increases.

The present study shows that the center of wall-attached streamwise vortex is located between $y^+ = 20$ and 30 wall units. As shown in Fig. 7.35, below this position the wall-normal fluctuations (v'_1, v'_2) are smaller than the maximum (v'_{max}) but the streamwise-spanwise cross-section passes through more rings. Beyond this position (Fig. 7.36 and

7.37), with increasing wall distance, the wall-normal fluctuations increase but the number of rings being cut decreases. This explains the result in Fig. 5.21 that the peak value is nearly constant in the region $y^+ < 22.2$ and decreases above it.

As shown in Fig. 5.22, the spanwise off-center distance increases with wall distance. Fig. 7.35 to 7.37 suggest that it results mainly from the increase in wall distance in the region $y^+ < 22$. In the region $y^+ > 22$, it may be caused by the increase in the diameter of the vortices (Fig. 7.24).

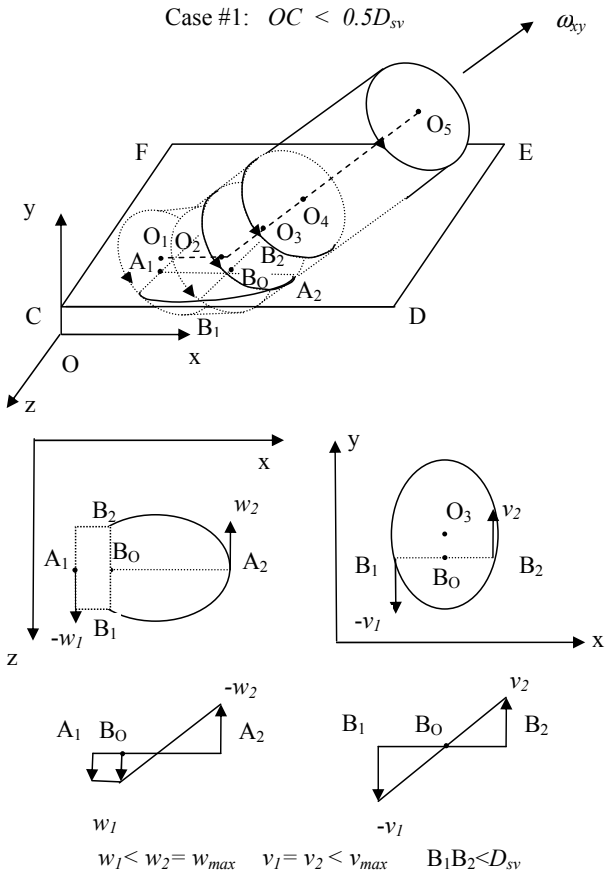

FIG. 7.35 – Conceptual model for cross-correlation $R_{v'w'}$ (case #1)

7.3.8 Vortex merging

In Fig. 7.10, the correlation $R_{NGSV-PGSV}$ shows two positive peaks at more or less symetric position with respect to Δz^+=0. The peak with a negative spanwise displacement Δz^+ is comparable to that with positive Δz^+. This seems to be in contradiction with the above hairpin model, which leads to the expectation of a peak only for positive Δz^+ as shown in Fig. 7.38. In order to explain this contradiction, one has to look at the possible ′merging′ of vortices.

This phenomenon has been reported and interpreted by previous authors. Perry and Chong (1982) assumed that the merging is a pure leg cancellation of the Λ-shape vortices, leaving only the merged portions contributing to the flow field. Wark and Nagib

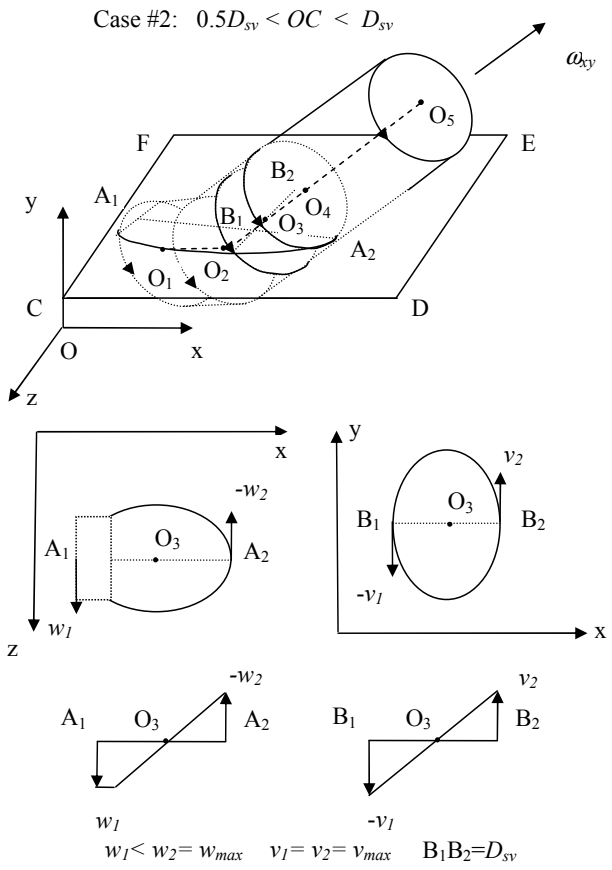

FIG. 7.36 – Conceptual model for cross-correlation $R_{v'w'}$ (case #2)

(1982) proposed an eddy-by-eddy basis via a vortex re-connection mechanism and suggested that it is complete annihilation of the legs of hairpin. Based on this eddy-by-eddy basis, Tomkins and Adrian (2003) concluded that the merging of vortex packets, and of associated low-momentum regions is a mechanism of spanwise scale growth. They have given three idealized potential spanwise merging scenarios based on hairpin vortices as shown in Fig. 7.39. The view is from above down to the wall with flow direction from left to right. Each merging scenario contains structures at three stages : before (t_0), during (t_1), and after (t_3) merging.

In Fig. 7.39a, two vortices with a comparable size are overlapped in the spanwise direction and move with slightly different convection velocities. When the vortices intersect, viscous re-connection occurs between the larger and smaller segments of the respective structures, resulting in two vortices (one with larger spanwise scale and one smaller) with rotation in the same direction as original ones. If the merging vortices happens to be aligned spanwise, such a streamwise interaction would result in only one stronger vortex of comparable scale. In Fig. 7.39b, the initial vortices interact in the spanwise direction, either growing or convecting into one another, resulting in a hairpin similar in shape as the original ones but larger in the spanwise scale. In Fig. 7.39c, initial hairpins interact in the spanwise direction, but the inner legs cross without annihilating. The same as the previous two cases, the dominant resulting structure is a hairpin vortex of larger spanwise

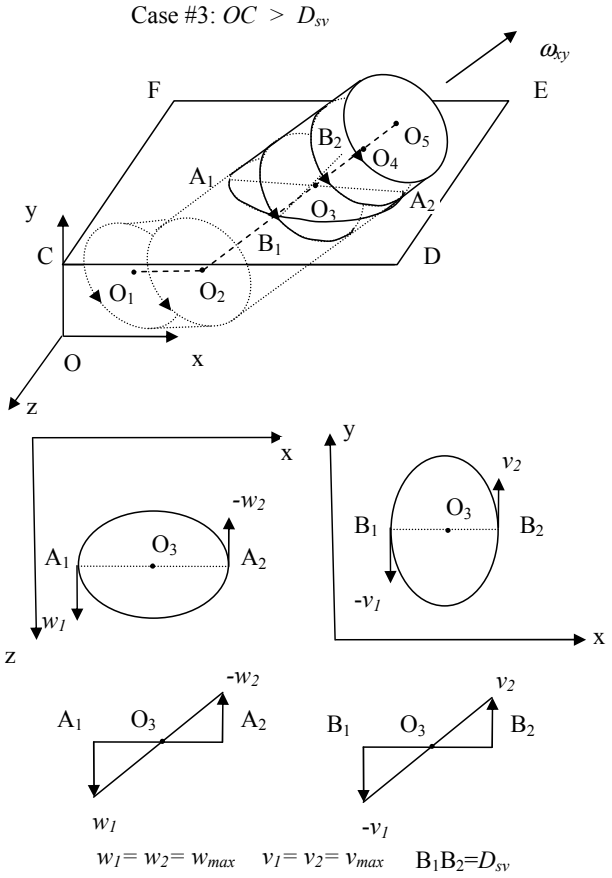

FIG. 7.37 – Conceptual model for cross-correlation $R_{v'w'}$ (case #3)

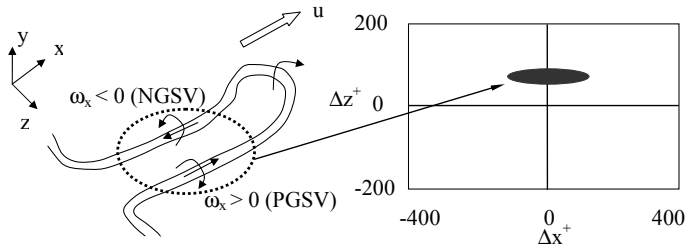

FIG. 7.38 – Theoretical correlation $R_{NGSV-PGSV}$ of hairpins

scale. The remaining fragments of the merged structures are also assumed to reconnect to form a smaller hairpin (black) which is rotating in the reverse direction.

As shown in Fig. 7.39, between t_0 and t_1, the interacting legs of two vortices are close to each other and have a relative position with the positive one on the left side of the negative one. This can correspond to the peak with negative Δz^+ in Fig. 7.9. Fig. 7.39 also shows that some pairs of interacting legs can take a Λ-shape. This is supported by the negative φ_c observed in Fig. 6.92b. The existence of this Λ-shape can explain in part the angle between regions with high correlations and the streamwise direction in Fig. 5.6 and 7.24.

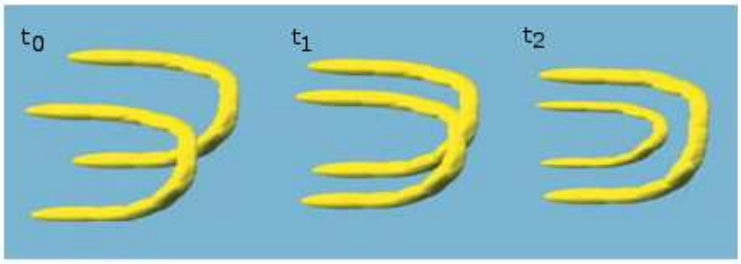

a : Overlap and pairing of outer structure, leaving a residual vortex with rotation in the same direction

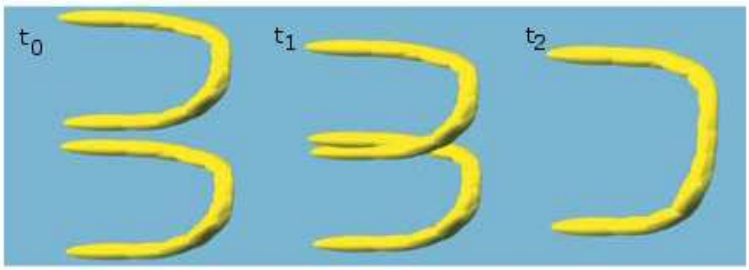

b : merging of outer structures with inner-leg annihilation

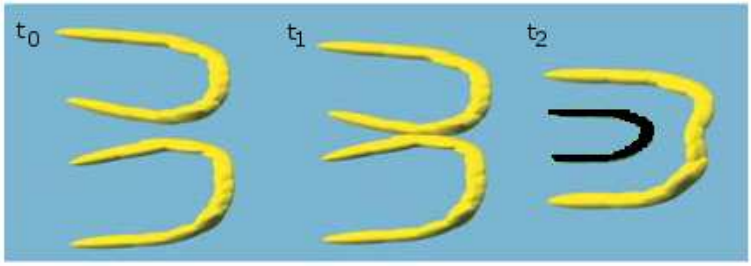

c : merging of outer structures without overlap, leaving a residual vortex with rotation in the opposite direction (black)

FIG. 7.39 – Idealized schematic of vortex merging scenarios (Tomkins and Adrian (2003))

Based on the scenarios in Fig. 7.39, Tomkins and Adrian (2003) have also given an idealized schematic of scale growth through vortex re-connection and packet merging (Fig. 7.40). Two packets are shown, each with 4 or 5 vortices. Upstream, at the time of observation, vortices in each packet induce an elongated low-speed region between their legs and underneath their heads. The downstream vortices in each packet have merged, or are in the process of merging, to create new structures with roughly double the spanwise scale. These larger vortices also induce a weaker low-speed region. Based on this scenario, Tomkins and Adrian (2003) evidenced the coalescence of low speed streaks. This is supported by the appearance of bifurcate streaks as shown in Fig. 6.7b.

Fig. 7.41 shows the ratio of the value of the peak with negative Δz^+ to that with the positive one of $R_{NGSV-PGSV}$ (Fig. 7.10) as a function of y^+. In the region $y^+ < 33$, the ratio is comparable. When $y^+ > 33$ this ratio decreases nearly linearly with wall distance and then levels off around $y^+ = 44$. This reveals that the merging occurs mainly between $y^+ = 33$ and 44. Below $y^+ = 33$, the large ratio suggests that the vortices involved in a merging, approach each other and prepare for this process. This is partly supported by

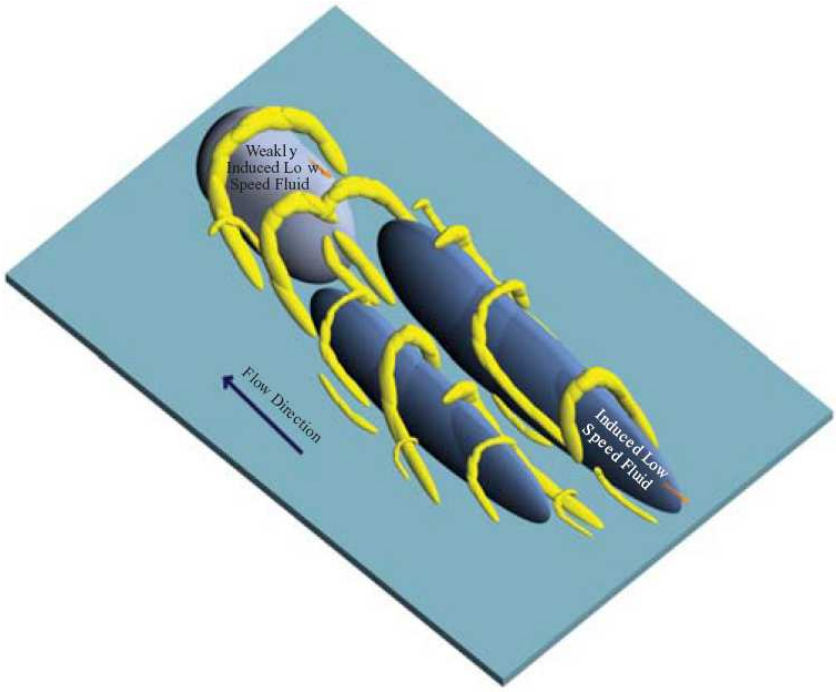

FIG. 7.40 – Idealized schematic of scale growth through vortex re-connection and packet merging (Tomkins and Adrian (2003))

the distribution of the frequency of appearance of low speed streaks with wall distance (Fig. 6.7) as well as the width of these streaks (Fig. 6.12). According to Tomkins and Adrian (2003), for low speed streaks, the main consequence of the merging is a decrease in the number but an increase in the width. In the present study, the frequency of appearance of low speed streaks is nearly constant at $y^+ < 33$ and decreases above $y^+ = 33$.

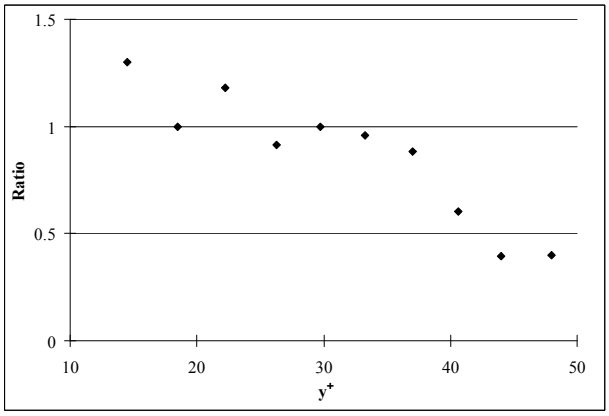

FIG. 7.41 – Ratio of the value of the negative peak to that of the positive one of the correlation $R_{NGSV-PGSV}$

As a conclusion, the present results support the idea of merging of individual hairpin vortices which is in the region $33 < y^+ < 44$.

Chapitre 8

Conclusions and Perspectives

8.1 Conclusions

The wall region of a turbulent boundary layer contains different coherent structures, which plays an important role in the turbulent energy generation and transport. Among them, three typical structures, namely low and high speed streaks, ejections and sweeps, and streamwise vortices, are the most documented. The objective of the present work was to study the characteristics of the turbulent flow in this region, to observe and quantify these structures and to investigate the spatial relations between them to provide an organization model near the wall.

To achieve this purpose, an experiment of stereo PIV was carried out on a fully developed turbulent boundary layer flow along a flat plate. This experiment was performed in a streamwise-spanwise plane parallel to the wall. 500 image pairs were recorded in each of 10 planes distributed between $y^+ = 14.5$ to 48. The Reynolds number based on the momentum thickness Re_θ was 7800.

In a first step, three methods, namely Image Mapping, Vector Warping and the Soloff technique, were compared in order to select the most suitable method of analysis for the present database. The comparison also took into consideration different interpolation and shift methods. The key parameters for the comparison were the computer time, the estimation of accuracy, the spatial spectra and velocity PDFs. It was concluded that the Soloff method with 3 calibration planes for projection and reconstruction, using integer shift for PIV analysis was the most suitable method to obtain the instantaneous 2D3C velocity fields.

Following that, using the obtained instantaneous 2D3C velocity fields, the basic statistical characteristics of the flow were studied. They include the mean streamwise velocity, velocity fluctuations, Reynolds shear stresses, spectra, PDFs, skewness and flatness. These results were validated by comparing them with those of Hot Wire Anemometry, DNS and the Van Driest model. The comparison shows that the results of SPIV are in good accordance with other results in the literature. This concludes that Stereoscopic PIV is a suitable method to study near wall turbulence.

In the next step, a detailed analysis of the spatial correlation was performed on the instantaneous velocity fields. The auto-correlations $R_{u'u'}$ and $R_{v'v'}$ evidence the existence

of streaks and streamwise vortices while the cross-correlation $R_{u'v'}$ reveals the existence of ejections and sweeps. Then, a detection of these coherent structures was set up based on a pattern recognition method. This method allows to create binary images of each structure. For streaks, ejections and sweeps, this detection procedure consists of four steps : Detection function definition thresholding, mathematical morphology and cleaning. The first one is to define the detection function according to the property of structures and the second one is to identify objects from the background. The third and the forth steps are to improve the quality of the detection. For streamwise vortices, it is the first time that a special method was applied to detect them in the streamwise-spanwise plane, based on the wall-normal velocity fluctuation and its spanwise gradient. This method first detects the objects with high fluctuation and gradient as for streaks, ejections and sweeps. Then, by considering the characteristics of the streamwise vortices, the relations between these objects were examined to detect the vortices.

Most of early research emphasizes on the mean statistics of these structures by means of conditional average and spatial or spatio-temporal correlations, etc. They can only provide an average behaviour. Benefiting from the binary image built here, not only the mean statistical characteristics but also the histograms and the variations with wall distance were analyzed for the first time in such a detail in the present study. The characteristics studied include mainly : frequency of appearance, spanwise angle, width, length, area, spanwise distance between the same structures.

The results show that the mean spanwise distance between low (or high) speed streaks is about 120 wall units. This value is nearly the same as those for ejections and sweeps as well as for negative (or positive) streamwise vortices. In general, it increases slowly with wall distance for all coherent structures under study. The present study also measures the distance between the closest low (or high) speed streaks. It is about 8-12% smaller than the distance between nearby streaks, indicating the misalignment property of this kind of structures. The distance between the two legs of counter-rotating vortices is about 45 wall units, which is comparable to the width of low speed streaks. Except for the frequency of appearance, histograms of the same characteristic of different structures follow the same distribution law : Laplace distribution for the spanwise angle, Lognormal distribution for the width and the length, Exponential distribution for the area and Rayleigh distribution for the spanwise distance. A significant number of the population of each structure have a spanwise angle when they travel downstream.

The present study shows that the wall attached streamwise vortices are centred in the region $20 < y^+ < 30$. In this region, the maximum or minimum of the characteristics studied was often observed, especially for ejections and streamwise vortices. The mean diameter of the steamwise vortices increases with wall distance.

Streaks are the largest structures in the present study. Low speed streaks have a width of about 35 wall units while high speed ones have about 45 wall units. Due to the limited size of the velocity field, the length of streaks cannot be measured directly if it is larger than 500 wall units (the streamwise dimension of the velocity field). In the present study, according to the two-point correlations, the length of streaks is estimated to be about 1000 wall units. Ejections have a width of about 20 wall units and a length of about 110 wall units. Sweeps are wider and shorter than ejections. Their mean width and length

are about 25 and 90 wall units respectively. The streamwise vortices have a comparable length with ejections and sweeps.

The correlations between structures show that ejections and sweeps are strongly linked to streamwise vortices. Ejections and sweeps are associated with low and high speed streaks respectively. The correlations also reveal that low speed steaks and ejections are on the upstream right of negative streamwise vortices and on the upstream left of positive ones while high speed steaks and sweeps are on the downstream left of negative streamwise vortices and downstream right of positive ones. Ejections and sweeps are closer to the streamwise vortices than streaks in both streamwise and spanwise directions.

The correlations of both velocity fluctuations and coherent structures show that for a streamwise vortex the part with negative wall normal fluctuations is on the upstream of the positive one. Moreover, the present results show that streaks are associated with a packet of streamwise vortices. This leads to the conclusion that low speed streaks are formed within a packet of streamwise vortices and high speed streaks are on the outside of them. As ejections and sweeps are associated with low and high speed streaks respectively, the above conclusion is also true for ejections and sweeps. The statistical analysis shows that the difference of the spanwise angle between positive and negative legs of a counter-rotating streamwise vortex has a positive value above $y^+ = 30$. This indicates that most of these vortices have a Ω-shape in this region. Besides, the analysis of correlation $R_{NGSV-PGSV}$ allows to evidence the merging phenomenon as described by Tomkins and Adrian (2003), mostly in the region $33 < y^+ < 44$.

The present results support the model of Adrian *et al.* (2000) except for the location of sweeps. Adrian *et al.* (2000) suggest that the sweeps are from out-layer while they are associated with the wall attached streamwise vortices in the present study. In this study, the model of Adrian *et al.* (2000) was improved and some characteristic dimensions were given. This modified model explains the fact that the peaks of conditional cross-correlations $R_{(v'>0)w'}$ and $R_{(v'<0)w'}$ have different off-centre distances in the spanwise as well as the streamwise directions. In addition, it interprets the appearance of the secondary peaks of these correlations.

8.2 Perspectives

In contrast to the rest of this thesis, in which we looked back and described what has been done, we look in this final section into the future. Here, the topics that are interesting for further investigation are listed.

As well known, the Reynolds number is important to the near wall turbulence. The characteristics of a turbulent flow can be very different between low and high Reynolds numbers. As the present study used only one Reynolds number, it would be interesting to investigate the effect of the Reynolds number on the statistics of coherent structures.

The present results as well as the literature show that the streamwise vortices are lifted up with an angle about 45 degrees with respect to the streamwise-spanwise plane when travelling downstream. This suggests several interesting extensions for the investigation of near wall turbulence. A plane inclined to the wall at about 45 degrees upstream can be used to measure the diameter of the vortices more precisely. A plane inclined to the

wall at about 45 degrees downstream can be used to show the evolution of the hairpin or Ω-shape vortices. In addition, the experiment on the streamwise-wall-normal plane is able to evidence the theory of hairpin packets and to study their characteristics (e.g. angle inclined to the wall, streamwise distance, secondary vortices, etc.).

The present experiment was performed with a low sampling rate, which makes it impossible to investigate the evolution of the structures with time. Taking advantage of the rapid development of high speed cameras, it is now possible to study the interactions between different structures as well as their consequences on the variation of characteristics with time. It could also be interesting to conduct the time dependent experiments for the different Reynolds numbers and different plane orientations.

Nearly no experimental techniques can measure the 3D3C velocity field. Therefore, it is difficult to visualize directly the spatial organization of the coherent structures in three dimension fields. Benefiting from the development of DNS, the turbulent flows can be simulated completely at low Reynolds numbers. It would be of interest to use the results of numerical simulations to examine and improve the findings of the experiments.

In the present study, above $y^+ = 40$, the variations of some characteristics with wall distance change their tendencies. In this region, the behaviours are different from those very near the wall and should be investigated in more detail.

The present study was done on a smooth wall, however, in practice, many surfaces are rough (e.g. the water flow over a barnacled ship's hull, oil flow through industrial pipework). Therefore, the characteristics of the flow near the wall can differ from those over smooth surfaces. This requires additional investigation. For example, the research can be done by comparing the characteristics of the structures and by determining the roughness beyond which the structure pattern becomes very different from the smooth wall.

Bibliographie

Acarlar MS, R SC (1987). "A study of hairpin vortices in a laminar boundary layer. I-Hairpin vortices generated by a hemisphere protuberance. II-Hairpin vortices generated by fluid injection." *Journal of Fluid Mechanics*, **175**, 1–41.

Achia BU, Thompson DW (1977). "Structure of the turbulent boundary in drag-reducing pipe flow." *Journal of Fluid Mechanics*, **81**, 439–464.

Adrian RJ (1991). "Particle imaging techniques for experimental Journal of Journal of Fluid Mechanicsanicsanics." *Ann. Rev. Journal of Journal of Fluid Mechanicsanics.*, **23**, 261–304.

Adrian RJ, Meinhart CD, Tomkins CD (2000). "Vortex organization in the outer region of the turbulent boundary layer." *Journal of Fluid Mechanics*, **422**, 1–54.

Adrian RJ, Moin P (1988). "Stochastic estimation of organized turbulent structure : homogeneous shear flow." *Journal of Fluid Mechanics*, **190**, 531–559.

Alfredsson PH, Johansson AV (1984). "On the detection of turbulence-generating events." *Journal of Fluid Mechanics*, **139**, 325–345.

Asai M, Sawada K, Nishioka M (1996). "Development of turbulent patch in a subcritical boundary layer." *Fluid Dynamics Research*, **18**, 1151–1168.

Aubry N, Holmes P, L LJ, Stone E (1988). "The dynamics of coherent structures in the wall region of a turbulent boundary layer." *Journal of Fluid Mechanics*, **192**, 115–173.

Bakewell HP, Lumley JL (1967). "Viscous Sublayer and Adjacent Wall Region in Turbulent Pipe Flow." *Physics of Fluids*, **10**, 1880–1889.

Balint JL, Wallace JM, vukoslavcecvic P (1991). "The velocity and vorticity vectro fields of a tubulent boundary layer. Part 2. Statistical preperties." *Journal of Fluid Mechanics*, **228**, 53–86.

Bandyopadhyay P (1980). "Large structure with a characteristic upstream interface in turbulent boundary layers." *Physics of Fluids*, **23**, 2326.

Benney DJ (1961). "A non-linear theory for oscillations in a parallel flow." *Journal of Fluid Mechanics*, **10**, 209–236.

Benney DJ, Gustavsson LH (1981). "A new mechanism for linear and nonlinear hydrodynamic instabilities." *Studies in Applied Mathematics*, **64**, 185–209.

Bernard PS, Thomas JM, Handler RA (1993). "Vortex dynamics and the production of Reynolds stress." *Journal of Fluid Mechanics*, **253**, 385–419.

Bippes H (1972). "Experimentelle Untersuchung des laminar-turbulenten Umschlags an einer parallel angestroemten konkaven Wand." *Heidelb. Akad. Wiss., Math. Naturwiss. Kl.*, pp. 103–180.

Blackwelder RF (1983). "Large scale motion in turbulent boundary layers." *In Von Karman Inst. for Fluid Dynamics Turbulent Shear Flows*, **N84-15448**, 06–34.

Blackwelder RF, Eckelmann H (1979). "streamwise vortices associated with the bursting phenomenon." *Journal of Fluid Mechanics*, **94**, 577–594.

Blackwelder RF, Kaplan RE (1976). "On the wall structure of the turbulent boundary layer." *Journal of Fluid Mechanics*, **76**, 89–112.

Bogard DG, Tiederman WG (1987a). "Burst detection with single-point velocity measurements." *Journal of Fluid Mechanics*, **162**, 389–413.

Bogard DG, Tiederman WG (1987b). "Characteristics of ejections in turbulent channel flow." *Journal of Fluid Mechanics*, **179**, 1–19.

Brooke JW, Hanratty TJ (1993). "Origin of turbulence producing eddies in a channel flow." *Physics of Fluids*, **5(4)**, 1011–1022.

Brown GL, Thomas ASW (2002). "Large structure in a turbulent boundary layer." *Physics of Fluids*, **20**, 243–252.

Butler KM, Farrell BF (1993). "Optimal perturbations and streak spacing in wall-bounded shear ows." *Physics of Fluids*, **5(3)**, 774–777.

Calluaud D, David L (2004). "3D PIV measurements of the flow around a surface-mounted block." *Experiments in Fluids*, **36**, 53–61.

Carlier J (2001). *Etude des structures cohérentes de la turbulence de paroi à grand nombre de Reynolds par vélocimétrie par images de particules.* Ph.D. thesis, Univercity Lille 1.

Carlier J, Stanislas M (2005). "Experimental study of eddy structures in a turbulent boundary layer using paritcle image velocimetry." *Journal of the Aeronautical Sciences*, **535**, 143–188.

Chen CHP, Blackwelder RF (1978). "Large-scale motion in a turbulent boundary layer : a study using temperature contamination." *Journal of Fluid Mechanics*, **89**, 1–31.

Chernyshenko SI, Baig MF (2005). "The mechanism of streak formation in near-wall turbulence." *Journal of Fluid Mechanics*, **544**, 99–131.

Christensen KT, Adrian RJ (2001). "Statistical evidence of hairpin vortex packets in wall turbulence." *Journal of Fluid Mechanics*, **431**, 433–443.

Corino ER, Brodkey RS (1969). "A visual investigation of the wall region in turbulent flow." *Journal of Fluid Mechanics*, **37**, 1–30.

Coudert S, Schon JP (2001). "Back projection algorithm with misalignment corrections for 2D3C Stereoscopic PIV." *Measurement Science and Technology*, **12**, 1371–1381.

Delo CJ, Kelso RM, Smits AJ (2004). "Three-dimensional structure of a low-Reynolds-number turbulent boundary layer." *Journal of Fluid Mechanics*, **512**, 47–83.

Doligalski TL, Walker JDA (1984). "The boundary layer induced by a convected two-dimensional vortex." *Journal of Fluid Mechanics*, **139**, 1–28.

Ersoy S, A WJD (1985). "Viscous flow induced by counter-rotating vortices." *Physics of Fluids*, **28**, 2687–2698.

Fei R, Merzkirch W (2004). "Investigations of the measurement accuracy of stereo particle image velocimetry." *Experiments in Fluids*, **37**, 559–565.

Fernholz HH, Finley PJ (1996). "The incompressible zero-pressure-gradient turbulent boundary layer : An assessment of the data." *Prog. Aerospace Sci.*, **32**, 245–311.

Ferrell JK, Richardson FM, Beatty KO (1955). "Dye displacement technique for velocity distribution measurement." *Industrial and engineering chemistry*, **47**, 29.

Fortuna G, Hanratty TJ (1972). "The influence of drag-reducing polymers on turbulence in the viscous sublayer." *Journal of Fluid Mechanics*, **53**, 575–586.

Foucaut J, Carlier J, Stanislas M (2004a). "PIV optimization for the study of turbulent flow using spectral analysis." *Measurement Science and Technology*, **15**, 1046–1058.

Foucaut J, Miliat B, Perenne N, Stanislas M (2004b). "Characterization of different PIV algorithms using the EUROPIV Synthetic Image Generator and real images from a turbulent boundary layer." *Proceeding of the EUROPIV 2 Workshop on Particle Image Velocimetry, Ed. Springer-Verlag*, pp. 163–186.

Foucaut JM, Stanislas M (2002). "Some considerations on the accuracy and frequency response of some derivative filters applied to particle image velocimetry vector fields." *Measurement Science and Technology*, **13**, 1058–1071.

Gonzalez R, Woods RE (2001). "Digital Image Processing." *Prentice-Hall. Inc. (2nd edition)*.

Grass A, Mansour-Tehrani M (1996). *Generalized Scaling of Coherent Bursting Structures in the Near-wall Region of Turbulent Flow over Smooth and Rough Boundaries*. Wiley.

Grass AJ (1971). "Structural features of turbulent flow over smooth and rough boundaries." *Journal of Fluid Mechanics*, **50**, 233–255.

Guezennec Y (1985). *Documentation of large coherent structures associated with wall events*. Ph.D. thesis, Ill. Inst. Technol., Chicago.

Guezennec YG, Choi WC (1989). "Stochastic estimation of coherent structures in turbulent boundary layers." *In Proc. Zoran P. Zaric Memorial International Seminar on Near Wall Turbulence (ed. S. J. Kline and N. H. Afgan)*, **May 1988, Hemisphere**, 420–436.

Guezennec YG, Piomelli U, Kim J (1987). "Conditionally-averaged structures in wall-bounded turbulent flows." In "Proc. 1987 Summer Program, Center for Turbulence Research," Stanford University. CTR-S87.

Gupta AK, Laufer J, Kaplan RE (1971). "Spatial structure in the viscous sublayer." *Journal of Fluid Mechanics*, **50**, 493–512.

Haidari AH, R SC (1994). "The generation and regeneration of single hairpin vortices." *Journal of Fluid Mechanics*, **277**, 135–162.

Hall P, Horseman NJ (1991). "The linear inviscid secondary instability of longitudinal vortex structures in boundary layers." *Journal of Fluid Mechanics*, **232**, 357–375.

Hama FR (1954). "Boundry Layer Characteristics for Smooth and Rough Surfaces." *Trans. Soc. Nav. Arch. Mar. Engrs*, **62**, 233–255.

Hama FR (1962). "Streaklines in a Perturbed Shear Flow." *Physics of Fluids*, **5**, 644.

Hama FR, J N (1963). "Detailed flow-field observations in the transition process in a thick boundary layer." Stanford University Press.

Hamilton J, Kim J, Waleffe F (1995). "Regeneration mechanisms of near-wall turbulence structures." *Journal of Fluid Mechanics*, **287**, 317–348.

Hastings NAJ, Peacock JB (1975). "Statistical Distribution : A Handbook for Students and Practitioners." *John Wiley, New York*.

Head MR, Bandyopadhyay PR (1981). "New aspects of turbulent boundary-layer structure." *Journal of Fluid Mechanics*, **107**, 297–338.

Heijmans HJAM (1994). "Morphological image operators." *Advances in Electronics and Electron Physics Suppl., Boston : Academic Press*.

Helmholtz H (1868). "On discontinuous movements of fluids." *Phil. Mag.*, **36**, 337–346.

Hetsroni G, Rozenblit R (1994). "Heat transfer to a liquid-solid mixture in a flume." *International Journal of Multiphase Flow*, **20(4)**, 671–689.

Hetsroni G, Rozenblit R, Yarin LP (1997). "Thermal streaks regeneration in the wake of a disturbance in a turbulent boundary layer." *International Journal of Heat and Mass Transfer*, **40**, 4161–4168.

Hinze JO (1975). *Turbulence*. McGraw Hill, New York.

Jang PS, Benney DJ, Gran RL (1986). "On the origin of streamwise vortices in a turbulent boundary layer." *Journal of the Aeronautical Sciences.*, **169**, 109–123.

Jeong J, Hussain F (1995). "On the identification of a vortex." *Journal of Fluid Mechanicsanics*, **285**, 69–94.

Jeong J, Hussain F, Schoppa W, Kim J (1997). "Coherent structures near the wall in a turbulent channel flow." *Journal of Fluid Mechanics*, **332**, 185–214.

Jimenez J, Moin P (1991). "The minimal flow unit in near-wall turbulence." *Journal of Fluid Mechanics*, **225**, 213–240.

Jimenez J, Orlandi P (1993). "The rollup of a vortex layer near a wall." *Journal of Fluid Mechanics*, **248**, 297–313.

Jimenez J, Pinelli A (1999). "The autonomous cycle of near-wall turbulence." *Journal of Fluid Mechanics*, **389**, 335–359.

Johansson AV, Alfredsson PH (1982). "On the structure of turbulent channel flow." *Journal of Fluid Mechanics*, **122**, 295–314.

Johansson AV, Alfredsson PH, Kim J (1991). "Evolution and dynamics of shear-layer structures in near-wall turbulence." *Journal of Fluid Mechanics*, **224**, 579–599.

Kaftori D, Hetsroni G, Banerjee S (1994). "Funnel-shaped vortical structures in wall turbulence." *Physics of Fluids*, **6**, 3035–3050.

Kahler CJ (2004). "Investigation of the spatio-temporal flow structure in the buffer region of a turbulent boundary layer by means of multiplane stereo PIV." *Experiments in Fluids*, **36**, 114–130.

Keane R, Adrian RJ (1990). "Optimisation of particle image velocimeters-Part I : Double pulsed systems." *Measurement Science and Technology*, **1**, 1202–1215.

Kim HT, Kline SJ, Reynolds WC (1971). "The production of turbulence near a smooth wall in a turbulent boundary layer." *Journal of the Aeronautical Sciences*, **50**, 133–160.

Kim J, Moin P, Moser R (1987). "Turbulence statistics in fully developed channel flow at low Reynolds number." *Journal of Fluid Mechanics*, **177**, 133–166.

Klebanoff PS, Tidstrom KD, Sargent LM (1962). "The three-dimensional nature of boundary layer instability." *Journal of Fluid Mechanics*, **12**, 1–34.

Kline SJ (1978). "The role of visualization in the study of the turbulent boundary layer." *Cohereent Structure of turbulent boundary layers*, **Lehigh ; AFOSR**, 1–26.

Kline SJ, Reynolds WC, FA S, W RP (1967). "The stucture of turbulent boundary layers." *Journal of the Aeronautical Sciences*, **30**, 741–773.

Kline SJ, Runstadler PW (1959). "Some preliminary results of visual studies of the flow model of the wall layers of the turbulent boundary layers." *Trans. ASME*, **Ser. E Vol 2**, 166–170.

Kreplin HP (1976). *An experimental investigation of the streamwise and spanwise velocity fluctuations in a turbulent channel flow.* Ph.D. thesis, George-August-University zu GSttingen.

Kreplin HP, Echelmann H (1979). "Propagation of pertubations in the viscous sublayer and adjacent wall region." *Journal of Fluid Mechanics*, **59**, 305–322.

Lagraa B, Labraga L, Mazouz A (2004). "Characterization of low speed streaks in the near-wall region of a turbulent boundary layer." *European Journal of Mechanics B/Fluids*, **23**, 587–599.

Landahl MT (1990). "On sublayer streaks." *Journal of Fluid Mechanics*, **212**, 593–614.

Lawson N, Wu J (1997). "Three-Dimensional particle image velocimety : experimental error analysis of digital angular stereoscopic system." *Measurement Science and Technology*, **8**, 1455–1464.

Lee M, Kim J, Moin P (1990). "Structure of turbulence at high shear rate." *Journal of Fluid Mechanics*, **216**, 561–583.

Lee MJ, Eckelman L, Hanratty TJ (1974). "Identification of turbulent wall eddies through the phase relation of the components of the fluctuating velocity gradient." *Journal of Fluid Mechanics*, **66**, 17–33.

Lele SK (1992). "Compact Finite Difference Schemes with Spectral-like Resolution." *Journal of Computational Physics*, **103**, 16–42.

Lin J, Foucaut JM, Laval JP, Stanislas M (2004). "Optimization de la PIV Stéréoscopique pour la caractérisation de la turbulence de paroi." *9ème Congrès Francophone de Vélocimétrie Laser*, **G1**, 1–8.

Lourenco L (1986). Von Karmann Institute for Fluid Dynamics, Lecture Series 1988-06.

Lu LJ, Smith CR (1991). "Use of flow visualization data to examine spatial-temporal velocity and burst-type characteristics in a turbulent boundary layer." *Journal of Fluid Mechanics*, **232**, 303–340.

Lu SS, Willmarth WW (1973). "Measurements of the structure of the Reynolds stress in a turbulent boundary layer." *Journal of Fluid Mechanics*, **60**, 481–511.

Maragos P, Schafer RW (1990). "Morphological systems for multidimensional signal processing." *Proceedings of the IEEE*, **78**, 690–710.

Marusic I (2001). "On the role of large-scale structures in wall turbulence." *Physics of Fluids*, **13(3)**, 735–743.

Matheron G (1975). "Random sets and Integral Geometry." *Wiley and sons. New York.*

Meyer F (1977). "Constrast features extraction." *In : Chermant JL, ed. Quantitative Analysis of microstructures in Materials Science, Biology and Medecine. Stuttgart : Riederer Verlag*, pp. 374–380.

Nakagawa H, Nezu I (1981). "Structure of space time correlations of bursting phenomena in an open channel flow." *Journal of the Aeronautical Sciences*, **104**, 1–43.

Nikitin NV, Chernyshenko SI (1997). "On the nature of the organised structures in turbulent near-wall flows." *Journal of Fluid Mechanics*, **32(1)**, 18–23.

Nychas SG, Hershey HC, Brodkey RS (1973). "A visual study of turbulent shear flow." *Journal of Fluid Mechanics*, **61**, 513–540.

Offen GR, Kline SJ (1974). "Combined dye-streak and hydrogen-bubble visual observations of a turbulent boundary layer." *Journal of Fluid Mechanics*, **62**, 223–239.

Oldaker oK, Tiederman WJ (1977). "Spatial structure of the viscous sublayer in drag-reducing channel flow." *Phys. Fluid*, **20**, S133–144.

Orlandi P (1990). "Vortex dipole rebound from a wall." *Physics of Fluids*, **A2**, 1429–1436.

Panton RL (1997). *Self-Sustaining Mechanisms of Wall Turbulence.* Computational Mechanics Publications, Southampton, UK.

Paulus DWR, Hornegge J (1998). "Applied Pattern Recognition." *Vieweg (2nd edition).*

Perry AE, Chong MS (1982). "On the mechanism of wall turbulence." *Journal of Fluid Mechanics*, **119**, 173–217.

Phillips WRC, Wu Z, Lumley J (1996). "On the formation of longitudinal vortices in a turbulent boundary layer over wavy terrain." *Journal of Fluid Mechanics*, **326**, 321–341.

Prasad AK, Adrian RJ (1993). "Stereoscopic particle image velocimetry applied to liquid flows." *Experiments in Fluids*, **15**, 49–60.

Praturi AK, Brodkey RS (1978). "A stereoscopic visual study of coherent structures in turbulent shear flowr." *Journal of Fluid Mechanics*, **89**, 251–272.

Pérenne N, Foucaut JM, Savatier J (2004). "Study of the accuracy of different stereoscopic reconstruction algorithms." *Proceeding of the EUROPIV 2 Workshop on Particle Image Velocimetry, ed. Springer-Verlag*, pp. 375–390.

Preston KJ, Duff MJB (1984). "Modern Cellular Automata." *Plenum Press, New York.*

Raffel M, Gharib M, Ronneberger O, Kompenhans J (1995). "Feasibility study of three-dimensional PIV by correlating images of particles within parallel light sheets." *Experiments in Fluids*, **19**, 69–77.

Rajagopalan S, Antonia RA (1984). "Conditional averages associated with the fine structure in a turbulent boundary layer." *Physics of Fluids*, **27(8)**, 1966–1973.

Rao KN, Narasimha R, Narayanan BMA (1971). "The bursting phenomenon in a turbulent boundary layer." *Journal of Fluid Mechanics*, **48**, 339–352.

Raupach MR (1981). "Conditional statistics of Reynolds stress in rough-wall and smooth-wall turbulent boundary layers." *Journal of Fluid Mechanics*, **108**, 363–382.

Reynolds WC, Hussain AKMF (1981). "The mechanics of an organized wave in turbulent shear flow." *Journal of Fluid Mechanics*, **54**, 263–288.

Robinson SK (1991). "Coherent Motions in the Turbulent Boundary Layer." *Annual Review of Journal of Journal of Fluid Mechanicsanicsanics*, **23**, 601–639.

Robinson SK (1993). "The kinematics of turbulent boundary layer structure." *NASA Technical Memorandum*, **103859**.

Rogers MM, Moin P (1987). "The structure of the vorticity field in homogeneous turbulent flows." *Journal of Fluid Mechanics*, **176**, 33–66.

Runstadler PC, Kline SJ, Reynolds WC (1963). "Dept Mech. Engng, Stanford University, Rep." *Trans. Soc. Nav. Arch. Mar. Engrs*, pp. MD–8.

Scarano F, David L, Bsibsi M, Calluaud D (2005). "S-PIV comparative assessment : image dewarping+misalignment correction and pinhole+geometric back projection." *Experiments in Fluids*, **39**, 257–266.

Scarano F, Riethmuller R (2000). "Advances in iterative multi-grid PIV image processing." *Experiments in Fluids [Suppl.]*, pp. S51–S60.

Schlichting H (1979). *Boundary Layer Theory*. McGraw Hill, New York.

Schoppa W, Hussain AKMF (1998). "Formation of near-wall streamwise vortices by streak instability." In "Tech. Rep. 98-3000. AIAA, 29th AIAA Fluid Dynamics Conf," Albuquerque, NM, U.S.A.

Schoppa W, Hussain F (1997). "Effective drag reduction by large-scale manipulation of streamwise vortices in near-wall turbulence." In "AIAA, Shear Flow Control Conference," Snowmass Village, CO ; UNITED STATES.

Schoppa W, Hussain F (2002). "Coherent structure generation in near-wall turbulence." *Journal of Fluid Mechanics*, **453**, 57–108.

Schraub FA, Kline SJ (1965). "A study of the structure of the turbulent boundary layer with and without longitudinal pressure gradients." *Thermosciences Division Stanford University*, pp. MD–12.

Schubauer GB, Skramstad HK (1948). "Laminar Boundary Layer Oscillation and Transition on a Flat Plate." *NACA Report*, **909**.

Serra J (1982). "Image Analysis and Mathematical Morphology." *Academic Press, London.*

Serra J (1988). "Image Analysis and Mathematical Morphology. Part II : Theoretical Advances." *Academic Press, London.*

Smith CR (1984). "A synthesized model of the near-wall behavior in turbulent boundary layers." In "Proc. 8th Symp. on turbulence," University of Missouri-Rolla.

Smith CR, Metzler SP (1983). "The characteristics of low speed streaks in the near wall region of a turbulent boundary layer." *Journal of the Aeronautical Sciences*, **129**, 27–54.

Smith CR, Walker JDA (1997). "Sustaining mechanisms of turbulent boundary layers-The role of vortex development and interactions." *Computational Mechanics Publications (Advances in Journal of Journal of Fluid Mechanicsanicsanics Series)*, **15**, 13–47.

Smith CR, Walker JDA, Haidari AH, Sobrun U (1991). "On the Dynamics of Near-Wall Turbulence." *Philosophical Transactions : Physical Sciences and Engineering*, **336 (1641)**, 131–175.

Soloff S, Adrian R, Liu Z (1997). "Distortion compensation for generalized stereoscopic particle image velocimetry." *Measurement Science and Technology*, **8**, 1441–1454.

Spalart PR (1988). "Direct simulation of a turbulent boundary layer up to R_{theta}=1410." *Journal of Fluid Mechanics*, **187**, 61–98.

Stanislas M, Carlier J, Foucaut J, Dupont P (1999). "Double spatial correlations, a new experimental insight into wall turbulence." *C. R. Acad. Sci. Paris. t. 327*, **Série 2b**, 55–61.

Stoesser T, Rodi W, Froehlich J (2005). "Large eddy simulation of open-channel flow over a layer of spheres." In "Proceedings of 31th IAHR Congress," Seoul.

Stuart JT (1965). "Hydrodynamic stability." *Appl. Mech. Rev*, **18**, 523–531.

Subramanian CS, Rajagopalan S, Antonia RA, Chambers AJ (1982). "Comparison of conditional sampling and averaging techniques in a turbulent boundary layer." *Journal of Fluid Mechanics*, **123**, 335–362.

Suzuki Y, Kasagi N (1993). "Drag Reduction Mechanism on Micro-Grooved Riblet Surface." In "International Conference on Near-Wall Turbulent Flows," Tempe-Arizona.

Swearingen JD, Blackwelder RF (1987). "The growth and breakdown of streamwise vortices in the presence of a wall." *Journal of Fluid Mechanics*, **182**, 255–290.

Talmon AM, Kunen JMG, Ooms G (1986). "Simultaneous flow visualization and Reynolds-stress measurement in a turbulent boundary layer." *Journal of Fluid Mechanics*, **163**, 459–478.

Theodorsen T (1952). "Mechanism of turbulence." In "Proc. 2nd. Midwestern Conf.on Journal of Journal of Fluid Mechanicsanicsanics," Ohio State Univ. Columbus, OH.

Tomkins CD, Adrian RJ (2003). "Spanwise structure and scale growth in turbulent boundary layers." *Journal of Fluid Mechanics*, **26**, 573–616.

Townsend AA (1976). "Structures of Turbulent Shear Flow." *Cambridge University Press, Cambridge and New York*.

Tritton DJ (1967). "Some new correlation measurements in a turbulent boundary layer." *Journal of Fluid Mechanics*, **28**, 439–462.

Tubergen RG, G TW (1993). "Evaluation of ejection detection schemes in turbulent wall flows." *Experiments in Fluids*, **15**, 255–262.

Ueda H, Hinze JO (1975). "Fine-structure turbulence in the wall region of a turbulent boundary layer." *Journal of Fluid Mechanics*, **61**, 125–143.

Ursenbacher T (2000). *Traitement de vélocimétrie par images digitales de particules par une technique robuste de distortion d'images*. Ph.D. thesis, Ecole Polytechnique de Lausanne. Switzeland.

Van Driest ER (1978). "On turbulent flow near a wall." *J.Aero. sci.*, **23**, 1007–1011.

Von Karman T (1937). "The Fundamentals of the Statistical Theory of Turbulence." *Journal of the Aeronautical Sciences*, **4**, 131–138.

Waleffe F (2003). "Homotopy of exact coherent structures in plane shear flows." *Physics of Fluids*, **A6**, 1517–1534.

Waleffe F, Kim J, Hamilton J (1993). "On the Origin of Streaks in Turbulent Shear Flows." In "Turbulent Shear Flows 8 : selected papers from the Eighth International Symposium on Turbulent Shear Flows," Springer-Verlag, Berlin, Munich, Germany.

Wallace JM, Eckelman H, Brodkey RS (1972). "The wall region of turbulent shear flow." *Journal of Fluid Mechanics*, **54**, 39–48.

Wark CE, Nagib HM (1982). "Relation between outer structures and wall layer events in boundary layers with and without manipulation. In Proc. 2nd IUTAM Symp. on Structure of Turbulence and Drag Reduction." *Switzerland (ed. A. Gyr). Springer*, pp. 467–474.

Wark CE, Nagib HM (1991). "Experimental investigation of coherent structures in turbulent boundary layers." *Journal of Fluid Mechanics*, **230**, 183–208.

Weisstein EW (1999). "Normal Distribution." *MathWorld–A Wolfram Web Resource*.

Westerweel J (1997). "Fundamentals of digital particle image velocimetry." *Measurement Science and Technology*, **8**, 1379–1392.

Westerweel J, van Oord J (1999). "Stereoscopic PIV measurements in a turbulent boundary layer." *EUROPIV : Progress Towards Industrial Application, Ed. M Stanislas et al. (Dordrecht : Kluwer)*, pp. 459–478.

Wieneke B (2005). "Stereo-PIV using self-calibration on particle images." *Experiments in Fluids*, **39**, 267–280.

Willert C (1997). "Stereoscopic digital particle image velocimetry for applications in wind tunnel flows." *Measurement Science and Technology*, **8**, 1465–1479.

Willert C (2004). "Prososal for netCDF (re)implementation for use with planar velocimetry data." *Proceedings of the EUROPIV 2 Workshop on Particle Image Velocimetry, (Springer Verlag), Ed. Stanislas M., Westerweel J., Kompenhans J.*, pp. 251–262.

Willmarth WW, Lu SS (1972). "Structure of the Reynolds stress near the wall." *Journal of Fluid Mechanics*, **55**, 65–92.

Yu X, Liu JTC (1991). "On the secondary instability in Gortler flow." *Physics of Fluids*, **A3**, 1845–743.

Zaric ZP (1975). "Wall turbulence structure and convection heat transfer." *International Journal of Heat and Mass Transfer*, **18**, 831–842.

Zaric ZP (1982). "Conditionally Averaged Patterns of Coherent Events in a Wall-bounded Turbulent Flow." *Structure of Turbulence in Heat and Mass Transfer*, pp. 7–28.

Zhou J, Adrian RJ, Balachandar S, Kendall TM (1999). "Mechanisms for generating coherent packets of hairpin vortices in channel flow." *Journal of Fluid Mechanics*, **387**, 353–396.

Annexe A

Comparison of SPIV and HWA

A.1 PDF

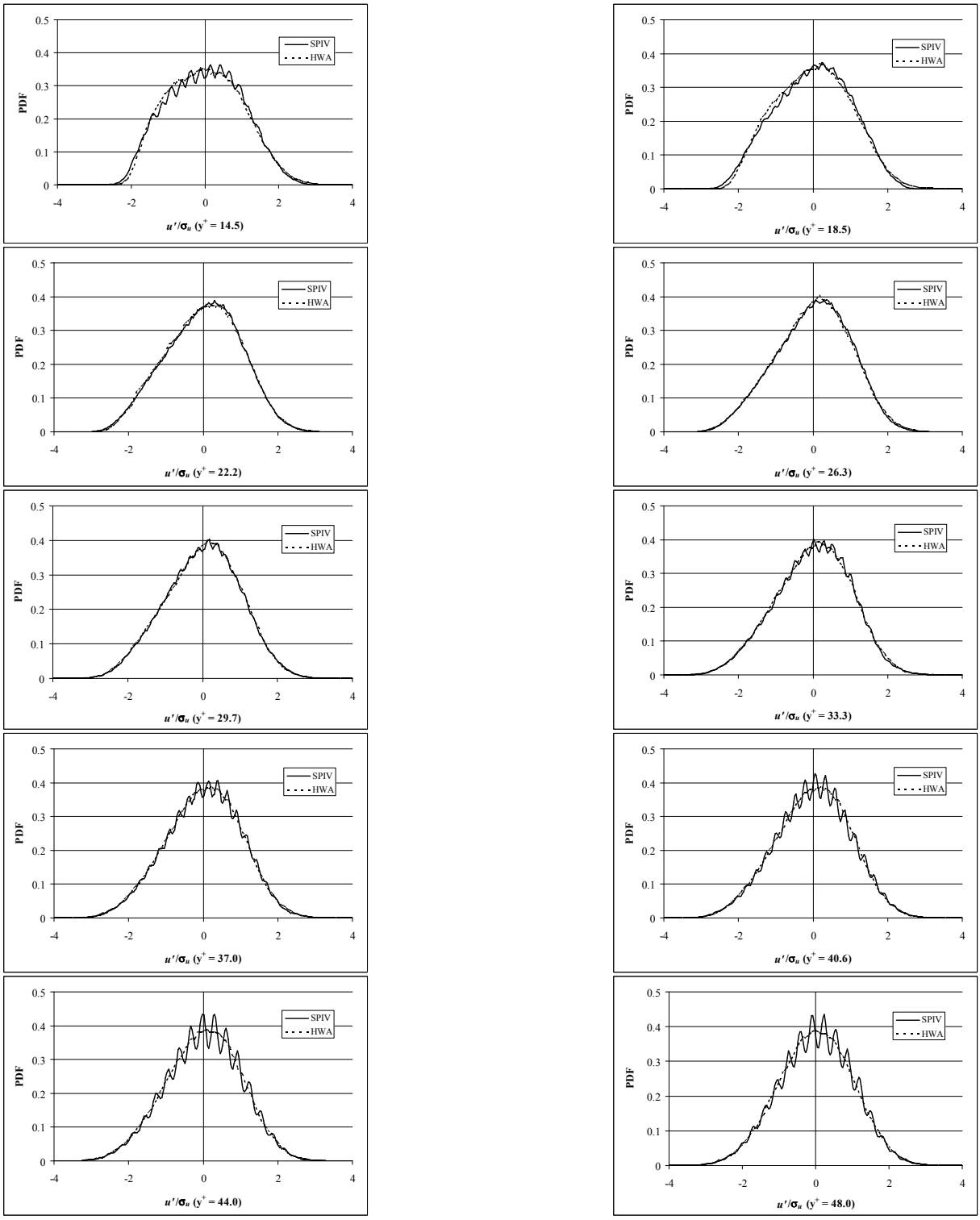

FIG. A.1 – Comparison on PDF of the normalized streamwise velocity fluctuation u'/σ_u of SPIV and HWA

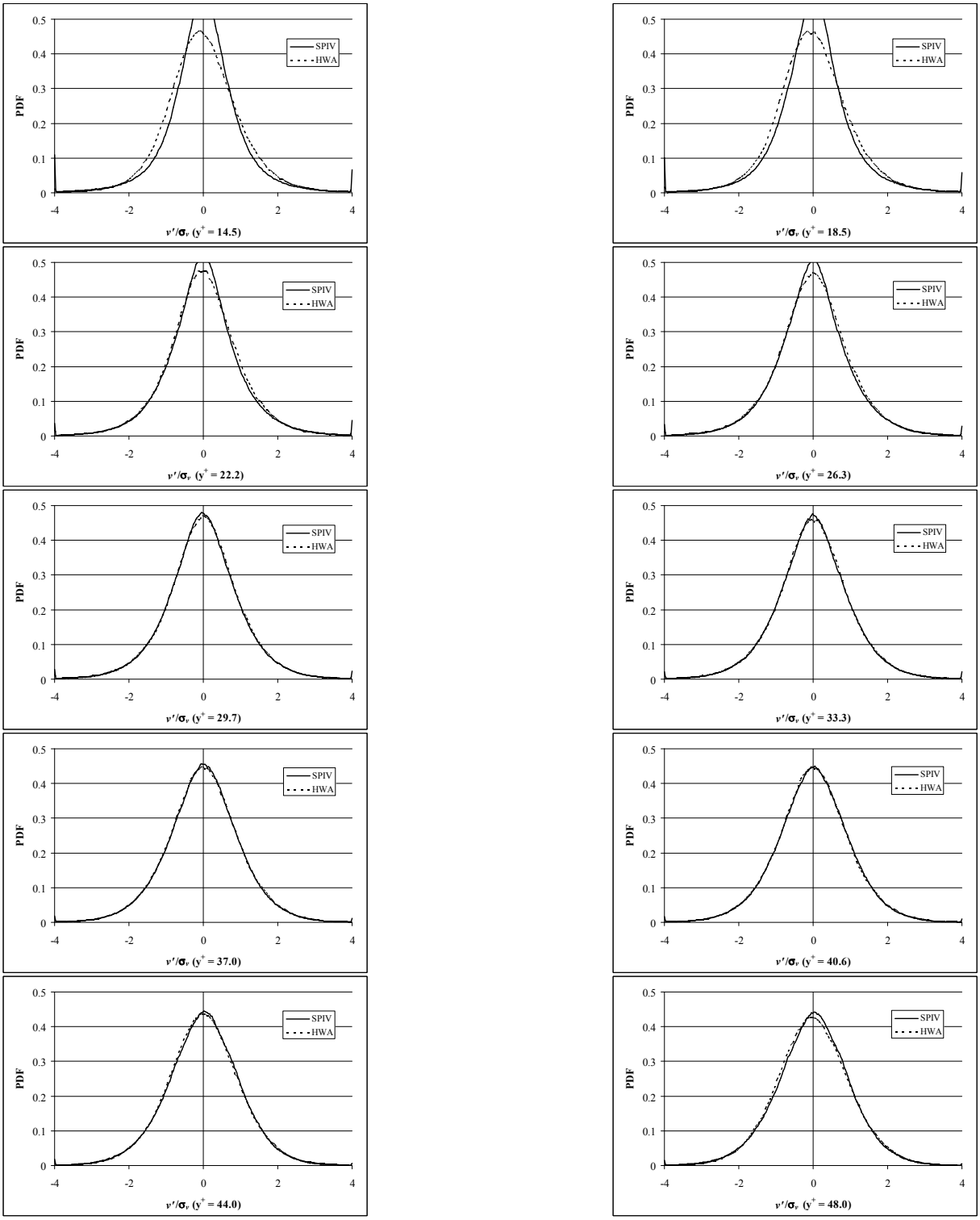

FIG. A.2 – Comparison on PDF of the normalized wall-normal velocity fluctuation v'/σ_v of SPIV and HWA

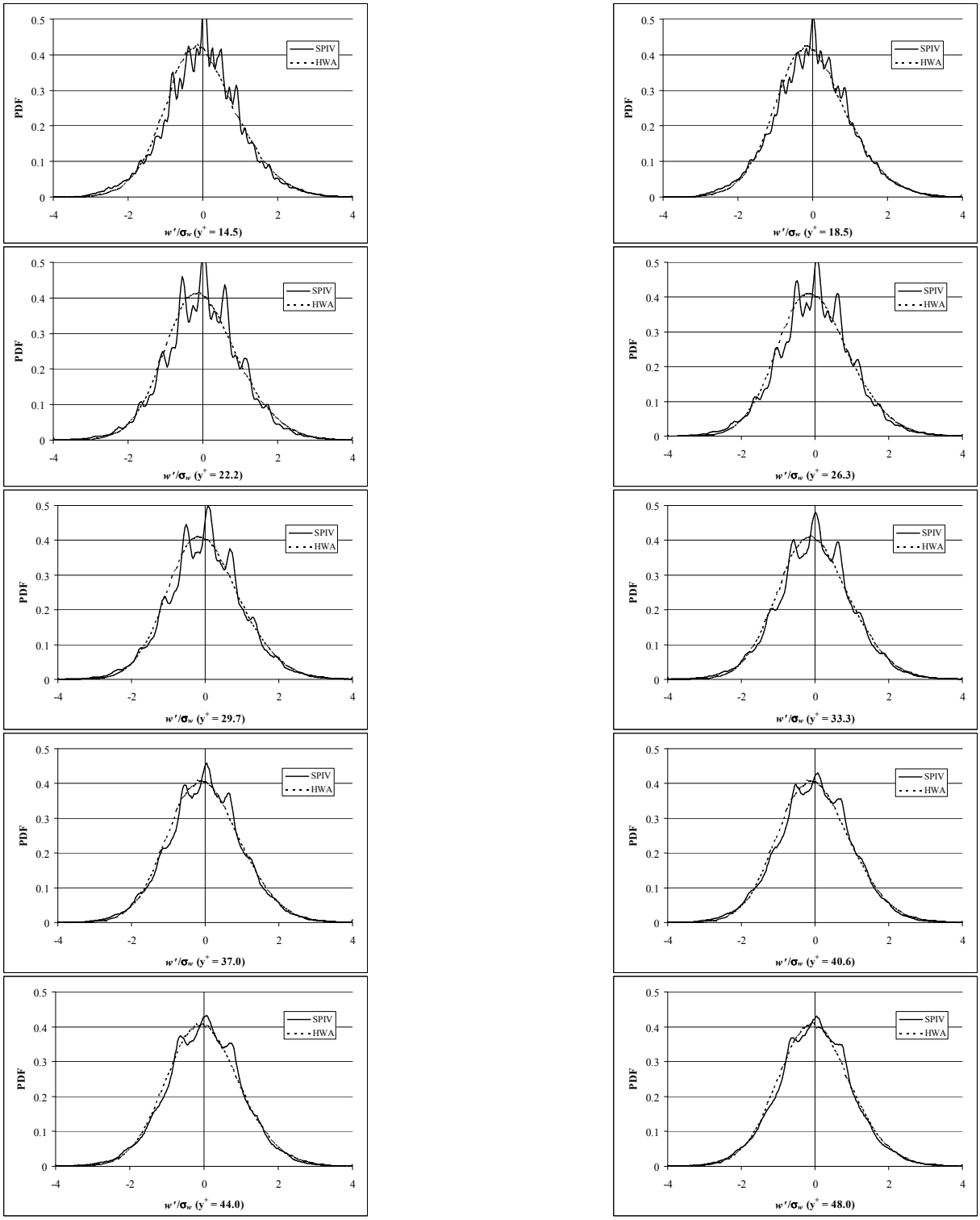

FIG. A.3 – Comparison on PDF of the normalized spanwise velocity fluctuation w'/σ_w of SPIV and HWA

A.2 Spectra

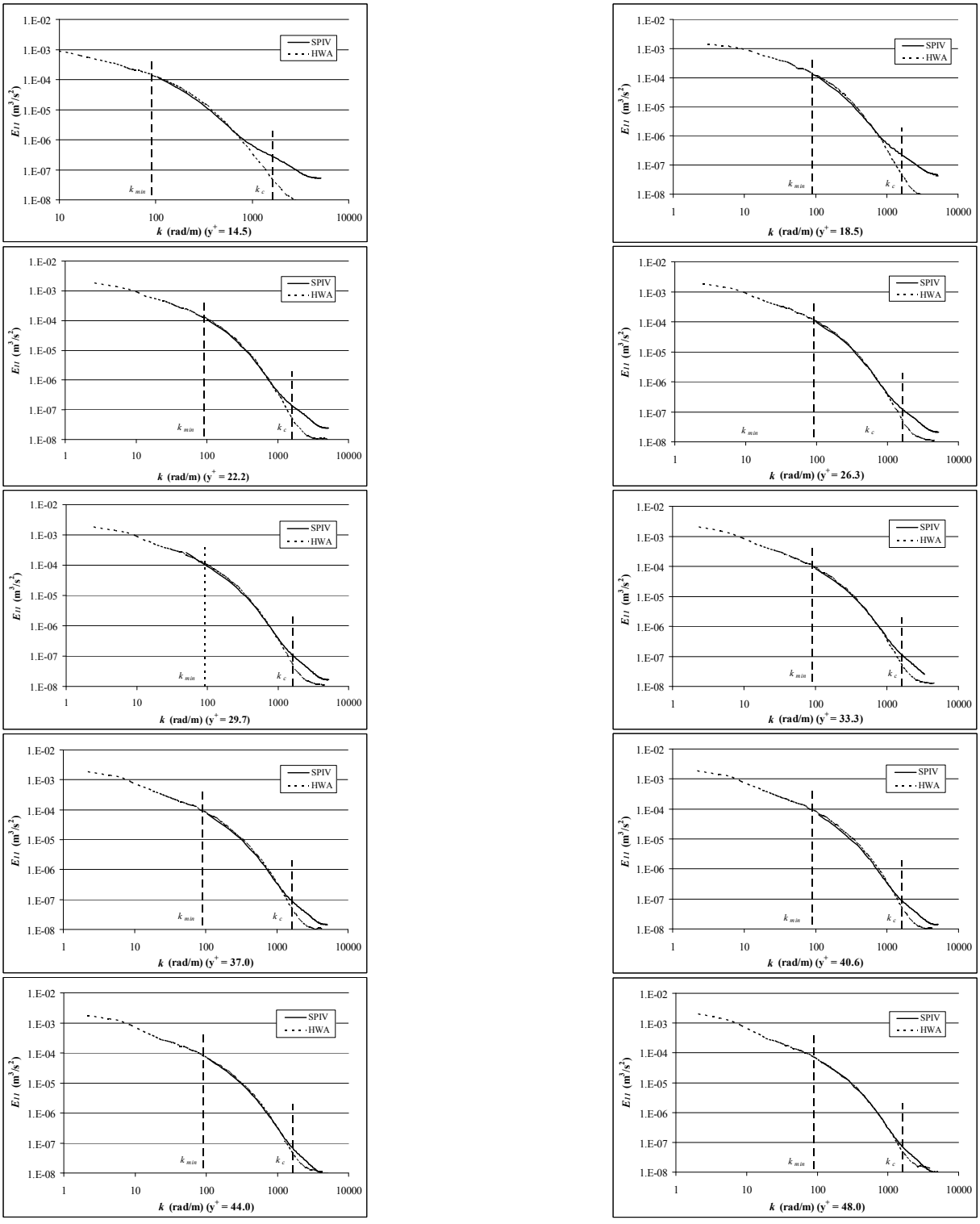

FIG. A.4 – Comparison on spectra of the streamwise velocity u of SPIV and HWA

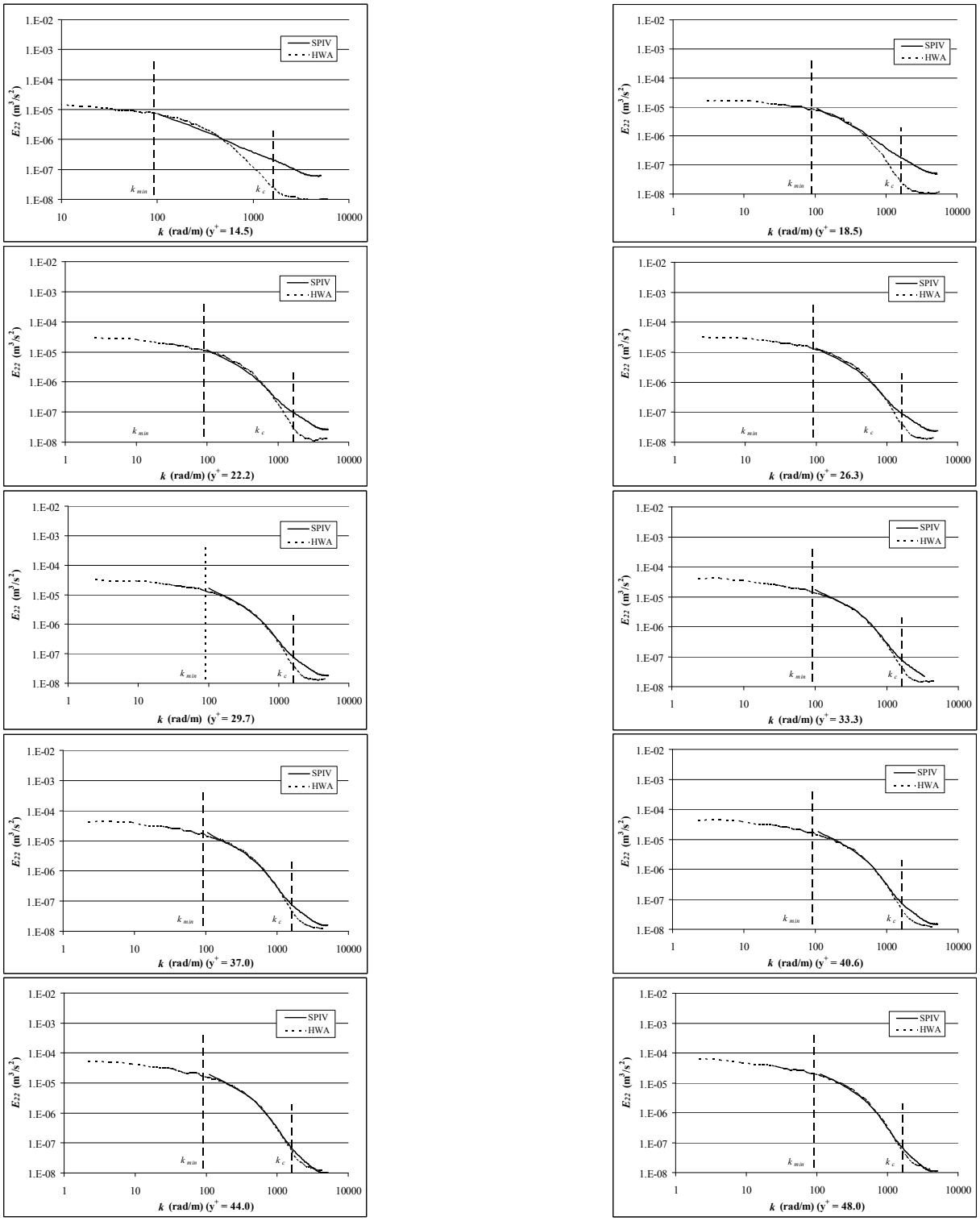

FIG. A.5 – Comparison on spectra of the wall-normal velocity v of SPIV and HWA

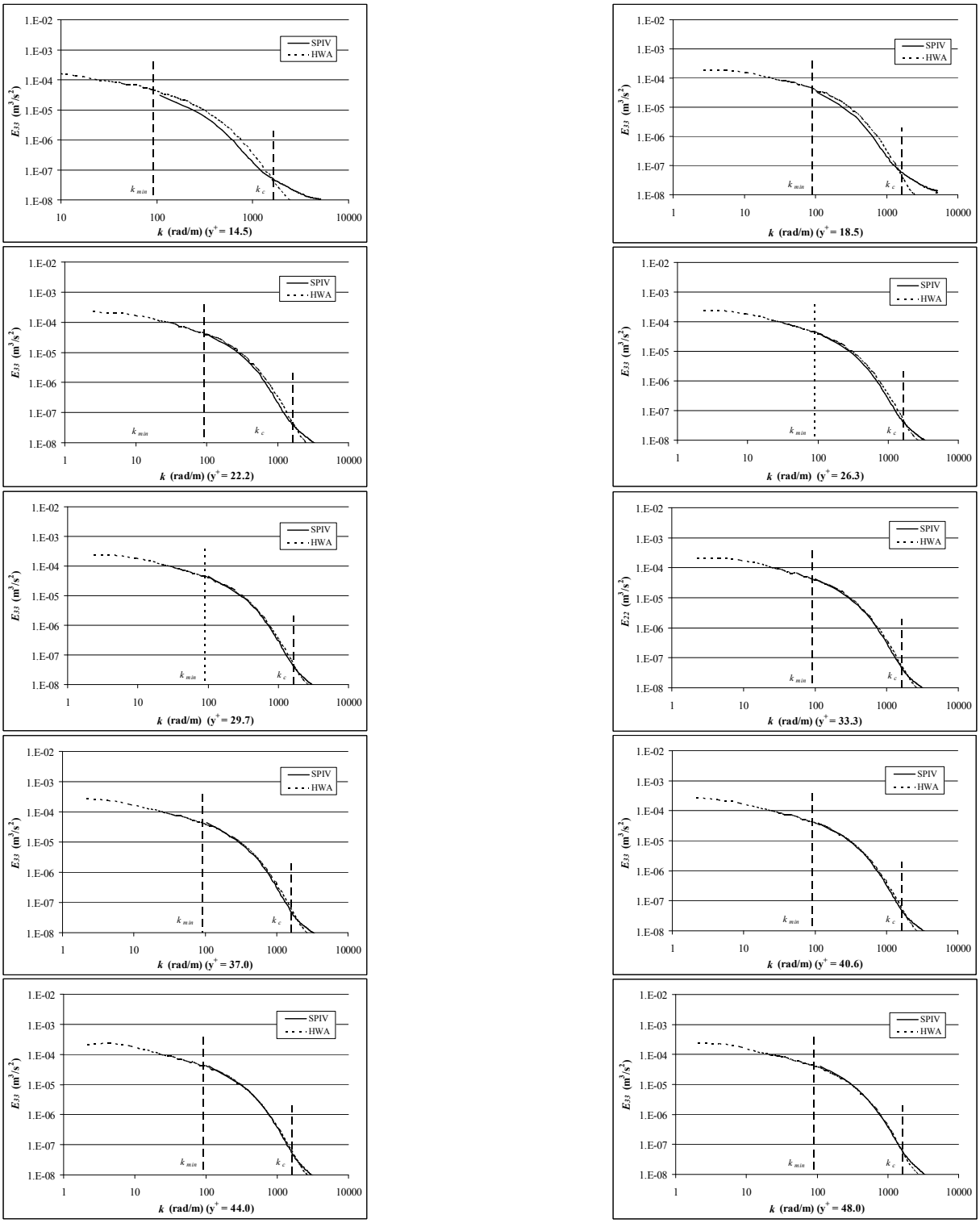

FIG. A.6 – Comparison on spectra of the spanwise velocity w of SPIV and HWA

Annexe B

Detection of Coherent Structures

B.1 Streaks

B.1.1 Detection function

A detection function F_d^u has been selected in Chapter 6.2.1 to detect low and high speed streaks respectively. This function is defined on a discrete (M, N) grid at 10 different wall distances :

$$F_d = f(u'(m,n,\mathrm{y}^+), \sigma_u(\mathrm{y}^+)) = \frac{u'(m,n,\mathrm{y}^+)}{\sigma_u(\mathrm{y}^+)} \tag{B.1}$$

Where u' is the instantaneous velocity fluctuation of the streamwise component u and σ_u is the standard deviation. This detection function is obtained from SPIV data and is also a scalar field defined on a discrete grid in real space R. This function will be used to identify streaky structures and to generate the corresponding binary indicative image that contains white objects (1) corresponding to streaks on a black background (0). With this binary image, streaks can be localized and measured. As explained in Chapter 6.1, three more steps are necessary to achieve this quantification : thresholding, mathematical morphology and cleaning. Four parameters are involved, namely the threshold (C_T) for the thresholding procedure, the structuring element (M_S) for the mathematical morphology procedure and the clean factors (C_B and C_C) for the cleaning procedure. Details of those parameters are described in this section. In order to obtain suitable parameters for each step, plane 1 (at 14.5^+ from the wall) was used to adjust all the parameters as it is close to the wall and streaks in this position are easy to recognize. Several statistical results (e.g. mean width, number of streaks), which have been studied by many researchers (e.g. Gupta *et al.* (1971), Smith and Metzler (1983), Carlier and Stanislas (2005)), are calculated in the present study to help choose the suitable value for these parameters. The reference parameters were set as : $C_T = 0.6$, $M_S = (10, 50)$, $C_B = 1750$ and $C_C = 2500$. The unit of M_S is wall unit and the unit of C_B and C_C is square wall unit. Each time when the statistics is calculated, only one parameter is varied.

B.1.2 Thresholding

Streaks are detected by applying a threshold C_T to the detection function F_d defined by Eq. (1). In the present study, the value of C_T is always positive. Using this threshold, the streaks are defined by :

$$\text{Low speed streaks } F_i = \begin{cases} 1 \text{ when } F_d \leq -C_T \\ 0 \text{ when } F_d > -C_T \end{cases} \tag{B.2}$$

$$\text{High speed streaks } F_i = \begin{cases} 1 \text{ when } F_d > C_T \\ 0 \text{ when } F_d \leq C_T \end{cases} \tag{B.3}$$

F_i is called an indicative function. By applying this procedure to the whole field, a binary indicative image of streaks is generated. As this thresholding procedure is the initial step to identify streaks, it can have a significant impact on the results and thus the value of C_T should be chosen carefully. To obtain the suitable value of C_T for the present SPIV database, six values from 0.5 to 1.0 were tested to detect low speed streaks.

In general, low value of C_T leads to identifying large objects that are strongly connected. In contrast, high value of C_T detects more small and isolated objects. Fig. B.1 gives a representative sample of the detection image for low speed streaks and the corresponding indicative images obtained by thresholding with various values of C_T. In the detection image, there are two objects. One is quite large which is considered as a streak, and the other is relatively small which can be related to other coherent structures (e.g. ejections and vortices). Comparing the detection image to the indicative images for the different values of C_T, we see that the large object is clearly separated into several small ones for large values of C_T (0.8, 0.9 and 1.0). The objects found by using $C_T = 0.5$, 0.6 and 0.7 are very similar to those in the detection image, thus a threshold between 0.5 and 0.7 seems to be the better choice. Examining a certain number of image samples, we found that this result is valid for most of the images.

Fig. B.2 shows the histograms of the width of low speed streaks for the different values of C_T. The two measurement methods ($\overline{W_a^+}$ and $\overline{W_t^+}$, defined in Chapter 6.1) give comparable results which are not very sensitive to C_T for $0.6 \leq C_T \leq 1.0$. Most of streaks are between 15 and 40 wall units in width. Table B.1 gives some statistical results that are computed with various values of C_T. As expected, the smaller the threshold, the smaller the width is. Table B.1 shows that the difference between $\overline{W_a^+}$ and $\overline{W_t^+}$ decreases from 3.5 wall units (about 11% of $\overline{W_a^+}$) with a $C_T = 0.5$ to 1.4 wall units (about 5% of $\overline{W_a^+}$) with a $C_T = 1.0$. At the same time, the number of streaks that have more than one branch decreases from 488 (about 34% of the total number of streaks) with a $C_T = 0.5$ to 252 (about 19% of the total number of streaks) with a $C_T = 1.0$. These two results indicate that the length of the branch part of a bifurcated streak is not small compared to its total length. However, as the branches of a bifurcated streak are apart, it is reasonable to consider the branches as a group of $'$single streak$'$ and thus the width of the bifurcate streak should be computed as the average of all the branches. Therefore, only the mean width $\overline{W_a^+}$ will be discussed hereafter. Table B.1 suggests that the mean width $\overline{W_a^+}$ of low speed streaks decreases nearly linearly with C_T. When C_T is varied from 0.5 to 1.0, the differenece in $\overline{W_a^+}$ is 5.5^+ (about 17% of $\overline{W_a^+}$ with a $C_T = 0.5$). This differenece results

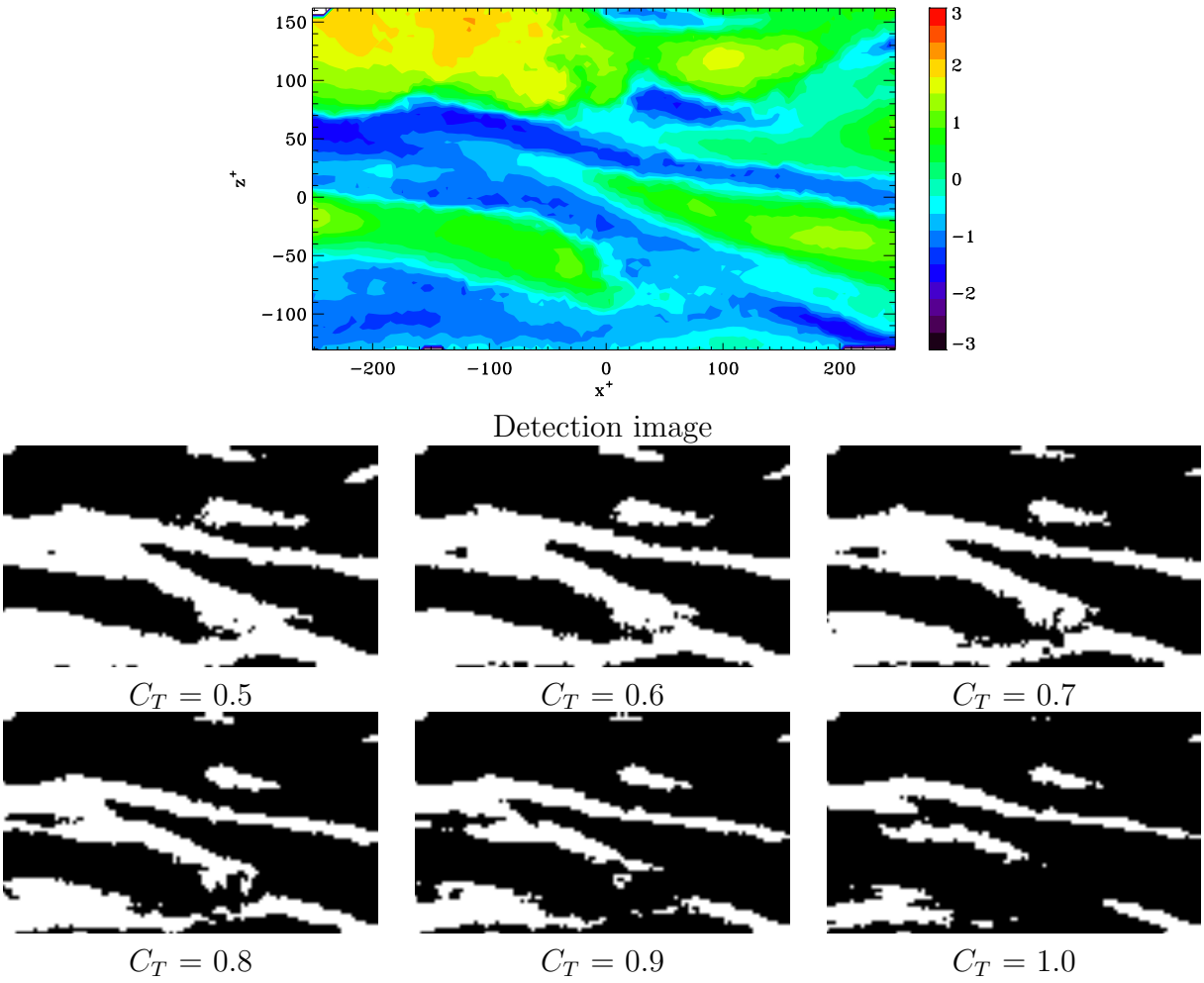

FIG. B.1 – Detection image and the corresponding indicative images with various C_T for low speed streaks

from the fact that a large threshold narrows the objects and separates them into several parts while a small one connects several parts of objects together. In Table B.1, the mean distance $\overline{d^+}$ between the streaks keeps nearly a constant value when varing the threshold. This can be explained by the fact that the distance is measured between the centers of nearby streaks, which is not affected by the threshold. Based on the above comparison, a threshold of $C_T = 0.6$ or 0.7 appears to be suitable for the detection. To detect all the potential streaks, $C_T = 0.6$ was finally chosen. Since the characteristics of high speed streaks are similar to those of low speed ones, this threshold was used to detect high speed streaks as well.

B.1.3 Mathematical morphology

The indicative image obtained by the thresholding procedure, for example the one with $C_T = 0.6$ in Fig. B.1, contains many small holes, sharp capes and isolated objects. To improve the indicative image, a mathematical morphology procedure is employed as

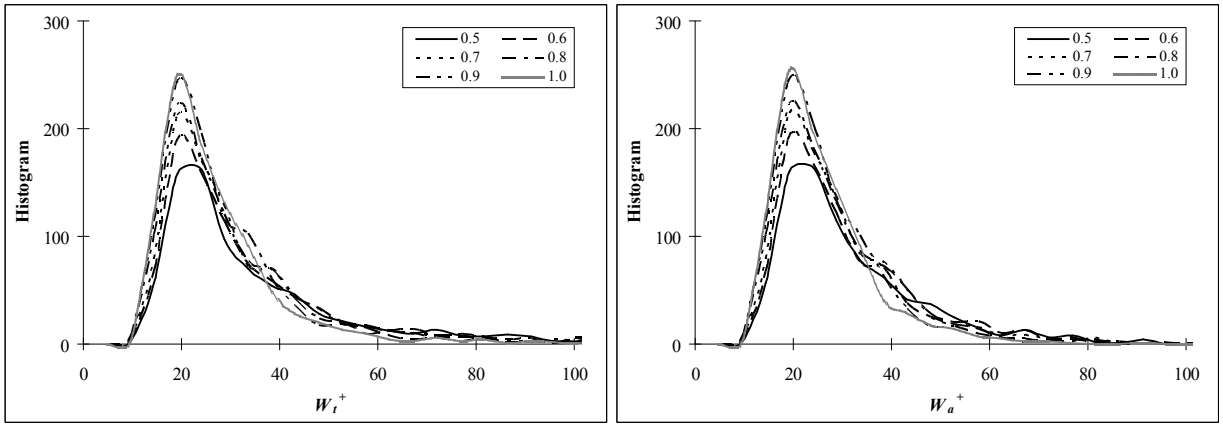

FIG. B.2 – Histogram of the width of low speed streaks with various C_T

Threshold C_T	0.5	0.6	0.7	0.8	0.9	1.0
Number of streaks	1437	1447	1445	1406	1405	1317
Number of bifurcate streaks	488	459	396	353	308	252
$\overline{W_a^+}$	31.6	30.6	29.4	28.3	27.1	26.1
$\overline{W_t^+}$	35.1	33.6	31.9	30.4	28.7	27.5
$\overline{d^+}$	103.9	104.4	103.7	104.4	103.5	106.2

TAB. B.1 – Threshold influence on the detection of low speed streaks

explained in Chapter 6.1. It requires a structuring element M_S. Since streaks are elongated in the streamwise direction, the structuring element was chosen as a rectangle or a square with two parameters : $M_S(W, L)$, in which W is the dimension in the spanwise direction and L in the streamwise direction. The values of W and L are presented in wall units. Large structuring element cannot be used in the detection of streaks due to the following reasons. First, they can connect several separated streaks. Second, structuring element with large values of L can cut streaks that have a large angle with the streamwise direction into several small pieces and eliminate short streaks and incomplete streaks cut by the streamwise border of the image. Also, large values of W can eliminate narrow streaks and incomplete streaks that are cut by the spanwise border of the image. In the present study, six different structuring elements were tested to detect low speed streaks.

Fig. B.3 gives an example to illustrate the effects of the mathematical morphology procedure on the indicative image (the one with $C_T = 0.6$ in Fig. B.1) with various structuring elements. This example shows clearly that mathematical morphology does improve the quality of the original indicative image by filling holes, removing small objects and capes, and reconnecting separated objects. In order to choose the appropriate parameter L, comparisons among indicative images have been done. When L is equal to 70 wall units, larger objects are cut into pieces. $L = 30^+$ and 50^+ seems usable. However, considering the fact that the length of streaks is generally larger than 500 wall units, in order to remove effectively the holes and to reconnect the separated objects, $L = 50^+$ was chosen to be used in the present study.

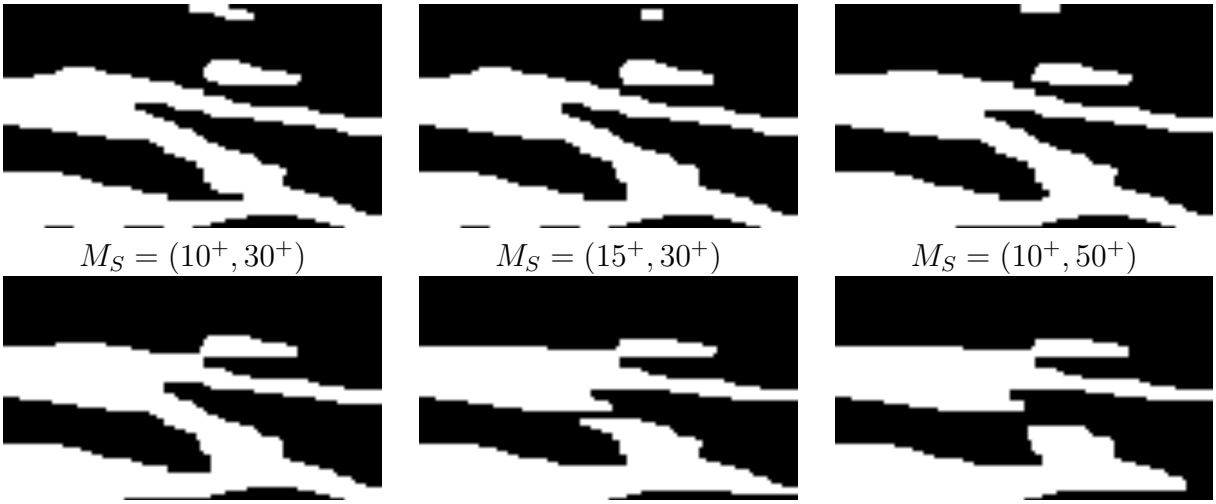

FIG. B.3 – Indicative images with various M_S for low speed streaks

Shape operator M_S	$(10^+,\ 30^+)$	$(15^+,\ 30^+)$	$(10^+,\ 50^+)$	$(15^+,\ 50^+)$	$(10^+,\ 70^+)$	$(15^+,\ 70^+)$
Number of streaks	1459	1439	1447	1403	1431	1380
$\overline{W_a^+}$	30.1	32.8	30.6	33.5	30.9	33.7
$\overline{d^+}$	104.7	107.0	104.4	107.9	103.7	108.1

TAB. B.2 – Structuring element M_S influence on the detection of low speed streaks

For various structuring elements, Fig. B.4 shows the histograms of the width of low speed streaks and Table B.2 gives some statistical results computed from the indicative images. Fig. B.4 and Table B.2 indicate that when M_S increases the total number of streaks decreases. This is due to the fact that larger M_S removes more small streaks and connects more separated streaks. In Fig. B.4, the peak is located at 25 wall units with $W = 15^+$ and situated at 20 wall units with $W = 10^+$. The difference in the position of peaks can be explained by the fact that $W = 15^+$ removes more edgy parts of streaks than $W = 10^+$. Since most of the streaks have a width between 20 - 40 wall units in the literature, $W = 10^+$ keeps more objects with a width of 20 wall units than $W = 15^+$ does and thus seem to be more suitable in the present study. Fig. B.4 shows that the peaks seem to be almost at the same position for the results with the same W but different L. Moreover, Table B.2 shows that statistical results with same L but different W are very different, while those with same W but different L are nearly the same. These results suggest that parameter W is more sensitive than L as the length of streaks is much greater than its width. Based on the above discussions, in the present study, the suitable parameters of the structuring element M_S were finally selected as $(10^+,\ 50^+)$ for both low and high speed streaks.

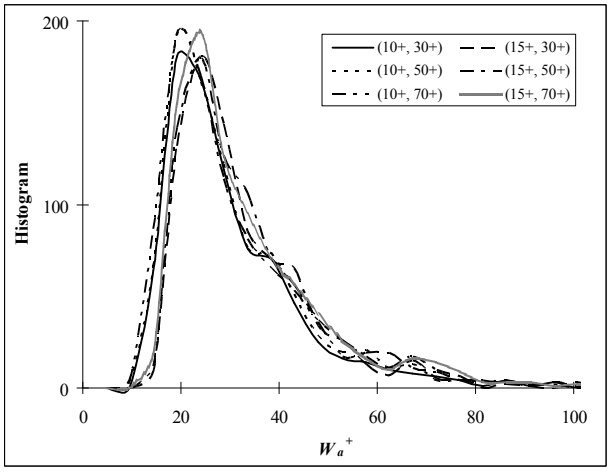

FIG. B.4 – Histogram of the width W_a^+ of low speed streaks with various M_S

B.1.4 Cleaning

Since the selected structuring element M_S is relatively small, many small objects remain in the indicative image. These small objects, which have an area larger than that of the structuring element, may result from mis-detection of the local disturbance of the flow or the small parts cut from the big objects. Therefore, they can not be considered as streaks and need to be removed before statistical analysis. Two parameters C_B and C_C are introduced to remove these objects on the basis of their area. For the small objects cut by image borders, the parameter C_B is used. Three values : $C_B = 1250^{+^2}, 1750^{+^2}$ and 2250^{+^2} were tested. The histograms of the width of the low speed streaks are presented in Fig. B.5a and statistical results are in the left part of Table B.3. The results show that C_B in general performs well in removing small objects. Fig. B.5a shows $C_B = 2250^{+^2}$ and $C_B = 1750^{+^2}$ remove more objects with a width of 10^+ - 15^+ than $C_B = 1250^{+^2}$ does. To avoid removing too many objects that are likely to be streaks, $C_B = 1750^{+^2}$ was selected in this study for both low and high speed streaks. For the small objects totally embedded in the images, the parameter C_C is used. Three values : $C_C = 1250^{+^2}$, 2500^{+^2} and 3750^{+^2} were tested. The histograms of the width $\overline{W_a^+}$ for low speed streaks are shown in Fig. B.5b. The right part of Table B.3 shows the statistical results for the three values of C_C. All results show that this clean factor removes a considerable amount of small objects. Fig. B.5b shows that $C_C = 2500^{+^2}$ and 3750^{+^2} removes more objects with a width of 10 - 15 wall units than $C_C = 1250^{+^2}$. In addition, $C_C = 3750^{+^2}$ removes more objects with an average width of 20 wall units than $C_C = 2500$ and $C_C = 1250^{+^2}$. As the width of low speed streaks is expected to be 20 - 40 wall units, the objects with an average width of 20^+ are more likely to be real streaks than the objects with an average width of 10 - 15 wall units. Taking this into account, an intermediate level $C_C = 2500^{+^2}$ was chosen for low speed streaks as well as for high speed ones in the present study. Fig. B.6 shows an example of the effect of the cleaning procedure on the indicative images (the one with $M_S = (10^+, 50^+)$ in Fig. B.3). This example illustrates that the selected clean factors remove some small objects and improve the indicative image.

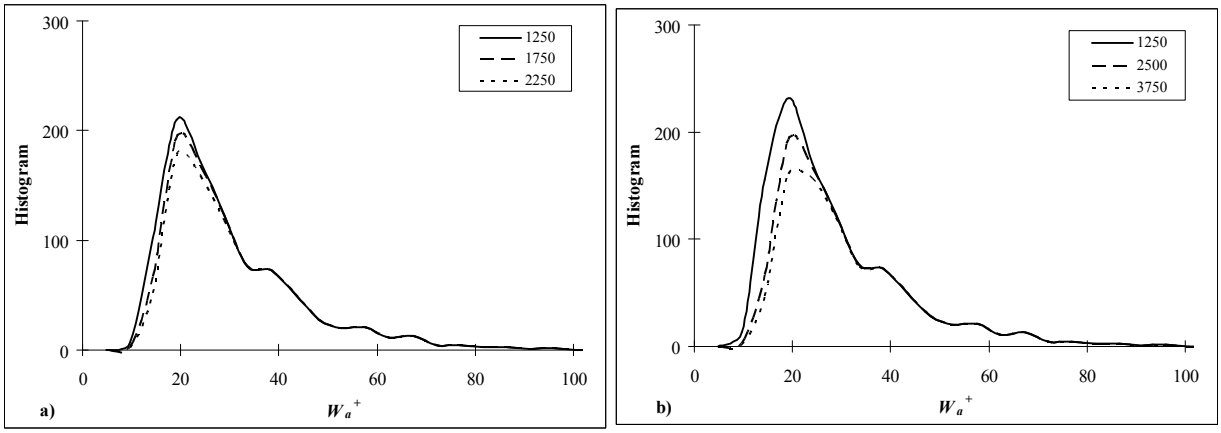

FIG. B.5 – Histogram of the width W_a^+ of low speed streaks with various C_B and C_C. a : C_B ; b : C_C

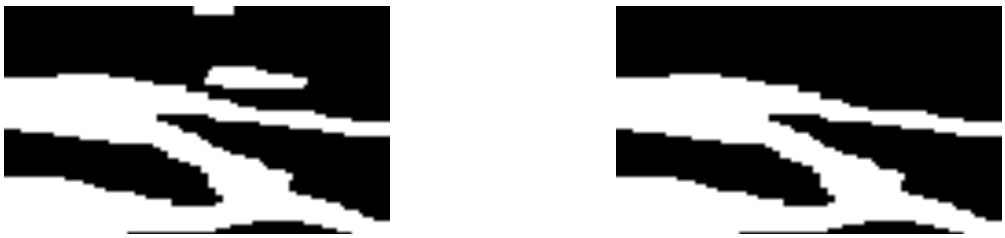

After the morphology procedure ($M_S = (10^+,\ 50^+)$)

After the cleaning procedure ($C_B = 1750^{+^2}$ and $C_C = 2500^{+^2}$)

FIG. B.6 – Example of the effect of the cleaning procedure for low speed streaks

Clean factor	$C_B(C_C = 2500)$			$C_C(C_B = 1250)$		
	1250^{+^2}	1750^{+^2}	2250^{+^2}	1250^{+^2}	2500^{+^2}	3750^{+^2}
Number of streaks before cleaning	2155					
Number of streaks after cleaning	1548	1447	1366	1589	1447	1379
Number of incomplete streaks before cleaning	1609					
Number of incomplete streaks after cleaning	1382	1281	1200	1281		
Number of complete streaks before cleaning	546					
Number of complete streaks after cleaning	166			308	166	98
$\overline{W_a^+}$	29.6	30.6	31.2	28.5	30.6	31.6
$\overline{d^+}$	103.9	104.4	104.2	103.0	104.4	104.7

TAB. B.3 – Clean factor influence on the detection of low speed streaks

y^+	14.5	18.5	22.2	26.3	29.7	33.3	37.0	40.6	44.0	48.0
Plane #	1	2	3	4	5	6	7	8	9	10
σ_u^n	0.348	0.344	0.329	0.322	0.316	0.307	0.298	0.293	0.288	0.281
C_T=0.6 $*$ $\sigma_u^{max}/\sigma_u^n$	0.60	0.61	0.63	0.65	0.66	0.68	0.70	0.72	0.72	0.74

TAB. B.4 – Threshold C_T in ten planes of measurement (σ_u^{max}= 0.35)

B.1.5 Parameters for all ten planes

Based on the above discussion for plane 1 ($y^+ = 14.5$), $C_T = 0.6$, $M_S = (10^+, 50^+)$, $C_B = 1750^{+^2}$ and $C_C = 2500^{+^2}$were chosen for both low and high speed streaks. For the other planes, the same parameters were used except for the threshold C_T which depends on the distance to the wall. In fact, σ_u^n decreases with wall distance when $y^+ > 10-15$. Also, beyond a certain distance from the wall streaks are known to disappear. Considering these facts, in the present study, the threshold C_T was chosen as $0.6 * \sigma_u^{max}/\sigma_u^n$. Here, the value of $'0.6'$ is the one used for plane 1, σ_u^n is the standard deviation of the streamwise velocity component u of plane n, and σ_u^{max} is the maximum standard deviation of the present flow and is equal to 0.35 according to our previous study (Lin et al., 2004). According to this method, there is a streak only when u' (velocity fluctuation of the streamwise component) is larger than a constant value whatever the wall distance is. Table B.4 gives the resulting values of C_T in each plane.

B.2 Ejections and Sweeps

B.2.1 Detection functions

As concluded in Chapter 6.3.1, three detection functions F_d^{uv}, F_d^u and F_d^v are employed to detect ejections and sweeps respectively on a discrete (M, N) grid at 10 different wall distances. They are defined as :

$$F_d^{uv} = \frac{u'v'(m,n,\mathrm{y}^+)}{\sigma_v(\mathrm{y}^+)} \tag{B.4}$$

$$F_d^{u} = \frac{u'(m,n,\mathrm{y}^+)}{\sigma_u(\mathrm{y}^+)} \tag{B.5}$$

$$F_d^{v} = \frac{v'(m,n,\mathrm{y}^+)}{\sigma_v(\mathrm{y}^+)} \tag{B.6}$$

Where u' and v' are the instantaneous velocity fluctuations of the streamwise and spanwise components u and v. σ_u and σ_v are the corresponding standard deviations. (m, n) is the position in the (M, N) grid and y^+ is the wall distance. Similar to streaks, these detection functions are also scalar fields defined on a discrete grid in the real space R. As explained in Chapter 6.1, after definition of the detection functions, three successive steps are used to identify ejections and sweeps : thresholding, mathematical morphology and cleaning. The parameters involved are : three thresholds, one structuring element, two clean factors. In order to obtain suitable parameters for each step, detection functions at $\mathrm{y}^+ = 48$ (plane #10) were used to adjust all the parameters, in respect that ejections and sweeps are well-developed and easy to recognize in this position. Since ejections and sweeps are similar in both dimension and shape, the parameters that are selected for ejections are used to detect sweeps as well.

B.2.2 Thresholding procedure

By thresholding three detection functions (F_d^{uv}, F_d^u and F_d^v), ejections and sweeps are identified. The corresponding thresholds are C_T^{uv}, C_T^u and C_T^v. The values of C_T^{uv} and C_T^v are always positive in the present study while $C_T^u = 0$ is used referring to Wallace et al. (1972). Indicative function (F_i) of ejections and sweeps are defined as :

$$\text{Ejection :} \quad F_i = \begin{cases} 1 & \text{when } F_d^{uv} < -C_T^{uv},\ F_d^u < 0 \text{ and } F_d^v > C_T^v \\ 0 & \text{otherwise} \end{cases} \tag{B.7}$$

$$\text{Sweep :} \quad F_i = \begin{cases} 1 & \text{when } F_d^{uv} < -C_T^{uv},\ F_d^u > 0 \text{ and } F_d^v < -C_T^v \\ 0 & \text{otherwise} \end{cases} \tag{B.8}$$

By applying this procedure to the whole field, a binary image of ejections (or sweeps) is generated. Thresholding is the initial step to identify ejections and sweeps and thus has a significant impact on the results. Therefore the value of C_T^{uv} and C_T^v should be analyzed thoroughly. Six values from 0.5 to 2.0 for $C_T^{uv}$and six values from 0.3 to 1.8 for C_T^v were tested in the present study.

Fig. B.7 shows an example of detection functions. The vector field refers to the detection functions F_d^u and F_d^v, and the contour is the detection function F_d^{uv}. Fig. B.8 shows the corresponding indicative image with various C_T^{uv} at $C_T^v = 0$, while Fig. B.9 shows indicative images of various C_T^v at $C_T^{uv} = 1.0$.

In Fig. B.8, the main differences appear in regions B, D, E, F and H (Fig. B.7). F_d^{uv} in regions B and F is slightly larger than that in regions D, E and H. In regions D and E, F_d^u is very small while F_d^v is large. Examining Fig. B.7, regions A and A1 are with high negative and positive wall-normal velocity fluctuations respectively. As explained in Chapter 6.4.1, regions A and A1 can be considered as parts of a streamwise vortex whose core is represented by the black line. Similarly, regions G and G1 are parts of a streamwise vortex represented by the black line. The vortices mentioned above are two separated ones. Therefore, it is logical to have a break between the ejections in regions A and G and thus regions D and E are not considered as parts of ejections. In region H, F_d^u is large but F_d^v is very small. This region is more likely to be a part of a streak than that of ejections. Therefore, it is not considered as part of ejections in the present study. To avoid detecting those regions, the threshold C_T^{uv} needs to be larger than 0.75. The region F can be taken as a part of the ejection in region C and thus need to be detected. F_d^{uv} in region B is comparable to that in region F and thus can also be detected. Since the region B and F cannot be detected when $C_T^{uv} \geq 1.25$, the value of C_T^{uv} should be less than 1.25 in order to detect all the possible ejections. Based on these discussions, an intermediate value $C_T^{uv} = 1.0$ was chosen in the present study.

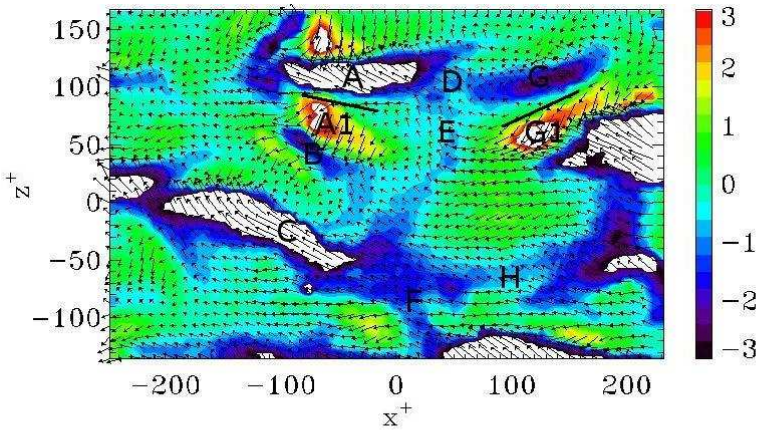

FIG. B.7 – Normalized velocity vector field (F_d^u and F_d^v) and contour of the function F_d^{uv}

In Fig. B.9, the images show clearly that C_T^v has an important influence on the detection of ejections. Since the threshold C_T^{uv} has already been applied, threshold C_T^v is mainly used to reject the objects with strong streamwise but weak normal fluctuations. Examining the indicative images in Fig. B.7, a large part of the region F is eliminated when $C_T^v > 0.9$ while there is not any improvement in the image when $C_T^v = 0.3$. Therefore, an intermediate value $C_T^v = 0.6$ was chosen for the present study.

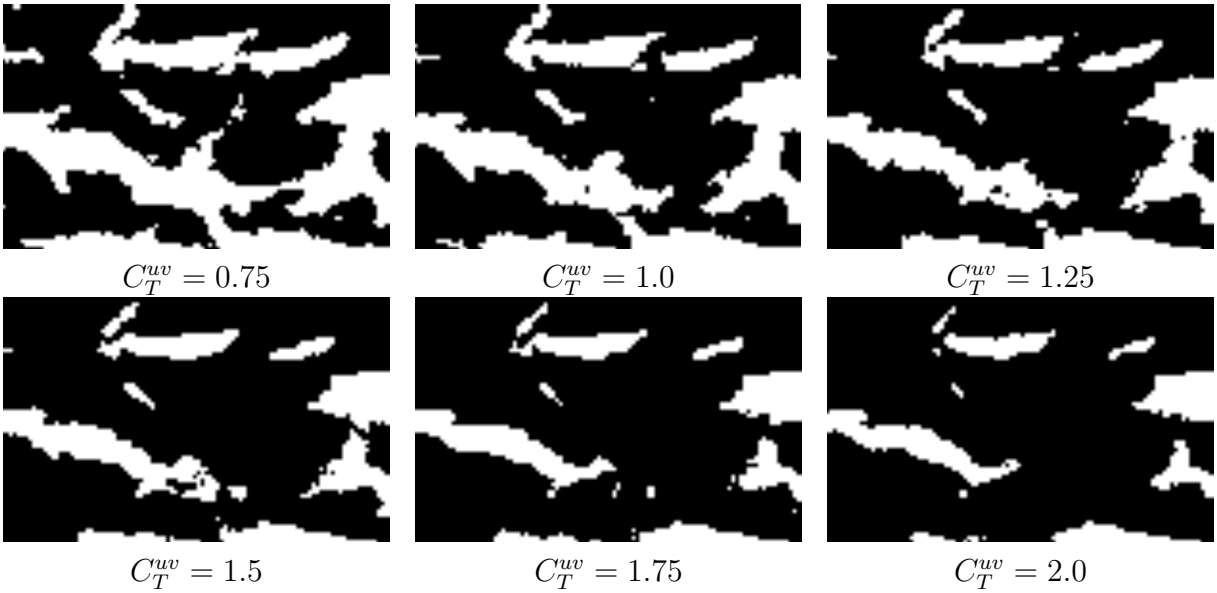

FIG. B.8 – Indicative images with various C_T^{uv} ($C_T^v = 0$)

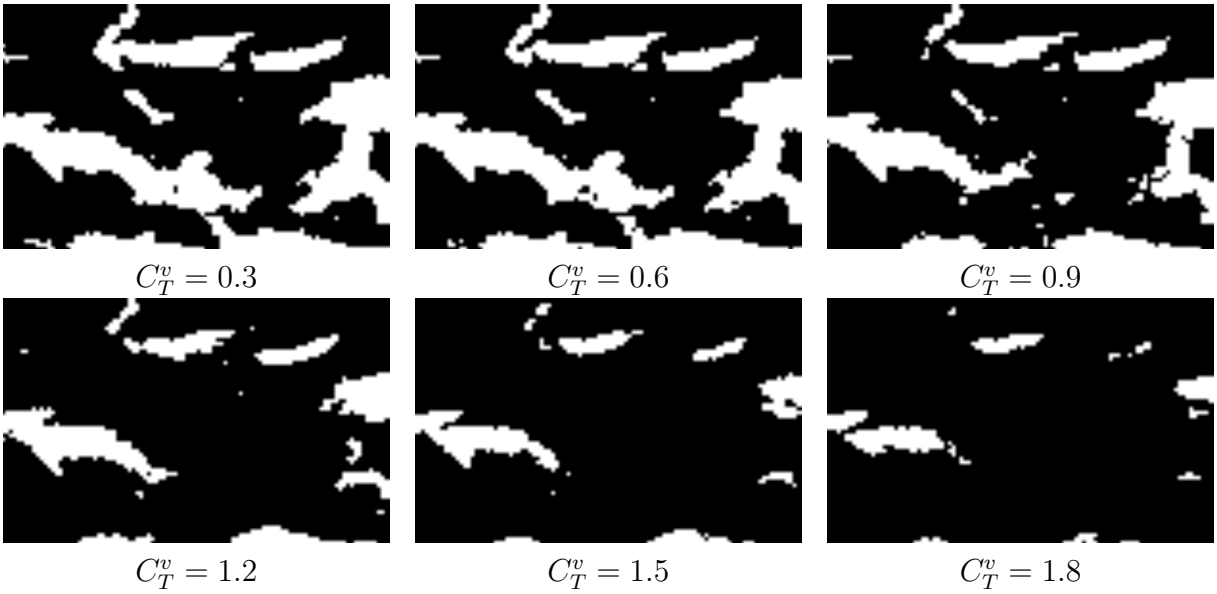

FIG. B.9 – Indicative images with various C_T^v ($C_T^{uv} = 1.0$) for ejections

B.2.3 Mathematical morphology

The same as for streaks, a mathematical morphology procedure is employed to remove the noise from the indicative images obtained by the thresholding described above. This procedure requires a suitable structuring element M_S. Examining the indicative images, most of the objects appear elongated in the streamwise direction. Therefore, a rectangular or a square structuring element was chosen with two parameters : $M_S(W, L)$, in which W is the dimension in the spanwise direction and L in the streamwise direction. Both W and L are presented in wall units. In the present study, six structuring elements were tested

to detect ejections.

Fig. B.10 shows an example about the effects of the mathematical morphology procedure on the indicative image obtained by thresholding with $C_T^{uv} = 1.0$ and $C_T^{v} = 0.6$ (see Fig. B.9). These images provide a direct visualization of the influence of this procedure. In Fig. B.10, large structuring elements, $M_S = (10^+,\ 20^+)$, $M_S = (10^+,\ 25^+)$ and $M_S = (10^+,\ 30^+)$, separate or even eliminate the region F (see Fig. B.7), which is considered as a part of an ejection. Moreover, applying $M_S = (10^+,\ 30^+)$, the regions A and G, which are two separated ejections, are connected. Therefore, large structuring elements are not suitable to use. For small structuring elements, such as $M_S = (10^+,\ 10^+)$, $M_S = (15^+,\ 10^+)$ and $M_S = (10^+,\ 15^+)$, the main difference appears in the region B. However, no matter which structuring element is used, this region will be cut into several small parts. Therefore, the three small structuring elements are usable in the present study.

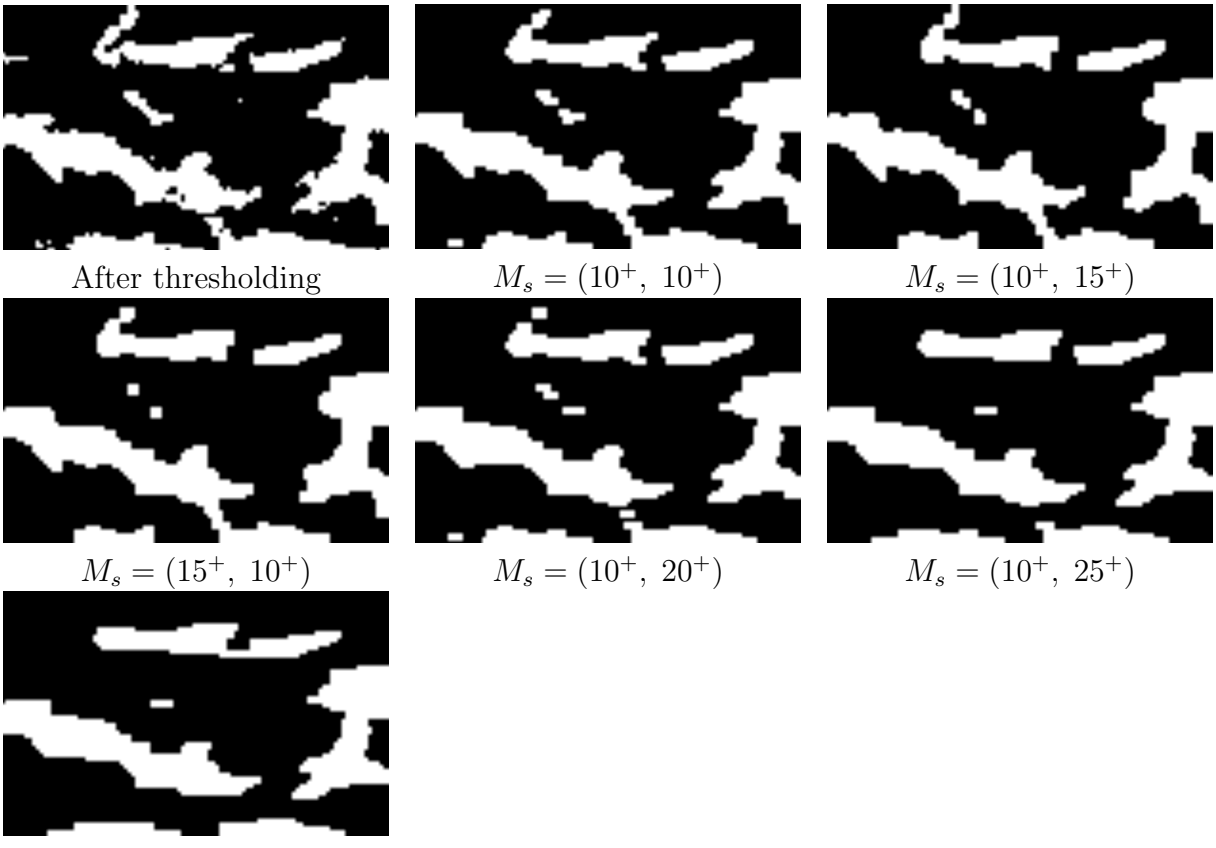

FIG. B.10 – Indicative images with various M_s for ejections ($C_T^{uv} = 1.0$ and $C_T^{v} = 0.6$)

To help choose the most suitable structuring element, Fig. B.11 gives the histograms of the area A_c^+ of the detected objects. Fig. B.11a is calculated directly by applying the mathematical morphology procedure to the indicative images obtained by thresholding. To obtain Fig. B.11b, a cleaning procedure was performed on the indicative images, before the mathematical morphology procedure, to remove the objects whose areas are equal to

or smaller than 300^{+^2} (the area of the largest structuring element tested in the present comparison ($M_S = (10^+, 30^+)$). Examining the indicative images obtained after thresholding, it appears that only few objects have holes. Consequently, the effect of holes filling by the mathematical morphology procedure is limited in this case. The main effects of this procedure in Fig. B.11a are : 1) removing small objects (smaller than the structuring element) ; 2) separating objects into several pieces ; 3) connecting close objects together. The main effects in Fig. B.11b are : 1) separating objects larger than 300^{+^2} into pieces, 2) connecting close objects which are larger than 300^{+^2}.

As can be seen from Fig. B.11, the main effect of both cleaning and mathematical morphology appears on the left part of the histogram (small scale). Fig. B.12 provides a detailed view of the histograms of Fig. B.11 in the range of $100^{+^2} \leq A_c^+ \leq 300^{+^2}$.

In Fig. B.12a, the histogram results from three sources : small objects which are larger than structuring elements but smaller than 300^{+^2}, combinations of small objects, and objects cut from larger ones. In Fig. B.12b, the histogram only shows the objects cut from larger ones ($> 300^{+^2}$). Comparing Fig. B.12a and B.12b, both results are very similar with large structuring elements : $M_S = (15^+,\ 10^+)$, $M_S = (10^+,\ 20^+)$, $M_S = (10^+,\ 25^+)$ and $M_S = (10^+, 30^+)$. This indicates that the histograms in both Fig. B.12a and B.12b contain mainly objects which are cut from large objects if those structuring elements are used. Moreover the histograms obtained with those structuring elements are fairly high, indicating a strong effect on the detected objects. Therefore, those structuring elements can not be used in the present study. Using smaller structuring elements $M_S = (10^+,\ 10^+)$ and $M_S = (10^+,\ 15^+)$, the histograms in Fig. B.12a are much higher than those in Fig. B.12b, indicating that the histograms are mainly from small objects that are larger than the structuring element but smaller than 300^{+^2}, or combinations of small objects. Thus, small structuring elements $M_S = (10^+,\ 10^+)$ and $M_S = (10^+,\ 15^+)$ can be used.

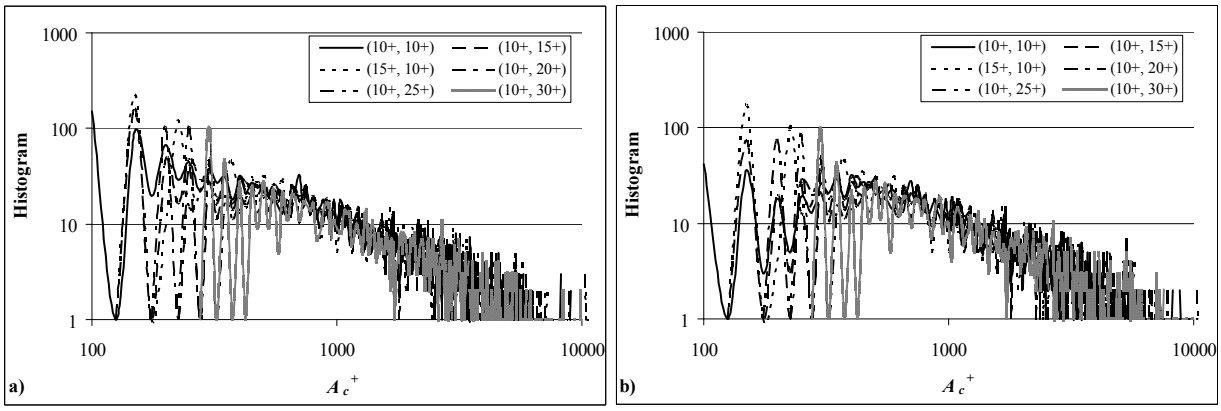

a : Without cleaning b : With cleaning

FIG. B.11 – Histogram of area A_c^+ of complete objects detected after the mathematical morphology procedure

Examining the indicative images, we find that many objects are thin and have angles with the streamwise direction. Therefore, to avoid separating too many objects into pieces, the structuring element $M_S = (10^+,\ 10^+)$ was finally chosen in the present study.

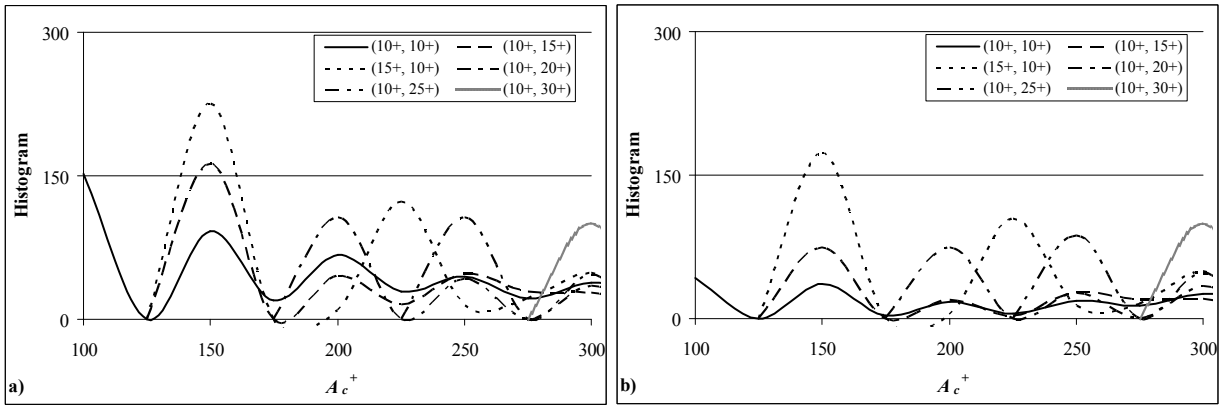

a : Without cleaning b : With cleaning

FIG. B.12 – Detailed histogram of the area A_c^+ of complete objects detected after the mathematical morphology procedure in the range $100^{+^2} \leq A_c^+ \leq 300^{+^2}$

B.2.4 Cleaning

After the mathematical morphology procedure, many small objects, which have area larger than that of the structuring element but not enough to be considered as ejections or sweeps, remain in the images (see Fig. B.10). They should be removed before statistical analysis. Two parameters C_B and C_C are employed to remove these kinds of objects on the basis of their area. The parameter C_B is for the small objects cut by image borders while the parameter C_C is for the small objects totally embedded in the images. In the present study, C_B was taken as half of C_C due to the fact that ejections and sweeps are much smaller than the image field ($530^+ * 300^+$). These two parameters are given in square wall unit. Three combination of C_B and C_C were tested : (250^{+^2}, 500^{+^2}), (375^{+^2}, 750^{+^2}) and (500^{+^2}, 1000^{+^2}).

Fig. B.13 gives an example of an indicative image after the mathematical morphology procedure and the corresponding images after cleaning procedure. The chosen sample is exceptional due to existence of many small objects, thus the effect of cleaning can be observed clearly. In Fig. B.13, small clean factors $C_B = 250^{+^2}$ and $C_C = 500^{+^2}$ can not remove effectively the small objects in the middle left of the image which are considered as noise. Large clean factors $C_B = 500^{+^2}$ and $C_C = 1000^{+^2}$ remove too many objects which are potential ejections (e.g. the one in the middle right and the one in the bottom of the image). In order to detect all the possible ejections and sweeps, clean factors C_B=375^{+^2} and C_C=750^{+^2} were chosen.

B.2.5 Parameters for all ten planes

Based on the above discussion, $C_T^{uv} = 1.0$, $C_T^v = 0.6$, $M_S = (10^+, 10^+)$, $C_B = 375^{+^2}$ and $C_C = 750^{+^2}$ were chosen to detect both ejections and sweeps at all the wall distances studied.

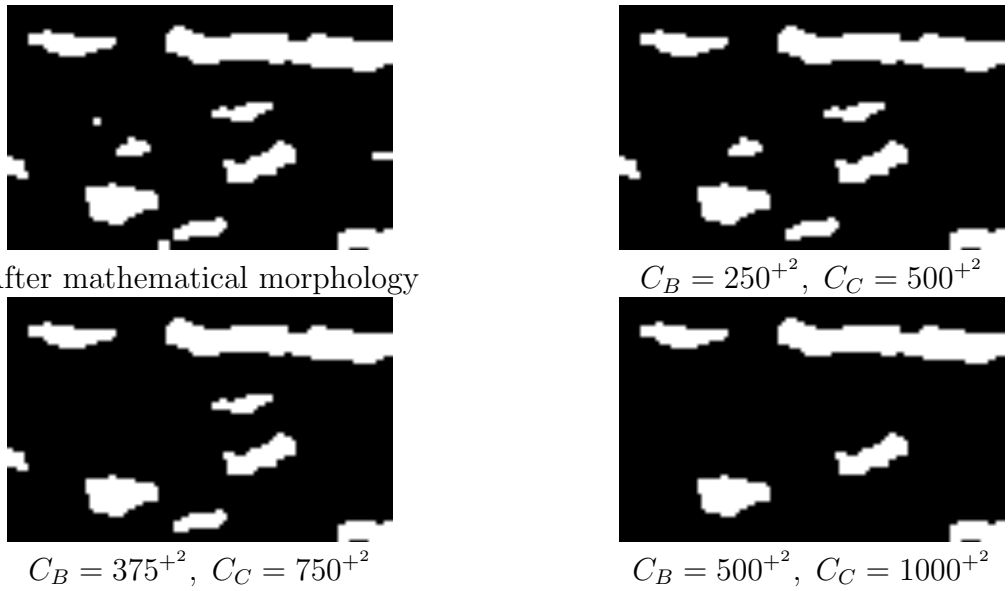

After mathematical morphology

$C_B = 250^{+^2}$, $C_C = 500^{+^2}$

$C_B = 375^{+^2}$, $C_C = 750^{+^2}$

$C_B = 500^{+^2}$, $C_C = 1000^{+^2}$

FIG. B.13 – Indicative images with various C_B and C_C for ejections ($C_T^{uv} = 1.0$, $C_T^v = 0.6$, $M_s = (10^+, 10^+)$)

B.3 VF and GO

B.3.1 Detection functions

As defined in Chapter 6.4, objects with high velocity fluctuation are referred to as VF while objects with high velocity gradient are named GO. According to the sign of the fluctuations, VF can be divided into NVF (negative) and PVF (positive). Similarly, according to the sign of gradient, GO are classified into NGO (negative) and PGO (positive). As concluded in Chapter 6.1, two detection functions F_d^{grad} and F_d^v, are employed to detect VF and GO respectively. They are defined as :

$$F_d^v = f_1(v', \sigma_v) = \frac{v'(m, n, \mathrm{y}^+)}{\sigma_v(\mathrm{y}^+)} \tag{B.9}$$

$$F_d^{grad} = f_2(v', \sigma_v) = \frac{1}{\sigma_v(\mathrm{y}^+)} \frac{\partial(v'(m, n, \mathrm{y}^+))}{\partial \mathrm{z}} \tag{B.10}$$

Similar to the detection procedure of streaks, ejections and sweeps, three procedures : thresholding, mathematical morphology and cleaning, are used to identify VF and GO and to create the corresponding indicative images. For both objects, the parameters involved in these procedures are one threshold for the thresholding procedure, one structuring element for the mathematical morphology procedure and two clean factors for the cleaning procedure. In order to find the suitable value for each parameter, field #3 of Plane #5 ($\mathrm{y}^+ = 29.7$) was selected as the reference image to test different values for each parameter. The corresponding detection functions F_d^v and F_d^{grad} were shown in Fig. B.14. The second order least square difference scheme was used to calculate F_d^{grad}.

VF can be divided into NVF and PVF according to the sign of fluctuation, while GO can be separated into NGO and PGO according to the sign of gradient. According to the spanwise homogeneity of the flow, the shape and size of NGO are the same as PGO. This is also true for NVF and PVF. Therefore, in the present study, only PGO and PVF were examined to select the suitable parameters if no other specification is made. The selected

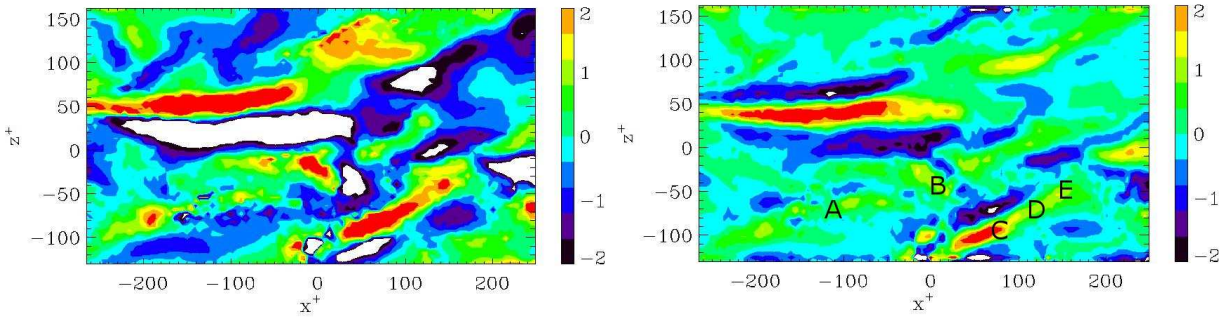

Detection function F_d^v Detection function F_d^{grad}

FIG. B.14 – Detection functions

B.3.2 VF

B.3.2.1 Thresholding

VF can be recognized from the background by thresholding the detection function F_d^v (Eq. B.10). The corresponding threshold is referred to as C_T^v. The corresponding indicative function of NVF and PVF F_i^v are defined respectively as :

$$\text{PVF}: \quad F_i^v = \begin{cases} 1 & \text{when } F_d^v > C_T^v \\ 0 & \text{otherwise} \end{cases} \tag{B.11}$$

$$\text{NVF}: \quad F_i^v = \begin{cases} 1 & \text{when } F_d^v < -C_T^v \\ 0 & \text{otherwise} \end{cases} \tag{B.12}$$

Binary images of PVF (or NVF) are generated by applying this procedure to the whole field. Since this procedure is the initial step to identify these objects that are used to detect the streamwise vortices. This procedure can have a significant effect on the quality of the detection of these vortices. Therefore, the value of threshold C_T^v should be examined thoroughly. In the present study, six different values of C_T^v from 0.6 to 1.6 with an interval of 0.2 were tested to detect PVF.

Fig. B.15 shows indicative images for PVF obtained by thresholding the detection function F_d^v (Fig. B.14) with various threshold C_T^v on the reference image. Comparing this figure with the original normalized wall-normal velocity fluctuation image in Fig. B.14, when $C_T^v < 1.0$, the indicative function is fairly noisy and many separate objects are connected. However, high value of C_T^v ($C_T^v > 1.4$) results in reduction or even removal of many objects that have strong velocity fluctuations. Therefore, the most suitable value is between 1.0 to 1.4. To make a further choice, indicative images for NVF after the thresholding procedure with various thresholds C_T^v, is presented in Fig. B.16. When $C_T^v = 1.0$, the two big objects in the middle of the image that belong to different vortices are connected together. When $C_T^v = 1.4$, the NVF in the upper-left that is potentially related to streamwise vortices is eliminated. Following this, an intermediate value of the threshold of $C_T^v = 1.2$ is chosen in the present study.

B.3.2.2 Mathematical morphology

Similar to the detection procedure of other coherent structures, a mathematical morphology filter is employed to remove the small objects, to fill the holes inside the objects, and to reconnect the separated parts that belong to the same object. This procedure requires a suitable structuring element (M_S). Examining the indicative images after threholding, we found that the VF are generally elongated in the streamwise direction. According to the shape of VF, a rectangular or a square structuring element $M_S(W, L)$ is chosen, where W is the width in the spanwise direction and L is the length in the streamwise direction. W and L are given in wall unit. To select a suitable structuring element, six M_S are tested in the present study.

Fig. B.17 shows the indicative images of PVF with various structuring elements after the mathematical morphology procedure. With these images, the influence of the structuring element is clearly evidenced. The images show that structuring elements with large

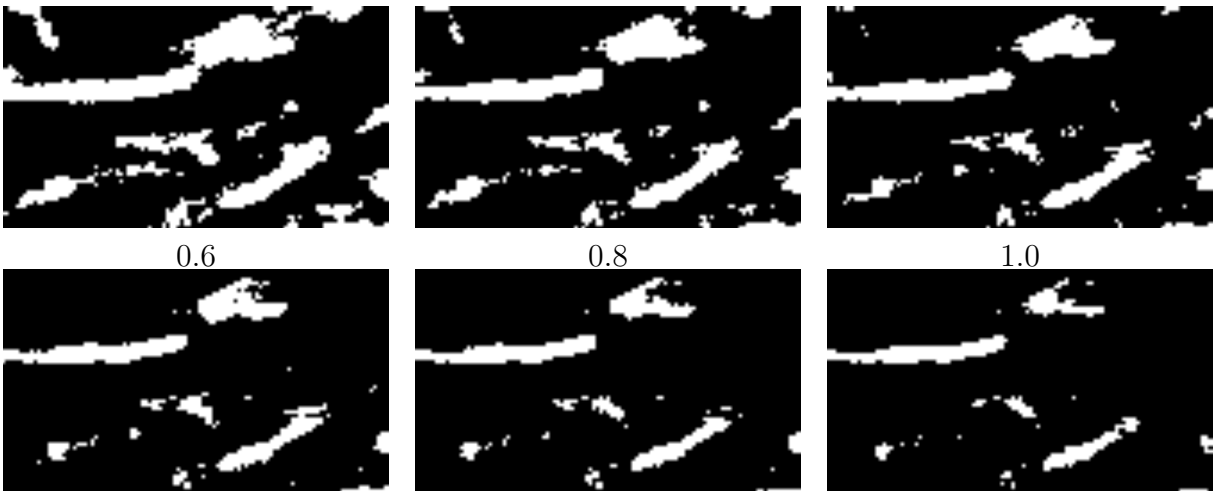

FIG. B.15 – Indicative images after the thresholding procedure with various C_d^v for PVF

FIG. B.16 – Indicative images after the thresholding procedure with various C_T^v for NVF

parameter W ($M_s = (15^+,\ 10^+)$, $(15^+,\ 15^+)$ and $(20^+,\ 10^+)$) can cut objects into pieces and reduce considerably the size of them, thus are not suitable in the present study. Furthermore, examining all 500 indicative images after thresholding, VF has a similar size as ejections and sweeps. Similar to the detection of ejections and sweeps, large structuring elements cannot be used in the detection of VF. Moreover, the examination of all 500 indicative images shows that some of VF are thin and have relatively large angles with the streamwise direction. Considering this effect, the square structuring element $M_s = (10^+,\ 10^+)$ was chosen to be used in the present study.

B.3.2.3 Cleaning

As shown in Fig. B.17, many small objects, whose areas are larger than that of the structuring element but not enough to be used to detect the streamwise vortices, remain in the images after the mathematical morphology procedure. The same as the detection of other coherent structures, a cleaning procedure with two parameters C_B and C_C, is introduced to remove these objects based on their area. The first one is for the objects that are cut by borders and the other is for the objects entirely embedded in the image. C_B and C_C are given in square wall units.

Fig. B.18 shows the effect of the cleaning procedure on the reference image. Small

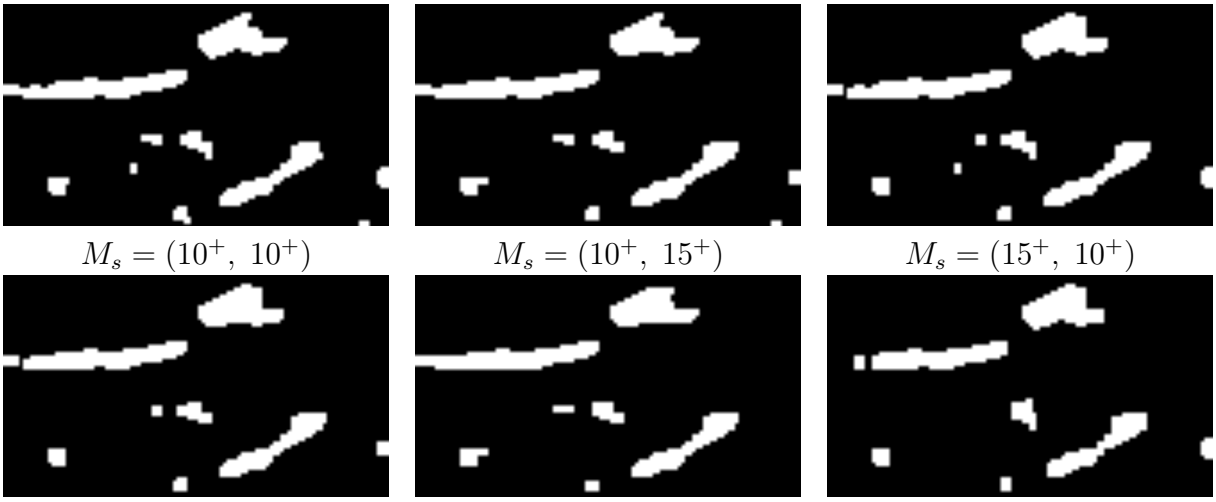

FIG. B.17 – Indicative images with various M_s after the mathematical morphology procedure for PVF

values of $C_B < 500^+$ and $C_C < 1000^{+^2}$ can not remove small objects as effectively as $C_B = 500^{+^2},\ 625^{+^2}$ and $C_C = 1000^{+^2},\ 1250^{+^2}$. In addition, the average surface of complete objects before the cleaning procedure is about 1000 square wall units. Therefore, the clean factors $C_B = 500^{+^2}$ and $C_C = 1000^{+^2}$ were chosen in the present study to detect VF.

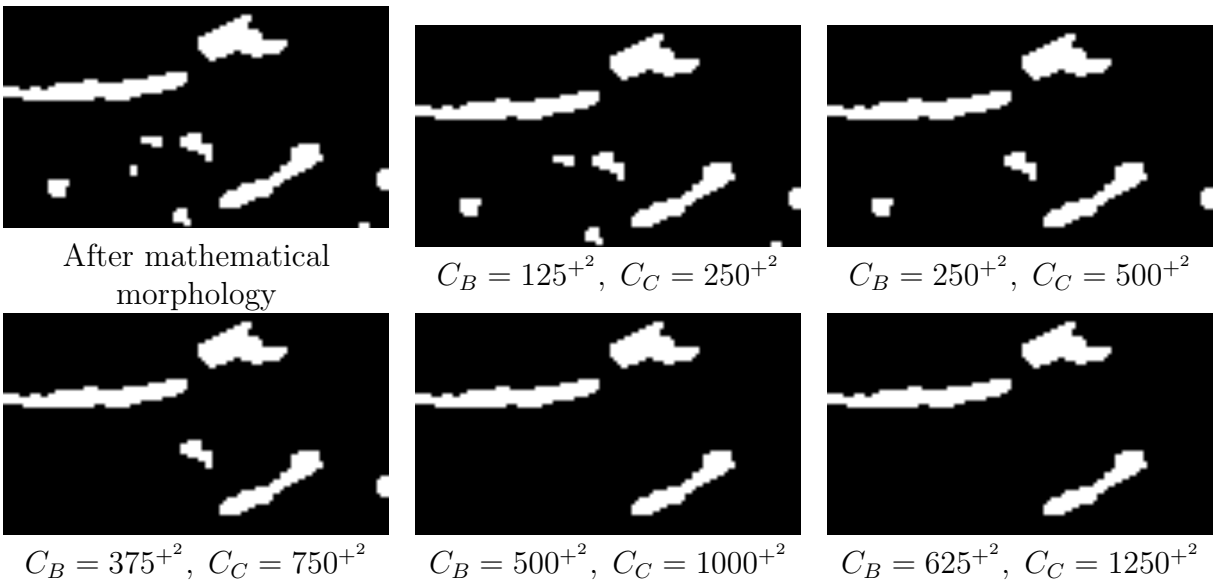

FIG. B.18 – Indicative images with various C_B and C_C after the cleaning procedure for PVF

B.3.2.4 Parameters for all ten planes

Based on the above discussion, $C_T^v = 1.2$, $M_S = (10^+, 10^+)$, $C_B = 500^{+^2}$ and $C_C = 1000^{+^2}$ were chosen to detect VF at all the wall distances studied.

B.3.3 GO

B.3.3.1 Thresholding

PGO and NGO are identified from the background by thresholding the detection function F_d^{grad} (Eq. B.10). The corresponding threshold is referred to as C_T^{grad}. The corresponding indicative function F_i^{grad} of PGO and NGO are defined respectively as :

$$\text{PGO}: \quad F_i^{grad} = \begin{cases} 1 & \text{when } F_d^{grad} > C_T^{grad} \\ 0 & \text{otherwise} \end{cases} \tag{B.13}$$

$$\text{NGO}: \quad F_i^{grad} = \begin{cases} 1 & \text{when } F_d^{grad} < -C_T^{grad} \\ 0 & \text{otherwise} \end{cases} \tag{B.14}$$

Applying this procedure to the whole field, binary images of PGO (or NGO) are generated. As explained in the detection of VF, It is mandatory of GO to reveal the existence of streamwise vortices. Their detection can thus have a significant impact on the quality of the detection of these vortices. Therefore the value of threshold C_T^{grad} should be selected carefully. In the present study, six different values from 0.6 to 1.6 with an interval of 0.2 were tested to detect PGO.

Fig. B.19 shows indicative images of PGO obtained by thresholding the detection function with various threshold C_T^{grad} in the reference field (field #3 of Plane 5). Comparing this figure with the detection functions F_d^{grad} in Fig. B.14, the indicative images are fairly noisy when $C_T^{grad} < 0.8$. However, high value of C_T^{grad} (i.e. $C_T^{grad} > 1.2$) leads to reduction or even removal of many objects that are potentially related to streamwise vortices. Examining Fig. B.14, regions A and B are considered as noise rather than parts of streamwise vortices thus the related PGO should be eliminated by thresholding. For regions C, D and E, according to Fig. B.14, they are parts of a streamwise vortex. However, in region D, this vortex seems to be disturbed. Therefore, it is logical to have a break on the related high gradient object. Based on the above discussions, the best choice of the threshold C_T^{grad} is 1.0 in the present study.

B.3.3.2 Mathematical morphology

As can be seen in Fig. B.19, the indicative image is still noisy even after thresholding. To improve the quality of the image, a mathematical morphology procedure is employed. This procedure is expected to remove the small objects, to fill the holes inside the objects and to reconnect the separated parts that belong to the same structure. It requires a suitable structuring element (M_S). Examining the indicative images after thresholding, we found that GO are elongated in the streamwise direction. Therefore, a rectangular or a square structuring element $M_S(W, L)$ is chosen, where W is the width in the spanwise

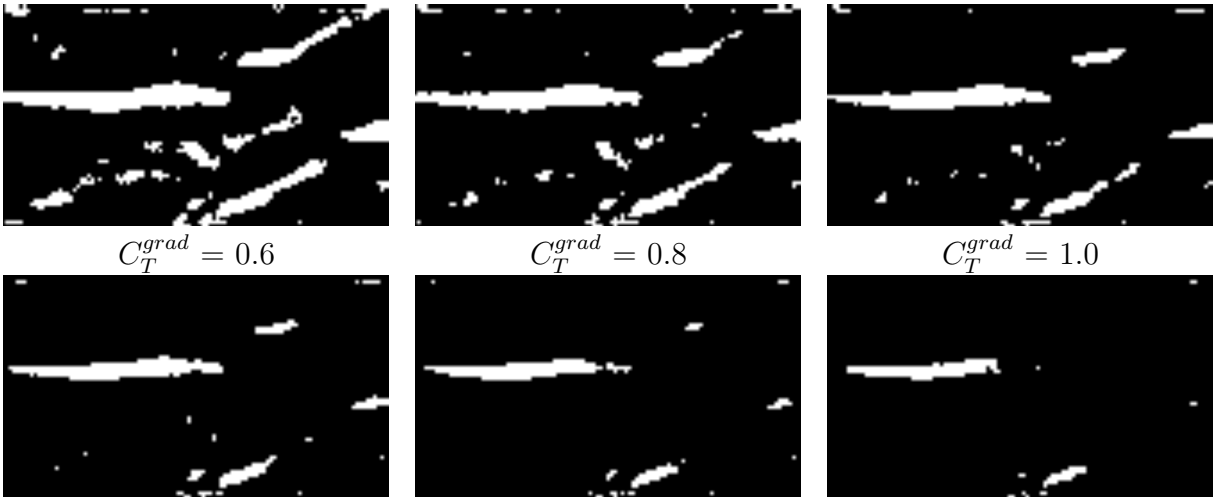

FIG. B.19 – Indicative images after the thresholding procedure with various C_T^{grad} for PGO

direction and L is the length in the streamwise direction. The values of W and L are given in wall unit. In the present study, six structuring elements are tested.

Fig. B.20 shows the indicative images with different structuring elements after the mathematical morphology procedure. These images provide a direct visualization of the influence of the structuring element. They show that large structuring elements ($M_s = (20^+,\ 10^+), (15^+,\ 15^+)$ and $(10^+,\ 20^+)$) can cut objects into pieces and reduce considerably the size of them, thus are not suitable to be used in the present study. In addition, structuring elements $M_s = (15^+,\ 10^+)$ and $(10^+,\ 15^+)$ may cause the same problem due to the fact that the high gradient objects are thin and may have angles with the streamwise direction. Therefore, only the square structuring element $M_s = (10^+,\ 10^+)$ can be used in the present study.

B.3.3.3 Cleaning

After the mathematical morphology procedure, many small objects, whose areas are larger than that of the structuring element but not enough to represent the streamwise vortices, remain in the images. A cleaning procedure with two parameters C_B and C_C, is employed to remove these objects based on their area. The first one is for the objects cut by borders and the second is for the small objects entirely embedded in the images. The unit of C_B and C_C is square wall unit. Fig. B.21 and Fig. B.22 shows the effect of the cleaning procedure on the reference image. In Fig. B.21, the indicative image after mathematical morphology procedure contains not only four large objects which are potentially related to the streamwise vortices but also several small ones. Large values ($C_B = 500^{+^2}$ and $C_C = 1000^{+^2}$) remove the object in the upper-right corner that represents a streamwise vortex. All the other clean factors remove efficiently the noise and keep the four large objects. To select the suitable clean factors, Fig. B.22 shows another example of cleaning procedure. In Fig. B.22, some small objects that are unlikely to be streamwise vortices,

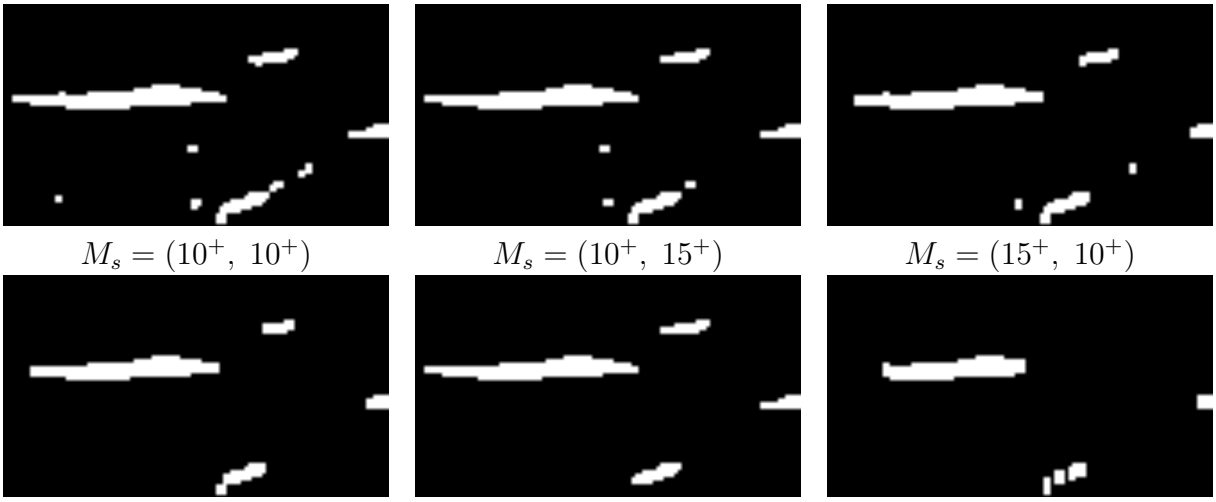

FIG. B.20 – Indicative images with various M_s after the mathematical morphology procedure for PGO

still remain in the indicative images with the small values ($C_B = 125^{+^2}$, $C_C = 250^{+^2}$) and ($C_B = 250^{+^2}$, $C_C = 500^{+^2}$)). In addition, the average surface of complete objects before the cleaning procedure is about 750^+. Based on the above discussion, the clean factor $C_C = 750^{+^2}$ was selected to detect PGO in the present study. The clean factor C_B was chosen as 375^{+^2} which is half of the value of C_C.

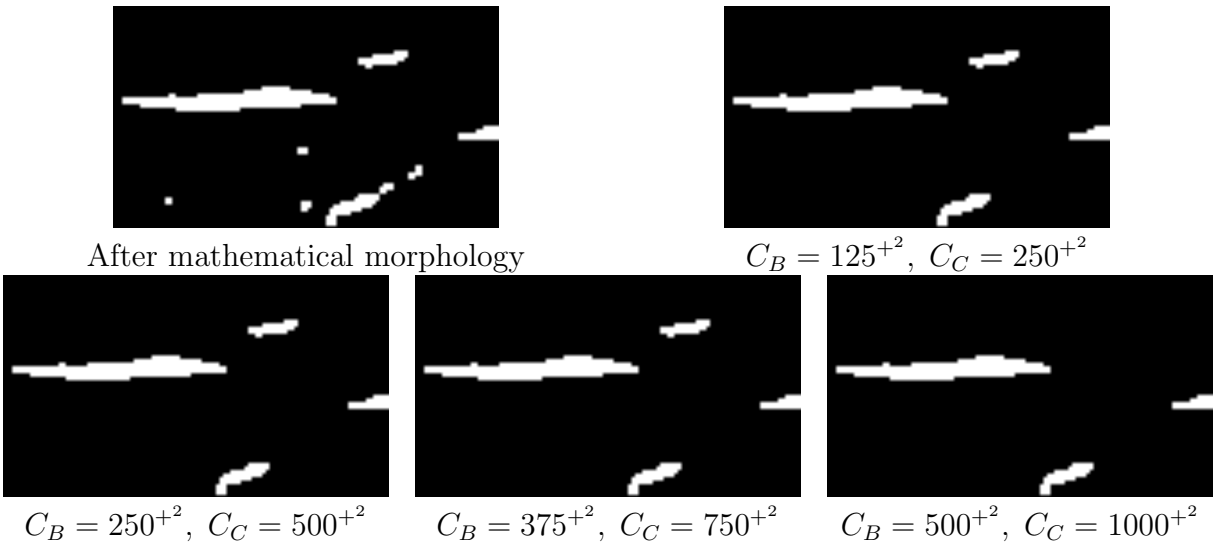

FIG. B.21 – Indicative images with various C_B and C_C after the cleaning procedure for PGO

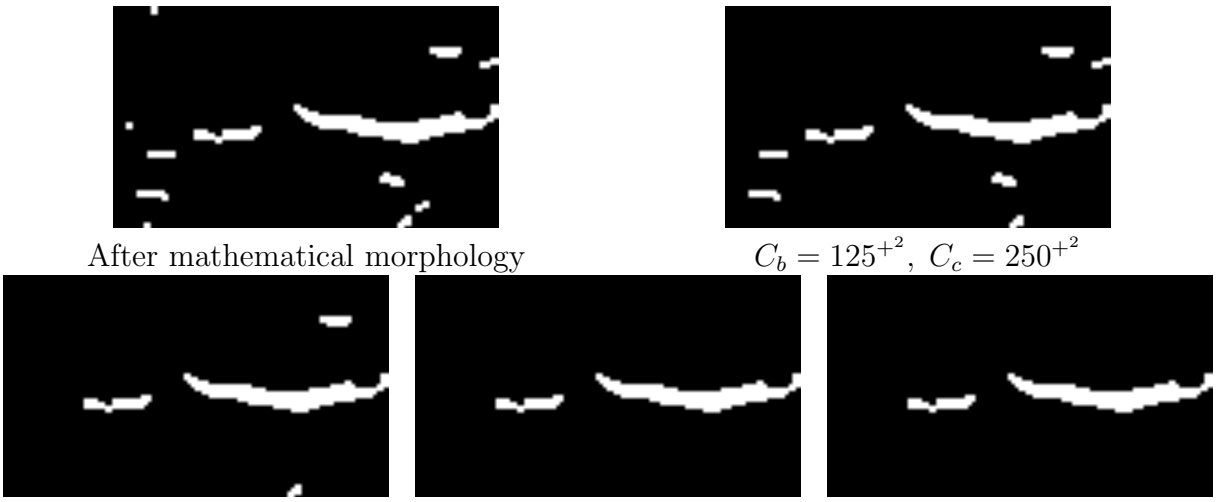

FIG. B.22 – Indicative images with various C_B and C_C after the cleaning procedure for PGO

B.3.3.4 Parameters for all ten planes

Based on the above discussion, $C_T^{grad} = 1.0$, $M_S = (10^+, 10^+)$, $C_B = 375^{+^2}$ and $C_C = 750^{+^2}$ were chosen to detect GO at all the wall distances studied.

All the parameters selected in Appendix A. 2.1 to A. 2.3 were used to detect the all possible structures including weak ones. If one needs to detect strong structures, these parameters can be changed to adapt the requirements according to the above mentioned selection criteria. Details will not be discussed here.

Annexe C

Correlation of coherent structures

C.1 Streaks

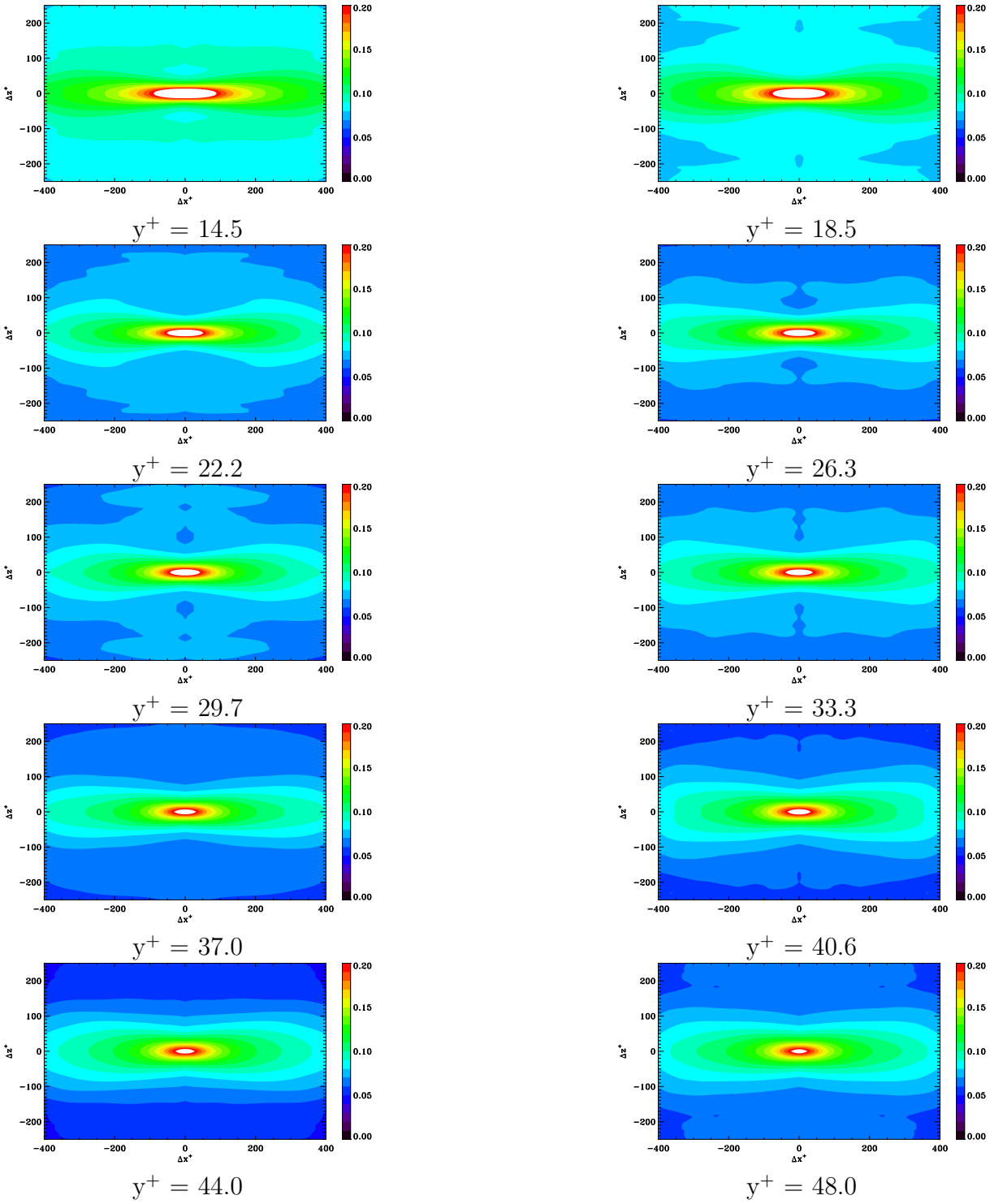

FIG. C.1 – Correlations of low speed streaks with low speed streaks $R_{LSS-LSS}$

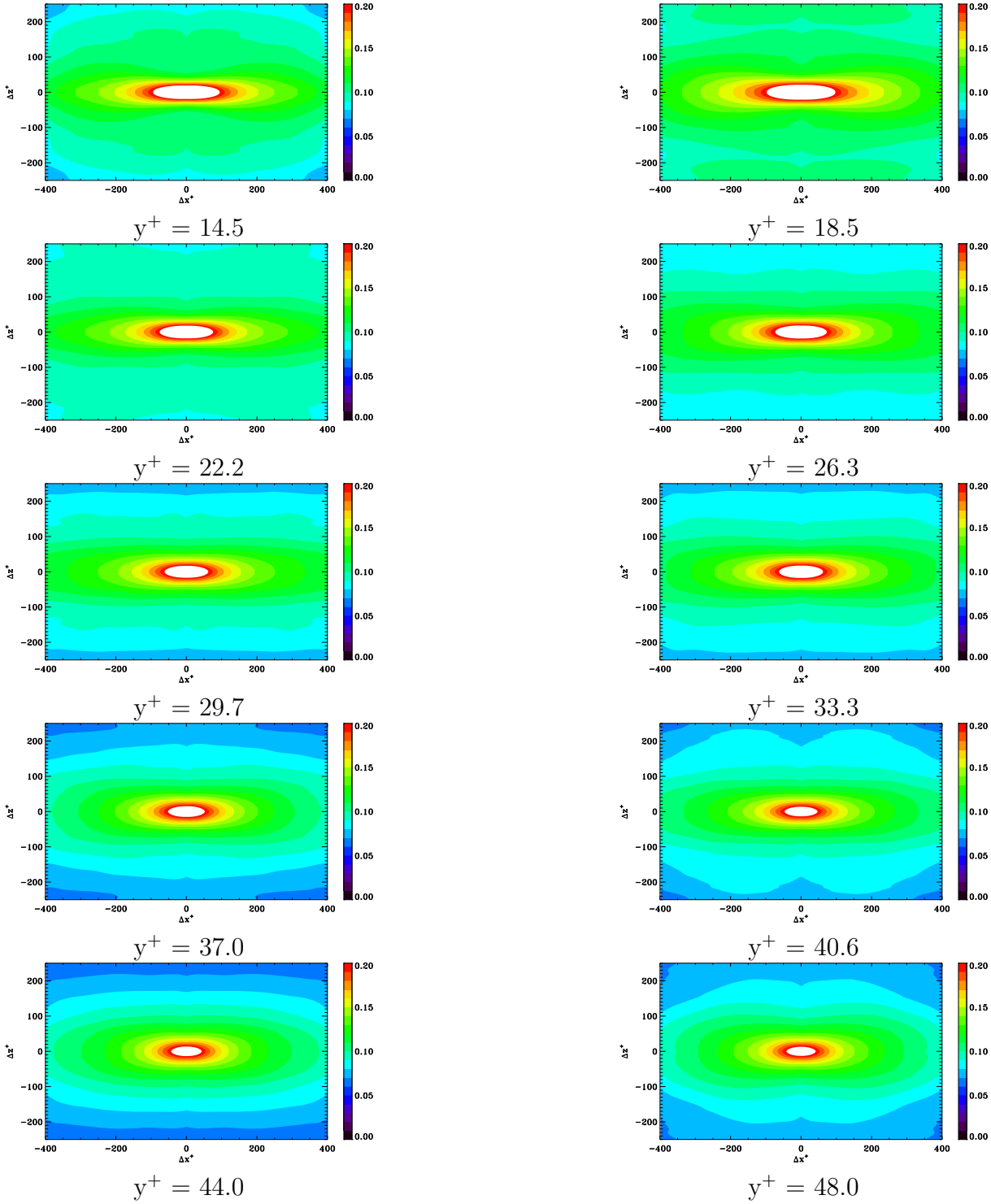

FIG. C.2 – Correlations of high speed streaks with high speed streaks $R_{HSS-HSS}$

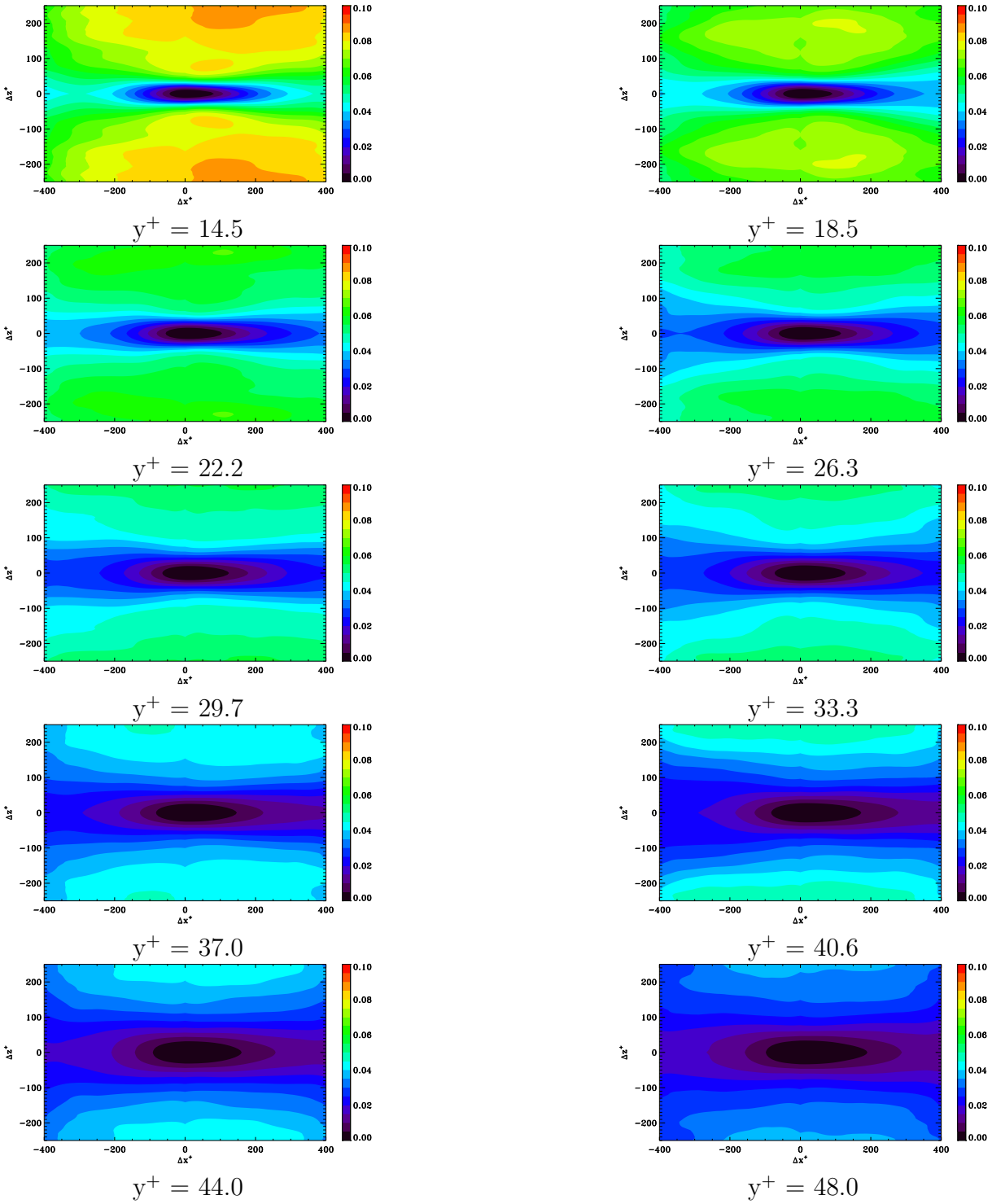

FIG. C.3 – Correlations of low speed streaks with high speed streaks $R_{LSS-HSS}$

C.2 Ejections and sweeps

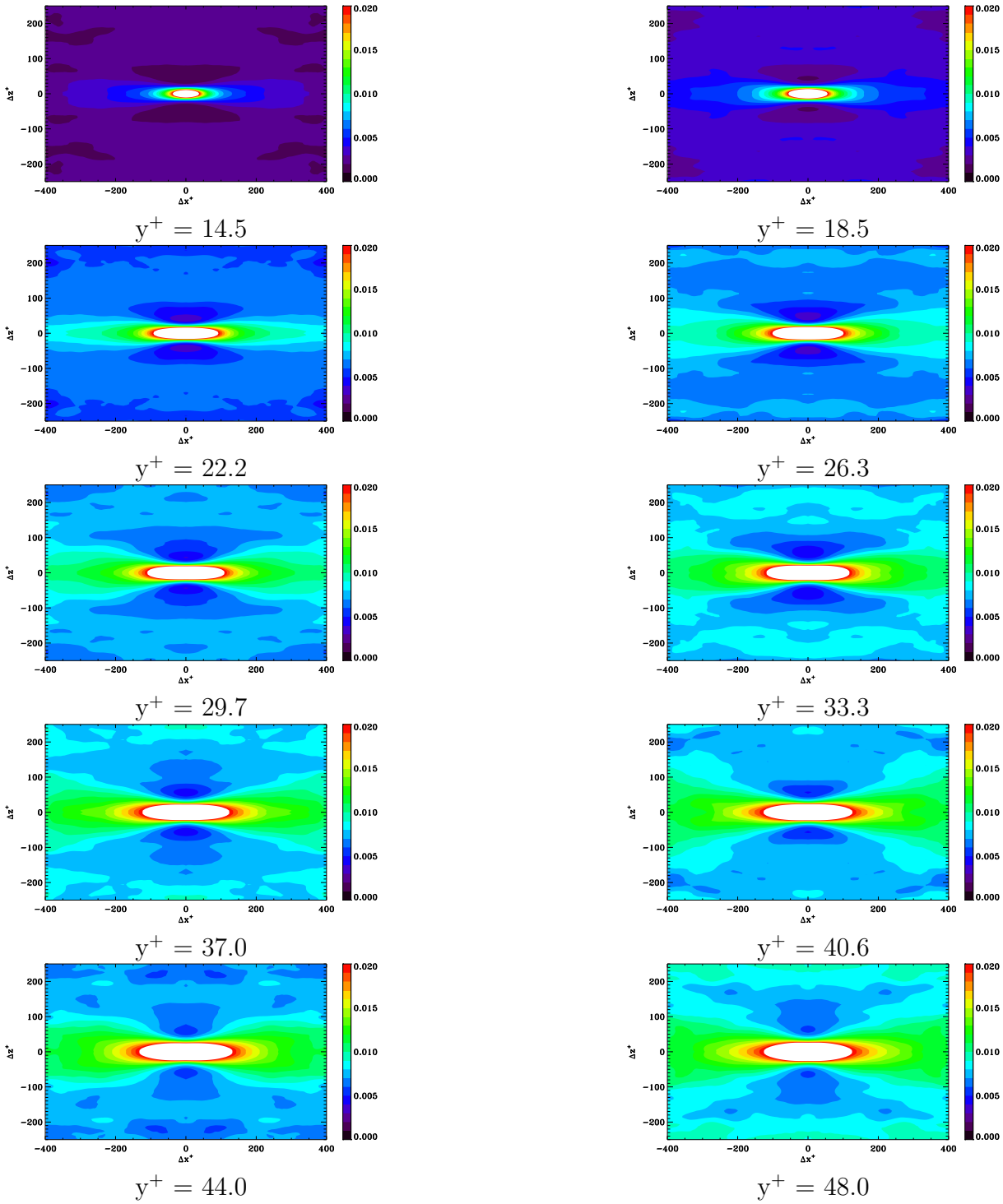

FIG. C.4 – Correlations of ejections with ejections R_{EJ-EJ}

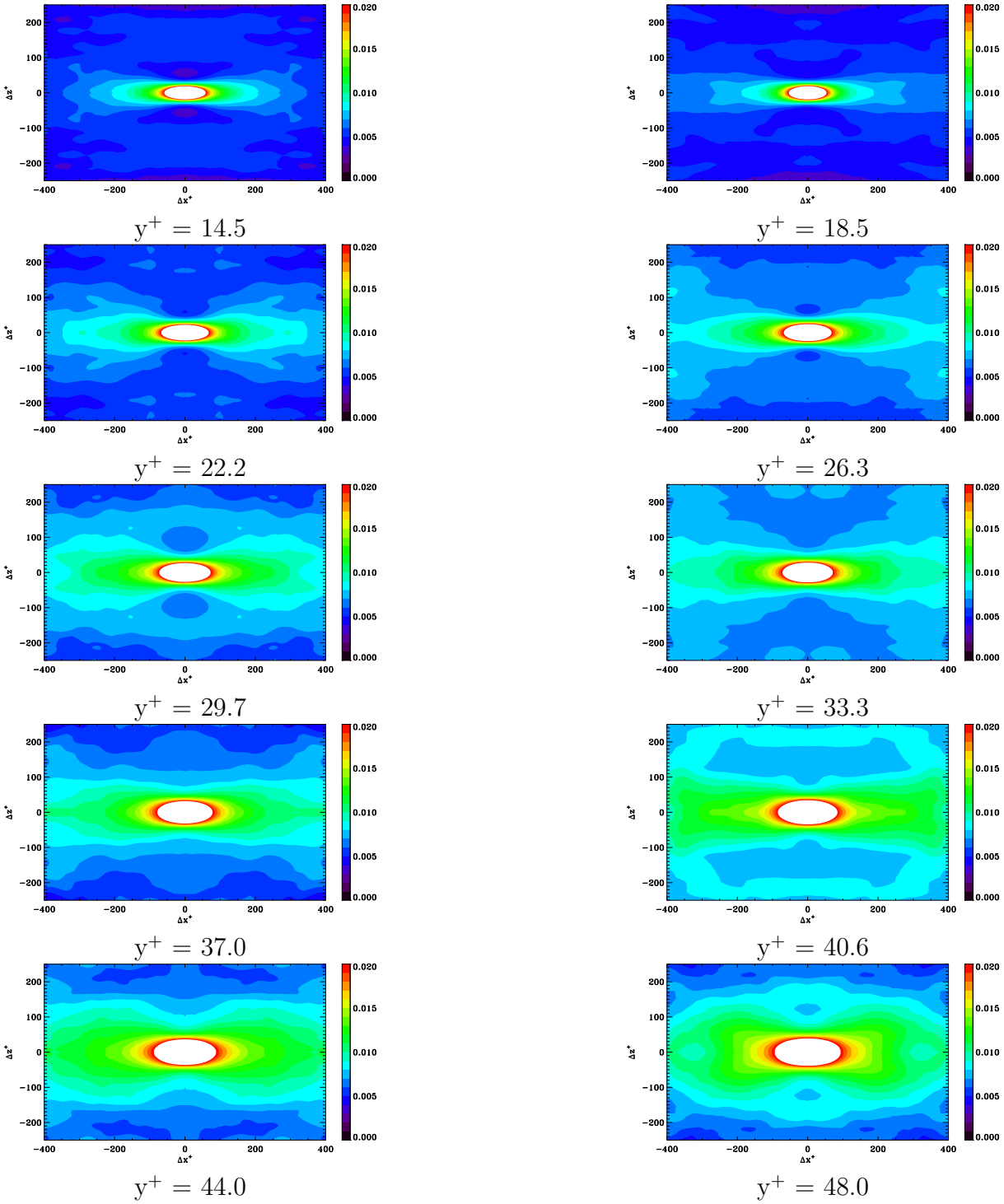

FIG. C.5 – Correlations of sweeps with sweeps R_{SW-SW}

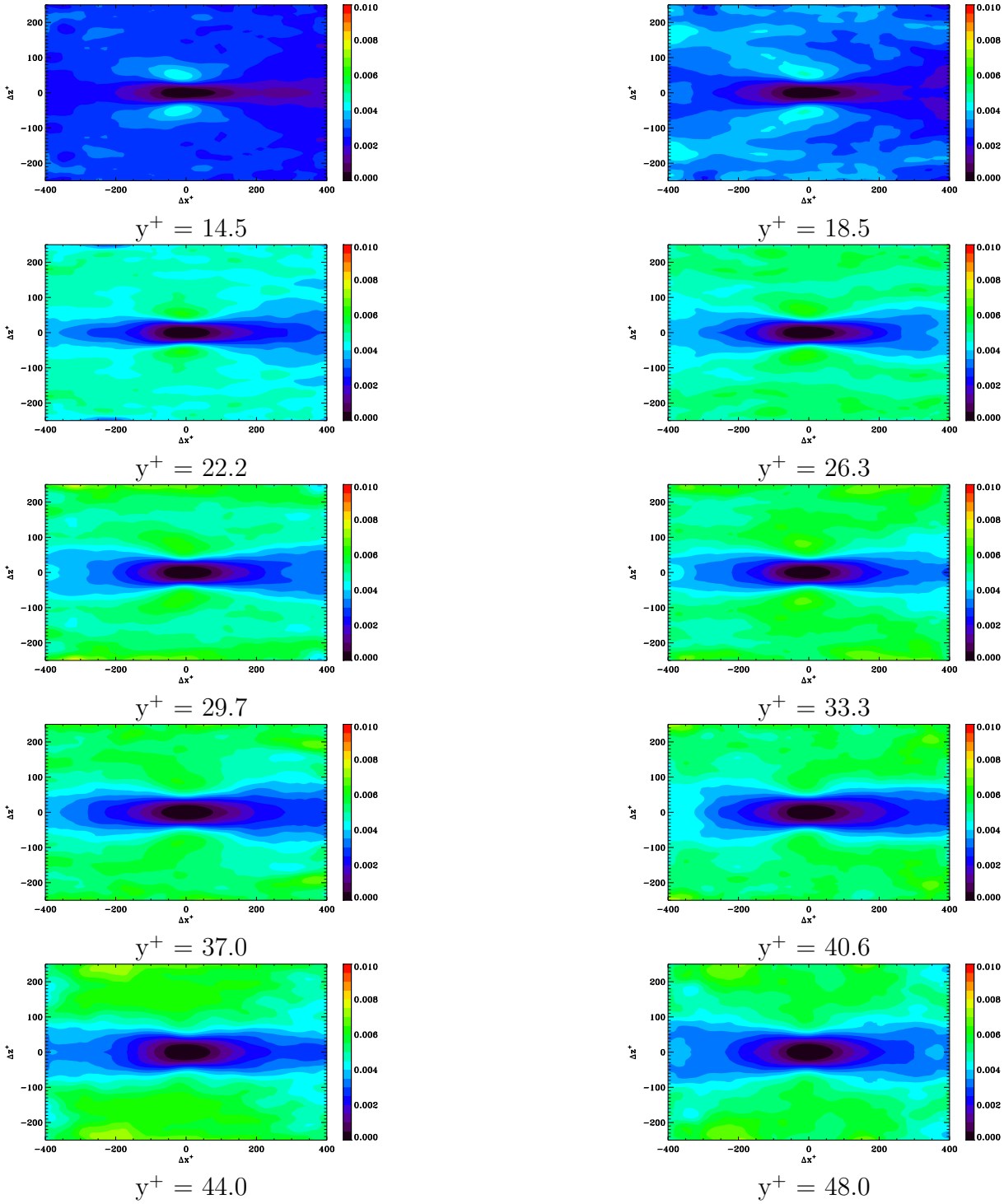

FIG. C.6 – Correlations of ejections with sweeps R_{EJ-SW}

C.3 NGSV and PGSV

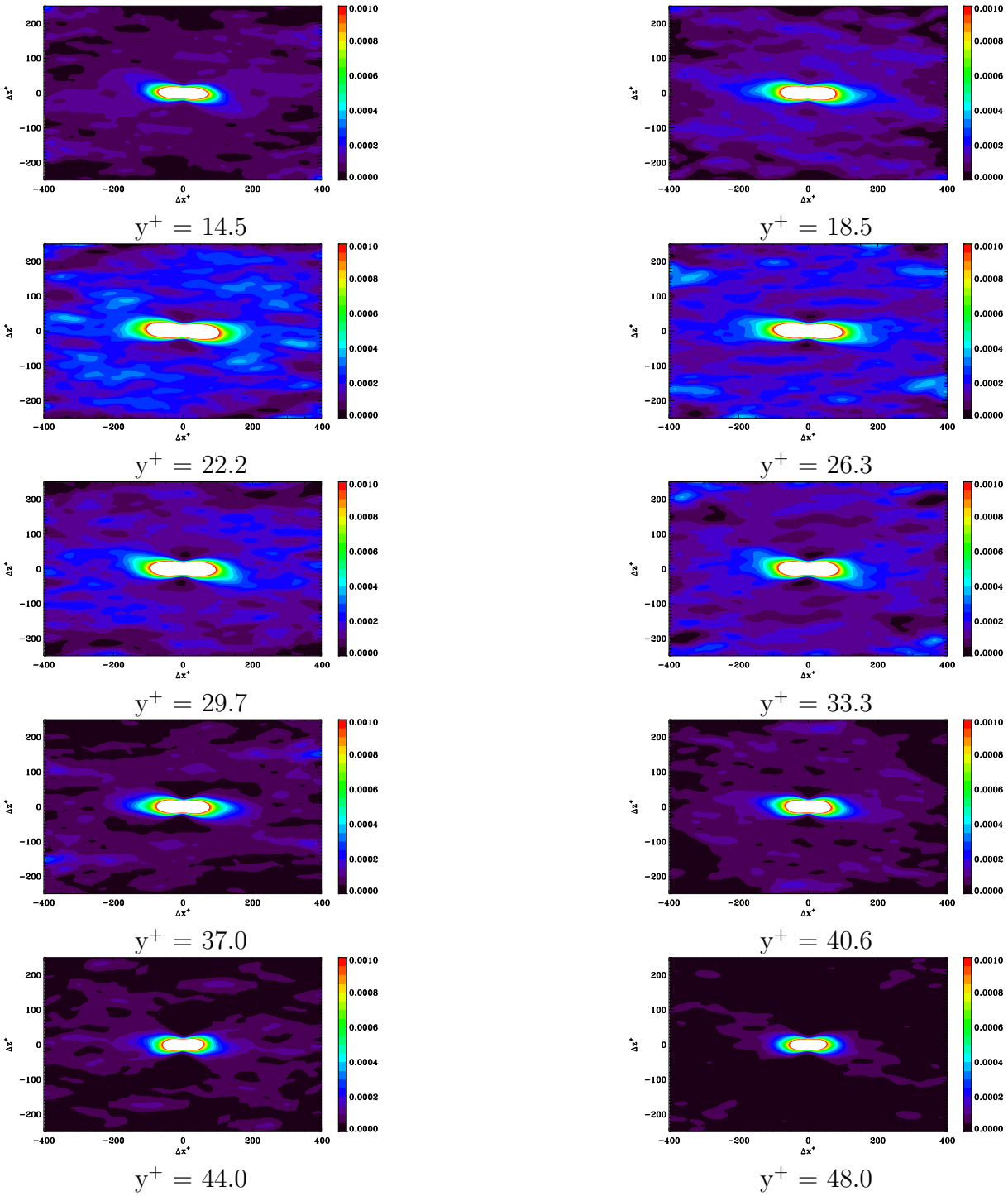

FIG. C.7 – Correlations of PGSV with PGSV $R_{PGSV-PGSV}$

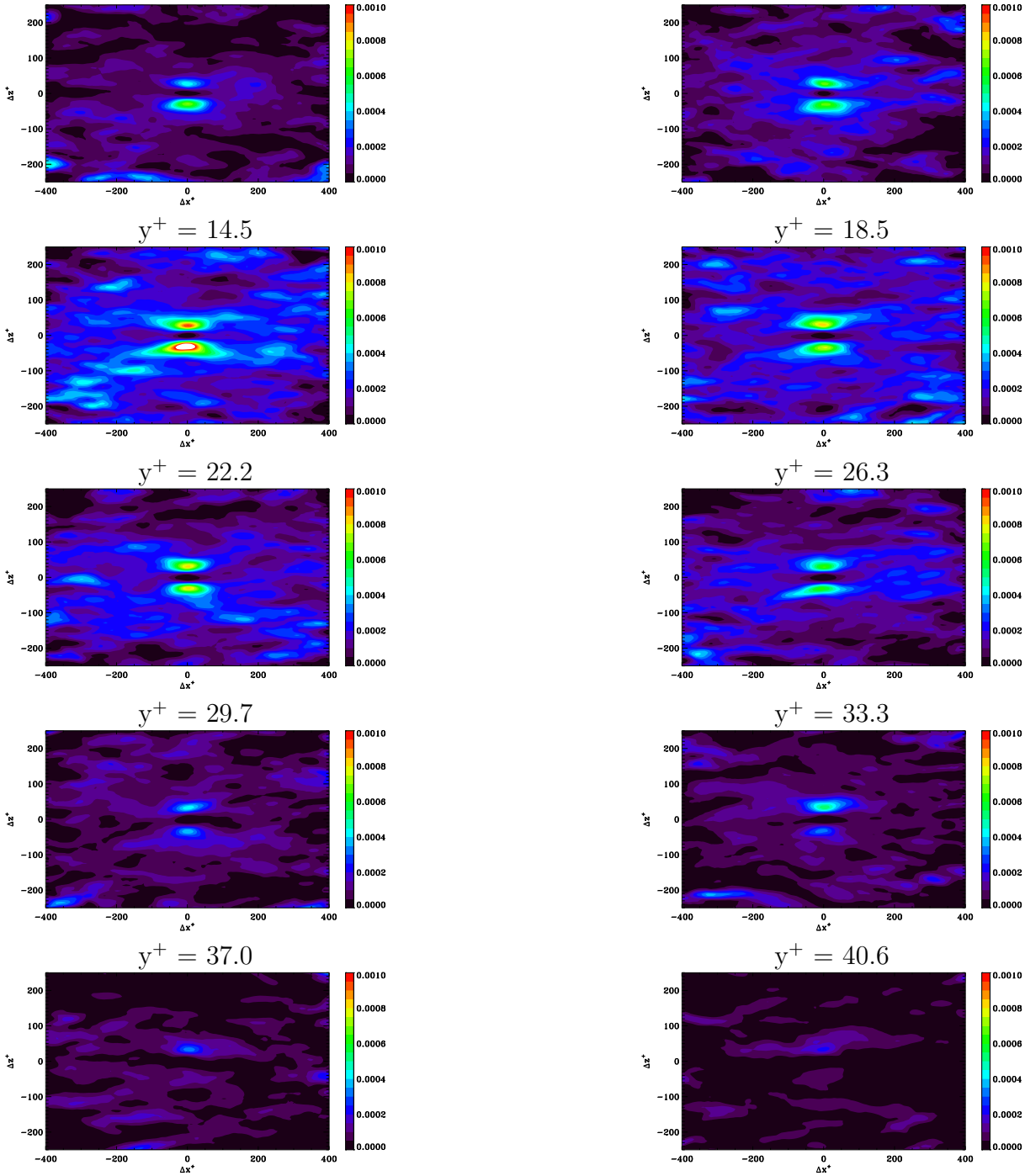

FIG. C.8 – Correlations of NGSV with PGSV $R_{NGSV-PGSV}$

C.4 NVF and PVF

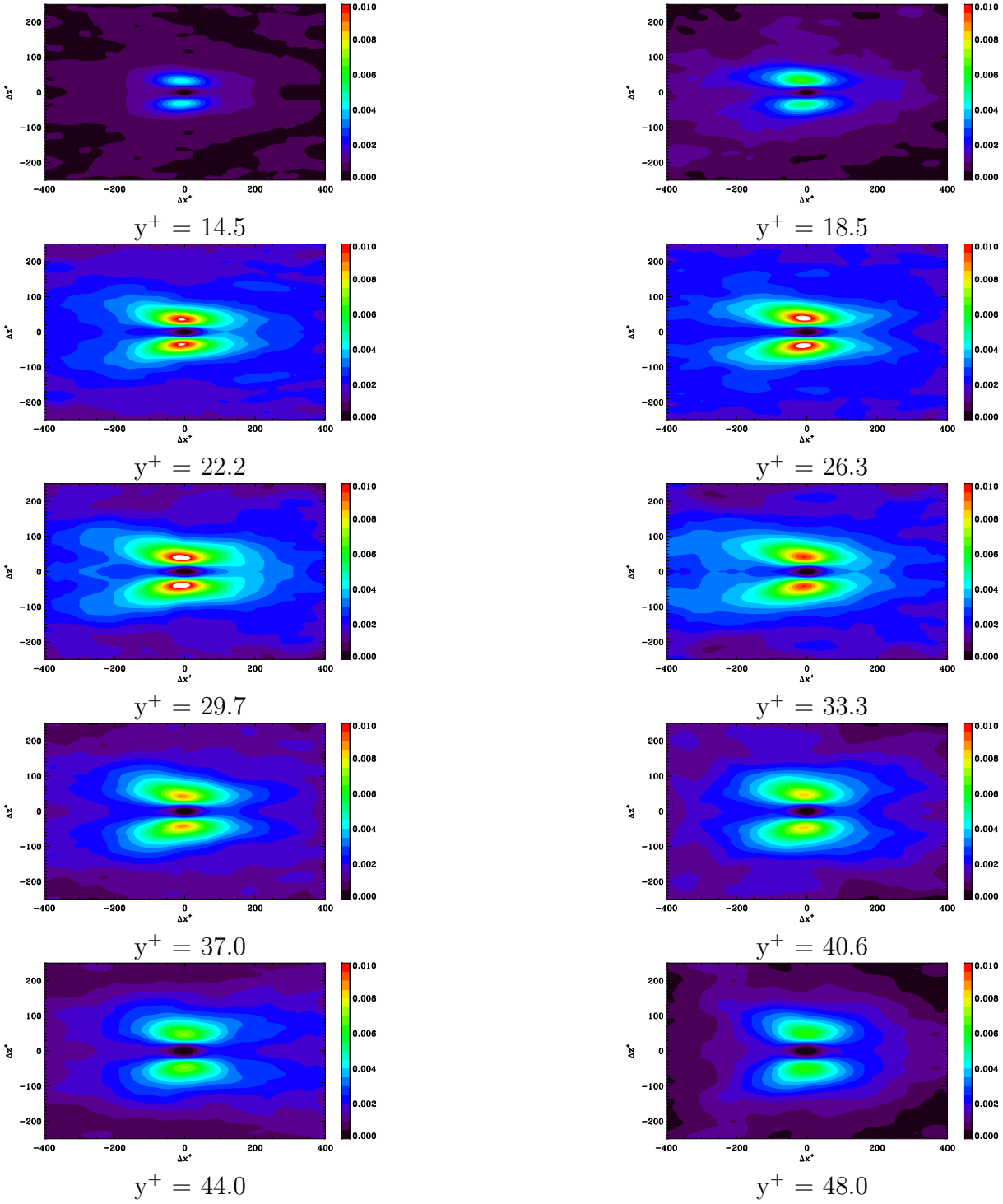

FIG. C.9 – Correlations of PVF with NVF $R_{PVF-NVF}$

C.5 Streaks with ejections and sweeps

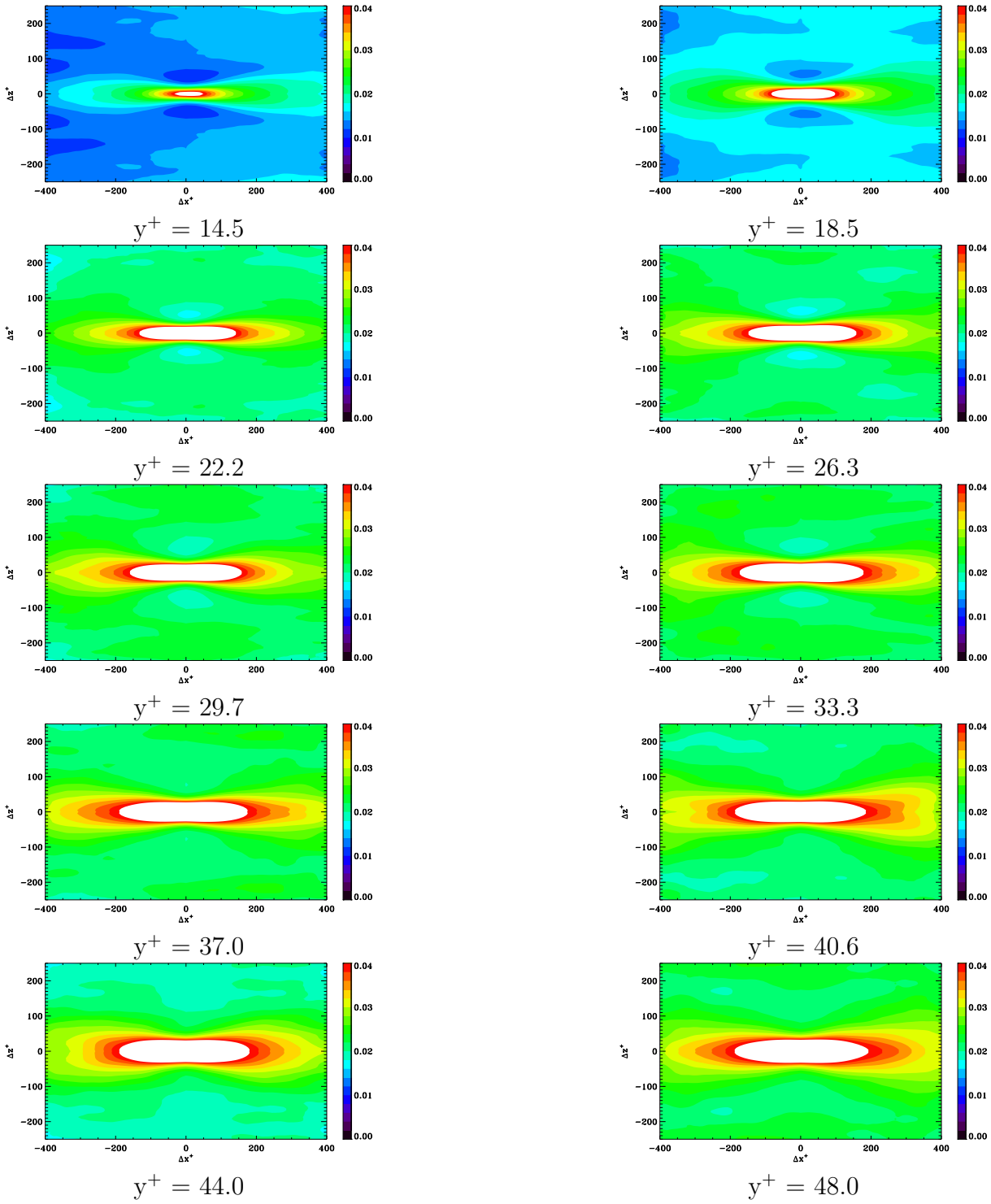

FIG. C.10 – Correlations of low speed streaks with ejections R_{LSS-EJ}

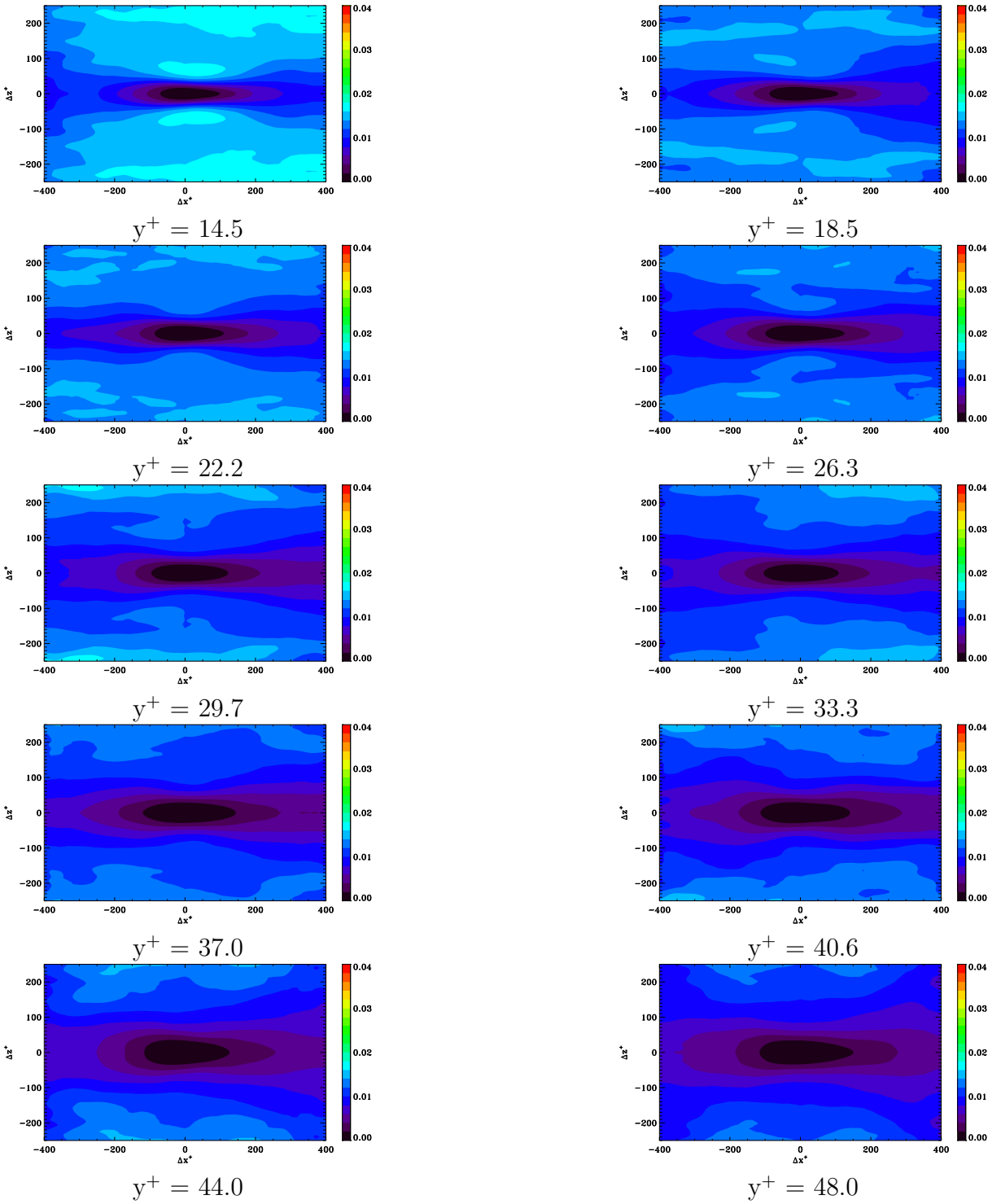

FIG. C.11 – Correlations of low speed streaks with sweeps R_{LSS-SW}

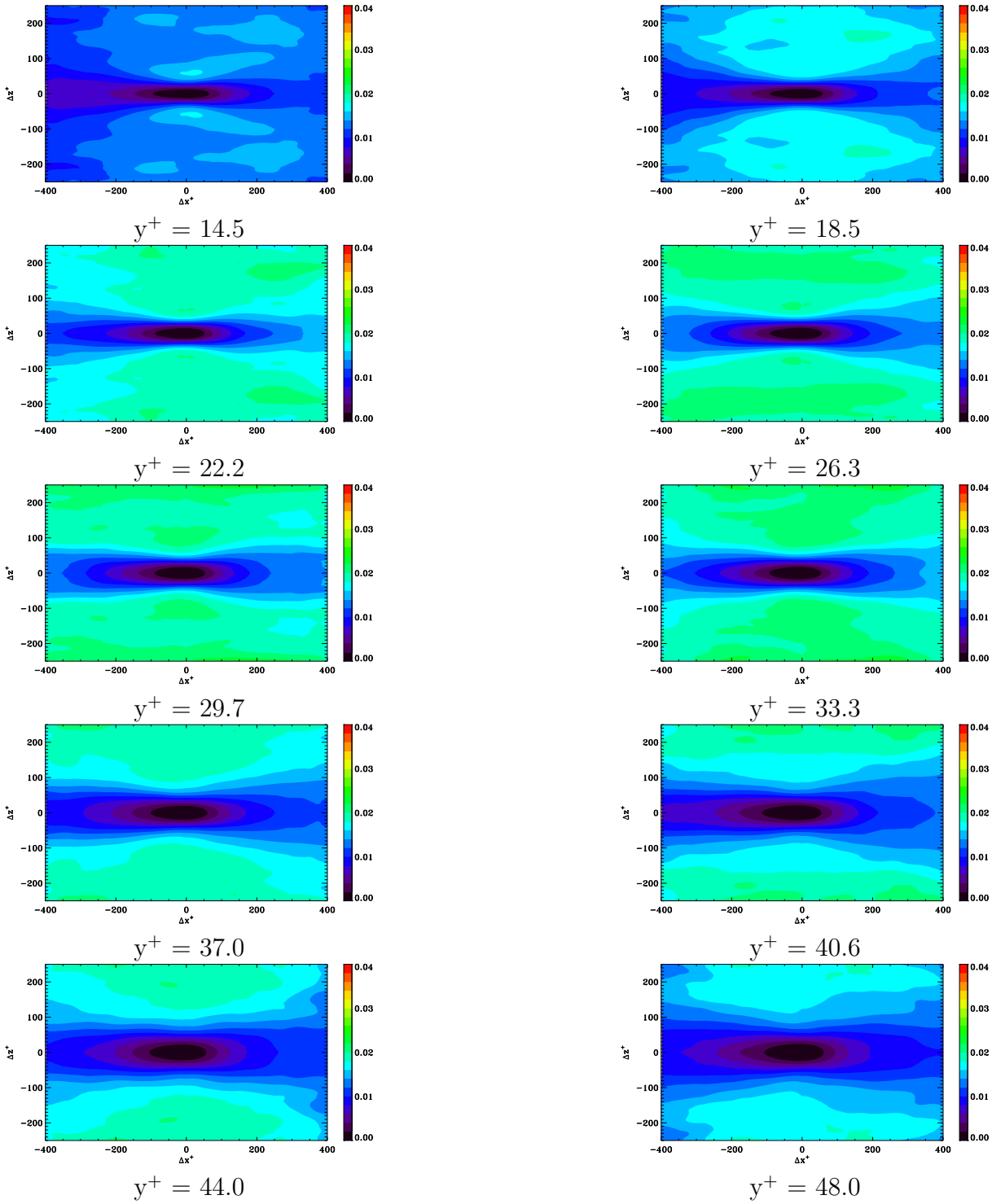

FIG. C.12 – Correlations of high speed streaks with ejections R_{HSS-EJ}

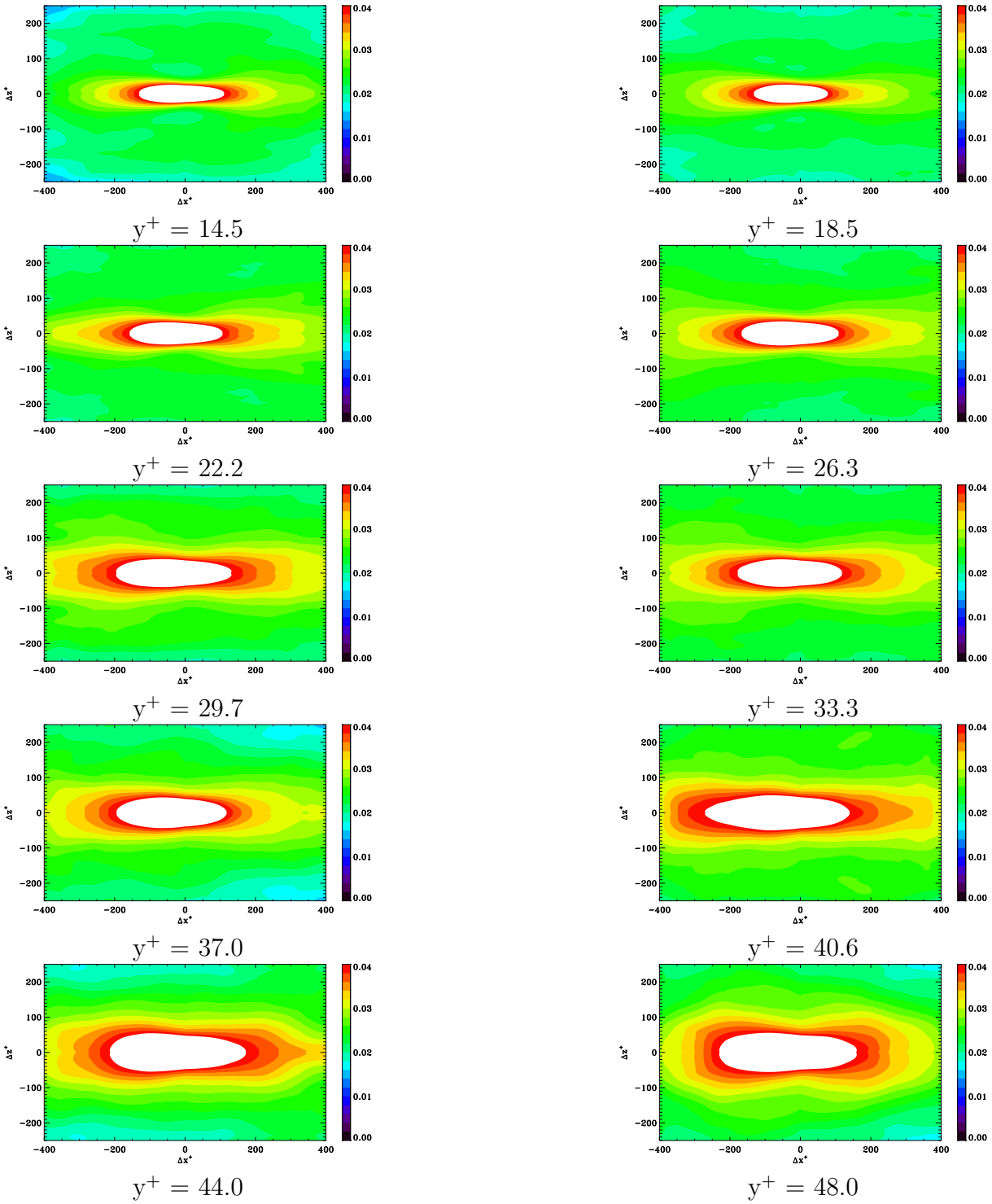

FIG. C.13 – Correlations of high speed streaks with sweeps R_{HSS-SW}

C.6 Streaks with NGSV and PGSV

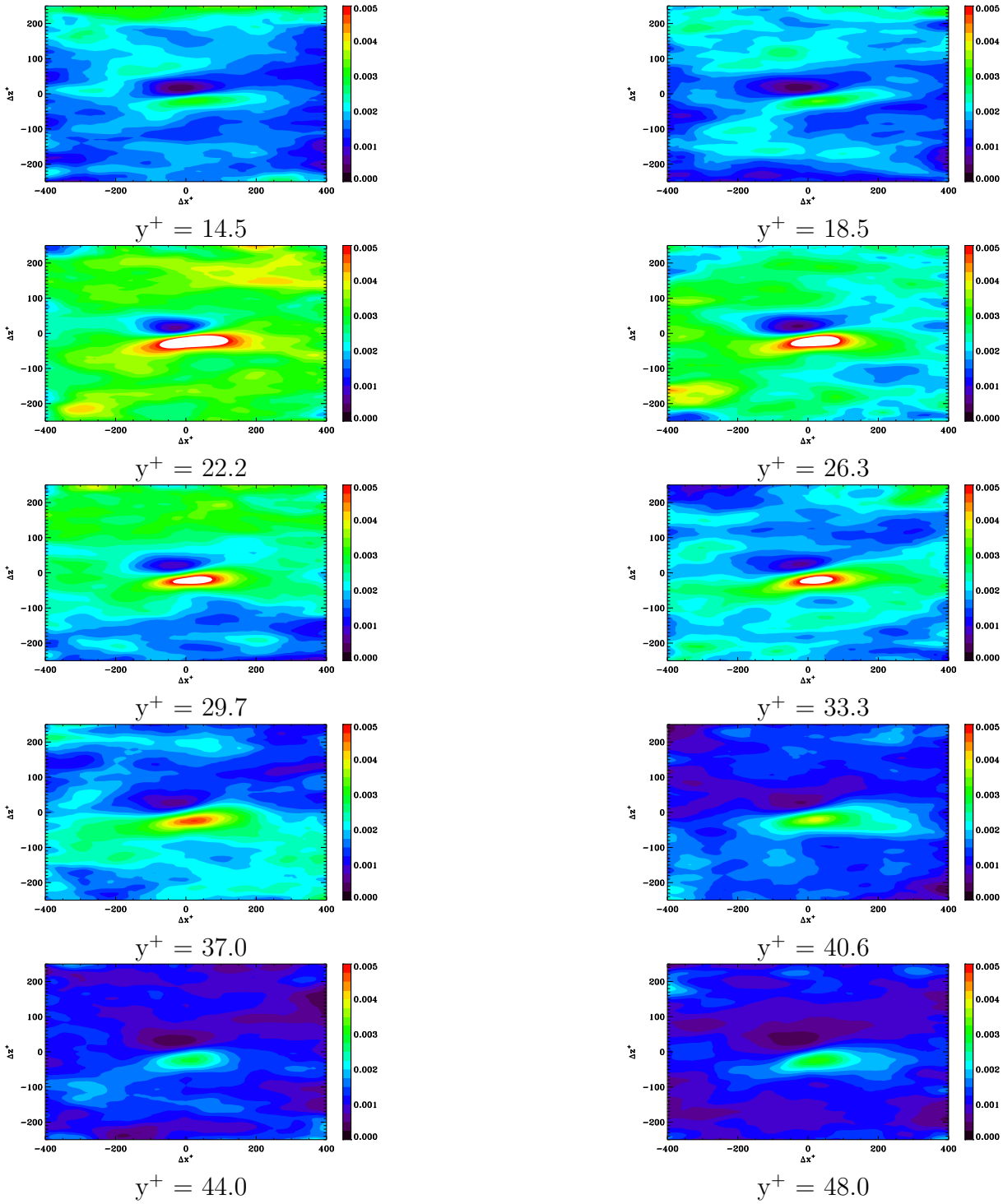

FIG. C.14 – Correlations of low speed streaks with NGSV $R_{LSS-NGSV}$

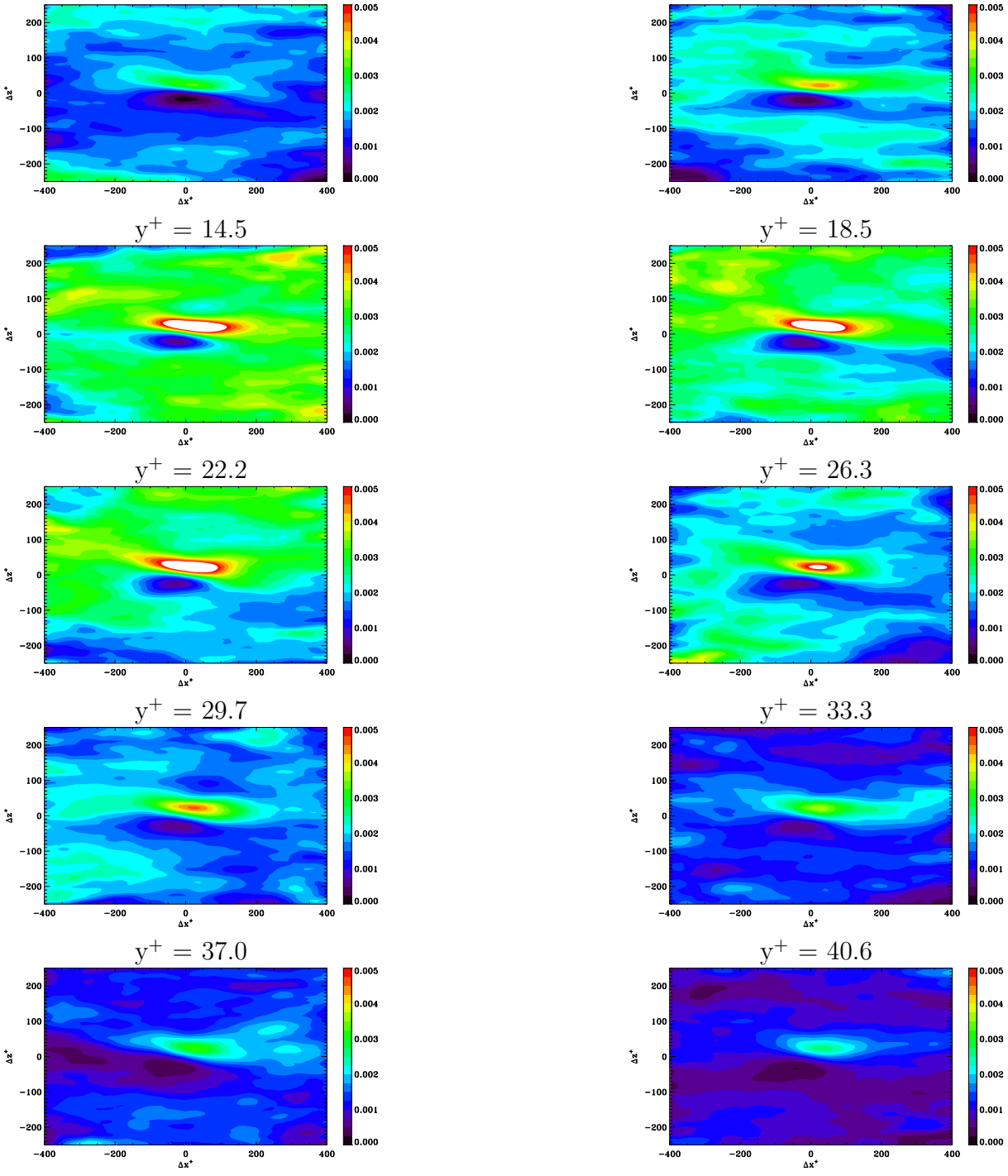

FIG. C.15 – Correlations of low speed streaks with PGSV $R_{LSS-PGSV}$

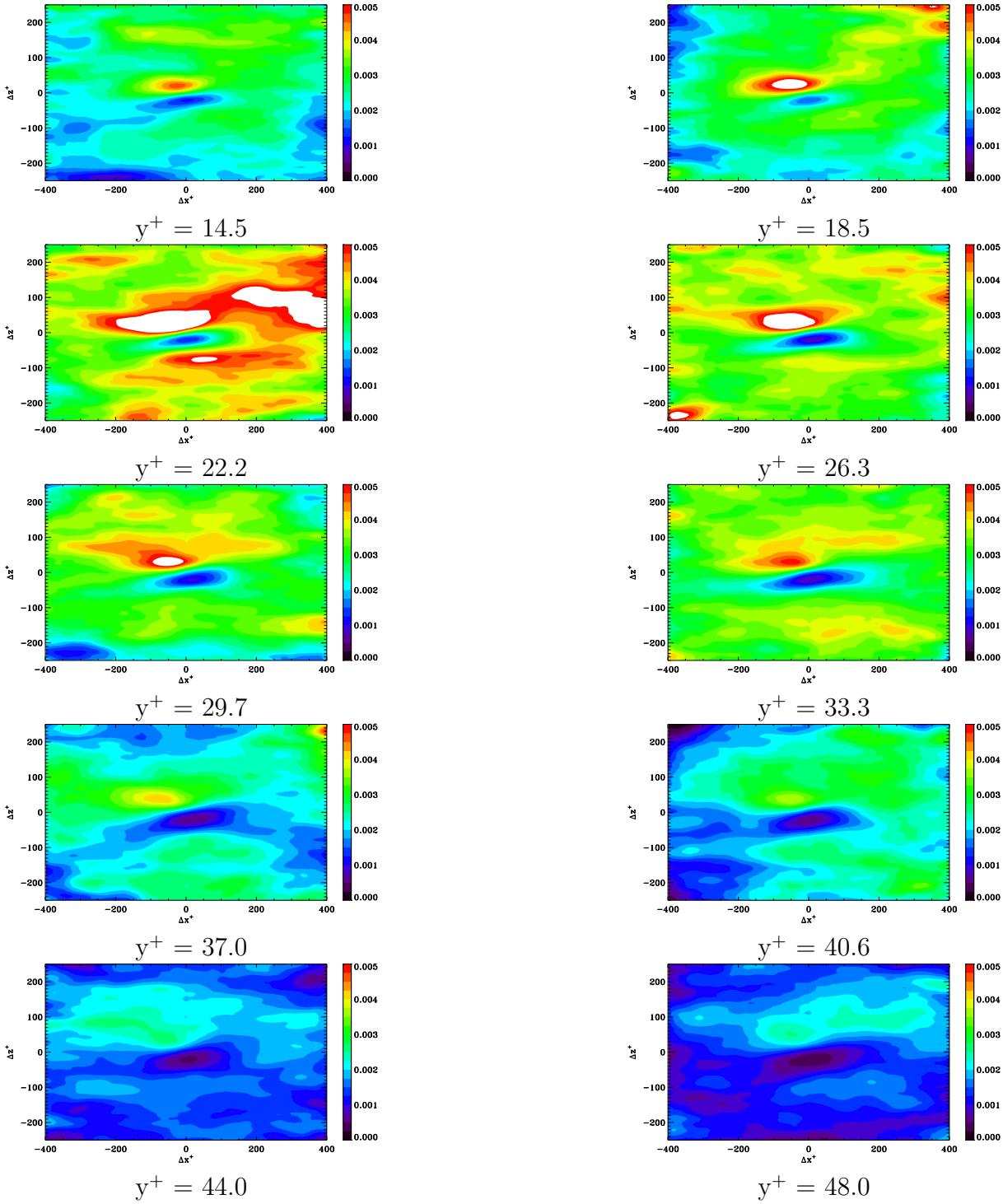

FIG. C.16 – Correlations of high speed streaks with NGSV $R_{HSS-NGSV}$

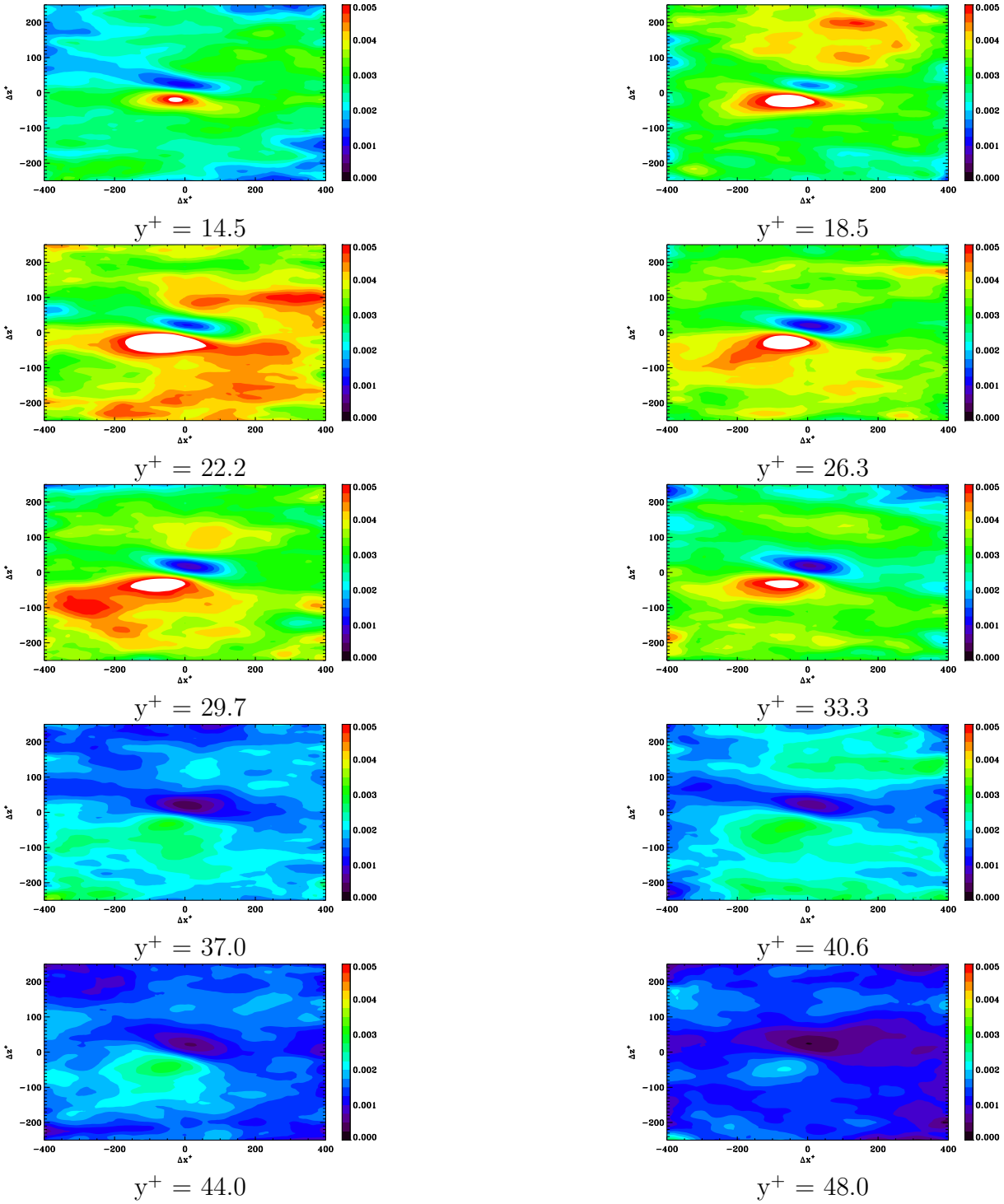

FIG. C.17 – Correlations of high speed streaks with PGSV $R_{HSS-PGSV}$

C.7 Ejections and sweeps with NGSV and PGSV

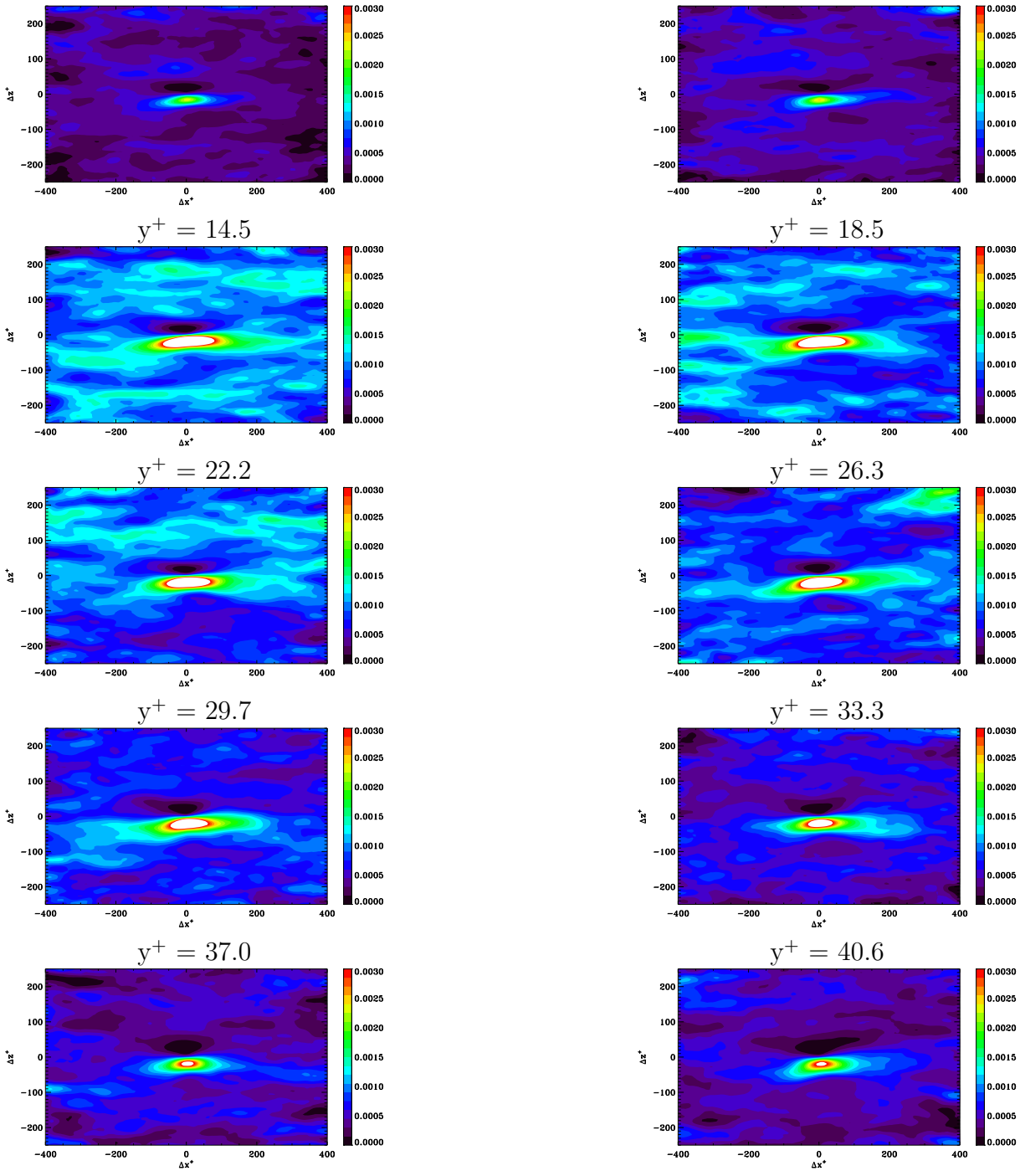

FIG. C.18 – Correlations of ejections with NGSV $R_{EJ-NGSV}$

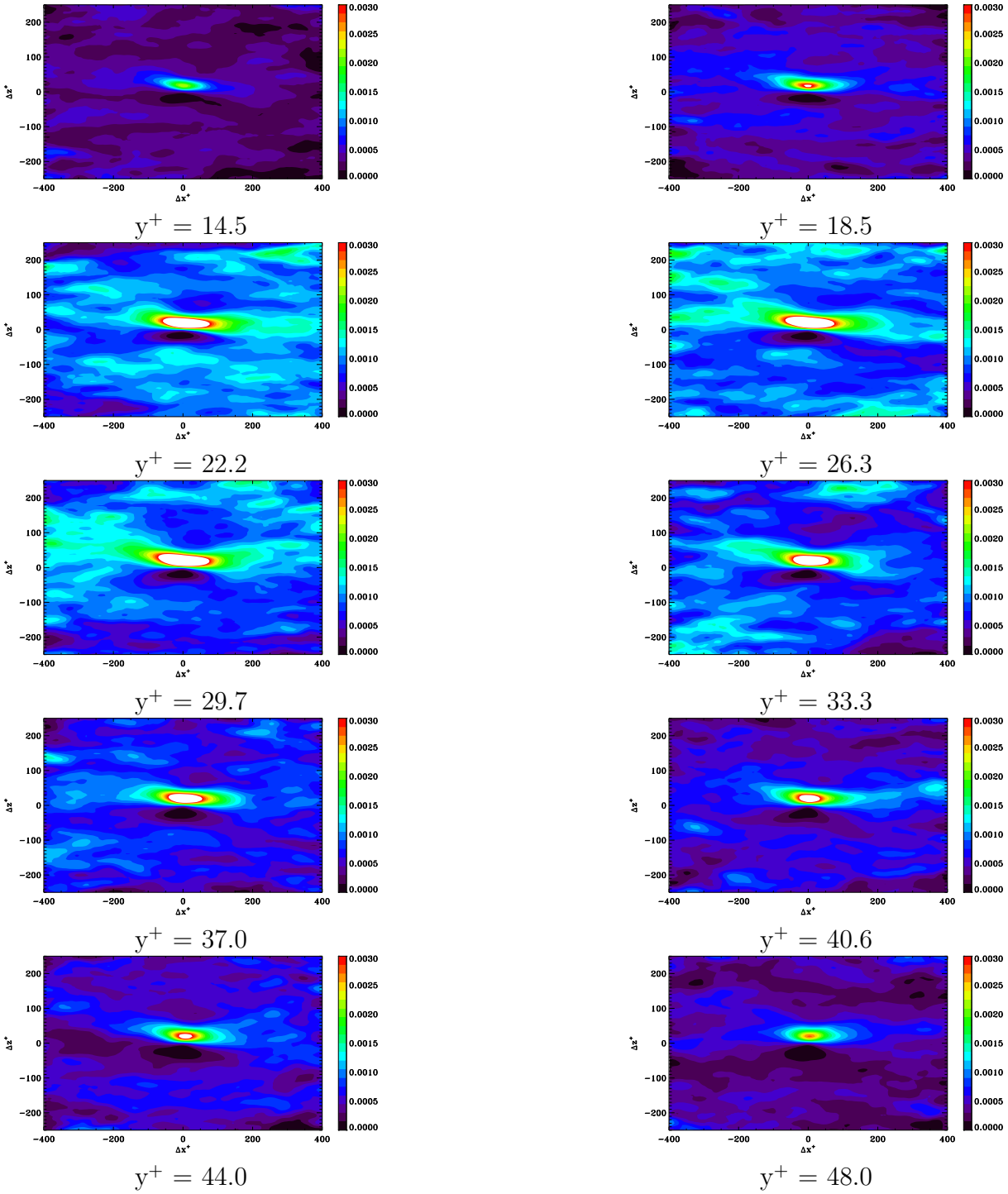

FIG. C.19 – Correlations of ejections with PGSV $R_{EJ-PGSV}$

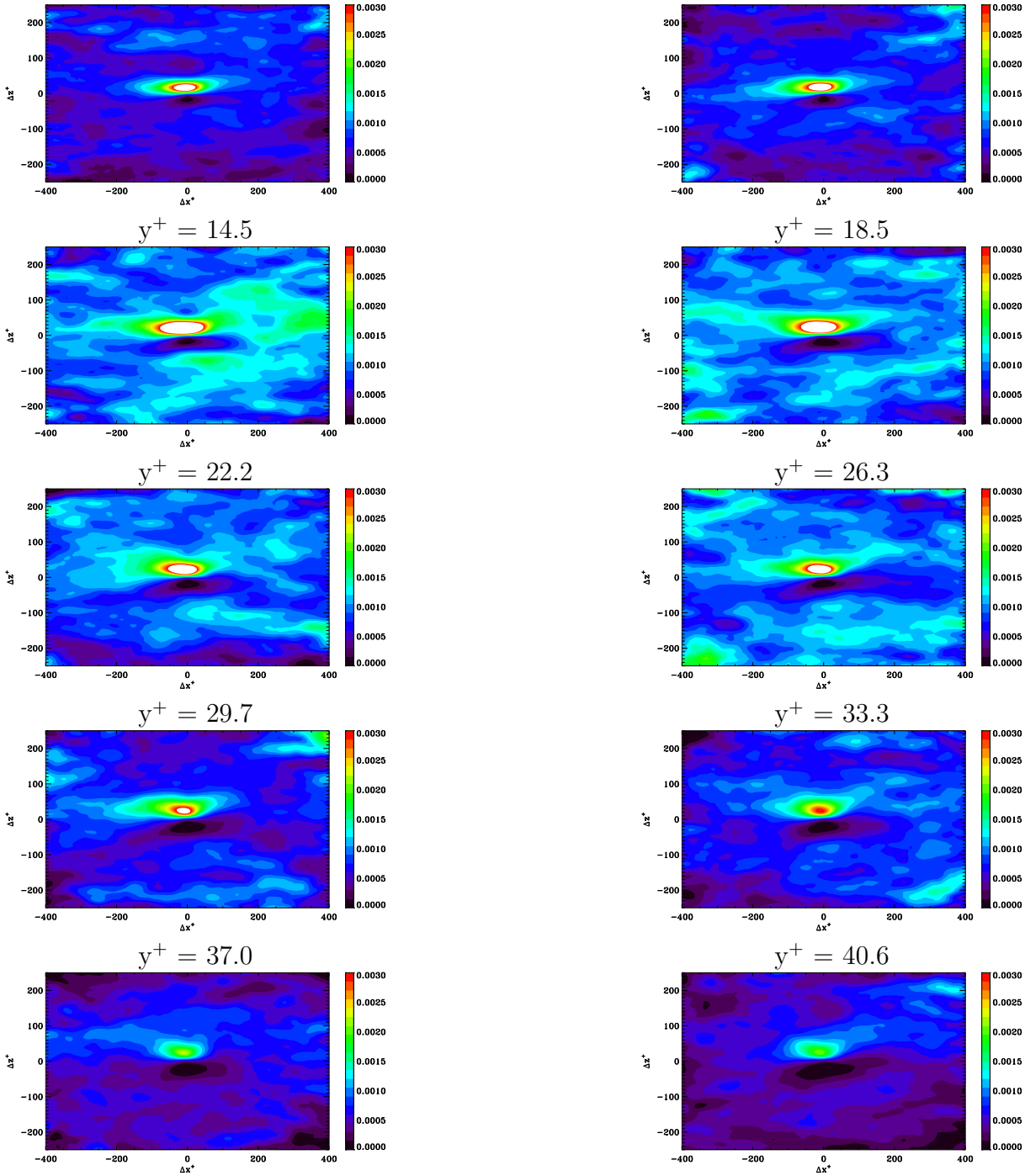

FIG. C.20 – Correlations of sweeps with NGSV $R_{SW-NGSV}$

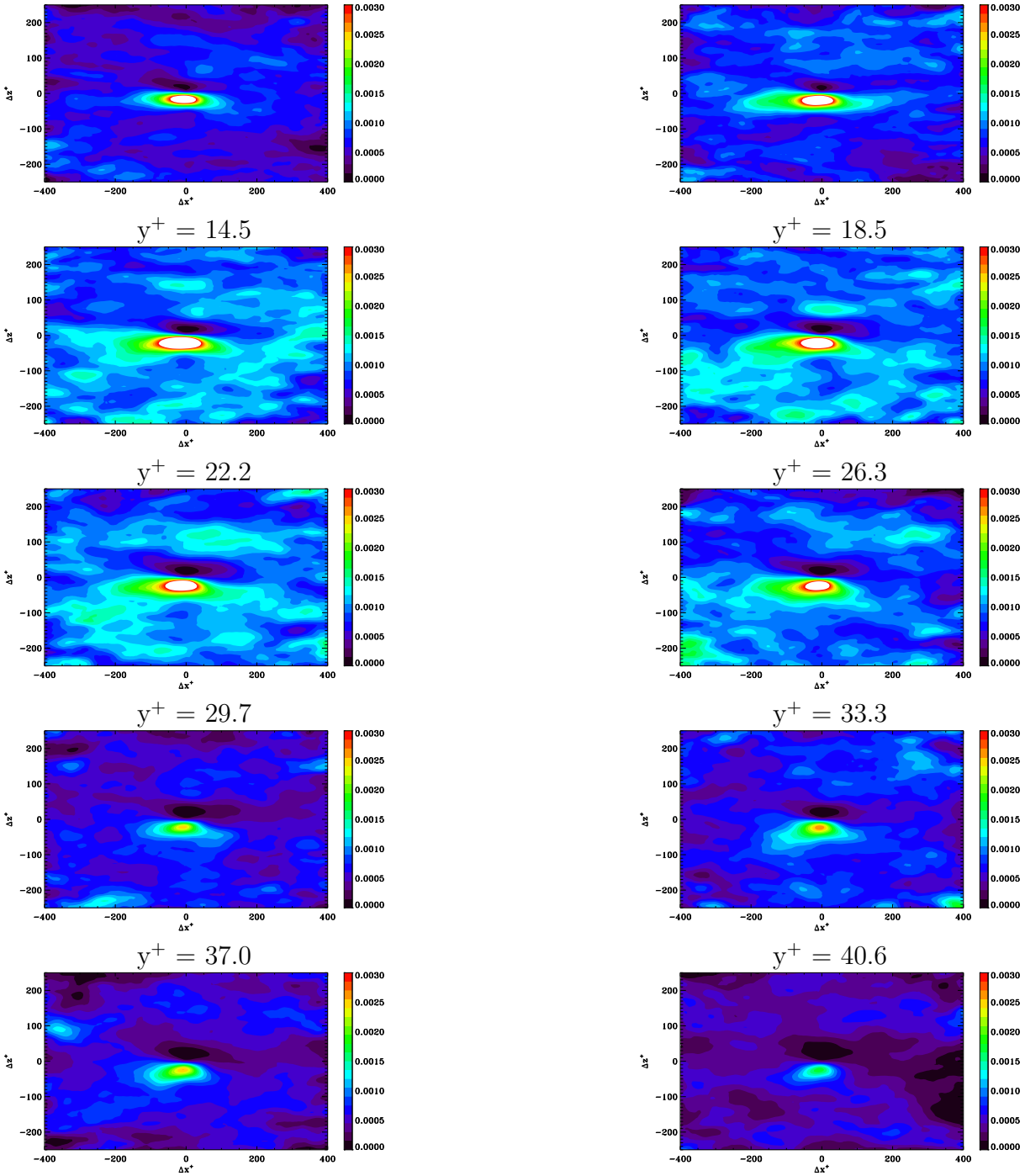

FIG. C.21 – Correlations of sweeps with PGSV $R_{SW-PGSV}$